ZAŠTITA MATERIJALA

Godina LXVII Beograd, 2026. Broj 1

Editor in Chief

Prof. dr **Časlav Lačnjevac**, University of Belgrade, Faculty of Agriculture, Belgrade, Serbia

Co - editors

Dr **Nebojša Nikolić**, University of Belgrade, Serbia

Dr **Vladimir Panić**, University of Belgrade, Serbia

Prof. dr **Abd El-Aziz S. Fouda,** El-Mansoura University, Egypt

Prof.dr **Branimir Grgur**, University of Belgrade, Serbia

Prof.dr **Susai Rajendran**, Department of Chemistry, Thamaraipady, India

Prof. dr **Iveta Vaskova**, Technikal University of Kosice, Slovakia

Prof.dr.habil. **Marian Jaskula**, Jagiellonian University, Poland

Prof.dr **Leonid Dvorkin**, National University of Water and Environmental Engineering, Ukraine

Prof. dr **Vaso Manojlović,** University of Belgrade, TMF, Belgrade, Serbia

Dr **Marija Ercegović,** Institute ITMNS, Serbia

Prof. dr. **Srećko Stopić***,* Aachen University, Germany

Editorial Board

Prof.dr **Benedetto Bozzini**, Italy
Prof.dr **J. G. Gonzalez-Rodriguez,** México
Prof.dr **Heiner Jakob** Gores, Germany
Prof.dr **Tor Henning Hemmingsen**, Norway
Dr **Mirjana Stojanovic**, Serbia
Prof.dr **K. F. Khaled**, Egypt
Prof. dr **Miomir G. Pavlović**, Serbia
Prof. dr **Liudmila Tsygankova**, Russian Federation
Dr **Andrzej Kowal**, Poland
Prof.dr **Dragica Chamovska**, R.N.Macedonia
Prof. dr **Svetlana Kaluzhina,** Russian Federation
Prof.dr **Srdjan Roncevic**, Serbia
Prof.dr **Refik Zejnilović,** Montenegro
Dr **Ronald Latanision**, USA
Prof.dr **Miodrag Maksimović,** Serbia
Prof.dr **Vesna Mišković-Stanković**, Serbia
Dr **Dorothy Rajendran**, India
Prof.dr **Milan Jaić,** Serbia
Prof.dr **Kozeta Vaso,** Albania
Prof.dr **A. S. Sarac**, Turkey
Prof.dr **Milorad Tomić**, BiH
Prof.dr **Jelena Bajat,** Serbia
Dr **Aleksandra Daković,** Serbia
Prof. dr **Ladislav Vrsalović,** Croacia
Prof.dr **Darko Vuksanović,** Montenegro
Prof.dr **Deana Wahyuningrum**, Indonesia
Dr **Nebojsa Marinkovic**, USA
Dr **Slavko Bernik**, Slovenia
Prof.dr **Milica Gvozdenovic**, Serbia
Dr **Tsvetina Dobrovolska,** Bulgaria
Prof.dr **Oguike Raphael Shadai**, Nigeria
Dr **Miroslav Sokic**, Serbia
Prof.dr **Djendji Vaštag,** Serbia
Prof. dr **Maria Joany Rajendran**, India
Prof.dr **Regina Fuchs Godec,** Slovenia
Prof.dr **Aurel Nuro,** Albania
Dr **Muhammed Ernur Akıner**, Turkey
Dr **Branimir Jugovic,** Serbia
Dr **Petar Ljumovic,** Croacia
Prof.dr **Manjeet Singh Goyat**, India
Prof.dr **Aleksandar Kost**ic, Serbia
Prof.dr **Borko Matijević,** Serbia
Dr **Miroslav Pavlovic**, Serbia
Prof.dr **Blažo Laličić**, Serbia
Dr. **Agha Inya Ndukwe**, Nigeria

Izdavački savet – Publisher board

Dr **Sreco Pavlin**, predsednik, R. Slovenia
Mr **Ivan Burić,** Montenegro
Zoran Ivljanin, Serbia
Gordana Miljević, Serbia
Dr **Ilija Nasev**, R. S. Macedonia
Dr **Zoran Avramović**, Serbia
Momir Ilić, Serbia

Dosadašnji glavni i odgovorni urednici

Prof. dr **Sreten Mladenović** (1967–2001)
Prof.dr **Miodrag Maksimović** (2002 – 2005)
Prof.dr **Milan Antonijević** (2006-2012)
Technical editor:**Slavka Vukašinović**

Za izdavača – For publisher

Prof. dr **Časlav Lačnjevac**, predsednik

Izdavač- Publisher:

INŽENJERSKO DRUŠTVO ZA KOROZIJU, Beograd, Kneza Miloša 9/I,
Tel/fax (011) 3860 - 867 i (011) 3230–028,
E-mail:editor@idk.org.rs; idk@idk.org.rs, www.idk.org.rs, E-mail:caslav.lacnjevac@gmail.com

EVROPSKA FEDERACIJA ZA KOROZIJU (EFC) SMATRA OVAJ ČASOPIS ZVANIČNOM PUBLIKACIJOM ZA OBJAVLJIVANJE IZVEŠTAJA I INFORMACIJA

EUROPEAN FEDERATION OF CORROSION (EFC) CONSIDERES THIS JOURNAL TO BE THE OFFICIAL PUBLICATION FOR PUBLISHING THE REPORTS AND INFORMATION

SADRŽAJ – CONTENT

SidorelaVishkulli, Ervin Suli, Spiro Drushku

Optimization of dyeing process of wool with extract of saffron petals using response surface methodology **5**

Ubanozie Julian Obibuike, Stanley Toochukwu Ekwueme, Nnaemeka Princewill Ohia,
Frank Chinedu Ukaeru, Ifeanyi Michael Onyejekwe, Mathew Chidubem Udechukwu

Modelling and optimisation of geothermal binary ORC systems using response surface methodology and artificial neural networks **14**

Ganesan Sundara Moorthy, Palaniappan Meyyappan

Study on the effectiveness of SAP, PEG-400, and PVA as self-curing agents: A comparative approach **36**

SivakumarDurairaj, Shankar Durairaj

Advancements and challenges in self-healing coatings for sustainable smart materials n industry applications **46**

Dinesh Kumar Vairavel, Sivasubramanian Mahadevan, Armstrong Michael,
Sivakumar Durairaj, Selvapalam Narayanan

Investigating the hydrophobic properties and corrosion resistance of copper surfaces via octadecanoic acid chemical deposition technique **62**

Pedro Henrique Poubel Mendonça Da Silveira, Jheison Lopes Dos Santos,
Alaelson Vieira Gomes, Andmarcelo Henrique Prado Da Silva

Study of crystallite size and lattice strain by Williamson-Hall analysis in sintered Al_2O_3 - Fe_2O_3 ceramics **76**

Ansam Ali Hashim

Development of a novel cementitious blend derived fromcalcined pozzolanic materials and nanoparticles of self-compacting high-performance concrete **85**

Mary Pramila Santhi, Susai Rajendran

Corrosion management in petroleum Industry **100**

Chandra Kant Bhardwaj, Sana Rafi, Abhilasha Mishra, Nouman

Synthesis, characterization, chromatographic and antimicrobial studies of transition metal complexes of cobalt(II) and iron(III) **112**

Jelena Lađarević, Bojan Božić, Dušan Mijin, Luka Matović, Nataša Valentić,
Evica Ivanović, Nebojša Banjac

Study of tautomerism and solvatochromism of 5-(substituted phenylazo)-3-cyano-6-hydroxy-4-methyl-2-pyridones **119**

Farzet Bikić, Dejana Kasapović

Investigation of pitting corrosion in austenitic stainless steels AISI304L and AISI317L: With particular emphasis on the role of molybdenum **133**

Nnaemeka Uwaezuoke, Emmanuel Ojecho, Onyebuchi Ivan Nwanwe,
Stanley Ibuchi Onwukwe

Batch adsorption using *C. aurantiifolia* peel as bio-adsorbent for the treatment of heavy metals in produced water from petroleum production **139**

Azuka N. Amitaye, Elias E. Elemike, Terngu T. Uzah

Valorization of african giant land snail shell waste (*Archachatinamarginata)* by extraction of chitosan from it ... 149

Ahlem Chahinez Kadri, M’hamed Ouadah, Abderrahmane Younes, Sofiane Chabane

Assessing the impact of AC, DC and hybrid AC/DC stray currents on cathodic protection efficiency ... 159

Abdelmadjid Atassi, Mounir Djellab, Hamza Bentrah, Abdelouahad Chala, Mohamed Cherif Ben Ameur, Slimane Kherief, Ridha Azzouz, Amir Eddine Kabouia, Bouzid Bouamra

Corrosion inhibitionefficiency of the Myrrh Gum on API 5CTP110 tubing in hydrochloric acid ... 171

Valentina Loganina, Vadim Pylaev, Roman Fediuk, Bassam A. Tayeh, Sergey Klyuev, Alexander Klyuev, Svetlana Shambina, German Fediuk

Lime compositions with polysaccharides for building walls restoration ad protection ... 181

Vladimir D. Jović

Adsorption of iodide anions onto Ag(111) ... 191

Instructions for manuscript preparation ... 199

SUIZDAVAČI

INSTITUT ZA TEHNOLOGJU NUKLEARNIH I DRIGIH MINERALNIH SIROVINA, BEOGRAD
UDRUŽENJE INŽENJERA SRBIJE ZA KOROZIJU I ZAŠTITU MATERIJALA
CRNOGORSKO DRUŠTVO ZA ZAŠTITU MATERIJALA

DONATORI

JP ELEKTROMREŽA SRBIJE, BEOGRAD
JKP DRUGI-OKTOBAR, VRŠAC
"NIS - FAM", KRUŠEVAC
GALFOS, BEOGRAD
PD DRINSKO LIMSKE ELEKTRANE, BAJINA BAŠTA
INSTITUT ZA PREVENTIVU, NOVI SAD
MAŠINSKI FAKULTET, BEOGRAD
TEHNOLOŠKO-METALURŠKI FAKULTET, BEOGRAD
TEHNIČKI FAKULTET, BOR
TEHNOLOŠKI FAKULTET, LESKOVAC
ALFA PLAM ad, VRANJE
„HELIOS“, DOMŽALE
ŠUMARSKI FAKULTET, BEOGRAD
AGRONOMSKI FAKULTET, ČAČAK
GRAĐEVINSKO-ARHITEKTONSKI FAKULTET, NIŠ
TEHNOSAM, SUBOTICA
"PITURA", NOVI BEOGRAD
UNIPROMET, ČAČAK
FAKULTET ZAŠTITE NA RADU, NIŠ
INSTITUT ZA VODOPRIVREDU „JAROSLAV ČERNI“, BEOGRAD
„GALVA“, KRAGUJEVAC
PERIĆ & PERIĆ, POŽAREVAC
HORIZONT PRES, BEOGRAD
VISOKA TEHNOLOŠKA ŠKOLA STRUKOVNIH STUDIJA, NOVI BEOGRAD
VISOKA STRUKOVNA ŠKOLA, NIŠ
VISOKA TEH. SKOLA STRUK. STUDIJA, NOVI SAD
INSTITUT ZA PUTEVE, BEOGRAD
IMPOL SEVAL, UŽICE
ALFATERM, ČAČAK
METALAC A.D., GORNJI MILANOVAC
SINVOZ DOO, ZRENJANIN

U finansiranju izdavanja časopisa "ZAŠTITA MATERIJALA" učestvuju:

MINISTARSTVO NAUKE, TEHNOLOŠKOG RAZVOJA I INOVACIJA REPUBLIKE SRBIJE

INŽENJERSKA KOMORA SRBIJE

CIP - Katalogizacija u publikaciji
Narodna biblioteka Srbije, Beograd

620.1
ZAŠTITA MATERIJALA = Materials Protection / Glavni urednik .Časlav Lačnjevac),
[Štampano izd.]. - God. 1, br. 1 (1953)-god. 22, br. 3/4 (1974) ; god. 23, br. 1 (1982)-. - Beograd:
Inženjersko društvo za koroziju, 1953-1974; 1982- (Zemun : Akademska izdanja). - 29 cm

Dostupno i na: https://www.zastita-materijala.org - Tromesečno. - Drugo izdanje na drugom medijumu:
Zaštita materijala (Online) = ISSN 2466-2585
ISSN 0351-9465 = Zaštita materijala
COBISS.SR-ID 4506626

Redakcija: Beograd, Kneza Miloša 9/I, Tel/fax (011) 3860 - 867, i (011) 3230 - 028,E-mail: idk@idk.org.rs;
E-mail:editor@idk.org.rs, www.idk.org.rs; www.zastita-materijala.org/index.php/home/issuse

Tekući račun: 205 - 24967 – 71, Komercijalna banka, Beograd; Časopis izlazi četiri puta godišnje
Rukopisi se ne vraćaju; Štampa: Akademska izdanja, Zemun

SidorelaVishkulli[1], Ervin Suli[2], Spiro Drushku[1]*

[1]*Department of Industrial Chemistry, Faculty of Natural Sciences, University of Tirana, Tirana, Albania*
[2]*Department of Information Technology and Communication, Professional College of Tirana, Tirana, Albania*

Scientificpaper
ISSN 0351-9465, E-ISSN 2466-2585
https://doi.org/10.62638/ZasMat1311

Zastita Materijala 67 (1)
5 - 13 (2026)

Optimization of dyeing process of wool with extract of saffron petals using response surface methodology

ABSTRACT

Recently the awareness of the demand on eco-friendly dyes in textile applications is increased, since the natural dyes can reveal better biodegradability and generally have a higher compatibility with the environment. There are ongoing attempts to overcome some disadvantages related to natural dyeing such as prolonged dyeing time, consumption of energy, and chemicals used. In this point of view, the optimization of process parameters is a good alternative. In this work, the dyeing of wool fibers with extract of saffron petals is presented. The response surface methodology is used to optimize the process parameters and to investigate the relationship between different factors taken into consideration, such as dyeing time, dye concentration, mordant amount, dyeing temperature and pH. The dye uptake was evaluated by absorbance measurements, using UV-Vis spectrophotometer and was used as response. The optimal dyeing conditions for obtaining the highest dye uptake value were as follows: dyeing time 69.89 minutes, dye concentration 3.7%, mordant amount 1.02g (0.56%) , dyebath pH 2.08, dyeing temperature 110°C.

Keywords: *natural dye, optimization, RSM, saffron extract, wool*

1. INTRODUCTION

Synthetic dyes are commonly used for the coloration of textiles because of wide variety of colors available with good fastness properties at a low cost and easy applications [1,2]. However, the synthetic dyes present in dyeing wastewater discharged into the environment cause health risks, and toxic and allergic reactions [3-5] to humans as well as threaten the ecosystems [1,2]. Global concern for environmental pollution has put rigorous rules forward for high level pollutant industries [6]. Textile industry with huge amount of hazardous wastewater production is one of such industries [7-9]. Germany has completely banned azo dyes [2]. The use of non-toxic, antimicrobial and eco-friendly natural dyes on textiles, and preferably natural fiber products, has become a matter of increasing importance due to the increased awareness of environmental impact caused by synthetic ones [7].

Natural dyes are known as sustainable and environmentally friendly materials for dyeing and functional finishing of textiles [3]. They can be obtained from vegetable, animal or mineral origin [1-8]. They are non-carcinogenic, biodegradable [4] and biocompatible with the environment [5,6,8-12]. Due to this fact they are in high demand nowadays.

Saffron is a perennial plant which belongs to the genius *Crocus Sativus.* It is cultivated in warm climate countries like Italy, Iran, Spain, Greece, Turkey, Morocco, etc. [13-17]. Recently, it is cultivated also in Albania, in Elbasan region. After harvesting stigma, the petals produced in huge amount remain as a waste and are reused as a source of natural colorant.

Wool is the fibre from the fleece of the sheep. It is a natural protein with multiple cellular structure. The wool fibre is a crimped, fine to thick, regular fibre [11]. Wool primarily consists of keratin, which consists of long chains of amino acids linked together by peptide bonds. Within the keratin structure, various types of chemical bonds and intermolecular forces play a role in determining the properties of wool. These include disulfide bonds, ionic bonds, hydrogen bonds, and van der Waals forces. The combination of these bonding forces and interactions results in a three-dimensional

---

*Corresponding author: Sidorela Vishkulli
E-mail: sidorela.vishkulli@fshn.edu.al

Paper received: 07.12.2024.
Paper corrected: 12. 06. 2025.
Paper accepted: 19.06.2025

network of intertwined keratin chains, forming the complex and unique structure of wool. This advanced structure provides wool with its desirable properties, such as elasticity, resilience, moisture absorption, insulation, and durability. Wool is recognized as a high-quality and mid-to-high-end fabric.

Natural dyes exhibit a high affinity for natural fibers, particularly for protein-based fibers [12]. However, there exist some disadvantages such as low color yield, prolonged time to dye, consumption of energy, dye, mordant and auxiliaries. Because of these disadvantages there is a need for optimization of natural dyeing [3]. Optimization of dyeing is definitely the substantial method to determine the optimum condition in order to get highest dyeing uptake exhaustion [14]. In the traditional method, one variable is examined at a time while the other is maintained constant. This method is time consuming and requires too much work [3]. Furthermore, this method may provide inaccurate outcomes, such as the belief that interaction effects cannot be observed, making it difficult to ascertain process parameters performance [13]. Response surface methodology is one of a perfect method to simulate the variables simultaneously. It has been widely used in process and product improvement because it can optimize the complex process and minimize the experimental number of trials [14]. The central composite design is widely used experimental design method due to the selection of appropriate pivot points and the retention of the rotatability and sequentiality of the experimental data, which greatly improves its prediction accuracy [15].

In this study, the dyeing conditions of wool fiber were optimized by response surface methodology. Extract of saffron petals is used as a natural dye source for coloration of wool fibers. Five independent factors including dye concentration, mordant amount, temperature, dyeing time and pH were selected as the most influencing factors according to preliminary experiments. The effect of these factors was examined on the dye uptake of the wool fibers. The optimum conditions were determined to achieve the maximum dye uptake percentage during the dyeing process.

2. MATERIALS AND METHODS

2.1. Wool fabrics:

The wool fabrics were sized in 4x10cm and prepared to be dyed with the pre-mordanting method using alum mordant. The method of mordanting and the alum mordant were determined by our previous experiments during the project.

2.2. Dye extraction:

Saffron petals were obtained from Victus Fed company. They were dried and prepared for extraction. The dye was extracted with traditional boiling method. The mixture was allowed to cool down and filtered to remove the petals. The extracted solution was kept in the dark box and further used in the dyeing process.

2.3. Dyeing process:

The dyeing experiments were performed according to the runs determined by RSM method. The proteinic fiber was dyed with saffron extracts with pre-mordanting method with liquor ratio of 1:45, while the other parameters were ranged as is showed in table 1. At the end, the absorbance of the extract remained in the dyeing bath was measured. The initial absorbance before the dyeing process was measured and the percentage of the dye uptake was calculated as the following equation:

$$E = \left(\frac{A_0 - A_f}{A_0}\right) x\, 100 \qquad (1)$$

Where: A_0 is the absorbance of the dyeing solution before the dyeing process

A_f is the absorbance of the dyeing solution after the dyeing process

2.4. Absorbance measurements:

The absorbance measurements were recorded by using UV-Vis spectrophotometer by using quartz cells at a maximum wavelength of 265nm, which was previously determined in our experiments.

2.5. Experimental design:

In this study the response surface methodology was applied to optimize the process variables. Prior designing the experimental runs, preliminary studies were done to determine the range for each parameter. Minitab18 statistical software was used for the design of experiments and statistical analysis of the process. The experimental ranges of factors are shown in table 1. A total number of 32 experiments were proposed by the software. Analysis of variance (ANOVA) was employed to select or to reject the model terms with a P-value with 95% confidence level. Dye uptake percentage was used as response. The experimental data were analyzed and fitted to the second-order polynomial model, including linear, quadratic and interaction. The following equation of the non-linear multiple regression quadratic model was used:

$$Y = b_0 + \sum_{j=1}^{5} b_j x_j + \sum_{i<j} b_{ij} x_i x_j + \sum_{j=1}^{5} b_{jj} x_j^2 \qquad (2)$$

Where: y is the response factor, b_0 is the constant term, b_j is the linear term, b_{ij} is the coefficient of interaction, b_{jj} is the quadratic coefficient.

Table 1. Independent variables and their levels used for response surface study

Factors	Unit	Levels				
		-2	-1	0	+1	+2
(x1) dyeing time	Minute	40	50	60	70	80
(x2) dye concentration	g/L	0.2	1.9	3.6	5.3	7
(x3) mordant amount	g	0	0.4	0.8	1.2	1.6
(x4) dyeing temperature	^{o}C	90	95	100	105	110
(x5) pH	pH	1.5	1.8	2.1	1.8	2.7

2.6. Fastness properties assessment on the dyed wool fabric

Color fastness is used to determine the degree to which dye holds fast to the fiber. A good or high fastness means that they do not bleed in washings and perspiration processes. The color fastness to washing test and acid and alkaline perspiration test were performed and evaluated according to ISO standards respectively ISO 105-C10:2006, ISO 105-E04, ISO 105-A02, ISO 105-A03.

Color fastness to washing: A specimen of the textile in contact with two specified adjacent fabrics is mechanically agitated under specified conditions of time and temperature in a soap solution, then rinsed and dried. The change in color of the dyed cotton specimen and the staining of the adjacent fabrics are assessed with reference to the original fabric with grey scale, ISO 105- C10:2006.

Color fastness to perspiration: Specimens of the textile in the contact with adjacent fabrics are treated in two different solutions, acidic and alkaline solution containing histidine, drained and placed between two plates under a specified pressure in a test device. The change in color of each specimen and the staining of the adjacent fabrics are assessed by comparison with grey scale ISO 105-E04.

3. RESULTS AND DISCUSSIONS

3.1. Model fitting and ANOVA results

In order to check the model adequacy, the experimental data were fitted to various models. According to the values of P and adjusted R – squared we can conclude that the dyeing process of wool fibers with saffron petals extract was most suitably described by a quadratic model. The analysis of variance was used for measuring up the significance of the effect of the dyeing process variables and their interactions on the dye uptake as the response. The ANOVA results of the fitted quadratic model are shown in table 2. According to the probability value of the independent variables, the significant or insignificant factors were determined. A probability value less than 0.05 indicates that the effect of this independent variable is significant. In our case, the primary impact towards the rate of dyeing uptake are dyeing time (x1), dyeing temperature (x4) and mordant amount (x3) were emerged to be the most substantial factors. Followed by the second order effect of dyeing time (x1*x1), dye concentration (x2*x2), mordant amount (x3*x3), dyeing temperature (x4*x4) and pH value of the dyebath (x5*x5) and the two-way interactions between dyeing time and dyeing temperature (x1*x4), between dye concentration and pH value (x2*x5) and between mordant amount and dyeing temperature (x3*x4). Furthermore, the primary influence of dye concentration (x2) and pH of the dyebath (x5), the 2-way interaction between dyeing time and mordant amount (x1*x3) and between dye concentration and mordant amount (x2*x3) were found to be corresponding to the secondary effect on the dyeing uptake percentage. The obtained second-order polynomial equation from the regression analysis of the experimental data is shown below:

$$Y = -597 + 0.72\ x1 + 6.69\ x2 - 54.3\ x3 + 6.65x4 + 238.9\ x5 - 0.04102\ x1*x1 - 2.333\ x2*x2 - 32.38\ x\ x3*x3 - 0.0479\ x4*x4 - 61.57\ x5*x5 + 0.114\ x\ x1*x3 + 0.0446\ x1*x4 + 0.535\ x2*x3 + 4.786\ x2*x5 + + 1.000\ x3*x4 \tag{3}$$

The obtained empirical model was used in the optimization and prediction of the dyeing uptake percentage within the range of variable factors in this experimental work. The coefficient of determination was 0.982 and adjusted R2 was 0.97. These values imply that the fitted model is highly significant and can explain the relationship among variables and response.

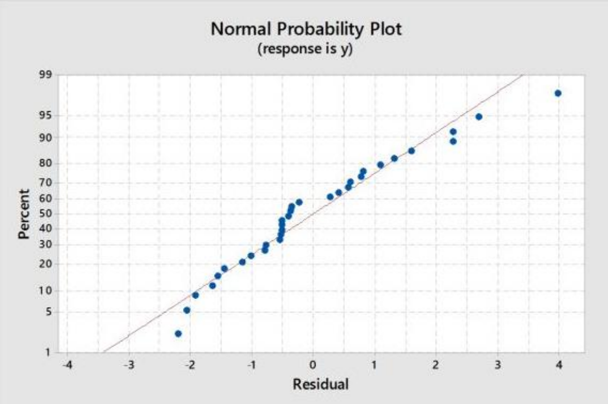

Figure 1. Normal plot of residuals

The fitted empirical model was examined by the normal plot of residuals. Residuals are the difference between actual and predicted values for each point and show how well the model satisfies the assumptions of the analysis of the variance. The normal probability plot of the residuals for the data tests the hypothesis that the residuals have a normal distribution. From figure 1 it is clear that the points were almost distributed in a line, which indicated that the model was satisfactory and accurate.

Table 2. ANOVA results of fitted quadratic model to the experimental data of wool dyeing process

Source	DF	Adj SS	Adj MS	F-value	P-value
Model	15	3608.14	240.54	58.11	0.000
Linear	5	519.77	103.95	25.11	0.000
x1	1	286.75	286.75	69.27	0.000
x2	1	9.57	9.57	2.31	0.148
x3	1	27.57	27.57	6.66	0.020
x4	1	183.15	183.15	44.24	0.000
x5	1	12.65	12.65	3.06	0.100
Square	5	2844.22	568.84	137.41	0.000
x1*x1	1	493.66	493.66	119.25	0.000
x2*x2	1	1333.33	1333.33	322.09	0.000
x3*x3	1	787.54	787.54	190.24	0.000
x4*x4	1	42.00	42.00	10.15	0.006
x5*x5	1	900.60	900.60	217.56	0.000
2-way interaction	5	244.44	48.89	11.81	0.000
x1*x3	1	3.31	3.31	0.80	0.384
x1*x4	1	79.64	79.64	19.24	0.000
x2*x3	1	2.12	2.12	0.51	0.485
x2*x5	1	95.31	95.31	23.02	0.000
x3*x4	1	64.06	64.06	15.48	0.001

The normal probability plot of the standardized effects is shown in figure 2. This graph was used to verify the statistically main and interaction effects that were included in the model. According to the normal probability plot, the points located closer to the fitted line are not considered as significant, whereas points located far away from the line tend to be more significant.

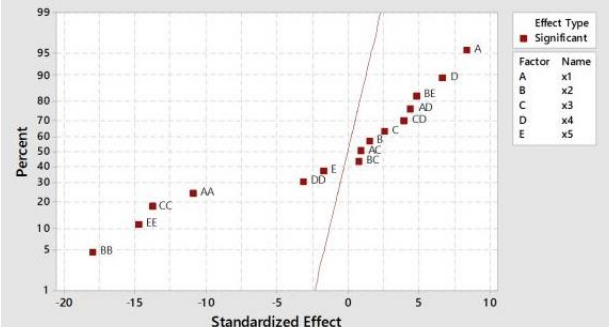

Figure 2. Normal probability plot of standardized effects

The main factors A, B, C and D on the right side have a positive effect on the adsorption efficiency, while the factor E lies in the left and has a negative effect. The time of dyeing (point A) has the largest effect since its point lies farthest from the line. The second important factor is the dyeing temperature (point D), which is more significant than amount of mordant, dye concentration and pH. The interaction and quadratic terms have significant effect on adsorption efficiency because they stay away from the line. Quadratic term of dye concentration has the most significant effect.

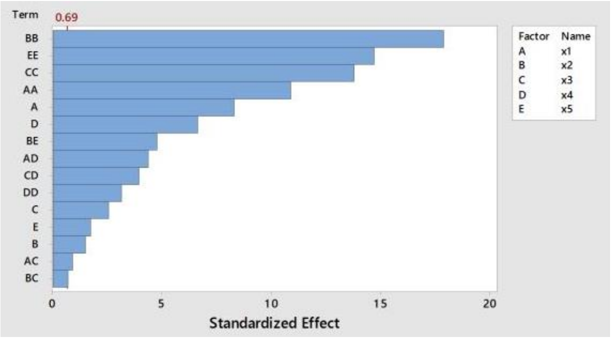

Figure 3. Pareto chart of the standardized effects of model variables

The Pareto chart of this experimental design is shown in figure 3. According to this chart the quadratic effect of dye concentration has the most significant effect on adsorption efficiency. The other quadratic effects EE, CC, AA, main terms A and D and 2-way interactions BE, AD, CD have greater effects on adsorption efficiency. Other factors C, E, B, AC and BC have significant effect and are statistically significant at 95% confidence level.

3.2 Three dimensional surface plots

The effect of process parameters on the dye uptake efficiency was further analyzed with the assistance of three dimensional plots. The plots were obtained by using Minitab18 software. In all response surface plots, three other variables which are not mentioned are in their midpoints. These plots are represented in figures 4, 5 and 6.

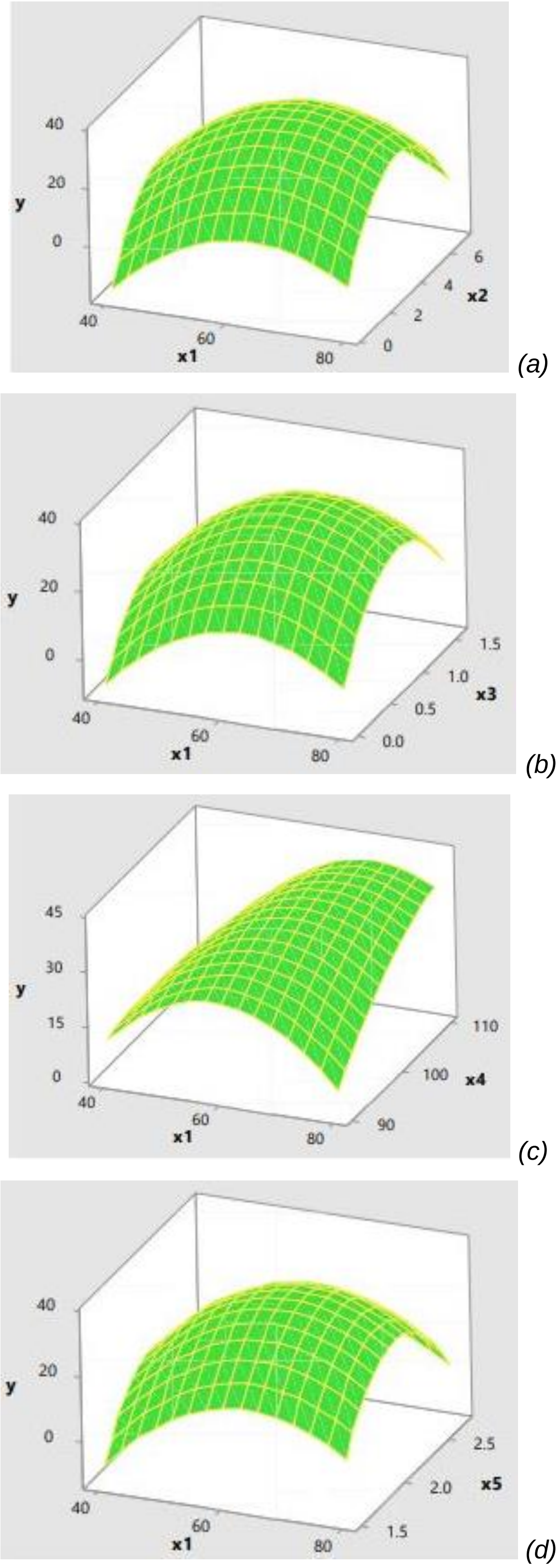

Figure 4. The 3D surface plots of the dye uptake for (a) dyeing time and dye concentration, (b) dyeing time and mordant amount, (c) dyeing time and dyeing temperature, (d) dyeing time and pH

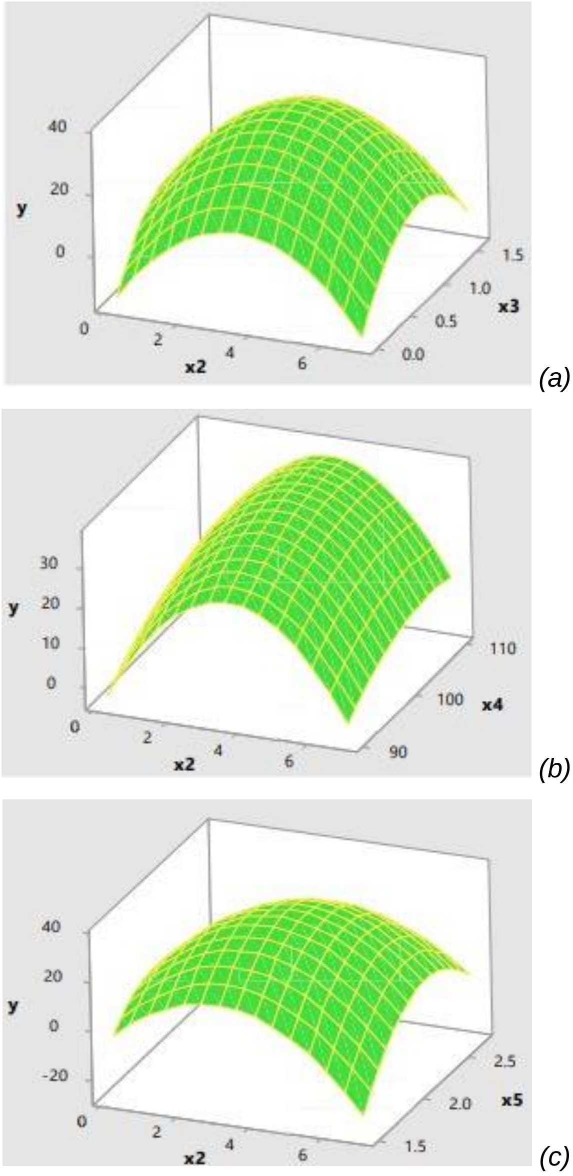

Figure 5. The 3D surface plots of the dye uptake for (a) dye concentration and mordant amount, (b) dye concentration and dyeing temperature, (c) dye concentration and pH

The effect of dyeing time, dye concentration, mordant amount, dyeing temperature and pH, illustrated in figures 4, 5 and 6, showed that the dye uptake percentage decreased when dyeing time, dye concentration, mordant amount and pH values increased and increases with increasing the dyeing temperature. The increase of the dyeing time from low values improves the dye uptake due to long contact time between the dye and the wool fiber, but prolonged dyeing time can cause to desorption or degradation of the natural colorant, resulting in lower dye uptake values. Increasing the initial dye concentration leads to an increase in mass gradient between the dye solution and the wool fiber.

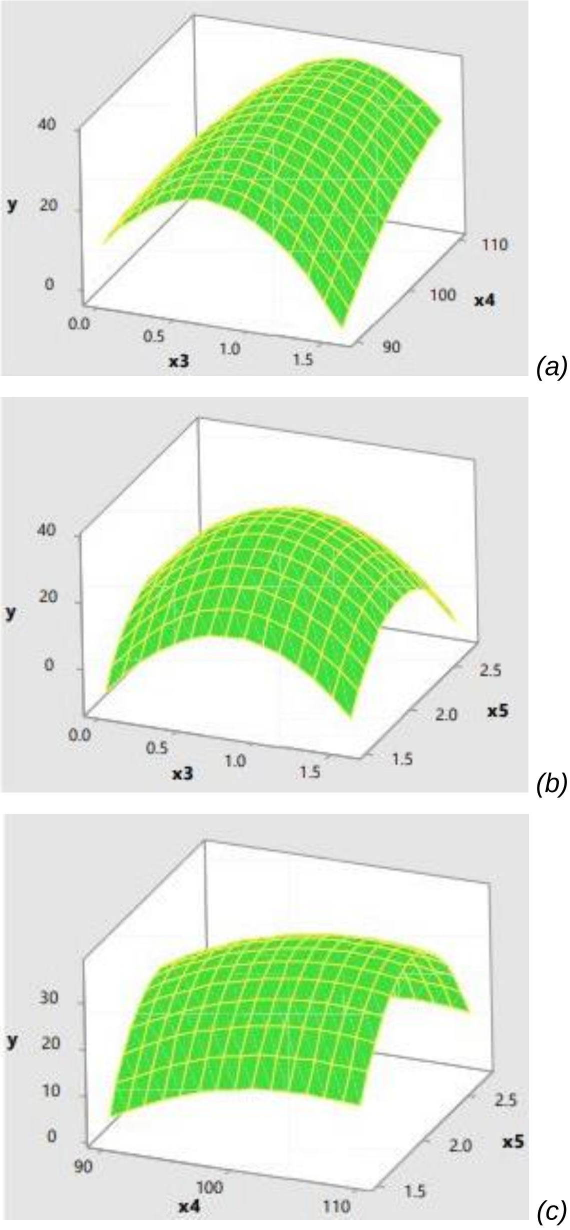

Figure 6. The 3D surface plots of the dye uptake for (a) mordant amount and dyeing temperature, (b) mordant amount and pH, (c) dyeing temperature and pH

This acts as a driving force leading to transfer of dye molecules from solution to fiber surface, but in high concentration values occurs the association of the dye molecules so they cannot penetrate into the fiber pores.

Mordanting increases the interaction between the functional groups of wool fibers (-COOH and –NH2) and the flavonoid and phenolic groups present in the saffron petals extract. Increasing the amount of mordant leads to a higher dye uptake until all the active sites present in the fiber are filled. Higher amounts of mordant can cause the agglomeration of dye molecules around the mordant molecules present in the dye bath. Increasing the pH beyond acidic values causes the neutralization of the functional groups of wool fiber and forming of unstable structures for the dyeing fixation. Thus acidic values are suitable for wool dyeing. Increasing the dyeing temperatures leads to increase in the dye uptake due to the intensification of molecular movement. This intensification leads to more hits with the fiber surface and successful fixation of the dye molecules. The 3 dimensional graphs show the simultaneous effects of parameters on the response in which the highest points of the curved surface plots indicate the values of factors resulting in maximum dye uptake. These graphs are useful for establishing response values and operating conditions that are needed. We can conclude that the dye uptake was higher near the optimum conditions (mentioned below) of the dyeing process.

3.3 Optimization of dyeing conditions

In our case the optimization of process parameters by using CCD method was done to maximize the response with desirability values of d=1.000 in order to obtain a response almost similar to optimum. From software the optimum conditions of dyeing wool with extract of saffron petals were found to be dyeing time 69.89 minutes, dye concentration 3.7%, mordant amount 1.02g, dyeing temperature 110°C and pH 2.08 (figure 7).

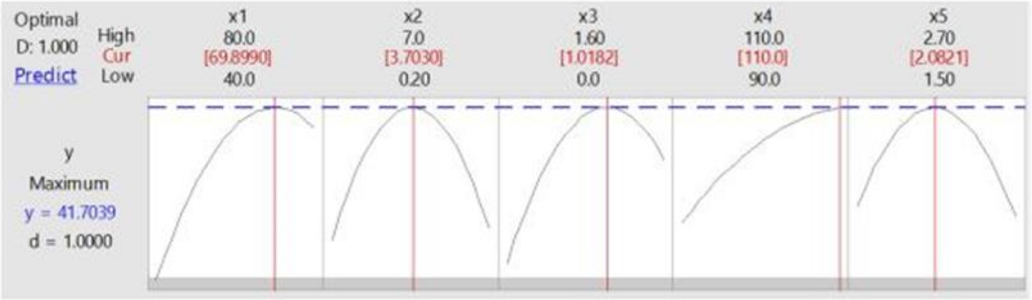

Figure 7. Optimum dyeing conditions for wool fiber

The good agreement between predicted values and the experimental ones means that the derived model can be used to adequately describe the relationship between factors and response in this study (figure 8 and 9).

The actual forecast graph shows how well the model fits the data. The diagonal line indicates that the predicted value and the actual value have the same position. If all the points are on or around this diagonal, it proves that the predicted value is more representative. The relationship between the predicted value and the actual value of the response in shown in figure 9. This figure shows that there is sufficient consistency between the actual data and the data obtained from the model.

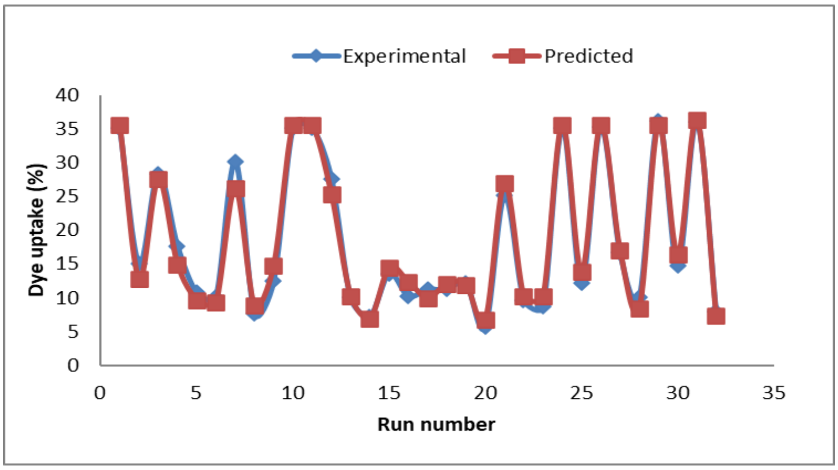

Figure 8. Relative deviation between experimental and predicted values of dye uptake for wool fiber dyed with extract of saffron petals

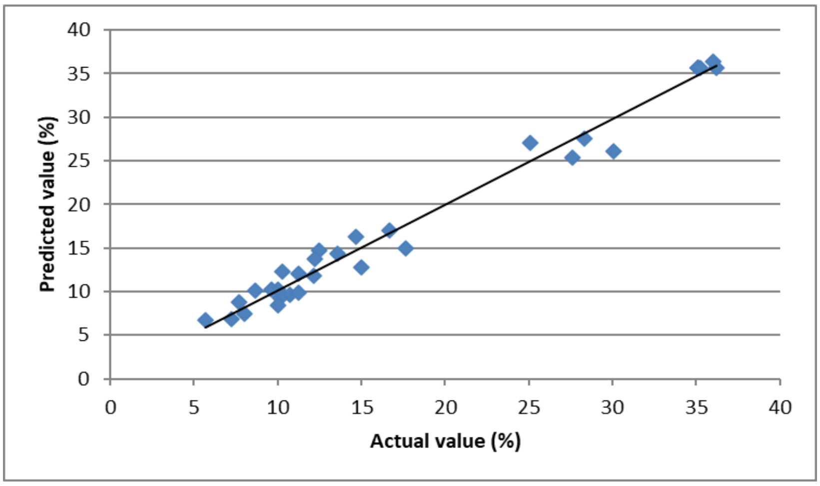

Figure 9. Experimental values versus predicted values for dye uptake for wool fiber dyed with extract of saffron petals

3.4 Fastness properties of dyed samples

The color fastness to washing and perspiration of wool fabrics dyed with extract of saffron petals is presented in table 3. The wool fabrics were pre-mordanted and dyed according to the proposed optimized conditions in order to find out the fastness properties.

Table 3. Fastness properties of dyed wool fabricswith proposed optimized conditions.

Washing fastness			Perspiration Color fastness					
			Basic			Acidic		
Color fastness	CS cotton	CS wool	Color fastness	CS cotton	CS wool	Color fastness	CS cotton	CS wool
4-5	5	4-5	5	5	5	5	5	5

From the experimental results, it can be concluded that the fastness properties of the dyed wool fibers were improved. The metal ions form a complex with the dye molecule; making it insoluble in water and resulting in a higher color fastness. Aluminium ions as mordant have a strong affinity to wool fabrics and fix several dye molecules onto the fiber, creating a larger complex and helping the fiber to retain the color and consequently increasing the color fastness. Both, the washing and perspiration color fastness tests gave good fastness grades for dyed wool fabric in the optimized dyeing conditions.

4. CONCLUSIONS

Wool fibers were successfully dyed with extract of saffron petals. Response surface methodology was used for the optimization of the dyeing conditions. The quadratic model was most suitably to describe the relationship between variables and the response. The optimum conditions of the process dyeing of wool fiber with extract of saffron petals were: dyeing time 69.89 minutes, dye concentration 3.7%, amount of mordant 1.02g (0.56%), dyeing temperature 110°C and pH 2.08. The R2 value of 0.982 shows the satisfactory explanatory of the fitted model. The experimental values were in good agreement with the model predicted values. The dyed wool fibers at optimal conditions proposed by RSM method have shown improvement in the washing and perspiration fastness properties. They gave good and increased fastness grades.

Acknowledgements

The authors want to thank the VICTUS FED Company for providing the saffron petals.

5. REFERENCES

[1] L. Lin, T. Jiang, L. Xiao, M. Pervez, N. Pervez, X. Cai, V. Naddeo, Y. Cai (2022) Sustainable fashion: eco-friendly dyeing of wool fiber with novel mixtures of biodegradable natural dyes. Scientific Reports, 12, 21040. https://doi.org/10.1038/s41598-022-25495-6

[2] N. Bhouri, S. Ltaief, N. Bhouri, S. B. Abdessalem (2023) Optimization of a green dyeing process using natural dyes extracted from Corchorus Olitorius leaves. Journal of Natural Fibers, 20(1), 2170946. https://doi.org/10.1080/15440478.2023.2170946

[3] A. Haji and S. S. Qavamnia (2018) The use of D-optimal design in optimization of wool dyeing with Juglans regia bark. Industria Textila, 69(2), 1-7.. DOI: 10.35530/IT.069.02.1509

[4] S. Manyim, A. K. Kiprop, J. I. Mwasiagi, C. M. Achisa, M. P. Odero (2021) Dyeing of cotton fabric with Euclea divinorum extract using response surface method. Research Journal of Textile and Apparel, 29(2), 6074. https://doi.org/10.1108/RJTA-10-2020-0115

[5] N. Habib, F. Batool, S. Adeel, M. Naveed, A. Ali, R. Mia, M. A. Assiri (2024) Free extraction and application of yellow natural curcumin colorant from Curcuma aromatic rhizomes for silk dyeing. Scientific Reports, 14, 13032, https://doi.org/10.1038/s41598-024-63927-7

[6] N. Nasirizadeh, H. Dehghanizadeh, M. E. Yazdanshenas, M. Rohani-Moghadam, A. Karimi (2012) Optimization of wool dyeing with rutin as natural dye by central composite design method. Industrial Corps and Products, 40, 361-366, https://doi.org/10.1016/j.indcrop.2012.03.035

[7] H. Barani and K. Rezaee (2017) Optimization of dyeing process using Achillea pachycephala as a natural dye for wool fibers. Chiang Mai Journal of Sciences, 44(4), 1548-1561, http://epg.science.cmu.ac.th/ejournal/

[8] S. Adeel, M. Azeem, N.Habib, M. Hussaan, A. Kiran, A. Haji, W. Haddar (2023) Sustainable application of microwave assisted extracted tea based tannin natural dye for chemical and bio-mordanted wool fabric. Journal of Natural Fibers, 20(1), 2136322 https://doi.org/10.1080/15440478.2022.2136322

[9] Y. Cai, L. Xiao, M.N. Ehsan, T. Jiang, M.N. Pervez, L. Lin, X. Xiong, V. Naddeo (2023) Green penetration dyeing of wool yarn with natural dye mixtures in D5 medium. Journal of Materials Research and Technology, 25, 6524-6541, https://doi.org/10.1016/j.jmrt.2023.07.081

[10] A. Etemadifar, H. Dehghanizadeh, N. Nasirizadeh, M. Rohani-Moghadam (2014) Statistical optimization of wool dyeing with alizarin red s as a natural dye via central composite design. Fibers and Polymers, 15(2), 254-260, https://doi.org/10.1007/s12221-014-0254-4

[11] A. Moiz, M.A. Ahmed, N. Kausar, K. Ahmed, M. Sohail (2010) Study the effect of metal ion on wool fabric dyeing with tea as natural dye. Journal of Saudi Chemical Society, 14(1), 69-76, https://doi.org/10.1016/j.jscs.2009.12.011

[12] Z. Zhao, C. Yan, F. Xu, J. Liu (2023) Study on dyeing properties and color characteristics of wool fabrics dyed with Geranium caespitosum L. extract – A new natural yellow dye. Coatings, 13(6), 1125. https://doi.org/10.3390/coatings13061125

[13] M. M. Pervez, W.S. Yeo, L. Lin, X. Xiong, V. Naddeo, Y. Cai. Optimization and prediction of the cotton fabric dyeing process using Taguchi design-integrated machine learning approach. Scientific Reports, 13, 12363. https://doi.org/10.1038/s41598-023-39528-1

[14] N. Hamid and M. S. A. Munaim (2017) Optimization on dyeing uptake exhaustion percentage of betacyanin pigment extracted from Hylocereus polyrhizus peel onto the spun silk using central composite design. Journal of Chemical Engineering and Industrial Biotechnology, 1, 72-487, https://doi.org/10.15282/JCEIB-V1-

12.31/3/2017/1.1.1

[15] M. Guo, L. Jiang, Q. Yang, C. Sun, J. Liu, W. Gao (2020) Optimization of dyeing parameters of cotton standardized samples for laundy test of dye transfer inhibition program. Fashion and Textiles, 7(38), 2-19. https://doi.org/10.1186/s40691-020-00226-5

[16] A.Kumar, M. Devi, R. Kumar, S. Kumar (2022) Introduction of high-value crocus sativus (saffron) cultivation in non-traditional regions of India through ecological modeling. Scientific Reports, 12,11925, https://doi.org/10.1038/s41598-022-15907-y

[17] D. Kothari, M. Thakur, R. Joshi, A. Kumar, R. Kumar (2021) Agro-climatic suitability evaluation for saffron production in areas of western Himalaya. Frontiers in Plant Science, 12, 657819. https://doi.org/10.3389/fpls.2021.657819

IZVOD

OPTIMIZACIJA PROCESA BOJENJA VUNE EKSTRAKTOM LATA ŠAFRANA KORIŠĆENJEM METODOLOGIJE ODGOVARAJUĆIH POVRŠINA

Nedavno je povećana svest o potražnji za ekološki prihvatljivim bojama u tekstilnoj primeni, jer prirodne boje mogu otkriti bolju biorazgradljivost i generalno imaju veću kompatibilnost sa životnom sredinom. Postoje stalni pokušaji da se prevaziđu neki nedostaci u vezi sa prirodnim bojenjem, kao što su produženo vreme bojenja, potrošnja energije i korišćene hemikalije. Sa ove tačke gledišta, optimizacija parametara procesa je dobra alternativa. U ovom radu je prikazano bojenje vunenih vlakana ekstraktom latica šafrana. Metodologija površine odgovora se koristi za optimizaciju parametara procesa i za istraživanje odnosa između različitih faktora koji se uzimaju u obzir, kao što su vreme bojenja, koncentracija boje, količina jedka, temperatura bojenja i pH. Upijanje boje je procenjeno merenjem apsorbancije, korišćenjem UV-Vis spektrofotometra i korišćeno je kao odgovor. Optimalni uslovi bojenja za dobijanje najveće vrednosti apsorpcije boje bili su sledeći: vreme bojenja 69,89 minuta, koncentracija boje 3,7%, količina jedila 1,02g (0,56%), pH kupke za farbanje 2,08, temperatura bojenja 110°C.

Ključne reči: prirodna boja, optimizacija, RSM, ekstrakt šafrana, vuna

Naučni rad
Rad primljen: 07.12.2024.
Rad korigovan: 12.06.2025.
Rad prihvaćen: 19.06.2025.

Sidorela Vishkulli: https://orcid.org/0009-0003-5671-6075
Ervin Suli: https://orcid.org/0009-0000-2991-3418
Spiro Drushku: https://orcid.org/0000-0003-0366-8578

Ubanozie Julian Obibuike[1], Stanley Toochukwu Ekwueme[1], Nnaemeka Princewill Ohia[2], Frank Chinedu Ukaeru[1], Ifeanyi Michael Onyejekwe[1], Mathew Chidubem Udechukwu[1]

[1]Department of Petroleum Engineering, Federal University of Technology, Owerri, Nigeria, [2]Africa Centre of Excellence in Future Energies and Electrochemical Systems (ACE-FUELS), Owerri, Nigeria

Scientific paper
ISSN 0351-9465, E-ISSN 2466-2585
https://doi.org/10.62638/ZasMat1329

Zastita Materijala 67 (1)
14 - 35 (2026)

Modelling and optimisation of geothermal binary ORC systems using response surface methodology and artificial neural networks

ABSTRACT

This study focuses on the modeling and optimization of geothermal binary Organic Rankine Cycle (ORC) systems to enhance power generation from geothermal systems using water as geofluid. Aspen HYSYS, utilizing the Peng-Robinson property package, was used to simulate the process, generating critical process data for subsequent modeling and optimization. Response Surface Methodology (RSM) and an Artificial Neural Network (ANN) were employed to model the relationships between input factors and output response, utilizing a Box-Behnken Design (BBD) for three key input variables: working fluid flow rate, working fluid outlet pressure, and turbine outlet pressure. Both RSM and ANN demonstrated strong predictive capabilities, with RSM achieving an R2 value of 0.9966 and an RMSE of 12.254, while ANN achieved an R2 value of 0.9886 and an RMSE of 23.722, indicating that RSM marginally outperformed ANN in terms of modelling accuracy. Optimization of the ORC system was conducted using RSM and ANN coupled with a Genetic Algorithm (ANN-GA), aimed at determining the optimal values for input and output parameters. The ANN-GA optimization results were validated using Aspen HYSYS and showed superior performance over RSM. ANN-GA predicted optimal values of working fluid flow rate, working fluid outlet pressure, and turbine outlet pressure as 12 kg/s, 19 bar, and 1.2 bar, respectively, which perfectly matched the Aspen HYSYS validation results. This optimization yielded a power output of 958.48 kW, which closely aligned with the Aspen HYSYS validation output of 952.9 kW, reflecting a minimal percentage error of 0.59%. Conversely, RSM predicted slightly deviated optimal values of 11.8 kg/s, 18.47 bar, and 1.2 bar, with a corresponding power output of 940.78 kW. When validated with HYSYS, the RSM-predicted output was 927.2 kW, resulting in a higher percentage error of 1.46%, thereby underperforming relative to ANN-GA. The study highlights the comparative strengths of RSM and ANN-GA, demonstrating that while RSM excels in accurately modeling the relationship and interactions between input factors and output responses, the ANN-GA framework exhibits a significantly higher capability in navigating complex nonlinear optimization landscapes. This highlights the effectiveness of integrating machine learning models with meta-heuristic algorithms for enhanced optimization performance. The findings contribute to advancing the methodology for optimizing geothermal ORC systems and offer a robust framework for improving power generation efficiency in geothermal energy applications.

***Keywords**: Geothermal energy, RSM, ANN, genetic algorithm, Hysys simulation, Power generation, binary ORC systems*

1. INTRODUCTION

The global reduction of fossil fuel resources and the need to mitigate carbon emissions are critical challenges faced worldwide. Despite these, energy demand continues to rise, necessitating alternative energy solutions to meet global requirements. Geothermal energy is a promising solution due to its abundance, eco-friendliness, and renewable nature [1, 2].

As a clean energy resource, geothermal energy offers numerous advantages over other renewable sources, including its higher reliability, sustainability, and capacity factor. It is less affected by climatic conditions, making it a reliable source of energy, particularly in regions with geothermal reserves.

Geothermal energy is derived from the Earth's subsurface, with temperatures ranging from 50°C to 350°C [3]. Geothermal resources can be classified into four main groups: hydrothermal, magma, hot-dry rock, and geo-pressured [4]. Among these, hydrothermal resources are the most commonly utilized, existing in either vapor-dominated or liquid-dominated forms, depending

---

*Corresponding author: Stanley ToochukwuEkwueme
E-mail: stanleyekwueme@yahoo.com

Paper received: 25.12.2024.
Paper corrected: 30.04. 2025.
Paper accepted: 09. 06.2025.

on geological conditions. Vapor-dominated systems typically exhibit temperatures between 250°C and 300°C and produce superheated (dry) steam [5]. In contrast, liquid-dominated systems can generate wet steam or water, making them versatile in energy production [5, 6].

The utilization of geothermal energy for power generation is divided into two main categories: power generation systems and reinjection facilities (or alternative solutions for non-condensable gases) [7]. The former includes the production well and closed power cycle, while the latter deals with compressor trains and reinjection wells [8]. Geothermal power plants are a key method for harnessing geothermal energy and fall into three main types: dry-steam, flash, and binary [9]. Each technology is suitable for different temperature ranges. Dry-steam and flash systems are used for high-temperature sources (above 180°C), while binary plants are employed for lower temperature resources (below 180°C).

Globally, dry-steam, flash, and binary technologies account for approximately 26%, 58%, and 15% of the market, respectively, with emerging technologies making up about 1% of facilities [1]. However, binary plants are becoming increasingly popular due to their flexibility in utilizing low-to-medium-temperature resources. In fact, over 270 binary power plants are currently operational worldwide [10].

In a dry-steam geothermal system, high-temperature and high-pressure steam is directly extracted from underground and expanded through a steam turbine to drive an electricity generator [8]. Wet-steam geothermal systems, on the other hand, involve separating the wet steam into saturated steam and geothermal water ([11]. The saturated steam is expanded through a turbine to generate electricity, while the geothermal water can be flashed at lower pressure to produce additional steam, which is also used for power generation. This configuration allows for efficient use of geothermal resources, particularly in areas where wet-steam conditions prevail.

While the traditional Rankine cycle using water as a working fluid is widely used for power generation, it is not always suitable for low- and medium-temperature geothermal resources. The boiling point of water is often too high for these resources, leading to inefficiencies [10]. Additionally, using steam cycles can result in issues such as turbine blade erosion, condensation during expansion, and the need for superheating, which complicates turbine design and increases costs. As a result, alternative cycles like the organic Rankine cycle (ORC), supercritical Rankine cycle, Kalina cycle, and flash cycle have been proposed for low-temperature heat conversion.

The ORC is particularly well-suited for low-to-medium-temperature geothermal applications due to its use of organic working fluids with lower boiling points than water. These organic fluids allow the ORC to utilize a wide range of heat sources [10]. The cycle operates similarly to the traditional Rankine cycle, where the working fluid is heated to boiling, and the resulting vapor drives a turbine that generates electricity. Afterward, the vapor is condensed back into a liquid and recirculated in the system.

Binary cycle technology, which includes ORC and Kalina cycles, is often used for liquid geothermal sources or medium-to-low-temperature resources (100–170°C) [1]. One of the key advantages of binary systems is their enclosed geothermal fluid loop, which prevents environmental pollution by reinjecting potentially harmful geothermal fluids back underground. In ORC-based binary geothermal power plants, the organic working fluids ensure system efficiency and environmental safety [12].

Despite the benefits, creating an efficient binary ORC system remains a significant challenge for the geothermal industry [13]. These systems require substantial capital investment, making proper planning and design essential. Research and development efforts focus on field tests, numerical modeling, simulation, and optimization to enhance system performance [1].

A successful binary ORC system must generate sufficient heat to produce electricity and maintain a production life of at least 30 years. Understanding and optimizing key parameters, including fluid properties, cycle efficiency, and resource characteristics, is crucial to improving system performance. By systematically testing various parameter combinations, engineers can design more efficient and cost-effective geothermal systems, thereby contributing to the global energy transition [14].

In optimization studies and experimental setups, process variables often depend on or interact with one another. Understanding the output-input relationships requires a deep comprehension of these interactions. Evaluating all possible combinations of parameters can be time-consuming, especially when running complex numerical simulations [13]. To address this challenge, numerical simulations are often used to study the effects of individual parameters, which are then used to design surrogate models. These models help streamline system development, reducing the time required for optimization while maintaining accuracy [14].

In the design of thermo-power generation blocks for binary Organic Rankine Cycle (ORC) systems using H_2O as the geothermal working fluid, various factors significantly influence performance, including cycle layout parameters, design specifications, and the variability of heat source and heat sink conditions [14]. Optimization of such systems is essential for maximizing efficiency and output, and the Response Surface Methodology (RSM) serves as a powerful and versatile tool for this purpose [15, 16]. RSM is a statistical and mathematical approach designed for constructing experimental models, analyzing variations in input factors, and generating a response surface that relates these variables to the desired output ([17]. By employing carefully structured experimental designs, such as Box-Behnken or Central Composite Designs, RSM facilitates the exploration of complex parameter spaces with high efficiency. This enables the identification of relationships between multiple input variables and the response variable, thereby allowing for simultaneous analysis and optimization [18].

The response surface generated by RSM provides a detailed map of how changes in input variables affect the system's output, making it a reliable method for identifying optimal ranges for key input parameters. This capability is particularly valuable in geothermal systems, where factors such as turbine inlet conditions, working fluid properties, and thermal efficiency must be fine-tuned to achieve maximum power output. RSM has been successfully applied in various studies to optimize and predict performance in ORC systems [18]. Its applications include turbine design optimization, where the geometry and operating conditions are adjusted for peak performance, and determining input parameters for maximizing thermal efficiency and output in geothermal power cycles [15]. By providing a systematic and statistically robust approach, RSM reduces the time and computational effort required for optimization while ensuring reliable and accurate predictions [17, 19].

Many scholars have investigated the use of RSM for modelling and optimisation of geothermal systems. Assareh et al. [18] employed RSM with Design-Expert software to optimize a geothermal-based energy system producing liquid hydrogen, cooling, hot water, and power. Using R123 as the working fluid, optimal exergy efficiency (43.91%) and cost rate (45.12 $/h) were determined. RSM effectively modeled and analyzed the impact of design variables, identifying Regina, Canada, as the optimal location based on performance and environmental benefits. Al Jubori et al. [20] employed RSM as part of a multi-objective optimization methodology integrating mean-line design, 3D CFD analysis, and ORC modeling for a small-scale radial-inflow turbine. Blade geometry was optimized using 20 design points, achieving 13.95% and 17.38% improvements in turbine and cycle thermal efficiencies, respectively. Kazemian et al. [21] utilized RSM with the central composite design to optimize input parameters for a combined GT/ORC/ARS system, demonstrating its superior economic performance over GT/ORC/GSHP systems. Sensitivity analysis further evaluated economic parameters like payback period and NPV. Azizi et al. [22] integrated RSM with grey wolf optimization for a geothermal-natural gas cogeneration system. Optimization achieved 45.2% exergy efficiency and a unit product cost of 3.82 $/GJ, highlighting RSM's role in enhancing performance and profitability.

In recent years, machine learning methods have revolutionized the optimization and performance enhancement of Organic Rankine Cycle (ORC)-based plants. Among these methods, Artificial Neural Networks (ANNs) have demonstrated exceptional capabilities in predicting, classifying, and approximating functions, particularly in handling complex and nonlinear relationships [23]. This has made ANNs an indispensable tool for solving real-world challenges across diverse applications, including shallow geothermal systems. ANNs, particularly those implementing backpropagation algorithms, have been pivotal in advancing geothermal energy operations, enhancing efficiency and sustainability [23]. The integration of machine learning techniques in ORC systems began with their application to predict and optimize system performance [24].

Tugcu and Arslan [25] applied a two-stage ANN model to optimize a geothermal absorption refrigeration system, analyzing 3660 designs with energy, exergy, and NPV metrics. ANN trained with backpropagation algorithms achieved error rates as low as 0.07%, effectively predicting and optimizing COP and exergy efficiency. Ziviani et al. [26] developed an ANN to predict performance in ORC experiments using scroll expanders, achieving high accuracy for turbine parameters like inlet pressure and rotation speed. Yilmaz and Koyuncu [27] modelled and optimized the Afyon Geothermal Power Plant using a multi-layer ANN with a genetic algorithm, achieving energy and exergy efficiencies of 10.4% and 29.7%. The optimized payback period and exergy cost were calculated as 2.87 years and $0.0176/kWh, respectively. Cetin et al. [28] modeled a binary geothermal power plant

(GPP) with ANN to optimize thermodynamic performance. By analyzing reference point data, the model estimated power output and exergy efficiency, determining the best parameter configurations for maximum performance. Yilmaz and Sen [29] utilized an ANN-based Genetic Algorithm (GA) to optimize a geothermal and solar-assisted energy and hydrogen production system under varying climatic and operational conditions. The ANN-GA model predicted power output and hydrogen production, achieving a cost of hydrogen at $1.576/kg and a unit electricity cost of $0.027/kWh.

Chanthamaly et al. [30] applied ANN classification algorithms to predict maintenance schedules for geothermal wells, achieving 99.83% accuracy using K-means clustering. The ANN-supported predictive maintenance ensured system reliability and minimized power loss. Xue et al. [23] proposed an ANN-Differential Evolution (DE) optimization framework for a three-horizontal-well EGS, achieving a low LCOE of $0.0376/kWh, with ANN models demonstrating high predictive accuracy ($R^2 > 0.996$) and significant time savings (36,000x faster than simulations). Hsieh et al. [31] trained an ANN using data from a 3D axial turbo-expander model to predict key cycle parameters under off-design conditions, enabling long-term performance analysis for geothermal fields. Zhou et al. [32] Introduced a hybrid framework combining ANN with mathematical programming to optimize ORCs, achieving high classification (99% accuracy) and regression (mean errors <1%) performance. The mixed-integer linear programming (MILP) approach significantly reduced computational time while optimizing net exergy to 28.66 MW.

Chitgar et al. [33] used ANN-GA for multi-objective optimization of geothermal-based desalination systems, identifying configurations that improved power generation by 150% and water production by 60%, while evaluating optimal working fluid combinations under different temperatures. Shakibi et al. [34] evaluated ANN algorithms for optimizing geothermal-hydrogen systems in Australia, achieving a 46.27% exergy efficiency, 1.84-year payback, and high accuracy (mean absolute error: 2.28×10^{-14}) in predicting system performance under multi-objective scenarios. Ling et al. [35] developed an ANN-based prediction and optimization model for a binary cycle geothermal power plant. The model controlled working fluid circulation rates, optimizing net power production and reducing costs, outperforming traditional physics-based approaches. Farajollahi et al. [36] combined ANN with response surface methodology (RSM) for hybrid power plant optimization, using ANN to map independent variables to thermal efficiency and cost. The GA-based optimization identified parameters achieving a thermal efficiency of 30.47% and a levelized product cost of $13.04/GJ.

2. LITERATURE REVIEW

2.1.ORC Cycle Working Fluids

The performance of an ORC system is highly dependent on the choice of working fluid, making this selection a critical factor in system design and efficiency. Selecting the most suitable organic working fluid involves considering a variety of parameters, including thermodynamic properties, environmental impact, safety concerns, and economic factors. These criteria collectively influence the overall efficiency, cost, and sustainability of the ORC system [1].

From an environmental and safety perspective, working fluids must comply with strict regulations related to Global Warming Potential (GWP) and Ozone Depletion Potential (ODP). Fluids used in ORC systems should have a GWP below 150 and exhibit no ODP to minimize environmental harm, in line with global climate targets and environmental protection efforts [33]. Furthermore, the working fluids should also possess favourable safety characteristics, such as low flammability and toxicity. The careful selection of non-hazardous fluids helps to reduce operational risks and ensures compliance with safety regulations in industrial settings [37].

When choosing a working fluid, other critical factors include thermodynamic properties that directly affect the system's efficiency. Fluids with low specific volumes are preferred because they reduce the size and cost of key components such as condensers [38, 39]. Additionally, fluids should exhibit favourable liquid-specific heat, viscosity, and thermal stability, which play essential roles in efficient heat transfer and long-term operation. High latent heat and density are also important as they enhance output power and ensure better performance, particularly in combined cycle applications [12, 13]. The molecular weight of the fluid should be compatible with the turbine’s design, and the fluid must be stable under the operational temperatures and pressures, avoiding issues like material degradation or chemical breakdown. Fluids must also be non-corrosive and compatible with turbine materials and lubricating oils to ensure system longevity and minimal maintenance.

Saturation pressure is another important consideration, as higher pressures (typically >100 kPa) are required to prevent air or gas infiltration, which could reduce system efficiency [39]. At the same time, fluids with moderate heat exchanger pressures are preferred because they allow for safer and more manageable system designs. Overall, the selection of a working fluid that balances these thermodynamic and material compatibility properties is essential for optimizing both performance and cost [40].

Working fluids can be categorized into three main types based on the slope of their temperature-entropy (T-S) saturation curve during the expansion process: wet fluids, dry fluids, and isentropic fluids. Wet fluids, such as water, exhibit a negative slope, which means that during expansion, condensation occurs, leading to two-phase mixtures of liquid and vapour [3]. This can cause erosion in turbines due to the presence of liquid droplets, making wet fluids less desirable for ORC systems. Dry fluids, including hydrocarbon gases such as propane, butane, pentane, and hexane, exhibit a positive slope, meaning that they remain in a superheated vapor state during expansion, avoiding condensation and preventing turbine erosion [41]. Isentropic fluids, such as toluene and R245fa, exhibit a vertical slope and maintain an ideal balance during expansion [1]. However, their high GWP has made them less favourable for use in ORC systems due to environmental concerns.

Historically, water has been widely used as a working fluid in large-scale Rankine cycles, especially in high-temperature, fossil fuel-fired plants. However, at lower temperatures, water becomes less efficient due to its high specific heat and latent heat of vaporization. This makes it unsuitable for ORC applications, which often operate at lower temperatures [42]. Organic fluids, on the other hand, offer significant advantages over water in ORC systems. They require less heat to evaporate and eliminate the need for superheating, making the cycle design simpler and more efficient [43]. These organic fluids generally maintain a superheated vapor state during isentropic expansion through a turbine, preventing the formation of two-phase mixtures and simplifying turbine design [44]. As a result, ORC systems can operate with less complexity, reduced risk of turbine erosion, and lower maintenance costs.

One of the most significant advantages of using dry working fluids in ORC systems is their ability to maintain the superheated vapor state throughout the expansion process [45]. This prevents the formation of liquid droplets that could damage turbine blades, making dry fluids more desirable than wet fluids for ORC applications. Although isentropic fluids offer good thermodynamic properties, their higher global warming potentials (GWP) has led to a decline in their use, especially as global efforts to reduce greenhouse gas emissions intensify. Additionally, organic fluids derived from petroleum exhibit lower evaporation energy than water, requiring less heat for vaporization [46, 47]. This makes them particularly well-suited for ORC systems that operate at lower temperatures, such as those used in geothermal, waste heat recovery, and solar thermal applications [48, 49].

As the need for sustainable and efficient energy solutions grows, the choice of working fluids in ORC systems is increasingly guided by both environmental considerations and performance metrics [50]. The focus is shifting towards fluids that not only offer high efficiency but also align with stricter environmental regulations. In response to these challenges, research and development efforts continue to focus on discovering new working fluids with low GWP, zero ODP, and optimal thermodynamic properties to improve the overall sustainability and performance of ORC systems.

2.2. Material challenges in Geothermal ORC systems

Geothermal Organic Rankine Cycle (ORC) systems operate under extreme conditions due to the high temperature, pressure, and chemically aggressive nature of geothermal fluids. These factors lead to significant material degradation, particularly corrosion in turbines, heat exchangers, and pipelines. The selection of corrosion-resistant materials is crucial to ensuring the long-term durability and efficiency of ORC components. This section explores the major corrosion mechanisms affecting these components and highlights materials that have demonstrated resilience in harsh geothermal environments [51].

Corrosion in geothermal ORC systems arises primarily due to the presence of dissolved gases such as carbon dioxide (CO_2) and hydrogen sulfide (H_2S), as well as chloride-rich geothermal brines. General corrosion occurs when the entire surface of a material undergoes uniform degradation due to its reaction with geothermal fluids, often leading to thinning and structural weakness over time. In contrast, localized corrosion, such as pitting and crevice corrosion, occurs in specific areas where aggressive ions concentrate, leading to rapid penetration and failure of the material [52]. Stress corrosion cracking (SCC) is another prevalent issue in geothermal environments, resulting from the combined effects of tensile stress and corrosive fluid interactions, which can lead to sudden material failure, particularly in turbine blades and piping. Additionally, erosion-corrosion accelerates material degradation due to the mechanical impact of high-velocity geothermal fluids carrying suspended particulates, leading to severe wear and loss of material integrity [53].

2.2.1. Corrosion-Resistant Materials for Geothermal ORC Systems

The selection of appropriate materials for geothermal ORC systems is essential to combat the detrimental effects of corrosion. Stainless steels such as 316L, Duplex 2205, and Super Duplex 2507 are commonly employed due to their excellent resistance to chloride-induced pitting and stress corrosion cracking. These materials contain high levels of chromium, molybdenum, and nitrogen, which enhance their protective passive film formation, thereby improving their resistance in aggressive geothermal environments [52]. Stress corrosion cracking (SCC) is another prevalent issue in geothermal environments, resulting from the combine. Nickel-based alloys, such as Inconel 625 and Hastelloy C-276, exhibit superior performance in highly acidic and oxidizing conditions, making them suitable for heat exchangers and other critical ORC components. Titanium alloys, particularly Ti-6Al-4V, are widely recognized for their exceptional resistance to corrosion in chloride-rich geothermal brines, preventing structural failures in pipelines and other submerged components [51].

Protective coatings and linings serve as additional barriers against corrosion by preventing direct contact between metal surfaces and aggressive fluids. Epoxy and polymer-based coatings are extensively used in pipelines and heat exchangers, providing a non-permeable barrier against chemical attack [52]. Stress corrosion cracking (SCC) is another prevalent issue in geothermal environments, resulting from the combine. Thermal spray coatings, which include metal-based, ceramic, and composite coatings, are often applied to high-temperature components to improve resistance to oxidation and erosion. Ceramic coatings, in particular, are highly effective in geothermal environments due to their excellent thermal stability and chemical inertness. Additionally, composite materials such as fiber-reinforced polymers (FRP) are gaining popularity due to their lightweight nature and remarkable resistance to chemical degradation [53]. Recent advancements in graphene-based coatings have also demonstrated promising results in enhancing the longevity of ORC components by providing ultra-thin, highly corrosion-resistant protective layers.

The effectiveness of corrosion-resistant materials and coatings has been demonstrated in several geothermal ORC plants worldwide. In Icelandic geothermal plants, extensive use of titanium alloys in heat exchangers has significantly reduced failures caused by chloride-induced corrosion [54]. At the Salton Sea Geothermal Field in the United States, nickel-based alloys have been successfully implemented in turbine components to withstand high concentrations of hydrogen sulfide, thereby enhancing operational longevity. In Japan, geothermal facilities have adopted duplex stainless steels in piping systems to prevent stress corrosion cracking, minimizing the risk of catastrophic failures. Ongoing research continues to focus on developing novel materials, hybrid coatings, and composite structures to further improve the durability and efficiency of geothermal ORC systems. Nanostructured materials and self-healing coatings represent particularly promising innovations, as they can actively repair micro-damages and extend the operational lifespan of components [55].

2.2.2. Protective Coatings for Erosion and Thermal Degradation

Protective coatings play a crucial role in enhancing the durability and performance of geothermal ORC system components. These coatings serve as a barrier against erosion, high-temperature degradation, and chemical attack from geothermal fluids. The selection of appropriate coatings depends on factors such as operating temperature, fluid composition, and mechanical stresses encountered in the system [54].

Thermal spray coatings, which include metallic, ceramic, and cermet-based solutions, provide high resistance to oxidation and wear in elevated-temperature environments. Metallic coatings, such as those based on nickel-chromium (NiCr) and molybdenum, form a protective oxide layer that minimizes the effects of high-temperature corrosion [56]. Ceramic-based coatings, including aluminum oxide (Al_2O_3) and zirconium oxide (ZrO_2), offer superior thermal insulation and resistance to chemical attack, making them ideal for use in turbine components and high-temperature heat exchangers. Cermet coatings, composed of tungsten carbide-cobalt (WC-Co) and chromium carbide-nickel-chromium (Cr_3C_2-NiCr), provide exceptional wear resistance, ensuring prolonged durability in harsh geothermal conditions [55].

Polymer-based coatings, including epoxy and polyurethane coatings, are widely used for corrosion protection in geothermal pipelines and heat exchangers. These coatings form an impermeable barrier that prevents direct exposure to aggressive geothermal fluids, thereby mitigating material degradation. Additionally, polytetrafluoroethylene (PTFE) and fluoropolymer coatings offer low surface energy, reducing scaling and biofouling in ORC systems. Recent advancements in nanostructured coatings, such as graphene and carbon-based solutions, have demonstrated remarkable chemical resistance and mechanical strength, making them attractive candidates for next-generation geothermal applications [56]. The development of self-healing coatings further enhances the reliability of ORC components by enabling autonomous repair of minor damages, thereby extending operational life and reducing maintenance costs [55].

2.2.3. Material Compatibility with Working and Geothermal Fluids

Material compatibility is a critical consideration in geothermal ORC systems to ensure that components can withstand the chemical and thermal conditions imposed by both working fluids and geothermal brines. High-salinity brines pose a significant challenge due to their aggressive nature, necessitating the use of corrosion-resistant materials such as titanium alloys and duplex stainless steels [57]. These materials exhibit exceptional resistance to chloride-induced corrosion, thereby preventing premature failure in pipelines and heat exchangers. Exposure to hydrogen sulfide (H_2S) can accelerate material degradation, particularly in carbon steels. Nickel-based alloys, such as Hastelloy C-276, have proven effective in mitigating sulfide-induced corrosion, ensuring long-term reliability in geothermal environments [58].

Working fluids used in ORC systems also impact material compatibility. Hydrocarbon-based ORC fluids, including isopentane and toluene, require elastomers and seals that resist swelling and degradation. Ammonia-water mixtures, commonly used in Kalina cycle systems, are highly corrosive to copper-based alloys, necessitating alternative material selections. Supercritical CO_2-based ORC systems impose additional challenges, as carbon steel components may experience accelerated degradation under high-pressure conditions. Stainless steels and ceramic coatings have demonstrated improved resistance in such environments, offering viable solutions for long-term durability [57].

2.3 Material Behavior under Geothermal Conditions

2.3.1. Impact of Geothermal Fluids on Material Degradation

The study of material degradation in geothermal Organic Rankine Cycle (ORC) systems requires a thorough investigation of the effects of geothermal fluids on structural materials over extended periods. Laboratory and field studies have been conducted to analyze corrosion, scaling, and material deterioration under geothermal conditions. These studies provide critical insights into how different material compositions perform in aggressive environments characterized by high salinity, dissolved gases, and elevated temperatures [59].

Electrochemical and accelerated aging tests serve as fundamental methods for evaluating corrosion rates and predicting material longevity. Electrochemical impedance spectroscopy (EIS) and potentiodynamic polarization techniques are widely used to assess the passivation behavior of metals and alloys in geothermal brines. Accelerated aging tests, including high-temperature autoclave exposure and cyclic immersion tests, replicate the long-term effects of geothermal fluids on materials within a controlled timeframe [60]. By systematically studying the degradation behavior of materials such as carbon steel, stainless steel, nickel-based alloys, and titanium alloys, researchers can determine their suitability for geothermal ORC applications.

Comparative studies between conventional and advanced materials reveal significant differences in their resistance to geothermal-induced degradation. While carbon steels remain susceptible to pitting and stress corrosion cracking in chloride-rich environments, duplex stainless steels and superalloys demonstrate superior resistance, attributed to their enhanced passive film stability and alloying elements such as chromium and molybdenum [60]. Titanium-based materials exhibit exceptional corrosion resistance but pose economic constraints due to their high cost. The incorporation of protective coatings further enhances material performance by providing an additional barrier against aggressive geothermal fluids [61].

2.3.2. Performance of Advanced Materials and Coatings

The effectiveness of corrosion-resistant alloys and coatings in geothermal ORC systems has been extensively investigated through experimental testing and numerical simulations. Numerous studies have examined the application of thermal spray coatings, polymer-based linings, and advanced ceramic coatings in mitigating wear, corrosion, and high-temperature degradation. Experimental methods, such as scanning electron microscopy (SEM) and X-ray diffraction (XRD), provide in-depth characterization of coating integrity and failure mechanisms under extreme conditions. These techniques help assess the adhesion strength, porosity, and microstructural evolution of coatings subjected to geothermal environments [62].

Computational methods play an increasingly vital role in predicting material behavior under geothermal conditions. Computational fluid dynamics (CFD) and finite element analysis (FEA) are widely employed to simulate fluid-material interactions and predict the effects of erosion, scaling, and thermal stress on ORC components. CFD modeling enables the evaluation of fluid velocity profiles and turbulence-induced degradation, allowing engineers to optimize pipeline and heat exchanger designs for reduced wear [63]. FEA simulations assess mechanical stresses imposed on materials due to cyclic thermal loading and pressure fluctuations, ensuring that critical components such as turbine blades and heat exchanger tubes maintain structural integrity over prolonged operational periods.

In addition to experimental and computational studies, ongoing research is dedicated to identifying novel materials that offer enhanced durability in geothermal ORC applications. Graphene-based coatings, self-healing polymers, and nano-structured surface modifications are among the emerging technologies being explored for their ability to resist corrosion and erosion while maintaining mechanical strength [63]. These advanced materials promise to extend component lifespan and reduce maintenance requirements, thereby improving the economic feasibility of geothermal ORC plants [64].

2.3.3. Strategies for Enhancing ORC Component Lifespan

Ensuring the longevity of ORC system components requires the implementation of effective maintenance, monitoring, and material selection strategies. The use of corrosion inhibitors, for example, has proven beneficial in reducing the rate of material degradation by forming protective films on metal surfaces. Chemical treatments involving phosphate- and molybdate-based inhibitors have demonstrated success in geothermal applications by minimizing localized corrosion in heat exchangers and pipelines [65].

Predictive maintenance, enabled by real-time monitoring technologies, provides a proactive approach to identifying material degradation before catastrophic failures occur (Izuwa et al., 2024). Sensors equipped with electrochemical monitoring capabilities can detect changes in material passivation and corrosion rates, allowing operators to take preventive action. Non-destructive testing (NDT) methods, such as ultrasonic thickness gauging and eddy current testing, further contribute to the early detection of material wear and structural defects, facilitating timely repairs and replacements [64].

Material innovations, including self-healing coatings and nano-structured materials, offer promising advancements in extending the service life of ORC components. Self-healing coatings, which contain microencapsulated corrosion inhibitors, can autonomously repair minor surface damages, preventing the initiation of corrosion sites. Nanostructured surface treatments, such as plasma-assisted deposition techniques, enhance material resistance to erosion and fouling by altering surface roughness and chemical reactivity [66].

Best practices in material selection remain paramount to optimizing ORC system durability. The integration of duplex stainless steels, nickel-based superalloys, and advanced ceramic coatings ensures that components can withstand the combined effects of geothermal fluid exposure and thermal cycling [67]. By aligning material selection with the specific operating conditions of geothermal ORC systems, engineers can minimize unplanned downtime, reduce maintenance costs, and enhance overall system efficiency [68]. Continuous research and technological advancements in material science will further contribute to the development of next-generation materials capable of withstanding the extreme conditions of geothermal ORC environments, thereby ensuring sustainable and long-term energy production [69].

3. METHODS

The method consists of three different parts including the process simulation of the geothermal binary ORC system for electricity generation, the implementation of the surrogate models comprising RSM and ANN to investigate the interrelationship between influencing parameters and output, and the model optimisation using RSM and ANN-GA for optimal parameter conditions. The methods comprise the following

- Process modelling using Hysys to conduct modelling and simulation of geothermal binary ORC system using water and isopentane as geofluid and working fluid respectively and in conducting simulation runs for different input datasets generated with the Box-Behnken design (BBD) method
- Developing surrogate model for RSMmodelling and ANN modelling using Design Experts and MATLAB respectively to determine the relationship between decision variables and output response and approximate the design space.
- Perform optimization based on the modelled design space using RSM optimization and a coupled artificial neural network model and genetic algorithm (ANN-GA)

3.1. Process Modelling and Simulation

3.1.1. Process Model

The model utilised by Hysys is based on mass and energy balance in steady state condition. The steady-state energy models for the ORC system are given below

$$\sum \dot{m}_{in} = \sum \dot{m}_{out} \quad (1)$$

$$\sum Q + \sum \dot{m}_{in} h_{in} = \sum W + \sum \dot{m}_{out} h_{out} \quad (2)$$

$$W_{net} = W_{turbine} - W_{pump} \quad (3)$$

$$W_{turbine} = \dot{m}_f (h_{in} - h_{out}) \quad (4)$$

Where $\dot{m}$ (kg /s) is the mass flow rate, h is the specific enthalpy of the system's working fluid streams, (kJ/kg), Q represent the heat energy passing via the component boundaries, (Watts), W is the work energy passing via the component boundaries, (Watts), Wnet is the net work, Watts, Wturbine is the turbine work, Watts, Wpump is the pump work, Watts, $\dot{m}_f$ is the mass flow rate, hin is the specific enthalpy at the turbine entry, hout is the specific enthalpy at the exit of the turbine

3.1.2. Model Simulation

The simulation model made with Aspen Hysys v11 software consists of; Evaporator, Turbine, Condenser, and Circulating Pump. The model consists of three different loops; first the heating loop which is the hot water rising from the abandoned oil and gas well, the ORC loop which is the working fluid (i-C_2H_5), and finally the cooling cycle for the condenser which is also water.

The scheme of the ORC power plant is shown in Fig. 1, displaying the heating loop which is the hot water rising from the abandoned oil and gas well, the ORC loop which is the working fluid (i-C_2H_5), and finally the cooling cycle for the condenser which is also water. An ORC power cycle utilizing i-C_2H_5 as working fluid is fed (stream #3) through a condensing heat exchanger (E100 and E101), which is pressurized at about 10 bars. The ORC scheme comprehends an evaporator, a turbine, a condenser, and a pump which were modelled as heat exchangers, expander, air cooler and pump in Hysys respectively. The process flow diagram (PFD) for the ORC process simulated in Hysys is given in Figure 3

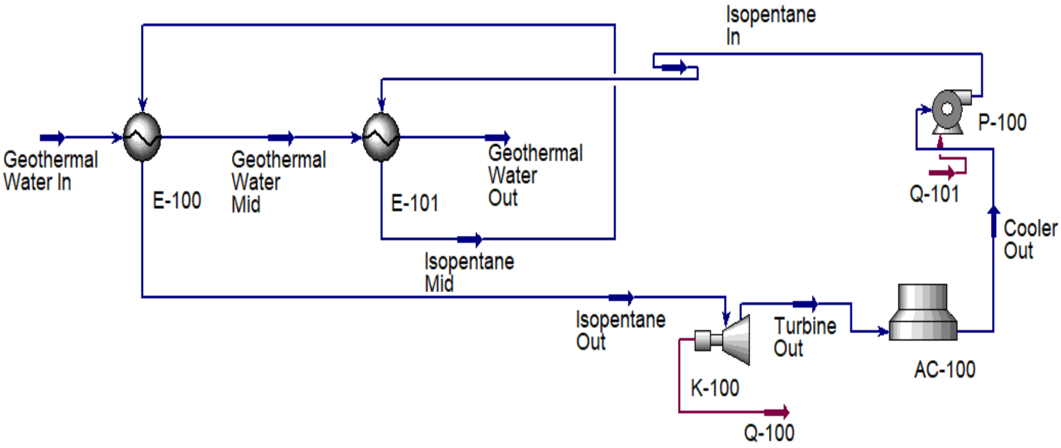

Figure 1. Process flow diagram (PFD) of the geothermal binary ORC system

The geofluid which is hot water comes from the wells and enters into HEX1 (E-100) and subsequently to HEX2 (E-101). iC_2H_5 is pumped into the heat exchangers and extracted heat both from HEX2 and HEX1 and then exits HEX1 towards the turbine. At the turbine, iC_2H_5 was vapourised andexpandedthus rotating the turbine leading to the generation electric power. The iC_2H_5 exits the turbine at lower temperature and pressure and goes to the air cooler where it is cooled and then pumped back to the HEXs to continue the cycle. Water that came out from the outlet of HEX2 was injected back into the well and the cycle continues. Throughout the process, the turbine, pump, and compressor stages are assumed to be adiabatic devices. Negligible pressure losses occur in the components of the ORC and its piping system. Neglecting the changes of kinetic and potential energies, the mass and energy balance equations in the steady-state condition can be applied to each component.

3.2. Development of Surrogate Model

The surrogate model comprises the RSM and ANN conducted to investigate the relationship between input parameters and power produced. The surrogate models are applied to dual functions which includes design space approximation and optimisation.

3.2.1.RSMModelling

A response surface methodology (RSM) model was implemented using Design-Expert software to predict geothermal power generation by applying regression analysis to the experimental data obtained through a Box-Behnken design (BBD). The BBD incorporated three independent variables which were found to have impact on the geothermal power generation; these include:

working fluid (iC2H5) flowrate (kg/s), working fluid inlet pressure (bar) and turbine outlet pressure (bar). Several regression models were tested and evaluated to identify the one with the highest performance and accuracy, most the independent variables. The flowchart in Figure 2 illustrates the steps involved in the RSM modelling. The RSM selected the best regression model based on statistical parameters such as R², adjusted R², predicted R², standard deviation, and coefficient of variation (COV). Multiple regression analyses facilitated the fitting of these models to the simulation data, allowing for the estimation of responses from independent variables using their general equations. Some of the equations for several models in RSM is given below.

The general form of the models for linear regression is given as

$$y = a_o + \sum_{i=1}^{k} a_i x_i + e \qquad (5)$$

The general form of the 2FI regression model is given as

$$y = a_o + \sum_{i=1}^{k} a_i x_i + \sum_{i<j}^{k} a_{ij} x_i x_j + e \qquad (6)$$

The general form of the quadratic regression model is given as

$$y = a_o + \sum_{i=1}^{k} a_i x_i + \sum_{i<j}^{k} a_{ij} x_i x_j + \sum_{i=1}^{k} a_{ii} x_i^2 + e \qquad (7)$$

Where x_i,x_j, x_l, are the input variables and a_i, a_{ij}, a_{ii},and a_{ijl} are the coefficient of each of the terms, a_o is the offset and e is the residual or error term

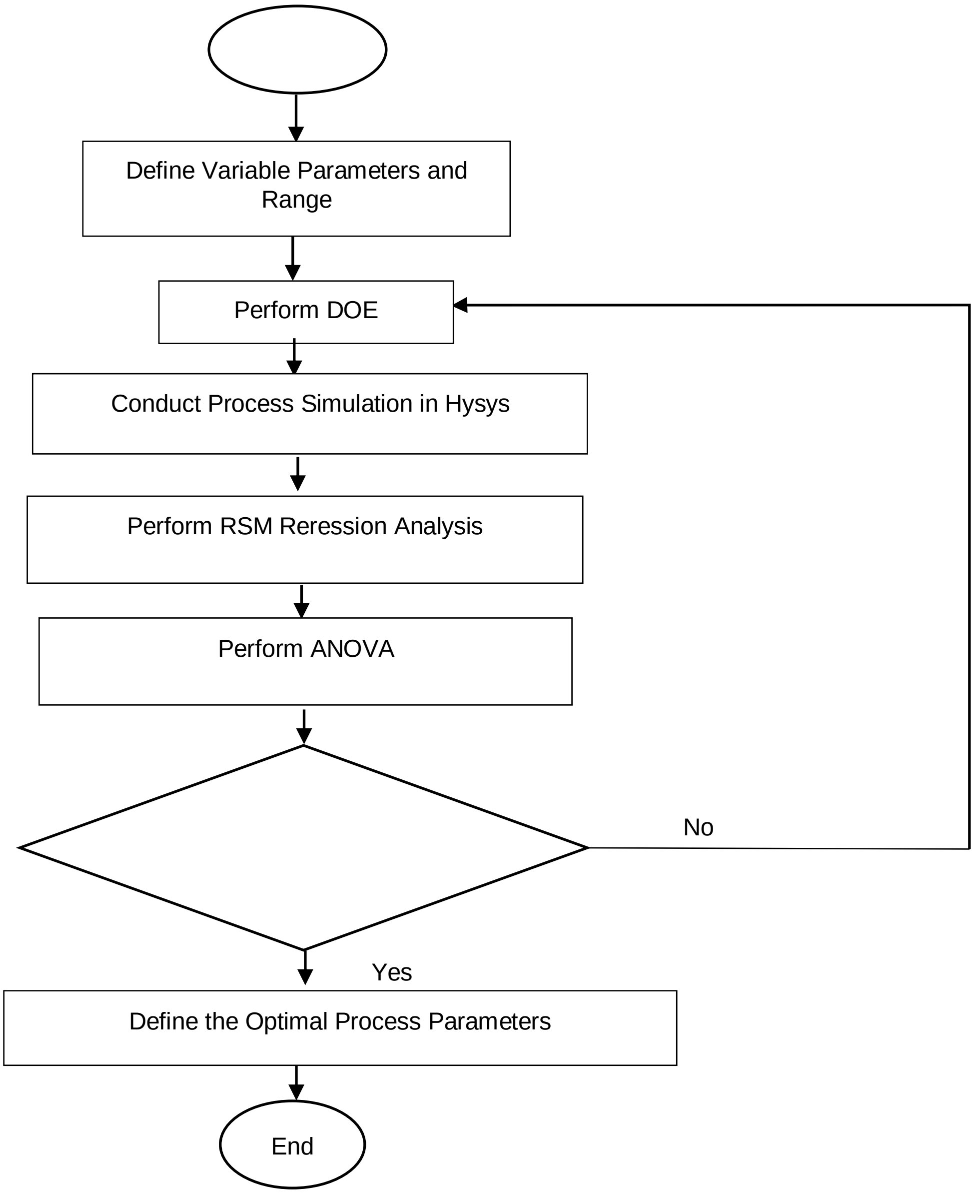

Figure 2. RSM Modelling Flowchart

3.5.2. ANN Modelling

The ANN model was developed using MATLAB by training with simulation data from the BBD, aiming to create a network capable of accurately modellinggeothermal power generation based on the input of independent variables. The model was constructed using a dataset of 17data points, with 70% of the data allocated for training, 15% for testing, and 15% for validation. The ANN model employed in this study utilizes a feed-forward neural network architecture, following the backpropagation learning principle. The network architecture consists of an input layer, a hidden layer, and an output layer. Various configurations of neurons in the hidden layer were tested, with the optimal network topology determined iteratively by evaluating network performance indices. Training of the network was performed using the Levenberg-Marquardt (LM) algorithm, with the Sigmoid function used as the transfer function. The optimal number of neurons in the hidden layer was selected based on the best performance, measured by the R² value and root mean squared error (RMSE).

The construction of an ANN model involves adjusting weights and biases. The output of a neuron is computed by summing the weighted inputs and adding a bias, which is then processed through a transfer function.

$$f_n = f\left[\left(\sum_{i=1}^{k} w_i\, x_i\right) + b\right] \tag{8}$$

Where k, wi, b, and f(n) are the number of elements in the input vector xi, the interconnection weight, the bias for the neuron (n), and the neuron output, respectively. ANNs feature various network architectures, training algorithms, transfer functions, and optimal neuron counts [70]. The ANN model employed in this study utilizes a feed-forward neural network architecture based on the backpropagation learning principle. For training nonlinear functions, such as those encountered in many chemical processes, the tangent sigmoid transfer function (tansig) is commonly used due to its effectiveness. The general formula for the tansig transfer function is given as follows:

$$f(x) = \frac{2}{1 + e^{-2x}} - 1$$

Additionally, following the recommendations of Hojjat et al. [71], input parameters were normalized by dividing each column by its maximum value, ensuring a range of zero to one (0–1). The study utilized these normalized parameters as inputs for modelling the artificial neural network.

The structure of the network is illustrated in Figure 3.

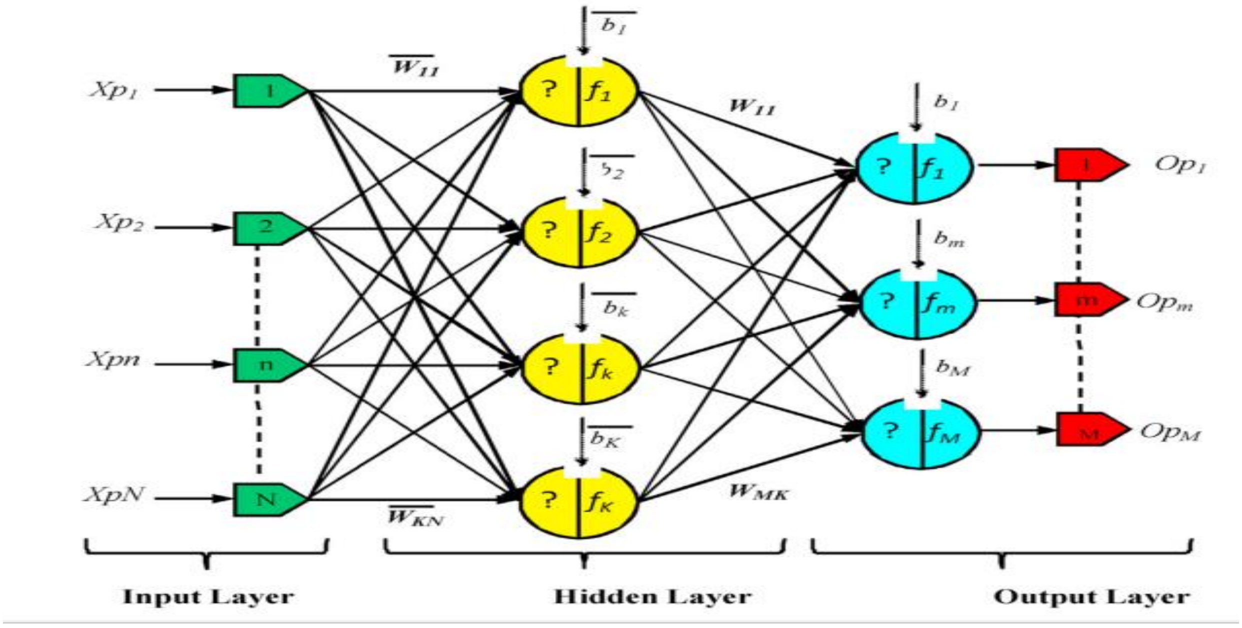

Figure 3. Sample network architecture for ANN modeling [27]

The flowchart in figure 3 describes the steps of the ANN modelling

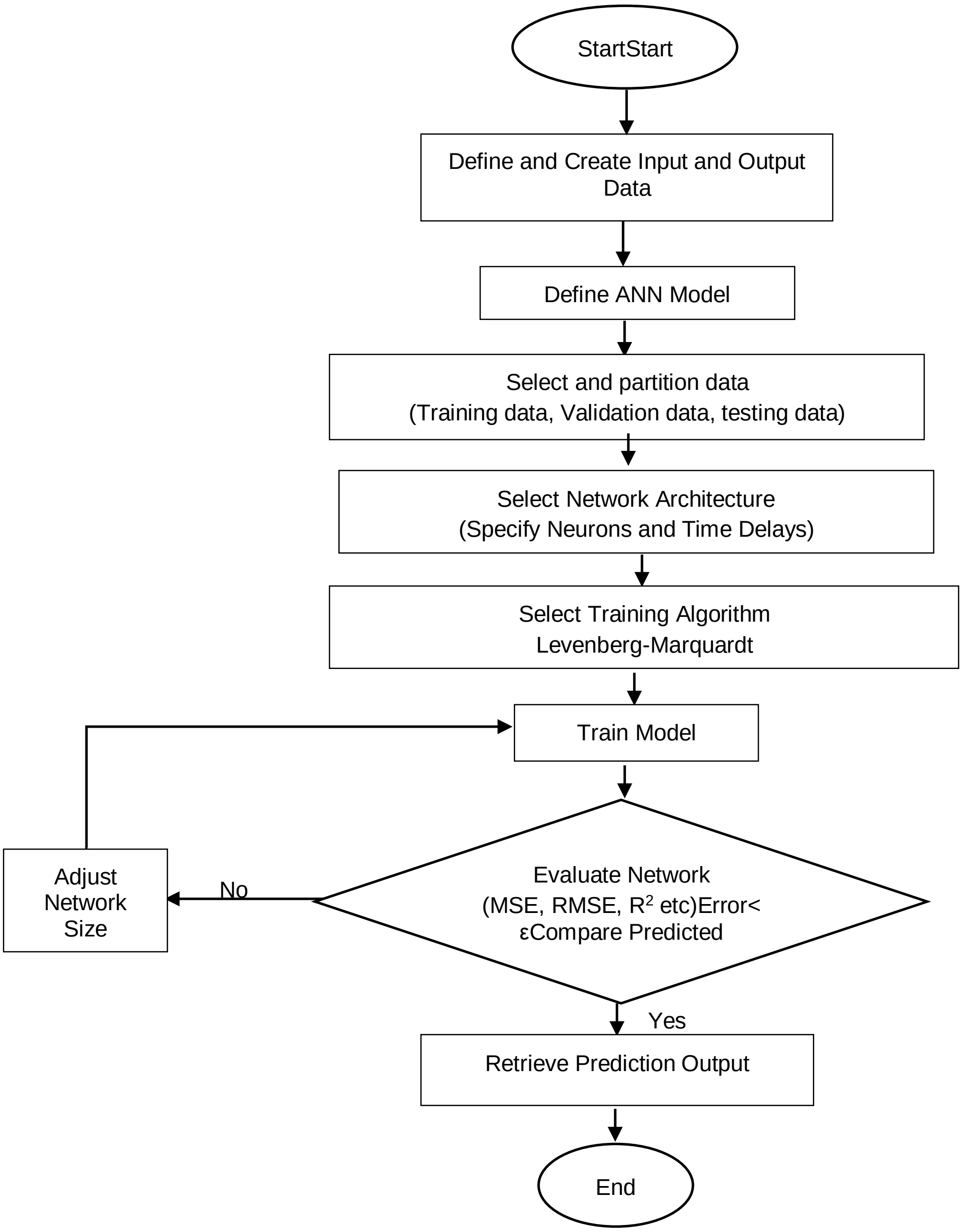

Figure 4. ANN Modelling Flowchart

3.2.3. Performance Metrics of Surrogate Models

The predicted power generation from RSM and ANN models were assessed and compared in terms of statistical performance metricsincluding coefficient of determination (R^2), adjusted, standard deviation and root mean squared error (RMSE). The formulas for these metrics are given:

$$R^2 = \frac{\sum_{i=1}^{n}\left(x_{a,i} - x_{p,i}\right)^2}{\sum_{i=1}^{n}\left(x_{p,i} - x_{a,ave}\right)^2} \quad (11)$$

$$Adjusted R^2 = 1 - \left[\left(1 - R^2\right) \times \frac{n-1}{n-k-1}\right] \quad (12)$$

$$RMSE = \sqrt{\frac{1}{n}\sum_{i=1}^{n}\left(x_{p,i} - x_{a,i}\right)^2} \quad (13)$$

Where n is the number of experimental runs $x_{p,i}$is the estimated values, $x_{a,i}$is the experimental values, $x_{a,ave}$ is the average experimental values, k is the number of input variables

3.6.4. Power Generation Optimization

Optimization was carried out using both Response Surface Methodology (RSM) and artificial neural network coupled Genetic Algorithm (ANN-GA). Initially, a quadratic model was developed through RSM. This model was optimized using RSM itself, and then it was exported to MATLAB, where GA was applied for further optimization. This process yielded two distinct optimization outcomes—one from RSM and the other from GA. These results were subsequently compared, focusing on the values of the independent variables and the resulting optimized power generated.

4. RESULTS

The results for power generationfrom the surrogate models conducted is presented in this section which model result results from RSM and ANN, and optimisation results from RSM and ANN-GA.

4.1. Results for RSM analyses

The results of the RSM modelling are presented and discussed in this section, encompassing Table 1, Table 2, and Table 3. These tables display both the actual output from the process simulation and the corresponding predicted output responses from RSM, considering input variables such as working fluid flowrate, working fluid outlet pressure and turbine outlet pressure. Among several regression models tested, the quadratic model demonstrated the highest fit to the actual data for as shown in Table 1 and was selected for its superior prediction accuracy. Equation 20 is the quadratic model generated by RSM for the power generation.

Table 1. Error data for RSM model analyses

Source	P value	R^2	Adjusted R^2	
Linear	<0.0001	0.8850	0.8145	
2FI	0.1381	0.9117	0.7587	
Quadratic	0.0001	0.9923	0.9462	Suggested
Cubic		1.0000		Aliased

$$\textit{Power Generation (kWh)} = 475.8 + 144.374\,A + 243.491B - 76.9425C + $$

$$+ 81.0775AB - 26.025AC + -3.99BC + 0.15625A^2 - 96.3788B^2 + 11.2188C^2$$

Where variables A, B, C represent working fluid flowrate (kg/s), working fluid inlet pressure (bar) and turbine outlet pressure (bar) respectively.This equation can be utilized to predict the response for given levels of each factor. To achieve accurate predictions, the levels must be specified in the original units of each factor, both for the input parameters and the response variables. To assess the significance of the model coefficients, Analysis of Variance (ANOVA) was conducted. Table 2 and Table 3 summarize the ANOVA results and fit metrics for the power generation output responses. These tables include degrees of freedom, mean square values, F-values, and p-values. In Table 5, the p-values are smaller than 0.0001, and the high F-values indicate that the models are statistically significant.

The RSM model's predictions closely matched the actual simulation data, as shown in Table 8. To evaluate the statistical significance of the model, an Analysis of Variance (ANOVA) was conducted on equation 14, as detailed in Table 2. The results indicated that the model was statistically significant ($p < 0.0007$), with a non-significant lack of fit. The adjusted R^2 value (0.9923) and predicted R^2 value (0.9462) further confirmed the model's robustness, suggesting that the key factors influencing power generated—such as working fluid flowrate (kg/s), working fluid inlet pressure (bar) and turbine outlet pressure (bar)—were effectively captured by the model.

Table 2. ANOVA

Source	Sum of Squares	df	Mean Square	F-value	p-value	
Model	7.57E+05	9	84093.51	230.56	< 0.0001	significant
A-Working Fluid Flowrate	1.67E+05	1	1.67E+05	457.19	< 0.0001	
B-Working Fluid Outlet Pressure	4.74E+05	1	4.74E+05	1300.42	< 0.0001	
C-Turbine Outlet Pressure	47361.19	1	47361.19	129.85	< 0.0001	
AB	26294.24	1	26294.24	72.09	< 0.0001	
AC	2709.2	1	2709.2	7.43	0.0295	
BC	63.68	1	63.68	0.1746	0.6886	
A^2	0.1028	1	0.1028	0.0003	0.9871	
B^2	39111	1	39111	107.23	< 0.0001	
C^2	529.94	1	529.94	1.45	0.2672	
Residual	2553.12	7	364.73			
Lack of Fit	2553.12	3	851.04			
Pure Error	0	4	0			
Cor Total	7.59E+05	16				

Figure 5 shows the relationship between the actual and predicted results from the RSM model

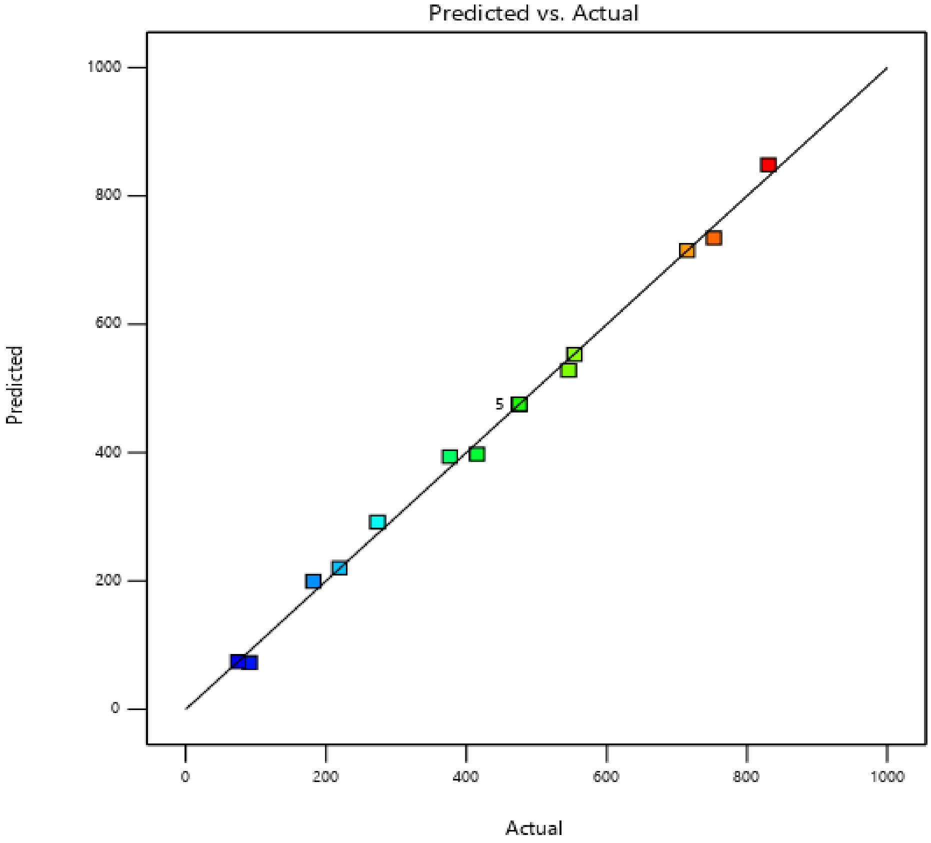

Figure 5.Parity plot of Actual vs Predicted values of power generated from RSM model

The parity plot in figure 4 shows how the data points from the actual (process simulation datal) and predicted power generated clustered aroun the 45° line. This figure demonstrate that the actual and predicted output responses closely align around the 45-degree line for all indicating strong regression and agreement between the two datasets. Thus, there exists an acceptable level of agreement between the actual process simulation data and the predicted responses from the RSM models.

4.2. Interaction Response of Input Parameters on Power Generated using 3D Plots

Figure 6 illustrates the 3D response surface plot depicting the interaction between independent variables and power production while figure 7 shows the contour plots for the power production from the RSM modelling. These plots visually represent how changes in the independent variables (such working fluid flowrate (kg/s), working fluid inlet pressure (bar) and turbine outlet pressure (bar)) influence the power production providing insights into their mutual interactions.

Both the 3D surface plots in figure 6a-c and the contour plots in Figure 7a-c are used to make analysis of the interactions between the independent variables and the response.

Figure 6a and Figure 7a shows the interactive effect of working fluid flowrate and working fluid outlet pressure on the power generated. As can be observed, increasing the working fluid flowrate increases the power generated by the binary ORC system at higher outlet pressures of the working fluid. In other words both the flowrate and outlet pressures of the working fluid have positive effect on the power generated as their increase results to higher power generated.

Figure 6b and Figure 7b shows the interactive effect of working fluid flowrate and turbine outlet pressure on the power generated. It can be observed that at lower turbine outlet pressures, increasing the flowrate of the working fluid increases the power generated by the turbine. However, when the flowrate of the working fluid is kept constant, the power generated by the turbine decreases as the turbine outlet pressure increases.

Figure 6c and Figure 7c shows the interactive effect of working fluid outlet pressure and turbine outlet pressure on the power generated. It is seen that at lower turbine outlet pressures, increasing the outlet pressure of the working fluid increases the power generated by the turbine. However, when the outlet pressure of the working fluid is kept constant, the power generated by the turbine decreases as the turbine outlet pressure increases.

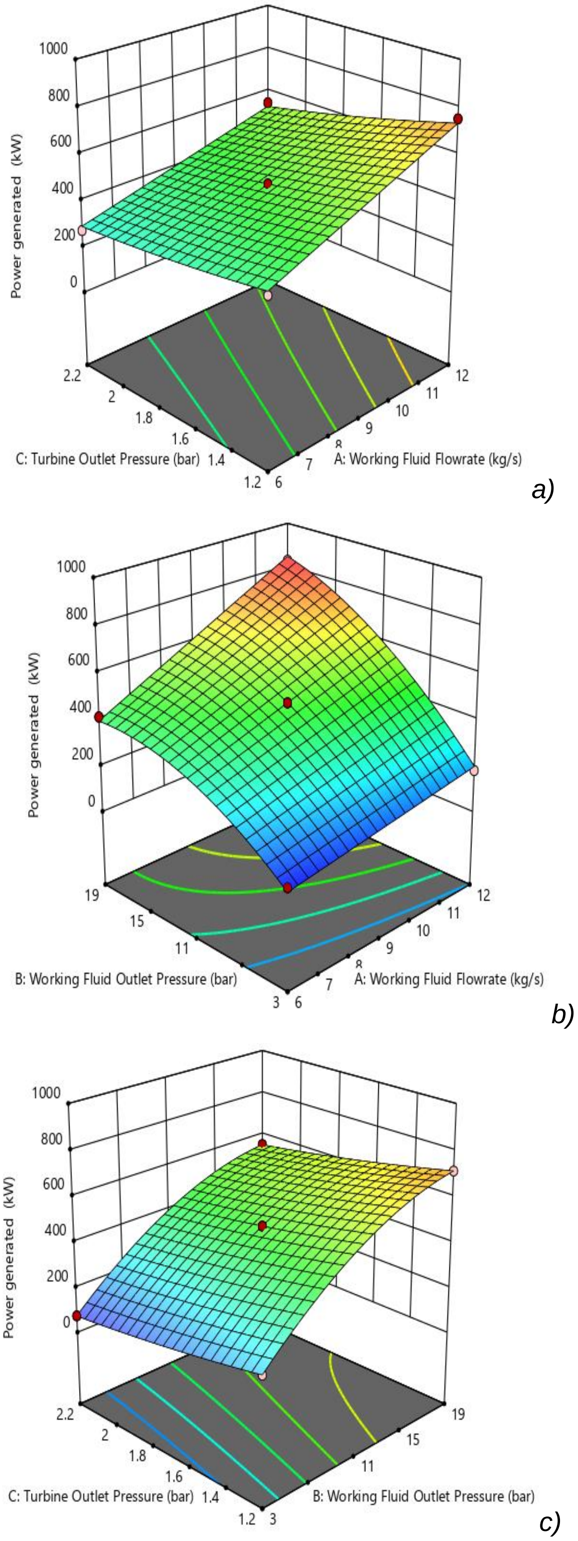

Figure 6. 3D response surface plots for power production from RSM

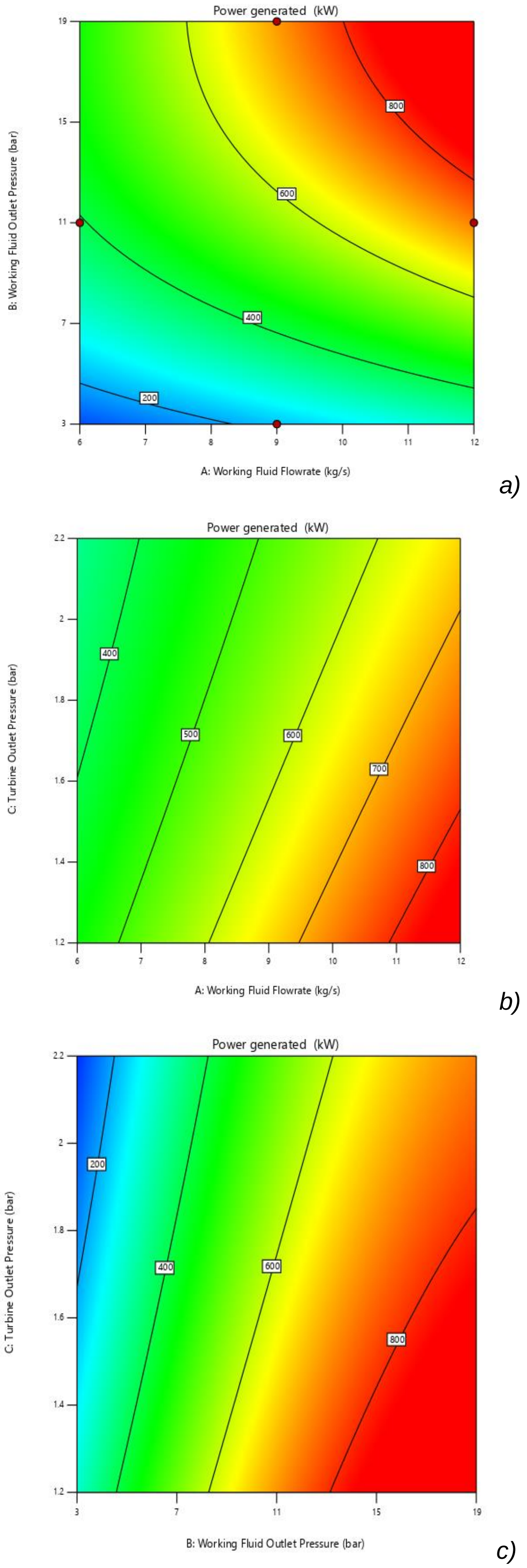

Figure 7. Contour plots for power production from RSM

4.3. Results for ANN Modelling

The ANN neural network model was employed to establish the relationship between the input factors and the output response. The selection of the optimal neural network for the ANN analysis was based on the performance of various transfer functions, training algorithms, network architectures, and the optimal number of neurons. Multiple training sessions were conducted, and the best-performing results were selected to represent the model. The performance of these factors was evaluated using metrics such as R² values, mean squared error (MSE), root mean squared error (RMSE), mean absolute error (MAE), and mean absolute percentage error (MAPE). A higher R² value, along with lower MSE, RMSE, MAE, and MAPE values, indicates better predictive accuracy in relation to the model's factors. The R-value corresponding to the selected trained ANN model is presented in Figure 6.

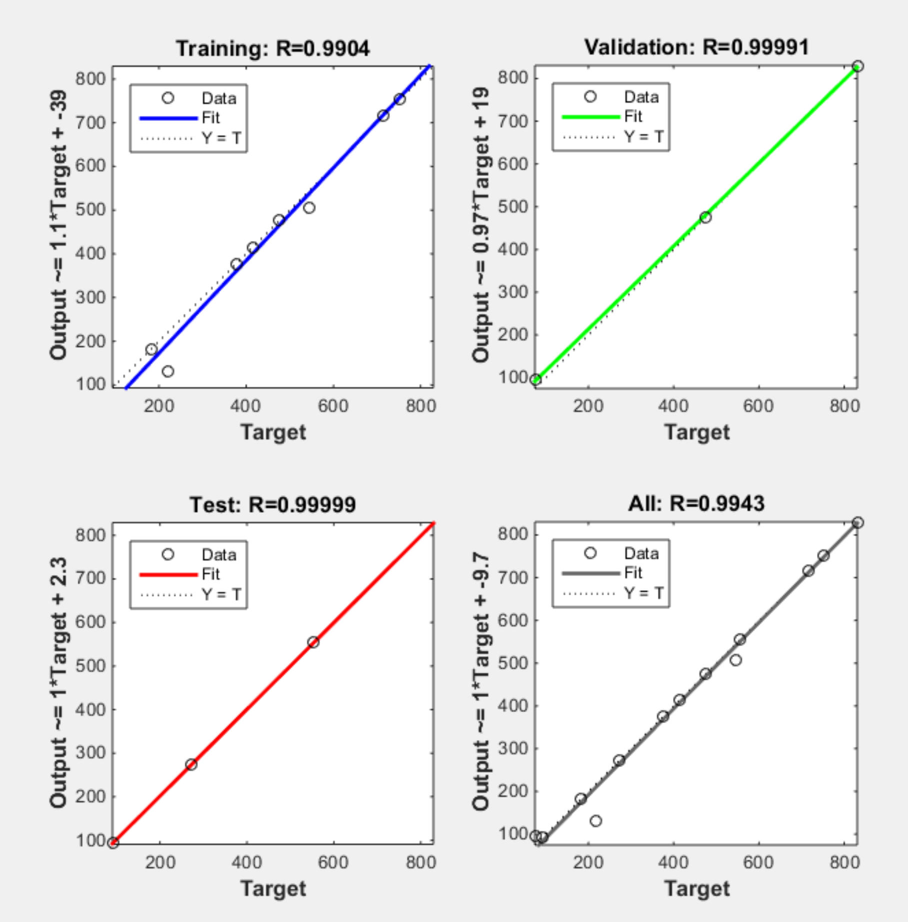

Figure 8.Regressionplot for the training in ANN

Figure 8 shows the Regression values corresponding to the ANN training performed. The Overall R values for the ANN model was 0.9943. It is seen that ANN gave notably high R values which indicate very good predictions for the power generated.

Table 4 shows the values predicted by RSM and ANN models for each of the input variables and actual output data. Table 4 shows that there is a high correlation between the actual and predicted results for the RSM and the ANN models.

Table 4. Actual and predicted results for power generated corresponding to RSM and ANN modelling.

Run	Working Fluid Flowrate, kg/s	Working Fluid Outlet Pressure bar	Turbine Outlet Pressure, bar	Actual Power Generated kW	RSM Predicted Power Generated, kW	ANN Predicted Power Generated, kW
1	9	11	1.7	475.8	475.8	475.9489
2	6	19	1.7	415.2	397.62	415.1577

3	9	11	1.7	475.8	475.8	475.9489
4	12	11	1.2	753	734.52	753.0379
5	9	19	1.2	714.7	715.06	714.7729
6	12	3	1.7	181.8	199.38	181.8843
7	6	11	1.2	376.5	393.72	376.4783
8	9	11	1.7	475.8	475.8	475.9489
9	9	3	2.2	74.56	74.2	94.31542
10	9	11	1.7	475.8	475.8	475.9489
11	6	3	1.7	90.91	72.79	93.33428
12	6	11	2.2	273.4	291.88	273.4133
13	9	19	2.2	554.1	553.2	554.146
14	9	11	1.7	475.8	475.8	475.9489
15	12	11	2.2	545.8	528.58	505.9555
16	9	3	1.2	219.2	220.1	132.1279
17	12	19	1.7	830.4	848.52	829.374

Table 5 shows the comparison of performance metrics for the RSM and the ANN predictions.

Table 5: Performance metrics for RSM and ANN Predictions

	RSM	ANN
MSE	150.1611	562.7336
RMSE	12.2540	23.7220
MAE	8.5482	8.8932
MAPE	0.0318	0.0450
R^2	0.9966	0.9886

From Table 5, it is seen that both RSM and ANN models gave realistic predictions of the actual/experimental data for the error metrics considered. In terms of R^2 values, both RSM and ANN gave predictions higher than 0.9 which indicates very good predictions of the test data. The R^2 values for RSM was 0.9966, while that for ANN was 0.9886. Thus, relative to R^2 values the RSM performed better than the ANN. The MSE and MAE of RSM model were 150.1611 and 12.2540 respectively while the MSE and MAE for ANN were 562.7336 and 23.722respectively. The MAPE of RSM and ANN models were 3.18% and 4.5% respectively it is evident that the RSM performed better than the ANN model.

Additionally, the model performance in this study were compared with performance of scholars who conducted modelling on geothermal systems as summarized in Table 6.

Table 6. Comparison of model performance of study with results from literature

Area of Study	Target Parameter	Model Used	R2	RMSE	Reference
Binary Geothermal Power Plant	Power Generated	ANN	0.999	0.272	[27]
Double Flash Cycle Geothermal Turbine to	Net Power Generated	Multiple Linear Regression	-	0.9997	[72]
Geothermal Binary ORC Systems	System Performance	Taguchi model	0.941	4.29	[73]
Geothermal ORC system	Power Generated	ANN	0.9986	51.2	[74]
Geothermal ORC system	Turbine performance	ANN	0.9989	0.0009	[25]
Enhanced Geothermal systems	Geothermal production temperature	ANN	0.998	0.067	[75]
Geothermal Binary ORC system	Power Generated	ANN	0.9886	23.7220	This Study
		RSM	0.9966	12.2540	

Table 6 shows the performance of various studies on geothermal systems using various modelling techniques in describing the relationship between the input parameters and the target output. It can be observed that from literature several models have been successfully utilised for modelling geothermal systems with excellent performance. Moreso, it is seen that the performance of the ANN and RSM model realised in this study are close to the performances seen in literature in several studies conducted on geothermal systems especially in the area of geothermal binary ORC systems for power generation.

4.4.Optimisation of Power Generated

Table 7 gives the summary of the optimisation results of power generated corresponding to RSM and ANN-GA optimisations performed.

Table 7. Optimisation results

Parameter	RSM	ANN-GA	Hysys Check
Working fluid flowrate, MMscfd	11.8	12	12
Working fluid outlet pressure, bar	18.47	19	19
Turbine outlet pressure	1.2	1.2	1.2
Power generated, kW	940.78	958.48	952.9
Power Generated from Hysys at optimal factors, kW	927.2	952.9	-
Percentage error	1.46	0.59	-

Table 7 provides a comparative analysis of the optimization results obtained using two distinct methodologies: Response Surface Methodology (RSM) and the coupled Artificial Neural Network-Genetic Algorithm (ANN-GA). These optimization techniques adopt fundamentally different approaches, which naturally result in variations in their outcomes. To evaluate their performance, an optimization check was conducted in Aspen HYSYS to determine the optimal input factors based on sensitivity analysis trends. The optimal input variables predicted by both methods were subsequently inputted into HYSYS to verify the corresponding power output.

From the results presented in the table, it is evident that ANN-GA demonstrated superior optimization capabilities. The method accurately predicted the ranges of input variables—working fluid flowrate, working fluid outlet pressure, and turbine outlet pressure—that yielded the optimal power output. The optimal values identified by ANN-GA were consistent with those determined directly by HYSYS, signifying excellent alignment and optimization performance. This consistency highlights the robustness and reliability of ANN-GA in predicting the key input parameters required for maximizing power generation.

In contrast, RSM struggled to accurately predict the optimal input values. Although RSM provided a set of predicted optimal factors, these values deviated from the actual optimal values determined by HYSYS. To further assess the optimization performance of both methodologies, their predicted input values were tested in HYSYS, and the corresponding power outputs were analyzed. ANN-GA achieved a power output of 958.48 kW when its predicted values were inputted, closely matching the 952.9 kW output determined directly by HYSYS. This resulted in a percentage error of just 0.59%, demonstrating the high accuracy of ANN-GA not only in parameter prediction but also in achieving optimal power generation.

On the other hand, the power output generated using the input factors predicted by RSM was 927.2 kW when tested in HYSYS. This value significantly deviated from the 940.78 kW predicted by RSM itself, resulting in a higher percentage error of 1.46%. The discrepancy between RSM's predicted and actual performance highlights its limitations in identifying the precise input variables required for maximum power generation. Moreover, the power output achieved by RSM was considerably lower than the optimal power output obtained via ANN-GA, further emphasizing the comparative weakness of RSM as an optimization tool for this process.

The analysis highlights the robustness and accuracy of the ANN-GA model, which not only closely aligned with HYSYS predictions but also consistently delivered power outputs that were nearly identical to the actual optimal values. Its integration of machine learning (via ANN) and evolutionary optimization (via GA) likely contributed to its superior performance by effectively capturing complex nonlinear relationships and exploring the solution space more comprehensively. ANN-GA significantly outperformed RSM in optimization performance. While RSM exhibited notable errors and limitations, ANN-GA proved to be a highly reliable and robust optimization technique, demonstrating its potential as a powerful tool for process optimization in scenarios where accuracy and efficiency are paramount.

5. CONCLUSION

Modelling and optimization of geothermal binary Organic Rankine Cycle (ORC) systems has been accomplished in this study, leveraging Aspen HYSYS process simulations with RSM and ANN models. Aspen HYSYS was utilized to model the process system and generate simulation data, which served as the foundation for developing RSM and ANN models. The RSM and ANN models were designed using the Box-Behnken Design (BBD) for three factors: working fluid flowrate, working fluid outlet pressure, and turbine outlet pressure, while optimization was performed independently using RSM and ANN-GA.

In terms of modelling, both RSM and ANN demonstrated excellent capabilities in capturing the nonlinear relationships between the input parameters and the system's power generation. The RSM model, however, outperformed ANN with a superior coefficient of determination (R^2) of

0.9966 compared to 0.9886 for ANN. Additionally, the RSM model achieved a lower root mean square error (RMSE) of 12.254 compared to ANN's RMSE of 23.722, highlighting its superior predictive accuracy and robustness in modeling the system’s behavior.

When applied to optimization, the ANN-GA demonstrated better performance than RSM, achieving optimal power generation values with a lower percentage error when validated against Aspen HYSYS. The power output predicted by ANN-GA was 958.48 kW, exhibiting a minimal error deviation of 0.59% compared to the Hysys-validated output. In contrast, RSM gave an optimal power output of 940.78 kW which gave a percentage error deviation of 1.46%. when validated in HYSYS. These results highlights the superior optimization capabilities of ANN-GA, which effectively integrated machine learning and evolutionary algorithms to achieve higher accuracy in navigating the solution space than RSM.

6. REFERENCES

[1] N.Izuwa, S. Ekwueme, N. Okereke, O.Nwanwe, N. Ohia (2024a) Comparative analysis of geothermal binary ORC systems: performance and environmental considerations for CO2 andwater as geofluids. Zastita Materijala, 65(1), 73-85.

[2] M.Haghghi, Z. Mohammadi, M. Delpisheh, E. Nadimi, H. Athari (2023) Multi-variable study/optimization of a novel geothermal-driven poly-generation system: application of a soft-computing intelligent procedure and MOGWO. Process Safety and Environmental Protection, 171, 507-531.

[3] N.Izuwa, N. Okereke, O. Nwanwe, E. Ejiga, S. Ekwueme, A. Chikwe, C. Ohaegbulam (2024b) Modeling of Wellbore Heat Transfer in Geothermal Production Well. In IOP Conference Series: Earth and Environmental Science, 1342(1), 012041. IOP Publishing.

[4] P.M.B. Abrasaldo, S.J. Zarrouk, A.W. Kempa-Liehr (2024) A systematic review of data analytics applications in above-ground geothermal energy operations. Renewable and Sustainable Energy Reviews, 189, 113998.

[5] N. C. Izuwa, V. E. Udigwe, O. I. Nwanwe, N. U. Okereke (2022) Investigation of the Potentials of Heat Extraction from Abandoned Oil Wells for Electricity Generation. Petroleum & Coal, 64(4).

[6] C. Temizel, U. Odi, C. Cetin, Y. Pamukcu, C. Yegin (2024, April) Challenges and Recent Advances in Modeling and Simulation of Geothermal Systems. In SPE Western Regional Meeting, p. D021S010R006. SPE.

[7] Z. Said, P. Sharma, A. K. Tiwari, Z. Huang, V. G. Bui, A. T. Hoang (2022) Application of novel framework based on ensemble boosted regression trees and Gaussian process regression in modelling thermal performance of small-scale Organic Rankine Cycle (ORC) using hybrid nanofluid. Journal of Cleaner Production, 360, 132194.

[8] J. Oyekale, B. Oreko (2023) Machine learning for design and optimization of organic Rankine cycle plants: A review of current status and future perspectives. Wiley Interdisciplinary Reviews: Energy and Environment, 12(4), e474.

[9] S. Ramachandran, S. S. Bhogilla, P. K. Vijayan (2024) Techno-economic analysis and optimization of a binary geothermal combined district heat and power plant for Puga Valley, India. Renewable Energy, 234, 121223.

[10] A. G. Sangesaraki, A. Gharehghani, J. R. Mehrenjani (2023) 4E analysis and machine learning optimization of a geothermal-based system integrated with ejector refrigeration cycle for efficient hydrogen production and liquefaction. International Journal of Hydrogen Energy, 48(82), 31875–31904.

[11] J. Xie, J. Wang (2022) Compatibility investigation and techno-economic performance optimization of whole geothermal power generation system. Applied Energy, 328, 120165.

[12] P. Ding, K. Zhang, Z. Yuan, Z. Wang, D. Li, T. Chen, … R. Shofahaei (2021) Multi-objective optimization and exergoeconomic analysis of geothermal-based electricity and cooling system using zeotropic mixtures as the working fluid. Journal of Cleaner Production, 294, 126237.

[13] R. DiPippo (2024) Extraction turbines and feed-heating in geothermal binary plants: A thermodynamic performance assessment. Geothermics, 116, 102857.

[14] M. A. Haghghi, Z. Mohammadi, M. Delpisheh, E. Nadimi, H. Athari (2023) Multi-variable study/optimization of a novel geothermal-driven poly-generation system: application of a soft-computing intelligent procedure and MOGWO. Process Safety and Environmental Protection, 171, 507–531.

[15] D. Pan, S. G. Farkoush (2023) Comprehensive analysis and multi-objective optimization of power and cooling production system based on a flash-binary geothermal system. Applied Thermal Engineering, 229, 120398.

[16] T. Parikhani, M. Delpisheh, M. A. Haghghi, S. G. Holagh, H. Athari (2021) Performance enhancement and multi-objective optimization of a double-flash binary geothermal power plant. Energy Nexus, 2, 100012.

[17] E. R. Khama, E. Z. Loyibo, W. Okologume, S. T. Ekwueme, C. V. Okafor, N. P. Ohia (2024) Investigation of the performance of activated carbon derived from ripe plantain peels for CO_2 capture: Modelling and optimisation using response surface methodology. Zastita Materijala, 65(2), 258–272.

[18] M. Assareh, P. Yavari, M. Jamil, B. Rafiei, E. Assareh (2024) Thermodynamic analysis of a multiple energy production system based on geothermal energy for commissioning in Canada and optimization by response surface method (RSM). Energy, 302, 131669.

[19] A. Haghighi, M. R. Pakatchian, M. E. H. Assad, V. N. Duy, M. Alhuyi Nazari (2021) A review on geothermal Organic Rankine cycles: modeling and optimization. Journal of Thermal Analysis and Calorimetry, 144, 1799–1814.

[20] A. M. Al Jubori, R. Al-Dadah, S. Mahmoud (2017) Performance enhancement of a small-scale organic Rankine cycle radial-inflow turbine through multi-objective optimization algorithm. Energy, 131, 297–311.

[21] M. E. Kazemian, S. G. Nassab, E. J. Javaran (2022) Comparative techno-economic investigation of CCHP combined by GSHP based on response surface methodology. Thermal Science and Engineering Progress, 34, 101386.

[22] S. Azizi, H. Shakibi, A. Shokri, A. Chitsaz, M. Yari (2023) Multi-aspect analysis and RSM-based optimization of a novel dual-source electricity and cooling cogeneration system. Applied Energy, 332, 120487.

[23] Z. Xue, S. Yao, H. Ma, C. Zhang, K. Zhang, Z. Chen (2023) Thermo-economic optimization of an enhanced geothermal system (EGS) based on machine learning and differential evolution algorithms. Fuel, 340, 127569.

[24] E. Assareh, S. Hoseinzadeh, N. Agarwal, M. Delpisheh, A. Dezhdar, M. Feyzi, … M. Lee (2023) A transient simulation for a novel solar-geothermal cogeneration system with a selection of heat transfer fluids using thermodynamics analysis and ANN intelligent (AI) modeling. Applied Thermal Engineering, 231, 120698.

[25] A. Tugcu, O. Arslan (2017) Optimization of geothermal energy aided absorption refrigeration system—GAARS: A novel ANN-based approach. Geothermics, 65, 210–221.

[26] D. Ziviani, N. A. James, F. A. Accorsi, J. E. Braun, E. A. Groll (2018) Experimental and numerical analyses of a 5 kWe oil-free open-drive scroll expander for small-scale organic Rankine cycle (ORC) applications. Applied Energy, 230.

[27] C. Yilmaz, I. Koyuncu (2021) Thermoeconomic modeling and artificial neural network optimization of Afyon geothermal power plant. Renewable Energy, 163, 1166–1181.

[28] G. Çetin, O. Özkaraca, A. Keçebaş (2021) Artificial neural network-based optimization of geothermal power plants. In Thermodynamic Analysis and Optimization of Geothermal Power Plants, pp. 263–278. Elsevier.

[29] C. Yilmaz, O. Sen (2022) Thermoeconomic analysis and artificial neural network based genetic algorithm optimization of geothermal and solar energy assisted hydrogen and power generation. International Journal of Hydrogen Energy, 47(37), 16424–16439.

[30] S. Chanthamaly, A. Promwungkwa, K. Ngamsanroaj (2023) Optimal operation of geothermal power plant by artificial neural network.

[31] J. C. Hsieh, Y. C. Li, Y. C. Lin, T. C. Yeh (2024) Off-design performance and economic analysis in coupled binary cycle with geothermal reservoir and turbo-expander. Energy, 305, 132274.

[32] J. Zhou, Y. T. Chu, J. Ren, W. Shen, C. He (2023) Integrating machine learning and mathematical programming for efficient optimization of operating conditions in organic Rankine cycle (ORC) based combined systems. Energy, 281, 128218.

[33] N. Chitgar, A. Hemmati, M. Sadrzadeh (2023) A comparative performance analysis, working fluid selection, and machine learning optimization of ORC systems driven by geothermal energy. Energy Conversion and Management, 286, 117072.

[34] H. Shakibi, M. Y. Faal, E. Assareh, N. Agarwal, M. Yari, S. A. Latifi, … M. Lee (2023) Design and multi-objective optimization of a multi-generation system based on PEM electrolyzer, RO unit, absorption cooling system, and ORC utilizing machine learning approaches; a case study of Australia. Energy, 278, 127796.

[35] W. Ling, Y. Liu, R. Young, T. T. Cladouhos, B. Jafarpour (2024) Efficient data-driven models for prediction and optimization of geothermal power plant operations. Geothermics, 119, 102924.

[36] A. Farajollahi, M. Baharvand, H. R. Takleh (2024) Modeling and optimization of hybrid geothermal-solar energy plant using coupled artificial neural network and genetic algorithm. Process Safety and Environmental Protection, 186, 348–360.

[37] J. Xie, J. Wang (2022) Compatibility investigation and techno-economic performance optimization of whole geothermal power generation system. Applied Energy, 328, 120165.

[38] A. Farajollahi, M. Rostami, M. Feili, H. Ghaebi (2023) Thermodynamic and economic evaluation and optimization of the applicability of integrating an innovative multi-heat recovery with a dual-flash binary geothermal power plant. Clean Technologies and Environmental Policy, 25(5), 1673–1698.

[39] A. A. Mana, S. I. Kaitouni, T. Kousksou, A. Jamil (2023) Enhancing sustainable energy conversion: Comparative study of superheated and recuperative ORC systems for waste heat recovery and geothermal applications, with focus on 4E performance. Energy, 284, 128654.

[40] A. D. P. Putera, A. N. Hidayah, A. Subiantoro (2019) Thermo-economic analysis of a geothermal binary power plant in Indonesia—A pre-feasibility case study of the Wayang Windu site. Energies, 12(22), 4269.

[41] M. Ozturk, I. Dincer (2021) Development of a combined flash and binary geothermal system integrated with hydrogen production for blending into natural gas in daily applications. Energy Conversion and Management, 227, 113501.

[42] H. Ghasemi, M. Paci, A. Tizzanini, A. Mitsos (2013) Modeling and optimization of a binary geothermal power plant. Energy, 50, 412–428.

[43] A. N. Hidayah, A. D. P. Putera, A. Subiantoro (2020, February) Selection of optimum working fluid and cycle configuration of organic Rankine cycle (ORC) as bottoming binary cycle at Wayang Windu geothermal power plant. In Proceedings of the 45th Workshop on Geothermal Reservoir Engineering, Stanford University, California.

[44] G. Buster, P. Siratovich, N. Taverna, M. Rossol, J. Weers, A. Blair, … J. Akerley (2021) A new modeling framework for geothermal operational optimization with machine learning (Gooml). Energies, 14(20), 6852.

[45] A. M. Moustafa, A. S. Shehata, A. I. Shehata, A. A. Hanafy (2022) Reuse of abandoned oil and

gas wells for power generation in Western Desert and Gulf of Suez fields of Egypt. Energy Reports, 8, 1349–1360.

[46] M. T. Islam, M. N. Nabi, M. A. Arefin, K. Mostakim, F. Rashid, N. M. S. Hassan, … S. M. Muyeen (2022) Trends and prospects of geothermal energy as an alternative source of power: A comprehensive review. Heliyon, 8(12).

[47] H. D. V. Venomhata, P. O. Oketch, B. B. Gathitu, P. Chisale (2023) Working fluid selection for the geothermal-solar hybrid cycle at Olkaria II power plant in Kenya. Heliyon, 9(1).

[48] Z. Zeng, Y. Chen, C. Li, Y. Li, X. Wu (2021) Parametric analysis and system optimization of a novel steam production system by synthetic cascade utilization of industrial waste heat. Energy Reports, 7, 5909–5921.

[49] P. H. Niknam, L. Talluri, D. Fiaschi, G. Manfrida (2021) Sensitivity analysis and dynamic modelling of the reinjection process in a binary cycle geothermal power plant of Larderello area. Energy, 214, 118869.

[50] P. Ziółkowski, R. Hyrzyński, M. Lemański, B. Kraszewski, S. Bykuć, S. Głuch, … J. Badur (2021) Different design aspects of an Organic Rankine Cycle turbine for electricity production using a geothermal binary power plant. Energy Conversion and Management, 246, 114672.

[51] S. N. Karlsdottir, H. Pálsson, A. Manadao Bravo Jr, A. Stefánsson, G. O. Boakye (2023, March) Corrosion Testing of Coatings in Simulated ORC Geothermal Heat Exchanger Environment. In AMPP CORROSION (pp. AMPP-2023). AMPP.

[52] S. Davíðsdóttir, B. G. Gunnarsson, K. B. Kristjánsson, B. A. Ledésert, D. I. Ólafsson (2021) Study of corrosion resistance properties of heat exchanger metals in two different geothermal environments. Geosciences, 11(12), 498.

[53] C. Penot, D. Martelo, S. Paul (2023) Corrosion and scaling in geothermal heat exchangers. Applied Sciences, 13(20), 11549.

[54] C. Tong, C. Tong (2019) Advanced Materials Enable Renewable Geothermal Energy Capture and Generation. In Introduction to Materials for Advanced Energy Systems, pp. 321–377.

[55] F. Fanicchia, S. N. Karlsdottir (2023) Research and development on coatings and paints for geothermal environments: A review. Advanced Materials Technologies, 8(18), 2202031.

[56] A. B. N. Jayakumari, N. G. Malik, G. Mittal, D. Martelo, N. Kale, S. Paul (2023) A review on geothermal heat exchangers: challenges, coating methods, and coating materials.

[57] M. AlGaiar, J. Afolabi (2024, May) Enhancing Geothermal Wells Integrity: Key Considerations and Challenges from Drilling to Production. In SPE Symposium: Well Integrity Management, p. D021S005R001. SPE.

[58] O. Jiang, L. Cao, W. Zhu, X. Zheng (2024) Review of Reservoir Damage Mechanisms Induced by Working Fluids and the Design Principles of Reservoir Protection Fluids: From Oil–Gas Reservoirs to Geothermal Reservoirs. Energies, 17(19), 4895.

[59] W. Kibikas, C. Chang, S. J. Bauer, S. Nakagawa, P.Dobson, T. Kneafsey, A. Samuel (2024) Time-dependent thermal degradation of lost circulation materials in geothermal systems. Geothermics, 121, 103038.

[60] B. Meng, G. Yan, P. He, Q. Zhou, W. Xu, Y. Qiao (2025) Nanotechnology applications in geothermal energy systems: Advances, challenges and opportunities. Advances in Geo-Energy Research, 15(2), 172–180.

[61] N. Olry, A. Cascone, M. Eils, L. Bussaglia, V. Smith (2024) Geothermal Drilling Fluid Meets Performance, Environmental, and Regulatory Challenges in the Alps. In Proceedings of the 2024 AADE Fluids Technical Conference and Exhibition. American Association of Drilling Engineers.

[62] S. Paul, C. Leahy (2024, March) Performance of Damaged Thermal Spray Coatings in Phase Change Materials (PCMs) Used in Geothermal Plants. In AMPP CORROSION (pp. AMPP-2024). AMPP.

[63] L. Wan, J. Wang, W. Yue, F. Lin, C. Gao, X. Liu, … Z. Huang (2024) Composites with Synergistically Enhanced Thermodynamic and Mechanical Properties for Geothermal Heat Exchangers. Advanced Engineering Materials, 26(22), 2401581.

[64] H. Yunpeng, Z. Mingming, D. Ji, C. Chunrong, L. Junfu, Z. Dongping, … M. Chunchi (2024) Study on the thermo-mechanical properties of adaptive thermal control anchoring materials in high-geothermal tunnels. Construction and Building Materials, 447, 138156.

[65] Q. Zhang, Y. Q. Feng, K. J. Xu, H. J. Liang, Z. N. Liu, C. Y. Zhao, C. N. Markides (2024) Dynamic behaviour and performance evaluation of a biomass-fired organic Rankine cycle combined heat and power (ORC-CHP) system under different control strategies. Applied Thermal Engineering, 248, 123236.

[66] J. Wu, Y. Liang, Z. Sun, Y. Zhu, J. Ye, J. Lu (2024) Dynamic analysis and control strategy of ORC coupled ejector expansion refrigeration cycle driven by geothermal water. Journal of Cleaner Production, 445, 141309.

[67] S. Davoodi, M. Al-Shargabi, D. A. Wood, S. Slivkin, G. Shishaev, V. S. Rukavishnikov (2024) Geothermal energy recovery from abandoned petroleum wells: A review of the challenges and opportunities. Sustainable Energy Technologies and Assessments, 68, 103870.

[68] S. Bilodeau, M. Carty (2024) Conversion of Waste Heat into Electricity Using Combined TESS-ORC Technology. SSRN Paper.

[69] I. Ekeke, C. Mgbemere, C. Nwanze, F. Aniukwu, C. Njoku (2025) Musa paradisiaca stem sap extract as corrosion inhibitor for aluminum protection in acidic environment. Zastita Materijala.

[70] M. H. E. Ahmadi, A. Mosayebi (2021) Fischer–Tropsch synthesis over Co-Ni/Al_2O_3 catalyst: Comparison between comprehensive kinetic modeling, Artificial Neural Network, and a novel hybrid GA-Fuzzy models. Journal of the Taiwan Institute of Chemical Engineers, 127, 32–45.

[71] M. Hojjat, S. G. Etemad, R. Bagheri, J. Thibault (2011) Thermal conductivity of non-Newtonian

nanofluids: experimental data and modeling using neural network. International Journal of Heat and Mass Transfer, 54(5–6), 1017–1023.

[72] E. H. Martinez, M. C. P. Carlos, J. I. C. Solis, M. C. P. Avalos (2020) Thermodynamic simulation and mathematical model for single and double flash cycles of Cerro Prieto geothermal power plants. Geothermics, 83, 101713.

[73] S. Ata, A. Kahraman, R. Şahin (2020) Prediction and sensitivity analysis under different performance indices of R1234ze ORC with Taguchi's multi-objective optimization. Case Studies in Thermal Engineering, 22, 100785.

[74] A. Khosravi, S. Syri, X. Zhao, M. E. H. Assad (2019) An artificial intelligence approach for thermodynamic modeling of geothermal-based organic Rankine cycle equipped with solar system. Geothermics, 80, 138–154.

[75] L. Zhou, Y. Zhang, Z. Hu, Z. Yu, Y. Luo, Y. Lei, … Y. Ma (2019) Analysis of influencing factors of the production performance of an enhanced geothermal system (EGS) with numerical simulation and artificial neural network (ANN). Energy and Buildings, 200, 31–46.

IZVOD

MODELIRANJE I OPTIMIZACIJA GEOTERMALNIH BINARNIH ORC SISTEMA KORIŠĆENJEM METODOLOGIJE POVRŠINE ODGOVORA I VEŠTAČKIH NEURONSKIH MREŽA

Ova studija se fokusira na modeliranje i optimizaciju geotermalnih binarnih sistema Organic Rankine Cicle (ORC) kako bi se poboljšala proizvodnja energije iz geotermalnih sistema koji koriste vodu kao geofluid. Aspen HISIS, koji koristi Peng-Robinsonov paket svojstava, korišćen je za simulaciju procesa, generišući kritične podatke procesa za naknadno modeliranje i optimizaciju. Metodologija površine odgovora (RSM) i veštačka neuronska mreža (ANN) su korišćene za modeliranje odnosa između ulaznih faktora i izlaznog odgovora, koristeći Bok-Behnken dizajn (BBD) za tri ključne ulazne varijable: brzinu protoka radnog fluida, izlazni pritisak radnog fluida i izlazni pritisak turbine. I RSM i ANN su pokazali snažne prediktivne sposobnosti, pri čemu je RSM postigao R2 vrednost od 0,9966 i RMSE od 12,254, dok je ANN postigao R2 vrednost od 0,9886 i RMSE od 23,722, što ukazuje da je RSM neznatno nadmašio ANNccura u smislu ANNccura. Optimizacija ORC sistema je sprovedena korišćenjem RSM i ANN u kombinaciji sa genetskim algoritmom (ANN-GA), sa ciljem određivanja optimalnih vrednosti za ulazne i izlazne parametre. Rezultati optimizacije ANN-GA su potvrđeni korišćenjem Aspen HISIS i pokazali su superiorne performanse u odnosu na RSM. ANN-GA je predvideo optimalne vrednosti protoka radnog fluida, izlaznog pritiska radnog fluida i izlaznog pritiska iz turbine od 12 kg/s, 19 bara i 1,2 bara, respektivno, što je savršeno odgovaralo rezultatima validacije Aspen HISIS. Ova optimizacija je dala izlaznu snagu od 958,48 kV, koja je bila usko usklađena sa izlazom validacije Aspen HISIS od 952,9 kV, što odražava minimalnu procentualnu grešku od 0,59%. Nasuprot tome, RSM je predvideo blago odstupanje optimalnih vrednosti od 11,8 kg/s, 18,47 bara i 1,2 bara, sa odgovarajućom izlaznom snagom od 940,78 kV. Kada je potvrđen sa HISIS-om, RSM-predviđena izlazna snaga je bila 927,2 kV, što je rezultiralo većom greškom u procentima od 1,46%, čime je lošiji učinak u odnosu na ANN-GA. Studija naglašava komparativne snage RSM-a i ANN-GA, pokazujući da, dok se RSM ističe u preciznom modeliranju odnosa i interakcija između ulaznih faktora i izlaznih odgovora, ANN-GA okvir pokazuje znatno veću sposobnost u navigaciji složenim nelinearnim optimizacijskim pejzažima. Ovo naglašava efikasnost integracije modela mašinskog učenja sa metaheurističkim algoritmima za poboljšane performanse optimizacije. Nalazi doprinose unapređenju metodologije za optimizaciju geotermalnih ORC sistema i nude robustan okvir za poboljšanje efikasnosti proizvodnje energije u primenama geotermalne energije.

Ključne reči: *Geotermalna energija, RSM, ANN, genetski algoritam, Hisis simulacija, Proizvodnja električne energije, binarni ORC sistemi*

Naučni rad
Rad primljen: 25.12.2024.
Rad korigovan: 30.04.2025.
Rad prihvaćen: 09.06.2025.

Ubanozie Julian Obibuike	https://orcid.org/0000-0003-1382-9160
Stanley ToochukwuEkwueme	https://orcid.org/0000-0003-3446-0905
NnaemekaPrincewillOhia	https://orcid.org/0000-0002-4219-7062
Frank ChineduUkaeru	Nil
Michael IfeanyiOnyejekwe	https://orcid.org/0000-0001-6489-6801

Ganesan Sundara Moorthy[1]***, *Palaniappan Meyyappan*[1]

[1]*Centre for Building Materials, Department of Civil Engineering, Kalasalingam Academy of Research and Education, Krishnankoil-626126, Tamilnadu, India.*

Scientific paper
ISSN 0351-9465, E-ISSN 2466-2585
https://doi.org/10.62638/ZasMat1336

Zastita Materijala 67 (1)
36 - 45 (2026)

Study on the effectiveness of SAP, PEG-400, and PVA as self-curing agents: A comparative approach

ABSTRACT

Concrete's performance essentially depends on the hydration process, requiring adequate moisture and a controlled environment for curing. The traditional curing is challenging in water-scarce regions and in high-altitude areas. The self-curing concrete as an emerging sustainable and efficient alternative in conventional curing method scenarios and in challenging environments. Self-curing, or internal curing, is an innovative solution that ensures sufficient moisture for hydration and minimizes evaporation to enhance properties of concrete. This study explores the impact of various self-curing agents Superabsorbent Polymers (SAP), Polyethylene Glycol-400 (PEG-400), and Polyvinyl Alcohol (PVA) on the fresh and mechanical properties of self-curing concrete. The nine mix designs were developed, with self-curing agents incorporated at dosages of 1%, 2%, and 3% by mass of cement. The mechanical properties analysed include compressive strength,splitting tensile strength, and flexural strength, while workability was assessed using slump tests.The results expose that PEG-400 at 1% dosage the highest performance in terms of strength and workability, with compressive, tensile, and flexural strengths of 26.29 N/mm², 2.19 N/mm², and 2.27 N/mm², respectively. The SAP exhibited moderate performance with enhanced internal curing, while PVA offered balanced hydration benefits but lower strength compared to PEG-400. The increasing dosages of all agents led to a decline in mechanical performance due to reduced hydration efficiency and increased viscosity.The PEG-400 of optimizing self-curing agents to achieve a balance between curing efficiency and mechanical performance, contributing to the development of sustainable, high-quality concrete with reduced water consumption.

Keywords: *Self-curing concrete, PEG-400, SAP, PVA, mechanical strength, sustainable construction*

1. INTRODUCTION

Concrete is a widely used construction material due to its workability and strength. Its durability is largely controlled by completing the hydration of cement, which requires sufficient moisture and favourable curing conditions. Improper curing can lead to incomplete hydration, porous concrete, reduced strength, and increased susceptibility to environmental attacks, resulting in accelerated corrosion, structural deterioration, and drying-shrinkage cracking [1, 2]. Traditional curing methods require high water resources, making it difficult in water-scarce regions and high-altitude areas to achieve adequate curing [3]. The construction industry consumes large amounts of water, necessitating the development of innovative solutions to minimize water consumption without compromising concrete quality [4].

Self-curing concrete is an alternative to traditional curing methods, addressing water scarcity and improper curing. It uses internal curing to ensure adequate hydration, conserving water resources and saving time and labour. This consistent hydration leads to uniform strength development and durability enhancement, making it a suitable solution for current construction challenges [5]. Self-curing concrete uses various agents to maintain water within itself during mix preparation. The research on self-curing agents includes water-soluble polymers, superabsorbent materials, and hydrophilic compounds. Superabsorbent polymers (SAPs), polyethylene glycol-400 (PEG-400), and polyvinyl alcohol (PVA) are most commonly used due to their ability to increase hydration and reduce evaporation [6].

SAPs reduce shrinkage due to hydration-induced water consumption, minimizing cracking and durability risk. They also prevent self-curing or internal curing, as moisture evaporation in concrete mix dries faster than wetting, which can affect the hydration process and reduce strength development in large structures or high- SAPs are

---

*Corresponding author:Ganesan Sundaramoorthy
E-mail id: sundarcivil2015@gmail.com

Rad primljen: 07.01.2025.
Rad korigovan: 02.05.2025.
Rad prihvaćen: 10.05.2025.

ionic polymers that absorb and retain water within their structure, ensuring moisture levels during concrete hydration [7, 8]. This is beneficial for low water content concrete mixes where conventional curing may not provide enough moisture temperature areas [9].SAPs enhance the hydration process in concrete, even in water-starved conditions, allowing better microstructure formation and enhanced properties. However, their incorporation requires careful optimization, as higher dosages may decrease mechanical strength due to excess water hindering bonding. Accurate dosing is crucial to enjoy SAP benefits without sacrificing strength. An optimized SAP can create a sustainable hydration solution and mitigate cracking and shrinkage problems, especially in self-curing concrete applications [5, 10].

PEG-400 is an efficient self-curing agent that ensures proper hydrogen bonding with water molecules in concrete mixtures, allowing for better hydration and better strength development. It maintains internal moisture levels, preventing surface moisture loss, which is beneficial in dry or hot climates where rapid evaporation can cause weaker concrete [11]. PEG-400 also prevents early age cracking and shrinkage, enhancing early strength and is particularly useful for prefabricated concrete elements or projects requiring rapid strength gains [12]. PEG-400 aids in moisture retention in concrete during early stages, but excessive usage can negatively affect its mechanical properties. Overdosing can disrupt the cement paste's structural framework and reduce particle bonding, leading to deterioration in strength and durability. Compatibility with other admixtures and additives is also crucial. To maximize effective ness, dosage needs to be optimized to strengthen early hydration without compromising long-lasting durability and mechanical properties [5, 13].

PVA is a versatile additive that enhances concrete's workability self-curing and. It acts as a lubricant between cement particles, allowing them to move smoothly and improve the concrete mix's consistency. PVA also aids in retaining moisture within the concrete matrix, which is crucial for hydration and strength build-up over time. This moisture supports cement particle reactions, completing hydration uniformly, especially during early stages of strength gain. PVA's unique properties make it an attractive addition to concrete construction. Self-curing concrete with PVA internal retention reduces the need for external curing methods. However, overuse of PEG-400 and PVA can negatively affect the concrete's long-term performance. Excessive use increases pore structure, causing shrinkage, cracking, and chemical attack, potentially reducing concrete durability. PVA increases workability and hydration, but its amount needs to be adjusted to prevent long-term damage. Proper dosage and careful integration with other self-curing agents are essential for optimizing PVA in concrete mixes [5, 14, 15].

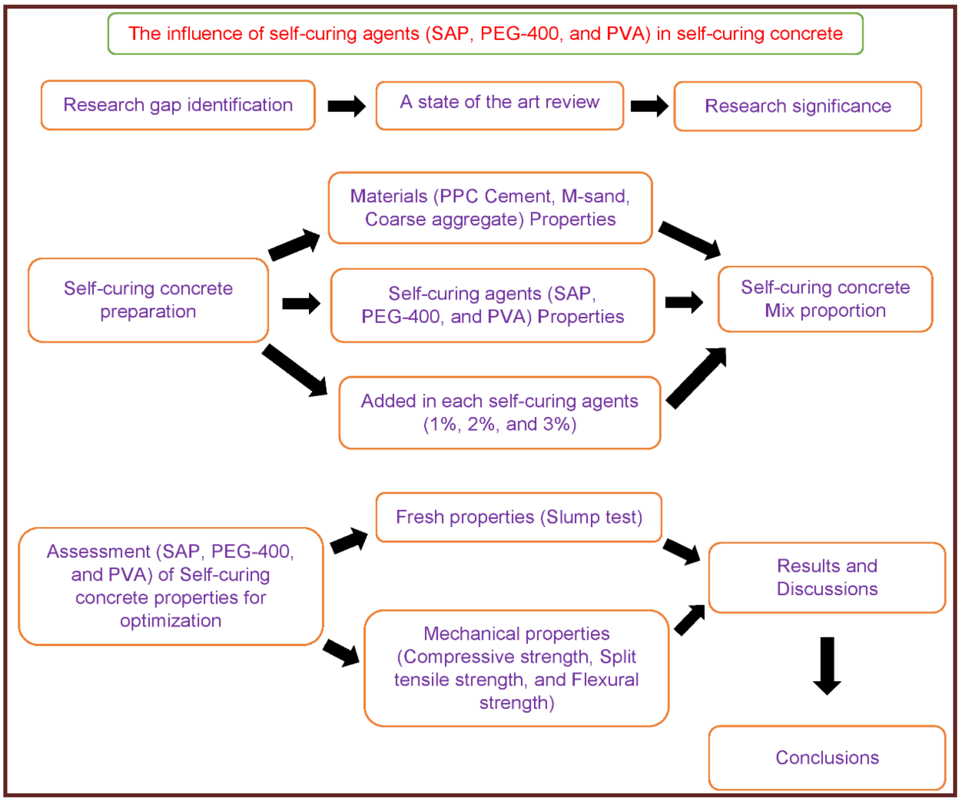

Figure 1. To identify the aim of study

2. RESEARCH SIGNIFICANCE

This study investigates the influence of different self-curing agents such as Superabsorbent Polymers (SAP), Polyethylene Glycol-400 (PEG-400), and Polyvinyl Alcohol (PVA) at varying dosages levels of 1%, 2% and 3% respectively on the mechanical properties (compressive strength, split tensile strength, and flexural strength) of M_{20} grade concrete. The main objective of this study is to identify the ideal self-curing agent and dose in order to bring out the possibility of improving the sustainable solution for the self-curing concrete. High dosage, however, might adversely affect the concrete's mechanical strength, hence careful optimization is required [16–18]. The detailed flow of this research study is given below in the Fig.1

3. MATERIALS USED

3.1. Cement

The Portland pozzolanic cement (PPC) of grade 53 was utilized in the experimental study. PPC is utilized in accordance with Indian Standard IS 12269-1987 [16]. Since it has a lesser heat of hydration at early ages and able to achieve higher durability. According to preliminary testing, this cement has a standard consistency of 32.5%, a specific gravity of 3.12, an initial setting time of 35 minutes, and a final setting time of 457 minutes and other properties such as compressive strength is 35 N/mm^2 respectively.

3.2 Fine aggregate

M-sand from a local source, as classified according to Zone II of IS: 383-2016 criteria, was utilized for this experimental investigation. The choice of M-sand was decided because it is fully concordance with the size distribution and the characteristics requirements [17]. The M-sand utilized in this investigation had a bulk density of 1640 kg/m^3, a specific gravity of 2.58, a fineness modulus of 2.23, a capacity to absorb water of 2.45%, and SO_3 content is 0.40% by mass respectively.

3.3. Coarse aggregate

A locally accessible coarse aggregate with a maximum size of 20 mm in accordance with IS: 383-2016 specifications [17], was utilized for this study. From the initial testing, it is found that, the bulk density of the coarse aggregate is 1728 kg/m^3, its specific gravity is 2.68, its fineness modulus is 6.54, and its water absorption capacity is 0.45%. Additionally, it is found that the aggregate's crushing value is 23.5%, impact strength is 21.5% and SO_3 content is 0.92% by mass.

3.4. Water

The water used for this study has met the required quality criteria and observed that there is no detrimental impact on the mixes characteristics. The water used is in complied with IS: 456-2000's standards, including having a pH value of 7.1 which quite fit in the acceptable range between 6.5 and 58.0 [18].

3.5. Self-curing agents

As described earlier, three self-curing agents Superabsorbent Polymers (SAP), Polyethylene Glycol-400 (PEG-400), and Polyvinyl Alcohol (PVA) were used in this study. The basic properties such as appearance, colour, density, molecular weight, particle size, pH and specific gravity of each of the self-curing agents are presented in the Table 1.

Table 1. Properties of self-curing agents

S.No	Property	SAP	PEG-400	PVA
1	Appearance	powder	Viscous liquid	Slightly cloudy liquid
2	Colour	White	Colourless	Colourless
3	Density	0.9 g/cm^3 (Dry state)	1.13 g/cm^3 at 20°C	1.12 g/cm^3 at 20°C
4	Molecular Weight	-	400 g/mol	-
5	Particle Size	500 µm	-	-
6	pH	7.5	7.3	7.1
7	Specific gravity	0.92	1.12	1.23

SAP is an ionic polymer, because it can collect and retain the large volume of water and gradually release the water during hydration process. This property helps in the reduction of autogenic shrinkage, especially for the concrete mixes with lower water content and also for the conditions where water curing is impossible [19-21].PEG-400 binds to the water molecules and thus forming hydrogen bonds. This process lowers the vapour pressure and thereby preventing the loss of moisture from the concrete surface. In the early phases of curing, this retained moisture helps in achieving better hydration and strength development [5, 22, 23]. PVA has a lubricating effect between the cement particles and thereby reducing water bleeding, which enhances the flow ability of concrete. It helps in supporting the strength development process by keeping the internal moisture, which is favourable for facilitating the hydration processes. The dosages must be careful, at larger dosages level, mechanical properties of concrete may get affected [24-26].

3.6. Mix proportion & casting

In this experimental investigation, nine different self-curing concrete mixtures were made in the proportion of 1:1.51:3.02 with a w/c ratio of 0.45 as per the confirmation of IS: 10262-2009 codal provisions [27]. The primary objective of the study is to assess the influence of the various self-curing agents, like SAP, PEG-400, and PVA, at different dosage levels of 1%, 2% and 3% on the M_{20} grade concrete. Table 2 indicates the mix proportions of the materials used for self-curing concrete made up of various self-curing agents.

Table 2. Mix proportions of conventional and self-curing concrete with various self-curing agents

Mix id	Self-curing agents	Self-curing agents (kg/m^3)	Cement (kg/m^3)	M-sand (kg/m^3)	Coarse aggregate (kg/m^3)	Water (kg/m^3)
CC Mix	---	---	420.25	634.58	1268.48	186.23
MSP1	1% SAP	4.20	420.25	634.58	1268.48	186.23
MSP2	2% SAP	8.40	420.25	634.58	1268.48	186.23
MSP3	3% SAP	12.60	420.25	634.58	1268.48	186.23
MPG1	1% PEG-400	4.20	420.25	634.58	1268.48	186.23
MPG2	2% PEG-400	8.40	420.25	634.58	1268.48	186.23
MPG3	3% PEG-400	12.60	420.25	634.58	1268.48	186.23
MPA1	1% PVA	4.20	420.25	634.58	1268.48	186.23
MPA2	2% PVA	8.40	420.25	634.58	1268.48	186.23
MPA3	3% PVA	12.60	420.25	634.58	1268.48	186.23

Cement, M-sand, and coarse aggregates were mixed together in a dry manner for about 3 minutes in a pan mixer. Then any one of the self-curing agents SAP, PEG-400, and PVA were added with the water according to the mix proportion specified and mixed for further 2 to 3 minutes so that wet mixing was properly completed with adequate consistency. The prepared self-curing concretes were cast in the moulds of cube of size 100 mm x 100 mm x 100 mm, cylinder of size 100 mm x 200 mm, and prism of size 100 mm x 100 mm x 500 mm with proper compaction allowing it to occupy all spaces in the mould. After casting, the specimens were allowed for 24 hours and then demoulded. Then the specimens were placed at ambient conditions for the period of 28 days to test the hardened properties [28-32]. Fig. 2 representative the preparation of self-curing concrete with different self-curing agents.

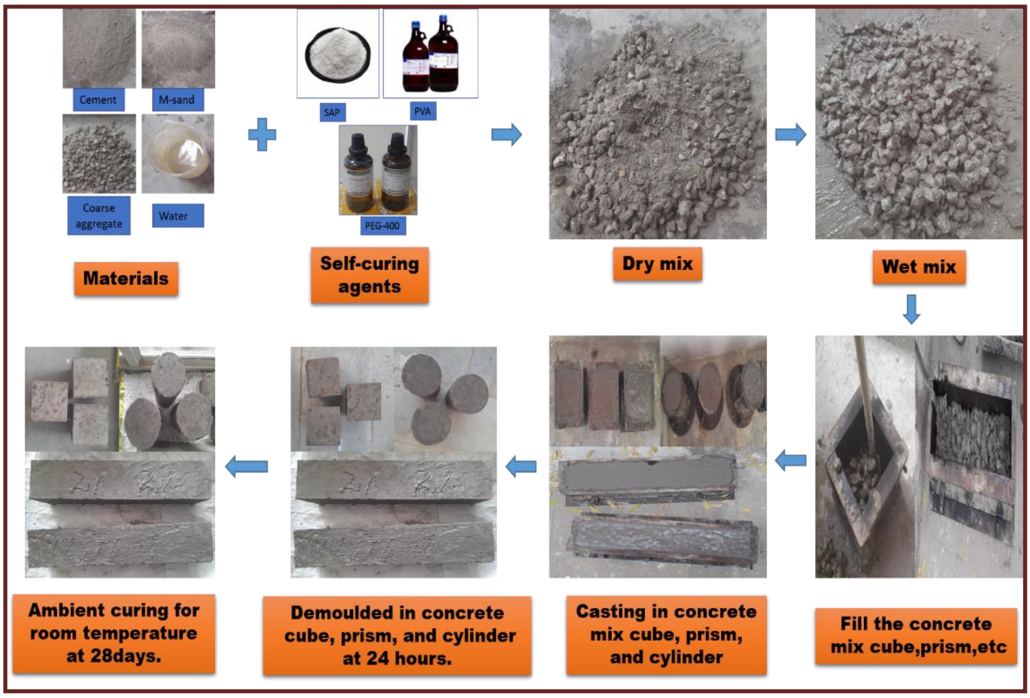

Figure 2. Mixing and Casting of Specimens

3.7. Experimental testing

Fresh properties of the self-curing concrete made up of various self-curing agents such as SAP, PEG-400, and PVA were tested for workability using the slump test. Mechanical properties such as compressive strength, splitting tensile strength, and flexural strength were conducted on self-curing concrete specimens of cubes, cylinder and prism respectively at the age of 28 days of curing at ambient conditions as per 516:1959 [33].

The tests on mechanical properties were performed on a 200 TON capacity compressive testing machine and a 400 KN capacity universal testing machine as shown in Fig. 3.

Figure 3. Experimental testing on specimens

4. RESULT AND DISCUSSION

4.1. Slump test

Table 3 presents the results of a measurement of the workability of conventional andvarious self-curing concrete mixtures using self-curing agents of SAP, PEG-400, and PVA. Fig.4 indicates the variation of slump values for the conventional mix andvarious self-curing agents (PVA, PEG-400, and SAP). The conventional concrete (control mixCC), without self-curing agents, achieved a slump value of 70 mm.

Table 3. Fresh and Mechanical properties of conventional and self-curing concrete based on self-curing agents

Mix id	Self-curing agents	Slump test in (mm)	Compressive strength (N/mm^2)	Splitting tensile strength (N/mm^2)	Flexural strength (N/mm^2)
CC Mix	---	70	20.18	1.09	1.03
MSP1	1% SAP	87	24.65	1.82	1.95
MSP2	2% SAP	79	23.21	1.48	1.52
MSP3	3% SAP	73	22.25	1.20	1.23
MPG1	1% PEG-400	108	26.29	2.19	2.27
MPG2	2% PEG-400	95	24.51	1.78	1.93
MPG3	3% PEG-400	80	23.36	1.36	1.51
MPA1	1% PVA	85	22.80	1.65	1.68
MPA2	2% PVA	76	21.58	1.29	1.35
MPA3	3% PVA	71	20.53	1.15	1.10

The addition of different self-curing agents, namely PVA, PEG-400, and SAP, led to an increased slump value than the conventional concrete. Since the PEG-400 retains water and has lubricating qualities, it had the highest slump values, measuring 108 mm at 1% (MPG1). At high viscosity, the slump value decreased to 80 mm when the dosage was increased to 3% (MPG3), further restricting particle mobility. The most significant impact on workability was shown in SAP, where slump values dropped from 87 mm at 1% (MSP1) to 73 mm at 3% (MSP3), mostly due to water absorption, which reduced the amount of free water in the mixture while simultaneously increasing internal curing. The PVA mixes showed a slump at moderate values, ranging from 85 mm at 1% (MPA1) to 71 mm at 3% (MPA3), despite their general tendency to thicken their mixes. These findings show that PEG-400 is ideal for workability-intensive applications such as self-curing concrete. SAP reduces workability but is beneficial for internal cures and shrinking issues. PVA provides in a balancing way of promoting hydration while maintaining moderate workability. The findings highlights an optimizing dosage to achieve workability within the intended curing performance, with each agent tailored to distinct construction requirements.

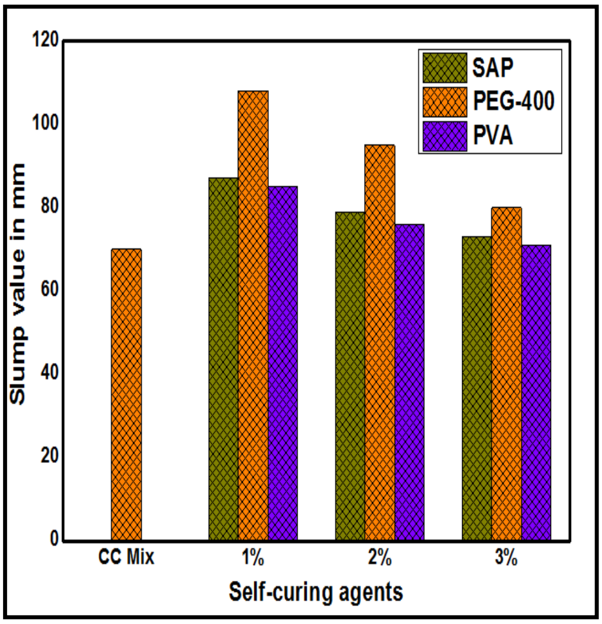

Figure 4. Test results of Slump test of conventional and self-curing concretes

4.2. Compressive strength

Table 3 shows the experimental test results of compressive strength of conventional and self-curing concrete mixes with varying dosages of self-curing agents (SAP, PEG-400, and PVA). Fig.5 depicts the variance in compressive strength values due to conventional concrete and different self-curing chemicals and dosage levels. The conventional concrete, showed a compressive strength value of 20.18 N/mm². The addition of various self-curing agents like PVA, PEG-400 and SAP gave increasing values of compressive strength compared to the control mix. The PEG-400-based mixes achieved the highest compressive strength, reaching 26.29 N/mm² at 1% dose (MPG1) which is 6.6% greater than SAP's 1% (MSP1) and 15.3% higher than PVA (MPA1). It is observed that, the compressive strength is dropped as dosage level is increased, by 6.8% at 2% (MPG2) and 11.1% at 3% (MPG3) compared to 1%. This degradation is caused by high water retention and increased viscosity factors, which slows down the hydration process. SAP-based mixes had a moderate compressive strength of 24.65 N/mm² at 1% dosing (MSP1), decreasing by 5.9% at 2% (MSP2) and 9.8% at 3% (MSP3). Although SAP promotes internal curing, the absorbed water reduces free water for hydration in cement, resulting in a slight decrease in the strength. PVA-based mixes had the lowest compressive strength among all, by dropping from 22.80 N/mm² at 1% (MPA1) to 20.53 N/mm² at 3% (MPA3). The drop percentages were 5.3% at 2% (MPA2) and 9.9% at 3% (MPA3). PVA's setting effects cause delays in hydration efficiency and strength development. PEG-400 will be preferred for situations requiring greater strength. SAP and PVA provide better curing and moisture retention. The optimal doses should be significant in balancing workability, curing, and strength.

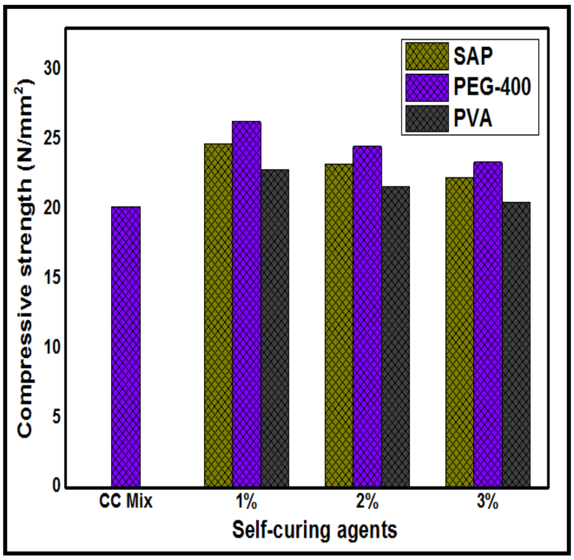

Figure 5. Test results of compressive strength of conventional and self-curing concretes

4.3. Splitting tensile strength

Table 3 shows the splitting tensile strength test results of conventional and self-curing concrete mixtures with varying dosages of self-curing agents such as SAP, PEG-400, and PVA. The effects of these without and with self-curing agents on tensile performances at different dose levels were shown in Fig. 6.

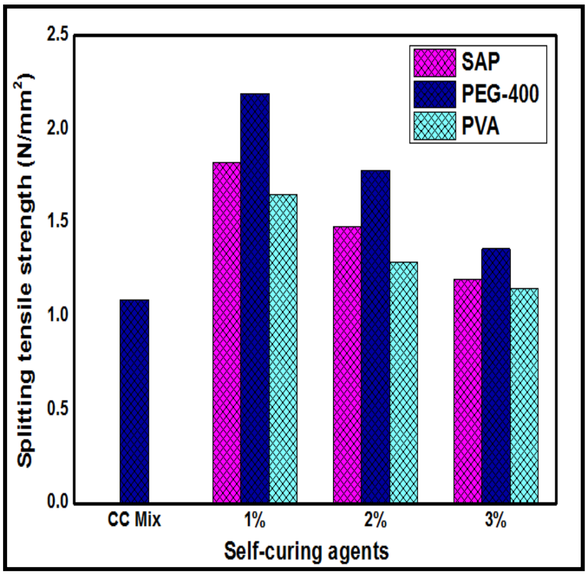

Figure 6. Test results of splitting tensile strength of conventional and self-curing concretes

The conventional concrete showed a splitting tensile strength of 1.09 N/mm². The incorporation of self-curing agents like PVA, PEG-400, and SAP leads to an increase in the splitting tensile strength values compared to the control mix. The tensile strength of the mix was highest for PEG-400 mix, with the maximum tensile strength of 2.19 N/mm² at 1% (MPG1), which is 20.3% more than SAP (MSP1) and 32.7% more than PVA (MPA1) with the same amount of dosage level. However, tensile strength decreased with the increase in dosage, which it dropped by 18.7% at 2% (MPG2) and 37.9% at 3% dosage level than at 1% dosage, and this is happened because of the weakened effect of the interfacial bond strengths by the increase in viscosity of the mix. While the split tensile strength test results is 1.82 N/mm² for 1% (MSP1) and further it is decreased by 18.7% (MSP2) and 34.1% (MSP3) for the dosage levels 2% and 3% respectively. This is because the SAP was absorbing water, which decreased the amount of water available for hydration and, as a result, there is a subsequent reduction in the tensile strength. The PVA mixes exhibited the lowest tensile strength, ranging from 1.65 N/mm² at 1% (MPA1) to 1.15 N/mm² at 3% (MPA3). Because of the setting effect that inhibited reverse hydration, the PVA mixes with the lowest tensile strength ranged from 1.65 N/mm² at 1% (MPA1) to 1.15 N/mm² at 3% (MPA3), which were declines of 21.8% at 2% (MPA2) and 30.3% at 3% (MPA3). PEG-400 considerably increased the tensile strength, while SAP and PVA are helpful for internal curing but show worse behaviour against tensile performance at higher dosages levels.

4.4. Flexural strength

The flexural strength performance of conventional and self-curing concrete with different dosage levels of SAP, PEG-400, and PVA is shown in Table 3. The flexural strength results of the conventional and self-curing concrete mixes with different SAP, PEG-400, and PVA doses are shown in Fig.7.

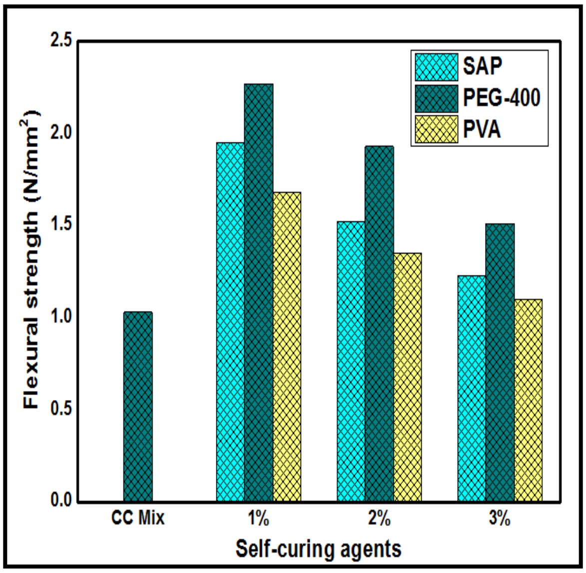

Figure 7. Test results of flexural strength of conventional and self-curing concretes

The flexural strength of the conventional concrete, which did not contain any self-curing agents, was 1.03 N/mm². With the addition of self-curing agents like PVA, PEG-400, and SAP, the values for flexural strength were higher than the control mix. The maximum flexural strength was achieved by the PEG-400 based mixtures, attaining 2.27 N/mm² at a 1% dosage (MPG1), which is 35.1% greater than that of PVA (MPA1) and 16.4% higher than that of SAP (MSP1). However, strength decreased by 15% at 2% (MPG2) and 33.5% at 3% (MPG3) as dosage levels increased. This is to be expected because of the higher viscosity which weakens the inter particle bonding strength of the self-curing concrete. At 1% dosage (MSP1), the SAP-based mixes' flexural strength was 1.95 N/mm2, but it decreased by 22% at 2% (MSP2) and 37% at 3% (MSP3). It corresponds with SAP's water absorption, which reduces the amount of water that is free to be used for hydration and, as a result, this lowers the mix's performance. PVA-based mixes exhibited the lowest flexural strength, measuring just 1.68 N/mm2 at 1% dosing, which decreased by 19.6% at 2% and 34.5% at 3%.This is because it has a condensing action that restricts bond formation and hydration. In general, PEG-400 suggests higher flexural strength, whereas PVA and SAP rely more on internal curing but at larger dosages compromise bending resistance. Hence, the optimal dosages ensure a balance between the mechanical performance and curing advantages.

5. CONCLUSION

The effects of the self-curing chemicals SAP, PEG-400, and PVA on the mechanical and fresh characteristics of conventional and self-curing concrete that has been cured in water and ambient circumstances have been studied. The major findings of this study are briefly described as follows:

1. The conventional concrete without self-curing agents, exhibited workability with a slump value of 70 mm. It had compressive, splitting tensile, and flexural strengths of 20.18 N/mm², 1.09 N/mm², and 1.03 N/mm², respectively.
2. With a dosage of 1%, PEG-400 had its highest slump value, of 108 mm, due to its exceptional water-retention ability. PVA and SAP has demonstrated a moderate level of workability. SAP's free water availability is decreased as a result of water absorption, while PVA has a condensing effect on the mix, which results in comparatively low slump values at higher dosages.
3. PEG-400 exhibited its finest performance at 1% dosage, with compressive strength of 26.29 N/mm², split tensile strength of 2.19 N/mm², and flexural strength of 2.27 N/mm², all of which were attributed to its capacity to retain water. By keeping internal curing and hydration in balance, SAP demonstrated moderate strength. As a result of its delayed hydration effects, PVA had the lowest strength.
4. At 1% dosage level, the optimum self-curing agents of PEG-400 were found to be most active self-curing agent providing improved workability and mechanical properties. At higher dosage level, SAP reduces strength and workability but is helpful in reducing shrinkage and encouraging internal curing. Although PVA advises mild hydration assistance, delayed hydration lowers mechanical performance.
5. Based on the study, it is found that, the PEG-400 is well suited for high-performance self-curing concrete. SAP is appropriate for shrinkage control applications where workability and strength are critical, but PVA can be utilized for applications needing curing improvement with significant endurance.

Acknowledgments

The author Ganesan Sundaramoorthy is grateful to the International Research Centre (IRC), Kalasalingam Academy of Research and Education (KARE) for providing University Research Fellowship (URF) and instrumental research facilities

6. REFERENCES

[1] D. Xu, J. Tang, X. Hu, C. Yu, F. Han, S. Sun, J. Liu (2023) The influence of curing regimes on hydration, microstructure and compressive strength of ultra-high performance concrete: A review, J. Build. Eng. 76, 107401. https://doi.org/10.1016/j.jobe.2023.107401

[2] C. Zhong, W. Lu, W. Mao, S. Xin, J. Chen, J. Zhou, C. Shi (2024) Research on capillary water absorption characteristics of modified recycled concrete under different freeze–thaw environments, Appl. Sci. 14(3), 1247. https://doi.org/10.3390/app14031247.

[3] H. Shemer, S. Wald, R. Semiat (2023) Challenges and solutions for global water scarcity, Membranes (Basel). 13(6), 612. https://doi.org/10.3390/membranes13060612.

[4] [M. N. Patil, S. D. Dubey, H. S. Patil (2023) Self-curing concrete: a state-of-the-art review, Innov. Infrastruct. Solut. 8(12), 313. https://doi.org/10.1007/s41062-023-01282-8.

[5] G. Sundaramoorthy, P. Meyyappan, (2024) Role of self-curing mechanism in lightweight concrete: A state-of-the-art report, Int. Rev. Appl. Sci. Eng. 15(2), 200-210. https://doi.org/10.1556/1848.2023.00695.

[6] K. V. S. Gopala Krishna Sastry, P. M. Kumar, (2018) Self-curing concrete with different self-curing agents, IOP Conf. Ser. Mater. Sci. Eng. (Vol. 330, p. 012120). https://doi.org/10.1088/1757-899X/330/1/012120.

[7] B. Zhou, K. Wang, P. C. Taylor, Y. Gu (2024) Superabsorbent Polymers for Internal Curing Concrete: An Additional Review on Characteristics, Effects, and Applications, J. Mater. *17*(22), 5462. https://doi.org/10.3390/ma17225462.

[8] X. Huang, X. Liu, H. Rong, X. Yang, Y. Duan, T. Ren (2022) Effect of super-absorbent polymer incorporation method on mechanical and shrinkage properties of internally cured concrete, J. Mater. *15*(21), 7854. https://doi.org/10.3390/ma15217854.

[9] L. Rachana, A. Venkateswararao (2021) Effect of self-curing agent on mechanical properties of concrete with GGBS replacement, IOP Conf. Ser. Earth Environ. Sci. (Vol. 796, No. 1, p. 012062). https://doi.org/10.1088/1755-1315/796/1/012062.

[10] J. Liu, M. Wang, N. Liu, L. Teng, Y. Wang, Z. Chen, C. Shi (2023) Development of ultra-fine SAP powder for lower-shrinkage and higher-strength cement pastes made with ultra-low water-to-binder ratio, Compos. B: Eng. 262, 110810. https://doi.org/10.1016/j.compositesb.2023.110810.

[11] S. Gowdra Virupakshappa, A. Shrishail Basappa, M. Thimmarayappa, C. K. N. Narayana, A. Buradi, A. F. Emma (2024) Modelling and analysis of strength and durability properties of internal curing concrete using PEG 400 and artificial neural network, Discov. Sustain. *5*(1), 80. https://doi.org/10.1007/s43621-024-00240-3.

[12] P. Magudeaswaran, V. Kumar, K. V. Krishna, A. Nagasaibaba, R. Ravinder (2023) Investigational studies on the impact of Supplementary Cementitious Materials for identifying the strength and durability characteristics in self-curing concrete, Mater. Today Proc. https://doi.org/10.1016/j.matpr.2023.03.161.

[13] S. Panwar, A. Jindal (2023) A review on self-curing agents, Innov. Infrastruct. Solut. 8 282. https://doi.org/10.1007/s41062-023-01237-z.

[14] N. Dharani, M.R. Nivitha (2024) Use of polyvinyl alcohol and polyethylene glycol as self-curing agents for concrete pavement. Eur. J. Environ. Civ. Eng. 1–21. https://doi.org/10.1080/19648189.2024.2312476.

[15] U. Nabi, S. Chauhan (2023) A study on self curing concrete incorporated with light weight aggregates, polyethylene glycol & polyvinyl alcohol, Mater. Today Proc. https://doi.org/10.1016/j.matpr.2023.04.286.

[16] IS-12269 (1987) Specification for 53 grade ordinary Portland cement, Bur. Indian Stand. New Delhi,India.

[17] IS:383 (2016) Specification for Coarse and Fine Aggregates From Natural Sources for Concrete, Indian Stand. 1–24.

[18] IS 456 (2000) Plain Concrete and Reinforced, Bur. Indian Stand. Dehli.1–114.

[19] V. Mechtcherine, M. Wyrzykowski, C. Schröfl, D. Snoeck, P. Lura, N. De Belie, A. Mignon, S. Van Vlierberghe, A.J. Klemm, F.C.R. Almeida, J.R. Tenório Filho, W.P. Boshoff, H.-W. Reinhardt, S.-I. Igarashi (2021) Application of super absorbent polymers in concrete construction update of RILEM state-of-the-art report, Mater. Struct. 54, 80. https://doi.org/10.1617/s11527-021-01668-z.

[20] Z. Ahmad, S. Salman, S.A. Khan, A. Amin, Z.U. Rahman, Y.O. Al-Ghamdi, K. Akhtar, E.M. Bakhsh, S.B. Khan, (2022) Versatility of Hydrogels: From Synthetic Strategies, Classification, and Properties to Biomedical Applications, Gels. 8. https://doi.org/10.3390/gels8030167.

[21] D. Thirumoolan, T. Siva, R. Ananthakumar, K.S.N. Nambi (2023) Alginate-Based Superabsorbents, In Bio-Based Superabsorbents Recent Trends, Types, Appl. Recycl. pp. 93–114. https://doi.org/10.1007/978-981-99-3094-4_6.

[22] J.P. Rizzuto, M. Kamal, H. Elsayad, A. Bashandy, Z. Etman, M.N. Aboel Roos, I.G. Shaaban (2020) Effect of self-curing admixture on concrete properties in hot climate conditions, Constr. Build. Mater. 261 119933. https://doi.org/10.1016/j.conbuildmat.2020.119933.

[23] T. Udayabanu, N.P. Rajamane, C. Makendran, R. Gobinath, S. Chandra Chary (2020) Self-Curing Concrete Using Water-Soluble Polymerfor Developing Countries, IOP Conf. Ser. Mater. Sci. Eng. 981. https://doi.org/10.1088/1757-899X/981/3/032088.

[24] J. Fan, G. Li, S. Deng, Z. Wang (2019) Mechanical properties and microstructure of polyvinyl alcohol modified cement mortar, Appl. Sci. 9. https://doi.org/10.3390/app9112178.

[25] K. S. Kumar, P. S., Reddy, E. Arunakanthi (2022) An experimental study on mechanical and durable properties of self-curing concrete by using Ferro silica slag aggregate, IOP Conf. Ser. Earth Environ. Sci. (Vol. 982, No. 1, p. 012025). https://doi.org/10.1088/1755-1315/982/1/012025.

[26] G. Modupeola, B. Olufunmi, A. Ibrahim (2023) Assessment of strength characteristics of propylene glycol self-curing concrete, 22, 49–54.

[27] IS 10262 (2009) Concrete mix proportioning - Guidelines, Bur. Indian Stand., New Delhi. 1–14.

[28] F.S. Aditto, M.H.R. Sobuz, A. Saha, J.A. Jabin, M.K.I. Kabbo, N.M.S. Hasan, S. Islam (2023) Fresh, mechanical and microstructural behaviour of high-strength self-compacting concrete using supplementary cementitious materials, Case Stud. Constr. Mater. 19, 02395. https://doi.org/10.1016/j.cscm.2023.e02395.

[29] Z. Wu, J. Zhang, H. Yu, Q. Wu, B. Da (2023) Computer-aided investigation of the tensile behavior of concrete: Relationship between direct and splitting tensile strength, Structures. 55, 453–467. https://doi.org/10.1016/j.istruc.2023.06.019.

[30] B.W. Darvell (2022) Mechanical test relevance-A personal perspective on some methods and requirements, Front. Dent. Med. 3 1–13. https://doi.org/10.3389/fdmed.2022.1084006.

[31] I.A. Ja'e, A.R. Salih, A. Syamsir, T.H. Min, Z. Itam, C.V. Amaechi, V. Anggraini, J. Sridhar(2023) Experimental and predictive evaluation of mechanical properties of kenaf-polypropylene fibre-reinforced concrete using response surface methodology, Dev. Built Environ. 16, 100262. https://doi.org/10.1016/j.dibe.2023.100262.

[32] B. Sen, D. Chanda, R. Saha (2024) Mechanical strength characterization and seismic performance of rammed earthen walls built on eco-friendly lateritic soil and sustainable stabilizing materials, Sādhanā. 49, 37. https://doi.org/10.1007/s12046-023-02375-x.

[33] IS 516 (1959) Method of Tests for Strength of Concrete, Bur. Indian Stand. 1–30.

IZVOD

STUDIJA O EFIKASNOSTI SAP, PEG-400 I PVA KAO SREDSTAVA ZA SAMOOČVRŠĆAVANJE: UPOREDNI PRISTUP

Performanse betona u suštini zavise od procesa hidratacije, što zahteva odgovarajuću vlagu i kontrolisano okruženje za očvršćavanje. Tradicionalno očvršćavanje je izazovno u regionima sa oskudicom vode i na velikim nadmorskim visinama. Samoočvršćavajući beton je nova održiva i efikasna alternativa u scenarijima konvencionalnih metoda očvršćavanja i u izazovnim okruženjima. Samoočvršćavanje, ili unutrašnje očvršćavanje, je inovativno rešenje koje obezbeđuje dovoljnu vlagu za hidrataciju i minimizira isparavanje kako bi se poboljšala svojstva betona. Ova studija istražuje uticaj različitih sredstava za samoočvršćavanje - superapsorbujućih polimera (SAP), polietilen glikola-400 (PEG-400) i polivinil alkohola (PVA) - na sveža i mehanička svojstva samoočvršćavajućeg betona. Razvijeno je devet mešavina, sa sredstvima za samoočvršćavanje ugrađenim u dozama od 1%, 2% i 3% po masi cementa. Analizirana mehanička svojstva obuhvataju čvrstoću na pritisak, zateznu čvrstoću na cepanje i čvrstoću na savijanje, dok je obradivost procenjena testovima sleganja. Rezultati pokazuju da PEG-400 u dozi od 1% ima najbolje performanse u pogledu čvrstoće i obradivosti, sa čvrstoćama na pritisak, zatezanje i savijanje od 26,29 N/mm², 2,19 N/mm² i 2,27 N/mm², respektivno. SAP je pokazao umerene performanse sa poboljšanim unutrašnjim očvršćavanjem, dok je PVA ponudio uravnotežene prednosti hidratacije, ali nižu čvrstoću u poređenju sa PEG-400. Povećanje doza svih agenasa dovelo je do pada mehaničkih performansi zbog smanjene efikasnosti hidratacije i povećane viskoznosti. PEG-400 optimizuje sredstva za samoočvršćavanje kako bi se postigla ravnoteža između efikasnosti očvršćavanja i mehaničkih performansi, doprinoseći razvoju održivog, visokokvalitetnog betona sa smanjenom potrošnjom vode.

Ključne reči: *Samoočvršćavajući beton, PEG-400, SAP, PVA, mehanička čvrstoća, održiva gradnja*

Naučni rad
Rad primljen: 07.01.2025.
Rad korigovan: 02.05.2025.
Rad prihvaćen: 10.05.2025.

Ganesan Sundaramoorthy : https://orcid.org/0009-0008-8683-3607
Palaniappan Meyyappan : https://orcid.org/0000-0002-6925-5277

SivakumarDurairaj[1], Shankar Durairaj[2]*

[1]Department of Agricultural Engineering, Kalasalingam Academy of Research and Education, Krishnankoil, Tamil Nadu, India, [2]Department of Pharmaceutical Chemistry, K.M. College of Pharmacy, Madurai, Tamil Nadu, India

Scientific paper
ISSN 0351-9465, E-ISSN 2466-2585
https://doi.org/10.62638/ZasMat1294
Zastita Materijala 67 (1)
46 - 61 (2026)

Advancements and challenges in self-healing coatings for sustainable smart materials in industry applications

ABSTRACT

This review examines the developing fields of self-healing coatings and smart materials, emphasizing how they have the potential to transform a number of sectors by improving efficiency, sustainability, and durability. A growing number of self-healing coatings incorporate smart materials, which react to environmental stimuli like temperature, pressure, and electric fields, allowing damage to be repaired without the need for outside assistance. Even with some improvements in self-healing processes, there is still a great deal to learn about the long-term functionality and real-world uses of these materials, especially when paired with cutting-edge technology like nanomaterials. The most recent studies on self-healing coatings are summarized in this study, which also offers insights into the mechanisms underlying these advancements, such as vascular systems, reversible chemical bonding, and microencapsulation. It also emphasizes the various ways that smart materials are being used in sectors including construction, automotive, healthcare, and aerospace, showcasing their potential to save maintenance costs and enhance sustainability in general. This study discusses current issues and suggests future lines of inquiry that may propel the development and commercialization of these technologies for practical uses.

Keywords:*Advanced coatings; industry applications; nanotechnology; self-healing coatings; smart coating systems; smart materials; sustainability*

1. INTRODUCTION

Smart materials are materials that have the ability to respond dynamically to external stimuli, such as mechanical, electrical, thermal, or chemical changes. These materials can adapt and modify their properties in response to environmental conditions, making them highly valuable in various technological applications. The growing interest in smart materials stems from their potential to enhance the performance, durability, and functionality of devices across numerous industries.One of the most inventive uses of smart materials is in self-healing coatings. The lifespan of the materials these coatings cover is increased since they are made to automatically fix damage brought on by mechanical wear or environmental conditions. Damage-induced alterations, like cracks, can activate self-healing coatings, which fix the harmed portions without the need for human assistance (Kessler, Sottos, & White, 2003).

The basic idea is to incorporate micro- or nanocapsules that contain healing agents. These chemicals are released when the coating is destroyed, starting the repair process. Numerous sectors make extensive use of this idea, and material design and engineering have advanced significantly (Wang & Urban, 2020).

The potential for enhancing the durability and sustainability of different systems has led to an increase in the significance of smart materials and self-healing coatings. These materials are essential in situations when more conventional repair techniques would be expensive or difficult (Yu et al., 2023). Self-healing coatings, for instance, have the potential to save maintenance costs and enhance the performance of structural materials in the fields of civil engineering, automotive engineering, and aerospace (Zhang et al., 2018). They can also be used in protective coatings for metal surfaces, which can effectively prevent corrosion and drastically cut down on the frequency of repairs or replacements (Zhang et al., 2020).Many different industries have showed promise in self-healing materials, particularly coatings (Kim et al., 2024). These materials contribute to increased vehicle and aircraft durability in the automotive and aerospace industries (MohdJani et al., 2014). Additionally, they can be applied to electronics to create protective layers for circuits and components, increasing their dependability and prolonging their

---

Corresponding author: SivakumarDurairaj
E-mail: shri.sivakumar1974@gmail.com
Paper received: 15.01.2025.
Paper corrected: 02.04. 2025.
Paper accepted: 09.04. 2025.

useful lives (Sekine&Nakao, 2023). Moreover, the application of self-healing coatings to building elements like steel and concrete has the potential to completely transform infrastructure maintenance. Long-term advantages include less maintenance needs, less of an influence on the environment, and more economical material management (Achal& Mukherjee, 2015; Jonkers et al., 2010).

Research on self-healing coatings is progressing quickly, with a focus on a variety of mechanisms, including stimuli-responsive materials, intrinsic healing polymers, and microcapsule-based systems (Rivero et al., 2014). These advancements hold the potential to improve self-healing systems' adaptability and effectiveness, enabling them to satisfy the demands of harsher and more complicated situations (Zhang et al., 2020). Self-healing coatings continue to develop as a game-changing technology by fusing nanotechnology, polymers, and composite materials (Kim et al., 2024).Self-healing systems' capacity to fix themselves, frequently without outside assistance, has significant ramifications for upcoming materials science applications. Performance and sustainability could be greatly enhanced in a number of industries by incorporating smart materials into commonplace products (VenkataChalapathi et al., 2023). These materials provide a sustainable substitute for conventional techniques, altering not just the way goods are created but also the approach to upkeep, durability, and repair (Yang & Urban, 2013; Wang & Urban, 2020).

An important knowledge gap about the long-term performance and practical uses of smart materials is highlighted by the paucity of prior studies in the field of sophisticated self-healing coatings. The integration of these coatings with cutting-edge technology, such nanomaterials, and their employment in many industries have received little attention, despite some research into self-healing processes. Comprehensive assessments that evaluate the latest developments, difficulties, and possibilities for scaling up these technologies in real-world settings are also lacking. This review is unique in that it synthesizes the most recent advancements in self-healing coatings and smart materials, offering a current viewpoint on the underlying principles, inventions, and applications that are now influencing the sector. It also provides fresh perspectives on future research avenues that might get past current obstacles and help create material systems that are more effective, long-lasting, and sustainable.

This review's primary goals are: (i) Smart materials alter their characteristics in a regulated manner in response to outside stimuli like pressure or temperature; (ii) Self-healing coatings, which frequently use microcapsules or polymers that release healing chemicals, are a sort of smart material that can mend itself when injured; (iii) Shape memory alloys (SMAs), electroactive polymers (EAPs), and piezoelectric materials are important categories of smart materials, each with specialized uses in flexible electronics, sensors, and actuators; (iv) Nanotechnology and real-time monitoring systems are used in recent developments in self-healing coatings to improve their functionality and efficiency; and (v) These materials improve durability, lower maintenance costs, and enable more sustainable solutions in a variety of industries, including construction, automotive, healthcare, and aerospace.

2. FUNDAMENTALS OF SMART MATERIALS

Smart materials are engineered to respond to external stimuli, enabling adaptive and innovative applications across fields. This section explores key types such as piezoelectric materials, SMAs, and EAPs, their unique properties, and how they interact with environmental factors for optimized performance.

Types of Smart Materials

Smart materials are engineered to respond to changes in their environment by altering their physical or chemical properties. These materials have been widely studied and implemented in various applications such as sensors, actuators, and self-healing systems. The following sections provide an overview of the most prominent types of smart materials:

1. Piezoelectric Materials: The ability to produce electrical charge under mechanical stress is a special property of piezoelectric materials. Applications such as EH, sensors, actuators, and transducers make extensive use of this feature. Technologies for EH and damage detection have greatly improved with the recent invention of carbon fiber-reinforced piezo-electric nanocomposites. These nanocomposites improve durability in harsh conditions and energy conversion efficiency by fusing the mechanical strength of carbon fibers with the piezoelectric qualities of certain polymers (Yu et al., 2023). Piezoelectric materials are indispensable in the civil engineering and aerospace sectors because they are essential to wireless sensor networks and devices that track the health of structures.
2. Shape Memory Alloys: Metallic compounds known as SMAs, a pre-programmed shape and revert to it in response to a certain heat stimulation. SMAs are especially helpful in applications like medical devices, robotics, and actuators that demand accuracy and reactivity. The most widely used SMAs are nickel-titanium (NiTi) alloys, which are distinguished by their exceptional capacity to experience reversible phase changes. Research is still being done to

improve their performance, such as making these alloys more fatigue resistant for longer service lives (Jani et al., 2014). Innovation in fields like micro-electro-mechanical systems (MEMS) and biomedical implants is being fueled by the incorporation of SMAs into flexible and compact systems. Furthermore, the use of SMAs in high-performance automotive and aerospace applications is growing as new models with wider operating temperature ranges are developed.

3. Thermochromic and Photochromic Materials: Materials that are thermochromic react to changes in temperature, but materials that are photochromic change colour when exposed to light, especially ultraviolet (UV) light. Applications for these materials are numerous and include smart packaging, car glass, clothing, and temperature-sensitive indicators. Thermochromic coatings have advanced to the point where they are used in energy-efficient windows. Depending on the ambient temperature, these coatings can either block or let solar radiation, helping to adjust temperature (Kuilla in 2010). Wearable electronics and sensors are incorporating photochromic materials to provide real-time input on environmental changes, like UV exposure (Kessler et al., 2003). The development of multicolourthermochromic materials is another area of innovation. These materials may find use in a variety of contexts, including thermometers, smart fabrics, and adaptive camouflage systems.
4. Electroactive Polymers: A type of intelligent materials known as EAPs undergoes deformation when exposed to an electric field. They are frequently referred to as "artificial muscles" because of their capacity to replicate the mechanical characteristics of real muscles. EAPs have clear advantages over conventional actuators since they are flexible, lightweight, and can function in a range of conditions, including space and underwater. Recent developments have produced conductive polymer composites for soft robotics (SR), in which electrical signals regulate movement and deformation (Wang & Urban, 2020). The ability of these materials to react to variations in electrical stimuli makes them a crucial part of next-generation medical, robotic, and automotive equipment. They are also being employed in adaptive optics (AO) and sensor applications.
5. Magnetostrictive Materials: Materials that undergo shape change in response to a magnetic field are known as magnetostrictive (MD) materials. The realignment of the material's magnetic domains under the effect of a magnetic field, which produces dimensional changes, is the mechanism underlying MD. Actuators, sensors, and EH devices frequently use these materials. One of the most well-known MD materials, terfenol-D (TFD) is an alloy of iron, terbium, and dysprosium that is frequently utilized in high-performance actuators (Zhang et al., 2020). Optimizing the material's speed, sensitivity, and efficiency for application in energy-harvesting systems and sophisticated sensors for structural health monitoring (SHM) has been the focus of recent advancements. Furthermore, multifunctional MD composites are being created to improve their mechanical and MD qualities, opening the door to better robotics and aerospace actuation systems.

Properties and Mechanisms of Smart Materials

Numerous characteristics of smart materials make them special and appropriate for a range of uses. Usually, these characteristics include the capacity to alter size, form, or colour in reaction to outside stimuli like heat, light, or mechanical force. Understanding the mechanisms underlying these changes is essential to comprehending how these materials function.An electric charge is produced by the displacement of charges brought on by mechanical stress in piezoelectric materials, for example, where the transformation takes place at the atomic level. Similarly, in SMAs, the material's form recovers when heated due to phase transitions between the austenitic and martensitic phases (Jani et al., 2014). However, when exposed to an electric field, electrostatic forces cause shape changes in EAPs, whereas MD materials create mechanical strain through domain reorientation brought on by magnetic fields (Wang & Urban, 2020).

These materials must be able to react reversibly to external stimuli in order to be used in devices that need adaptive functionality, such as actuators that move, sensors that respond to pressure changes, or self-healing materials that can repair themselves after being damaged (Sekine&Nakao, 2023).Certain smart materials can also heal themselves, allowing them to bounce back from damage on their own. This capability has been shown in a variety of polymers and composites, where damage triggers the release of microencapsulated healing agents, promoting material repair (Kessler et al., 2003). Chemical events, such as polymerization or other healing processes, are part of the mechanisms of self-healing and are brought on by outside stimuli like light or temperature.

Interaction between Smart Materials and Environmental Stimuli

The way smart materials react to external stimuli is their basic behaviour. When temperature, pressure, light, electric field, or magnetic field changes, these materials react by changing their properties or behaviour accordingly. To detect damage in buildings, for instance, piezoelectric materials are perfect since they can produce electrical signals and are sensitive to mechanical stress (Yu et al., 2023). SMAs react similarly to temperature fluctuations, recovering a certain shape when heated above a critical temperature.Temperature indicators and smart textiles frequently incorporate thermochromic and photochromic materials, such as thermochromic inks, which change colour in response to temperature changes (Kuilla et al., 2010). Photochromic materials react more readily to UV light, they can be used in adaptive eyeglasses and smart windows that change their tint in response to changes in the surrounding light (Kessler et al., 2003). Soft robotics, artificial muscles, and actuators can all benefit from the shape-changing properties of EAPs, which interact with electric fields (Wang & Urban, 2020). The intensity of the electric field determines the rate and magnitude of deformation that these polymers can undergo when subjected to an applied voltage.High sensitivity to magnetic fields causes dimensional changes in MD materials, which are used in actuators and sensors for high-precision applications like motion sensing and vibration control (Zhang et al., 2020). Furthermore, self-healing materials exhibit distinct interactions with environmental stimuli. For example, self-healing polymers release encapsulated healing chemicals that can fix the material on their own when it is mechanically damaged. The polymerization or healing events that restore material integrity are triggered by external cues such as heat or UV light in certain self-healing materials (Sekine&Nakao, 2023).

Significant advancements have been made in the design and functionality of smart materials for a variety of applications, and innovation in this field is still developing quickly. EAPs give SR flexibility and adaptability, SMAs transform actuation systems, and piezoelectric materials facilitate effective EH and damage detection. MD materials improve actuation and sensor precision, while thermochromic and photochromic material innovations enable the development of systems that visually react to environmental changes. Certain smart materials' capacity for self-healing opens up new avenues for lifespan and endurance in structural applications. When taken as a whole, these developments show how smart materials are becoming more and more promising across a wide range of high-performance industries, such as robotics, healthcare, aerospace, automotive, and construction.

Table 1. Overview of Key Smart Materials, Properties, Mechanisms, and Applications

Type of Smart Material	Key Properties and Mechanisms	Applications	References
Piezoelectric Materials	Generate electrical charge under mechanical stress. React to mechanical forces by generating electric signals at the atomic level.	EH, sensors, actuators, damage detection, wireless sensor networks in civil engineering and aerospace sectors.	Yu et al., 2023
Shape Memory Alloys	Recover a pre-programmed shape when heated, transitioning between austenitic and martensitic phases.	Medical devices, robotics, actuators, MEMS, automotive, aerospace.	Jani et al., 2014
Thermochromic and Photochromic Materials	Change color in response to temperature (thermochromic) or UV light (photochromic).	Smart packaging, car glass, adaptive eyewear, energy-efficient windows, temperature-sensitive indicators.	Kuilla, 2010; Kessler et al., 2003
Electroactive Polymers	Undergo deformation when exposed to electric fields, acting as "artificial muscles".	Soft robotics, actuators, AO, biomedical devices, automotive systems.	Wang & Urban, 2020
Magnetostrictive Materials	Change shape in response to magnetic fields, caused by the reorientation of magnetic domains.	Actuators, sensors, EH, SHM, vibration control.	Zhang et al., 2020
Self-healing Materials	Materials that can repair themselves when damaged, triggered by external stimuli such as heat or UV light.	Self-healing composites, damage detection, structural applications.	Sekine&Nakao, 2023

Table 1 highlights the diverse range of smart materials, showcasing their properties, operational mechanisms, and wide-ranging applications in modern technologies. Each material type is tied to its core properties and innovations, indicating their ongoing importance in the development of adaptive and intelligent systems.

3. UNDERSTANDING SELF-HEALING COATINGS

Self-healing coatings are innovative materials that can repair themselves after damage, restoring their protective and functional properties without external intervention. These coatings have become crucial in fields like corrosion protection, automotive applications, and infrastructure, offering notable improvements in material longevity and performance. This section explores self-healing coatings, their mechanisms, types, and applications.

Self-Healing Mechanisms

The purpose of self-healing coatings is to increase surface protection, save maintenance costs, and extend the lifespan of materials by automatically fixing mechanical damage such cracks and scratches (Acharya et al., 2021). These coatings are especially useful in settings like the automotive, marine, and aerospace industries where routine maintenance is expensive or impossible. Reactive agents, such as microcapsules or reversible chemical bonds, are usually embedded within the coatings' structure and triggered upon damage (Liu et al., 2012). Important mechanisms consist of:

1. Autonomous Self-Healing: Certain coatings have inherent qualities, such as reversible chemical bonds or molecular interactions that enable the material to mend itself under normal circumstances without the need for an outside trigger. Hydrogen bonds, for instance, can be broken and then reformed, offering effective and affordable repair for real-world uses (Liu et al., 2012).
2. Microencapsulation: This technique, which is one of the most studied self-healing systems, entails encasing healing chemicals (such as monomers or resins) in coated microcapsules. These capsules rupture when they are broken, releasing the healing chemicals that subsequently polymerize to repair damaged surfaces. This technique, which is frequently used in epoxy-based coatings, increases coating lifetime and decreases the requirement for manual repairs (Karaxi et al., 2019; Chen et al., 2023).
3. Vascular Systems: The coating's networks of microchannels carry healing materials to places that have been injured. These substances move to the crack site, simulating organic healing. This method works well for bigger cracks because it guarantees that the healing ingredients are distributed evenly (Sanyal et al., 2024).
4. Reversible Chemical Bonds: Diels-Alder reactions and other dynamic bonds are used in some coatings to enable the material to establish new bonds in response to particular stimuli, such as light or heat. These coatings are perfect for applications that need several healing cycles and long-term durability because this procedure can be repeated (Brunsveld et al., 2001; Hager et al., 2015).

Types of Self-Healing Coatings

Self-healing coatings vary by the materials used and healing mechanisms, each offering unique advantages for different applications:

1. Polymer-Based Coatings: These are among the most adaptable self-healing coatings; they are based on polymers, such as polyurethane or polyaniline composites, which have the ability to self-heal via processes like polymerization or hydrogen bonding. These coatings are appropriate for corrosion prevention and biodegradable applications due to recent advancements that include the use of graphene oxide and other nanomaterials to enhance mechanical qualities and healing effectiveness (Lei et al., 2020; Liu et al., 2022). They are frequently utilized in biodegradable materials, automotive, and aerospace (Ren et al., 2024).
2. Ceramic-Based Coatings: Despite their reputation for resilience to wear and high temperatures, ceramic coatings frequently suffer from brittleness. However, self-healing ceramics, including silica-based coatings that mend by silica condensation or hydrolytic bonding, have been made possible by developments in microcapsule embedding or the use of vascular systems. These coatings are perfect for high-temperature applications where traditional repairs are difficult, like thermal barriers for turbines and aircraft components (Zhang et al., 2018).
3. Hybrid Coatings: These coatings combine inorganic ceramics and organic polymers to provide both thermal stability and mechanical strength. These coatings produce improved mechanical, thermal, and self-healing capabilities by embedding nanostructured particles, such as carbon nanotubes, in polymer matrices. Applications in the automotive, aerospace, electronic, and marine industries benefit greatly from hybrid systems since they use a variety of processes, such as reversible bonding and microencapsulation (Wang et al., 2024).

Applications and Benefits

Self-healing coatings are gaining traction in industries that require high material integrity and where repairs are costly or impractical:

1. Corrosion Protection: These coatings shield metal surfaces from corrosive substances by patching fractures that may otherwise expose them to them. This is particularly helpful in sectors where corrosion drastically shortens material lifespan, such as the automotive, aerospace, and marine industries (Banerjee et al., 2020).

2. Aerospace and Automotive: Self-healing coatings reduce maintenance requirements and increase the lifespan of automobiles and aircraft by providing resilience and damage resistance against environmental stressors such UV radiation, mechanical wear, and temperature fluctuations (Kontiza&Kartsonakis, 2024).
3. Smart electronics: Self-healing coatings increase the dependability of devices by shielding circuits and other parts from harm, extending their lifespan and reducing the need for replacements or repairs (Jung et al., 2023).
4. Sustainable and Biodegradable Coatings: Biodegradable self-healing coatings, which provide environmentally friendly substrate protection, have gained popularity as environmental concerns have grown. Green building materials and sustainable packaging are perfect for these coatings (Liu et al., 2012).

Materials science is being advanced by self-healing coatings, which solve problems like corrosion, wear, and durability on their own. These coatings drastically lower the requirement for maintenance by repairing damage on their own through the use of mechanisms including vascular networks, microencapsulation, and reversible bonding. Applications for coatings based on polymers, ceramics, and hybrids are growing in a variety of sectors, including electronics, automotive, aerospace, and sustainable technologies. The ongoing advancement of self-healing coatings demonstrates how they have the potential to completely transform durability and material maintenance in a variety of industries.

4. TECHNOLOGIES BEHIND SMART MATERIALS AND SELF-HEALING COATINGS

Smart materials and self-healing coatings are reshaping industries with their ability to adapt to environmental changes, damage, and wear. These technologies incorporate advanced manufacturing, nanotechnology, and real-time monitoring systems to enable dynamic responses to damage. This section outlines recent advancements in smart material and self-healing coating technologies.

Advanced Manufacturing Techniques for Smart Materials

The production of smart materials requires specialized techniques that embed responsive elements into materials at molecular or macroscopic scales. Methods like layer-by-layer deposition, sol-gel processing, and nanostructuring allow for precise control over material properties, enhancing their response to environmental stimuli. Nanostructured coatings, for instance, improve self-healing by allowing efficient diffusion and activation of healing agents (Wang et al., 2019; Li et al., 2024). These methods yield coatings resistant to corrosion, abrasion, and environmental degradation. Recent progress in 3D printing and additive manufacturing enables the design of complex coatings with self-healing capabilities, allowing precise control over material structure and facilitating the inclusion of mechanisms like microcapsules and vascular networks (Li et al., 2023). These methods produce customizable coatings suited to specific industry needs, including aerospace, marine, and automotive applications.

Nanotechnology in Self-Healing Coatings

Nanotechnology is pivotal in enhancing the durability and self-healing efficiency of coatings. Nanomaterials such as nanoparticles, nanocapsules, and nanotubes strengthen coatings at the nanoscale, improving both mechanical and chemical properties. For example, nanocapsules filled with healing agents like epoxy or resins are incorporated into polymeric coatings, releasing healing agents upon rupture to repair cracks and prevent further damage (Li et al., 2024; Liu et al., 2021). Additionally, carbon nanotubes and graphene create conductive networks that facilitate rapid self-repair in cases of mechanical failure (Xu et al., 2024). Materials like graphene oxide and lignin derivatives enhance anticorrosive properties, making them ideal for protecting metals in harsh environments. These nanomaterials improve adhesion, flexibility, and thermal stability, allowing self-healing coatings to endure extreme conditions while maintaining functionality.

Smart Coating Systems with Sensors and Real-Time Monitoring

Integrating sensors with self-healing coatings represents a major innovation in smart materials. These sensors allow coatings to detect and respond to damage, such as corrosion or cracks, by releasing healing agents as needed. Coatings with embedded corrosion sensors, for example, can detect wear onset and activate a protective response, making them especially valuable in aerospace, automotive, and marine applications (Li et al., 2023). Embedded sensors can detect changes in mechanical, thermal, or chemical conditions and even biofouling. These capabilities enable predictive maintenance by providing real-time data on potential failures before they become critical, enhancing the efficiency and longevity of protective coatings (Li et al., 2024).

Additive Manufacturing and 3d Printing of Smart Materials

Additive manufacturing and 3D printing enable the design of self-healing materials with intricate geometries and embedded functionalities. These methods support the integration of microchannels, capsules, or encapsulated healing agents directly into the material. For example, certain 3D-printed structures incorporate patterns that optimize the controlled release of healing agents upon damage (Wang et al., 2019). Furthermore, multi-material 3D printing allows the creation of layers with distinct functions, some providing mechanical strength, others containing healing agents. The customization offered by these techniques improves the performance of self-healing coatings across a range of applications, from aerospace to biomedical devices (Li et al., 2024; Liu et al., 2022).

Computational Modelling and Simulation of Self-Healing Processes

Computational modelling and simulations are crucial for optimizing self-healing coatings, allowing researchers to predict material behaviour under different conditions. Techniques like finite element analysis (FEA) and molecular dynamics (MD) simulations model interactions between healing agents, polymers, and nanoparticles in coatings (Li et al., 2023). Machine learning and Artificial Intelligence(AI) further support these advancements by predicting coating responses under various stresses. Simulation tools provide insights into healing kinetics, structural integrity, and lifetime predictions, allowing for precise fine-tuning of self-healing mechanisms before production (Li et al., 2024).

Smart materials and self-healing coatings are advancing industries by enabling autonomous damage repair, improved performance, and reduced maintenance costs. Innovations in advanced manufacturing, nanotechnology, sensor integration, and computational modelling make it possible to design coatings with highly specialized functions. Real-time monitoring capabilities and self-triggered healing processes provide a significant advantage for industries reliant on durable and efficient protective materials, including corrosion protection, aerospace, and automotive sectors. Table 2 summarizes the technologies behind smart materials and self-healing coatings, with relevant citations that highlight the innovative advancements shaping their development and applications.

Table 2. Technologies behind Smart Materials and Self-Healing Coatings

Technology	Description	Applications	References
Advanced Manufacturing Techniques	Methods like layer-by-layer deposition, sol-gel processing, and nanostructuring allow precise control over material properties.	Aerospace, automotive, marine applications, energy-efficient coatings, 3D printed smart materials.	Wang et al., 2019; Li et al., 2024
Nanotechnology	Utilizes nanomaterials such as nanoparticles, nanotubes, and nanocapsules to enhance mechanical, chemical, and self-healing properties.	Protection of metals, corrosion-resistant coatings, flexible coatings, conductive networks.	Li et al., 2024; Liu et al., 2021; Xu et al., 2024
Smart Coating Systems with Sensors	Coatings embedded with sensors that can detect damage, like cracks or corrosion, and trigger self-repair mechanisms.	Aerospace, automotive, marine applications, predictive maintenance, corrosion control.	Li et al., 2023; Li et al., 2024
Additive Manufacturing &3D Printing	Allows for intricate design and embedding of healing agents, microchannels, and capsules directly into the material.	Aerospace, biomedical devices, custom smart coatings, 3D printed self-healing systems.	Wang et al., 2019; Li et al., 2024; Liu et al., 2022
Computational Modelling& Simulation	Utilizes tools like FEA and MD simulations to predict material behavior, healing kinetics, and optimize coating designs.	Coating optimization, material behavior prediction, failure analysis, enhanced self-healing processes.	Li et al., 2023; Li et al., 2024

5. INNOVATIVE APPLICATIONS OF SMART MATERIALS AND SELF-HEALING COATINGS

Smart materials and self-healing coatings are increasingly applied across various industries, offering durable, low-maintenance, and safety-enhancing solutions. These materials self-repair damage in real time, ensuring sustained performance and protection in harsh environments. Below are the innovative applications of smart materials and self-healing coatings across multiple industries.

Aerospace Industry: Protective Coatings for Aircraft and Satellites

Protective coatings are essential to the longevity and dependability of satellites and airplanes in the aerospace industry. Severe degradation is brought on by extreme circumstances like high-speed collisions, UV rays, and temperature changes. Self-healing coatings increase resistance to erosion, abrasion, and corrosion by fixing damage on their own. To prevent environmental degradation to aircraft surfaces, such as those made of aluminum and composite materials, nano-enabled self-healing coatings have been developed (Shakirzyanov et al., 2023; Zhang et al., 2018). These coatings contain microcapsules that automatically release healing chemicals to fix small cracks or abrasions.Embedded sensors in smart coatings provide real-time structural integrity monitoring, minimizing the need for expensive inspections and warning maintenance teams of possible damage early on (George et al., 2022). In aerospace applications, these technologies improve cost-effectiveness, durability, and safety.

Automotive Industry: Self-healing Paints and Materials for Vehicles

Automotive production is being revolutionized by self-healing materials, which can be used to create coatings that can fix tiny abrasions, cracks, and scratches. When a surface is damaged, these coatings' microcapsules or nanocontainers containing agents like epoxy or linseed oil activate, repairing the surface's appearance and providing protection from environmental elements like corrosion (Zhang et al., 2018; Morshed-Behbahani et al., 2022). Additionally, self-healing coatings are applied to car interiors to safeguard delicate electronic parts. Manufacturers improve car systems' dependability and safety by incorporating self-healing materials into electronics, protecting against environmental damage, wear, and moisture (George et al., 2022).

Construction Industry: Smart Coatings for Buildings and Infrastructure

Self-healing coatings are very advantageous to the construction sector for the upkeep of buildings and infrastructure. Smart coatings provide long-lasting defense against weathering, corrosion, and cracking when applied to steel, glass, and concrete. The self-healing concrete reduces the need for frequent repairs by containing bacteria or chemical agents that, when exposed to moisture, automatically mend cracks (Xia et al., 2022). These materials prolong the life of infrastructure and buildings, which promotes sustainability. Sensor-embedded intelligent coatings can track the health of the structure, giving maintenance crews up-to-date information on material quality and warning them of possible problems before they become serious.

Electronics and Sensors: Self-Healing coatings in consumer devices

Self-healing coatings improve the operation and longevity of consumer devices including wearables, tablets, and smartphones. These coatings frequently employ nanoencapsulation, which releases healing chemicals in response to damage, preventing problems from moisture, drops, or scratches (Li et al., 2017; Leal et al., 2018).Self-healing polymers are especially advantageous for flexible electronics, enabling wearable sensors and bendable screens to fix cracks without sacrificing functionality. These coatings will be more and more crucial for boosting the dependability and durability of electrical gadgets.

Energy Sector: Smart Materials in Renewable Energy Technologies

Self-healing coatings are used on wind turbines, solar panels, and storage devices in the energy sector to increase the lifetime of renewable technologies and combat environmental deterioration. The self-healing coatings on wind turbine blades fix impact damage, guaranteeing peak performance and lowering maintenance requirements (Erdogan et al., 2021). The reliability of renewable energy infrastructure is also supported by coatings on solar panels, which keep efficiency high by sealing fractures and keeping moisture out.

Healthcare and Biomedical Applications of Self-Healing Materials

Self-healing materials are used in the biomedical and healthcare sectors for devices, implants, and wound healing. In biomedical equipment like implants and prostheses, self-healing polymers fix themselves when they wear down, guaranteeing patient safety and lifespan. Self-healing hydrogel coatings in wound care protect and encourage tissue regeneration by simulating the skin's natural healing process (Behzadnasab et al., 2017). Self-healing materials, in which environmental factors induce the targeted release of medicines or healing agents, are also advantageous for drug delivery systems.

Marine and Offshore Applications: Protecting Structures in Harsh Environments

Materials that can withstand high pressure, harsh temperatures, and saltwater are necessary for the marine and offshore industries. Offshore platforms, ship hulls, and undersea structures are shielded from corrosion, abrasion, and biofouling by self-healing coatings. Offshore structures are coated to prevent corrosion, which lowers the need for repairs and increases the lifespan of the infrastructure (Hou et al., 2017). Marine coatings with antifouling and self-healing qualities keep organisms from building up, maintaining structural integrity and effectiveness (Erdogan et al., 2021).

Self-healing coatings and smart materials provide revolutionary solutions for a variety of sectors by boosting long-term performance in demanding settings, reducing maintenance, and improving durability. These developments, which tackle wear, deterioration, and environmental issues in fields ranging from healthcare to aerospace, highlight the promise of self-healing materials as crucial instruments for industrial resilience and efficiency as technology advances. Table 3 highlights the innovative applications of smart materials and self-healing coatings across various industries, from aerospace to healthcare. These technologies improve durability, reduce maintenance, and enhance performance in challenging environments.

Table 3. Innovative Applications of Smart Materials and Self-Healing Coatings

Industry	Application	Technology/Benefit	References
Aerospace	Protective Coatings for Aircraft and Satellites	Nano-enabled self-healing coatings with microcapsules that repair damage and embedded sensors for structural integrity	Shakirzyanov et al., 2023; Zhang et al., 2018
Automotive	Self-Healing Paints and Materials for Vehicles	Coatings that repair abrasions, cracks, and scratches using microcapsules containing epoxy or linseed oil	Zhang et al., 2018; Morshed-Behbahani et al., 2022
Construction	Smart Coatings for Buildings and Infrastructure	Self-healing concrete with bacteria or chemical agents to mend cracks and sensor-embedded coatings to monitor structural health	Xia et al., 2022
Electronics & Sensors	Self-Healing Coatings in Consumer Devices	Nanoencapsulation-based coatings for wearables, tablets, smartphones to prevent damage from moisture and scratches	Li et al., 2017; Leal et al., 2018
Energy	Smart Materials in Renewable Energy Technologies	Self-healing coatings for wind turbines and solar panels to repair damage and maintain efficiency	Erdogan et al., 2021
Healthcare	Biomedical Applications of Self-Healing Materials	Self-healing hydrogels for wound care and polymers for implants and prostheses	Behzadnasab et al., 2017
Marine &Offshore	Protecting Structures in Harsh Environments	Self-healing coatings for offshore platforms and ship hulls to resist corrosion and biofouling	Hou et al., 2017; Erdogan et al., 2021

6. CHALLENGES AND LIMITATIONS OF SMART MATERIALS AND SELF-HEALING COATINGS

Despite the many benefits of developing smart materials and self-healing coatings, a number of obstacles still stand in the way of their widespread use and efficacy. These difficulties cover a wide range of topics, including as integration with current infrastructure, environmental concerns, economic viability, scalability, and durability. For these materials to continue to improve in practical applications, these problems must be resolved.

Durability and Performance Under Extreme Conditions

Sustaining performance and durability under harsh conditions is a major problem for self-healing coatings. Variations in temperature, moisture content, and UV rays can all lower these materials' capacity for self-healing, which can occasionally result in partial or delayed recovery (Zhang et al., 2018). Mechanical wear can weaken coatings over time, reducing their capacity for self-healing. Researchers are looking into more durable choices, like graphene-based composites for corrosion protection and strong healing capabilities, to improve long-term performance (George et al., 2022).

Scaling up Production and Commercialization Challenges

Smart materials and self-healing coatings are still challenging to produce on a large scale. Despite their success in the lab, many self-healing coatings have difficulties in industrial manufacture because of intricate synthesis procedures (Samadzadeh et al., 2010). It can be difficult to maintain consistency over big batches, particularly for components that are nanoscale and susceptible to environmental changes. Technological advancements in nanoencapsulation may assist solve these scaling problems and increase production efficiency (Wang et al., 2017).

Cost and Economic Feasibility of Smart Coatings

The wider application of smart coatings is hampered by high production costs since sophisticated materials like graphene and nanoparticles are very expensive. Self-healing coatings can save maintenance costs, but because of their high initial cost, they are less accessible to cost-conscious industries like electronics and construction (George et al., 2022). Performance and economic viability must be balanced, especially in sectors where cost reduction is critical, such as renewable energy (Hou et al., 2017).

Environmental Impact and Sustainability Concerns

Smart materials' potential to contribute to plastic pollution raises concerns about their effects on the environment, especially those made of synthetic, non-biodegradable polymers. The environmental advantages of less maintenance may be outweighed by the energy-intensive manufacturing of nanoparticles (Xia et al., 2022). The development of biodegradable self-healing coatings and environmentally friendly encapsulation is promoted in order to improve sustainability (Grigoriev et al., 2017).

Integration with Existing Systems and Infrastructure

The integration of self-healing coatings with existing infrastructure presents an additional hurdle. Retrofitting efforts may be complicated by the incompatibility of modern coatings with traditional materials utilized in sectors such as construction (Leal et al., 2018). Furthermore, existing technological infrastructure must be modified in order to include these materials into sensor-based or automated maintenance systems (Dieleman et al., 2018).

Despite its potential, self-healing coatings and smart materials have problems with integration, scalability, cost, durability, and environmental effect. Innovations in sustainability, manufacturing, and materials science are needed to overcome these challenges. Future studies will probably concentrate on enhancing the effectiveness of self-healing, cutting production costs, and guaranteeing compatibility with a range of industrial applications.

7. RECENT INNOVATIONS IN SMART MATERIALS AND SELF-HEALING COATINGS

Recent developments in self-healing coatings and smart materials have produced important achievements, especially in enhancing usefulness, sustainability, and corrosion resistance. These developments are making it possible to create multifunctional coatings that react to a range of environmental stimuli in addition to improving the functionality of self-healing mechanisms.

Advances in Materials and Mechanisms for Self-Healing

The effectiveness of protective coatings has been greatly increased by recent developments in self-healing processes. The triple-stimuli-responsive nanocontainers, which react to light, moisture, and temperature stimuli to improve corrosion protection, have been created for anticorrosion coatings on aluminium alloys (Wang et al., 2019). Furthermore, to improve performance in harsh environments, dense Aluminium Oxide (Al_2O_3) sealing has been investigated as a means of preventing high hydrostatic pressure corrosion inChromium/Glassy Carbon(Cr/GLC) coatings (Li et al., 2024).

New Developments in Hybrid and Multi-functional Coatings

The creation of multipurpose coatings with improved qualities is the result of hybrid coatings, which combine several elements. Composite silicon dioxide and zinc oxide (SiO_2@ZnO) core-shell nanospheres have been shown to be used in polymer coatings that offer corrosion resistance and anti-fouling qualities for marine applications. Additionally, the use of porous microspheres in coatings has created new opportunities for active corrosion prevention and real-time damage detection (Li et al., 2023).

Advancements in Nano-enabled Self-Healing Coatings

More focused healing processes have been offered by developments in nano-enabled self-healing coatings. Liu et al. (2021) used nanoparticles to detect damage and initiate healing in order to create smart coatings with autonomous self-healing and early corrosion reporting capabilities. Waterborne polyurethane coatings containing chitosan-modified graphene oxide exhibit improved anti-corrosion and self-healing properties, making them perfect for extended outdoor use (Xie et al., 2022).

Role of Artificial Intelligence and Machine Learning in Material Design

Optimizing self-healing coatings is mostly dependent on machine learning and AI. Artificial intelligence algorithms simulate environmental conditions to help forecast material behavior and build more effective coatings (Li et al., 2024). Additionally, machine learning algorithms are employed to pinpoint performance trends and direct the creation of more resilient coatings.

Self-Healing Coatings for Extreme Environmental Applications

In challenging environmental applications where conventional coatings are ineffective, self-healing coatings are becoming more and more important. A mimosa-inspired anti-corrosive composite coating, for example, was created by Xu et al. (2024) and offers improved corrosion protection in challenging conditions. These developments hold the potential to completely transform industries by providing high-performing, environmentally friendly corrosion protection solutions.

Industries that depend on durable corrosion protection are undergoing a revolution thanks to recent advancements in smart materials and self-healing coatings. More effective and sustainable coatings are being developed thanks to developments in nano-enabled coatings, multifunctional hybrid coatings, and the fusion of AI and machine intelligence. These developments hold the potential to tackle some of the most difficult corrosion prevention issues, providing solutions that are resilient to harsh environments and extend the life of vital infrastructure.

8. ENVIRONMENTAL IMPACT AND SUSTAINABILITY OF SMART MATERIALS

The environmental impact and sustainability of smart materials and self-healing coatings are critical considerations in their development and implementation. As these materials become more advanced, it is essential to evaluate their eco-friendliness, life cycle, and ability to contribute to more sustainable practices.

Eco-friendly Smart Materials and Sustainable Alternatives

Reducing the environmental impact of coatings is a key component of the growing trend toward eco-friendly smart materials. The creation of self-healing and self-lubricating nano-hybrid smart coatings, which provide greater durability while reducing the need for frequent replacements, was emphasized by Vafaeenezhad and Eslami-Farsani (2024). This method offers a more environmentally friendly substitute for conventional coatings, which frequently need more upkeep. Furthermore, because bio-based materials improve sustainability and lessen dependency on hazardous chemicals, their application in protective coatings is growing (Zhang et al., 2018).

Smart Coatings and Materials Life Cycle Assessment

Assessing the environmental impact of smart materials from manufacture to disposal requires life cycle assessment (LCA). Jung et al. (2023) discussed about how LCA can be used to optimize dual-function smart materials that combine self-healing and damage detection in order to reduce resource consumption. According to life cycle studies that contrast self-healing coatings with conventional coatings, the latter offer advantages for the environment by lowering the need for replacement and maintenance (Sabet-Bokati et al., 2024).

Recyclability and End-of-life Management of Self-Healing Materials

Recyclability and the handling of self-healing materials at the end of their useful lives are also aspects of sustainability. Intelligent anti-corrosion coatings that use recyclable and less hazardous ingredients were investigated by Liu et al. in 2024. Microcapsules containing natural polyelectrolytes in water-based polyurethane coatings are an example of a biodegradable material trend that enhances self-healing and recyclability while lowering environmental impact over the material's lifecycle (Li et al., 2022).

Role in Reducing Maintenance and Resource Consumption

Self-healing coatings minimize the usage of raw materials and the related environmental effects by reducing the need for frequent maintenance. Wang et al. (2019) showed how anticorrosion coatings using triple-stimuli-responsive smart nanocontainers improve long-term durability while using fewer resources. Similarly, active protection is integrated into porous microspheres with corrosion sensing, maximizing material efficiency and minimizing unnecessary resource use (Li et al., 2023).

By lowering resource consumption and environmental effects, self-healing coatings and smart materials are advancing sustainability in protective coatings. These coatings offer long-term cost benefits and support more sustainable business practices because to developments in eco-friendly materials, LCA, and recyclability.

9. FUTURE DIRECTIONS OF SMART MATERIALS AND SELF-HEALING COATINGS

The future of smart materials and self-healing coatings is marked by continuous innovation, which aims to enhance their performance, sustainability, and integration with advanced technologies. As these materials evolve, they are expected to play a pivotal role in next-generation protective systems and contribute significantly to sustainable development.

Innovations on the Horizon: New Materials and Technologies

Recent innovations in smart materials focus on enhancing self-healing properties and improving efficiency. Martin et al. (2014) highlighted the development of poly(urea-urethane) elastomers with aromatic disulfide bridges, which enable reversible crosslinking and improved self-healing performance, offering durability and flexibility. Liu et al. (2012) explored biodegradable poly(urea-urethane) elastomers, based on hydrogen bonding, providing both environmental benefits and self-healing capabilities, addressing sustainability concerns in industrial applications.

The Role of Smart Coatings in Sustainable Development

Smart coatings are increasingly crucial for promoting sustainability across industries. Rivero et al. (2014) introduced thermo-remendable shape memory polyurethanes, which reduce material waste by extending coating lifespan. Additionally, supramolecular polymers with dynamic bonds, as noted by Brunsveld et al. (2001), improve material durability and energy efficiency, contributing to long-term sustainability and reducing the frequency of coating replacements.

Integrating Artificial Intelligence, Internet of Things, and Smart Materials for Next-generation Protection Systems

Integrating AI and the IoT with smart materials is transforming protective systems. Hager et al. (2015) discussed the integration of shape memory polymers with AI-driven systems, enabling real-time damage detection and adaptive self-healing coatings. Lei et al. (2020) highlighted the potential of IoT sensors combined with corrosion inhibitors, offering advanced corrosion monitoring, predictive maintenance, and reduced manual inspections.

Potential Markets and Future Applications in Emerging Industries

Smart materials are expanding into industries like aerospace, automotive, and marine. Karaxi et al. (2019) assessed self-healing coatings for galvanized steel, highlighting their potential in high-durability sectors. Chen et al. (2023) reviewed self-healing coatings for magnesium alloys, indicating promising applications in lightweight automotive components and energy-efficient buildings, improving resource efficiency and reducing maintenance costs.

Challenges for Widespread Adoption and Scaling

Challenges remain in scaling self-healing materials. Acharya et al. (2021) identified cost and production complexity as barriers. Sanyal et al. (2024) emphasized the need for standardized testing protocols to ensure reliability and safety. Addressing these issues is crucial for the widespread adoption of smart materials across industries.

The future of smart materials and self-healing coatings is exciting, with innovations in materials, technology integration, and applications paving the way for more sustainable and efficient solutions. By embracing advancements in biodegradable materials, AI, and IoT, the next generation of smart coatings will offer enhanced performance, durability, and environmental benefits, supporting their widespread adoption across diverse industries.

10. RECOMMENDATION OF REVIEW

The field of self-healing coatings has made significant strides, but there are still key areas that require further research to enhance their functionality, scalability, and sustainability for real-world applications.

1. Integration with Emerging Technologies: To unlock the full potential of self-healing coatings, research should focus on integrating nanomaterials, real-time monitoring, and advanced sensors. Combining these technologies could enable coatings to not only heal but also detect and assess damage before it spreads, offering multifunctional protection within a single system (Zhao et al., 2020).

2. Enhancing Durability: Future research must address the challenge of maintaining long-term durability under harsh conditions, such as extreme temperatures and mechanical wear, especially in industries like aerospace, marine, and industrial applications. Developing coatings that retain their healing ability and protective performance over time is crucial for their practical deployment (White et al., 2016).

3. Development of Multifunctional and Sustainable Coatings: There is growing demand for coatings that offer multiple protective functions, such as corrosion resistance, fouling prevention, and SHM, in addition to healing damage. Future research should aim to combine these features in a single coating system, while also exploring eco-friendly and biodegradable materials that reduce environmental impact without compromising performance (Srinivasan&Pospisil, 2021; Liu & Zhang, 2021).

4. Advanced Manufacturing and Scalability: A significant barrier to the widespread adoption of self-healing coatings is the ability to produce them at scale. Cost-effective manufacturing methods, such as 3D printing and roll-to-roll processing, need to be explored to ensure these coatings can be mass-produced for commercial use without exorbitant costs (Song et al., 2023).

5. AI and IoT Integration for Real-time Monitoring: Integrating AI and IoT with self-healing coatings could enable autonomous monitoring and triggered healing at the optimal time. This integration could be especially beneficial in high-precision industries, such as aerospace or healthcare, where timely repairs are critical to safety (Chen et al., 2022).

Self-healing coatings show great promise but require further research to enhance functionality, scalability, and sustainability. Key areas for improvement include integrating emerging technologies, enhancing durability, developing multifunctional and sustainable coatings, advancing scalable manufacturing methods, and incorporating AI and IoT for real-time monitoring.

11. CONCLUSIONS

The development of smart materials, particularly self-healing coatings, has emerged as a groundbreaking innovation with significant advantages across industries such as aerospace, automotive, construction, and healthcare. These coatings, capable of repairing themselves when damaged, offer enhanced durability, reduced maintenance costs, and promote sustainability by extending the lifespan of materials. The integration of emerging technologies such as nanomaterials, AI, and real-time monitoring is crucial for optimizing the functionality of these coatings. Despite these promising advancements, challenges such as the lack of long-term performance data, scalability issues, and high manufacturing costs still need to be addressed. The future of self-healing coatings depends on the successful integration of nanotechnology, AI, and IoT. These technologies have the potential to enhance the responsiveness and efficiency of self-healing materials, enabling real-time monitoring and automated damage detection. Advanced nanomaterials, like nanoparticles and nanocapsules, could significantly improve the healing process by enabling faster and more efficient recovery from damage. Additionally, AI algorithms could optimize the self-healing process, adapting the coatings to different environments and conditions. This convergence of emerging technologies will not only improve the functionality of self-healing coatings but also expand their potential applications.However, for self-healing coatings to achieve widespread adoption and commercial success, several challenges must be overcome.

These include enhancing the coatings' durability under real-world conditions, making them cost-effective for mass production, and ensuring their scalability across various industries. Additionally, the development of multi-functional coatings that can offer self-healing, corrosion resistance, and other protective properties simultaneously presents another challenge. To make these coatings commercially viable, collaboration between researchers, engineers, manufacturers, and industry stakeholders will be essential. By addressing these challenges, self-healing coatings can transition from lab-based concepts to commercially viable solutions, revolutionizing material science and leading to more resilient, sustainable, and efficient industries.

Nomenclatures

AI	Artificial Intelligence
Al_2O_3	Aluminum Oxide
AO	Adaptive Optics
Cr/GLC	Chromium/Glassy Carbon
EAP	Electroactive Polymer
EH	Energy Harvesting
FEA	Finite Element Analysis
IoT	Internet of Things
LCA	Life Cycle Assessment
MEMS	Micro-Electro-Mechanical Systems
MD	Molecular Dynamics
MS	Magnetostrictive
NiTi	Nickel-Titanium
SMA	Shape Memory Alloy
SHM	Structural Health Monitoring
SiO_2	Silicon Dioxide
SR	Soft Robotics
TFD	Terfenol-D
UV	Ultraviolet
ZnO	Zinc Oxide

Statement and declaration

The research presented in this manuscript is original and has not been submitted or published elsewhere. All sources and references have been duly acknowledged, and the authors have taken all necessary steps to ensure the accuracy and integrity of the work.

Acknowledgement

The authors would like to express their sincere gratitude to Kalasalingam Academy of Research and Education and K.M. College of Pharmacy for providing the necessary support and infrastructure throughout this study. The authors also acknowledge the valuable contributions of researchers whose work has shaped this field and helped in the development of this manuscript. Special thanks are extended to their families for their unwavering encouragement during this research process.

Highlights

1. Self-healing coatings enhance efficiency, sustainability, and durability by autonomously repairing damage in various industries.
2. Recent advancements include vascular systems, reversible bonding, and microencapsulation for autonomous damage repair.
3. Smart materials improve sustainability and reduce costs across sectors like construction, automotive, healthcare, and aerospace.
4. Challenges remain in long-term functionality, requiring further research on integrating nanomaterials and advanced technologies.

12. REFERENCES

[1] Y. Yu, Y. Shi, H. Kurita, Y. Jia, Z. Wang, F. Narita (2023) Carbon Fiber-Reinforced Piezoelectric Nanocomposites: Design, Fabrication and Evaluation for Damage Detection and Energy Harvesting, Compos. Part A Appl. Sci. Manuf., 172, 107587. https://doi.org/10.1016/j.compositesa.2023.107587

[2] J. MohdJani, M. Leary, A. Subic, M.A. Gibson (2014) A review of shape memory alloy research, applications and opportunities, Mater. Des., 56, 1078–1113. https://doi.org/10.1016/j.matdes.2013.11.084

[3] T. Kuilla, S. Bhadra, D. Yao, N.H. Kim, S. Bose, J.H. Lee (2010) Recent advances in graphene based polymer composites, Prog. Polym. Sci., 35, 1350–1375. https://doi.org/10.1016/j.progpolymsci.2010.07.005

[4] M.R. Kessler, N.R. Sottos, S.R. White (2003) Self-healing structural composite materials, Compos. Part A Appl. Sci. Manuf., 34, 743–753. https://doi.org/10.1016/S1359-835X(03)00138-6

[5] S. Kim, H. Jeon, J.M. Koo, D.X. Oh, J. Park (2024) Practical Applications of Self-Healing Polymers Beyond Mechanical and Electrical Recovery, Adv. Sci., 11, e2302463. https://doi.org/10.1002/advs.202302463

[6] S. Zhang, N. van Dijk, S. van der Zwaag (2020) A Review of Self-healing Metals: Fundamentals, Design Principles and Performance, Acta Metall. Sin., 33, 1167–1179. https://doi.org/10.1007/s40195-020-01102-3

[7] N. Sekine, W. Nakao (2023) Advanced Self-Healing Ceramics with Controlled Degradation and Repair

by Chemical Reaction, Materials, 16, 6368.https://doi.org/10.3390/ma16196368

[8] S. Parihar, B. Gaur (2023) Self healing approaches in polymeric materials-an overview, J. Polym. Res., 30, 217.https://doi.org/10.1007/s10965-023-03590-0

[9] K. VenkataChalapathi, M.N. Prabhakar, D.-W. Lee, J.-I. Song (2023) Development of thermoplastic self-healing panels by 3D printing technology and study extrinsic healing system under low-velocity impact analysis, Polym. Test., 119, 107923. doi.org/10.1016/j.polymertesting.2023.107923

[10] S. Wang, M.W. Urban (2020) Self-healing polymers, Nat. Rev. Mater., 5, 562–583. https://doi.org/10.1038/s41578-020-0202-4

[11] Y. Yang, M.W. Urban (2013) Self-healing polymeric materials, Chem. Soc. Rev., 42, pp. 7446–7467. https://doi.org/10.1039/C3CS60109A

[12] D.V. Zakharova, A.A. Pavlov, A.V. Polezhaev (2019) Synthesis of self-healing polymers precursors from available bio-renewable raw materials, IOP Conference Series: Materials Science and Engineering, 683, 012002. https://doi.org/10.1088/1757-899X/683/1/012002

[13] F. Zhang, P. Ju, M. Pan, D. Zhang, Y. Huang, G. Li, X. Li (2018) Self-healing mechanisms in smart protective coatings: A review, Corros. Sci., 144, 74–88. https://doi.org/10.1016/j.corsci.2018.08.005

[14] N.A. Johari, J. Alias, A. Zanurin, N.S. Mohamed, N.A. Alang, M.Z.M. Zain (2022) Anti-corrosive coatings of magnesium: A review, Mater. Today Proc., 48, 1842–1848. https://doi.org/10.1016/j.matpr.2021.09.192

[15] S.F. Da Costa, M. Zuber, M. Zakharova, A. Mikhaylov, T. Baumbach, D. Kunka, S.H. Pezzin (2021) Self-healing triggering mechanism in epoxy-based material containing microencapsulated amino-polysiloxane, Nano Sel., 3, 577–593. https://doi.org/10.1002/nano.202100091

[16] N.F. MohdSani, H.J. Yee, N. Othman, A.A. Talib, R.K. Shuib (2022) Intrinsic self-healing rubber: A review and perspective of material and reinforcement, Polym. Test., 111, 107598. https://doi.org/10.1016/j.polymertesting.2022.107598

[17] V. Achal, A. Mukherjee (2015) A review of microbial precipitation for sustainable construction, Constr. Build. Mater., 93, 1224–1235. https://doi.org/10.1016/j.conbuildmat.2015.04.051

[18] H.M. Jonkers, A. Thijssen, G. Muyzer, O. Copuroglu, E. Schlangen (2010) Application of bacteria as self-healing agent for the development of sustainable concrete, Ecol. Eng., 36, 230–235.https://doi.org/10.1016/j.ecoleng.2008.12.036

[19] A. Rekondo, R. Martin, A. Ruiz de Luzuriaga, G. Cabañero, H.J. Grande, I. Odriozola (2014) Catalyst-free room-temperature self-healing elastomers based on aromatic disulfide metathesis, Mater. Horiz., 1, 237–240.10.1039/C3MH00061C

[20] R. Martin, A. Rekondo, A. Ruiz de Luzuriaga, G. Cabañero, H.J. Grande, I. Odriozola (2014) The processability of a poly(urea-urethane) elastomer reversibly crosslinked with aromatic disulfide bridges, J. Mater. Chem. A, 2, 5710. https://doi.org/10.1039/C3TA14927G

[21] C.-C. Liu, A.-Y. Zhang, L. Ye, Z.-G. Feng (2012) Self-healing biodegradable poly(urea-urethane) elastomers based on hydrogen bonding interactions, Chin. J. Polym. Sci., 31, 251–262.https://doi.org/10.1007/s10118-013-1211-1

[22] G. Rivero, L.-T.T. Nguyen, X.K.D. Hillewaere, F.E. Du Prez (2014) One-Pot Thermo-Remendable Shape Memory Polyurethanes, Macromolecules, 47, 2010–2018. https://doi.org/10.1021/ma402471c

[23] L. Brunsveld, B.J. Folmer, E.W. Meijer, R.P. Sijbesma (2001) Supramolecular polymers, Chem. Rev., 101, 4071–4098. https://doi.org/10.1021/cr990125q

[24] M.D. Hager, S. Bode, C. Weber, U.S. Schubert (2015) Shape memory polymers: Past, present and future developments, Prog. Polym. Sci., 49–50, 3–33. https://doi.org/10.1016/j.progpolymsci.2015.04.002

[25] Y. Lei, Z. Qiu, N. Tan, H. Du, D. Li, J. Liu, T. Liu, W. Zhang, X. Chang (2020) Polyaniline/CeO_2 nanocomposites as corrosion inhibitors for improving the corrosive performance of epoxy coating on carbon steel in 3.5% NaCl solution, Prog. Org. Coat., 139, 105430. https://doi.org/10.1016/j.porgcoat.2019.105430

[26] E.K. Karaxi, I.A. Kartsonakis, C.A. Charitidis (2019) Assessment of Self-Healing Epoxy-Based Coatings Containing Microcapsules Applied on Hot Dipped Galvanized Steel, Front. Mater., 6, 222.https://doi.org/10.3389/fmats.2019.00222

[27] Y. Chen, L. Wu, W. Yao, J. Wu, M. Serdechnova, C. Blawert, M.L. Zheludkevich, Y. Yuan, Z. Xie, F. Pan (2023) “Smart” micro/nano container-based self-healing coatings on magnesium alloys: A review, J. Magnes. Alloys, 11, 2230–2259. https://doi.org/10.1016/j.jma.2023.06.006

[28] A. Ghazi, E. Ghasemi, M. Mahdavian, B. Ramezanzadeh, M. Rostami (2015) The application of benzimidazole and zinc cations intercalated sodium montmorillonite as smart ion exchange inhibiting pigments in the epoxy ester coating, Corros. Sci., 94, 207–217. https://doi.org/10.1016/j.corsci.2015.02.007

[29] Y. Ren, W. Sun, J. Fan, Z. Yu, L. Wang, Z. Yang, G. Liu (2024) Functionalization and morphology control of graphene oxide for intelligent barrier coatings against corrosion, Surf. Coat. Technol., 494, 131326. https://doi.org/10.1016/j.surfcoat.2024.131326

[30] N. Acharya, G.J. Weng, J.W. Fisher, P.L. Hudson, X. Li, X. Wu (2021) A review of self-healing materials: Theories, methods and applications, J. Mater. Sci., 56, 12679–12718. https://doi.org/10.1016/j.electacta.2021.139730

[31] A. Kontiza, I.A. Kartsonakis (2024) Smart Composite Materials with Self-Healing Properties: A Review on Design and Applications, Polymers, 16(15), 2115.https://doi.org/10.3390/polym16152115

[32] D. Banerjee, X. Guo, J. Benavides, B. Rameau, S.G. Cloutier (2020) Designing green self-healing anticorrosion conductive smart coating for metal protection, Smart Mater. Struct., 29(10), 105027. 10.1088/1361-665X/aba849

[33] R. Wang, L. Cao, W. Wang, Z. Mao, D. Han, Y. Pei, Y. Chen, W. Fan, W. Li, S. Chen (2024)

Construction of Smart Coatings Containing Core–Shell Nanofibers with Self-Healing and Active Corrosion Protection, ACS Appl. Mater. Interfaces, 16(32), 42748–42761. https://doi.org/10.1021/acsami.4c09260

[34] S. Sanyal, S. Park, R. Chelliah, S.J. Yeon, K. Barathikannan, S. Vijayalakshmi, Y.J. Jeong, M. Rubab, D.H. Oh (2024) Emerging Trends in Smart Self-Healing Coatings: A Focus on Micro/Nanocontainer Technologies for Enhanced Corrosion Protection, Coatings, 14(3), 324. https://doi.org/10.3390/coatings14030324

[35] H. Vafaeenezhad, R. Eslami-Farsani (2024) Self-Healing and Self-Lubricating Nano-hybrid Smart Coatings, in Nano-hybrid Smart Coatings: Advancements in Industrial Efficiency and Corrosion Resistance, p. 303–352, American Chemical Society.10.1021/bk-2024-1469.ch014

[36] F. Zhang, P. Ju, M. Pan, D. Zhang, Y. Huang, G. Li, X. Li (2018) Self-healing mechanisms in smart protective coatings: A review, Corros. Sci., 144, 74–88.https://doi.org/10.1016/j.corsci.2018.08.005

[37] S. Jung, H.G. Jang, J.Y. Jo, Y.S. Kim, D.C. Lee, J. Kim (2023) Smart Materials with Dual Functionality: Repeatable Damage-Detection and Self-Healing, ACS Appl. Mater. Interfaces, 15(21), 26028–26036.https://doi.org/10.1021/acsami.3c04194

[38] Z. Sabet-Bokati, K. Sabet-Bokati, Z. Russell, K. Morshed-Behbahani, S. Ouanani (2024) Anticorrosion shape memory-assisted self-healing coatings: A review, Prog. Org. Coat., 188, 108193. https://doi.org/10.1016/j.porgcoat.2023.108193

[39] Y. Liu, Y. Zhou, L. Tian, J. Zhao, J. Sun (2024) Intelligent anti-corrosion coating with self-healing capability and superior mechanical properties, J. Mater. Sci., p. 1–19. https://doi.org/10.1007/s10853-024-10175-9

[40] B. Li, D. Njuko, M. Meng, A. Tang, Y. Li (2022) Designing smart microcapsules with natural polyelectrolytes to improve self-healing performance for water-based polyurethane coatings, ACS Appl. Mater. Interfaces, 14(47), 53370–53379. https://doi.org/10.1021/acsami.2c18339

[41] T. Wang, J. Du, S. Ye, L. Tan, J. Fu (2019) Triple-stimuli-responsive smart nanocontainers enhanced self-healing anticorrosion coatings for protection of aluminum alloy, ACS Appl. Mater. Interfaces, 11(4), 4425–4438. https://doi.org/10.1021/acsami.8b19950

[42] S.Y. Li, H. Li, Y. Zhang, W. Yang, P. Guo, X.W. Li, A.Y. Wang (2024) Dense Al_2O_3 sealing inhibited high hydrostatic pressure corrosion of Cr/GLC coating, npj Mater. Degrad., 8, 1–10.https://doi.org/10.1038/s41529-024-00469-3

[43] W. Li, J.J. Tao, Y.X. Chen, K.Y. Wu, J. Luo, R. Liu (2023) Porous microspheres with corrosion sensing and active protecting abilities towards intelligent self-reporting and anti-corrosion coating, Prog. Org. Coat., 178, 107468. https://doi.org/10.1016/j.porgcoat.2023.107468

[44] Y.S. Liang, B. He, G. Fu, S.J. Wu, B. Fan (2023) Effects of ambient temperature and state of galvanized layer on corrosion of galvanized steel in high-humidity neutral atmosphere, Materials, 16, 3656. https://doi.org/10.3390/ma16103656

[45] C.A. Xu, X.C. Li, Z.B. Tong, Z.Z. Chu, H. Fang, Y. Hu, Z.H. Yang (2024) Mimosa inspired intelligent anti-corrosive composite coating by incorporating lignin and pyridine derivatives grafted graphene oxide, Chem. Eng. J., 483, 149316. https://doi.org/10.1016/j.cej.2024.149316

[46] C.B. Liu, H. Wu, Y.J. Qiang, H.C. Zhao, L.P. Wang (2021) Design of smart protective coatings with autonomous self-healing and early corrosion reporting properties, Corros. Sci., 184, 109355. https://doi.org/10.1016/j.corsci.2021.109355

[47] C. Xie, Y. Jia, M.S. Xue, Z.Z. Yin, Y.D. Luo, Z. Hong, W.Q. Liu (2022) Anti-corrosion and self-healing behaviors of waterborne polyurethane composite coatings enhanced via chitosan-modified graphene oxide and phosphate intercalated hydrotalcite, Prog. Org. Coat., 168, 106881.https://doi.org/10.1016/j.porgcoat.2022.106881

[48] F.G. Agayev, S.V. Trukhanov, A.V. Trukhanov, S.H. Jabarov, G.S. Ayyubova, A.V. Trukhanov (2022) Study of structural features and thermal properties of barium hexaferrite upon indium doping, J. Therm. Anal. Calorim., 147, 14107–14114. https://doi.org/10.1007/s10973-022-11742-5

[49] D.A. Vinnik, A.Y. Starikov, V.E. Zhivulin, K.A. Astapovich, V.A. Turchenko, A.V. Trukhanov (2021) Structure and magnetodielectric properties of titanium substituted barium hexaferrites, Ceram. Int., 47, 17293–17306. https://doi.org/10.1016/j.ceramint.2021.03.041

[50] R.I. Shakirzyanov, A.L. Kozlovskiy, M.V. Zdorovets, A.L. Zheludkevich, D.I. Shlimas, A.V. Trukhanov (2023) Impact of thermobaric conditions on phase content, magnetic and electrical properties of the $CoFe_2O_4$ ceramics, J. Alloys Compd., 954, 170083. https://doi.org/10.1016/j.jallcom.2023.170083

[51] K. Morshed-Behbahani et al. (2022) A review on the role of surface nanocrystallization in corrosion of stainless steel, J. Mater. Res. Technol., 19, 1120–1147. https://doi.org/10.1016/j.jmrt.2022.05.094

[52] D.-H. Xia et al. (2022) Electrochemical measurements used for assessment of corrosion and protection of metallic materials in the field: a critical review, J. Mater. Sci. Technol., 112, 151–183. https://doi.org/10.1016/j.jmst.2021.11.004

[53] S.A. Umoren et al. (2019) Protective polymeric films for industrial substrates: a critical review on past and recent applications with conducting polymers and polymer composites/nanocomposites, Prog. Mater. Sci., 104, 380–450. https://doi.org/10.1016/j.pmatsci.2019.04.002

[54] C. Erdogan et al. (2021) Conceptual sacrificial anode cathodic protection design for offshore wind monopiles, Ocean Eng., 235, 109339. https://doi.org/10.1016/j.oceaneng.2021.109339

[55] G. Grundmeier, et al. (2000) Corrosion protection by organic coatings: electrochemical mechanism and novel methods of investigation, Electrochim. Acta, p.1–12,https://doi.org/10.1016/S0013-4686(00)00348-0

[56] J.S. George, et al. (2022) Advances and future outlook in epoxy/graphene composites for anti-corrosive applications, Prog. Org. Coat., p. 1–15. https://doi.org/10.1016/j.porgcoat.2021.106571

[57] A.A. Nazeer, et al. (2018) Potential use of smart coatings for corrosion protection of metals and alloys: a review, J. Mol. Liq., 261, 495–510. https://doi.org/10.1016/j.molliq.2018.01.027

[58] M. Samadzadeh, et al. (2010) A review on self-healing coatings based on micro/nanocapsules, Prog. Org. Coat., 69(1), 3–14. https://doi.org/10.1016/j.porgcoat.2010.01.006

[59] F. Zhang, et al. (2018) Self-healing mechanisms in smart protective coatings: a review, Corros. Sci., 144, pp. 74–88. https://doi.org/10.1016/j.corsci.2018.08.005

[60] X. Li, D. Zhang, Z. Liu, Z. Li, C. Du, C. Dong (2015) Materials science: share corrosion data, Nature, 527, 441–442.https://doi.org/10.1038/527441a

[61] B. Hou, X. Li, X. Ma, C. Du, D. Zhang, M. Zheng, W. Xu, D. Lu, F. Ma (2017) The cost of corrosion in China, npj Mater. Degrad., 1, 4-12. https://doi.org/10.1038/s41529-017-0005-2

[62] D. Grigoriev, E. Shchukina, D.G. Shchukin (2017) Nanocontainers for self-healing coatings, Adv. Mater. Interfaces, 4, 1600590. https://doi.org/10.1002/admi.201600318

[63] W. Wang, L. Xu, F. Liu, X. Li, L. Xing (2017) Synthesis of isocyanate microcapsules and micromechanical behavior improvement of microcapsule shells by oxygen plasma treated carbon nanotubes, J. Mater. Chem. A, 1(5), 776–782. https://doi.org/10.1039/C2TA00612J

[64] J. Li, Q. Feng, J. Cui, Q. Yuan, H. Qiu, S. Gao, J. Yang (2017) Self-assembled graphene oxide microcapsules in Pickering emulsions for self-healing waterborne polyurethane coatings, Compos. Sci. Technol., 151, 282–290. https://doi.org/10.1016/j.compscitech.2017.07.031

[65] M. Mahmoudian, E. Nozad, M.G. Kochameshki, M. Enayati (2018) Preparation and investigation of hybrid self-healing coatings containing linseed oil loaded nanocapsules, potassium ethyl xanthate and benzotriazole on copper surface, Prog. Org. Coat., 120, 167–178. https://doi.org/10.1016/j.porgcoat.2018.03.014

[66] D.A. Leal, I.C. Riegel-Vidotti, M.G.S. Ferreira, C.E. B. Marino (2018) Smart coating based on double stimuli-responsive microcapsules containing linseed oil and benzotriazole for active corrosion protection, Corros. Sci., 130, 56–63. https://doi.org/10.1016/j.corsci.2017.10.009

[67] M. Behzadnasab, S. Mirabedini, M. Esfandeh, R. Farnood (2017) Evaluation of corrosion performance of a self-healing epoxy-based coating containing linseed oil-filled microcapsules via electrochemical impedance spectroscopy, Prog. Org. Coat., 105, 212–224. https://doi.org/10.1016/j.porgcoat.2017.01.006

[68] C.D. Dieleman, P.J. Denissen, S.J. Garcia (2018) Long-term active corrosion protection of damaged Coated-AA2024-T3 by embedded electrospun inhibiting nanonetworks, Adv. Mater. Interfaces, 5, 1800176. https://doi.org/10.1002/admi.201800176

IZVOD

NAPREDAK I IZAZOVI U SAMOZALEČIVIM PREMAZIMA ZA ODRŽIVE PAMETNE MATERIJALE U INDUSTRIJSKIM PRIMENAMA

Ovaj pregled ispituje razvoj oblasti samozalečivih premaza i pametnih materijala, naglašavajući kako oni imaju potencijal da transformišu brojne sektore poboljšanjem efikasnosti, održivosti i izdržljivosti. Sve veći broj samozalečivih premaza uključuje pametne materijale, koji reaguju na stimuluse iz okoline poput temperature, pritiska i električnih polja, omogućavajući popravku oštećenja bez potrebe za spoljnom pomoći. Čak i uz neka poboljšanja u procesima samozalečivosti, još uvek ima mnogo toga da se nauči o dugoročnoj funkcionalnosti i stvarnoj upotrebi ovih materijala, posebno kada se upare sa najsavremenijom tehnologijom poput nanomaterijala. Najnovije studije o samozalečivim premazima sumirane su u ovoj studiji, koja takođe nudi uvid u mehanizme koji leže u osnovi ovih napretka, kao što su vaskularni sistemi, reverzibilno hemijsko vezivanje i mikroenkapsulacija. Takođe naglašava različite načine na koje se pametni materijali koriste u sektorima, uključujući građevinarstvo, automobilsku industriju, zdravstvenu zaštitu i vazduhoplovstvo, pokazujući njihov potencijal da uštede troškove održavanja i poboljšaju održivost uopšte. Ova studija razmatra aktuelna pitanja i predlaže buduće pravce istraživanja koji bi mogli da podstaknu razvoj i komercijalizaciju ovih tehnologija za praktičnu upotrebu.

Ključne reči: *Napredni premazi; industrijske primene; nanotehnologija; samozalečivi premazi; pametni sistemi premaza; pametni materijali; održivost*

Naučni rad
Rad primljen: 15.01.2025.
Rad korigovan: 02.04.2025.
Rad prihvaćen: 09.04.2025.

Sivakumar Durairaj: https://orcid.org/0009-0008-5889-7005
Shankar Durairaj: https://orcid.org/0000-0001-5228-0145

Dinesh Kumar Vairavel[1], Sivasubramanian Mahadevan[2], Armstrong Michael[3],Sivakumar Durairaj[4], Selvapalam Narayanan[5]*

[1,2]School of Mechanical, Aero, Auto and Civil Engineering, Kalasalingam Academy of Research and Education, Krishnankoil, Virudhunagar, Tamil Nadu, India, [3]Department of Mechanical Engineering, PSN College of Engineering and Technology, Tirunelveli, Tamil Nadu, India, [4]School ofBio, Chemical and Processing Engineering, Kalasalingam Academy of Research and Education, Krishnankoil, Virudhunagar, Tamil Nadu, India, [5]School of Advanced Sciences,Kalasalingam Academy of Research and Education, Krishnankoil,. Virudhunagar, Tamil Nadu, India

Scientific paper
ISSN 0351-9465, E-ISSN 2466-2585
https://doi.org/10.62638/ZasMat1390

Zastita Materijala 67 (1)
62 – 75 (2026)

Investigating the hydrophobic properties and corrosion resistance of copper surfaces via octadecanoic acid chemical deposition technique

ABSTRACT

This study investigates the enhancement of copper's hydrophobicity and corrosion resistance through the chemical deposition of octadecanoic acid. Structural and chemical modifications of the treated copper surfaces were analyzed using X-ray Diffraction (XRD), Scanning Electron Microscopy (SEM), and Energy-Dispersive X-ray Spectroscopy (EDS). SEM images revealed significant alterations in surface topography, promoting water repellency, while EDS confirmed the uniform coating of octadecanoic acid. XRD analysis showed that the crystalline structure of copper was preserved. Hydrophobicity was quantitatively assessed through contact angle measurements, which increased from 75° for bare copper to 121.5° for the octadecanoic acid-coated copper, confirming the transition to a hydrophobic surface. Water jetting and water bouncing tests demonstrated superior water repellency and self-cleaning efficiency of the coated surfaces. The contact angle measurement for the coated surface reached approximately 160° during the bouncing tests, indicating highly hydrophobic behaviour. Corrosion resistance was evaluated using dynamic potential polarization and electrochemical impedance spectroscopy (EIS). The dynamic polarization curve indicated a corrosion potential (Ecorr) of -0.0700 V for the coated copper, compared to -0.2036 V for the uncoated copper. The corrosion current density (Icorr) for the coated copper was 3.577×10^{-6} *A/cm², significantly lower than the bare copper's value of* 2.214×10^{-5} *A/cm². The corrosion rate of the coated copper was reduced to* 1.388×10^{-1} *mm/a from* 3.226×10^{-1} *mm/a for the uncoated copper, resulting in an efficiency of 83.8%. These findings demonstrate that octadecanoic acid is an effective and cost-efficient protective coating for enhancing copper's durability and functionality, especially in moisture-prone environments.*

Keywords: *Copper, Corrosion Resistance,Hydrophobicity, Octadecanoic Acid, Self-Cleaning, Surface Modification*

1. INTRODUCTION

Copper, renowned for its exceptional electrical and thermal conductivities, stands as a cornerstone in the advancement of modern technology and infrastructure[1,2]. Its significance in the global market is projected to escalate, with forecasts indicating a surge in demand comparable to that of gold. The global copper market insight for 2024 anticipates a robust expansion from $199.67 billion in 2023 to $252.33 billion by 2031, driven by acompound annual growth rate (CAGR) of 3.98%[3].

Figure 1 illustrates the significance of copper in diverse sectors.

Exhibiting a distinct pinkish-orange hue when freshly exposed, copper is extensively utilized in heat and electricity conduction, as well as a fundamental building material in the form of wires, rods, and pipes[4, 5]. Despite its widespread use, copper's Achilles' heel is its susceptibility to corrosion, particularly in humid environments. This limitation has spurred research into enhancing copper's corrosion resistance, with hydrophobic films emerging as a promising solution[6]. These films significantly increase the water contact angle on surfaces, thereby reducing the interaction between corrosive agents and the metal, preserving the metal's inherent mechanical properties.

---

*Corresponding author: Dinesh Kumar Vairavel
E-mail: autodinesh@gmail.com

Paper received: 27.01.2025
Paper corrected: 28.02.2025.
Paper accepted: 05.03.2025.

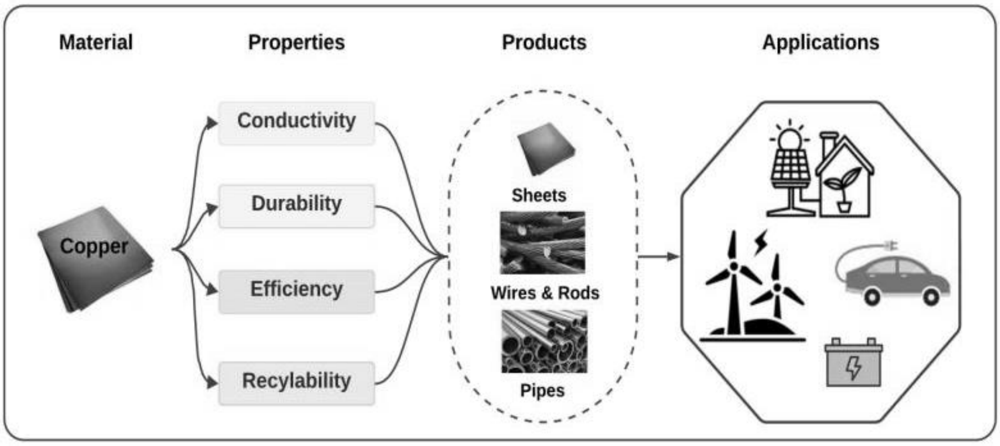

Figure 1. Significance of copper in different sectors

The quest for hydrophobic surfaces on copper has led to various methods, including etching[7], sol-gel techniques[8], and chemical vapor deposition[9]. Yet, the practical deployment of these surfaces is often hampered by their mechanical and chemical stability, as well as cost considerations. Hydrophobic coatings have demonstrated utility across diverse applications, from consumer electronics to marine and automotive components, offering enhanced durability and performance [10, 11]. Improving copper's hydrophobicity through coatings could yield substantial benefits, enhancing its water repellence, corrosion resistance, wear resistance, friction resistance, self-cleanability, and antimicrobial properties.

In the realm of hydrophobic coating technology, octadecanoic acid has emerged as a pivotal component due to its unique properties. Octadecanoic acid (OA) chemical deposition has proven to be a promising method for developing hydrophobic surfaces on many materials, offering improved corrosion resistance in aggressive environments [6]. OA prevents the diffusion of corrosive ions, such as chloride, and reduces the accumulation of moisture, a key factor in electrochemical corrosion processes. OA-treated metal surfaces exhibit reduced corrosion rates, as water and contaminants are kept from reaching the metal substrate The preparation and corrosion resistance of superhydrophobic coating on Cu plate via two-step electrodeposition[12, 13]. The key benefits of octadecanoic acid include its biodegradability, surface compatibility, cost-effectiveness, enhanced protection, longevity, versatility, and ease of application. These attributes make it highly suitable for the extensive variety of applications in hydrophobic coatings[14].

Recent studies have highlighted the potential of octadecanoic acid in various applications. Kim et al.[15] inspected the enhancement of hydrophobicity in zeolite composites coated with octadecanoic acid, finding a significant increase in impact strength compared to uncoated zeolites. Similarly, Jeong et al.[16] observed improvements in the flowability and floodability of $CaCO_3$ powder when coated with octadecanoic acid, with the coated powder outperforming uncoated calcium carbonate.Ng et al. [17] synthesized organic coatings on magnesium through hydrothermal treatment followed by immersion in octadecanoic acid, resulting in superior corrosion resistance, although they noted that long-term immersion led to coating degradation. Gupta et al. [18] compared the corrosion resistance of magnesium coated with phytic acid followed by immersion in octadecanoic acid, concluding that the latter provided better protection than both phytic acid-coated and uncoated magnesium.In another study, Nguyen et al.[19] explored the effect of octadecanoic acid over the dispersion of inorganic fillers, finding that treated fillers exhibited enhanced dispersion without affecting the melting temperature. Additionally, the mechanical properties of films treated with octadecanoic acid were superior to those of untreated films, suggesting significant improvements in material performance.Advanced applications have also been explored, such as Liu et al.[20] developing a novel superhydrophobic coating for magnesium ions through a hybrid approach integrating electro-deposition with immersion techniques. Their study revealed that the resultant coatings exhibited enhanced super hydrophobicity, chemical stability, and anti-corrosioncharacteristics. Concurrently, Hu et al.[21] synthesized a stearic acid-TiO_2/zinc composite superhydrophobic coating on carbon steel employing electrochemical deposition and surface modification processes. The fabricated coating demonstrated superior mechanical and chemical toughness, self-cleaning functionality, and improved corrosion resistance.Rongjun Ma et al. [22] investigated the superhydrophobic properties of copper mesh substrates using octadecanethiol. The resulting surfaces exhibited superhydrophobic and superoleophilic characteristics, which enhanced the self-cleaning, wettability, durability, and anticorrosive properties of the samples.

Building on this background, the present research study evaluated the hydrophobic performance of copper by applying an octadecanoic acid-based coating. The hydrophobic properties of copper surfaces are influenced primarily by surface roughness and chemical composition. OA deposition forms a self-assembled monolayer (SAM) that reduces surface energy, resulting in a water-repellent layer. This interaction between the carboxyl group of OA and the copper surface creates a stable hydrophobic layer. Surface roughening enhances this effect, leading to a Cassie-Baxter wetting state, where water droplets maintain minimal contact with the surface. The behaviour of the coated copper was documented and assessed to determine its effectiveness, further emphasizing the potential of octadecanoic acid in enhancing material properties across various applications.

2. METHODS AND MATERIALS

2.1 Preparation of the Samples

The preparation process involved modifying copper surfaces using high-purity chemicals sourced from Otto ChemiePvt. Ltd and Avra Synthesis Pvt. Ltd in India, as well as Sigma Aldrich in the USA. Two distinct sets of copper plate samples, each measuring 1 × 1 × 1 cm, were prepared. One set underwent a comprehensive cleaning and coating process, while the second set remained uncoated, serving as a control sample to evaluate the efficacy of the treatment (Figure 2).

The cleaning process began by immersing the copper plates in an ammonium persulfate solution, prepared by dissolving 0.1 g of ammonium persulfate salt in 50 ml of distilled water (Figure 3a). The plates were immersed in this solution at 60 °C for one hour to ensure the removal of any surface contaminants and to enhance surface reactivity. This step is crucial for preparing the copper surface for subsequent coating, thereby improving the adhesion of the coating material.

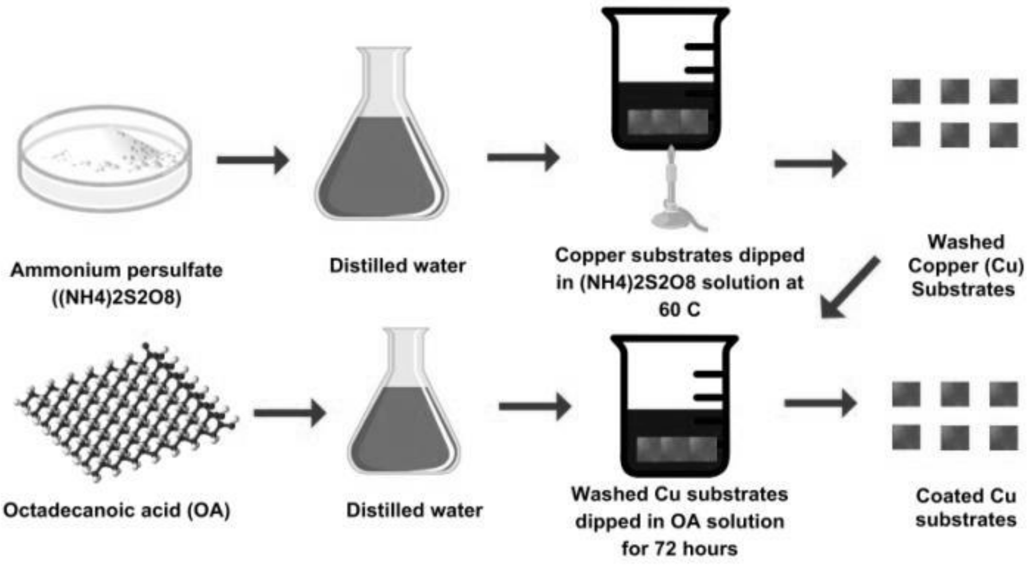

Figure 2. Illustration of Copper Washed and Copper Coated Substrates

The coating process involved immersing cleaned copper plates in a solution of octadecanoic acid (OA), prepared by dissolving 1 g of OA in 50 ml of ethanol (Figure 3b). The copper plates were submerged in this ethanol-OA solution for 72 hours at ambient temperature, ensuring the formation of a uniform and adherent coating on the surface. After the treatment, the coated plates were removed from the solution and air-dried using heated air for 30 minutes to eliminate any residual solvent. The treated surfaces were then systematically documented through both schematic and photographic representations. The effects of the surface treatment are illustrated in Figures 3(a) and 3(b), highlighting the physical transformations of the copper plates before and after coating.

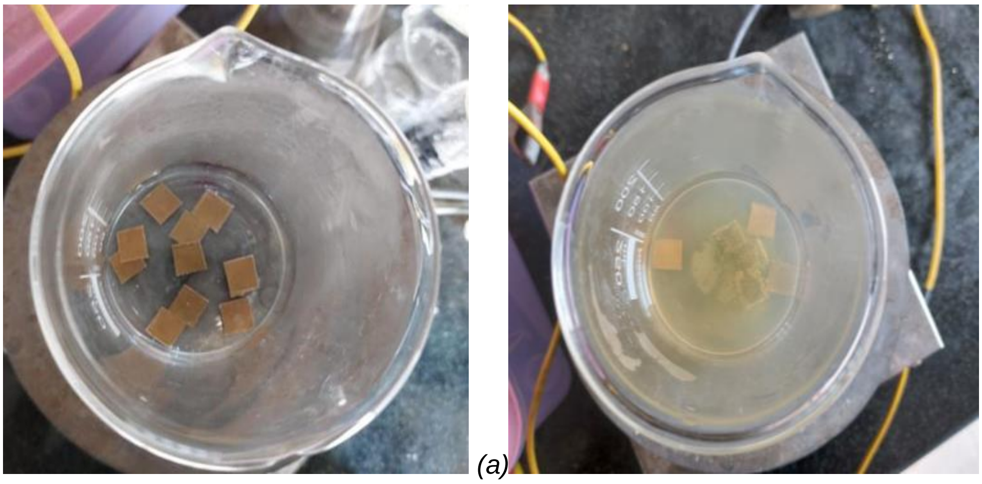

(a) (b)

Figure 3.(a) Cleaning, and (b) Coating of the Copper plates

3. RESULT AND DISCUSSION

3.1.X-Ray Diffraction (XRD) Analysis

The structural and surface composition of the octadecanoic acid-coated copper plate were determined using X-ray diffraction (XRD) analysis with an ECO Brukerdiffractometer equipped with a copper anode (Cu-Kα radiation source, λ = 1.54060 Å). The analysis spanned a 2θ range of 10° to 80° to capture potential diffraction peaks from both the octadecanoic acid coating and the underlying copper substrate. Diffractometer settings, including voltage, current, and scan rate, were optimized to ensure high-resolution data. Special attention was given to sample preparation to maintain uniform coating and reduce surface irregularities, ensuring accurate and reproducible results.

Observed diffraction peaks of the octadecanoic acid-coated copper were compared with those of uncoated copper to validate the successful deposition of octadecanoic acid and assess the interaction between the coating and the substrate. The degree of crystallinity of the copper samples was calculated using Equation 1:The occurrence of crystalline elements can be identified through the diffractograms illustrate sharp peaks and broad patterns [23].

$$Percent\ Crystallinity(\%) = \frac{\sum I_{crystalline\ peaks}}{\sum I_{crystalline\ peaks} + \sum I_{amorphous\ background}} * 100 \qquad (1)$$

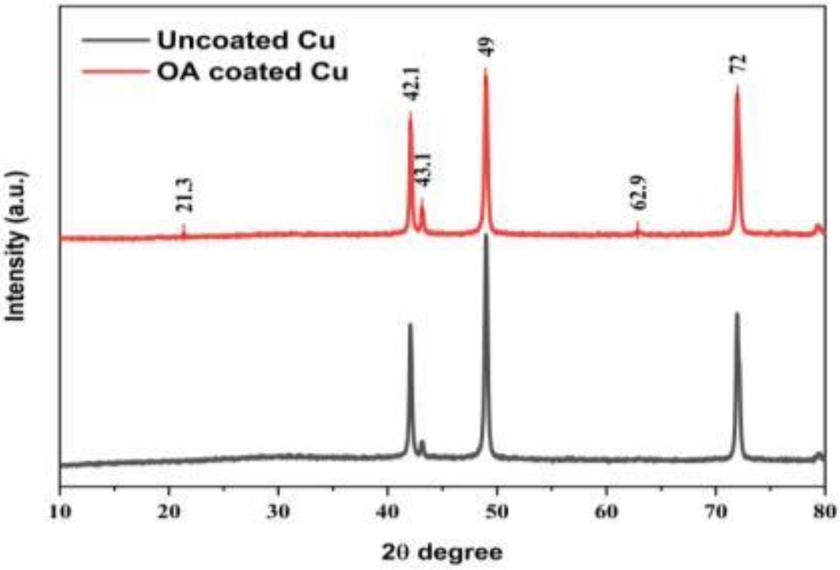

Figure 4. XRD Analysis of Uncoated and Octadecanoic Acid-Coated Copper (Cu) Samples

XRD analysis revealed significant structural modifications, confirming the successful deposition of the octadecanoic acid coating (Figure 4). New peaks at 21.3° (d-value = 4.16042 Å)and 62.8° (d-value = 1.47739 Å), with net intensities of 497 and 112, respectively, were observed in the coated sample but were absent in the uncoated sample. Additionally, the intensity of key copper peaks decreased in the coated samples, such as at 42.1° (d-value = 2.14517 Å) and 48.9° (d-value = 1.85745 Å), with net intensities dropping from 3634 to 2884 and 6244 to 4275, respectively (Table 2). These changes suggest that the octadecanoic acid coating alters the copper's crystal structure.

Figure 4 showcases the XRD diffraction patterns of both samples, highlighting new peaks exclusive to the coated copper, indicating structural changes and increased crystallinity. The emergence of new peaks at 21.3° and 62.8° signifies the presence of crystalline elements unique to the coating, further confirming successful deposition of octadecanoic acid.

Table 2. Comparative Analysis of XRD Spectrograms for Uncoated and Octadecanoic Acid-Coated Copper (Cu) Samples

Peaks	Angle	d-Value	Net-Intensity		Gross-Intensity		New Peaks
	2θ	(A)	Uncoated	Coated	Uncoated	Coated	
1	21.3	4.16042	-	126	-	497	Yes
2	42.1	2.14517	3634	2884	4233	3375	No
3	43.1	2.0952	433	642	1022	1130	No
4	48.9	1.85745	6244	4275	6822	4769	No
5	62.8	1.47739	-	112	-	556	Yes
6	71.9	1.31079	4076	3901	4602	4389	No
7	79.3	1.20441	122	215	615	687	No

These structural modifications and increased crystallinity improve the copper's water-repellent properties, enhancing its hydrophobicity and corrosion resistance. These findings align with studies by Chen et al. [24] and Ma et al. [22], who observed similar structural changes and enhanced hydrophobicity following surface modifications.

3.2.Scanning Electron Microscopy (SEM) Analysis

The surface morphology of uncoated and octadecanoic acid-coated copper (Cu) samples was examined using scanning electron microscopy (SEM). This analysis aimed to compare the surface features of the uncoated and coated samples and evaluate the uniformity and coverage of the octadecanoic acid coating. Observations were conducted at magnifications of 100x, 500x, 1000x, and 5000x to provide a comprehensive view of the surface textures and the distribution of the coating material.

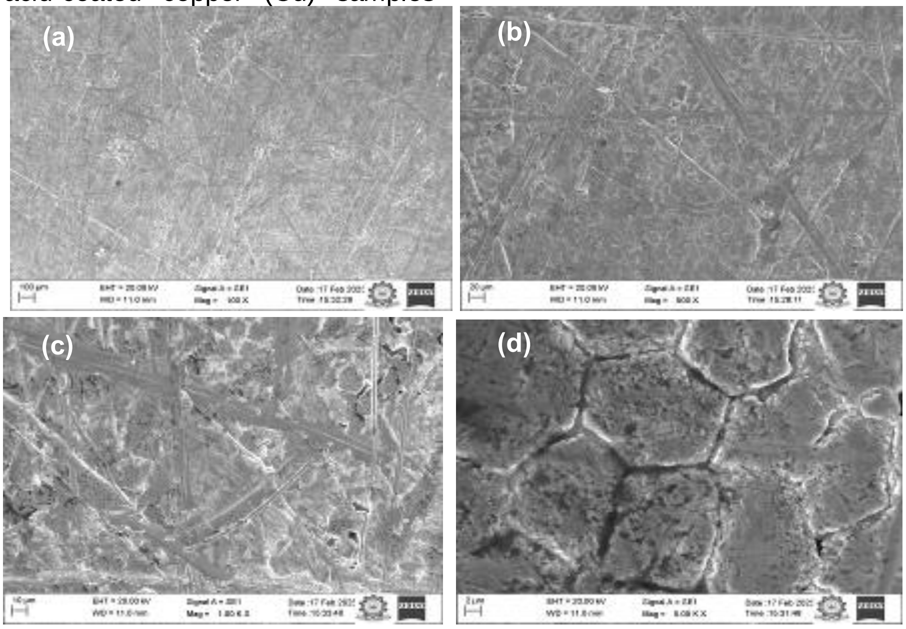

Figure 5. SEM Analysis of Uncoated Cu

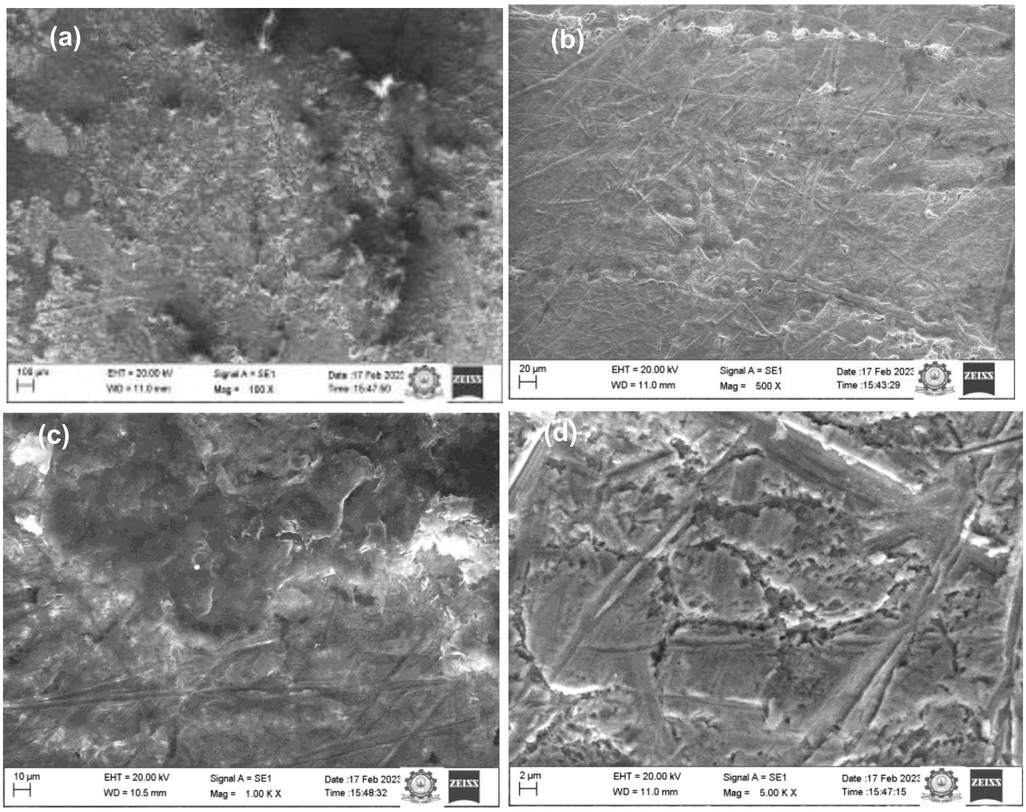

Figure 6.SEM Analysis of Octadecanoic Acid-Coated Cu

The uncoated Cu surface, as depicted in Figure 5, exhibited numerous micro-cracks, which increase susceptibility to corrosion and water absorption. In contrast, the octadecanoic acid-coated Cu surface, shown in Figure 6, appeared smoother and more uniform, suggesting that the coating contributes to surface smoothening and may enhance hydrophobicity. SEM analysis confirmed the formation of a self-assembled monolayer (SAM) of long-chain fatty acids on the copper surface.

The result illustrates strong bonding between the copper and the octadecanoic acid, contributing to the smoother surface and enhanced protection. Additionally, the coated Cu surface exhibited reduced accumulation of dust and other foreign materials, which is crucial for improving corrosion resistance. This finding suggests that the octadecanoic acid coating improves a degree of self-cleaning effect, further enhancing the long-term performance of the copper surface.

3.3 Energy-Dispersive X-ray (EDX) Spectroscopy

The elemental composition of the uncoated and octadecanoic acid-coated copper (Cu) samples was analysed using energy-dispersive X-ray (EDX) spectroscopy. This technique was employed to identify and quantify the elements present on the sample surfaces, providing crucial information about the chemical composition of the coating.

Table 3. Estimated elemental compositions from the samples

Element	Uncoated Cu			Coated Cu		
	Weight %	Atomic %	Error %	Weight %	Atomic %	Error %
C K	4.8	19.5	15.8	45.1	74.4	9.1
O K	3.2	9.9	11.7	9	11.1	10.9
Cu K	58	44.9	2.6	27.9	8.7	3.1
Zn K	34	25.6	3.3	17.1	5.2	3.9
P K	-	-	-	0.9	0.6	12.1

EDX measurements were conducted in conjunction with scanning electron microscopy (SEM) to accurately localize the areas under analysis. The spectroscopic data were acquired by directing an electron beam onto the sample surface, inducing characteristic X-ray emissions that were subsequently detected and analysed.

From the EDX compositional investigations, spectrograms were obtained and are presented in Figure 7. Table 3 quantifies these variations, demonstrating a significant increase in carbon and oxygen content and a decrease in copper and zinc content after coating.From Figure 7, it may be noted that the uncoated Cu displayed predominant copper (58 wt%) and zinc (34 wt%), with minor carbon (C) and oxygen (O) content, indicating surface oxidation. In contrast, the coated Cu revealed a significant increase in carbon (45.1 wt%) and oxygen (9%), and a reduction in copper (27.9 wt%) and zinc, confirming the deposition of octadecanoic acid.

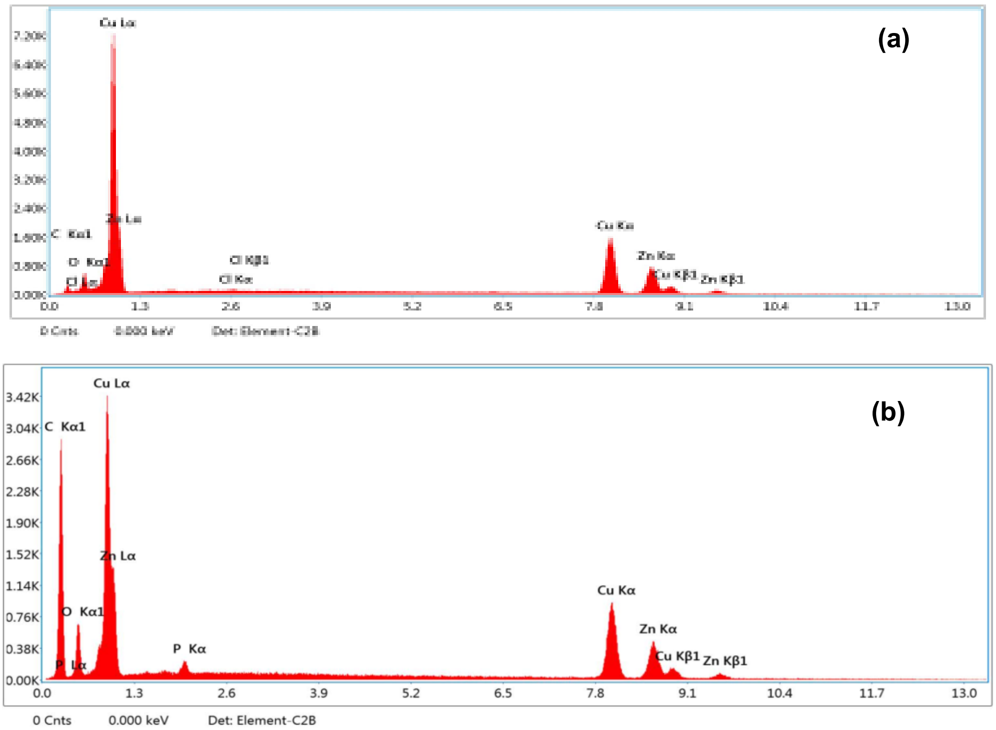

Figure 7.EDX compositional investigations of (a) bare Cu, (b) OA coated Cu

3.4 Contact Angle Measurements

To quantify the hydrophobic nature of the octadecanoic acid-coated copper (Cu) samples, contact angle measurements were performed using a goniometer equipped with a high-resolution camera. A controlled volume of deionized water (5 μL) was deposited onto the sample surface, and the contact angle formed between the water droplet and the surface was recorded. Measurements were taken at multiple locations to ensure surface uniformity and coating consistency. Uncoated copper samples were tested under identical conditions for comparison. The results, compared to standard hydrophobicity benchmarks, confirmed a significant increase in water repellency due to the octadecanoic acid coating, validating the hydrophobic properties observed in the material characterization studies.

The contact angle measurements, as illustrated in Figure 8, quantified the hydrophobic nature of the octadecanoic acid-coated copper (Cu) samples. The uncoated Cu surface exhibited a contact angle of 98.3°, indicating its less hydrophobic nature, whereas the coated Cu sample achieved a contact angle of 121.5°, indicating a transition to hydrophobic behaviour. This enhancement is attributed to the deposition of octadecanoic acid, which forms a continuous air gap between water droplets and the copper surface, characteristic of the Cassie-Baxter phenomenon[25]. According to Table 4, surfaces with contact angles exceeding 90° are classified as hydrophobic. The results affirm the efficacy of the immersion method for creating hydrophobic surfaces, highlighting its potential for applications requiring anti-wetting and corrosion resistance.

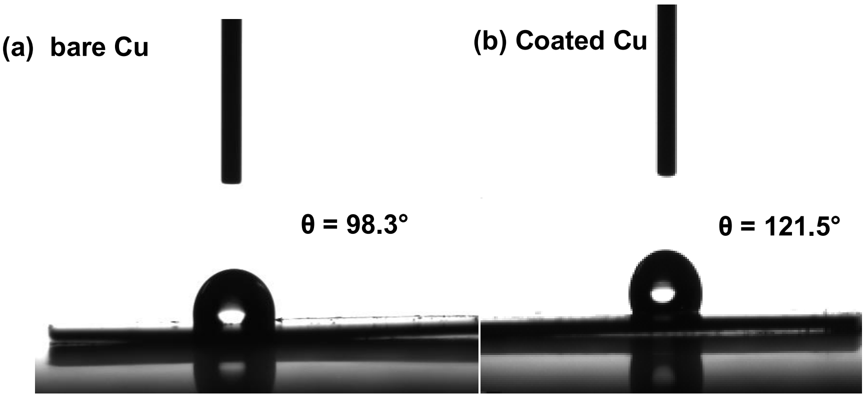

Figure 8. Contact angle measurements of (a) Bare Cu, (b) Coated Cu

Table 4. Wettability Nature of Metal Surface[26]

Contact Angle Measurement	Wettability Nature
0-90	Hydrophilic Nature
Above 90	Hydrophobic Nature

3.5.Water Jetting Investigations

The hydrophobic behaviour of octadecanoic acid-coated copper (Cu) samples was further evaluated through water jetting investigations. A fine stream of water droplets was directed at both uncoated and coated samples using a controlled nozzle setup. The water droplets were retained on the uncoated copper surface, indicating its hydrophilic nature. In contrast, the octadecanoic acid-coated samples exhibited pronounced water repellency, with droplets being repelled upon contact. This behaviour is attributed to the low-surface-energy layer formed by the octadecanoic acid coating, which minimizes interaction between the water droplets and the substrate. The water droplet dynamics during the jetting process were recorded and analyzed, providing a qualitative comparison between the coated and uncoated samples. These results validated the enhanced hydrophobicity of the coated copper, confirming the effectiveness of the octadecanoic acid treatment.

During the water jetting investigations, a significant contrast was observed between the uncoated and octadecanoic acid-coated copper (Cu) samples, illustrating the influence of the coating on the surface properties. The uncoated Cu samples retained water droplets, indicative of their lower hydrophobic nature, where high surface energy promotes water adhesion[27]. On the other hand, the octadecanoic acid-coated Cu samples exhibited strong water repulsion, demonstrating hydrophobicity. This behaviour is attributed to the formation of a low-surface-energy layer from the octadecanoic acid, which minimizes the interaction between water and the surface. The hydrophobicity follows the Cassie-Baxter model, where air pockets are trapped beneath water droplets, reducing the contact area. Figure 9 shows these observations, with panel (a) illustrating water retention on the uncoated surface and panel (b) showing the repulsion on the coated surface.

(a) Uncoated Cu (b) Coated Cu

Figure 9. Water Jetting Investigations

3.6.Water Bouncing Investigations

The hydrophobic nature of octadecanoic acid-coated copper (Cu) samples was further confirmed through water bouncing investigations. In this test, 5 μL water droplets were dispensed from a height of 5 cm onto both uncoated and coated Cu surfaces. The uncoated samples showed adhesion, with droplets spreading and remaining stationary. In contrast, the coated samples exhibited a bouncing effect, with droplets rebounding off the surface. This behaviour is attributed to the low-surface-energy layer formed by the octadecanoic acid coating, reducing adhesive forces and enhancing water repellency, consistent with findings from water jetting and contact angle measurements.

Figure 10 compares water bouncing on (a) an uncoated Cu and (b) a coated Cu sample. In uncoated Cu, droplets spread and adhered due to high surface energy. In coated Cu, droplets rebounded completely, demonstrating superhydrophobicity. This confirms the coating's effectiveness in reducing surface energy and enhancing water repellency. The observed behaviour in the coated sample supports the conclusion that the surface treatment significantly improves droplet mobility[28]. The contrast between the two surfaces visually highlights the impact of the octadecanoic acid coating on surface properties.

The study demonstrated that the coated Cu surface exhibited a superhydrophobic nature with a contact angle of approximately 160°. The coated surface enabled complete droplet rebound, indicating minimal adhesion and high mobility, while the uncoated surface showed no bounce behaviour.

(a) Bare Cu (b) Coated Cu

Figure 10. Water Jetting Investigation

3.7.Self-Cleaning Investigations

The self-cleaning properties of octadecanoic acid-coated copper (Cu) samples were evaluated by observing the removal of soil particles under water application. Soil particles were uniformly sprinkled onto both uncoated and coated Cu surfaces, followed by the application of water droplets. The uncoated Cu samples showed water adhesion, failing to dislodge the particles, indicating the absence of self-cleaning properties. In contrast, the coated Cu samples demonstrated a self-cleaning effect, with water droplets rolling off and carrying the soil particles with them. This behaviour is attributed to the enhanced hydrophobicity and low-surface-energy characteristics of the octadecanoic acid coating.

(a) Bare Cu (b) Coated Cu
Figure 11: Self-Cleaning Investigations

Figure 11(a) shows the uncoated Cu sample with soil particles adhering to the surface due to its high surface energy, preventing the removal of dirt by water droplets. Figure 11(b) illustrates the coated Cu sample, where soil particles are efficiently washed away by the water droplets, demonstrating the surface's self-cleaning ability.

3.8. Corrosion Resistance Analysis

Corrosion resistance analysis is crucial for assessing the durability of copper surfaces in aggressive environments. Superhydrophobic coatings have been widely recognized for their effectiveness in mitigating corrosion by reducing metal exposure to corrosive media. Among these, octadecanoic acid (OA) chemical deposition has been established as a reliable method to enhance corrosion resistance due to the hydrophobic properties of fatty acids. To further investigate the effectiveness of this approach, this study evaluates the corrosion resistance of uncoated and OA-coated copper (Cu) samples using electrochemical impedance spectroscopy (EIS) and potentiodynamic polarization techniques[29].

In this analysis, the experimental setup consisted of a three-electrode electrochemical cell, where the copper sample served as the working electrode, a saturated calomel electrode (SCE) acted as the reference electrode, and a platinum wire functioned as the counter electrode. A 3.5 wt% NaCl solution was used as the electrolyte to simulate seawater conditions, ensuring a realistic assessment of the corrosion behaviour. Prior to testing, copper samples underwent ultrasonic cleaning in acetone, ethanol, and deionized water, followed by air drying. OA-coated samples were prepared for uniform surface properties. Initial weights were recorded, and surface conditions were analysed. Post-corrosion weight loss measurements assessed material degradation. To evaluate the corrosion resistance, EIS measurements were performed by immersing the sample in NaCl solution. Impedance analysis was conducted over a frequency range of 100 kHz to 0.01 Hz with a 10 mV AC perturbation, and the resulting Nyquist plots were used to determine the charge transfer resistance (R_{ct}), a key indicator of corrosion resistance[30].

Additionally, Tafel slopes were extracted using the Tafel extrapolation method, where the linear regions of the anodic and cathodic branches of the potentiodynamic polarization curves were fitted to determine the anodic (β_a) and cathodic (β_c) slopes. These slopes were used to derive the corrosion current density (I_{corr}) and corrosion potential (E_{corr}) for both bare and OA-coated Cu samples. The polarization scans were performed in the range of -250 mV to +250 mV relative to OCP, at a scan rate of 1 mV/s, following 30 minutes of stabilization at OCP. This enabled a comparative evaluation of the corrosion rates between uncoated and OA-coated samples. To ensure data reliability, all experiments were repeated three times for reproducibility. The results, as presented in Table 5, indicate that OA-coated Cu exhibited a significantly lower corrosion rate, confirming the enhanced protective effect of the OA coating. These findings demonstrate the effectiveness of OA-based superhydrophobic coatings in improving the corrosion resistance of copper in aggressive environments.

To quantify the corrosion resistance, the corrosion rate (Y_1) was calculated using Equation (2), the efficiency of corrosion resistance (η) was determined using Equation (3) and (4) provides the tafel equation:

$$Y_1 = \frac{87600*(w_a - w_b)}{\rho*A_s*t} \tag{2}$$

$$Efficiency, \eta = \frac{I_{corr(Cu)} - I_{corr(coated\ Cu)}}{I_{corr(Cu)}} \tag{3}$$

$$Overpotential\ \vartheta = \beta\ \log i + constant \tag{4}$$

where w_a (g) represents the sample's weight before the corrosion test, w_b (g) is the sample's weight after the test, A_s (cm^2) is the sample's surface area, ρ (g/cm^3) is the sample's density, t (h) is the duration of the test, β is the Tafel slope, and i is the current density.

Table 5 shows the dynamic potential polarization curve results, illustrating the corrosion resistance performance of uncoated and OA coated copper samples in a 3.5 wt.%NaCl solution.

The results reveal that uncoated Cu substrates exhibit a corrosion potential (Ecorr) of −0.2036 V and a corrosion current density (Icorr) of 2.214×10^{-5} A/cm², leading to a corrosion rate of 3.226×10^{-1} mm/a. In contrast, OA-coated Cu samples demonstrate significantly enhanced corrosion resistance, with an Ecorr of −0.0700 V, an Icorr of 3.577×10^{-6} A/cm², and a notably reduced corrosion rate of 1.388×10^{-1} mm/a. The efficiency of corrosion resistance for the OA coating is calculated to be 83.8%, as summarized in Table 5.

Table 5.Results on dynamic potential polarization curves

Name of the sample	E_{corr} (VSCE-Subscript Font for SCE)	I_{corr} (A/cm^2)	Corrosion rate, (mm/a)	Efficiency ( )
Bare Cu	-0.2036	2.214 X 10^{-5}	3.226x10^{-1}	-
Coated Cu	-0.0700	3.577 X 10^{-6}	1.388 x 10^{-1}	83.8

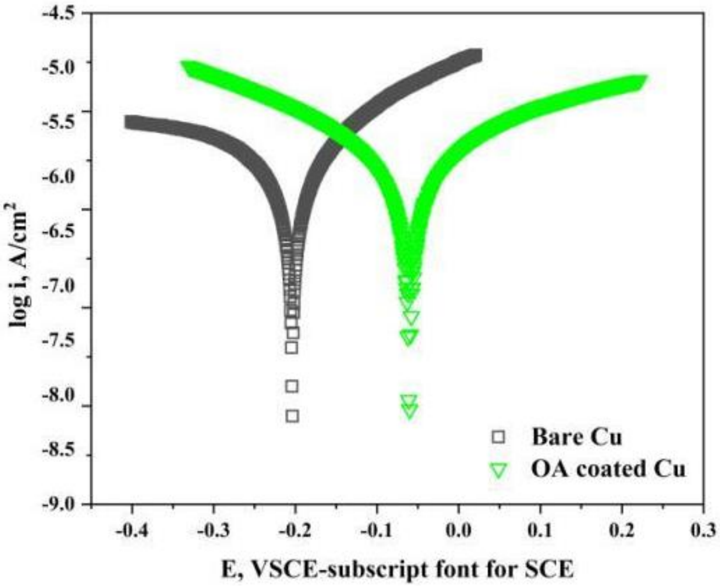

Figure 12. Tafel Polarization curve of bare and coated Cu substrate

In addition, as illustrated in figure 12, the Tafel polarization curves indicate that bare copper samples exhibit a higher corrosion current density (Log I, A/cm²), with their corresponding curve positioned higher on the log I axis compared to coated Cu. This positioning signifies an increased corrosion rate in uncoated samples. Additionally, the corrosion potential (E, VSCE) for bare Cu was more negative, suggesting a greater susceptibility to corrosion compared to OA-coated Cu. These findings further validate the effectiveness of the octadecanoic acid coating in enhancing the corrosion resistance of copper surfaces, making it a viable protective solution for mitigating degradation in aggressive environments.

Electrochemical impedance spectroscopy (EIS) data presented in Table 6 further substantiate the corrosion resistance improvement in OA-coated Cu.

Table 6.EISData Equivalent Circuit Fitting Outcomes

Material	R_s (Ωcm^2)	R_{ct} (Ωcm^2)	R_f (Ωcm^2)	CPEdl (μF cm^{-2})
Bare Cu	18	878.7	340.42	5.48 x 10^{-4}
Coated Cu	14.7	3.52x10^3	1180.3	2.36 x 10^{-6}

The solution resistance (R_s) values for both uncoated and coated Cu samples are comparable, with bare Cu at 18 Ω·cm² and coated Cu at 14.7 Ω·cm², indicating that the OA coating does not significantly influence the electrolyte's resistance. However, a notable increase in charge transfer resistance (R_{ct}) was observed for the coated sample, with bare Cu exhibiting 878.7 Ω·cm² and OA-coated Cu reaching 3.52 × 10³ Ω·cm². This substantial increase highlights the OA coating's ability to impede charge flow, thereby enhancing corrosion resistance.

Additionally, the coating resistance (Rf) is significantly higher for OA-coated Cu (1180.3 Ω·cm²) compared to bare Cu (340.42 Ω·cm²), further confirming the protective nature of the OA layer. The capacitance of the double layer (CPEdl) is notably lower for the coated sample (2.36 × 10⁻⁶ μF·cm² vs. 5.48 × 10⁻⁴ μF·cm² for bare Cu), indicating reduced electrochemical activity at the copper surface due to the OA coating. These findings are further validated by the Nyquist plots (Figure 13), where the larger semicircular arc for OA-coated Cu reflects its superior corrosion resistance.

The EIS data were not fitted due to challenges in selecting an appropriate equivalent circuit model that accurately represents the corrosion behaviour of OA-coated Cu. Instead, charge transfer resistance (R_{ct}) was directly extracted from the Nyquist plots, which provided a reliable comparative measure of corrosion resistance between uncoated and coated samples. This approach ensured that the analysis remained focused on evaluating the protective effectiveness of the OA coating without introducing potential errors from arbitrary circuit fitting. However, future studies could explore refined circuit modelling to further enhance electrochemical characterization.

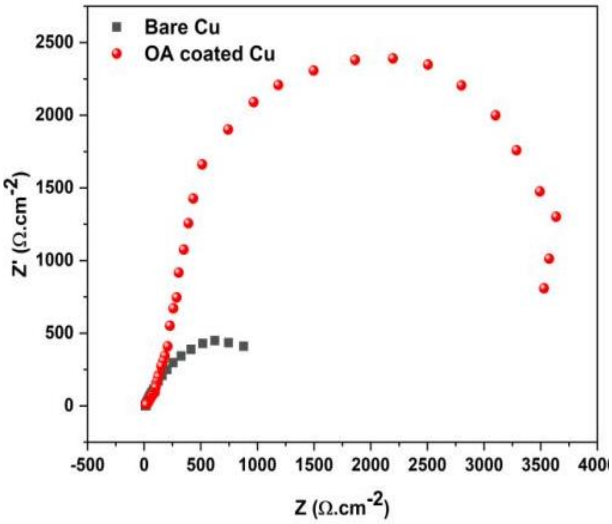

Figure 13. NyqusitImageof OA Coated and Uncoated Cu Substrates in 3.5 wt.%NaCl

The significant improvement in corrosion resistance observed in this study is primarily attributed to the superhydrophobic nature of the OA coating, which minimizes direct contact between the substrate and the corrosive medium. This effect aligns with findings from Jia et al. [29], who demonstrated that chemically treated copper surfaces exhibited enhanced corrosion resistance due to their hydrophobic properties. Similar to previous studies on electrodeposited superhydrophobic coatings, the OA coating effectively reduces ion transport at the metal-electrolyte interface, leading to lower corrosion current densities and improved corrosion resistance efficiency.The higher charge transfer resistance (R_{ct}) and impedance values observed for OA-coated Cu confirm its superior corrosion resistance compared to bare Cu. These results demonstrate that OA-based superhydrophobic coatings significantly reduce electrochemical activity and enhance surface protection, making them a promising solution for corrosion mitigation in aggressive environments.

4. CONCLUSIONS

This study demonstrates that octadecanoic acid (OA) coating significantly enhances the corrosion resistance and hydrophobicity of copper surfaces, making it a highly promising protective solution for industrial applications. Structural analysis using XRD, SEM, and EDS confirmed the uniformity of the coating, which preserved the copper's crystalline integrity while improving surface roughness, leading to superior water repellency. The contact angle increased from 75° (bare copper) to 121.5° (OA-coated copper), with water jetting and droplet rebound tests indicating enhanced self-cleaning properties, achieving a maximum contact angle of 160°.Electrochemical evaluations further validated the effectiveness of the OA coating. The corrosion potential of coated copper improved from -0.2036 V (bare Cu) to -0.0700 V, while the corrosion current density decreased from 2.214×10^{-5} A/cm² to 3.577×10^{-6} A/cm². This resulted in a substantially lower corrosion rate of 1.388×10^{-1} mm/a and an impressive corrosion resistance efficiency of 83.8%. Electrochemical impedance spectroscopy (EIS) measurements revealed a significantly higher charge transfer resistance (3.52×10^3 Ω.cm²) for OA-coated copper, underscoring its superior barrier properties.

To further optimize the industrial viability of OA coatings, future work should focus on enhancing corrosion resistance through multi-layer coatings or synergistic integration high performing nanoparticles with other protective compounds. Fine-tuning coating thickness and chemical composition could elevate hydrophobicity beyond 150°, making it even more effective for marine and pipeline applications. In summary, OA coatings offer a robust, cost-effective, and environmentally friendly solution for mitigating copper corrosion in aggressive environments.

Acknowledgment

The authors felt sincere gratitude to Kalasalingam Academy of Research and Education (Deemed to be University), to perform all the investigations.

Competing Interests

The authors found no conflicting interests in the research work.

5. REFERENCES

[1] Copper drives electric vehicles [Internet]. Copper Alliance: Copper Development Association Inc. 2023. Available form: www.copper.org

[2] K.K. Jha, M. Armstrong, S. Kumar, M. Kumar, G.S. Charan (2022). A recent examination on the performance of heat pipes in nanofluids in enhancing the thermodynamic properties. Materials Today: Proceedings, 60(3), 1920-1926. https://doi.org/10.1016/j.matpr.2021.12.587

[3] Copper Market Size, Share, and Trends 2024 to 2034 [Internet]. Semiconductor and Electronic: Copper Market 2024. Available form: www.precedenceresearch.com.

[4] M. Armstrong, M. Sivasubramanian (2019). Experimental examination over heat exchanging capacity on the hollow pipe incorporated with corrugated copper plate dividend and baffles. International Journal of Innovative Technology and Exploring Engineering, 9(2S2), 411-414. https://doi.org/10.35940/ijitee.B1070.1292S219

[5] M. Armstrong, S. Mahadevan, N. Selvapalam, C. Santulli, S. Palanisamy, C. Fragassa (2023). Augmenting the double pipe heat exchanger efficiency using varied molar Ag ornamented graphene oxide (GO) nanoparticles aqueous hybrid nanofluids. Frontiers in Materials, 10, 1240606. https://doi.org/10.3389/fmats.2023.1240606

[6] Y. Lv, M. Liu(2019). Corrosion and fouling behaviours of copper-based superhydrophobic coating.Surface Engineering, 35(6), 542-549. https://doi.org/10.1080/02670844.2018.1433774

[7] Q. Tong, Z.Fan, B. Wang, Q. Liu, Y. Bo, L. Qian (2021). Preparation and application of superhydrophobic copper mesh by chemical etching and in-situ growth.Frontiers in Chemistry, 9, 737550.https://doi.org/10.3389/fchem.2021.737550

B. Aikaterini, F. Stergioudi, N. Patsatzis, L. Malletzidou, G. Vourlias,S. Skolianos(2023). Preparation and characterization of stable superhydrophobic copper foams suitable for treatment of oily wastewater.Coatings, 13(2), 13020355. https://doi.org/10.3390/coatings13020355

[8] M. Armstrong, M. Sivasubramanian, N. Selvapalam, K.K. Jha (2024). Exploring the heat transfer performance of cylindrical heat pipes with varied molar Ag-doped GO hybrid nanofluids — an empirical study. Heat Transfer Research, 55(2), 55-71. https://doi.org/10.1615/HeatTransRes.2023049011

[9] H. Li, Y. Lu, X. Zou, C. Wang, H. Wei (2020). One-step preparation of superhydrophobic surface on copper substrate with anti-corrosion and anti-icing performance.International Journal of Electrochemical Science, 15(11), 10674-10683. https://doi.org/10.20964/2020.11.16

[10] M. Armstrong, M. Sivasubramanian, N. SelvaPalam, M. Adam Khan, C. Rajaganapathy (2021). A recent examination on the nano coating techniques in heat transfer applications.Materials Today: Proceedings, 46, 7942-7947. https://doi.org/10.1016/j.matpr.2021.02.660

[11] Z.Song, S.Zhang, L. Ding, X. Wu, N. Long (2024). The preparation and corrosion resistance of superhydrophobic coating on Cu plate via two-step electrodeposition. Anti-Corrosion Methods and Materials, 71(1), 92-102. https://doi.org/10.1108/ACMM-09-2023-2903

[12] M. Kaseem, A.R. Safira, A. Fattah-Alhosseini(2024). Development of superhydrophobic protective coatings through surface functionalization of porous MgO with transition metal salts of palmitic acid. Journal of Industrial and Engineering Chemistry, 136, 440-452. https://doi.org/10.1016/j.jiec.2024.02.033

[13] G. Žerjav, A. Lanzutti, F. Andreatta, L. Fedrizzi, I. Milošev (2017). Characterization of self-assembled layers made with stearic acid, benzotriazole, or 2-mercaptobenzimidazole on surface of copper for corrosion protection in simulated urban rain. Materials and Corrosion, 68(1), 30-41. https://doi.org/10.1002/maco.201608954

[14] H. Kim, J. Biswas, S. Choe (2006).Effects of stearic acid coating on zeolite in LDPE, LLDPE, and HDPE composites.Polymer, 47(11), 3981-3992. https://doi.org/10.1016/j.polymer.2006.03.068

[15] S.B. Jeong, Y.C. Yang, Y.B. Chae, B.G. Kim (2009). Characteristics of the treated ground calcium carbonate powder with stearic acid using the dry process coating system. Materials Transactions, 50(2), 409-414. https://doi.org/10.2320/matertrans.MRP2008351

[16] W.F. Ng, M.H. Wong, F.T. Cheng (2010).Stearic acid coating on magnesium for enhancing corrosion resistance in Hanks' solution.Surface and Coatings Technology, 204(11), 1823-1830. https://doi.org/10.1016/j.surfcoat.2009.11.024

[17] R.K. Gupta, K. Mensah-Darkwa, J. Sankar, D. Kumar (2013). Enhanced corrosion resistance of phytic acid coated magnesium by stearic acid treatment. Transactions of Nonferrous Metals Society of China, 23(5), 1237-1244. https://doi.org/10.1016/S1003-6326(13)62588-1

[18] T.T. Nguyen,V.K. Nguyen, T.T.H. Pham, T.D.Nguyen (2021). Effects of surface modification with stearic acid on the dispersion of some inorganic fillers in PE matrix. Journal of Composites Science, 5(10), 270. https://doi.org/10.3390/jcs5100270

[19] W. Liu, X. Qiao, S. Liu, S. Shi, J. Li, (2019).Study of hydrophobic modification of copper-coated mica and its spectrum, molecular structure, and properties.Journal of Molecular Structure, 1186, 440-447. https://doi.org/10.1016/j.molstruc.2019.03.043

[20] C. Hu, X. Xie, K. Ren(2021) A facile method to prepare stearic acid-TiO_2/zinc composite coating with multipronged robustness, self-cleaning property, and corrosion resistance.Journal of Alloys and Compounds 882, 160636. https://doi.org/10.1016/j.jallcom.2021.160636

[21] R. Ma, R. Li, Q. Niu, Y. Zeng, J. Li, S. Bai, Y. Cheng(2023). Preparation of superhydrophobic surfaces based on copper mesh substrates and its application performance. ACS Omega, 8(48), 45616-45625. https://doi.org/10.1021/acsomega.3c05834

[22] M. Armstrong, M. Sivasubramanian, N. Selvapalam, R. Pavitra, P. Rajesh Kanna, H. Lenin (2023).Synthesis and empirical analysis of the thermophysical characteristics of GO-Ag aqueous hybrid nanofluid using environmentally friendly reducing and stabilizing agents.Advances in Materials Science and Engineering, 2023(1), 5585132. https://doi.org/10.1155/2023/5585132

[23] Y. Chen, X. Zhang, B. Wang, M. Lv, Y. Zhu, J. Gao(2017). Fabrication and characterization of novel shape-stabilized stearic acid composite phase change materials with tannic-acid-templatedmesoporous silica nanoparticles for thermal energy storage. RSC Advances, 7(26), 15625-15631. https://doi.org/10.1039/c7ra00964j

[24] W. Hou, Y. Shen, J. Tao, Y. Xu, J. Jiang, H. Chen, Z. Jia(2020). Anti-icing performance of the superhydrophobic surface with micro-cubic array structures fabricated by plasma etching.Colloids and Surfaces A: Physicochemical and Engineering Aspects, 586, 124180. https://doi.org/10.1016/j.colsurfa.2019.124180

[25] M. Armstrong, M. Sivasubramanian, N. Selvapalam, R. Pavitra (2024). Green synthesis, characterization, and thermophysical properties of diverse molar Ag decorated GO hybrid nanofluids. Chemical Engineering Communications 211(10), 1610-1629. https://doi.org/10.1080/00986445.2024.2365766

[26] M.E. Mohamed, B.A. Abd-El-Nabey (2020).Facile and eco-friendly method for fabrication of superhydrophobic surface on copper metal.ECS Journal of Solid State Science and Technology 9(6), 061006.https://doi.org/10.1149/2162-8777/ab9dc7

[27] R. Jain, R. Pitchumani (2017).Facile fabrication of durable copper-based superhydrophobic surfaces via electrodeposition.Langmuir 34(10), 3159-3169. https://doi.org/10.1021/acs.langmuir.7b02227

[28] C. Jia, J. Zhu, L. Zhang(2022). An anti-corrosion superhydrophobic copper surface fabricated by milling and chemical deposition.Coatings 12(4), 442.https://doi.org/10.3390/coatings12040442

[29] S.R. Trisnanto, I. Setiawan, G.K. Sunnardianto, F. Triawan(2019). Stearic acid-modified CuO coating metal surface with superhydrophobicity and anti-corrosion properties.Journal of Engineering Research (Kuwait), 2019, 63-75. https://www.researchgate.net/publication/337590508

IZVOD

ISTRAŽIVANJE HIDROFOBNIH SVOJSTAVA I OTPORNOSTI BAKRA NA KOROZIJU TEHNIKOM HEMIJSKOG TALOŽENJA OKTADEKANSKOM KISELINOM

Ova studija istražuje poboljšanje hidrofobnosti i otpornosti bakra na koroziju hemijskim taloženjem oktadekanske kiseline. Strukturne i hemijske modifikacije tretiranih bakarnih površina analizirane su pomoću rendgenske difrakcije (XRD), skenirajuće elektronske mikroskopije (SEM) i energetski disperzivne rendgenske spektroskopije (EDS). SEM slike su otkrile značajne promene u topografiji površine, što je doprinelo vodoodbojnosti, dok je EDS potvrdio ujednačen premaz oktadekanskom kiselinom. XRD analiza je pokazala da je kristalna struktura bakra očuvana. Hidrofobnost je kvantitativno procenjena merenjem kontaktnog ugla, koji se povećao sa 75° za goli bakar na 121,5° za bakar obložen oktadekanskom kiselinom, potvrđujući prelazak na hidrofobnu površinu. Testovi mlaznog pranja vode i odbijanja vode pokazali su superiornu vodoodbojnost i efikasnost samočišćenja obloženih površina. Merenje kontaktnog ugla za obloženu površinu dostiglo je približno 160° tokom testova odbijanja, što ukazuje na visoko hidrofobno ponašanje. Otpornost na koroziju je procenjena korišćenjem dinamičke polarizacije potencijala i elektrohemijske impedansne spektroskopije (EIS). Kriva dinamičke polarizacije je pokazala potencijal korozije (Ecorr) od -0,0700 V za obloženi bakar, u poređenju sa -0,2036 V za neobloženi bakar. Gustina struje korozije (Icorr) za obloženi bakar bila je $3{,}577 \times 10^{-6}$ *A/cm*^{2}*, što je značajno niže od vrednosti za goli bakar od* $2{,}214 \times 10^{-5}$ *A/cm*^{2}*. Brzina korozije obloženog bakra je smanjena na* $1{,}388 \times 10^{-1}$ *mm/a sa* $3{,}226 \times 10^{-1}$ *mm/a za neobloženi bakar, što je rezultiralo efikasnošću od 83,8%. Ovi nalazi pokazuju da je oktadekanska kiselina efikasan i isplativ zaštitni premaz za poboljšanje izdržljivosti i funkcionalnosti bakra, posebno u okruženjima sklonim vlazi.*

Ključne reči: *Bakar, otpornost na koroziju, hidrofobnost, oktadekanska kiselina, samočišćenje, modifikacija površine*

Naučni rad
Rad primljen:27.01.2025
Rad korigovan: 28.02.2025.
Rad prihvaćen: 05.03.2025.

Dinesh Kumar Vairavel:	(0000-0001-7343-887X)
Sivasubramanian Mahadevan:	(0000-0003-0467-3766)
Armstrong Michael:	(0000-0001-6967-7579)
Sivakumar Durairaj:	(0000-0001-5228-0145)
Selvapalam Narayanan:	(0000-0002-6502-9694)

Pedro Henrique PoubelMendonça Da Silveira[1]**,*
Jheison Lopes Dos Santos[2]*, Alaelson Vieira Gomes*[1]*,*
Andmarcelo Henrique Prado Da Silva[1]

[1]*Graduate Programme in Materials Science and Engineering, Military Institute of Engineering—IME, Praça General Tibúrcio 80, Urca,Rio de Janeiro 22290-270, Brazil,* [2]*Brazilian Institute of Medicine and Rehabilitation, IBMR, Rio de Janeiro, RJ, Brazil*

Scientific paper
ISSN 0351-9465, E-ISSN 2466-2585
https://doi.org/10.62638/ZasMat1403
Zastita Materijala 67 (1)
76 – 84 (2026)

Study of crystallite size and lattice strain by Williamson-Hall analysis in sintered Al_2O_3 - Fe_2O_3 ceramics

ABSTRACT

This study investigates the influence of hematite (Fe_2O_3) as a sintering aid in alumina-based (Al_2O_3) ceramics. Samples with Fe_2O_3 concentrations ranging from 0.5 to 8 wt.% were produced and sintered at 1400 °C. The structural characterization of the samples was carried out using X-ray diffraction (XRD). Crystallite size and lattice strain were calculated by the Debye-Scherrer and Williamson-Hall equations. The results showed that Fe_2O_3 addition fostered crystallite size increase in almost all compositions, leading to a distortion in the Al_2O_3 lattice. Furthermore, the increase in crystallite size resulted in a reduction in dislocation density within the ceramics. This work contributes to a better understanding of the Al_2O_3 – Fe_2O_3 system and its applications in advanced ceramic materials, highlighting the importance of proper composition in ceramics of this compound for optimizing the properties of these materials.

Keywords*: Al_2O_3, Fe_2O_3, Crystallite size, XRD, Williamson – Hall*

1. INTRODUCTION

Alumina ceramics (Al_2O_3) are widely studied for their exceptional properties, such as dimensional stability, high-temperature resistance, and high hardness, making them suitable for various structural and technological applications [1]. However, alumina's brittle behavior is a significant limitation compared to metals and alloys. As an ionic-covalent solid, alumina lacks plastic deformation under load, causing cracks to propagate without energy dissipation, leading to abrupt failure. This brittleness is exacerbated by defects, notches, or thermal shock. Alumina's strong chemical bonds contribute to its low electrical and thermal conductivity, high melting point, and hardness [2].

Advances in materials science have led to new synthesis and processing methods to enhance alumina's properties and mitigate its limitations. One approach is adding low-melting-point sintering additives to create a liquid phase during sintering, bonding ceramic particles at lower temperatures. This is crucial for alumina, as its pure sintering requires temperatures above 1600 °C, increasing production costs and complexity [3,4].

Metallic oxides, such as CaO, MgO, Nb_2O_5, and ZrO_2, are commonly used as sintering additives for alumina. These additives create a liquid phase that "wets" ceramic particles, facilitating rearrangement and densification by removing pores [5-13]. In some cases, ternary eutectic compositions generate low-melting-point phases tailored for specific ceramic properties [6].

The Al_2O_3-Fe_2O_3 composite, formed by combining alumina and hematite, has garnered attention due to its applications in sorbents and catalysts [14,15] Alumina is known for its surface acidity, high surface area, mechanical strength, and sintering stability, while hematite offers redox behavior and semiconducting properties [18,19] Combining these oxides enhances mechanical, thermal, and catalytic performance, with high-temperature treatment forming new crystalline phases like $FeAlO_3$. This orthorhombic phase, produced under specific conditions, exhibits properties distinct from its parent oxides [20]

Studies on the Al_2O_3–Fe_2O_3 system have explored phase formation and properties. Muan and Gee [21,22] investigated $FeAlO_3$ formation under varying temperatures and oxygen pressures (PO_2), noting its instability below 1318 °C. $FeAlO_3$ stability increases with higher PO_2, with stabilization temperatures ranging from 1318 to 1495°C. Further studies characterized its orthorhombic structure [23], coexisting phases[24], and phase

---

*Corresponding author: P. H. P. M. Da Silveira
E-mail: pedroo.poubel@gmail.com

Paper received: 12.01.2025.
Paper accepted: 09.04.2025.

diagrams [25]. Thermodynamic properties indicate $FeAlO_3$ is unstable under high-temperature and pressure conditions [26].

Few studies have explored alumina's physical and mechanical properties with hematite as a sintering additive. Cai et al. [27] added hematite at 1–5 molar fractions to alumina, pressing discs at 100 MPa and sintering at 1550 °C. Densification reached 89–91%, with flexural strength increasing from 47 MPa at 1 molar fraction to 67 MPa at 5. Silveira et al. [28] combined Fe_2O_3 and Nb_2O_5 in alumina-based ceramics, observing densification, phase formation, and mechanical strength. Sintering at 1400°C improved properties, with flexural strength rising from 90 MPa to 252 MPa and compressive strength from 529 MPa to 705 MPa at 1–2 wt.% Fe_2O_3. However, higher hematite concentrations reduced densification and strength due to porosity.

In a previous study[29], Fe_2O_3 concentrations of 0.5–8 wt.% were added to alumina, sintered at 1400 °C. Results showed that 4–6 wt.% Fe_2O_3 decreased densification and strength due to porosity, while 0.5–2 wt.% enhanced sintering, increasing densification and mechanical performance. These findings highlight the significant influence of Fe_2O_3 concentration on alumina's final properties.

Characterization of ceramics in the Al_2O_3–Fe_2O_3 system is crucial to understanding additive effects. X-ray diffraction (XRD) identifies and quantifies phases while providing crystallite size and microstrain data. Williamson-Hall analysis, derived from XRD, separates crystallite size and microstrain contributions to peak broadening.[30] This method correlates microstructure with mechanical properties, aiding the understanding of Fe_2O_3's impact on sintering and material performance [31 - 33].

This study investigates Fe_2O_3 as a sintering additive in Al_2O_3, focusing on phase formation, crystallite growth, and microstructural changes during sintering. Scherrer calculations and Williamson-Hall analysis elucidate the relationships between sintering and material structure.

2. EXPERIMENTAL PROCEDURE

2.1.Materials

The materials used in the fabrication of ceramic bodies are: α-Al_2O_3 (ρ = 3.96 g/cm³; Alcoa P-913, Brazil), with a particle size of 1μm, glycine (Sigma Aldrich), and iron nitrate (Neon Química, Brazil), employed for the preparation of hematite (Fe_2O_3) powders (ρ = 5.26 g/cm³). Polyethylene glycol (PEG) (Isofar, Brazil) was added to provide mechanical strength to the green bodies.

2.2.Fe_2O_3 Powder Synthesis

The Fe_2O_3 powders were obtained through the spontaneous combustion synthesis method. In this process, ferric nitrate [$Fe(NO_3)_3 \cdot 9H_2O$] was used as the oxidizer, and glycine [NH_2CH_2COOH] as the fuel. This method was similar to the one performed in the study by Cao et al.[34] To prepare the powders, $Fe(NO_3)_3 \cdot 9H_2O$ and NH_2CH_2COOH were dissolved in 150 mL of distilled water and the solution was stirred to achieve a homogeneous mixture. Subsequently, the mixture was poured into a 500 mL beaker and heated to 100 °C. During the heating process, the water in the solution evaporated, transforming the mixture into a gelatinous mass. After a few minutes of heating, the mixture expanded, releasing a significant amount of gases. This was followed by a non-explosive exothermic reaction, resulting in spontaneous combustion. After the burn, a foam composed of iron oxide was obtained, which was crushed to produce the Fe_2O_3 powders used as sintering additives.

2.3. Ceramic Processing

The theoretical density of the samples was determined using the Rule of Mixtures, excluding PEG which is eliminated during sintering. Table 1 presents the theoretical density (TD) values and nomenclature of each sample.

Table 1. Composition, nomenclature and theoretical density of sample groups of this paper

Sample	Composition	Density (g/cm³)
AL	100 wt.% Al_2O_3	3.960
ALFE05	99.5 wt.% Al_2O_3 – 0.5wt.%Fe_2O_3	3.966
ALFE10	99 wt.% Al_2O_3 – 1 wt.% Fe_2O_3	3.973
ALFE20	98 wt.% Al_2O_3 – 2 wt.% Fe_2O_3	3.986
ALFE40	96 wt.% Al_2O_3 – 4 wt.% Fe_2O_3	4.012
ALFE60	94 wt.% Al_2O_3 – 6 wt.% Fe_2O_3	4.038
ALFE80	92 wt.% Al_2O_3 – 8 wt.% Fe_2O_3	4.064

Al_2O_3, Fe_2O_3, and PEG were homogenized in a ball mill for 8h, using distilled water in a 1:1 ratio to facilitate the mixture. After this process, the powders were dried for 48h at a temperature of 120 °C, manually deagglomerated, and sieved through a 60-mesh screen. Using these materials, discs with a diameter of 15 mm and a mass of 0.5 g were produced through cold uniaxial pressing with a load of 50 MPa. Sintering was conducted in a JUNG furnace, without the application of pressure, with a maximum temperature of 1400 °C, followed by inertial cooling. The heating ramp utilized is illustrated in Figure 1.

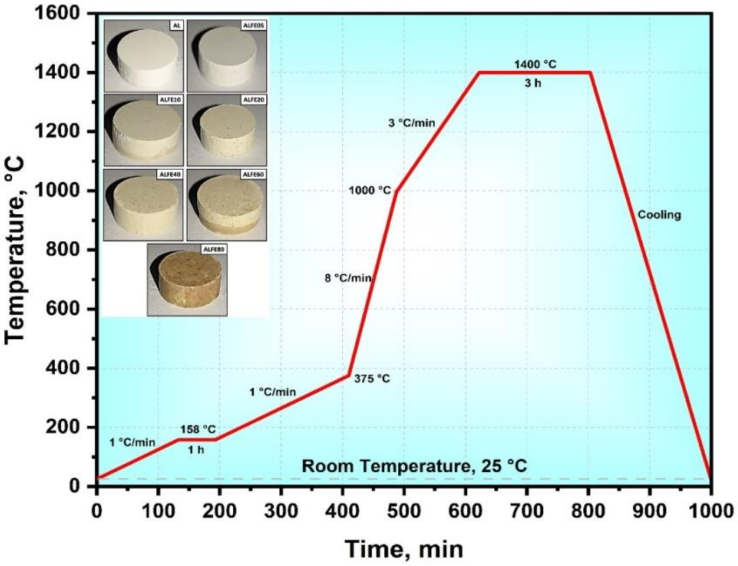

Figure 1. Sintering ramp used for sintering of Al_2O_3 – Fe_2O_3ceramics. The samples displayed in the graph are the groups of sintered samples

The X-Ray diffraction analysis of the sintered samples was conducted using the X'Pert Pro MRDdiffractometer from Panalytical (São Paulo, Brazil). The scanning range extended from 20° to 90°, with an increment of 0.02° and an acquisition time of 2s. Employing a Co-Kα tube (λ = 1,79 Å), the analysis was carried out with a voltage of 40 Kv and a current of 40 Ma. The qualitative identification of the formed phases was performed using the Panalytical`sHighScore Plus software.

3. RESULTS AND DISCUSSION

3.1.XRD Analysis of Al_2O_3 – Fe_2O_3 Ceramics

Figure 2(a) shows the diffraction patterns of the sintered ceramics with the peaks indexing. The primary identified phase corresponds to α-Al_2O_3 (corundum), a highly stable phase with a rhombohedral crystal structure and space group R-3c, as confirmed by the JCPDS 00-073-1512 reference card.

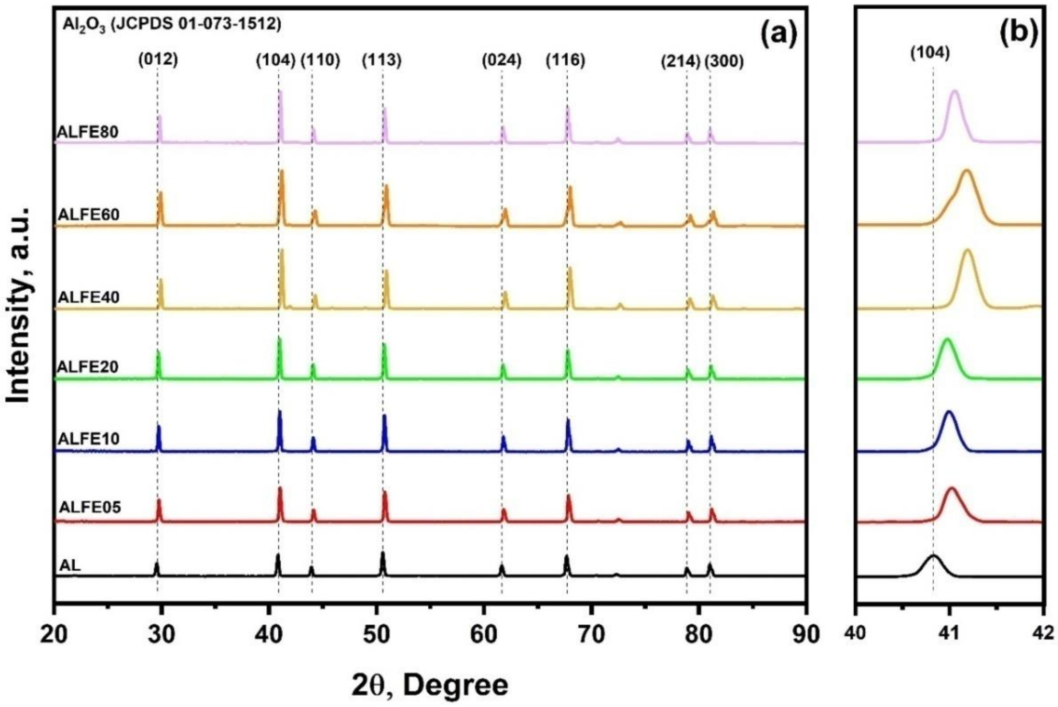

Figure 2. XRD patterns of sintered Al_2O_3 – Fe_2O_3 ceramics: (a) Complete diffractogram; (b) Amplified XRD pattern in the (104) diffraction peaks

The presence of only α-Al_2O_3 at 1400 °C, even with Fe_2O_3 additions ranging from 0.5 to 8 wt.%, aligns with the thermodynamic predictions based on the Al_2O_3–Fe_2O_3 binary phase diagram (Figure 3). This stability of the corundum phase suggests limited solubility of Fe_2O_3 in Al_2O_3 under the experimental conditions.

According to Kawasaki et al. [35], the corundum structure persists due to the very high thermal stability of α-Al_2O_3 and the strong ionic bonding within its lattice, which prevents the formation of additional phases such as $FeAlO_3$ unless the Fe_2O_3 concentration exceeds 18 wt.%. At this threshold, significant Fe^{3+} diffusion and substitution occur, leading to the formation of the $FeAlO_3$ phase with an orthorhombic structure (space group Pna21) characterized by a complex combination of hexagonal and cubic oxygen packing [36,37].

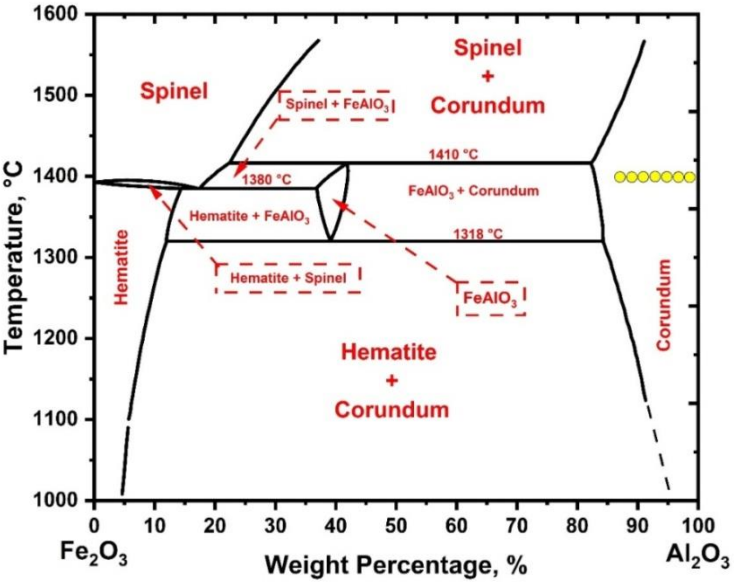

Figure 3. Phase diagram of Fe_2O_3 – Al_2O_3 compound indicating the phase of the sintered samples with yellow dots

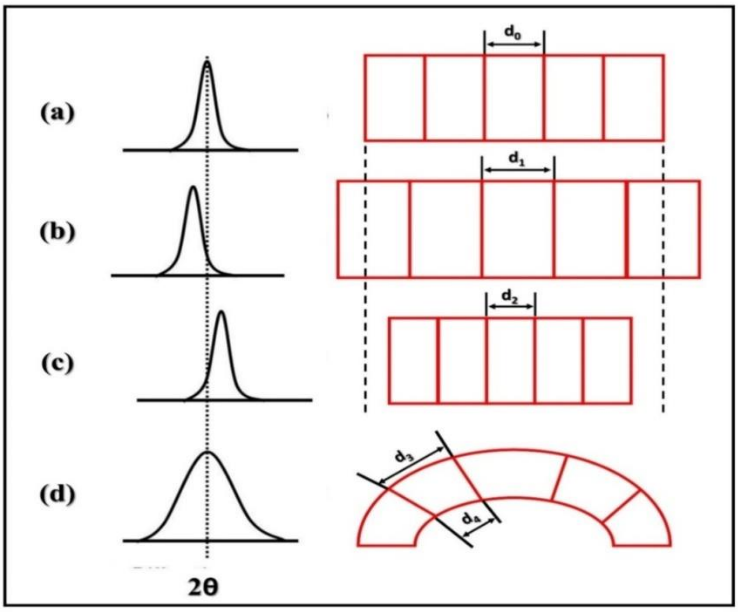

Figure 4.Diagram showing the effect of lattice strain on peak broadening and position shifts: (a) No strain at the original lattice spacing, (b) Peak shifts to lower angles when the lattice spacing is larger (d_0<d_1), (c) Peak shifts to larger angles when the lattice spacing is smaller (d_2<d_0), and (d) Peak is broadened because the peak gradually shifts from lower angles (top of the crystal: d_3) to larger angles (bottom of the crystal: d4) (d_4<d_0<d_3).

The process of $FeAlO_3$ phase formation involves Al^{3+} substitution by Fe^{3+} ions, which leads to lattice distortions and significant atomic rearrangement during sintering. This substitution process is kinetically limited at lower concentrations and temperatures due to the slow diffusion of Fe ions within the alumina matrix. Additionally, the narrow stability range of the $FeAlO_3$ phase makes its synthesis inherently challenging. The formation of a single-phase multiferroic ceramic, which could have practical applications in advanced technologies, requires precise control over the Fe_2O_3 content, temperature, and sintering conditions [37].

A closer analysis of the (104) diffraction peak, detailed in Fig.2(b), reveals significant changes in peak position, broadening, and intensity with increasing Fe_2O_3 content. These changes are attributed to microstructural effects such as lattice strain, crystallite size reduction, and local distortions caused by the Fe^{3+} substitution into the Al_2O_3 lattice. As illustrated in Figure 4, tensile and compressive lattice strains influence the d-spacing of the crystal planes, shifting the peak positions to smaller or larger 2θ values. Uniform tensile strain increases the interplanar spacing, while non-uniform strain causes asymmetry in peak broadening. The relative contributions of strain and crystallite size can be quantified by analyzing the peak width variation as a function of 1/cosθ, which highlights the significance of microstructural defects [38,39].

3.2.Crystallite size and dislocation density by scherrer analysis

The broadening of X-ray diffraction peaks typically arises from instrumental broadening, crystallite size effects, and lattice strain caused by dislocations. To separate these contributions, the instrumental broadening β_{hkl} must first be determined using a standard material like silicon. The corrected instrumental broadening is calculated using Equation 1:

$$\beta_D^2 = [(\beta_{measured}^2) - (\beta_{instrumental}^2)] \quad (1)$$

The crystallite size (CS) can then be estimated using the Scherrer equation:

$$CS = \frac{k\lambda}{\beta_D cos\theta} \quad (2)$$

Where

CS is the crystallite size (nm), k is the shape factor (k = 0.9), λ is the X-Ray wavelength (λ = 1.789 Å), θ is the Bragg angle, and β is the corrected peak width at half maximum (FWHM). The dislocation density (δ), defined as the length of dislocation lines per unit crystal volume, is calculated using Equation 3:

$$\delta = \frac{1}{D^2} \quad (3)$$

The crystallite size (CS) and dislocation density (δ) results from Table 2 reveal a nuanced relationship between Fe_2O_3 content and microstructural properties. For the base sample (AL), the crystallite size is 35.15 nm, with a dislocation density of 11.48 nm^{-2}. With the addition of 0.5 wt.% Fe_2O_3 (ALFE05), there is a slight increase in crystallite size to 35.36 nm and a corresponding decrease in dislocation density to 10.89 nm^{-2}, suggesting improved grain growth and reduced lattice imperfections.

Table2. Crystallite size and dislocation density values obtained by Scherrer equation

GROUPS	CS (nm)	**δ** (nm^{-2})
AL	35.15	11.48
ALFE05	35.36	10.89
ALFE10	39.79	9.29
ALFE20	38.89	10.17
ALFE40	37.20	11.12
ALFE60	25.82	24.48
ALFE80	43.34	9.61

At 1 wt.% Fe_2O_3 (ALFE10), the crystallite size peaks at 39.79 nm, with a significant drop in dislocation density to 9.29 nm^{-2}, reflecting improved microstructural integrity due to a minor fluxing effect. At 2 wt.% Fe_2O_3 (ALFE20), the crystallite size slightly decreases to 38.89 nm, and dislocation density rises to 10.17 nm^{-2}, suggesting initial lattice distortions. Higher Fe_2O_3 concentrations exacerbate these effects: at 4 wt.% (ALFE40), the crystallite size drops to 37.20 nm, and dislocation density increases to 11.12 nm^{-2}; at 6 wt.% (ALFE60), crystallite size sharply declines to 25.82 nm, with dislocation density reaching 24.48 nm^{-2}, indicating severe lattice imperfections. At 8 wt.% Fe_2O_3 (ALFE80), crystallite size rebounds to 43.34 nm, and dislocation density drops to 9.61 nm^{-2}, suggesting grain coalescence and reduced distortions. Low Fe_2O_3 levels enhance structural integrity, intermediate levels introduce strain, and high levels foster recovery.

3.3.Williamson-Hall Method (W-H)

According to Williamson and Hall, for the coherent scattering region, the line broadening due to finite size and internal stress in the prepared samples can be estimated. Through mathematical manipulations, Equation 4 represents the used formula.

$$\beta_{hkl} \, cos(\theta) = \frac{k\lambda}{D} + 4\varepsilon \cdot sin(\theta) \quad (4)$$

Using Equation 4, based on the manipulation of the equation, it is possible to obtain the crystallite size by the W-H method. Figure 5 is a plot of $\beta_{hkl}\cos(\theta)$ *vs*$4\sin(\theta)$ for the samples. From the slope and intercept, both lattice strain (ε) and crystallite size were obtained. The equation above represents a model of uniform deformation in all crystallographic directions, given the high value of R in the plots. The value of ε represented by the slope in Fig.5 shows that additions of 0.5 and 1% wt.% Fe_2O_3 caused low distortions in the lattice of Al_2O_3. Additions above 2 wt.% caused a greater distortion in the crystal lattice, which may have contributed to the low mechanical performance as stated in [34].

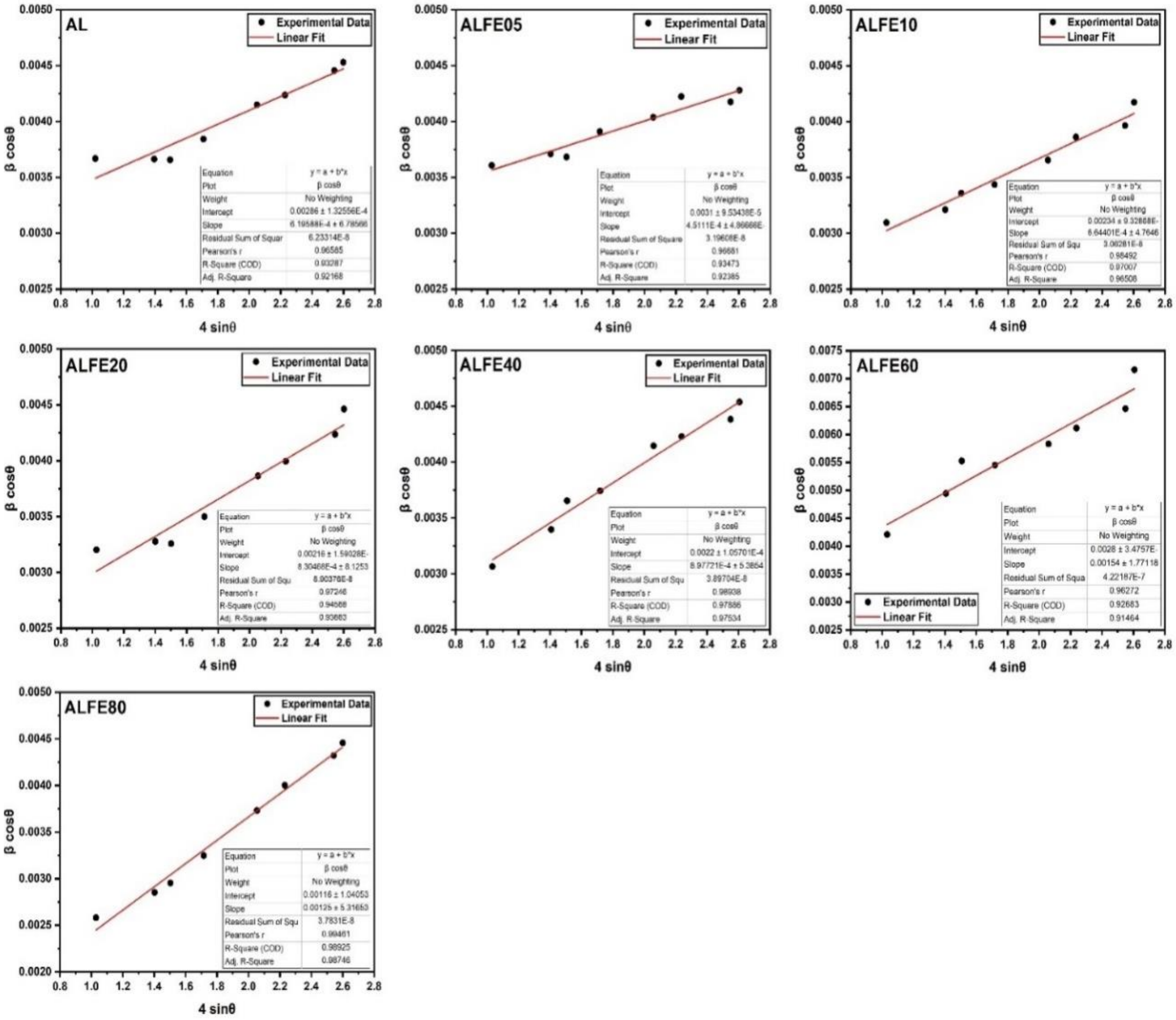

Figure 5. Williamson – Hall (W – H) plot of 4·sinθvs β·cosθ of Al_2O_3 – Fe_2O_3 ceramics

The crystallite size (CS) and lattice strain (ε) values obtained using the Williamson-Hall (W-H) method, as shown in Table 3, provide a detailed view of the microstructural behavior of alumina-based ceramics with varying Fe_2O_3 concentrations. The W-H method incorporates peak broadening effects, including internal stresses and crystal distortions, offering more reliable insights compared to simpler models.

Table 3. Crystallite size and lattice strain values obtained by Williamson-Hall method

GROUPS	CS (nm) (W-H Method)	ε
AL	58.80	0.62
ALFE05	54.25	0.45
ALFE10	71.86	0.64
ALFE20	77.85	0.83
ALFE40	76.44	0.90
ALFE60	60.06	1.54
ALFE80	144.97	1.20

The addition of Fe_2O_3 significantly influences crystallite size and lattice strain in Al_2O_3-Fe_2O_3 ceramics. For pure alumina (AL), the crystallite size is 58.80 nm. At 0.5 wt.% Fe_2O_3 (ALFE05), it decreases slightly to 54.25 nm (-7.8% compared to AL), likely due to minor structural changes. As Fe_2O_3 increases to 1 wt.% (ALFE10), crystallite size grows to 71.86 nm (+22.2%), reaching 77.85 nm (+32.4%) at 2 wt.% (ALFE20). At 4 wt.% (ALFE40), it slightly reduces to 76.44 nm (-1.8%), then drops to 60.06 nm (-21.4%) at 6 wt.% (ALFE60), suggesting structural disruptions. At 8 wt.% Fe_2O_3 (ALFE80), crystallite size surges to 144.97 nm (+146.5%), indicating relaxation and coalescence at high Fe_2O_3 levels.

Lattice strain (ε) shows an inverse trend. It decreases from 0.62 (AL) to 0.45 (-27.4%) at 0.5 wt.% Fe_2O_3, then rises progressively: 0.64 (+42.2%) at 1 wt.%, 0.83 (+29.7%) at 2 wt.%, and 0.90 (+8.4%) at 4 wt.%. At 6 wt.% Fe_2O_3, strain spikes to 1.54 (+71.1%), indicating significant distortions, before decreasing to 1.20 (-22.1%) at 8 wt.%, aligning with the large crystallite size and suggesting structural relaxation.

The Fig. 6 illustrates the comparison between crystallite size values obtained using the Scherrer equation and the Williamson-Hall method for Al_2O_3 - Fe_2O_3 samples. A clear disparity in the values can be observed, with the W-H method consistently yielding larger crystallite sizes across all compositions.

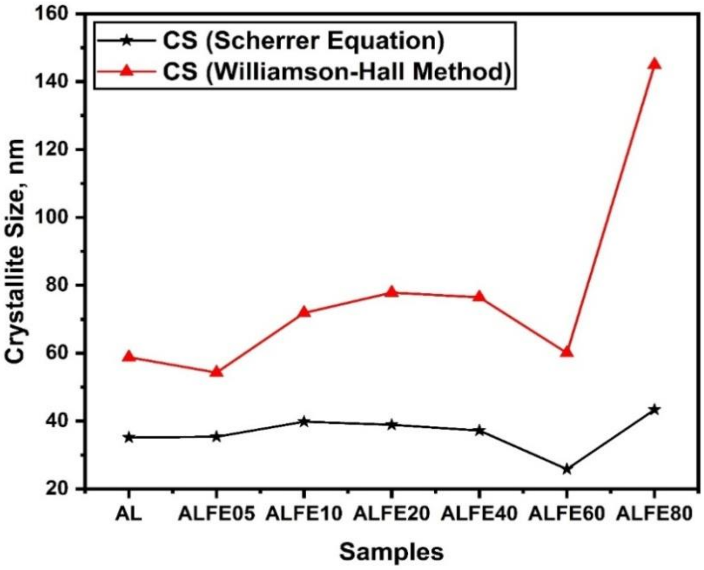

Figure 6.Comparison of Crystallite Size of Al_2O_3 - Fe_2O_3 Samples Using the Scherrer Equation and Williamson-Hall Analysis

This consistent difference arises from the distinct principles underlying the two methods. The Scherrer equation primarily considers the broadening of diffraction peaks caused by the crystallite size and assumes that broadening is solely due to this factor. It does not account for contributions from microstrain, dislocations, or other defects in the material. In contrast, the W-H method incorporates both size-induced and strain-induced broadening, offering a more comprehensive analysis of diffraction peak broadening. This additional consideration of lattice distortions and microstrain leads to the generally higher crystallite size values calculated using the W-H method.

4. CONCLUSION

In this paper, the variation of crystallite size, lattice strain, and dislocation density as a function of Fe_2O_3 content in Al_2O_3 was investigated. Fe_2O_3 addition promoted an increase in crystallite size, identified by both the Scherrer equation and W-H method, except for the addition of 6 wt.% of Fe_2O_3, which caused a reduction in crystallite size and an increase in dislocation density. Peak identification only showed the Al_2O_3 phase, without the presence of Fe_2O_3 or another phase, corroborating with the Fe_2O_3-Al_2O_3 phase diagram. Both techniques for determination showed the same trend of crystallite size growth, although the values obtained by the W-H method were higher.

Acknowledgements

The authors Pedro Henrique Poubel Mendonça da Silveira and Marcelo Henrique Prado da Silva thank the Fundação de Amparo à Pesquisa do Estado do Rio de Janeiro (FAPERJ) for their support - grant numbers E-26/200.338/2024 and E-26/200.339/2024.

5. REFERENCES

[1] J. Baltazar, M. F. R. P. Alves, C. dos Santos, S. Olhero (2022) Ceramics, 5, 1–12. https://doi.org/10.3390/ceramics5010001

[2] P. H. P. M. Da Silveira, T. T. da Silva, M. P. Ribeiro, P. R. R. Jesus, P. C. R. S. Credmann, A. V. Gomes (2021) Acad. Let., 1–11. http://dx.doi.org/10.20935/al3742

[3] E. Keramat, B. Hashemi (2021) Cer. Int., 47, 3159–3172.https://doi.org/10.1016/j.ceramint.2020.09.153

[4] R. M. German, P. Suri, S. J. Park (2009) J. Mat. Sci., 44, 1–39. https://doi.org/10.1007/s10853-008-3008-0

[5] D. Yin, J. Wang, M. Ni, P. Liu, Z. Dong, D. Tang (2021) Materials, 14, 444. https://doi.org/10.3390/ma14020444

[6] J. W. Lee, J. M. Cha, B. H. Bae, S. W. Choi, H. D. Jung, C. B. Yoon (2021) J. Alloy. Compd., 858, 157710. https://doi.org/10.1016/j.jallcom.2020.157710

[7] C. Pan, G. Zhao, S. Li, J. Wang, L. Yin, W. Song, et al. (2021) J. Appl. Phys., 130, 244102. https://doi.org/10.1063/5.0075730

[8] P. H. P. Da Silveira, P. R. R. De Jesus, M. P. Ribeiro, S. N. Monteiro, J. C. S. De Oliveira, A. V. Gomes (2020) Mat. Sci. For., 1012, 190–195. https://doi.org/10.4028/www.scientific.net/MSF.1012.190

[9] K. Shan, R. Li, J. Liu (2022) J. Eur. Cer. Soc., 42, 1815–1821. https://doi.org/10.1016/j.jeurceramsoc.2021.11.010

[10] C. Zhang, S. Qu, W. Xi, Y. Liang, J. Zhao, T. Yu (2022) Cer. Int., 48, 26269–26277. https://doi.org/10.1016/j.ceramint.2022.02.090

[11] N. C. De Carvalho, J. J. De Sousa Melo, F. H. S. Sales (2022) Braz. J. Dev., 8, 6871–6899. https://doi.org/10.34117/bjdv8n1-464

[12] V. Gomes, É. Lima Jr, P. R. R. De Jesus, L. F. C. Nascimento, J. L. Dos Santos, S. N. Monteiro, et al. (2020) Mat. Sci. For., 1012, 196–201. https://doi.org/10.4028/www.scientific.net/MSF.101.196

[13] H. P. Corado, P. H. Silveira, V. L. Ortega, G. G. Ramos, C. N. Elias (2022) Int. J. Biomater., 1–9. https://doi.org/10.1155/2022/5896511

[14] J. Hu, H. Li, S. Chen, W. Xiang (2022) Ind. Eng. Chem. Res., 61, 1022–1031. https://doi.org/10.1021/acs.iecr.1c03933

[15] Y. Jiang, Q. Mao, T. Ma, X. Liu, Y. Li, S. Ren (2021) Cer. Int., 47, 13884–13894. https://doi.org/10.1016/j.ceramint.2021.01.255

[16] L. Liu, M. R. Zachariah (2013) Energ. Fuel., 27, 4977–4983. https://doi.org/10.1021/ef400748x

[17] P. Yan, K. Zhang, Y. Peng (2022) Chem. Eng. Sci., 117410. https://doi.org/10.1063/5.0075730

[18] Z. Ma, G. Liu, Y. Lu, H. Zhang (2022) Fuel, 310, 122381. https://doi.org/10.1016/j.fuel.2021.122381

[19] Abyzov (2019) Refract. Ind. Cer., 60, 24–32. https://doi.org/10.1007/s11148-019-00304-2

[20] P. Bercoff, H. Bertorello (2010) Appl. Phys. A, 100, 1019–1027. https://doi.org/10.1007/s00339-010-5983-7

[21] Muan (1958) Am. J. Sci., 256, 413–422. https://doi.org/10.2475/ajs.256.6.413

[22] Muan, C. Gee (1956) J. Am. Cer. Soc., 39, 207–214. https://doi.org/10.1111/j.1151-2916.1956.tb15647.x

[23] R. Dayal, J. Gard, F. Glasser (1965) Acta Crystallogr., 18, 574–575. https://doi.org/10.1107/s0365110x65001329

[24] Feenstra, S. Sämann, B. Wunder (2005) J. Petrol., 46, 1881–1892. https://doi.org/10.1093/petrology/egi044

[25] L. Dreval, T. Zienert, O. Fabrichnaya (2016) J. Alloy. Compd., 657, 192–214. https://doi.org/10.1016/j.jallcom.2015.10.017

[26] Y. Q. Cai, Z. F. Wang, L. X. Yu, J. L. Bu, R. L. Wang, R. S. Wang (2011) Adv. Mat. Res., 284–286, 242–245. https://doi.org/10.4028/www.scientific.net/AMR.284-286.242

[27] P. H. P. Silveira, A. E. Eltom, A. V. Gomes, M. H. P. Silva (2024) Mat. Let., 359, 135966. https://doi.org/10.1016/j.matlet.2024.135966

[28] P. H. P. M. Silveira, A. E. Eltom, J. L. Santos, G. C. G. Delaqua, C. M. F. Vieira, P. R. R. Jesus, M. H. P. Silva, A. V. Gomes (2024) Tecnol. Met. Mat Min., 21, 2978. http://dx.doi.org/10.4322/2176-1523.20242978

[29] Himabindu, N. S. M. P. Latha, B. R. Kanth (2021) Mater. Today: Proc., 47, 4891–4896. https://doi.org/10.1016/j.matpr.2021.06.256

[30] J. S. Lim, F. K. Yam (2025) Physica B Condens. Matter, 699, 416798. https://doi.org/10.1016/j.physb.2024.416798

[31] Q. Huang, C. Wang, Z. Zhou, J. Peng, Q. Shan (2025) Mater. Sci. Eng. A, 920, 147545. https://doi.org/10.1016/j.msea.2024.147545

[32] M. K. Alam, M. S. Hossain, N. M. Bahadur, S. Ahmed (2024) J. Mol. Struc., 1306, 137820. https://doi.org/10.1016/j.molstruc.2024.137820

[33] Z. Cao, M. Qin, B. Jia, Y. Gu, P. Chen, A. A. Volinsky, X. Qu (2015) Cer. Int., 41, 2806–2812. https://doi.org/10.1016/j.ceramint.2014.10.100

[34] T. Kawasaki, T. Adachi, H. Ohfuji, Y. Osanai (2019) J. Miner. Petrol. Sci., 114, 238–251. https://doi.org/10.2465/jmps.190509

[35] R. Saha, A. Shireen, S. N. Shirodkar, U. V. Waghmare, A. Sundaresan, C. N. R. Rao (2012) Solid State Commun., 152, 1964–1968. https://doi.org/10.1016/j.ssc.2012.07.018

[36] Bhushan, S. Mukherjee, A. Basumallick, S. K. Bandopadhyay, D. Das (2008) Hyperfine Interact., 187,101–107.https://doi.org/10.1007/s10751-008-9889-0

[37] N. S. Ramgir, Y. K. Hwang, I. S. Mulla, J. S. Chang (2006) Solid State Sci., 8, 359–362. https://doi.org/10.1016/j.solidstatesciences.2006.02.008

[38] Y. Liao (2006) Practical Electron Microscopy and Database, S.L.: S.L.

IZVOD

PROUČAVANJE VELIČINE KRISTALITA I DEFORMACIJE REŠETKE VILLIAMSON-HALL ANALIZOM U SINTEROVANOJ Al_2O_3 - Fe_2O_3 KERAMICI

Ova studija istražuje uticaj hematita (Fe_2O_3) kao pomoćnog sredstva za sinterovanje u keramici na bazi aluminijuma (Al_2O_3). Uzorci sa koncentracijama Fe_2O_3 u rasponu od 0,5 do 8 tež.% su proizvedeni I sinterovani na 1400°C. Strukturna karakterizacija uzoraka je izvršena pomoću rendgenske difrakcije (XRD).Veličina kristalita I deformacija rešetke su izračunati pomoću Debie-Scherrer I Villiamson-Hall jednačina. Rezultati su pokazali da dodavanje Fe_2O_3 podstiče povećanje veličinekristalitau skorosvimkompozicijama, štodovodi do izobličenja u Al_2O_3 rešetki. Štaviše, povećanje veličine kristalita je dovelo do smanjenja gustine dislokacija unutar keramike. Ovaj rad doprinosi boljem razumevanju sistema Al_2O_3 – Fe_2O_3I njegove primene u naprednim keramičkim materijalima, naglašavajući važnost pravilnog sastava u keramici ovog jedinjenja za optimizaciju svojstava ovih materijala.

Ključnereči: *Al_2O_3, Fe_2O_3, veličina kristala, XRD, Villiamson – Hall.*

Naučni rad
Radprimljen: 12.01.2025.
Rad prihvaćen: 09.04.2025.

Pedro Henrique PoubelMendonça da Silveira: https://orcid.org/0000-0002-2651-1285
Jheison Lopes dos Santos: https://orcid.org/0000-0002-7075-1665
Alaelson Vieira Gomes: https://orcid.org/0000-0003-1651-2804
Marcelo Henrique Prado da Silva: https://orcid.org/0000-0002-1182-5345

Ansam Ali Hashim

Technical Institute of Babylon, Al-Furat Al-Awsat Technical University, Iraq

Scientific paper
ISSN 0351-9465, E-ISSN 2466-2585
https://doi.org/10.62638/ZasMat1357

Zastita Materijala 67 (1)
85 – 99 (2026)

Development of a novel cementitious blend derived fromcalcined pozzolanic materials and nanoparticles of self-compacting high-performance concrete

ABSTRACT

This research includes an experimental study of the potential use of pozzolanic and nanomaterials, including nano calcium carbonate (CC) and calcined clay (CK), throughout the manufacturing process of self-compacting high-performance concrete (SCHPC). Binary and ternary mix systems were prepared using 475 kg/m3 of cement and a fixed water-to-binder ratio (0.35). CK was used in proportions ranging from 6 to 24% of the total mass of cementitious materials. As for the ternary mixes, samples of (6% CK 1.5% CC, 12% CK 1.5 CC, 18% CK 1.5 CC, and 24% CK 1.5% CC) were prepared by partially replacing the weight of cement with CK and CC. The properties of the new SCHPC were assessed by slump flow (D (mm) and T500 (s)), V-funnel, L-box, and segregation resistance tests. Mechanical properties, including compressive and tensile strengths, were measured, and an ultrasonic pulse velocity test of the concrete was performed. Durability properties, including porosity and water absorption, were also measured. The findings demonstrated that adding calcined kaolin clay to concrete significantly improved its durability and mechanical properties. The best improvement was for binary and ternary mixtures at a 12% replacement ratio of calcined kaolin clay, where compressive strength improved by 20.9% and porosity and water absorption decreased by 15.6% and 19.9%, at 56 days compared to the reference mixture. The ternary mixtures also improved better than the ternary mixtures for the same replacement ratios of calcined kaolin clay for all ages. For example, the 12CK1.5CC mixture recorded a 25.5% improvement in compressive strength and a 21.3% and 40.8% reduction in porosity and water absorption compared to the reference mixture at the age of 56 days. This study accomplished its goals by sustainably producing eco-friendly concrete through the reduction of cement content via pozzolanic and nanoparticles.

Keywords: *Calcinedclay; nano calcium carbonate; segregation resistance; eco-friendly concrete;durability properties*

1. INTRODUCTION

Self-compacting concrete (SCC) is an advanced concrete employed in ground-breaking projects and practical uses. It infiltrates the thick reinforcement, penetrates every nook of the formwork, and is consolidated by its mass. SCC ensures stability while delivering various features without segregation or leakage [1, 2]. Benefits include reduced concrete construction time due to high efficiency, reduced noise from vibrating and concrete pouring operations, significantly enhanced components, and improved consistency of concrete on site, resulting in superior working conditions and exceptional surface quality of the concrete produced[3].Moreover, high-performance concrete is engineered to provide superior strength and exceptional durability. Over the last several decades, HPC has been widely utilized in the construction sector but has undoubtedly evolved. This arises from the growing need for durable concrete with extended service life while simultaneously minimizing maintenance expenses for concrete structures. A novel concrete variant, termed high-performance self-compacting concrete (SCHPC), has been created to incorporate the attributes of both SCC and HPC[4]. A SCHPC is a unique type of concrete that meets service life requirements under certain materials, loads, and exposure conditions. It has outstanding flowability and stability, high strength, and remarkable durability qualities. Constructing concrete buildings

---

Corresponding author: Ansam Ali Hashim
E-mail: ansamly2@atu.edu.iq

Paper received: 31.01.2025
Paper corrected: 28.02.2025.
Paper accepted: 06.03.2025.

requires meticulous placement and effective compaction of new concrete to get superior hardened characteristics and endurance[3].The optimal placement and compaction of standard concretes, even when executed by proficient labor, was not consistently attainable. The deficiency of skilled labor was a significant issue in the building sector as well [5]. The SCHPC concept initially emerged in Japan to construct resilient concrete structures and address the shortage of construction labor. Over the past decade, SCHPC's technology has been modified and advanced in Japan. SCHPC was marketed by the Japanese concrete industry under the trade name "Non-vibrated concrete" [6]. During the same era, SCHPC has grown extensively established in North America, Europe, and other regions globally [7].

In its fresh and hardened forms, self-compacting high-performance concrete (SCHPC) differs from conventional concrete primarily due to exceptional constituent components and combination proportions. This requires a lot of special ingredients in addition to the basic materials used for normal vibrated concrete (NVC), such as high-range water-reducing (HRWR) admixture for sufficient flowability and a large quantity of powder materials and/or viscosity-modifying admixture (VMA) to attain high segregation resistance. SCHPC's component material proportions frequently deviate significantly from NVC's[8].Compared to normal concrete, SCHPC has a significantly greater binder concentration, less water, more fine aggregate, and less coarse aggregate. SCHPC's water/binder ratio (W/B) is also significantly lower than NVC's [9],[10].A modest amount of coarse aggregate and expanded cementing materials at a low W/B ratio, or the use of a VEA can provide maximum resistance to segregation [11,12].Additionally, the aggregate size influences SCHPC's resistance to segregation as well as its capacity to flow [13].

Adeyemi[14] examined the combined effects of limestone as an inert additive and metakaolin as a pozzolanic additive on the microstructure, strength, and rheological characteristics of SCC. SCC mixes were created with different amounts of metakaolin and limestone added. Samples of seven different SCC concrete formulations were examined at 7, 28, and 56 days. The addition of limestone improves the flowability of SCC while preserving a suitable viscosity, according to preliminary findings. When metakaolin is used in place of limestone, there are encouraging gains in workability and compressive strength. After 56 days, samples with 100% metakaolin had the highest strength, closely followed by samples with 80% metakaolin and 20% limestone. The samples that included 80% limestone and 20% metakaolin also had the lowest strength. According to the SEM Microstructural data, concrete mixes with a high metakaolin concentration have less voids and are more homogeneous and consistent.In the study conducted by Hashem et al.[15], Portland cement was partially substituted with metakaolin and nano-silica. Two mixing schemes were used: binary and ternary. As a partial cement replacement for the two mixes, the metakaolin replacement ratios were 4%, 8%, 12%, and 16% (by weight). Nano silica was added to the ternary system mix at a rate of 2%, using the metakaolin at the same ratios as in the binary mixes. With increasing partial replacement by metakaolin and nano silica (viscosity, filling capacity, and resistance to segregation), the results showed that the slump flow and V-funnel flow times decreased. The SCC mixes with 2% nano-silica as a partial replacement, and metakaolin demonstrated better compressive strength at ages 7, 28, 56, and 90 days when compared to the control mix. For all ages, the compressive strength performance of ternary mixes comprising metakaolin and 2% nano-silica was shown to be superior to that of mixtures including metakaolin for the same replacement levels.Du and Pang [16] investigated the characteristics of high-performance concrete made using limestone and burnt kaolin clay at cement replacement percentages of 30% and 45%, respectively. The medium-grade kaolin clay was heated to 800 degrees Celsius. For a maximum of six months, the hydration, strength, shrinkage, and transport characteristics were assessed. The XRD results showed that within the first week, burnt clay will undergo a pozzolanic reaction and work in concert with limestone. The self-shrinkage was noticeably greater. The synthesized carbon aluminate phases and C-A-S-H gels may significantly improve the elastic modulus and compressive strength after seven days.

Meanwhile, more convoluted pathways were found to greatly boost the concrete's resistance to moisture and fluid infiltration. An investigation by Hashem et al. [17],examined the effects of partially substituting cement material with nanomaterials, specifically nano-metakaolin (NMK), on the fresh and hardening properties of High-Performance Self-Compacting Concrete (SCHPC). The substitution was made in varying proportions, specifically 1.25, 2.5, and 3.75. Four combinations were created: the first reference mixture and the other three, in which the cement was partially substituted with the amounts previously stated.

According to the results, the L-box and slump flow values drop as the proportion of cement that is partially replaced by nano-metakaolin rises. T 50 cm and V- funnel time, on the other hand, rise when the partial substitution rate for cement with nano metakaolin increases. As the fraction of cement that is partially replaced with nano-metakaolin rises, so do the compressive and tensile strengths.

Considering the current focus in civil engineering on sustainable development, it is essential to create a new generation of concrete, termed self-compacting high-performance concrete (SCHPC), utilizing eco-friendly materials in the construction sector while maintaining cost-effectiveness and minimizing environmental impacts to mitigate carbon dioxide emissions from the cement industry overall. Furthermore, SCHPC is indisputably novel to the Middle East region. No comprehensive research studies have been conducted to address the pertinent difficulties related to its use, as the technology remains relatively nascent in the region. The production and use of SCHPC, which includes pozzolanic materials and nanoparticles, appears to be a promising and energy-efficient development in the field of sustainable building and construction technology. Consequently, more research on the properties of this newly formulated concrete is required. The main goal of this study was to develop SCHPCs as cement replacements using nano-calcium carbonate (CC) and calcined kaolin clay (CK) in binary and ternary mix systems.The fresh properties of SCHPC were assessed for flowability, pass ability, and viscosity, and the solid properties were determined by measuring compressive strength, splitting tensile strength, and ultrasonic pulse velocity. Additionally, the durability performance of the SCHPC created in the study was evaluated by evaluating water absorption and porosity.

2. MATERIALS AND METHODOLOGY

2.1. Materials

2.1.1. Cement

For all concrete combinations, ordinary Portland cement type I (OPC), which complies with ASTM C150 [18], was utilized. The chemical and physical characteristics of the cement are displayed in Tables 1 and 2, respectively.

Table 1. Cement's physical characteristics

Physical property	Test Result
Setting Time, min Initial Final	 110 180
Fineness (Blaine), in m2/Kg	376
Compressive Strength in MN/m^2, at 3 days 7 days	 21 32
Specific gravity	3.13
Median particle size (µm) (d50)	10.96
Colour	Grey

2.1.2.Calcined clay

Locally sourced calcined clay (CK) was employed, and its chemical composition was confirmed using XRF analysis, as can be seen in Table 2. Figure1 illustrates the incinerated clay (KC). The fineness (m²/kg), specific gravity, and average particle size (µm) are 2.59, 487, and 9.53, respectively.


(A) (B)

Figure 1. (A) Calcined clay and (B) nano calcium carbonate utilized in this investigation

Table 2. Chemical makeup of cement (OPC)and calcined clay (KC)

Chemical composition (%)	OPC	CK
Silicon dioxide (SiO_2)	19.36	52.5
Aluminium trioxide (Al_2O_3)	4.82	39.6
Iron oxide (Fe_2O_3)	3.28	1.38
Calcium oxide (CaO)	62.43	0.95
Magnesium oxide (MgO)	3	0.48
Sodium oxide (Na_2O)	0.29	0.41
Potassium oxide (K_2O)	0.56	0.61
Sulfur trioxide (SO_3)	2.26	0.14
Phosphorus pentoxide(P_2O_5)	-	0.28
Titanium dioxide (TiO_2)	-	0.66
Loss on ignition (LOI)	0.96	2.94

2.1.3. Nano calcium carbonate

The commercially available nano $CaCO_3$ material, which is between 15 and 40 nm in particle size, has a 97.5% calcite ($CaCO_3$) content, and is white, as seen in Figure 1 (B), was made by the Sky Spring nanomaterials firm and used in this investigation.

2.1.4. Aggregate

Fine and coarse aggregates locally available in Iraq which comply with the requirements of IQS NO.45/1984 were used. The fineness modulus of natural sand used as fine aggregate is 2.34 and its maximum size, specific gravity, and water absorption are 4.75 mm, 2.62, and 1.22% respectively. The coarse aggregate is crushed gravel with a maximum size of 10 mm and has a specific gravity of 2.57 and water absorption of 0.4%.

2.1.5. Superplasticiser

Sika's ViscoCrete 180G, a water-reducing superplasticizer, wasemployed in this investigation. It satisfies ASTM C-494 (2015)'s specifications [19],type F.It was described as having a light-brownish colour, a specific gravity of 1.065±0.005 g/cm3, and a pH of 4-6 percent.

2.2. The proportions of the mixture

This work utilized the European standard (EFNARC, 2005) [20]to formulate concrete mixes for self-compacting concrete. The composition of the raw materials utilized in concrete mixes consisted of a total binder content of 475 kg/m3 and a water/binder ratio of 0.35. The superplasticizer is included in varying concentrations of 1.4% to 1.6% of the cement's weight. Nine concrete mixes were created to test high-performance self-compacting concrete. The initial mixture (control-CT) serves as a standard for binary blends with varying degrees of cement substitution by calcined clay CK in proportions of 6%CK, 12%CK, 18%CK, and 24%CK based on the weight of cement. Four ternary combinations were developed in which cement was partlysubstituted with calcined clays (CK) and Nano calcium carbonate (CC) in varying ratios: 6% CK and 1.5% CC, 12% CK and 1.5% CC, 18% CK and 1.5% CC, and 24% CK and 1.5% CC, based on the weight of the cement. It underwent curing for 28, 56, and 90 days following the molding process.

Table 3. Proportions of concrete mixture components

Mixture	W/C	Quantities of mix ingredients (kg/m3)					Superplasticizer (%)
		OPC	CK	CC	Fine Agg.	Coarse Agg.	
CT	0.35	475	--	--	840	852	1.4
6CK	0.35	446.5	28.5	--	840	852	1.4
12CK	0.35	418	57	--	840	852	1.4
18CK	0.35	389.5	85.5	--	840	852	1.4
24CK	0.35	361	114	--	840	852	1.4
6CK1.5CC	0.35	439.375	28.5	7.125	840	852	1.6
12CK1.5CC	0.35	410.875	57	7.125	840	852	1.6
18CK1.5CC	0.35	382.375	85.5	7.125	840	852	1.6
24CK1.5CC	0.35	353.875	114	7.125	840	852	1.6

2.3. Curing regimes

All concrete specimens must be cured before testing. After de-moulding, the specimens were positioned in a curing tank, where they were completely submerged in water whose temperature was regulated at 25 ± 2 °C to ensure uniform curing conditions. The specimens were maintained in the curing tanks until they attained the designated testing ages of 7, 28,56, and 90 days.

2.4. Testing procedures

2.4.1. Test of fresh properties

As to the [EFNARC, [20], fresh assessments of self-compacting high-performance concrete (SCHPC) are essential for evaluating the three workability characteristics: filling ability (flowability and viscosity), passing ability, and segregation resistance. To measure the three traits collectively, there isn't a single exam, though. In this experimental study, slump flow (D (mm) and T500 (s)), V-funnel, L-box, and resistance tests to segregation were used to evaluate the new characteristics of SCHPC. As shown in Figure 2 (A), the slump flow instrument was Abram's cone, which measured 30 cm in height, 10 cm in diameter at the top, and 20 cm at the bottom. The diameter average (D max. and d perp.) to the closest (10) mm is the slump flow. The slump flow time T500 mm, which is measured in seconds to the closest 1/10 second, is the interval between the cone's departure from the base plate and the SCC's initial contact with the 500 mm diameter circle.

The V-funnel examination is the test used to assess SCHPC's filling abilityas shown in Figure 2 (B). European self-compacting concrete guidelines, 2005, describe the test protocol and equipment utilized. Concrete from SCHPC is poured into the funnel without any pressure. A straight edge is used to trim any extra concrete from the funnel's top. We open the gate after waiting for 10 ± 2 seconds, and the stopwatch begins at the same time. Next, we examine the funnel and stop the watch when we notice visible portions.

The L-Box assessment may be used to determine SCHPC's passage capacity to flow freely in the face of reinforcing obstacles, as shown in Figure 2 (C). to the extent specified in the 2005 European Self-Compacting Concrete Guidelines. Fresh SCC is poured into the L-box's vertical section. Allow the concrete to remain in the vertical part for one minute. During this period, concrete will be on show, regardless of its stability (segregation). The concrete is then allowed to flow out into the horizontal section when we raise the sliding gate. Consequently, the L-box's height was calculated by averaging the concrete heights at the start and finish of the horizontal section.

Segregation tests can evaluate the resistance to segregation (stability), the apparatus, and the testing technique as outlined in the European recommendations of 2005, as shown in Figure 2 (D). The capacity of a new blend to preserve the original, generally constant distribution of component items is known as resistance to segregation. A bucket was filled with around 10 liters of concrete, which was then covered to prevent moisture loss and left to settle for about 15 minutes. Then, using a sieve pan and a weight scale, a concrete specimen weighing 4.8 ± 0.2 kg was placed on a 5 mm by 350 mm sieve and given time to settlefor two minutes to allow some mortar to pass through. The weight of the mortar divided by the weight of the original material on the sieve was employed to determine thesegregation index.

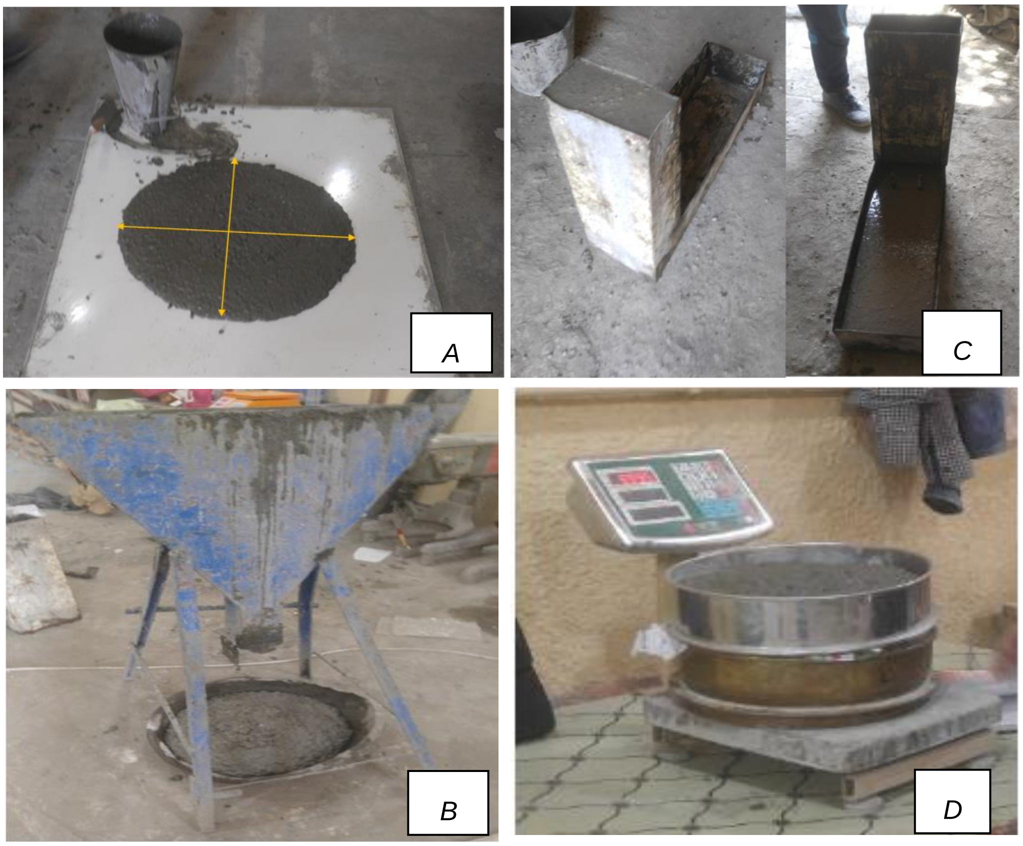

Figure 2. Fresh test procedures

2.4.2. Test of hardened properties

2.4.2.1.Compressive strength

A compressive strength test was performed under BS EN 12390 [21], utilizing a 2000 KN hydraulic compression apparatus at 18 MPa/minute for (100×100×100 mm3) cubes. At each test age (7, 28, 56, and 90 days), three cubes (100×100×100 mm3) were examined

2.4.2.2. Splitting tensile strength

The method outlined in ASTM 496/C 496M-2004 was used to assess the splitting tensile strength [22]. The cylinders that were used were 100 × 200 mm in size and were evaluated at 7, 28, and 90 days.

2.4.2.3. Ultrasonic pulse velocity

According to ASTM C597[23], the UPV was measured using a portable ultrasonic non-destructive digital indicating tester (PUNDIT). The identical cube specimens used to assess compressive strength were examined after 3, 7, 28, 56, and 90 days of curing to calculate the UPV.

2.4.3. Test of durability properties

2.4.3.1. Water absorption

To evaluate the voids in hardened concrete and ascertain the rise in resistance towards water penetration in concrete, the concrete specimens' water absorption test was carried out in compliance with ASTM C642, 2013[24], After the first 28-day curing period, three 100 mm cubic specimens of each SCHPC combination were made, and evaluated, and their average values were noted at the ages of 28, 56, and 90 days.

2.4.3.2. Porosity

The porosity of concrete was measured under ASTM C642, 2013[24], and three cubes (100×100×100 mm3) of concrete samples were made for the test. The Samples have been examined following 28, 56, and 90 days of water curing

3.RESULTS AND DISCUSSION

3.1. Fresh tests results

Table 4,Fig.3, 4, and 5 show slump flow diameter, T500mm, and V-funnel flow time, respectively, to display the degree of SCHPC viscosity. The figures show that the T500mm and V-funnel flow time rose while the slump flow diameter (mm) reduced when comparing the binary mixes (6CK, 12CK, 18CK, and 24CK) to the reference mix. T500mm and V-funnel flow time rose by 12.90, 45.62, 51.61%, and 8.33, 18.05, 41, 66, and 56.94%, respectively, whereas slump flow decreased by around 2.61, 5.22, 7.32, and 12.41.

Table 5 shows that whereas the control concrete had the lowest T500 mm and V-funnel flow durations (3.1 s and 7.2 s, respectively), the mixture including 24CK had the highest T500 mm and V-funnel flow times (4.9 s and 11.3 s). When CK was introduced to the binary system, the concrete generally became more viscous. This might be because, in addition to the fine particle size of CK, which has much larger surface areas than cement that absorbs water, the CK particles are long, hexagonal plates that become obstacles in the fresh mix and increase friction between the particles [25].

Table 4. The results of rheological properties tested of SCHPC

Types of Mixes	Slump flow(mm)	T500 (Sec)	V- Funnel Time (Sec)	L-Box height ratio (H2/H1)	GTM (%)	Classification		
						Flow class	Viscosity class	Passing ability
CT	765	3.1	7.2	0.940	11.7	SF3	VS2\VF1	PA1
6CK	745	3.5	7.8	0.921	10.5	SF2	VS2\VF1	PA1
12CK	725	4.5	8.5	0.889	9	SF2	VS2\VF2	PA1
18CK	709	4.7	10.2	0.870	8.4	SF2	VS2\VF2	PA1
24CK	670	4.9	11.3	0.838	7.5	SF2	VS2\VF2	PA1
6CK1.5CC	735	3.8	8.1	0.903	10.1	SF2	VS2\VF2	PA1
12CK1.5CC	720	4.6	9.6	0.871	8.8	SF2	VS2\VF2	PA1
18CK1.5CC	695	4.8	11.2	0.839	8.2	SF2	VS2\VF2	PA1
24CK1.5CC	662	5.3	12.4	0.819	7.3	SF2	VS2\VF2	PA1

When compared to the reference mixture, the ternary mixtures (6CK1.5CC, 12CK1.5CC, 18CK1.5CC, and 24CK1.5CC) showed a decrease in slump flow diameter value and an increase in T500mm and V-funnel flow time, similar to the binary mixtures. However, it was more evident that the flow diameter decreased by approximately 3.92, 5.88, 9.15, and 13.46 percent, while the T500 and funnel flow time V increased by 22.58, 48.39, 54.83, and 70.96%, and 12.5, 33.33, 55.54, and 72.22 percent, respectively. The calcined kaolin clay particles' size and shape, as well as the finer CK and CC particles' surface areas, which absorb water more readily and leave less free water to contribute to flowability, may be the cause. Additionally, because CC particles are finer than OPC particles, the filler effect occurs, allowing finer CC particles to fill in the gaps between cement particles. [16, 26,27].

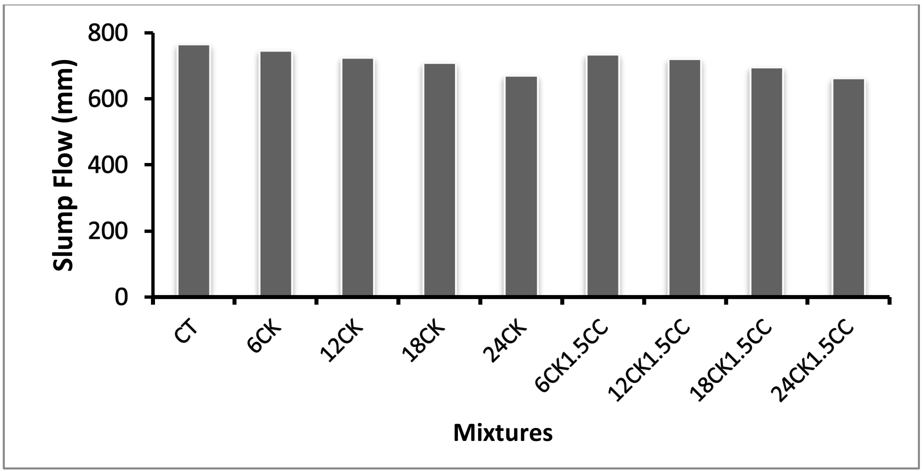

Figure 3. Slump flow diameter test results

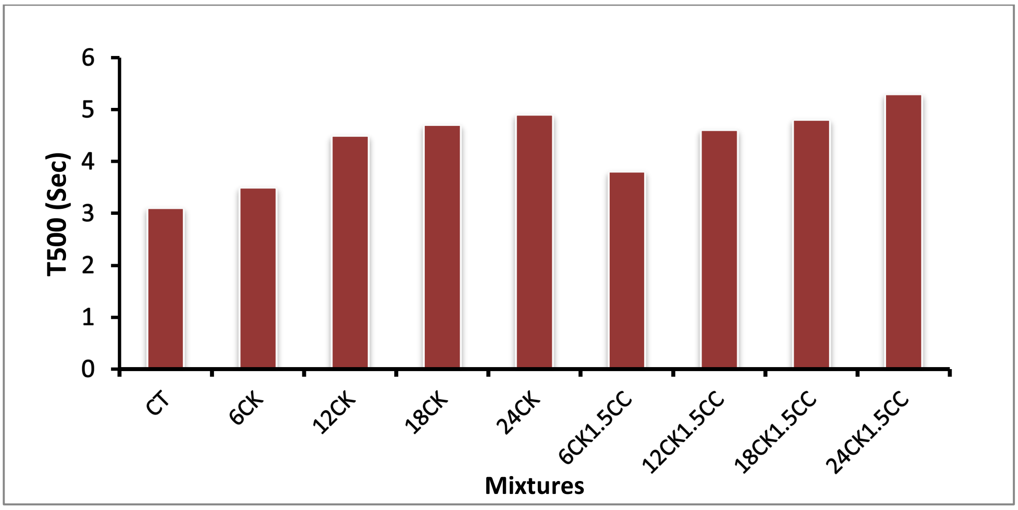

Figure 4. T500 results test results

The binary mixes (6CK, 12CK, 18CK, and 24CKC) had an inferior passing ability than the CT mixture, by around 2.02%, 5.42, 7.45%, and 10.85%, respectively, as shown in Figure 6. The more cement that was partially substituted, the lower the L-Box height ratio value. Similar to how it decreases the capacity to fill, the percentage and fineness of calcined clay (CK) also decrease the ability to pass. Comparable outcomes were reported by [27].

This impact amplifies with the ternary combinations (6CK1.5CC, 12CK1.5CC, 18CK1.5CC, and 24CK1.5CC) by about (3.93, 7.43, 10.74, and 12.87) % relative to the unblended mixture (100% OPC). No blocking or segregation phenomena were seen in the mixtures during the testing process. These findings are analogous to the results of the research [27].

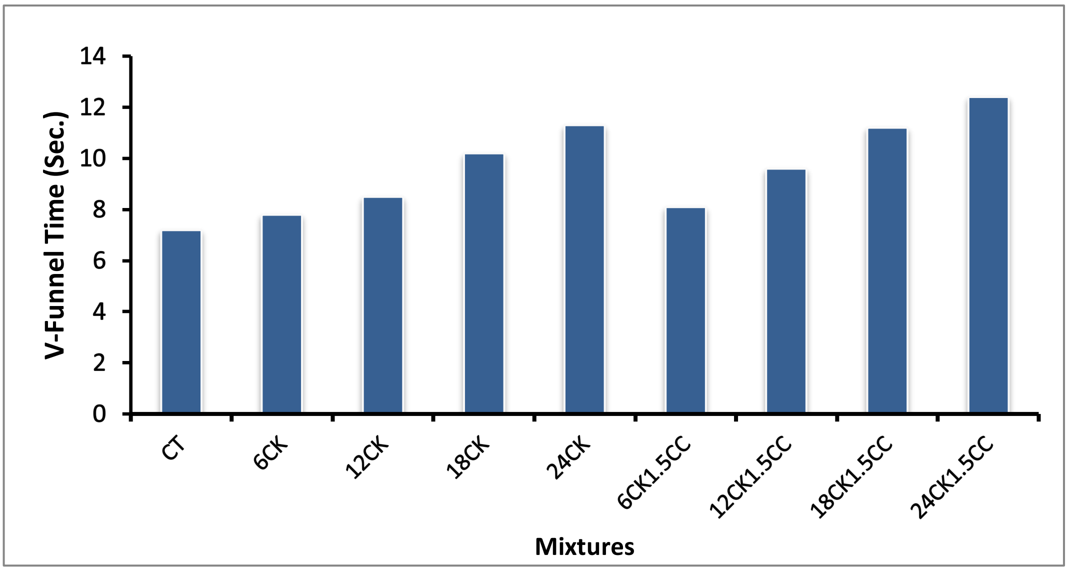

Figure 5. V-funnel time test result

Previous studies on fresh testing of blended SCHPC indicate that substituting CK or CK+CC for cement increases water use because of their reactivity with cement and fineness [26], [28].

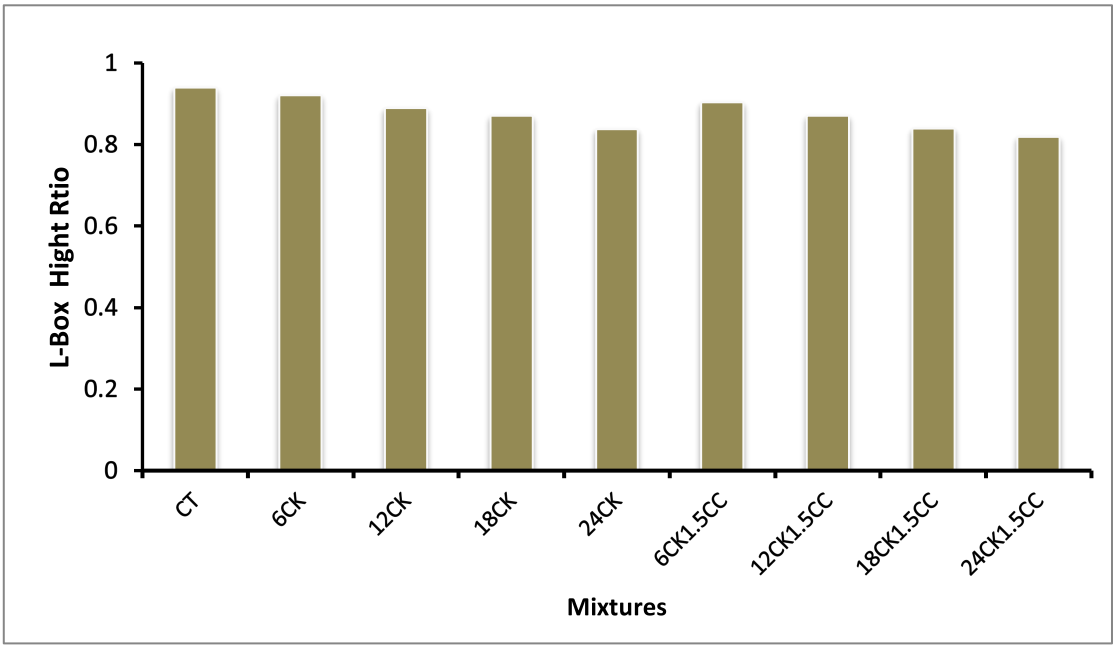

Figure 6. L-Box test results

Figure 7 displays the segregation resistance test outcomes for SCHPC mix binary and ternary blends. The binary mixtures (6CK, 12CK, 18CK, and 24CK) have greater segregation resistance than the CT mix, as the percentage of segregation falls as the percentage of partial replacement increases. For the binary mixes mentioned above, the percentage of reduction was around (10.25, 23.08, 28.21, and 35.90) %, respectively. In contrast, reference mixes and binary mixtures of comparable proportions exhibit lower segregation resistance than ternary combinations (6CK1.5CC, 12CK1.5CC, 18CK1.5CC, and 24CK1.5CC). In other words, the segregation ratio drops by around (13.67, 24.78, 29.91, and 37.60) %, respectively, in the ternary mixtures. This could be the result of the nanoparticles' increased surface area, which raises their viscosity and, in turn, their segregation resistance. Results were comparable to earlier studies [28].

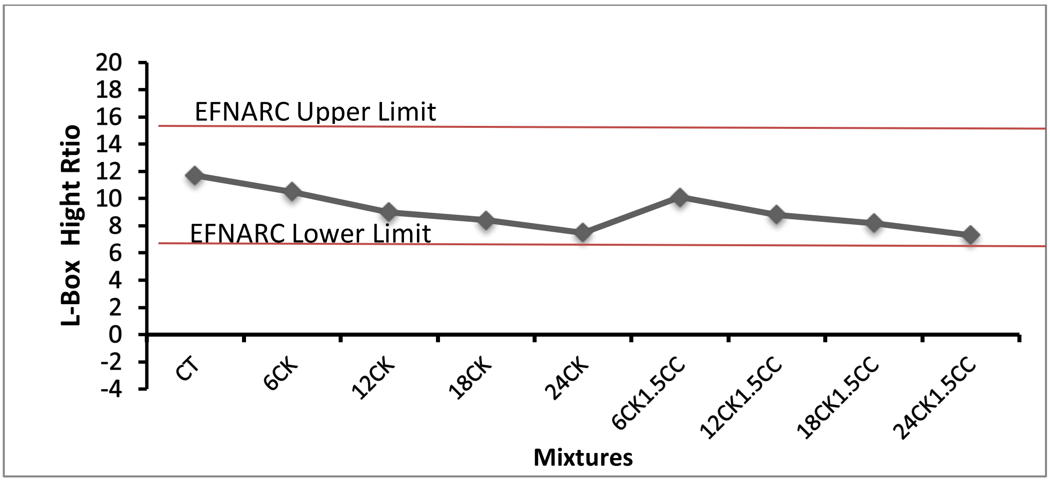

Figure 7. Segregation resistance test results

EFNARC [20], states that SCC is classed as VS1/VF1 when T500 mm and V-funnel flow time are less than or equal to 2 s and 8 s, and as VS2/VF2 when T500 mm is more than or equal to 2 s and V-funnel flow time is between 9 and 25 s. As a result, according to EFNARC, as indicated in Table 4, all ternary blends may be categorized into the VS2/VF2 class, whereas all binary blends of CK, except for the 6CK combination, fall within the ranges of the VS2/VF1 class.

3.2. Hardened examination results

3.2.1.Compressive strength of SCHPC

Fig.8 shows the compressive strength findings obtained for the experiment's binary and ternary mixtures. At 7 days, the SCHPC mixture (6CK, 12CK, 18CK, and 24CKC) had a compressive strength that was roughly (11.9, 19.3, 16, and 12.8) % higher than the control-CT mixture; at 28 days, it was (9, 19.9, 13.5 and 13) % higher; at 56 days, it was (10.4, 21, 14 and 12.7) % higher; and at 90 days, it was roughly (9.6, 17, 11.3, and 7.7) % higher.

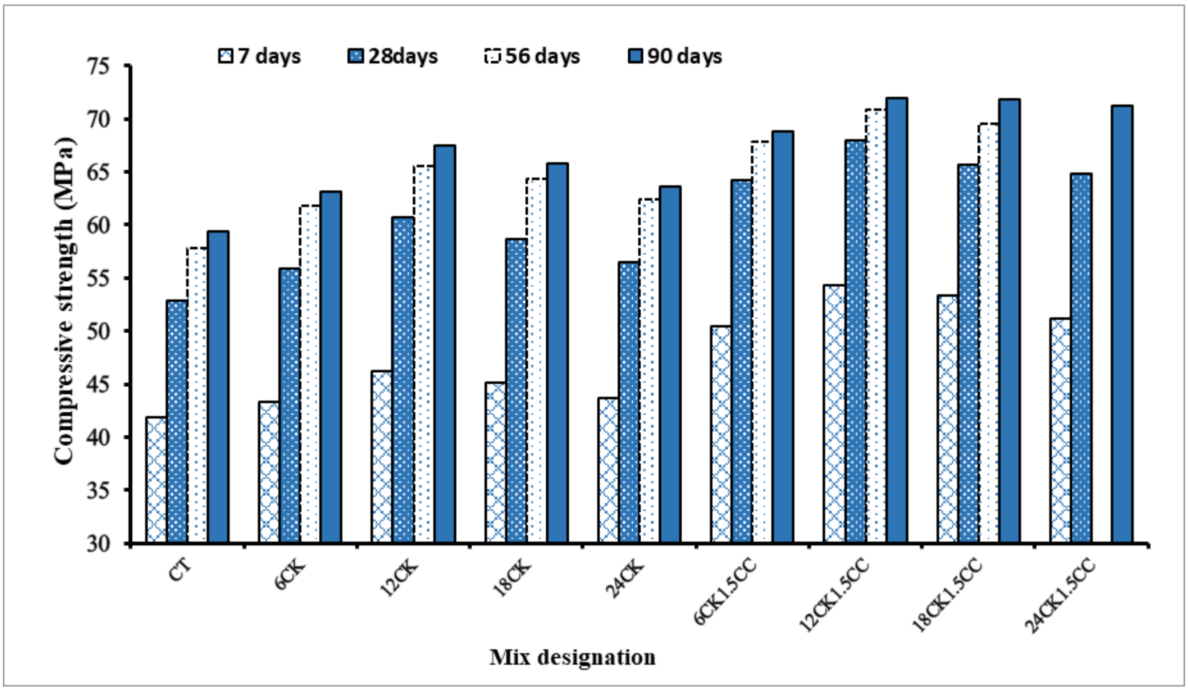

Figure 8. Compressivestrengthexamines results at (7, 28, 56, and 90)days

The pozzolanic processes of the calcined clay are responsible for the increase in compressive strength. For ternary mixes,12CK1.5CC mix revealed the maximum enhancement by about (34, 31.2, 25.5, and 21.8) % at (7, 28, 56, and 90) days, respectively. followed by 18CK1.5CC by (31.7, 26, 23, and 21.5) %, 24CK1.5CC by (26, 25.5, 20.9, and 20.5) %, and finally 6CK1.5CC by (11.9, 9, 10.4 and 9.7) %, respectively, compared with CT mix. Several factors contributed to this result: The impact of CK particle filling and its pozzolanic interaction with CaOH2 liberated during cement hydration. It significantly reduces concrete's CaOH2 content and forms C-S-H gel, (iii) accelerating early cement hydration (mainly at early ages), and (iv) a nano CaCO3 reaction with the aluminate phase from the hydration product's higher volume. Previous research on pozzolanic materials and nanoparticle concrete mixtures supported this tendency [5, 29, 30].

3.2.2.Splitting tensile strength

Fig. 9 showed that, in comparison to the CT mix, binary mixes (6% CK, 12% CK, 18% CK, and 24% CK) have a greater indirect tensile strength. Where the increase rate was (2, 9.4, 6.9, and 3.8) %, (3.3, 12.7, 9.6,and 4.9) %,(7.1, 11.4, 9.5, 7.7) %, and about (4.7, 12.3, 9.4, and 6.6) at 7, 28, 56, and 90 days, respectively. The causes include the fact that calcined clay has a larger surface area than cement, which causes the reaction to speed up. Adding 1.5 % nano-CaCO3 to ternary mixtures as a partial cement weight replacement (6% CK+1.5% CC, 12% CK+1.5% CC, 18% CK+1.5% CC, and 24% CK+1.5% CC),for ages (7, 28, 56, and 90) days, the values of splitting tensile strength rise further by (8.5, 14.8, 10.5, and 9.5) %, (26.6, 33.9, 30.8, and 29.3) %, (27.4, 33.3, 31.1, and 28.5), and (41.1, 31.6, 30.3, and 26.2) %, over the CT mix.as seen in Fig. 12. This may be the same reason indicated in compressive strength. The results were confirmed with previous studies[31]. Overall, the effect of CK and CC on the splitting tensile strength is similar to that on the compressive strength due to the stronger bonding between the cement paste and aggregate[32].

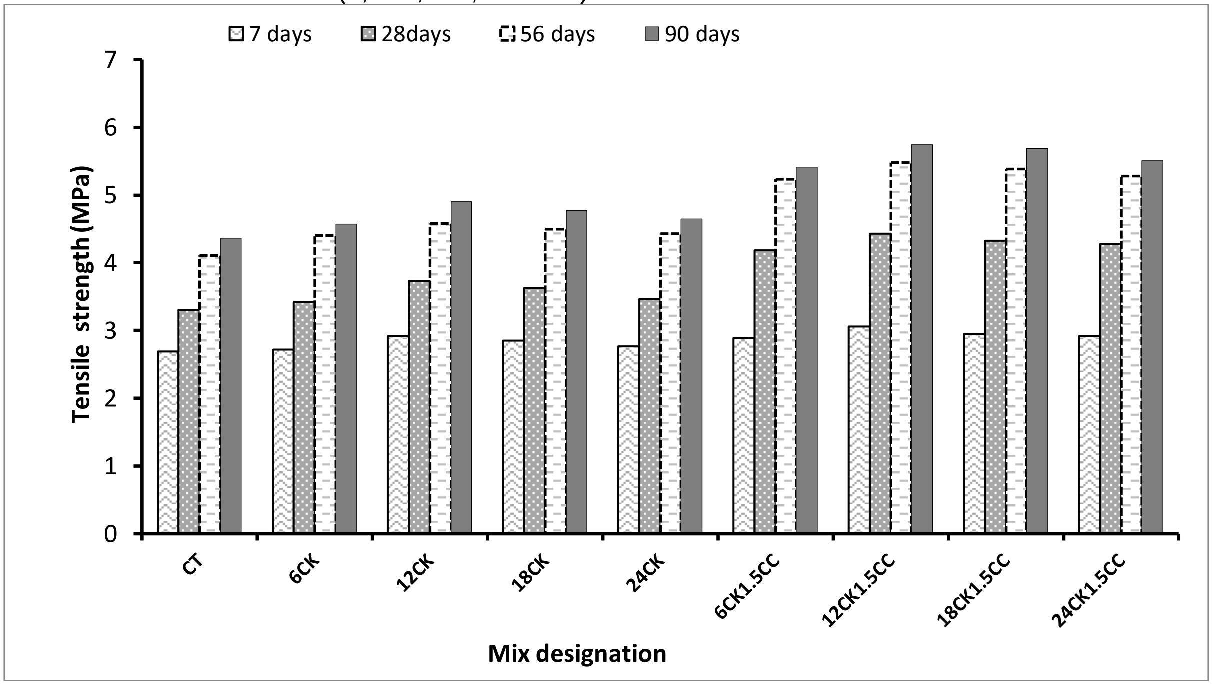

Figure 9. Splitting tensile strength results of control, binary, and ternary blended SCHPC mixes

3.2.3. Ultrasonic Pulse Velocity

Fig.10illustrates the results of the UPV experiment of binary blended mixes (6CK, 12CK, 18CK, and 24CK) and ternary blended mixes (6CK1.5CC, 12CK1.5CC, 18CK1.5CC, and 24CK1.5CC) at 7, 28, 56, and 90 days. As expected, the results of the UPV showed a similar general trend to the compressive strength results, increasing with the age of the specimens. At the same age,the UPV of the concrete incorporating CK and CC as ternary blends were observed to be better than those of concrete containing CK as the binary blends with the same replacement levels. This can be due to the rapid pozzolanic reaction of CC at 7 days and later ages, which produced additional C-S-H leading to declined porosity. The pulse velocity through voids is lower than that through solid matter, so the lower porosity and denser internal structure of the concrete lead to an increase in pulse velocity [33,34]. At the age of 7 days onward, the effect of CK on UPV value was generally increased at different partial replacement percent 6%CK, 12%CK, 18%CK, and 24%CK were ranged from 4405 to 4460 m ⁄s; at 7 days, 4560 to 4590 m ⁄s at 28 days, 4640 to 4750 m ⁄s at 56 days and 4750 to 4820 m ⁄s at 90 days. It also can be noticed that the UPV measurements for the mixture containing 12% CK were higher than for the specimens with 6%, 12%, 18%, and 24% CK and CT mixture. For ternary mixes at 7 days onward, the UPV values changed from (4340 to 4845), (4440 to 4920), (4425 to 4890), and (4380 to 4860)m/s for 6CK1.5CC, 12CK1.5CC, 18CK1.5CC, and 24CK1.5CC mixes respectively. This result is affected by the pozzolanic reactive (high silica content) with $Ca(OH)_2$ and produces additional C-S-H, adding to that the small size of CK and CC which can fill the voids between the large cement particles and the reduction of porosity which that leading to a higher UPV. Previous experiments on SCC incorporating pozzolanic materials provided similar findings [35,36].

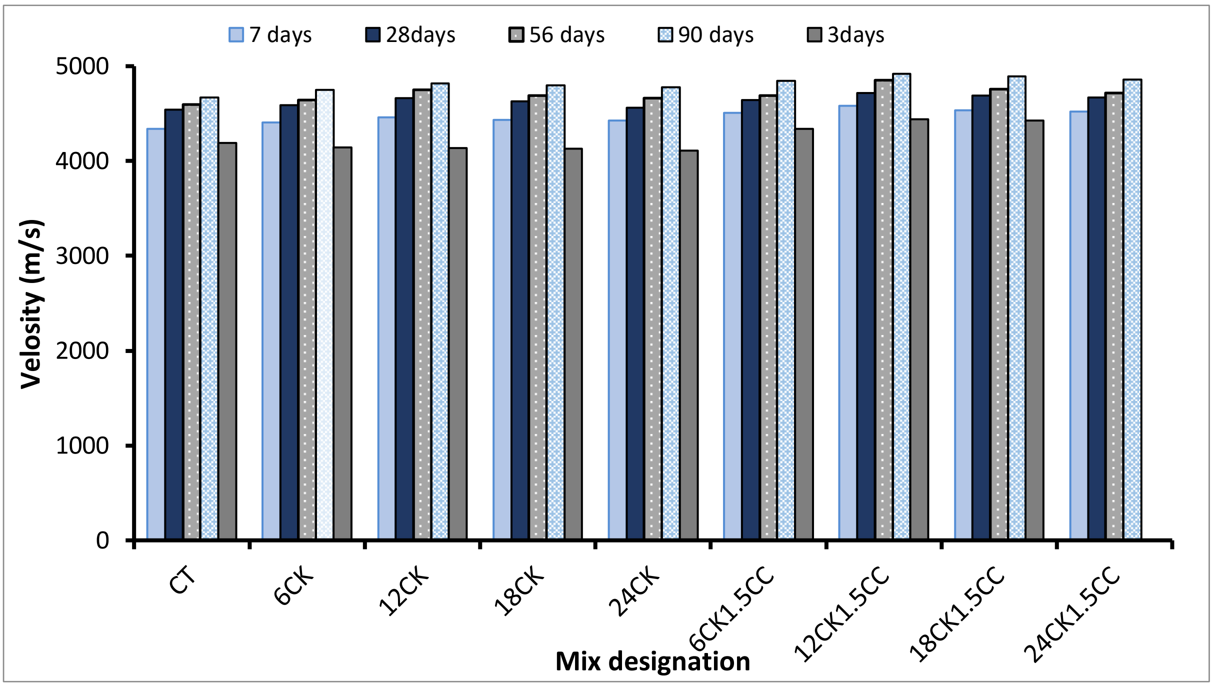

Figure 10. Ultrasonic pulse velocity values for control, binary, and ternary blended SCHPC mixtures incorporating CK and nano-CaCO3 at various ages

3.3. Durability examination results

3.3.1. Water absorption

The average results of the tests of self-compacting high-performance water-absorbing concretes (SCHPC), made of calcined kaolin clay and nano-calcium carbonate from binary and ternary mixtures, at 28, 56, and 90 days are shown in Fig. 11. It can be observed that the water absorption values decrease with increasing curing period for all binary and ternary SCHPC mixtures containing CK and nano-calcium carbonate in different proportions, compared to the reference CT concrete, due to the decrease in pore volume with hydration products, The lowest water absorption value was obtained at long-term ages (90 days) for all concrete mixtures. Compared to T C mix, CK concrete experienced a decrease in WA for 6% CK, 12% CK, 18% CK and 24% CKC mixes, which were recorded at about (9.22, 18.69, 17, and 22.65) %, (9.44, 19.90, 18.11 and 13.78) % and (3.98, 18.75, 11.64 and 7.95) %, respectively at 28, 56 and 90 days.

This finding can be attributed to the fact that these mixes have fewer interconnected pores as C-S-H is formed from the primary hydration and secondary pozzolanic reactions of CK, gradually filling the water-filled spaces. In addition, CK had high fineness as it acts as a filler between cement particles and may also contribute to this phenomenon. Hence, the CK-containing SCHPC blends produced in this study were of low absorption type and showed improved durability[27,37]. As for the ternary blends, the water absorption ratios of 6 CK1.5CC, 12 CK1.5CC, 15 CK1.5CC, and 24 CK1.5CC blends were 2.65 to 2.94; 2.32 to 2.63; 2.23 to 2.61 and 2.23 to 2.45% at ages ranging from 28 to 90 days, respectively. It can be observed that the water absorption ratio improved with lower values in the ternary blends upon partial replacement of cement with different proportions of calcined kaolin clay and nano calcium carbonate compared to the control CT blend. Due to the activity of pozzolanic material, it reacts with Ca $(OH)_2$, forming C-S-H addition in the pores and reducing water absorption, as well as the fineness of CKand CC which plays an important role in reducing water absorption. The research found that the 12% CK1.5 CC mixture was the best as it gave lower absorption rates for all ages. In general, all the binary and ternary blended SCHPC mixes investigated in the present study had a water absorption rate of less than 5%, which can be classified as good quality [38]. This reading indicates the durability of “good” concrete.

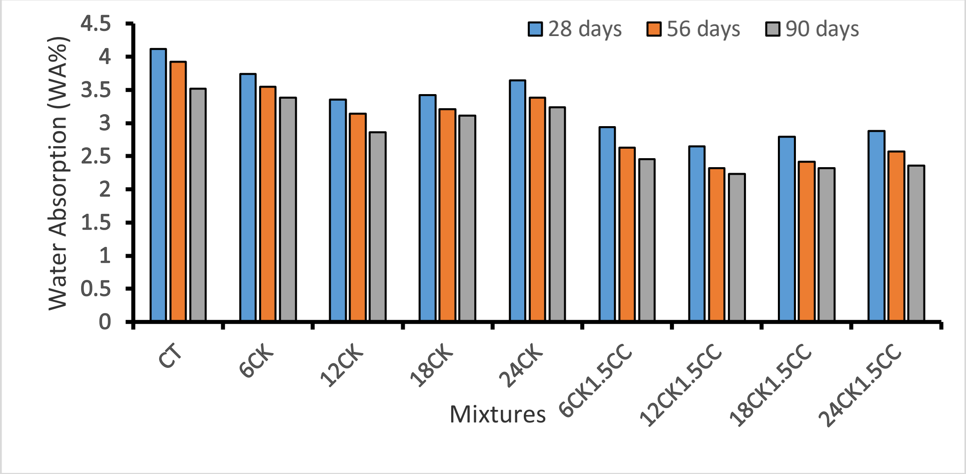

Figure 11. Water absorption of binary and ternary mixes for SCHPCsincorporating CK and nano-$CaCO_3$ at various ages

3.3.2. Porosity

The porosity results for all SCHPC containing calcined clay (CK) and nano calcium carbonate (CC) in binary and ternary mix systems at 28, 56, and 90 days are shown in Fig. 12. The incorporation of burnt kaolin clay up to 24% for binary mixes of SCHPC resulted in more reduction in porosity than the standard mix at different ages of 28, 56 and 90 days, as shown in Fig. 13. The recorded porosity of the mix using 12% CK was lower for all ages compared to the other binary concrete samples. However, the porosity of all mixes containing CK remained significantly lower than the standard concrete. The replacement mixes of CK at 6%, 12%, 18% and 24% were found to have significantly lower porosities of (10.34%, 9.63%, 9.78%, and 10.26%); (9.42%, 8.32%, 8.52 and 9.34%) and (8.52%, 7.86%, 8.14%, and 8.28%) for the progressive curing age of 28, 56, and 90 days, respectively. This may be attributed to the smaller size of CK particles and pozzolanic reaction, where CK particles fill the porous system because they are finer than cement, and CK reduces porosity by producing additional C-S-H gel[32,39].

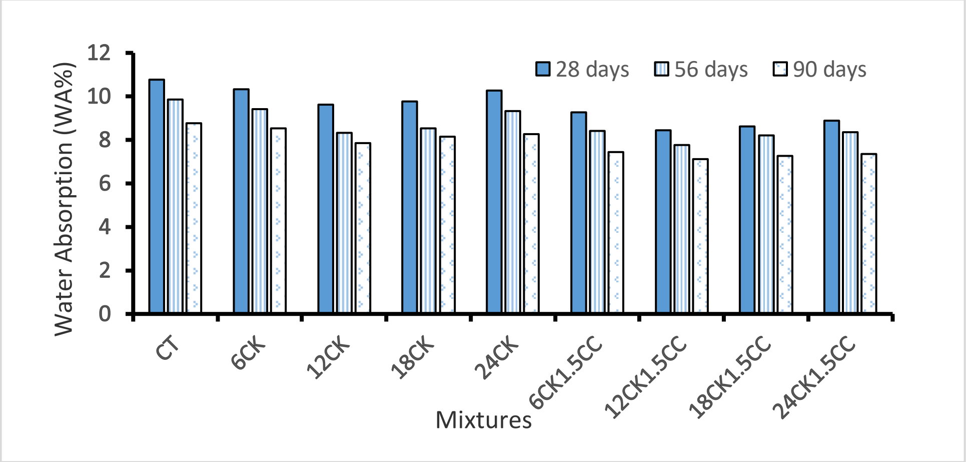

Figure 12. Porosity of binary and ternary mixes for SCHPCincorporating CK and nano-$CaCO_3$ at various ages

From Figure 12, the 12CK1.5CC mixture gave the lowest porosity values of 8.45%, 7.76%, and 7.12%, followed by 18CK1.5CC with 8.63%, 8.22% and 7.26%, then 24CK1.5CC with 8.77%, 8.35% and 7.39%, and finally, 6% CK1.5CC mixture gave 9.28%, 8.42% and 7.44% at (28, 56 and 90) days respectively. It was observed that all ternary mixtures performed better in terms of porosity than binary mixtures with CK for the same replacement levels. We conclude that the presence of C in SCHPC provides a more prominent effect in reducing absorption. The high fineness of burnt pozzolanic materials and nanoparticles used in this research may provide a filler effect for ternary composite concrete and contribute to reducing the absorption value. These results conformed with the study [39].

4. CONCLUSION

- The following conclusions may be made based on the findings of this experimental investigation.
- In binary mixed mixes comprising calcined clay (CK), fresh properties such as slump flow diameter, L-box height ratio, and segregation resistance decrease when CK is partially substituted. T500mm and V-funnel time, however, both increases.
- Compared to binary mixes, the fresh qualities of ternary blended mixtures (which contain CK and nano-CaCO3 (CC)) have a greater impact.1.5% dose of CC as partial substitution of cement weight in ternary SCHPC blend improves the strength of all mixtures for all ages.
- The binary mixes of SCHPC with 12% CK had better compressive strength than those with 6%, 18%, and 24% CK in all ages. The optimal CK concentration for sustaining SCHPC is 12%.
- The SCHPC ternary mixes had higher compressive strength at 7, 28, 56, and 90 days. CK-containing ternary blends with 1.5% CC had superior compressive strength than binary blends at all ages. SCHPC ternary blends with CK at 12% and 1.5% CC had greater compressive strength than binary, control, and other ternary mixes at all ages.
- SCHPC mixes' splitting tensile strength generally showed a similar pattern to their compressive strength, but the increases were slower than those shown in the SCHPC mixes' compressive strength.
- In general, the durability properties such as(water absorption, and porosity) were adversely impacted by increasing the partial substitute of CK and CC by cement weight.
- The UPV results showed a similar trend to the results of increasing compressive strength with age. At the age of 7 days onwards, the effect of CK on UPV value is a general increase at different partial replacement ratios.
- The UPVvalues of SCHPC ternary mixes at ages 7, 28, 56, and 90 days were higher than those of standard CT concrete. The UPV value of both concretes containing CK and NC as ternary mixes was higher than that of concretes including CK as binary mixes at the same replacement rates
- The optimal for calcined clay was 12% by cement weight for improvement of the strength and durability properties values.

5. REFERENCES

[1] N. A. Libre, R. Khoshnazar, M. Shekarchi (2012) Repeatability, responsiveness and relative cost analysis of SCC workability test methods, Mater. Struct., 45, 1087–1100. https://doi.org/10.1617/s11527-011-9818-6.

[2] A. A. Hashim, H. M. Owaid (2024) A Review of Workability and Mechanical Behavior of Self-Compacting Construction Composites Incorporating Nanomaterials, J. Univ. Babylon Eng. Sci., 32, 119–131.https://doi.org/10.29196/5sjfe077.

[3] M. Safiuddin, J. S. West, K. A. Soudki (2010) Hardened properties of self-consolidating high performance concrete including rice husk ash, Cem. Concr. Compos., 32, 708–717. https://doi.org/10.1016/j.cemconcomp.2010.07.006.

[4] A. O. Kadhum, M. O. Haider (2020) Experimental investigation of self-compacting high performance concrete containing calcined kaolin clay and nano lime, Civ. Eng. J., 6, 1708–1798. https://doi.org/10.28991/cej-2020-03091583.

[5] A. A. Hashim, R. Anaee, M. S. Nasr (2025) Improving the Mechanical, Corrosion Resistance, Microstructural and Environmental Performance of Recycled Aggregate Concrete Using Ceramic Waste Powder as an Alternative to Cement, Ceramics, 8, 11. https://doi.org/10.3390/ceramics8010011.

[6] P. J. M. Bartos (2000) Measurement of Key Properties of Fresh Self-compacting Concrete, CEN/STAR PNR Workshop, 6.

[7] O. Wallevik, I. Nielsson (2003) Self-compacting concrete, in Proceedings of the third International RILEM symposium, Reykjavik, RILEM Proceedings PRO, 1030.

[8] H. Okamura, K. Ozawa (1996) Self-compactable high-performance concrete in Japan, Spec. Publ., 159, 31–44. 10.14359/10052.

[9] B. Persson (2001) A comparison between mechanical properties of self-compacting concrete and the corresponding properties of normal concrete, Cem. Concr. Res., 31, 193–198. https://doi.org/10.1016/S0008-8846(00)00497-X.

[10] F. Dehn, K. Holschemacher, D. Weiße (2000) Self-compacting concrete (SCC) time development of the material properties and the bond behaviour, Selbstverdichtendem Bet., 5, 115–124.

[11] H. Okamura, K. Ozawa (1995) Mix design for self-compacting concrete, Concr. Libr. JSCE, 25, 107–120.http://dx.doi.org/10.1201/9781482271782.

[12] H. Okamura (1994) Seif-compacting high performance concrete in Japan, in Proceedings of International Workshop on High Performance Concrete, Bangkok Thailand, 1–2.

[13] V. K. Bui, D. Montgomery, I. Hinczak, K. Turner (2002) Rapid testing method for segregation resistance of self-compacting concrete, Cem. Concr. Res., 32, 1489–1496. https://doi.org/10.1016/S0008-8846(02)00811-6.

[14] F. Adeyemi (2023) Influence of Calcined Clay and Limestone Addition on the Strength Properties of Self-Compacting Concrete, Kwara State University (Nigeria). http://dx.doi.org/10.1007/978-981-15-2806-4_81.

[15] [15]A. A. Hashim, N. S. Azeez, A. S. Naje, H. A. M. Al-Zubaidi (2021) Eco friendly enhancement of self-compacting concrete mechanical properties using metakaolin and nanosilica, J. Green Eng., 11, 2.

[16] H. Du, S. Dai Pang (2020) High-performance concrete incorporating calcined kaolin clay and limestone as cement substitute, Constr. Build. Mater., 264, 120152. https://doi.org/10.1016/j.conbuildmat.2020.120152

[17] A. A. Hashim, Z. kazem Rodhan, S. J. Abbas (2020) Fresh and hardened properties of self-compacting high performance concrete containing nano-metakaolin as a partial replacement, in IOP Conference Series: Materials Science and Engineering, IOP Publishing, 22036. http://dx.doi.org/10.1088/1757-899X/928/2/022036.

[18] ASTM C150-92. (1992) Stand. Specif. Portl. Cem. Annu. B. ASTM Stand., 4.

[19] H. R. W. R. Admixture, “ASTM C494, Type F or G. One of the following: a. Euclid Eucon 37 or 537. b. Sika Sikament 300. c. Master Builders-Rheobuild 1000. e. WR Grace & Co,” Conn.–Daracem, 19.

[20] EFNARC (2005) European Guidelines for Self-Compacting Concrete, Specification and Production and Use, Association House, UK.

[21] BS EN, 12390–12393 (2009) Testing hardened concrete, Compressive Strength Test Specimens.

[22] ASTM C496 (2004) Standard Test Method for Splitting Tensile Strength of Cylindrical Concrete Specimens, ASTM Int. West Conshohocken, PA.

[23] ASTM C 597 (2002) Standard Test Method for Pulse Velocity Through Concrete’ ASTM Int.

[24] ASTM C642 (2013) Standard test method for density, absorption, and voids in hardened concrete.

[25] S. Dadsetan, J. Bai (2017) Mechanical and microstructural properties of self-compacting concrete blended with metakaolin, ground granulated blast-furnace slag and fly ash, Constr. Build. Mater., 146, 658–667. https://doi.org/10.1016/j.conbuildmat.2017.04.158.

[26] W. Li, Z. Huang, F. Cao, Z. Sun, S. P. Shah (2015) Effects of nano-silica and nano-limestone on flowability and mechanical properties of ultra-high-performance concrete matrix, Constr. Build. Mater., 95, 366–374. https://doi.org/10.1016/j.conbuildmat.2015.05.137.

[27] S. Lenka, K. C. Panda (2017) Effect of metakaolin on the properties of conventional and self compacting concrete, Adv. Concr. Constr, 5, 31–48. https://doi.org/10.12989/acc.2017.5.1.031.

[28] M. Liu (2009) ditions in self-compacting concrWider application of adete, UCL (University College London).

[29] X. Wang, K. Wang, J. Li, N. Garg, S. P. Shah (2014) Properties of self-consolidating concrete containing high-volume supplementary cementitious materials and nano-limestone, J. Sustain. Cem. Mater., 3, 245–255. https://doi.org/10.1080/21650373.2014.954155.

[30] M. M. Khotbehsara, B. M. Miyandehi, F. Naseri, T. Ozbakkaloglu, F. Jafari, E. Mohseni (2018) Effect of SnO2, ZrO2, and CaCO3 nanoparticles on water transport and durability properties of self-compacting mortar containing fly ash: Experimental observations and ANFIS predictions, Constr. Build. Mater., 158, 823–834. https://doi.org/10.1016/j.conbuildmat.2017.10.067.

[31] F. U. A. Shaikh, S. W. M. Supit (2014) Mechanical and durability properties of high volume fly ash (HVFA) concrete containing calcium carbonate (CaCO3) nanoparticles, Constr. Build. Mater., 70, 309–321. https://doi.org/10.1016/j.conbuildmat.2014.07.099.

[32] Z. Wu, C. Shi, K. H. Khayat, S. Wan (2016) Effects of different nanomaterials on hardening and performance of ultra-high strength concrete (UHSC), Cem. Concr. Compos., 70, 24–34. https://doi.org/10.1016/j.cemconcomp.2016.03.003.

[33] R. Madandoust, S. Y. Mousavi (2012) Fresh and hardened properties of self-compacting concrete containing metakaolin, Constr. Build. Mater., 35, 752–760. https://doi.org/10.1016/j.conbuildmat.2012.04.109.

[34] M. Shariq, J. Prasad, A. Masood (2013) Studies in ultrasonic pulse velocity of concrete containing GGBFS, Constr. Build. Mater., 40, 944–950. https://doi.org/10.1016/j.conbuildmat.2012.11.070.

[35] V. Kannan (2015) Relationship between ultrasonic pulse velocity and compressive strength of self compacting concrete incorporate rice husk ash and metakaolin, Int. J. Eng. Appl. Sci., 2, 5.

[36] A. E. M.-S. G. Nehme (2016) A comparative study on ultrasonic pulse velocity for normally vibrated and self-compacting concretes.

[37] M. Gholhaki, M. Hajforoush, M. Kazemi (2018) An investigation on the fresh and hardened properties of self-compacting concrete incorporating magnetic water with various pozzolanic materials, Constr. Build. Mater., 158, 173–180. https://doi.org/10.1016/j.conbuildmat.2017.09.135.

[38] B. Alsubari, P. Shafigh, Z. Ibrahim, M. F. Alnahhal, M. Z. Jumaat (2018) Properties of eco-friendly self-compacting concrete containing modified treated palm oil fuel ash, Constr. Build. Mater., 158, 742–754. https://doi.org/10.1016/j.conbuildmat.2017.09.174.

[39] H. Du, S. Du, X. Liu (2014) Durability performances of concrete with nano-silica, Constr. Build. Mater., 73, 705–712. https://doi.org/10.1016/j.conbuildmat.2014.10.014.

IZVOD

RAZVOJ NOVE CEMENTNE MEŠAVINE DOBIJENE OD KALCINISANIH PUCOLANSKIH MATERIJALA I NANOČESTICA SAMOZBIJAJUĆEG BETONA VISOKIH PERFORMANSI

Ovo istraživanje uključuje eksperimentalnu studiju o potencijalnoj upotrebi pucolanskih i nanomaterijala, uključujući nano kalcijum karbonat (CC) i kalcinisanu glinu (CK), tokom procesa proizvodnje samozbijajućeg betona visokih performansi (SCHPC). Binarni i ternarni sistemi mešanja pripremljeni su korišćenjem 475 kg/m3 cementa i fiksnog odnosa vode i veziva (0,35). CK je korišćen u proporcijama od 6 do 24% ukupne mase cementnih materijala. Što se tiče ternarnih mešavina, uzorci (6% CK 1,5% CC, 12% CK 1,5 CC, 18% CK 1,5 CC i 24% CK 1,5% CC) su pripremljeni delimičnom zamenom mase cementa sa CK i CC. Osobine novog SCHPC-a su procenjene testovima sleganja (D (mm) i T500 (s)), V-levka, L-kutije i otpornosti na segregaciju. Izmerena su mehanička svojstva, uključujući čvrstoću na pritisak i zatezanje, i izvršeno je ultrazvučno ispitivanje brzine pulsa betona. Takođe, merena su svojstva izdržljivosti, uključujući poroznost i upijanje vode. Nalazi su pokazali da dodavanje kalcinisane kaolinske gline u beton značajno poboljšava njegovu trajnost i mehanička svojstva. Najbolje poboljšanje je bilo za binarne i ternarne smeše sa 12% zamene kalcinisane kaolinske gline, gde je čvrstoća na pritisak poboljšana za 20,9%, a poroznost i upijanje vode smanjeni za 15,6% i 19,9%, za 56 dana u poređenju sa referentnom smešom. Trostruke mešavine su se, takođe, poboljšale bolje od ternarnih mešavina za iste omere zamene kalcinisane kaolinske gline za sve uzorke. Na primer, mešavina 12CK1.5CC zabeležila je poboljšanje čvrstoće na pritisak od 25,5% i smanjenje poroznosti i upijanja vode od 21,3% i 40,8% u poređenju sa referentnom smešom u periodu od 56 dana. Ova studija je ostvarila svoje ciljeve održivom proizvodnjom ekološki prihvatljivog betona kroz smanjenje sadržaja cementa putem pucolanskih i nanočestica.

Ključne reči: *Kalcinisana glina; nano kalcijum karbonat; Otpor segregaciji; ekološki prihvatljiv beton; Durabiliti Properties*

Naučni rad
Rad primljen: 31.01.2025.
Rad korigovan: 28.02.2025
Rad prihvaćen: 06.03.2025.

Ansam Ali Hashim: https://orcid.org/0000-0002-5389-1527

Mary Pramila Santhi[1], *Susai Rajendran*[2]*

[1]Department of Commerce and The Principal, [2]Corrosion Research Centre, Department of Chemistry,St.Antony's College of Arts and Sciences for Women, Thamaraipadi, Dindigul,Tamil Nadu,India. (Affiliated to Mother Teresa Women's University, Kodaikanal, India)

Rewiev paper
ISSN 0351-9465, E-ISSN 2466-2585
https://doi.org/10.62638/ZasMat1383

Zastita Materijala 67 (1)
100 - 111 (2026)

Corrosion management in petroleum Industry

ABSTRACT

The world is swiftly advancing towards the development of sustainable infrastructure, emphasizing the use of corrosion-resistant materials to effectively optimize corrosion control and reduce lifecycle costs. Addressing corrosion control and mitigation during the initial design and construction phases of assets proves to be more beneficial in the long term, particularly regarding enhanced safety, performance, asset longevity, environmental protection, and operational cost-effectiveness.Overall, the global cost attributed to corrosion is estimated to reach trillions. In general, corrosion is thought to affect approximately 4 percent of anation's GDP, and the continuously escalating environmental threat necessitates immediate and suitable actions.This article will concentrate on the different types of "Corrosion and its Prevention in the Oil and Gas Industry" that impact equipment, pipelines, and infrastructure within the oil and gas sector, along with strategies to alleviate these problems. Corrosion poses a significant challenge in the industry, resulting in safety risks, operational interruptions, and considerable financial losses. This article will address the following essential topics: Types of Corrosion in Oil and Gas, Impact of Corrosion on the Oil and Gas Industry, Corrosion Monitoring and Detection, Corrosion Prevention Methods, Best Practices in Corrosion Management, Case Studies and Industry Standards, and Future Trends in Corrosion Prevention.

Keywords: *corrosion, management, oil and gas industry, petroleum industry, pipe line corrosion*

1. INTRODUCTION

Management

Industrial management represents a distinct area of engineering dedicated to the advancement of management systems, while simultaneously integrating diverse engineering processes.This field includes industrial design, construction, and the utilization of scientific and engineering principles, all focused on improving the overall industrial infrastructure and processes.

The main focus of industrial management is to supervise industrial processes.Industrial managers are responsible for guaranteeing the optimal and efficient interaction of the four fundamental components referred to as the 4Ms: Man, Material, Machine, and Method, which are crucial for every organization.

Industrial management involves the evaluation of both machinery and employee performance. Experts are responsible for keeping equipment in peak operational condition and ensuring the quality of production results.The flow of materials throughout the facility is tracked to avoid any interruptions for either personnel or machinery.Regular inspections are performed to confirm that production rates align with set standards.

The economic consequences of corrosion in the oil sector total billions of dollars each year. This issue affects every aspect of exploration and production, including offshore platforms and casing materials. The conversation covers different methods for controlling and monitoring corrosion, along with an examination of the chemical elements that lead to its development.

A multitude of research articles has been published regarding corrosion management in the petroleum sector [1-25]. These studies are enumerated in the present research.

1. *An analytical risk-oriented methodology for determining the ideal inspection frequencies of a caustic soda recovery facility: a case analysis.*

Inspection and maintenance activities are crucial for guaranteeing the mechanical integrity and the safe, efficient functioning of systems and equipment.The organization of bare assets is of utmost importance, and it is essential to take into account the inspection and testing of equipment through suitable methods and procedures.The Risk

---

*Corresponding author: Susai Rajendran
E-mail: susairajendran@gmail.com

Paper received: 22.02.2025.
Paper corrected: 01.06. 2025.
Paper accepted: 04. 06.2025.

Based Inspection (RBI) methodology, as specified by the American Petroleum Institute (API), currently acts as the primary practical standard for overseeing and scheduling in-service or on-site inspection activities within the chemical sector.This paper introduces the RBI technique, based on the API 581 standard, aimed at determining optimal inspection intervals for a caustic soda recovery facility.By evaluating inspection data concerning significant damage factors such as corrosion and wear, both the probability and implications of potential failures have been analyzed, along with the annual expenses related to the inspection program.

The innovation is found in the application of this analysis specifically to a caustic soda recovery facility, filling the voids in the current literature regarding this application and integrating various damage mechanisms to facilitate a more precise evaluation. As a result, the pertinent scenarios and possible failure outcomes are recognized, which leads to the suggestion of suitable inspection schedules and maintenance practices, based on the assumption that risk remains within acceptable limits between two scheduled intervals. This paper concludes that Risk-Based Inspection (RBI) is an effective maintenance approach for assessing hazardous equipment impacted by multiple damage mechanisms, offering a robust framework for inspection programs that improve operational availability and reduce unplanned shutdowns. [1].

2. *A model for predicting corrosion, developed through data analysis, aimed at enhancing the digitization of subsea operations.*

Corrosion significantly contributes to the failure of subsea processing operations, especially in subsea crude oil pipelines. The pressing requirement for a data-driven corrosion prediction model emerges from the digitization of subsea processing systems within the Industry 4.0 framework, which is vital for improving the intelligent risk management capabilities of these systems. This paper presents an innovative data-driven model that utilizes hybrid methodologies to evaluate corrosion degradation in subsea operations. The model incorporates three data-driven techniques: principal component analysis (PCA), artificial bee colony algorithm (ABC), and support vector regression (SVR). Its effectiveness in forecasting the corrosion rate of subsea crude oil pipelines has been assessed, facilitating proactive monitoring of corrosion levels. In this hybrid methodology, PCA is employed to diminish the dimensionality of factors affecting corrosion, with the resulting principal components acting as input variables for the model.

The ABC algorithm is utilized to enhance the hyperparameters of the SVR. The model is developed using a segment of historical data, and its efficacy is later assessed against the remaining dataset. A case study exemplifies the model's practicality and efficiency, contrasting it with four other models: SVR, PCA-SVR, PCA-GA-SVR, and PCA-PSO-SVR. The PCA-ABC-SVR model exhibited greater prediction accuracy and resilience, attaining metrics of MAE = 7.10%, RMSE = 9.19%, and R^2 = 0.976. This proposed model is expected to serve as a significant online resource for improving safety and aiding the digitization of processing systems[2].

3. *Creating a fuzzy goal programming model to address health, safety, and environmental risks utilizing a hybrid fuzzy FMEA-VIKOR approach.*

The operations of the oil industry, ranging from the exploration stage to the management of oil fields, pose considerable negative impacts on both public health and the environment. Therefore, organizations involved in this industry are required to recognize and mitigate their related risks. This document intends to emphasize the known risks arising from various elements such as expenses and volume. Furthermore, it aims to pinpoint the most essential corrective measures through the implementation of a goal-programming approach. To evaluate health, safety, and environmental (HSE) risks, the Fuzzy Delphi technique was utilized. The failure mode and effects analysis (FMEA) along with the fuzzy VlseKriterijumska Optimizacija Kompromisno Resenje (VIKOR) methods were employed to overcome the shortcomings of FMEA in prioritizing HSE risks.

In contrast to other research, the FMEA–VIKOR method proposed here does not compute a risk priority number. Rather, it employs the Eigenvector method to assign weights to parameters such as time, cost, and quality, along with severity, occurrence, and detection, for the purpose of risk ranking. Following this, a fuzzy goal-programming model was created to identify optimal solutions for risk response. The findings of the study indicated that the most critical risks encompass fire and explosion threats associated with tanks and pipelines, as well as leaks from connections and pipelines, in addition to industrial waste. The main strategies for risk mitigation identified include the enhancement of alarm and fire suppression systems, the use of fiberglass tanks to reduce pipeline corrosion, and the implementation of advanced technologies for more efficient oil refining. The significant contribution of this paper is the integration of the FMEA–VIKOR methodology for risk ranking, which considers various factors such as time, cost, and quality, alongside severity, occurrence, and detection.

Furthermore, the establishment of a fuzzy goal-programming framework for pinpointing key risk responses adds additional value to this research.[3]

4. A probabilistic framework for evaluating the rate of corrosion affected by microbiological factors.

This research presents an innovative probabilistic method, in conjunction with traditional techniques, for estimating the rate of microbiologically influenced corrosion (MIC). The suggested approach considers the variability of factors that lead to corrosion, the complex interrelations of structures, and the necessity to adjust the corrosion rate in response to evolving conditions. This method aims to establish a highly parameterized Bayesian network specifically designed for evaluating the MIC rate. The model's validation is performed using field data associated with MIC. The results reveal that iron-oxidizing bacteria and methanogens are the key contributors to the corrosion rate. Furthermore, the study highlights the most intricate parameters influencing this rate. The model developed is crucial for safety evaluations and the management of corrosion risks in oil and gas production and processing facilities. [4].

5. Investigation into the technology for managing corrosion in petroleum pipelines and pressure vessels.

At present, there exists a considerable deficiency in localized corrosion rate data, understanding of corrosion mechanisms, and knowledge of inspection cases related to the corrosion of the upper module weight vessel and weight pipeline for both the fixed oil construction platform and the mobile oil storage and delivery platform. This shortcoming results in inaccurate evaluation outcomes and a fragile basis for integrity management. In response to this issue, the paper investigates the key factors that contribute to the corrosion process and performs a detailed analysis of the primary instruments involved. By meticulouslyexamining elements such as pressure vessel design, material selection, engineering practices, coatings, and slow-release methods, in conjunction with various corrosion instruments, a thorough analysis of corrosion protection for pressure vessels is conducted. The objective is to determine the most effective system for weather protection and rust prevention, thereby ensuring that weight vessels function safely and efficiently within the realm of petrochemical production [5].

6. Generating Value from Existing Gas Fields by Evaluating Well Integrity Assurance through a Thorough Analysis of Different Logs and Inspected Tubular Surfaces.

The Sharjah National Oil Corporation (SNOC) oversees four above-ground gas condensate tanks, three of which are well-established, containing over 50 wells that have been extracting corrosive hydrocarbons for more than thirty years. The dependability of these legacy wells is often examined before any development activities, which complicates the evaluation of well integrity. The costs related to retrieving plugs for assessment and performing logging operations across all wells are considerable, and the range of advancing technologies for corrosion evaluation available in the market complicates the selection of the most dependable option. This paper presents a thorough analysis and comparison of electromagnetic thickness measurements obtained from 10% of the wells, covering the period from 2016 to the post-workover surface inspections of the downhole completion systems in 2020/21. Additionally, it explores how correlating different assessment methods for well integrity improves the reliability of the electromagnetic technology applied to these legacy wells.

Moreover, the document offers a comparison between automated and electromagnetic evaluations of thickness for the production casing in situ.Data from all accessible fuel sources over the last five years were gathered for six wells. After retrieving the downhole completion tubing via a hydraulic workover, an ultrasonic (UT) inspection was conducted at shallow depths. Both sets of results (logs and surface inspections) were examined on the same classification track to deliver a thorough comparison of actual surface observations against measurements acquired through in-situ logging.Furthermore, a multi-barrier corrosion and caliper log was performed in the production casing to assess their findings in conjunction with historical data. The concluding phase involved comparing all available data to create a comprehensive well integrity profile. It was observed that the remaining metal thickness of the production tubing, as identified by the electromagnetic tool (logs) and surface ultrasonic measurements, demonstrated good correlation within a margin of +/-10%.

In evaluating corrosion within the production casing, the electromagnetic tool exhibited an impressive correlation with the results derived from the caliper log. This suggests a significant degree of reliability for this technology in measuring corrosion in offset wells.The relationship between log data and surface inspection results across wells in the same reservoir did not indicate a notable presence of external corrosion. This research provides management with crucial insights for making well-informed business decisions concerning the future use of the well stock.This study marks the first thorough and critical assessment of electromagnetic thickness logging technology, contrasting its findings on remaining wall thickness with various in-situ and surface technologies. The analysis includes comparisons between technologies from different providers, as well as mechanical versus electromagnetic measurements, emphasizing their respective benefits in maintaining well integrity.Furthermore, the paper presents insights into the condition of L-80 tubulars that have been operational for over 30 years [6].

7. Implementation of Non-Metallic Technologies for the Future ADNOC Production Facilities

Throughout the industry, the widespread occurrence of poverty and the decline of steel structures, coupled with the essential actions required to avert or alleviate these challenges, present considerable conservation and operational hurdles across multiple sectors. In light of these obstacles, ADNOC Group Technology, guided by our Non-Metallic Steering Committee and ADNOC Upstream, is partnering with selected specialized product companies to execute a series of innovative solutions as pilot trials within a thorough research and development initiative. This program is designed to transform our production and processing services, with a specific focus on integrity management. In particular, we are assessing the application of non-metallic pipelines, storage vessels, and downhole tubing and casing.

This paper will focus on the piloting of RTP Onshore, emphasizing a unique trial carried out in an ultra-sour gas field where the technology has successfully met the required performance standards. This encompasses the safe transportation of gas with hydrogen sulfide (H2S) concentrations of up to 10% by volume. The trial also illustrates that specially engineered non-metallic products can function effectively under the high temperature and high pressure (HPHT) conditions typical of our reservoirs. Consequently, as a result of this qualification program, ADNOC is anticipated to see an improvement in the durability of pipeline assets, along with a significant increase in reliability and availability, while also enjoying reduced maintenance costs over time. It has been demonstrated that RTP can provide life-cycle investment savings exceeding 60% in comparison to conventional carbon steel pipes.

The polymer feedstock employed in the creation of these products can be obtained locally, including resources supplied by Borouge in the UAE. This strategy promotes a thorough and sustainable cycle that includes manufacturing, usage, and recycling, thus improving In-Country Value (ICV) and creating additional economic opportunities within the developing non-metallic industrial sector of the country. A comprehensive description of this intricate value proposition is depicted in Figure 1 below. This illustrates how ADNOC and the UAE are demonstrating global leadership by cultivating and investing in sustainable, energy-efficient solutions across the entire value chain, while concurrently strengthening the national economy [7].

8. Assessment of an Accidental Emission of Liquefied Petroleum Gas at a Petrochemical Plant: A Case Study.

The Oil and Gas industry is presently experiencing considerable changes in knowledge, spurred by the increasing demand for energy. This industry continues to be a major source of risk, rendering risk assessment crucial for the protection of individuals, equipment, and the environment. Such assessments enhance management by alleviating these risks and establishing a proactive prevention and defense strategy to fulfill the goals of the Health, Safety, and Environment (HSE) management system. This research entails a quantitative evaluation of the risks linked to a Liquefied Petroleum Gas (LPG) storage and supply facility, suggesting a risk assessment methodology that allows for the analysis of various accidental scenarios that could result from an LPG release and their possible repercussions. It is vital to highlight that the triggering event is a complete and immediate rupture of the pipeline, leading to the uncontrolled discharge of a substantial quantity of liquid gas.

The analysis also takes into account small, medium, and large leaks. The main failure mechanisms identified for the pipelines consist of external leaks, blockages, and structural failures resulting from distortion or corrosion (in the absence of leaks or blockages). The primary causes of these failures are mechanical problems, frequently arising from overload, along with inadequate design and corrosion. Furthermore, external forces and human error may also play a role in these incidents. According to the event tree analysis, the recognized hazardous outcomes encompass an Unconfined Vapor Cloud Explosion (UVCE)/flash fire, pool fire, jet fire, and the release of a toxic cloud that leads to atmospheric pollution. The scenario concerning the release of the toxic cloud was excluded from our study. As a result, for minor leaks, the phenomena of pool fire, UVCE/flash fire, and jet fire are considered significant due to their relatively low occurrence rates, even though they have high frequencies of occurrence exceeding Ft = E-5 per year (in line with the ALARP principle).

The disappearance of the butane pool can be noted in the context of medium or large leaks, where the impacts are relatively minor.

Nevertheless, this situation is considered unacceptable in the event of a slick detonation. For average and large leaks, the occurrences of UVCE, flash fire, and jet fire are regarded as intolerable due to their severe consequences, despite their infrequent occurrence rates (1.28 E-5 and 3.2 E-5 per year for average leaks, and 1.092 E-5 and 1.82 E-5 per year for large leaks, respectively). The identified high-risk scenarios were examined using the ALOHA simulator, which enabled us to identify areas susceptible to various accidental effects, including thermal, toxic, and overpressure impacts. This analysis also aided in the formulation or revision of response strategies and emergency plans..[8].

9. Assessment of Fuzzy Criticality in Evaluating External Corrosion Risks of Systems in the Petroleum Industry—A Case Study.

Corrosion is the most common type of damage found in offshore installations and serves as a key factor influencing the longevity and reliability of these assets.Modern maintenance approaches are increasingly emphasizing risk and reliability.In the realm of intricate technical systems, such as offshore platforms, a variety of maintenance management techniques can be utilized, including reliability-centered maintenance (RCM).This method employs failure mode and effects analysis (FMEA) to evaluate the significance of potential failure modes by ranking the associated risks, especially those related to corrosion rates and the asset's remaining lifespan.Nevertheless, in some real-world situations, the conventional use of FMEA may become unfeasible due to the subjective nature involved in assessing risk factors.

As a result, this research seeks to present a more effective and practical approach for assessing the criticality of risks linked to external corrosion failures within the system. The suggested methodology incorporates fuzzy scale techniques, risk space diagrams, and weighted Euclidean distance, drawing on the expertise of specialists in external corrosion. Theoretically, this study highlights the significance of utilizing RCM for corrosion management in practical applications. From a practical perspective, the aim is to provide a tool that merges RCM with fuzzy logic and a multicriteria framework to prioritize systems for inspection. This groundbreaking FMEA model is intended to improve efficiency by reducing time and costs while minimizing fieldwork, thus enhancing quality, safety, and technical effectiveness in inspection and maintenance activities [9].

10. The 26th International Joint Conference on Industrial Engineering and Operations Management, IJCIEOM 2021.

The proceedings consist of 48 papers. This conference particularly focuses on Industrial Engineering and Operations Management. The subjects covered include: Contributions of Industry 4.0 to Sustainable Operations; fuzzy Criticality Assessment of External Corrosion Risks in the Petroleum Sector—A Case Study; Evaluation of the Coverage of Sustainability Dimensions by Maintenance Objectives and KPIs; Circular Economy and Supply Chain Management: Key Publications and Themes; Implementation Agenda for Autonomous Maintenance Utilizing the HTO Approach; Identification of Critical Risk Factors in an Effluent Drainage Network Project through AHP: A Case Study; Methodical Literature Review on Decision-Making Processes Related to Sustainability; Comparative Analysis of Business Simulation Games for Teaching Production Engineering; Descriptive Bibliometric Study on Vaccine Supply Chain Management during COVID-19; Evaluation of Circular Economy Impacts on Companies within a Brazilian Industrial Ecosystem; Analysis of Disaster Effects on Travel Movements through System Dynamics; Examination of Deprivation Costs in Humanitarian Logistics:

A Comprehensive Review; Evaluation of Universities' Strategic Commitment to the Sustainable Development Goals; Modification of the Framework for the Service Sector while Preserving Economic, Social, and Environmental Sustainability; Examination of Biosafety Protocols in Supermarkets: Insights from Customers; Development Framework for Skills Utilizing a Decision-Making Matrix: A Case Analysis; Significance of Advanced Manufacturing or Industry 4.0 Research to Technological Advancement; Assessment of CO2 Emissions in the Soil–Cement Brick Sector: An Educational Example in Southwest Paraná; Examination of Attitudes Towards Target Costing through a Teaching Case Study; Management of the Packaging Recycling Network in Brazil. [10].

11. Improving the mean time before failure (MTBF) in rod-pumped wells by analyzing corrosion barriers.

Subsurface pumps and production tubulars are essential for extracting crude oil from underground reservoirs to surface facilities in established oil and gas fields.The integrity of downhole pumps and tubulars is greatly affected by electrochemical degradation, which will be analyzed concerning the operational environment.The extent of damage to sucker rods that reach the pump in rod pump wells will be discussed.A self-enhancing corrosion management strategy is proposed through a discussion of inspection, monitoring, and mitigation techniques.The corrosion decision tree is vital for assessing corrosion failures and offers a unique method for risk evaluation.Both qualitative and quantitative assessments of the Mean Time Between Failures (MTBF) for rod-pumped wells have been performed.An action plan was formulated to tackle corrosion and/or friction-related failures.Consequently, the annual trend of workovers has shown a decline due to the implementation of the action plan.On average, oil and gas companies dedicate a specific percentage of their operational budget to address corrosion issues.Factors such as physical failure, presentation development, costs, and maintenance present considerable risks to erosion control.

Review and monitoring techniques alone are inadequate for accurately forecasting future performance. By integrating inspection, monitoring, mitigation, and predictive methodologies, a thorough corrosion management program can be developed. Following this, necessary remedial actions can be systematically executed to mitigate the effects of corrosion barriers. The Mean Time Before Failure (MTBF) can be considerably improved by following the practices specified in the action plan. For operators involved in extracting subsurface oil from difficult environments, the suggested method is to employ go-gauging and inhibitor washing for tube-shaped structures. The corrosion decision tree assesses the risks linked to corrosion, while corrosion management comprises a series of barriers aimed at preventing material failure. Performing MTBF analysis can offer operators critical insights into the reasons behind failures in subsurface pumps and downhole tubing..[11].

12. Society of Petroleum Engineers - SPE International Conference and Exhibition on Oilfield Corrosion 2021, OFCS 2021

The proceedings consist of 17 papers. The topics addressed include: the use of electrochemical noise for assessing green corrosion inhibitors; leveraging industry data to improve strategies for managing corrosion beneath insulation; the improvement of mean time before failure (MTBF) in rod-pumped wells through the examination of corrosion barriers; crevice corrosion in oxygen scavenger injection systems; discussions on the oxygen threshold level for corrosion processes in seawater injection systems; risk-based management strategies for corrosion under insulation; the dissolution of sulfate and sulfide field scales using a newly developed scale dissolver; and metrics in microbial biology to assess the effects of biocides on souring control and to enhance curdling modeling. [12].

13. Tackling the challenges related to pigging pipelines that are considered unpiggable.

Carbon steel tubes are extensively used for the transportation of hydrocarbons globally, owing to their relatively simple manufacturing process, safety in application, availability of raw materials, and cost-effectiveness. Nevertheless, in spite of these benefits, carbon steel is prone to considerable corrosion and various other complications. Pipeline corrosion presents a significant challenge in the oil and gas industry, resulting in numerous minor and major incidents of containment failure, which can lead to fatalities, environmental harm, asset loss, and production disruptions. The rising incidence of failures in operational pipelines has led the Department of Petroleum Resources (DPR) to strengthen its regulatory oversight of pipeline integrity assessments and operations in Nigeria, ensuring that Oil Producing Companies comply rigorously with regulatory standards.

According to the DPR Act (Section 2.5.2.1), all pipelines with a diameter greater than 6 inches must be inspected every five years utilizing intelligent pigs (inline inspection tools) to effectively evaluate their condition. However, numerous pipelines in Nigeria are either unpiggable or difficult to inspect with intelligent pigs due to the unavailability of pigging services (especially in brownfield areas), along with complications arising from short bend radii, dual lengths, and flow parameters. This paper provides case studies that investigate the use of advanced inline inspection methods to enable the simultaneous inspection of complex dual-diameter pipelines. [13]

14. A semi-empirical model that addresses the erosion-corrosion of carbon steel pipelines exposed to wet gas-solid flow conditions

The examination of erosion-corrosion (E-C) phenomena affecting carbon steel pipelines exposed to wet gas-solid flow is receiving considerable focus in the domain of oil and gas engineering. This research introduces a semi-empirical model designed to predict and evaluate the risks linked to the combined CO2 E-C rate under these particular circumstances. The model incorporates the changes in fluid characteristics that are affected by the system environment during gas-solid flow. By employing the Eulerian-Lagrangian method, the Navier-Stokes equations are utilized to investigate the flow field within the computational domain, while the force balance equation is applied to monitor the migration paths of solid particles within the simulation environment, ensuring a comprehensive analysis of fluid-solid interactions. An empirical model for CO2 corrosion, along with its revised version, has been created and validated, in addition to an erosion wear model, both specifically developed for carbon steel. Moreover, the synergistic impacts of these models are also considered.

The CFD-DPM technology, which utilizes the previously mentioned test data, is used to derive parameters relevant to both models. This facilitates the calculation of the overall CO2 E-C rate, the distinct erosion rate, and the separate CO2 corrosion rate at various points along the pipeline wall. Furthermore, the dominant rate is identified and analyzed, which allows for the evaluation of the severity of the combined CO2 E-C effects based on the total CO2 E-C rate. The proposed model is designed to efficiently and accurately compute the dominant rate and severity at different locations, thus identifying vulnerable areas and conditions that could potentially lead to pipeline failures. This model aims to provide theoretical insights for the prevention and management of risks related to carbon steel pipeline failures during oil and gas production and transportation, ultimately ensuring the safe and reliable achievement of established manufacturing objectives and the realization of economic benefits..[14].

15. An initial assessment of the corrosion issues faced by pipelines transporting hydrocarbons.

Pipelines are widely acknowledged as a secure and environmentally friendly, as well as economically feasible, method for the transportation of multiphase fluids of various kinds. Nevertheless, in the absence of adequate monitoring, they can present considerable risks to both health and the environment. Although progress is being made in operational and maintenance practices, new challenges continue to arise, particularly regarding the quality of the fluids being transported, with hydrocarbons being a primary concern. For example, crude oil often contains hydrogen sulfide (H2S); new pipelines are currently being developed to transport and inject supercritical fluids; and emerging corrosion issues may occur due to the—partially understood—damage mechanisms linked to biofuels, as well as from external aggressive environments such as deep seawater. Drawing on over 40 years of expertise in the field of corrosion, especially in pipeline-related projects, the author of this paper seeks to summarize the key damage mechanisms, current understanding, and potential future threats, from the viewpoint of a former Oil & Gas industry professional who is now working as a consultant in the field..[15].

16. Thorough evaluation of hybrid approaches for the suppression of gas hydrates.

In the ***subsea oil and gas sector***, shifting from a strategy that solely aims to avoid gas hydrates to one that incorporates risk-based hydrate management may result in considerable cost savings and improve the viability of new projects.A comprehensive evaluation of the probability of hydrate formation, conducted through the gathering of statistically significant data from independent hydrate formation occurrences, is crucial for accurately assessing the risk of hydrate blockages.This evaluation is especially vital when employing low-dosage kinetic hydrate inhibitors (KHIs), which affect the kinetics of hydrate formation rather than the thermodynamic stability envelopes, unlike thermodynamic hydrate inhibitors (THIs).In this regard, we introduce the use of a second-generation, Peltier-cooled, high-pressure, stirred, automated lag time apparatus (HPS-ALTA) that is specifically designed to accurately measure hydrate formation under conditions that simulate a methane-rich natural gas environment.Over 2,500 hydrate formation events were documented using a low-salt-content brine, which enabled the creation of smooth, high-resolution hydrate probability distributions in the presence of three chemical inhibitor additives and their combinations (including a corrosion inhibitor, a KHI, and a conventional THI).Furthermore, this approach not only allows for swift and accurate testing of potential interactions among inhibitors but also clearly demonstrates the ability to effectively modify the boundaries of formation likelihood through a combination of thermodynamic and kinetic inhibition effects.These hybrid inhibition strategies can result in prolonged induction times at operationally relevant formation temperatures (surpassing 2 days at 2.5 °C in this study) and may be more beneficial and/or cost-effective compared to methods focused solely on complete hydrate prevention..[16].

17. The conveyance of oil and water in segments to reduce pipeline corrosion.

A novel strategy for reducing pipeline corrosion during the transport of oil-water mixtures has been introduced, marking a departure from conventional techniques. This strategy employs a flow management concept that begins with the separation of the mixed fluids into oil and water. Following this, a batch transportation system for both oil and water is utilized to modify the water wetting condition at the pipeline's bottom. This modification significantly lowers the corrosion risk at the base of the pipe with only minimal changes to the transportation process. The theoretical and experimental validation of this approach has shown its effectiveness in reducing corrosion when compared to traditional oil gathering systems utilized in CO2-enhanced oil recovery (EOR) operations. It was noted that the effectiveness of corrosion mitigation is positively related to the dimensionless span of the oil phase, which is affected by the input lengths of the oil and water batches as well as the resulting flow pattern at the oil/water interface. This method is especially beneficial in situations where large volumes of free water cannot be integrated into the oil phase. The proposed strategy for corrosion reduction presents significant potential for use in the transportation of corrosive oil-water mixtures within the petroleum sector, including CO2-EOR and offshore oil extraction..[17].

18. Evaluation and oversight of corrosion within a shale gas collection and transportation system: A case analysis from the Changning-Weiyuan National Shale Gas Demonstration Zone

In the Changning-Weiyuan National Shale Gas Demonstration Area, situated in the southern Sichuan Basin, volumetric fracturing technology is primarily utilized for the extraction of shale gas. The amount of fracturing fluid and proppant, specifically quartz sand ceramsite, consumed per horizontal well generally falls between 40,000 to 50,000 cubic meters and 2,500 to 3,000 tons, respectively. After the fracturing process is completed, the flowback fluid from shale gas extraction can cause varying levels of corrosion in the surface drainage and gathering systems, which may lead to equipment and pipeline failures that threaten the safe operation of the production system. To improve the safety of the shale gas gathering and transportation infrastructure, an analysis was performed on the corrosion characteristics and control strategies for the gathering and transportation system in the southern Sichuan Basin.

This analysis encompassed the evaluation of the corrosion environment and production performance, the assessment of material failures, the optimization of materials, and the application of bactericides and corrosion inhibitors, in addition to the control and optimization of production parameters. This initiative was backed by the natural gas corrosion control technology platform of PetroChina Southwest Oil &Gasfield Company. The results revealed that the main types of corrosion impacting the shale gas gathering and transportation system in the southern Sichuan Basin are erosion corrosion and electrochemical corrosion.

Erosion corrosion primarily occurs during the technological processes at the shale gas station, presenting as ongoing mechanical wear induced by sand particles at bends, tee joints, valves, and other components.

Electrochemical corrosion mainly occurs in the gas gathering pipeline outside the shale gas station, defined by the combined corrosion effects of CO2 and sulfate-reducing bacteria in a liquid loading environment.Effective management of erosion corrosion can be accomplished by improving desanding efficiency and refining process design.Likewise, electrochemical corrosion can be effectively controlled through the application of bactericides and erosion inhibitors, in addition to implementing supportive production management strategies.It is crucial to take into account corrosion evaluation and the redesign of the shale gas gathering and transport system during the initial design phase.[18].

19. An extensive examination of permeation damage in polymer liners utilized in oil and gas pipelines

Non-metallic pipe (NMP) resources function as both internal coatings and standalone piping solutions in the oil and gas industry, representing an innovative strategy for managing erosion.These NMP materials are naturally susceptible to gradual degradation due to factors including creep, fatigue, permeation, manufacturing flaws, and installation mistakes.

When subjected to acid gases (CO2, H2S) and hydrocarbons under high pressures and temperatures, the primary type of damage occurs due to infusion.

The comprehension of potential damage from permeation is still insufficiently defined, posing difficulties in managing asset integrity.

At present, the assessment of permeation damage is performed through a variety of evaluations of mechanical, thermal, chemical, and structural properties, employing techniques such as Tensile Testing, Differential Scanning Calorimetry (DSC), Fourier-transform Infrared Spectroscopy (FTIR), and Scanning Electron Microscopy (SEM)/Transmission Electron Microscopy (TEM) to examine alterations in tensile strength, elongation, weight changes, crystallinity, chemical properties, and molecular structure.Typically, coupons are utilized to study the degradation of polymers; however, they operate as separate devices and do not yield real-time data.Their weight and mechanical characteristics are evaluated for assessment.

Since polymers are dielectric materials, their dielectric properties can be analyzed using Impedance Analyzers and Dielectric Spectroscopy.This review presents a succinct summary of the challenges associated with the failure of polymer liners in pipelines, which is linked to the presence of acid gases, hydrocarbons, and various contaminants. The discussion includes permeation, examples of liner failures, the current status of monitoring practices, and the introduction of new exclusive dielectric properties. A thorough perspective is offered, emphasizing the difficulties related to monitoring the polymer liner material within the pipeline, especially concerning the requirements for lifetime prediction..[19].

20. Developments in the Progress of Safety Technologies for Oil Storage Tanks.

Petroleum is a vital element of the national economy and serves as an essential strategic resource for the country's survival and growth. At present, tank storage is the primary method utilized for the storage of raw materials and products in the petroleum and petrochemical industries. As a result, the operation, maintenance, and anti-corrosion strategies for storage tanks are crucial for ensuring industrial safety throughout the entire sector. This paper evaluates the latest advancements in tank anti-corrosion technology within the petrochemical industry, investigates the challenges associated with both internal and external corrosion of tanks, outlines various anti-corrosion approaches, highlights the significance of tank anti-corrosion protection, and anticipates future trends in this area. Petroleum acts as the driving force behind modern industry and plays a significant role in national security. The adoption of effective anti-corrosion measures for storage tanks is especially critical for the strategic management of oil reserves in China..[20].

21. Forecasting the internal corrosion rate of gas pipelines: A novel approach utilizing transformer architecture

The precise evaluation of internal corrosion rates in steel natural gas pipelines is an essential aspect of managing the integrity of oil and gas pipelines. Nevertheless, the current models employed for forecasting internal corrosion rates frequently encounter several challenges, including low accuracy, inadequate generalization, and insufficient interpretability. To effectively tackle these issues, we introduce CNN-BO-Transformer and utilize DeepSHAP to enhance the model's interpretability. The CNN-BO-Transformer is designed to predict the corrosion rate in natural gas pipelines, while DeepSHAP is applied to examine the causal relationships between input variables and the model's predictions. The proposed model is validated using a real pipeline excavation dataset sourced from a gas field in Northwest China, achieving an average error of 0.21mm/y. This indicates reductions of 69.74% and 66.67% compared to the errors associated with support vector regression (SVR) and the Transformer model, respectively. The suggested method significantly enhances the accuracy and reliability of corrosion rate predictions in natural gas gathering and transportation pipelines, thereby offering an effective strategy for predictive maintenance and repair of steel gathering in transmission pipelines within gas fields [21].

22.A Bayesian methodology that incorporates real-time monitoring data to estimate the dynamic Remaining Useful Life (RUL) of equipment impacted by sulfidation and corrosion from naphthenic acids.

Corrosion caused by sulfidation and naphthenic acids is a prevalent mechanism in the processing of crude oils that contain high levels of sulphur. This study highlights the necessity for dependable corrosion management strategies within the chemical industry, particularly in the context of energy transition and the simultaneous impact of emerging scenarios such as economic and geopolitical factors. The aim is to create a dynamic model that estimates the remaining lifespan of equipment by utilizing predictive modeling techniques alongside monitoring data of process variables that affect the deterioration mechanism. The model developed will aid in preventing adverse outcomes resulting from equipment degradation and will enhance the optimization of inspection and maintenance programs. By providing an innovative tool for corrosion management, this research seeks to contribute to ongoing initiatives aimed at improving the efficiency and sustainability of energy production processes. Given the emergence of certain scenarios, refineries may be inclined to increase the processing of raw materials with high sulphur content; these materials are more readily available and cost-effective, yet they accelerate the deterioration of equipment materials, thereby heightening the associated risks. The method proposed in this article facilitates more effective safety management through the monitoring of the conditions of critical components [22].

23.The co-gasification of blast furnace dust with petroleum coke for sustainable waste management.

This research utilized a lab-scale fluidized bed steam gasification system to conduct co-gasification experiments involving blast furnace dust (BFD) and petcoke (PC), which are by-products from the steel and refining sectors, respectively.A series of experiments were carried out under optimized conditions to analyze the influence of the mineralogical composition of the feed samples on the parameters of gasification performance. The introduction of the iron and zinc-rich BFD sample into the PC resulted in a significant improvement in the gasifier's capacity to generate hydrogen-rich synthesis gas, which was linked to an increase in the number of surface active sites that enhance gasification reactivity.

The catalytic influence of the iron and zinc-containing components in the resultant ash led to an increase of nearly 3% in cold gas efficiency and approximately 12% in carbon conversion efficiency, which in turn contributed to a notable rise in both the heating values and the yields of the product gas.

To understand the catalytic effect, the feed and product samples were analyzed using analytical techniques including XRF, XRD, TGA, FTIR, and SEM with EDX analysis. The co-gasification product ash sample revealed the presence of various minerals dominated by zinc and iron, such as franklinite ($ZnFe2O4$), zincite (ZnO), hematite ($Fe2O3$), and magnetite ($Fe3O4$), to meet the increasing global mineral demands as a secondary mineral resource. This study presented an innovative approach to repurpose industrial waste while simultaneously eliminating toxic substrates. In summary, the potential for energy recovery from industrial by-products was emphasized, offering valuable insights for the development of sustainable waste management technologies with scalable opportunities within a circular industrial economy [23].

24.The engineering design and implementation of a large-scale project for the treatment of oil-based drilling cuttings.

Thermal phase separation technology represents an innovative and comprehensive treatment method that involves heating oil-based cuttings to a specific temperature to vaporize both oil and water components.This analysis is based on a significant project focused on the comprehensive utilization of oil-based drilling cuttings, examining the engineering design and the effectiveness of thermal phase separation technology in practice.

Results indicate that this technology can lower the oil content of the purified residue to between 0.1% and 0.2%, achieving an average base oil recovery rate of 94.12%, with an annual recovery of approximately 4800 tons of base oil. Furthermore, the purified residue is free from corrosive, leaching toxicity, and other hazardous characteristics, making it suitable for use in the production of bricks or building materials.Overall, thermal phase separation technology is a highly effective treatment and utilization method that offers significant engineering and environmental advantages, demonstrating considerable potential for widespread application[24].

25. A thorough review of polymeric anti-corrosion coatings integrated with fluorescent materials

Corrosion has a profound effect on metallic structures, leading to significant safety risks and financial losses. The catastrophic incidents resulting from unnoticed corrosion, including the 2013 oil pipeline explosion in Qingdao, China, and the 2014 explosion in Kaohsiung, Taiwan, underscore the critical need for effective detection methods. Worldwide, the financial burden of corrosion surpasses $4 trillion each year—accounting for 6% of the global GDP—divided between maintenance expenditures and losses due to damage.

Identifying early-stage corrosion is essential yet difficult with traditional techniques. Recently, fluorescent material-based polymeric coatings have emerged as a groundbreaking solution for the early detection of corrosion. These advanced coatings utilize fluorescence-based indicators that respond to corrosion byproducts, such as metal ions or acidic compounds, by changing their fluorescence characteristics. This innovation offers a real-time, non-invasive approach to monitor the integrity of metals, facilitating timely interventions and lowering maintenance expenses.This review explores the mechanisms involved in fluorescence-based corrosion detection, focusing specifically on the types of fluorescent indicators utilized, their incorporation into polymeric matrices, and the analytical techniques employed for fluorescence monitoring.These coatings provide considerable advantages, such as ongoing monitoring and early detection of corrosion, which helps to avert damage in advanced stages. Nonetheless, challenges persist in optimizing these systems for various environments and enhancing their sensitivity and durability.

Nevertheless, progress in this domain holds the potential for substantial benefits for industries that depend on metal infrastructure. The future is oriented towards the integration of these coatings with real-time monitoring systems, utilizing predictive analytics and fostering collaboration between industry and academia. Such advancements are set to transform corrosion management, rendering it more proactive, cost-efficient, and standardized [25].

CONCLUDING REMARKS

- Corrosion represents the foremost threat to integrity in oil and gas pressure containment and processing facilities.
- Effectively managing corrosion serves as the foundation for integrity management, and establishing a corrosion management strategy is crucial for fulfilling the requirements of a corrosion management policy.
- Additionally, corrosion is the primary risk factor driving Risk Based Inspection (RBI) activities; it is the essential mechanism through which the inspection strategy, vital for maintaining integrity, is implemented.

- Several methods have been examined to evaluate and manage the integrity of assets, including topside facilities, processing plants, utilities, marine terminals, tank farms, pipelines, and more.
- We have to assess qualitative, semi-qualitative, and quantitative risk assessment methodologies.
- Risk assessment is a key criterion for optimizing RBI.
- We have to explore how different risk assessment approaches affect the resulting risk and the implications for integrity management.
- Furthermore, we have toanalyze the influence of risk assessment on the Asset Integrity Management (AIM) strategy and reference software developed by WGK(Wood Group Kenny), highlighting how its application can lead to the safe and cost-effective operation and management of oil and gas facilities.
- RBI has progressed into a sophisticated approach for optimizing inspection processes and frequencies to achieve cost-effective AIM.
- The design of RBI integrates multi-disciplinary expertise and considers conditional factors, variations in operating conditions, asset operation and maintenance, asset criticality, data interpretation, and condition forecasting.

Acknowledgement

The authors express their gratitude to MahalakshmiMuthukumar, GayathriNandha Kumar, JameenaafrinAkbarAli, NagaatchayaGaneshavenkatasubramanian, and Suga Priya Jaisankar for their assistance and support.

REFERENCES

[1] S.Arena, R.Perna, M.T.Pilloni (2022) A quantitative risk-based approach for assessing optimal inspection intervals of a caustic soda recovery plant: a case study, Proceedings of the Summer School Francesco Turco.

[2] X.Li, L.Zhang, F.Khan, Z.Han(2021) A data-driven corrosion prediction model to support digitization of subsea operationsProcess Safety and Environmental Protection, 153, 413–421.https://doi.org/10.1016/j.psep.2021.07.031

[3] M.Nabizadeh,M.Khalilzadeh,S.Ebrahimnejad,M.J.Ershadi(2021) Developing a fuzzy goal programming model for health, safety and environment risks based on hybrid fuzzy FMEA-VIKOR method. Journalof Engineering, Design and Technology, 19(2), 317–338.
http://dx.doi.org/10.1108/JEDT-09-2019-0245

[4] A -W. Dawuda, M.Taleb-berrouane, F. Khan (2021) A probabilistic model to estimate microbiologically influenced corrosion rate Process Safety and Environmental Protection, 148, 908–926,2021.
https://doi.org/10.1016/j.psep.2021.02.006

[5] Z.Wan, J. Yang (2021) Research on corrosion management technology of petroleum pipeline and pressure vessel IOP Conference Series: Earth and Environmental Science, 692(4), 042057.
http://dx.doi.org/10.1088/1755-1315/692/4/042057

[6] C., Jain, S., Obaid, S., Nakeeb, F.A. (2021) Generating Value from Mature Gas Fields by Quantifying Well Integrity Assurance with a Critical Analysis of Multiple Logs & Retrieved Tubular Surface Inspection Golaco, Society of Petroleum Engineers - Abu Dhabi International Petroleum Exhibition and Conference, ADIP 2021.
http://dx.doi.org/10.2118/208204-MS

[7] R.N. Burke, A.M.A.R.AlTamimi, W.S. Al Shouly,D.E.Baetsen(2021) Non-Metallic Technology Deployment for the Next Generation of ADNOC Production Facilities.Society of Petroleum Engineers-Abu Dhabi International Petroleum Exhibition and Conference, ADIP 2021.
https://doi.org/10.2118/207830-MS

[8] A. Imane, C. Samia, H. Djamel(2021) Assessment of an Accidental Liquified Petroleum Gas Release at a Petrochemical Site: a Case Study Proceedings of the International Conference on Industrial Engineering and Operations Management, 113.
http://dx.doi.org/10.46254/AP01.20210071

[9] R. Caiado,M. Rios, G.C. Martins, P.IvsonNetto, F.RamosElmas(2021) Fuzzy Criticality Assessment of Systems External Corrosion Risks in the Petroleum Industry—A Case Study F.,Springer Proceedings in Mathematics and Statistics, 367, 153–166.
http://dx.doi.org/10.1007/978-3-030-78570-3_12

[10] A.M.T.Thome, R.G.Barbastefeno, L.F.Scavarda,J.C.G.D.Reis, M.P.C.Amorim (2021) 26th International Joint Conference on Industrial Engineering and Operations Management, IJCIEOM 2021, Springer Proceedings in Mathematics and Statistics, 367.

[11] K.L.Chanchlani, N.Khanduja, D.Gunwant (2021) Improving mean time before failure MTBF in rod pumped wells by analyzing corrosion barriersSociety of Petroleum Engineers - SPE International Oilfield Corrosion Conference and Exhibition 2021, OFCS 2021.
http://dx.doi.org/10.2118/205043-MS

[12] (2021) Society of Petroleum Engineers - SPE International Oilfield Corrosion Conference and Exhibition 2021, OFCS 2021 [No Authors Found]

[13] C.Oragwu, D.Molyneux, L.Lawal, S.Ameh (2021) Overcoming challenges of pigging the unpiggable pipelines Oragwu, Society of Petroleum Engineers - SPE Nigeria Annual International Conference and Exhibition 2021, NAIC 2021.
http://dx.doi.org/10.2118/207147-MS

[14] L.Zhao, Y.Yan, X.Yan (2020) A semi-empirical model for CO2 erosion-corrosion of carbon steel pipelines in wet gas-solid flow, Journal of Petroleum Science and Engineering, 196, 107992.
https://doi.org/10.1016/j.petrol.2020.107992

[15] G.Gabetta (2024) A tentative summary of corrosion issues in pipelines transporting hydrocarbons Lecture Notes in Civil Engineering, 102, 77–87.
http://dx.doi.org/10.1007/978-3-030-58073-5_6

[16] P.J.Metaxas, V.W.S.Lim, S.F.McKay,Z.M.Aman, E.F.May (2020)High-fidelity evaluation of hybrid gas hydrate inhibition strategies Metaxas, Energy and Fuels, 34(12), 15983–15989.
http://dx.doi.org/10.1021/acs.energyfuels.0c02803

[17] K.Wang, Z.M. Wang, G-L Song(2020)Batch transportation of oil and water for reducing pipeline corrosion Journal of Petroleum Science and Engineering, 195, 107583.
http://dx.doi.org/10.1016/j.petrol.2020.107583

[18] M.Xie, Y. Tang, B.Song, W.Zhao, G.Wu (2022) Corrosion evaluation and control of a shale gas gathering and transportation system: A case study of the Changning-Weiyuan National Shale Gas Demonstration Area | Natural Gas Industry, 40(11), 127–134.
http://dx.doi.org/10.1088/1742-6596/2539/1/012039

[19] H.U.Khalid, M.C.Ismail, N.Nosbi (2020) Permeation damage of polymer liner in oil and gas pipelines: A review Polymers, 12(10), 1–31, 2307.
https://doi.org/10.3390/polym12102307

[20] M-Y.Dou, X-H. Liao, S.-J .Yang, S.Zou, F.-C.Huang (2020) Development trend of protection technology for oil storage tank IOP Conference Series: Earth and Environmental Science, 526(1),012117.
http://dx.doi.org/10.1088/1755-1315/526/1/012117

[21] L.Tan, Y. Yang, K. Zhang, K.Liao, G.He, J.Tian, X. Lu (2025) Prediction of internal corrosion rate for gas pipeline: A new method based on transformer architecture,Computers and Chemical Engineering, 198, 109084.
https://doi.org/10.1016/j.compchemeng.2025.109084

[22] G.Ancione, P. Bragatto, M.F. Milazzo (2025)A Bayesian approach integrating real-time monitoring data for the estimation of a dynamic RUL of equipment affected by sulfidation and naphthenic acids corrosion,Journal of Loss Prevention in the Process Industries, 95, 105582.
https://doi.org/10.1016/j.jlp.2025.105582

[23] R.Saini, D.S.Rao, S.D.Barma (2025)Co-gasification of blast furnace dust with petcoke for sustainable waste management,Waste Management, 193, 506–516.https://doi.org/10.1016/j.wasman.2024.12.027

[24] Y.Zhou, C. Deng, X. Chen, X, Y.He, G.Fang, Z.Jin, Y. Liu(2025)Engineering design and application of large-scale oil-based drilling cuttings treatment project, Waste Management and Research, 43(2),282–292.
http://dx.doi.org/10.1177/0734242X241231393

[25] S.Arshad, S.Habib, R.A.Shakoor(2025)Fluorescent material-integrated polymeric anti-corrosion coating: A comprehensive review,Journal of Industrial and Engineering Chemistry,
https://doi.org/10.1016/j.jiec.2025.02.056

IZVOD

UPRAVLJANJE KOROZIJOM U NAFTNOJ INDUSTRIJI

Svet brzo napreduje ka razvoju održive infrastrukture, naglašavajući upotrebu materijala otpornih na koroziju kako bi se efikasno optimizovala kontrola korozije i smanjili troškovi životnog ciklusa. Rešavanje problema kontrole i ublažavanja korozije tokom početnih faza projektovanja i izgradnje imovine pokazalo se korisnijim na duži rok, posebno u pogledu poboljšane bezbednosti, performansi, dugovečnosti imovine, zaštite životne sredine i operativne isplativosti. Ukupno, procenjuje se da globalni troškovi koji se pripisuju koroziji dostižu trilione. Generalno, smatra se da korozija utiče na približno 4 procenta BDP-a nacije, a kontinuirano rastuća pretnja po životnu sredinu zahteva hitne i odgovarajuće akcije. Ovaj članak će se fokusirati na različite vrste „korozije i njene prevencije u naftnoj i gasnoj industriji" koje utiču na opremu, cevovode i infrastrukturu u naftnom i gasnom sektoru, zajedno sa strategijama za ublažavanje ovih problema. Korozija predstavlja značajan izazov u industriji, što rezultira bezbednosnim rizicima, prekidima u radu i značajnim finansijskim gubicima. Ovaj članak će se baviti sledećim osnovnim temama: Vrste korozije u naftnoj i gasnoj industriji, Uticaj korozije na naftnu i gasnu industriju, Praćenje i otkrivanje korozije, Metode sprečavanja korozije, Najbolje prakse u upravljanju korozijom, Studije slučaja i industrijski standardi i Budući trendovi u sprečavanju korozije.

Ključne reči: *korozija, upravljanje, naftna i gasna industrija, naftna industrija, korozija cevovoda*

Pregledni rad
Rad primljen: 22.02.2025.
Rad korigovan: 01.06.2025.
Rad prihvaćen: 04.06.2025.

Susai Rajendran https://orcid.org/0000-0002-0040-2435

Chandra Kant Bhardwaj[1], Sana Rafi[2],*
AbhilashaMishra[3], Nouman[4]

[1]Department of Chemistry, Graphic Era Hill University, Dehradun, Uttarakhand, India, [2]Department of Geography, School of Earth Sciences,HemwatiNandanBahugunaGarhwal University, S.R.T Campus, Tehri, India, [3]Department of Chemistry, Graphic Era (Deemed to be University), Dehradun, Uttarakhand, India, [4]Molecular and Biophysical lab, Department of Chemistry, Jamia Milia Islamia, New Delhi,India

Scientific paper
ISSN 0351-9465, E-ISSN 2466-2585
https://doi.org/10.62638/ZasMat1087

Zastita Materijala 67 (1)
112 - 118 (2026)

Synthesis, characterization, chromatographic and antimicrobial studies of transition metal complexes of cobalt(II) and iron(III)

ABSTRACT

Metal complexesCobalt(II) and iron(III) were synthesized by reacting metal nitrate with alprazolam. During this study,The elemental analyses of complexes confine to the stoichiometry of the type[(L)M(NO_3)$_2$], [(L)M(NO_3)$_3$]where M= Cobalt(II) and Iron(III) and L= alprazolam.Alprazolam's IR bands shift to confirm metal ion coordination. Complexes of metal ions were found to be bidentate and tridentate with"N(1) and N(4)"positions on the ligand.This study examined alprazolam and its complexes for their antimicrobial properties against selected bacteria and fungi. StreptomycinandNyastatin were used as standard drugs for antimicrobial and antifungal studies, respectively. These complexes are bioactiveas the complexes of Iron(III) and Cobalt(II) ions of alprazolam are more effective against selected bacterial and fungal species than the drug Alprazolam. The increased chelating tendency of metal complexes results in enhanced activity and these inhibits more of bacterial and fungal growth than ligand alprazolam.

Keywords:*-Metal complexes, infra-red, alprazolam, and antimicrobialandbioactive*

1. INTRODUCTION

Alprazolam (APZ) belongs to the benzodiazepine andtranquilizerdrugs family. It is a hypnotic drug,anxiety disorders are treated with this medication[1].Benzodiazepines are drugs derived from diazepam and benzene.It has been reported that 1,4-benzodiazepine complexes with transition metal ions possess anticancer and biological properties [2-4]. Complexes of benzodiazepine drugsshowed higherantimicrobial activity as compared to free ligands [5]. It is imperative that during complex formation the ligand molecule occupies all coordination sites of the metal ion, with the solvent molecule occupying vacant sites[6].Alprazolam complexes are more active than their ligands. The complexes of the benzodiazepine drug nitrazepam etc. in which the ligand acts as an anion were reported [7].APZ used as a ligand in this study, has the following structure(**Fig. 1**).

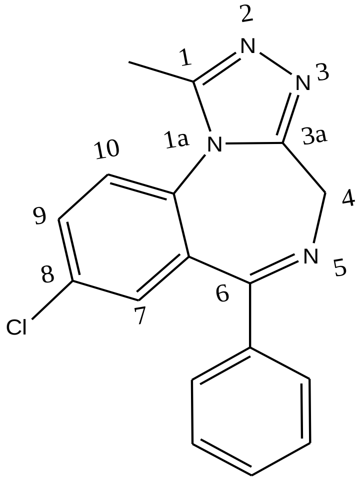

Figure 1. Alprazolam (APZ)

This study examines, the synthesis and characterization of Cobalt and Iron complexes based on elemental analysis and spectral analysis and chromatographic study.The coordination of Iron and Cobalt(II) with Alprazolam and these complexes showed improved antimicrobial activity in this study.The formation of alprazolam complexes influences its pharmacological effects by modifying drug release kinetics and receptor binding affinity. The complexation of drugs with

---

*Correspondig author: Chandra Kant Bhardwaj
E-mail: drckb2012@gmail.com

Paper received: 28.02.2025.
Paper corrected: 15.03.2025.
Paper accepted: 22.04.2025.

polymeric carriers can facilitate controlled drug release, minimizing the side effects of sedation and dependence[8].The antimicrobial activities of complexes of Iron (III) and Cobalt(II)are reported in the reviewed literature [9]. The antimicrobial study explains the application of metal complexes.

2. EXPERIMENTAL

Analytical reagents (E. Merck) are used in experimental analysis.A stock solution of [$Co(NO_3)_2.6H_2O$] and [$Fe(NO_3)_3.9H_2O$]in double distilled water and these solutions were standardized by using standard methods [10].A solution of cobalt nitrate and iron nitrate was treated with nitric acid to assess hydrolysis.In ethanol, alprazolam ligand solution was prepared. An equimolar amount of drug alprazolam and metal nitrates of [$Co(NO_3)_2.6H_2O$]and[$Fe(NO_3)_2.9H_2O$] were mixed in 1:1 ratio then precipitation took place which confirms the complex formation.In order to remove soluble impurities from complexes, the precipitate was washed with hot water and then washed with C_2H_5OH.By using Job's method[10], the stoichiometry of metal and ligand was determined, which is also confirmed by the elemental analysis and the results of experimental and calculated values were approximately the same which are listed in(Table 2).A gravimetric method is used in elemental analysis of metal complexes to determine chlorine content.

The precipitate of metal complexes was dried in an oven at about 100^0C and stored in desiccators.The purityof metal complexes was checked by TLC[11] by calculating the Rf factor. Rf values are listed in(Table1).

Table 1. Retention factor (Rf) values of different complexes

Solvent	Complex of metal ions	Retention factor value	Sample Impurities
Ethanol:Benzene 80:20	Cobalt(II)-APZ complexes	0.73	Invisible
	Iron(III) – APZ complexes	0.78	Invisible

The Rf values of both Cobalt(II) and iron(III)complexes are 0.73 and 0.78 respectively. Present results confirm no impurities in the sample of metal complexes.

2.1. Antimicrobial study

The antimicrobial activity of the ligand APZ and its complexes have been carried out against some selected bacterial species and antifungal activity against selected fungal species by using the "Filter paper disc method andbroth serial dilution method" [12]. To obtain 1000 ppm solution, a calculated amount of DMF (dimethylformamide) 0.5 ml was dissolved with sterilized distilled water and added to the metal complexes of alprazolam. A stock solution of different concentrations (250 ppm, 500 ppm, 1000 ppm) was prepared by further dilution.These solutions are named stock solutions. Some standard antibacterial and antifungal drugs were used for comparisonand verification of the activity of compounds.

2.2. Infra-red and Elemental Analysis

IR spectra of the APZ and their complexes in the KBr matrix were recorded on Perkin –Elmer 842- IR spectrophotometer. C, H, and N were estimated by using an elemental analyzer at CDRI, Lucknow.

3. RESULT AND DISCUSSIONS

Alprazolam ligand molar formula is $C_{16}H_{11}ClN_4$, and its complexes with Fe(III) and Co(II) is [$(C_{16}H_{11}ClN_4)Fe(NO_3)_3$] and [$(C_{16}H_{11}ClN_4)Co(NO_3)_2$] as explained in (table 2).Various types of elements, such as carbon, hydrogen, and nitrogen, were analyzed to determine) and Iron(III).A Coblt(II) complex has a molar mass of 491.73 and iron(III) complex has a molar mass of 550.64.Quantitative yields of complexes were obtained are colored and stable at room temperature. They are both stable and non-hygroscopic.

Table 2. Elemental and physical data of ligand and their complexes

Compounds	Molecular Mass	Analysis of elements found [calculated]%					Colour	M.P.
		Carbon	Hydrogen	Nitrogen	Chlorine	Metal(M)		
[$C_{17}H_{13}ClN_4$]	308.8	[66.06] 67.02	[4.21] 3.50	[18.13] 19.50	[11.5] 10.20	--	White	228.5
APZ $Fe(NO_3)_3$	550.64	[37.05] 38.15	[2.36] 1.43	[17.79] 18.16	(6.45] 7.23	[10.14] 11.12	Brick Red	327
APZ $Co(NO_3)_2$	491.73	[41.49] 40.12	[2.64] 2.18	[17.08] 16.52	[7.21] 6.98	[11.98] 10.50	Brown	345

Table 3. The IR frequencies of ligand and their complexes

Compounds	$\upsilon(>C=N)$	$\upsilon\left({}^{\backslash\backslash}_{/}C{-}N{-}\right)$	$\upsilon(C_6H_5)$	$\upsilon(Cl)$	$\upsilon(>CH_2)$	$\upsilon(CH_3)$	$\upsilon(M\text{-}N)$	$\upsilon(NO_3)$	$\upsilon(H_2O)$
Alprazolam(APZ)	1628	1280	1600	740	2960	1355	-	-	-
Fe-APZ Complex	1615	1259	1611	756	2962	1353	500 and 490	1370, 920 and 860	-
Co-APZ Complex	1614	1264	1608	760	2965	1360	493 and 341	1371 and 891	-

Table 3 shows a band of ligands at 1628 cm-1 which was shifting to 1614and 1615 cm^{-1} in Cobalt(II) and iron(III) complexes, respectively. A stretching vibration is observed in the double bond between carbon and nitrogen in the IR region, between 1610 and 1640 cm-1. In the present research paper, the band observed at 1628 cm ¹ in infrared (IR) spectroscopyis characteristic of the C=N stretching vibration in azomethine compounds. This represents that the "azomethine nitrogen" N(5) atom of the benzodiazepine ring is coordinated with the metal ion in complexes.

The complexes of Cobaltand Iron ions exhibit vibration modes:

$$\left[\upsilon\left({}^{\backslash\backslash}_{/}C{-}N{-}\right)\right]$$

at 1264 and 1259 cm^{-1}, respectively, showing lower shifting than ligand [1280 cm^{-1}],this shows that Nitrogen (1a) contributes to the formation of complexes.The IR spectrumof alprazolam shows the bands associated with the vibrationalmode "$\upsilon(-C_6H_5)$, $\upsilon(-Cl)$, $\upsilon(CH_2)$, $\upsilon(CH_3)$ "appear at 1600, 740, 2960, 1355 cm^{-1}as a result, complex formation has shown small positive shifts. In the Cobalt(II) complex, bands at 493 and 341 cm^{-1}andin the iron(III) complex, 500and 490 cm^{-1}, suggest a (M-N) linkage [13]. There are strong bands at 1371 $cm^{-1}$and 891 cm^{-1} inthe cobalt(II) complex and1370, 920, and 860 cm^{-1} inIron(III) complex, suggesting the presence of monodentate nitrate groups in existing complexes [14].Finally, infrared studies support the formation of complexes between alprazolam ligands and Iron(III) and Cobalt(II) metal ions. Fig. 3, 4and**5** show the IR spectra of APZ andcomplexes. APZ and complexes can be summarized as followsin Fig. 2,3,4,5, 6,7 and 8.

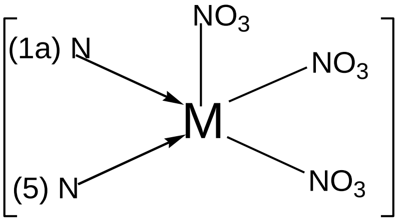

Figure 2. Metal complex (trivalent), M= Iron

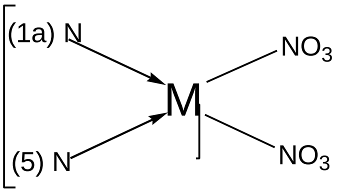

Figure 3. Metal complex (bivalent), M= Cobalt

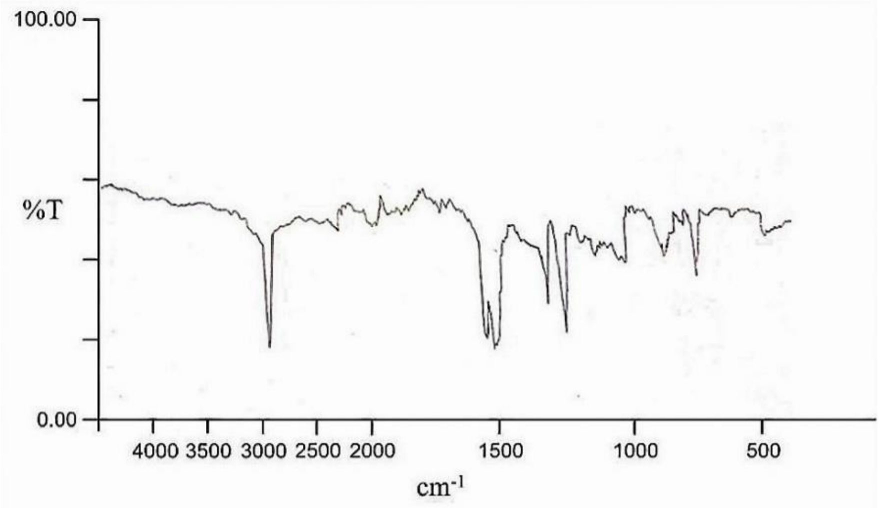

Figure 4. Infra-red spectrum of APZ

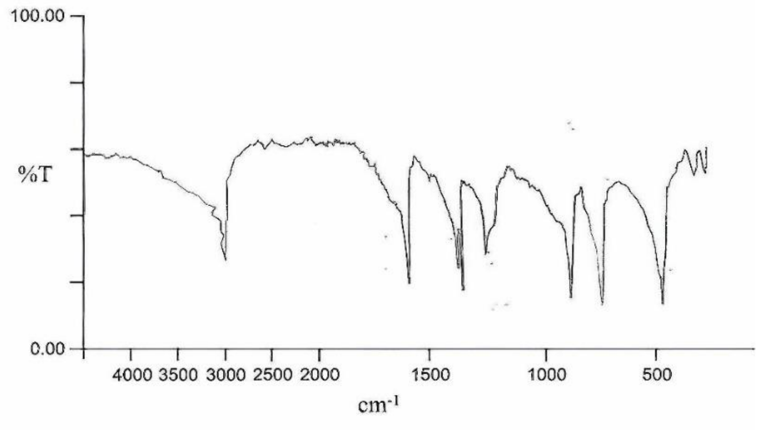

Figure 5. Infra-red spectrum of Cobalt(II) complex

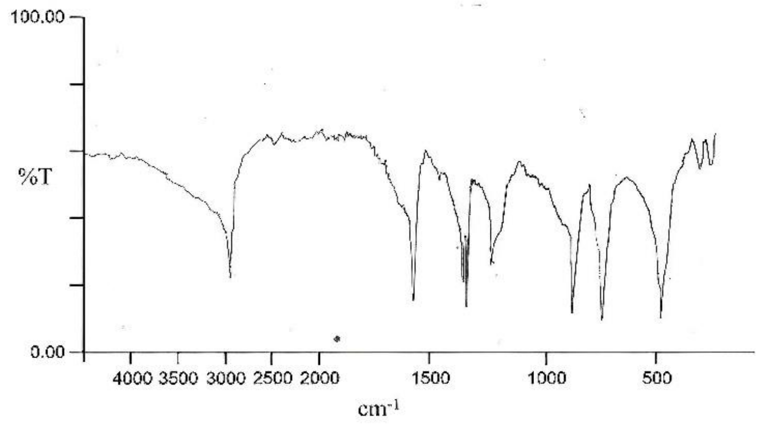

Figure 6.Infra-red spectrum of Iron (III) complex

It is evident from the results that the antimicrobial and antifungal activity of APZ complexes is higher than the ligand alprazolam and activity enhancement can be explained by chelation theory. However, it is known that chelating tends to make the Schiff base act as a more powerful and effective antibacterial agent, therefore inhibiting the growth of bacteria and fungi more than the original APZ ligand. This research confirms that the complexes of alprazolam showed much activity at a lower concentration and selected microbial species have been placed for incubation at 24±1^{0}C for 20 hours. Experimental results of antimicrobial studies are represented in table no. 4.

3.1. Antimicrobial studies of ligand and complexes

Antimicrobial activity of Cobalt and Iron complexes, metallic nitrates and used ligand were conducted on fungal species and bacterial speciesin this study[15-19]. Selected species of fungi-"*Fusarium species, A. flavous, A. niger, P. triticena*" and bacteria are "*S. aureus, S. typhi, B. subtilis, E. coli*". The percentage inhibition was calculated by measuring the diameter of the microbial colony in the control plate and test plate by using the formula *%inhibition = " [(C-T)/ C] X 100]"* C is the diameter of the microbial colony in the control plate in mm and T is the diameter of the microbial colony in the treated (test) plate. *Streptomycin*and*Nyastatin*were used as standard drugs for antimicrobial and antifungal studies respectively for comparison under similar conditions.

The results of the present antimicrobial study were presented as a (Table 4) which indicated that the inhibited zone at 500 ppm showed the best results. Comparative studies were conducted using standard drugs with metal complexes. According to the results of table no. 4, the complexes of Iron(III) and Cobalt(II) ions of alprazolam are more effective against selected bacterial and fungal species than the drug Alprazolam itself. In **Fig. 7** and **8** the Graphs are plotted between the percentage zone of inhibition and compounds used in antimicrobial studies at 500 ppm. In graph 7, the zone of inhibition against bacteria is plotted; in graph 8, the zone of inhibition against fungi is plotted. Metal complexes inhibit bacterial and fungal growth much more than the ligand alprazolam, which is shown in graphs 7 and 8.The increased chelating tendency of metal complexes results in enhanced activity andthis fact has been proven by many researchers[20-21].As a result of the chelating tendency of metal complexes, complexes are stronger inhibitors of bacteria and fungi than APZ. Metal complexes are more active due to their increased chelating tendency and lipo-soluble nature [22-23].When chelation occurs, the metal ion's polarity significantly decreases due to the interaction between its positive charge and the donor groups of the ligand. This interaction involves orbital overlap and partial charge sharing. Additionally, chelation increases the delocalization of π-electrons across the entire chelate ring, which in turn enhances the complex's lipophilicity.The higher lipophilicity allows the complexes to penetrate lipid membranes more effectively, preventing metals from binding to key enzyme sites in microorganisms[24].These metal complexes interfere with the cellular respiration process, preventing protein synthesis and ultimately inhibiting the organism's growth [25].

Table 4. Results of antimicrobial activity of APZ and complexes

Compounds	Zone of Inhibition against bacteria (mm).				Zone of inhibition against fungi (mm).			
Alprazolam (APZ)	-	-	-	-	-	-	-	-
Fe(NO$_3$)$_3$	-	-	-	-	-	-	-	-
Co(NO$_3$)$_2$	-	-	-	-	-	-	-	-
DMF	-	-	-	-	-	-	-	-
Fe APZ(NO$_3$)$_3$	27.55	33.00	34.50	37.55	34.00	39.17	35.00	35.10
Co APZ(NO$_3$)$_2$	28.57	34.50	35.44	39.00	35.56	39.87	39.14	35.56
Streptomycin	31.00	35.00	37.00	36.00	-	-	-	-
Nyastatin	-	-	-	-	35.00	41.00	42.00	37.00

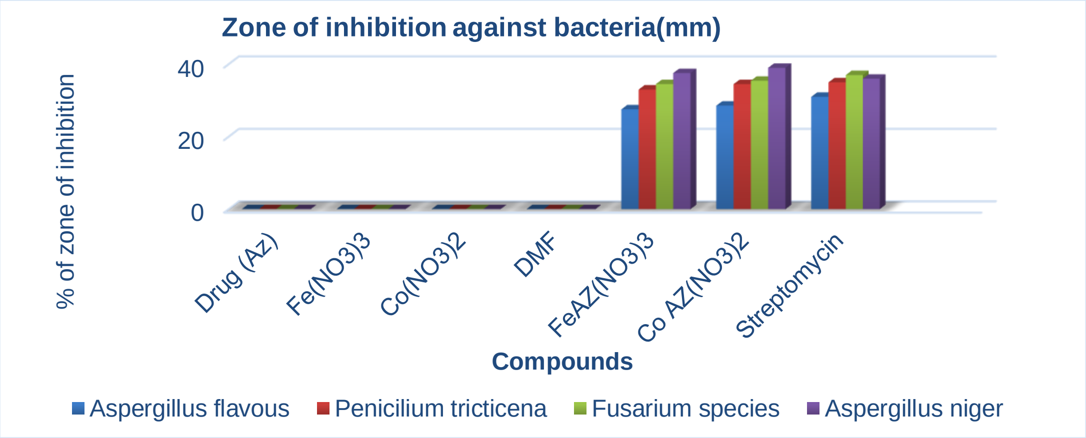

Figure 7. Zone of inhibition against bacteria(mm)

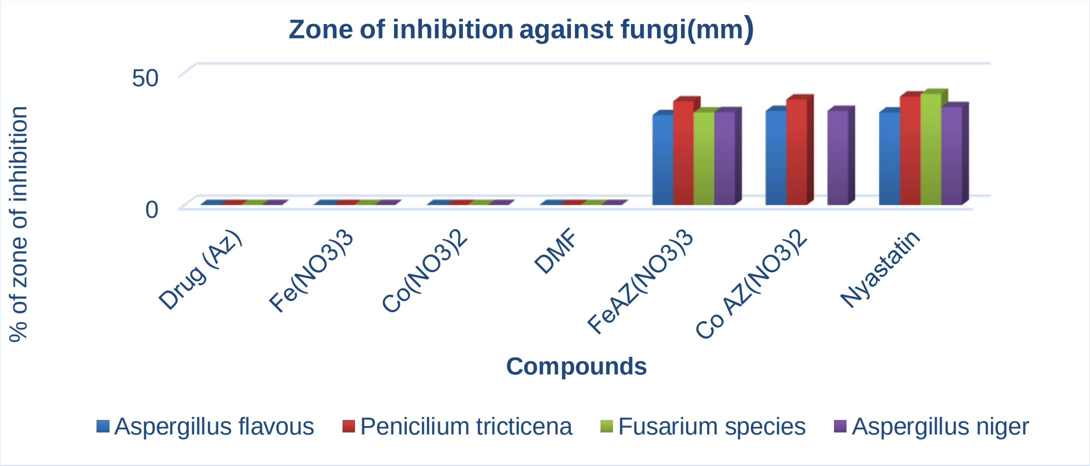

Figure 8. Zone of inhibition against fungi(mm)

4. CONCLUSION

In this study, iron(III) and Cobalt(II) complexes with alprazolam ligand were synthesized, IR studies, chromatographic as well as antibacterial and antifungal studies.By elemental analysis, the molecular weights, molecular formulae, and melting points of complexes of metal ions iron(III) and Cobalt(II) have been determined andcompound purity is confirmed by TLC. IR studies confirm the complexation of Iron(III) and Cobalt(II) with APZ. The Fe(III) complex exhibited a bacterial inhibition zone of 37.55 mm, while the Co(II) complex showed a slightly larger zone of 39.00 mm. Against fungal strains, the inhibition zones measured 39.17 mm for the Fe(III) complex and 39.87 mm for the Co(II) complex.This research shows that the complexes of Cobalt(II) andIron(III) are more effective on bacteria and fungi than APZ alone.

Acknowledgments

The authors are thankful to RAFM-2024 for providing this platform for the submission of the manuscript.

Conflict ofinterest

The authors declare that they have no conflicts of interest.

Availability of data and materials

The datasets used and/or analyzed during the current study are available from the corresponding author upon reasonable request.

5. REFERENCES

[1] G.O.Ildiz, A.M.Tabanez, A.Nunes, J.P.Roque, L.L.Justino, M.L. Ramos, R.Fausto (2022). Molecular structure, spectroscopy and photochemistry of alprazolam. *Journal of Molecular Structure*, *1247*, 131295.

[2] CH.Sharma,SH.Sharma,NA.Hussain, GL.Talesara(2009)Synthesis and antimicrobial activity of some new phthalimidoxy derivatives of triazine containing pyrimidine and isoxazole,J. Ind. Council Chem. 26(1),31-6.

[3] SA.Patil, R.Patil, RS.Keri, S.Budagumpi, GR.Balakrishna, M.Tacke(2015 Jul) N-heterocyclic carbene metal complexes as bio-organometallic antimicrobial and anticancer drugs, Future Medicinal Chemistry,7(10),1305-33.

[4] M.Marloye, G.Berger, M.Gelbcke, F. Dufrasne(2016 Dec) A survey of the mechanisms of action of anticancer transition metal complexes, Future medicinal chemistry,8(18),2263-86.

[5] SA.Khan, SAA.Nami, SA. Bhat, A.Kareem, N.Nishat (2017) Synthesis,characterization and antimicrobial study of polymeric transition metal complexes of Mn(II), Co(II), Ni(II), Cu(II) and Zn(II), Microbial Pathogenesis,110,414–25. Available from: http://dx.doi.org/10.1016/j.micpath.2017.07.008

[6] V.Kumar, R.Dhakarey(2003)Interaction of Schiff base derived from 4-aminoantipyrine and meta-bromobenzaldehyde with manganese (II), cobalt (II), nickel (II), copper (II), chromium (III), iron (III), Journal of the Indian Council of Chemists,20(1),46-51.

[7] SR.Kelode, PR. Mandlik (2012) Synthesis, characterization, thermal and antibacterial studies of cobalt (II), nickel (II), copper (II) and zinc (II) complexes of hydrazone Schiff base, Red.,804(7.98),8-13.

[8] L.J.Penkler (2007). *U.S. Patent No. 7,202,233*. Washington, DC: U.S. Patent and Trademark Office.

[9] A.Brandelli, D.Bizani, M.Martinelli, V .Stefani, AE.Gerbase(2004 Jun)Antimicrobial activity of 1, 4-naphthoquinones by metal complexation,RevistaBrasileira de CiênciasFarmacêuticas, 40(2), 247-53.

[10] A.I. Vogel, (1962) “A text book of Quantitative Inorganic Analysis”, E.L. B.S., 358.

[11] EJ.Olson, P. Bühlmann (2011)Getting more out of a job plot: Determination of reactant to product stoichiometry in cases of displacement reactions and n: N complex formation, Journal of Organic Chemistry,76(20), 8406–12. https://doi.org/10.1021/jo201624p.

[12] Ian Isherwood(August 1991) Book Reviews, Brain, Volume 114, Issue 4, Pages 2016–2017 https://doi.org/10.1093/brain/114.4.2016-b

[13] AW.Baur, WM.Kirby, JC.Sherris, M. Turch (1966) Antibiotic susceptibility testing by a standardized single disk method, Am J clinpathol,45(4),493-6.

[14] DX.West, AE. Liberta, SB. Padhye, RC.Chikate, PB.Sonawane, AS. Kumbhar, RG.Yerande(1993 Feb1)Thiosemicarbazone complexes of copper (II): structural and biological studies, Coordination Chemistry Reviews,123(1-2),49-71.

[15] K. Nakamoto, J. Fujita, H. Murata (1958 Sep) Infrared Spectra of Metallic Complexes. V. The Infrared Spectra of Nitro and Nitrito Complexes1, Journal of the American Chemical Society,80(18), 4817-23.

[16] MH. Salunke, ZA.Filmwala, AD. Kamble(2011) Synthesis, Characterization, Spectral Studies, Biocidal Activities of Fe (III), Co (II), Zn (II), Cd (II), Y (III), and In (III) Complexes of Schiff base derived from L-Phenylalanine, Oriental Journal of Chemistry,27(3),1243.

[17] B.Basavaraju, Bh. Naik, M.C.Prabhakara(2007) Transition metal complexes of quinolino [3, 2-b] benzodiazepine and quinolino [3, 2-b] benzoxazepine: synthesis, characterization, and antimicrobial studies. Bioinorganic Chemistry and Applications,34,123-131. doi: 10.1155/2007/639828

[18] VK. Sharma, S. Srivastava (2007 Feb 8)Template synthesis and structural characterization of homo binuclear chromium (III), manganese (III), iron (III), cobalt (III), and ruthenium (III) complexes with

octaazamacrocyclic ligands, Turkish Journal of Chemistry, 30(6), 755-67.

[19] V. Kumar, R. Dhakarey(2003) Interaction of Schiff base derived from 4-aminoantipyrine and meta-bromobenzaldehyde with manganese (II), cobalt (II), nickel (II), copper (II), chromium (III), iron (III) dioxouranium, Journal of the Indian Council of Chemists,20(1), 46-51.

[20] SE. Etaiw, DM. Abd El-Aziz, EH. Abd El-Zaher, EA. Ali (2011 Sep1)Synthesis, spectral, antimicrobial and antitumor assessment of Schiff base derived from 2-aminobenzothiazole and its transition metal complexes,SpectrochimicaActa Part A: Molecular and Biomolecular Spectroscopy,79(5),1331-7.

[21] S. Murugavel, S.Deepa, C. Ravikumar, R. Ranganathan, P. Alagusundaram (2020) Synthesis, structural, spectral and antibacterial activity of 3,3a,4,5-tetrahydro-2H-benzo[g]indazole fused carbothioamide derivatives as antibacterial agents,Journal of Molecular Structure, 1222. https://doi.org/10.1016/j.molstruc.2020.128961.

[22] KN. Thimmaiah, WD.Lloyd, GT. Chandrappa (1985)Stereochemistry and fungitoxicity of complexes of p-anisaldehydethiosemicarbazone with Mn(II), Fe(II), Co(II) and Ni(II). Inorganica Chimica Acta,106(2),81–3. https://doi.org/10.1016/S0020-1693(00)82252-5.

[23] R. Nair, A. Shah, S. Baluja, S. Chanda(2006) Synthesis and antibacterial activity of some Schiff base complexes, Journal of the Serbian Chemical Society, 71(7), 733-44. https://doi.org/10.2298/JSC0607733N

[24] S.A.Khan, S. A..Nami, S. A., Bhat, A., Kareem, N.Nishat (2017). Synthesis, characterization and antimicrobial study of polymeric transition metal complexes of Mn (II), Co (II), Ni (II), Cu (II) and Zn (II). *Microbial pathogenesis*, *110*, 414-425.

[25] L.H.Abdel-Rahman, H., Abu-Dief,M.Ahmed,F.Newair, K.Hamdan (2016)Some new nano-sized Cr(III), Fe(II), Co(II), and Ni(II) complexes incorporating 2-((E)-(pyridine-2-ylimino)methyl)napthalen-1-ol ligand: Structural characterization, electrochemical, antioxidant, antimicrobial, antiviral assessment and DNA interaction. Journal of Photochemistry and Photobiology B: Biology, 160(62), 18-31**.**

IZVOD

SINTEZA, KARAKTERIZACIJA, HROMATOGRAFSKA I ANTIMIKROBNA ISTRAŽIVANJA KOMPLEKSA PRELAZNIH METALA KOBALT(II) I GVOŽĐA(III)

Metalni kompleksi kobalt(II) i gvožđe(III) su sintetizovani reakcijom metalnog nitrata sa alprazolamom. Tokom ove studije, elementarne analize kompleksa su ograničene na stehiometriju tipa [(L)M(NO3)2], [(L)M(NO3)3] gde je M= kobalt(II) i gvožđe(III) i L= alprazolam. Alprazolamovi IR pojasevi se pomeraju da bi se potvrdila koordinacija metalnih jona. Utvrđeno je da su kompleksi metalnih jona bidentatni i tridentatni sa „N(1) i N(4)" pozicijama na ligandu. Ova studija je ispitivala alprazolam i njegove komplekse na njihova antimikrobna svojstva protiv odabranih bakterija i gljivica. Streptomicin i niastatin su korišćeni kao standardni lekovi za antimikrobne i antigljivične studije. Kao kompleksne studije I, odnosno antifungalne, su kompleksne studije I. III. Joni kobalta(II) alprazolama su efikasniji protiv odabranih bakterijskih i gljivičnih vrsta od leka Alprazolam. Povećana sklonost heliranju metalnih kompleksa dovodi do pojačane aktivnosti i one više inhibiraju rast bakterija i gljivica nego ligand alprazolam.

Ključne reči: *Metalni kompleksi, infracrveni, alprazolam, antimikrobni i bioaktivni*

Naučni rad
Rad primljen: 28.02.2024.
Rad korigovan: 15.03.2025.
Rad prihvaćen: 22.04.2025.

Jelena Lađarević[1]*, Bojan Božić*[2]*, Dušan Mijin*[1]*, Luka Matović*[3]*,*
Nataša Valentić[1]*, Evica Ivanović*[4]*, Nebojša Banjac*[4]***

[1]*Faculty of Technology and Metallurgy, University of Belgrade, Belgrade, Serbia,* [2]*Institute of Physiology and Biochemistry "Ivan Djaja", Faculty of Biology, University of Belgrade, Belgrade, Serbia,* [3]*Innovation Centre of the Faculty of Technology and Metallurgy, University of Belgrade, Belgrade, Serbia,* [4]*Faculty of Agriculture, University of Belgrade, Belgrade, Serbia*

Scientific paper
ISSN 0351-9465, E-ISSN 2466-2585
https://doi.org/10.62638/ZasMat1394

Zastita Materijala 67 (1)
119 - 132 (2026)

Study of tautomerism and solvatochromism of 5-(substituted phenylazo)-3-cyano-6-hydroxy-4-methyl-2-pyridones

ABSTRACT

In this study, ten 5-(substituted phenylazo)-3-cyano-6-hydroxy-4-methyl-2-pyridone dyes were synthesized, differing in both the position and the nature of substituents on the phenyl ring. The structural characterization of the dyes was performed using melting point analysis, FT-IR, NMR, and UV-Vis spectroscopy. The study includes spectral determination of the possible tautomeric forms in both the solid state and various solvents. Solvatochromic properties are investigated in 21 solvents with varying properties to assess the impact of solvent-solute interactions and effects of substituents electronic nature on the absorption maxima. For quantitative evaluation of the non-specific and specific solvent effects on the UV-Vis absorption maxima, the principles of the linear solvation energy relationships are used, i.e. models proposed by Kamlet-Taft and Catalán. Based on electronic distribution and substituent effects, methoxy-substituted dyes in ortho- and para-positions of phenyl ring have emerged as the most promising candidates for corrosion inhibition.
Keywords: *pyridone azo dyes, tautomerism, hydrazone, LSER*

1. INTRODUCTION

Azo dyes, as synthetic compounds, are extensively utilized in food, pharmaceutical, cosmetic, and textile industries, characterized by their structurally diverse molecules [1,2]. Additionally, it should be noted that azo dyes account for over 60% of the total production of all types of dyes, while approximately 70% make up the share of applied dyes in the industry [3].

Pyridone azo dyes are easy to synthesize and have good stability, whereby their structure consists of a pyridone ring, coupled with a heterocyclic or carbocyclic ring. Pyridone azo dyes have different applications. Alongside their usage as dyeing textiles, they are used in LCD screens, as liquid crystals, and in inkjet printing as pigments [4-7].

The use of organic compounds as corrosion inhibitors is commonly employed to extend the lifecycle of metals. These inhibitors form a protective barrier by adsorption onto the metal surface, shielding it from the harmful environment. The adsorption is facilitated by their active centers, which include polar functional groups, heteroatoms (such as N, S, O, P), aromatic rings, and π-electrons [8]. Corrosion prevention commonly involves the use of various heterocyclic organic compounds, particularly those belonging to the pyridine, imidazole, quinoline and azole groups [9]. On the other hand, the polar functional groups like hydroxyl, nitro, azo, carboxylic, cyano, carbonyl, imine, also, act as adsorption centers [10]. The ability of a particular organic compound to inhibit metal corrosion is influenced by two factors: the electronic distribution and the chemical structure [11].

Azo dyes function as corrosion inhibitors in various mixtures of electrolytes and metals and are one of the most commonly used anti-corrosion materials [12, 13, 14,15] due to their molecular structures, which contain numerous donor sites that allow them to act as chelating ligands when interacting with metal surfaces [12,16]. Non-bonding electrons from the nitrogen atom as well as the π-orbitals of the azo group (–N=N–) can participate in electron donation [13, 17,18]. Moreover, the empty p-orbitals of the nitrogen atoms can participate in the acceptance of electrons from the metal d-orbitals (retro donation)

∗Corresponding author: Nebojša Banjac
E-mail: nbanjac@agrif.bg.ac.rs
Paper received: 06.03. 2025.
Paper corrected: 28.05. 2025.
Paper accepted: 02. 06.2025.

[17]. Studies suggest that the nature of substituents can significantly affect their corrosion inhibition efficiency, with electron-donating groups, particularly in the *para*-position to azo bridge, often enhance performance by increasing electron density and promoting stronger interactions with metal surfaces [14,15,18].

In our previous study [19], we demonstrated that azo pyridone dyes act as effective chelating agents, as evidenced by the successful synthesis of two Cu(II) complexes. Having this in mind, the present study reports synthesis of ten 5-(substituted phenylazo)-3-cyano-6-hydroxy-4--methyl-2-pyridones altering both the position (-*ortho*, -*meta* and -*para*) and the nature (–OMe, $–NO_2$ and –Cl) of substituents in the phenyl group(Fig.1). The structures of the synthesized compounds are confirmed by FT-IR, ^{1}H NMR, ^{13}C NMR and UV-Vis spectroscopy and elemental analysis for compounds **2** and **6**. Literature data on similar azo pyridone dyes [20,21] suggest that these dyes exhibit azo-hydrazone tautomerism, due to the presence of the –OH group conjugated with the azo bridge (Fig. 1). Notably, most studies on the corrosion inhibition of azo dyes neglect this phenomenon, despite its critical importance for understanding the structure-property relationship since the migration of the proton within the molecule leads to a change in the structural skeleton, electron density distribution and physicochemical properties. Therefore, the primary aim of this study is to identify the dominant tautomeric form of the synthesized dyes in both the solid state and in various solvents by different spectroscopic techniques. The effects of the electronic nature of the substituents on the position of UV-Vis spectra are assessed. The nature of solvent-solute interactions plays a key role in stabilizing a particular tautomer, affecting electron distribution at different functional groups and molecular geometry [22]. To quantify these effects, the influence of both non-specific and specific solvent-solute interactions on the UV-Vis absorption maxima was evaluated using the LSER (Linear Solvation Energy Relationship) approach. The resulting solvatochromic data were analyzed using Kamlet-Taft and Catalán equations. As such, this study offers a theoretical framework focused on the structural and molecular characteristics of azo dyes that affect their potentialas corrosion inhibitors, providing a pathway for the design of more efficient corrosion-resistant materials.

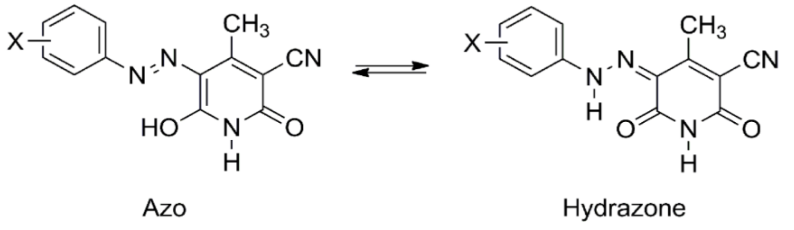

Copmounds	X
1	4-OCH_3
2	3-OCH_3
3	2-OCH_3
4	4-NO_2
5	3-NO_2
6	2-NO_2
7	4-Cl
8	3-Cl
9	2-Cl
10	H

*Figure 1. Azo-hydrazone tautomerism of the investigated dyes **1**–**10***

2. EXPERIMENTAL

2.1. Materials and measurements for the compounds

The reagents used for the synthesis were purchased from Merck, Sigma Aldrich and Fluka, and were used without purification. Additionally, solvents of spectroscopic purity were taken from the same manufacturers. Microwave-assisted syntheses were carried out using a household microwave oven Samsung M182 DN. The structure of the synthesized molecules was confirmed by determining the melting point, FT-IR, ^{1}H NMR, ^{13}C NMR and elemental analysis.The melting point of the synthesized compounds was determined by using the melting point system Stuart SMP30. ^{1}H NMR, ^{13}C NMR spectra of the compounds were recorded using a Varian Gemini 2000 (400 Hz and 100 Hz respectively) in deuterated DMSO-d_6 and CF_3COOD with TMS as an internal standard. The FTIR spectra of the synthesized compounds were determined using a Nicolet™ iS™ 10 FT-IR Spectrometer (Thermo Fisher SCIENTIFIC) with Smart iTR™ Attenuated Total Reflectance (ATR) Sampling accessories in the range of 500–4000 cm^{-1}, with 32 scans per spectrum. Elemental analysis was performed on a Vario EL III elemental analyzer. UV-Vis absorption spectra of the synthesized dyes were determined by using a Shimadzu 1700 spectrophotometer. The concentrations of all tested compounds in solvents were 5×10^{-5} M.

2.2. Synthesis of arylazo pyridone dyes

The synthesis of arylazo pyridone dyes was carried out in two steps. The first step involved the microwave synthesis of the starting 3-cyano-6-hydroxy-4-methyl-2-pyridone (Fig. 2) [23], which was carried out according to the following procedure. Ethyl-acetoacetate (0.02 mol, 2.6 g), cyanoacetamide (0.02 mol, 1.68 g) and powdered potassium hydroxide (0.02 mol, 1.12 g) were mixed in a test tube and heated in a commercial microwave oven at 200 W by irradiation for 4 minutes.

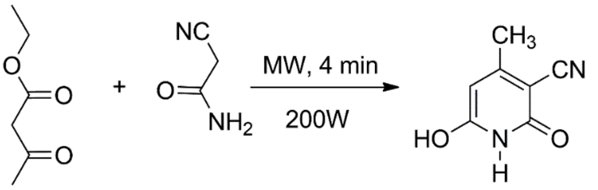

Figure 2. Microwave synthesis of 3-cyano-6--hydroxy-4-methyl-2-pyridone

The resulting reaction mixture was treated three times with 10 mL of H_2O under gentle heating until the precipitate completely dissolved. After cooling, the solution was filtered, and the filtrate was then acidified with HCl, whereby a white precipitate was separated. The product was separated by filtration, washed twice with water (5 mL) and air-dried. A white substance was obtained, with a yield of 60%; m.p. 315–316 °C (lit. m.p. 315–320 °C [24]), FT-IR (KBr, ν/cm^{-1}): 3294 (OH), 2223 (CN), 1593 (C=O); ^{1}H NMR (200 MHz, DMSO-d_6, δ/ppm): 2.51 (3H, s, CH_3), 5.61 (1H, s, C_5).

The second step in the synthesis of the dyes represents a classical diazo-coupling reaction (Fig. 3). Substituted aniline derivatives (10 mmol) were dissolved in concentrated hydrochloric acid (2.5 mL) and cooled to –5 °C. Sodium nitrite (1.23 g, 11 mmol) was dissolved in cold water (4 mL) and added in drops to the aniline solution. The mixture was stirred for 1 h to give the diazonium salt of the corresponding aniline. The obtained pyridone (10 mmol) was dissolved in an aqueous solution (4 mL) of potassium hydroxide (0.56 g, 10 mmol) and cooled to –5 °C. The diazonium salt was added dropwise to the pyridone solution, which was stirred for half an hour. The mixture was then stirred for an additional 3 hours, while the temperature was maintained between 0 and 5 °C. Once the mixture had been refrigerated overnight, it was filtrated, rinsed with water, and dried. The compounds **1**–**3** were recrystallized from chloroform, while the rest of the compounds were recrystallized from *N*,*N*-dimethylformamide (DMF). It should be noted that eight compounds are already known and registered in the literature, while compound **6** is present in the patent literature, and compound **2** is a new molecule.

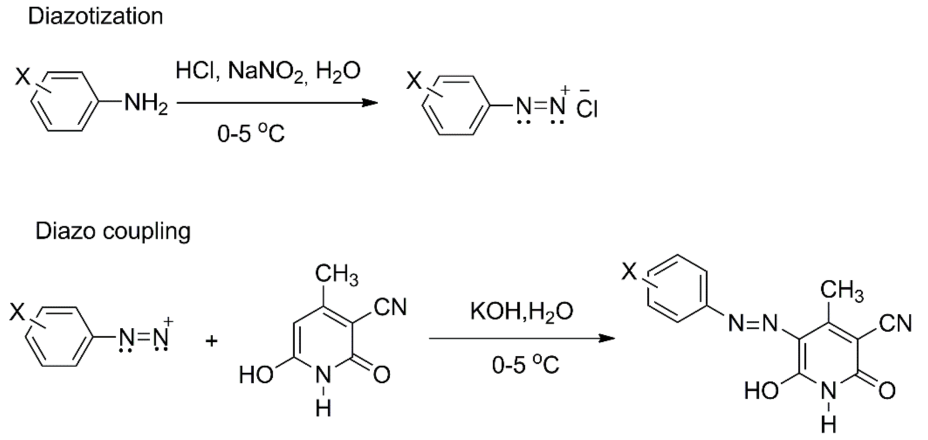

*Figure 3. Synthesis of compounds **1–10***

5-(4-Methoxyphenylazo)-3-cyano-6-hydroxy-4--methyl-2-pyridone (**1**). Dark red powder, yield: 59%, m.p. 270.3–271.1 °C (lit. m.p. 272–273 °C [25,26], 270–271 °C [27]); M = 284.3 g mol^{-1}; FT-IR (KBr, ν/cm^{-1}): 3433 (NH hydrazone form), 3121 (NH pyridone), 2221 (CN), 1675, 1630 (C=O pyridone); ^{1}H NMR (200 MHz, DMSO-d_6, δ/ppm): 2.50 (3H, s, CH_3), 3.80 (3H, s, OCH_3), 7.06 (2H, d, J = 8.4 Hz, Ar–H), 7.65 (2H, d, J = 8.4 Hz, Ar–H), 11.96 (1H, s, NH pyridone), 14.78 (1H, s, NH hydrazone form); ^{13}C NMR (50 MHz, DMSO-d_6, δ/ppm): 161.7 (Py), 161.1 (Py), 160.5 (Py), 158.8 (Ar), 134.7 (Ar), 122.8 (Py), 119.2 (Ar), 115.5 (CN), 115.3 (Ar), 99.5 (Py), 55.7 (OCH_3), 16.6 (CH_3); UV-Vis (EtOH) (λ_{max}/nm (log ε)): 457 (3.99).

5-(3-Methoxyphenylazo)-3-cyano-6-hydroxy-4--methyl-2-pyridone (**2**). Dark red powder; yield: 33%; m.p. 287.3–288.1 °C; M = 284.3 g mol^{-1}; Calculated $C_{14}H_{12}N_4O_3$ (%): C, 59.15; H, 4.25; N, 19.71; Found (%): C, 59.05; H, 4.29 ; N,19.68; FT-IR (KBr, ν/cm^{-1}): 3436 (NH hydrazone form), 3137 (NH pyridone), 2226 (CN), 1668, 1649 (C=O pyridone); ^{1}H NMR (200 MHz, DMSO-d_6, δ/ppm): 2.50 (3H, s, CH_3), 3.80 (3H, s, OCH_3), 6.81 (1H, d, J = 8.4 Hz, Ar–H), 7.18–7.20 (2H, m, Ar–H), 7.34 (1H, t, J = 8.2 Hz, Ar–H), 12.01 (1H, s, NH pyridone), 14.44 (1H, s, NH hydrazone form); ^{13}C NMR (50 MHz, DMSO-d_6, δ/ppm): 161.7 (Py), 161.0 (Py), 160.7 (Py), 160.6 (Ar), 142.5 (Ar), 131.0 (Ar), 123.8 (Py), 115.2 (CN), 112.8 (Ar), 109.7 (Ar), 102.8 (Ar), 101.1 (Py), 55.6 (OCH_3), 16.7 (CH_3); UV-Vis (EtOH) (λ_{max}/nm (log ε)): 435.6 (4.51).

5-(2-Methoxyphenylazo)-3-cyano-6-hydroxy-4-methyl-2-pyridone (**3**). Red powder; yield: 61%; m.p. 317.1–318.5 °C (lit. m.p. 324–325 °C [25], 314–315 °C [27]); M = 284.3 g mol^{-1}; FT-IR (KBr, ν/cm^{-1}): 3436 (NH hydrazone form), 3143 (NH pyridone), 2221 (CN), 1669, 1650 (C=O pyridone); ^{1}H NMR (200 MHz, DMSO-d_6, δ/ppm): 2.50 (3H, s, CH_3), 3.92 (3H, s, OCH_3), 7.00–7.33 (2H, m, Ar–H), 7.61 (1H, d, J = 7.2 Hz, Ar–H), 7.75 (1H, d, J = 7.4 Hz, Ar–H), 12.06 (1H, s, NH pyridone), 14.91 (1H, s, NH hydrazone form); ^{13}C NMR (50 MHz, DMSO-d_6, δ/ppm): 161.4 (Py), 160.9 (Py), 160.0 (Py), 149.0 (Ar), 142.3 (Ar), 131.0 (Ar), 128.2 (Ar), 122.1 (Py), 121.5 (Ar), 115.7 (CN), 112.6 (Ar), 101.0 (Py), 56.6 (OCH_3), 16.6 (CH_3); UV-Vis (EtOH) (λ_{max}/nm (log ε)): 453.0 (4.01).

5-(4-nitrophenylazo)-3-cyano-6-hydroxy-4-methyl-2-pyridone (**4**). Dark orange powder; yield: 54%; m.p. 326.2–327.8 °C (lit. m.p. 326–327 °C [25,26], 324 °C [28], 326–328 °C [29], > 320 °C [30]); M = 299.2 g mol^{-1}; FT-IR (KBr, ν/cm^{-1}): 3446 (NH hydrazone form), 3110 (NH pyridone), 2229 (CN), 1680, 1638 (C=O pyridone); ^{1}H NMR (200 MHz, CF_3COOD, δ/ppm): 2.89 (3H, s, CH_3), 7.92 (2H, d, J = 9.0 Hz, Ar–H), 8.53 (2H, d, J = 9.0 Hz, Ar–H), 8.56 (1H, s, Ar–H), 11.4 (1H, s, NH pyridone), 14.87 (1H, s, NH hydrazone form); ^{13}C NMR (50 MHz, CF_3COOD, δ/ppm): 163.9 (Py), 162.4 (Py), 161.5 (Py), 147.2 (Ar), 146.5 (Ar), 126.8 (Py), 123.8 (CN), 118.1 (Ar), 112.5 (Ar), 106.9 (Py), 16.7 (CH_3); UV-Vis (EtOH) (λ_{max}/nm (log ε)): 432 (4.36).

5-(3-nitrophenylazo)-3-cyano-6-hydroxy-4-methyl-2-pyridone (**5**). Orange-yellow powder; yield*:* 52 %; m.p. 275.3–276.6 °C (lit. m.p. 279–280 °C [31]); M = 299.2 g mol^{-1}; FT-IR (KBr, ν/cm^{-1}): 3447 (NH hydrazone form), 3089 (NH pyridone), 2224 (CN), 1692, 1645 (C=O pyridone); ^{1}H NMR (200 MHz, CF_3COOD, δ/ppm): 2.80 (3H, s, CH_3), 7.74 (1H, t, J = 8.0 Hz, Ar–H), 8.01 (1H, d, J = 8.0 Hz, Ar–H), 8.26 (1H, d, J = 8.0 Hz, Ar–H), 8.56 (1H, s, Ar–H), 11.3 (1H, s, NH pyridone), 14.87 (1H, s, NH hydrazone form); ^{13}C NMR (50 MHz, CF_3COOD, δ/ppm): 163.5 (Py), 162.6 (Py), 161.8 (Py), 150.3 (Ar), 142.8 (Ar), 132.5 (Py), 125.2 (Ar), 124.2 (Ar), 124.1 (CN), 118.5 (Ar), 112.9 (Ar), 107.2 (Py), 17.0 (CH_3); UV-Vis (EtOH) (λ_{max}/nm (log ε)): 415.5 (4.16).

5-(2-nitrophenylazo)-3-cyano-6-hydroxy-4-methyl-2-pyridone (**6**). Orange powder; yield: 44%; m.p. 288.5–289.6 °C; M = 299.2 g mol^{-1}; Calculated $C_{13}H_9N_5O_4$ (%): C, 52.18; H, 3.03; N, 23.40; Found (%): C, 52.21; H, 3.09; N, 23.45;FT-IR (KBr, ν/cm^{-1}): 3447 (NH hydrazone form), 3157 (NH pyridone), 2227 (CN), 1673, 1654 (C=O pyridone); UV-Vis (EtOH) (λ_{max}/nm (log ε)): 433.5 (3.85).

5-(4-Chlorophenylazo)-3-cyano-6-hydroxy-4-methyl-2-pyridone (**7**). Orange powder; yield: 61%; m.p. 300.2–301.7 °C (lit. m.p. 301–302 °C [25,26], 288–289 °C [29], 302–303 °C [27]); M = 288.7 g mol^{-1}; FT-IR (KBr, ν/cm^{-1}): 3446 (NH hydrazone form), 3132 (NH pyridone), 2228 (CN), 1680, 1641 (C=O pyridone); ^{1}H NMR (200 MHz, CF_3COOD, δ/ppm): 2.60 (3H, s, CH_3), 7.31 (2H, d, J = 8.0 Hz, Ar–H), 7.43 (2H, d, J = 8.0 Hz, Ar–H), 11.4 (1H, s, NH pyridone), 14.84 (1H, s, NH hydrazone form); ^{13}C NMR (50 MHz, CF_3COOD, δ/ppm): 163.8 (Py), 162.9 (Py), 162.1 (Py), 139.8 (Ar), 137.7 (Ar), 131.6 (Py), 124.1 (CN), 118.5 (Ar), 112.9 (Ar), 107.2 (Py), 17.0 (CH_3); UV-Vis (EtOH) (λ_{max}/nm (log ε)): 433.5 (4.39).

5-(3-Chlorophenylazo)-3-cyano-6-hydroxy-4-methyl-2-pyridone (**8**). Orange powder; yield: 33%; m.p. 295.3–296.8 °C (lit. m.p. 288–290 °C [31], 298–300 °C [27]); M = 288.7 g mol^{-1}; FT-IR (KBr, ν/cm^{-1}): 3436 (NH hydrazone form), 3105 (NH pyridone), 2227 (CN), 1680, 1636 (C=O pyridone); ^{1}H NMR (200 MHz, CF_3COOD, δ/ppm): 2.81 (3H, s, CH_3), 7.39–7.55 (3H, m, Ar–H), 7.71 (1H, s, Ar–H), 11.3 (1H, s, NH pyridone), 14.91 (1H, s, NH hydrazone form); ^{13}C NMR (50 MHz, CF_3COOD, δ/ppm): 163.8 (Py), 162.8 (Py), 161.9 (Py), 142.3 (Ar), 137.7 (Ar), 132.2 (Py), 130.9 (Ar), 124.1 (CN), 118.7 (Ar), 118.5 (Ar), 112.9 (Ar), 107.2 (Py), 16.9 (CH_3); UV-Vis (EtOH) (λ_{max}/nm (log ε)): 423.5 (4.39).

5-(2-Chlorophenylazo)-3-cyano-6-hydroxy-4-methyl-2-pyridone (**9**). Orange powder; yield: 42%; m.p. 345.6–346.9 °C (lit. m.p. 347–348 °C [25], > 320 °C [27]); M = 288.7 g mol^{-1}; FT-IR (KBr, ν/cm^{-1}): 3430 (NH hydrazone form), 3141 (NH pyridone), 2228 (CN), 1670, 1629 (C=Opyridone); ^{1}H NMR (200 MHz, CF_3COOD, δ/ppm): 2.83 (3H, s, CH_3), 7.38–7.57 (3H, m, Ar–H), 7.98 (1H, d, J = 7.8 Hz, Ar–H), 11.3 (1H, s, NH pyridone), 15.29 (1H, s, NH hydrazone form); ^{13}C NMR (50 MHz, CF_3COOD, δ/ppm): 163.7 (Py), 162.9 (Py), 162.0 (Py), 137.9 (Ar), 131.5 (Ar), 131.4 (Ar), 129.8 (Py), 126.3 (Ar), 124.1 (CN), 118.5 (Ar), 112.9 (Ar), 107.2 (Py), 16.9 (CH_3); UV-Vis (EtOH) (λ_{max}/nm (log ε)): 429.5 (4.06).

3-cyano-5-phenylazo-6-hydroxy-4-methyl-2-pyridone (**10**). Orange powder; yield: 41%; m.p. 280.6–281.9 °C (lit. m.p. 288.1 °C [28], 278–279 °C [25,26], 278–280 °C [29], 285–286 °C [27]); M = 254.2 g mol^{-1}; FT-IR (KBr, ν/cm^{-1}): 3447 (NH hydrazone form), 3149 (NH pyridone), 2229 (CN), 1688, 1647 (C=O pyridone); ^{1}H NMR (200 MHz, DMSO-d_6, δ/ppm): 2.51 (3H, s, CH$_3$), 7.29 (1H, t, J = 7.2 Hz, Ar–H), 7.48 (2H, t, J = 7.5 Hz, Ar–H), 7.66 (2H, d, J = 7.2 Hz, Ar–H), 12.04 (1H, s, NH pyridone), 14.55 (1H, s, NH hydrazone form); ^{13}C NMR (50 MHz, DMSO-d_6, δ/ppm): 160.4 (Py), 159.7 (Py), 158.4 (Py), 140.6 (Ar), 129.3 (Ar), 126.7 (Ar), 122.6 (Py), 116.8 (Ar), 114.5 (CN), 97.8 (Py), 16.9 (CH$_3$); UV-Vis (EtOH) (λ_{max}/nm (log ε)): 431.0 (4.72).

3. RESULTS AND DISCUSSION

3.1. Spectral analysis

Based on the FT-IR data, it can be concluded that the investigated pyridone dyes adopt hydrazone form in the solid state. The spectra of the compounds have pronounced peaks originating from carbonyl groups in the ranges 1629–1650 cm^{-1} and 1669–1692 cm^{-1}. The broad spectral bands originating from the –NH vibrations of the hydrazone form are located in the range 3433–3447 cm^{-1}, while the bands originating from the –NH ofpyridone are located in the range 3089–3157 cm^{-1}. ^{1}H NMR and ^{13}C NMR spectra of these compounds were recorded in DMSO-d_6 (**1**–**3**, **10**) and CF$_3$COOD (**4**, **5**, **7**–**9**) and unambiguously indicate the dominance of hydrazone form in these solvents. It should be noted that spectra of compound **6** were not recorded due to poor solubility in available NMR solvents. ^{1}H NMR chemical shifts assigned to the –N–H proton of the hydrazone form are in the ranges 14.44–14.91 ppm in DMSO-d_6 and 14.87–15.29 ppm in CF$_3$COOD. Furthermore, the presence of two carbonyl signals in ^{13}C NMR (range 159.7–161.7 ppm in DMSO-d_6 and 163.9–162.4 ppm in CF$_3$COOD) additionally confirms the presence of hydrazone form. The results obtained by NMR spectral analysis are in accordance with literature data [20,21,29,31]. The great stability and high planarity of the hydrazone form is considered to be mainly influenced by the formation of cooperative intramolecular hydrogen bond of –NH hydrazone and carbonyl group [20,21].

UV-Vis absorption spectra of the mentioned series of compounds in ethanol show an intense peak in the region between 415.5–457 nm (Fig. 4a), which is attributed to the π–π* transition of the hydrazone tautomer [20,21]. The absorption maxima are highly dependent on the position and the electronic nature of the substituents wherein the largest bathochromic shift ($\Delta\lambda_{max}$ = 26 nm) with respect to unsubstituted dye (**10,** 431 nm) is observed for the 4-methoxy substituted dye (**1**), while the largest hypsochromic shift ($\Delta\lambda_{max}$ = 15.5 nm) is observed for 3-nitro substituted dye (**5**).

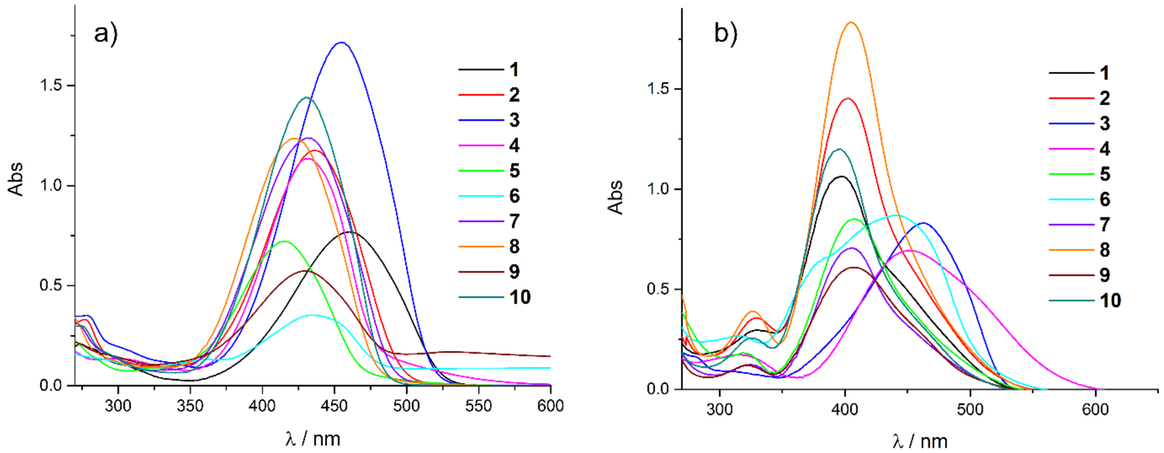

Figure 4. UV-Vis spectra of the synthesized compounds in ethanol (a) and formamide (b)

3.2. Solvatochromic properties of compounds and LSER analysis

The solvatochromic behavior of the investigated dyes was examined in 21 solvents of different dipolarity/polarizability and hydrogen bond capabilities covering a wide range of properties. The UV-Vis spectra in these solvents indicate that the most dominant form in all solvents is hydrazone form [32-34], whereas in amide solvents (DMF, formamide and *N*,*N*-dimethyl acetamide (DMA)) UV-Vis spectra reveal the coexistence of two forms in solution, as evidenced by the appearance of a shoulder in the spectra of all investigated compounds (Fig. 4b). Literature reports on structurally related pyridone azo dyes indicate that azo-hydrazone tautomerism does not occur in these solvents [21,32], instead, deprotonation of the hydrazone form takes place, leading to an equilibrium between the hydrazone and its anionic form, as illustrated in Fig. 5. Furthermore, in formamide, as well as in DMF and DMA, all spectra exhibit absorption bands in the 300–340 nm range, consistent with the presence of the anionic form in amide solvents [21]. The absorption maxima of hydrazones form in selected solvents are given in Table 1.

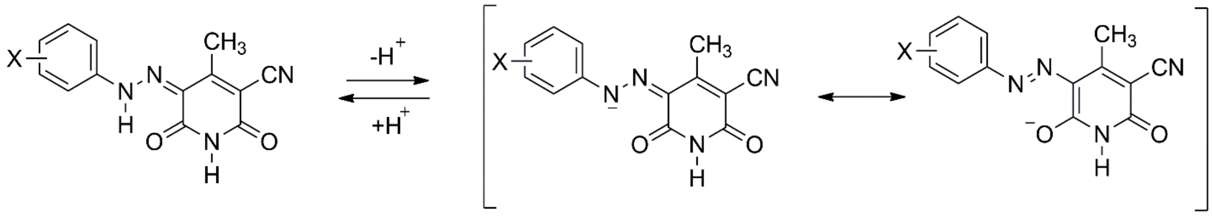

Figure 5. Equilibrium between hydrazone and anionic form in amide solvents.

*Table 1. Absorption maximaof the hydrazone form of compounds (**1–10**) in different solvents.*

	λ_{max} (nm)									
Solvent	**1**	**2**	**3**	**4**	**5**	**6**	**7**	**8**	**9**	**10**
Ethylene glycol	464	440.4	460	429.5	414	437	432	424	430	428.5
Methanol	456.8	435.6	453.5	432	415.5	434	434	424	429.5	431
Ethanol	457	435.6	453	432	415.5	433.5	433.5	423.5	429.5	431
1-Propanol	455	433	455.5	433	414	435.5	431.5	422	431.5	432.5
2-Propanol	456.4	434	443	423	408.5	425	426	419	424.5	423.5
1-Butanol	455.8	435.4	454	434	416.5	434	434.5	425	430.5	432.5
1-Pentanol	460	438.4	450	426	410.5	427	426.5	418	424.5	425
Acetonitrile	456.8	433.4	452	430.5	416.5	436.5	431	425	428.5	429
DMSO	461.2	439.2	459	443.5	424	444	435	427.5	433	432
DMF	458	436.5	453.5	437	422.5	441.5	433	426	430	429
DMA	455	432.5	450.5	431.5	420	439.5	430	424	426	428
Acetone	456.3	432.6	451.5	430.5	415.5	434.5	430.5	423	426.5	428.5
Chloroform	467.4	443	462	434.5	423	440	440.5	433	438	436
Ethyl acetate	453.6	431	449.5	428	414	432	429	421	426.5	427
Methyl acetate	455.2	431.6	449	428	416	432	428.5	422	427	427.5
Tetrahydrofuran	455.8	435	451	431	416	434	430.5	424	427.5	430
Acetic acid	462.5	441	460	434.5	421.5	438	438.5	430	433.5	435.5
Diisopropyl ether	452	431	446	425	413.5	428	430.5	420.5	429	426.5
Dioxane	453.4	433.2	449.5	436	418	435	433	426	427.5	429.5
Pyridine	462	441.5	458	442	425.5	445.5	438.5	432.5	435.5	436.5
Formamide	467.5	444	464	441.5	426.5	450.5	441	433	438	438

According to literature data, the electron density in these dyes is suggested to transfer from the hydrazone bridge to the cyano group, acting as the primary electron acceptor, as well as to the carbonyl group at position 6 of the pyridone ring [20,35]. Corresponding resonance structures are depicted in Fig. 6. It can be observed that the electron rich sites are cyano and carbonyl groups which may serve as suitable donor centers for adsorption onto metal surface. The electron-donating and electron-withdrawing nature of substituents as well as their position on the phenyl ring significantly influence the electronic distribution of these dyes, thereby affecting electron availability on oxygen and nitrogen atoms of carbonyl and cyano groups, respectively.

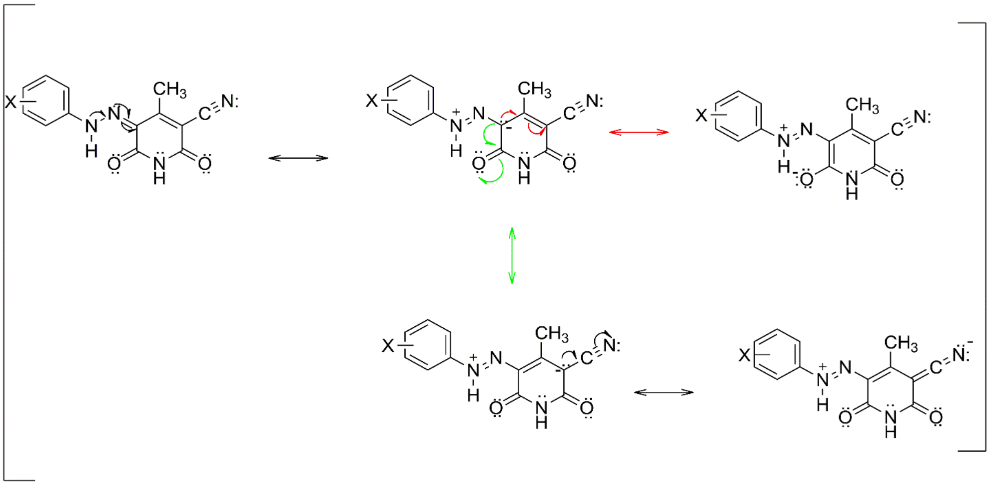

Figure 6. Possible resonance structures of the investigated dyes

The largest bathochromic shift in all solvents is observed for methoxy-substituted dyes (**1**–**3**) when compared to unsubstituted dye (**10**) (Table 1). Electron-donating group such as methoxy stabilize the structure by enhancing intramolecular charge transfer (ICT), thereby increasing electron density at the cyano and carbonyl groups. The UV-Vis absorption maxima of the meta-substituted dyes (**2**, **5**, and **8**) exhibit hypsochromic shift compared to their corresponding *para*- and *ortho*-substituted analogs, as only the inductive effect is operative in the *meta*-position, while resonance stabilization is not feasible. Absorption maxima of *ortho*-substituted dyes (**3**, **7** and **9**) are slightly shifted to lower wavelengths with respect to the corresponding *para*-substituted dyes which can be attributed to steric hindrance that prevents the pyridone and phenyl rings from adopting a planar conformation, thereby reducing effective π-electron delocalization. Electron-accepting nitro groups in the *ortho*- (**6**) and *para*-positions (**4**) are expected to cause a hypsochromic shift, likely due to structural destabilization arising from the development of positive charge on the nitrogen atom, but, in fact,exerts a small bathochromic or negligible (either bathochromic or hypsochromic) shifts which may be due to the counteracting effect of this group to the extended delocalization. Chlorine substituted dye in the *para*-position (**7**), despite strong electron-withdrawing inductive effect, induce a bathochromic shift in the UV-Vis absorption maxima due to their weak resonance effect.

Among the studied solvents, the largest bathochromic shift is observed in highly polar formamide, while shortest wavelengths are found in diisoporpyl ether, 2-propanol and 1-pentanol. According to Table 1, the UV-Vis spectra of the dyes are more affected by changes in the nature and position of the substituents than by alteration in solvent nature.

As shown in Table 1, the solvent effects on the absorption maxima are complex and cannot be attributed to a particular type of solvent interaction. Thus, in order to quantitatively describe manifold solvent-solute interactions LSER models developed by Kamlet-Taft and Catalán are used.Applied to UV-Vis absorption frequencies ν_{max} of hydrazone form of dyes (**1**–**10**) Kamlet-Taft model [36] is given as follows:

$$\nu_{max} = \nu_0 + a\alpha + b\beta + s\pi^* \qquad (1)$$

Each parameter represents a specific type of interaction contributing to the overall solvation ability. The Kamlet-Taft π^* parameter indicates the solvent's dipolarity/polarizability, while α and β correspond to the hydrogen bond donor (HBD) and hydrogen bond acceptor (HBA) capacities, respectively, with their values listed in Table 2. The solvent-independent correlation coefficients *a*, *b*, and *s* quantify the individual contributions of solvent effects on the UV-Vis absorption shifts (ν_{max}). The coefficient ν_0 represents the absorption frequency of the solute in the reference system. The results of regression analysis using the Kamlet-Taft model for compounds **1**–**10**are given in Table 3, while the percentages of solvatochromic parameters for these compounds are given in Table 4. The correlation coefficients (*R*) are above 0.93 indicating high validity of the applied model.

Table 2. Kamlet-Taft [37] and Catalán [38] solvent parameters

No	Solvent	Kamlet-Taft			Catalán			
		*π**	*β*	*α*	*SP*	*SdP*	*SB*	*SA*
1	Ethylene glycol	0.92	0.52	0.9	0.777	0.91	0.534	0.717
2	Methanol	0.6	0.66	0.98	0.608	0.904	0.545	0.605
3	Ethanol	0.54	0.75	0.86	0.633	0.783	0.658	0.4
4	1-Propanol	0.52	0.90	0.84	0.658	0.748	0.782	0.367
5	2-Propanol	0.48	0.84	0.76	0.633	0.808	0.83	0.283
6	1-Butanol	0.47	0.84	0.84	0.674	0.655	0.809	0.341
7	1-Pentanol	0.4	0.86	0.84	0.687	0.587	0.86	0.319
8	Acetonitrile	0.75	0.40	0.19	0.645	0.974	0.286	0.044
9	DMSO	1	0.76	0	0.83	1	0.647	0.072
10	DMF	0.88	0.69	0	0.759	0.977	0.613	0.031
11	DMA	0.88	0.76	0	0.763	0.987	0.65	0.028
12	Acetone	0.71	0.43	0.08	0.651	0.907	0.475	0
13	Chloroform	0.58	0.10	0.20	0.783	0.614	0.071	0.047
14	Ethyl acetate	0.55	0.45	0	0.656	0.603	0.542	0
15	Methyl acetate	0.6	0.42	0	0.645	0.637	0.527	0
16	Tetrahydrofuran	0.58	0.55	0	0.714	0.634	0.591	0
17	Acetic acid	0.64	0.45	1.12	0.651	0.676	0.39	0.689
18	Diisopropyl ether	0.27	0.49	0	0.625	0.324	0.657	0
19	Dioxane	0.55	0.37	0	0.737	0.312	0.444	0
20	Pyridine	0.87	0.64	0	0.842	0.761	0.581	0.033
21	Formamide	0.97	0.48	0.71	0.814	1.006	0.414	0.549

*Table 3. Results of the regression analysis obtained by the Kamlet-Taft equation (**1-10**)*

No	$\nu_0 \cdot 10^{-3}$ (cm^{-1})	$s \cdot 10^{-3}$ (cm^{-1})	$b \cdot 10^{-3}$ (cm^{-1})	$a \cdot 10^{-3}$ (cm^{-1})	R^a	sd^c	F^b	n^d
1	22.427 (±0.101)	–0.899 (±0.101)	0.222 (±0.110)	–0.250 (±0.042)	0.956	0.066	36	14
2	23.289 (±0.117)	–0.685 (±0.104)	0.262 (±0.131)	–0.188 (±0.053)	0.933	0.080	20	13
3	22.478 (±0.114)	–0.739 (±0.112)	0.408 (±0.153)	–0.360 (±0.051)	0.951	0.082	34	15
4	23.570 (±0.143)	–0.969 (±0.173)	0.605 (±0.154)	–0.254 (±0.076)	0.930	0.108	19	13
5	24.478 (±0.108)	–1.385 (±0.131)	0.701 (±0.107)	–0.136 (±0.058)	0.966	0.085	51	15
6	23.839 (±0.143)	–1.841 (±0.174)	0.639 (±0.146)	–0.168 (±0.076)	0.956	0.115	43	16
7	23.630 (±0.143)	–0.999 (±0.137)	0.549 (±0.140)	–0.382 (±0.059)	0.945	0.085	28	14
8	23.883 (±0.122)	–0.979 (±0.127)	0.678 (±0.129)	–0.240 (±0.056)	0.947	0.082	29	14
9	23.836 (±0.107)	–1.002 (±0.113)	0.394 (±0.117)	–0.270 (±0.048)	0.957	0.070	33	13
10	23.459 (±0.101)	–0.822 (±0.125)	0.788 (±0.103)	–0.295 (±0.055)	0.950	0.080	31	14

[a] Correlation coefficient, [b] Standard deviation, [c] Fisher's test,
[d] Number of solvents included in the correlation.

Based on the values of the independent coefficients (Table 3), it can be concluded that the positions of the UV-Vis absorption maxima depend much more on the change in polarity/polarizability (non-specific interactions) of the solvent than on the change in the HBA and HBD abilities of the solvent. Regression analysis showed that the independent coefficients *s* and *a* are always negative indicating a bathochromic shift by increasing the polarity/polarizability and ability of the solvent todonate hydrogen bonds. Based on this, it can be concluded that the excited state is more stabilized compared to the ground state, as a consequence of solvation. By comparing the absolute values of coefficient *s* (Table 3), it can be observed that this coefficient increases with increasing of electron-withdrawing capability of the substituents, being highest for nitro-substituted dyes. Potential interaction sites between the dye molecules and protic solvents include the cyano and carbonyl groups in the pyridone ring, as well as the nitrogen atom of the hydrazone moiety. Interaction of the hydrogen atom from the protic solvent with the pyridone carbonyl and cyano groups reduces the electron density on oxygen and nitrogen atoms, thereby reinforcing ICT [39] and resulting in a bathochromic shift of the UV-Vis absorption maxima. Conversely, when HBD solvents interact with the lone pair on the N–H group of the hydrazone, the ICT is disrupted, leading to a hypsochromic shift. Overall, the predominant effect is a bathochromic shift with increasing solvent acidity, suggesting that the interaction of HBD solvents is more pronounced with the pyridone ring than with other regions of the molecule.

The positive value of the coefficient *b* for all compounds indicates a hypsochromic shift by increasing the HBD ability of the solvent. The possible interaction sites of the molecule with protophilic solvents are both –NH groups, hydrazone and at the pyridone ring. Considering first interaction, solvent molecules compete with the intramolecular N–H···O hydrogen bond for the hydrogen atom, thereby weakening and elongating the N–H bond and increasing its acidity [40]. As the basicity of the solvent increases, this weakening becomes more pronounced, enhancing electron donation from the –NH group and promoting π-electron delocalization. This enhanced delocalization would lead to a bathochromic shift in the UV–Vis absorption maxima, but in fact in the real system the shift is hypsochromic which could suggest that the interactions with –NH pyridone group are dominant and more intense.

*Table 4. Percentages of solvatochromic parameters determined using the Kamlet-Taft equation (**1–10**).*

Compound	Pπ* (%)	Pβ (%)	Pα (%)
1	65.6	16.2	18.2
2	60.4	23.0	16.6
3	49.1	27.1	23.9
4	53.0	33.1	13.9
5	62.3	31.6	6.1
6	69.5	24.1	6.4
7	51.8	28.4	19.8
8	51.6	35.7	12.7
9	60.1	23.7	16.2
10	43.2	41.3	15.5

Based on Table 4, it is evident that non-specific interactions contribute the most significantly, particularly in the case of nitro-substituted compounds (**4**–**6**). The percentage of dipolarity/ /polarizability of the unsubstituted dye (**10**) is reduced in comparison to the substituted dyes (Table 4), indicating that the substituents on the phenyl core of these compounds intensify non-specific interactions between the dye molecule and the solvent. Additionally, as indicated by Table 4, these dyes show greater sensitivity to the HBA ability of solvents rather than their HBDproperties.

While the Kamlet-Taft approach is quite successful in quantitatively interpreting solvation effects, it does have certain limitations. First, the π* empirical scale combines both solvent dipolarity and polarizability, rather than treating them separately. Second, the empirical solvent parameter scales are derived from the averaged experimental data of multiple solvatochromic probes, which may introduce some generalizations. For this reason, Catalán's four-parameter model was usedfor a more precise analysis [38].

$$v_{max} = v_0 + aSA + bSB + cSP + dSdP \qquad (2)$$

The advantage of this approach lies in the separation of general interactions into distinct polarizability (*SP*) and dipolarity (*SdP*) components, while scales SA and SB correspond to Kamlet-Taft's *α* and *β* scales (Table 2). Regression analysis according to Eq. 2 is given in Table 5, while percentage contributions of individual parameters are given in Table 6. Thecorrelation coefficient (*R*) of the tested compounds is greater than 0.94.

*Table 5. Results of regression analysis obtained by Catalán's equation (**1–10**).*

No	$\nu_0 \cdot 10^{-3}$ (cm^{-1})	$c \cdot 10^{-3}$ (cm^{-1})	$d \cdot 10^{-3}$ (cm^{-1})	$b \cdot 10^{-3}$ (cm^{-1})	$a \cdot 10^{-3}$ (cm^{-1})	R^a	sd^c	F^b	n^d
1	22.996 (±0.172)	–1.481 (±0.227)	–0.244 (±0.088)	0.271 (±0.113)	–0.374 (±0.065)	0.953	0.068	32	18
2	24.340 (±0.202)	–2.359 (±0.280)	0.253 (±0.110)	0.292 (±0.101)	–0.617 (±0.085)	0.948	0.079	29	18
3	23.356 (±0.200)	–1.939 (±0.268)	–0.209 (±0.100)	0.557 (±0.115)	–0.465 (±0.077)	0.963	0.079	38	17
4	25.638 (±0.290)	–3.600 (±0.426)	–0.275 (±0.132)	0.421 (±0.193)	–0.437 (±0.127)	0.952	0.100	24	15
5	25.907 (±0.172)	–2.803 (±0.231)	–0.153 (±0. 083)	0.228 (±0.096)	–0.184 (±0.086)	0.973	0.065	52	17
6	25.166 (±0.269)	–3.478 (±0.371)	–0.338 (±0.129)	0.895 (±0.167)	–0.297 (±0.113)	0.964	0.104	42	18
7	24.200 (±0.223)	–2.240 (±0.309)	0.353 (±0.125)	0.537 (±0.114)	–0.626 (±0.093)	0.946	0.086	27	18
8	24.951 (±0.202)	–2.609 (±0.286)	0.245 (±0.115)	0.534 (±0.104)	–0.486 (±0.080)	0.970	0.069	47	17
9	24.362 (±0.215)	–2.304 (±0.298)	0.412 (±0.121)	0.499 (±0.114)	–0.508 (±0.091)	0.947	0.083	26	17
10	24.281 (±0.195)	–1.904 (±0.275)	0.250 (±0.110)	0.317 (±0.112)	–0.576 (±0.083)	0.944	0.075	23	16

^{a}Correlation coefficient, ^{b}Standard deviation,
^{c}Fisher's test, ^{d}Number of solvents included in the correlation

Considering the correlation coefficients (*R*) and number of solvents (*n*), the results of the regression analysis with this model are better than in the case of analysis with the Kamlet-Taft model. Based on Tables 5 and 6, it can be concluded that the most significant influence of the solvent on the absorption maxima of the examined compounds is its polarizability, while dipolarity has a very small influence.

Table 6. Percentages of solvatochromic parameters determined by Catalán's equation (1–10).

Compound	P_{SP} (%)	P_{SdP}(%)	P_B(%)	P_A(%)
1	62.5	10.3	11.4	15.8
2	67.0	7.2	8.3	17.5
3	61.2	6.6	17.6	14.7
4	76.1	5.8	8.9	9.2
5	83.2	4.5	6.8	5.5
6	69.4	6.7	17.9	5.9
7	59.6	9.4	14.3	16.7
8	67.3	6.3	13.8	12.5
9	61.9	11.1	13.4	13.6
10	62.5	8.2	10.4	18.9

As solvent polarizability increases, the π-system distribution is more affected, leading to a bathochromic shift, which is reflected by the negative *c* coefficient for all compounds. The independent *d* coefficient varies depending on the substituent patterns.The polarizability of the solvent have the most profound impact on the solvato chromic behavior of nitro-substituted compounds expressed as the highest values of *c.*

The signs of the coefficients obtained by the Kamlet-Taft and Catalán models are in good agreement. According to the Catalán model, non-specific interactions account for a larger portion of the solvatochromism of these dyes, while solvent basicity accounts for a smaller portion, in contrast to the correlation results produced by the Kamlet-Taft model.The differences between the results from these two models arise from the use of distinct solvatochromic probes to derive the parameters, which consequently reflect different solvent-solute interactions.In contrast, Catalán's empirical solvent scales are based on a well-defined reference system [38], offering a clearer understanding of the interactions between dye and solvent molecules.

In both cases, excellent linear dependences of the calculated wavenumbers on the experimental values were obtained and are given by the following equations:

The Kamlet-Taft model:

$$\nu_{calc} = 0.987\ \nu_{exp} + 0.292\ (R = 0.993,\ n = 141) \qquad (3)$$

The Catalán model:

$$\nu_{calc} = 0.988\ \nu_{exp} + 0.263\ (R = 0.994,\ n = 171) \qquad (4)$$

3.3. Structural aspects for the potential application of synthesized azo dyes as corrosion inhibitors

The ability of a particular organic compound to inhibit metal corrosion is influenced by two factors: the electronic distribution and the chemical structure [11]. Therefore, accurate determination of its structure is essential, as it serves as a fundamental prerequisite for understanding and optimizing its inhibitory performance. Adopting hydrazone form, investigated dyes are multifunctional organic compounds bearing electron-rich sites (Fig. 6), such as carbonyl (–C=O) and cyano (–CN) groups, along with various substituents on the phenyl ring. Substituent nature and position on the phenyl ring significantly affect dye electron distribution, influencing electron availability at oxygen and nitrogen of the carbonyl and cyano groups. Electron-donating groups like methoxy, particularly in *para*- and *ortho*-positions in phenyl ring, enhance ICT, increasing electron density at these sites which in turn could improve their ability to adsorb onto metal surfaces. The structural features of dyes allow them to act as polydentate and chelating ligands when adsorbed onto metal surfaces. Additionally, the presence of the phenyl ring can enhance corrosion inhibition by increasing electron density and improving surface coverage [11,41]. It can be suggested that the hydrazone form favors interaction with metal d-orbitals due to the increased electron density on nitrogen and oxygen atoms. It should also be noted that the increased interaction of free electrons from nitrogen atoms with d-orbitals of metals causes a greater ability to inhibit corrosion. Given these favorable properties, the investigated dyes could be considered a promising corrosion inhibitors for further research studies.

4. CONCLUSION

In this work, the synthesis of ten azo dyes 5--(substituted phenylazo)-3-cyano-6-hydroxy-4--methyl-2-pyridones of different substitution patterns in phenyl ring was carried out. The synthesized dyes adopt hydrazone form in the solid state and deuterated solvents. UV-Vis analysis indicates that solely hydrazone form exists in most of the solvents, while in amide solvents acid-base equilibrium exist. The position of absorption maxima of the hydrazone form is determined by the substitution patterns. UV-Vis spectra of the dyes are more affected by changes in the nature and position of the substituents than by alteration in solvent nature. LSER analysis revealed that the electronic distribution of the synthesized dyes is highly sensitive to the solvent environment, showing increased stabilization in solvents with higher polarizability. Excellent linear dependences of the calculated wavenumbers on the experimental values were obtained in both cases with a slightly better correlation obtained by Catalán model. It should be noted that the hydrazone form of these dyes favors interaction with the d-orbitals of metals due to the increased electron density on the nitrogen and oxygen atoms. Additionally, these compounds serve as a promising starting point for further investigation of their potential to act as corrosion inhibitors. Considering electronic distribution and electronic effect of substituents, dyes bearing electron-donating methoxy groups, particularly in the *ortho*- and para- positions, emerge as most promising candidates for corrosion inhibition.

Acknowledgements

This research has been financially supported by the Ministry of Science, Technological Development and Innovation of the Republic of Serba (Contract No: 451-03-136/2025-03/200287, 451-03-136/2025-03/200135, 451-03-136/2025-03/200178 and 451-03-136/2025-03/200116).

5. REFERENCES

[1] R.I. Alsantali, Q.A. Raja, A.Y.A. Alzahrani, A. Sadiq, N. Naeem, E.U. Mughal, M.M. Al-Rooqi, N.E. Guesmi, Z. Moussa, S.A. Ahmed (2022) Miscellaneous azo dyes: a comprehensive review on recent advancements in biological and industrial applications, Dyes Pigments, 199, 110050. https://doi.org/10.1016/j.dyepig.2021.110050

[2] K. T. Chung (2016) Azo dyes and human health: a review, J. Environ. Sci. Health C, 34(4), 233–261. https://doi.org/10.1080/10590501.2017.1284570.

[3] S. Benkhaya, S. M'rabet, A. El Harf (2020) Classifications, properties, recent synthesis and applications of azo dyes, Heliyon, 6(1), e03271. https://doi.org/10.1016/j.heliyon.2020.e03271

[4] M.S. Kim, B.D. Kwak, G.J. Min, S.H. Park, B.G. Oh, G. Bu, S.H. Cho, J.S. Park, O.Y. Jung (2019), Optical film having good contrast for polarizer and liquid crystal display device. KR Patent, No. *2019078428*.

[5] T. Kawakami, J. Sekiya (2000), Pyridone azo compounds, sublimation-type thermal transfer

pigments, and thermal transfer sheets therefrom. JP Patent, No. *2000239549*.

[6] S. Park, Y. Kang, H. Kwon, H. Kim, S. Kang, H. Lee, C. Yoon, J. Park (2022) Novel Yellow Azo Pyridone Derivatives with Different Halide Atoms for Image-Sensor Color Filters, Molecules, 27(19), 6601. https://doi.org/10.3390/molecules27196601

[7] M. Matsui, R. Aoki, D. Nishiwaki, Y. Kubota, K. Funabiki, J. Jin, T. Yoshida, S. Higashijimad, H. Miura (2015) Importance of fluorescence lifetimes for efficient indoline dyes in dye-sensitized solar cells, RSC Adv., 5, 57721–57724. https://doi.org/10.1039/C5RA09455K

[8] O.M.A. Khamaysa, Selatnia, H. Lgaz, A. Sid, H. Lee, H. Zeghace, M.Benahmed, I.H. Ali, P. Mosset (2021)Hydrazone-based green corrosion inhibitors for API grade carbon steel in HCl: Insights from electrochemical, XPS, and computational studies, Colloid. Surface A, 626, 127047. https://doi.org/10.1016/j.colsurfa.2021.127047

[9] D.S. Chauhan, P. Singh, M. Quraishi (2020) Quinoxaline derivatives as efficient corrosion inhibitors: current status, challenges and future perspectives, J. Mol. Liq., 320, 114387. https://doi.org/10.1016/j.molliq.2020.114387

[10] C. Verma, E.E. Ebenso, M.A. Quraishi, C.M. Hussain (2021) Recent developments in sustainable corrosion inhibitors: design, performance and industrial scale applications, Mat. Adv., 2, 3806-3850. https://doi.org/10.1039/d0ma00681e

[11] N.N. Hau, D.Q. Huong (2023) Effect of aromatic rings on mild steel corrosion inhibition ability of nitrogen heteroatom-containing compounds: Experimental and theoretical investigation, J. Mol. Struct., 1277, 134884. https://doi.org/10.1016/j.molstruc.2022.134884

[12] A.A. Abdulridha, M.A.A.H.Allah, S.Q. Makki, Y. Sert, H.E. Salman, A.A. Balaki(2020) Corrosion inhibition of carbon steel in 1 M H_2SO_4 using new Azo Schiff compound: Electrochemical, gravimetric, adsorption, surface and DFT studies, J. Mol. Liq., 315, 113690 https://doi.org/10.1016/j.molliq.2020.113690

[13] H.M. Elaryian, M.A. Bedair, A.H. Bedair, R.M. Abou shahba, A.E.S. Fouda (2022) Synthesis, characterization of novel coumarin dyes as corrosion inhibitors for mild steel in acidic environment: Experimental, theoretical, and biological studies, J. Mol. Liq., 346, 118310. https://doi.org/10.1016/j.molliq.2021.118310

[14] M.M. Youssif, M.N. El-Nahass, T.A. Fayed, H. A. El-Daly, M.M. El-Gamil, A.M. Eldesoky (2023) Tunable Anticorrosive Effects of Newly Synthesized Benzothiazole Azo Dyes by Potassium Iodide Synergism for Carbon Steel in 1 M HCl: Combined Experimental and Theoretical Studies, ACS Omega, 8(31), 28314-28332. https://doi.org/10.1021/acsomega.3c02105

[15] M. Alfakeer, R.N. Felaly, S.S. AlJuaid, D.F. Seyam, E.M. Mabrouk, M. Abdallah (2025) Synthesis and cyclic voltammetric studies of azo dye compounds derived from 1,5-dihydroxynaphthalene and their application as corrosion inhibitors for carbon steel in hydrochloric acid solution, Int. J. Electrochem. Sc. 20(1), 100892. https://doi.org/10.1016/j.ijoes.2024.100892

[16] K. Shalabi, H.M.A. El-Lateef, M.M. Hammouda, A.A. Abdelhamid (2024) Green Synthesizing and Corrosion Inhibition Characteristics of Azo Compounds on Carbon Steel under Sweet Conditions: Experimental and Theoretical Approaches, ACS Omega, 9(17), 18932–18945. https://doi.org/10.1021/acsomega.3c09072

[17] R. Ganjoo, C. Verma, A.Kumar, M.A. Quraishi (2023) Colloidal and interface aqueous chemistry of dyes: Past, present and future scenarios in corrosion mitigation, Adv. Colloid. Interfac., 311, 102832. https://doi.org/10.1016/j.cis.2022.102832

[18] M.S. Shihab, H.H. Al-Doori (2014) Experimental and theoretical study of [N-substituted] p-amino-azobenzene derivatives as corrosion inhibitors for mild steel in sulfuric acid solution, J. Mol. Struct. 1076, 658–663. https://doi.org/10.1016/j.molstruc.2014.08.038

[19] J. Lađarević, L. Radovanović, B. Božić, A. Mašulović, T. Lunić, Ž. Radovanović, J. Rogan, D. Mijin (2023) New copper (II) complexes derived from azo pyridone dyes: Structure characterization, thermal properties, and molecular docking studies, Appl. Organomet. Chem., 37(10), e7219. https://doi.org/10.1002/aoc.7219

[20] J. Mirković, J. Rogan, D. Poleti, V. Vitnik, Ž.Vitnik, G. Ušćumlić, D. Mijin (2014) On the structures of 5-(4-, 3- and 2-methoxyphenylazo)-3-cyano-1-ethyl-6-hydroxy-4-methyl-2-pyridone: An experimental and theoretical study, Dyes Pigments, 104, 160–168. https://doi.org/10.1016/j.dyepig.2014.01.007

[21] J. Mirković, B. Božić, V. Vitnik, Ž. Vitnik, J. Rogan, D. Poleti, G. Ušćumlić, D. Mijin (2018) Structural, spectroscopic and computational study of 5-(substituted phenylazo)-3-cyano-1-ethyl-6-hydroxy-4-methyl-2-pyridones, Color. Technol., 134(1), 33–43. https://doi.org/10.1111/cote.12321

[22] A. Jezuita, P.A. Wieczorkiewicz, H. Szatylowicz, T.M. Krygowski (2021)Effect of the Solvent and Substituent on Tautomeric Preferences of Amine-Adenine Tautomers, ACS Omega, 6(29),18890–18903. https://doi.org/10.1021/acsomega.1c02118

[23] J.M. Dostanić, D.R. Lončarević, P.T. Branković, Cvetković, D. Jovanović, D.Ž. Mijin (2011) Influence of process parameters on the photodegradation of synthesized azo pyridone dye in TiO2 water suspension under simulated sunlight, J. Environ. Sci. Heal. A, 46(1), 70–79. https://doi.org/10.1080/10934529.2011.526905

[24] J.M. Bobbit, D.A. Scola (1960) Synthesis of Isoquinoline Alkaloids. II. The Synthesis and

Reactions of 4-Methyl-3-pyridinecarboxaldehyde and Other 4-Methyl-3-substituted Pyridines, J. Org. Chem., 25(4), 560–564. https://doi.org/10.1021/jo01074a018

[25] Y.P. Wang, I.J. Wang (1990) Photofading of Azo Pyridone Dyes in Solution: Part II: Substituent Effects on the UV Absorption Spectra and Photostability of 3-(mono- and di-substituted arylazo)-2-hydroxy-4-methyl-5-cyano-6-pyridone in N,N-dimethylformamide, Text. Res. J.,60(9), 519–524.https://doi.org/10.1177/004051759006000090

[26] Y.P. Wang, I.J. Wang (1991) Effects of Substituent and Aggregation on the Photofading of Some Azo Pyridone Dyes on Polyester Substrates, Text. Res. J., 61(3), 162–168. https://doi.org/10.1177/004051759106100308

[27] J. Dostanić, N. Valentić, G. Ušćumlić, D. Mijin (2011) Synthesis of 5-(substituted phenylazo)-6-hydroxy-4-methyl-3- -cyano-2-pyridones from ethyl 3-oxo-2-(substituted phenylazo)butanoates, J. Serb. Chem. Soc.76(4), 499–504. https://doi.org/10.2298/JSC100618044D

[28] C.C. Chen, I.J. Wang (1991) Synthesis of some pyridone azo dyes from 1-substituted 2-hydroxy-6-pyridone derivatives and their colour assessment, Dyes Pigments,15(1), 69–82. https://doi.org/10.1016/0143-7208(91)87008-B

[29] N. Ertan, P. Gurkan (1997) Synthesis and properties of some azo pyridone dyes and their Cu(II) complexes, Dyes Pigments, 33(2), 137–147. https://doi.org/10.1016/S0143-7208(96)00044-7

[30] C.M. Moldovan, O. Oniga, A. Pârvu, B. Tiperciuc, P. Verite, A. Pîrnău, O. Crişan, M. Bojiţă, R. Pop (2011)Synthesis and anti-inflammatory evaluation of some new acyl-hydrazones bearing 2-aryl-thiazole, Eur. J. Med. Chem., 46(2), 526–534. https://doi.org/10.1016/j.ejmech.2010.11.032

[31] A. Alimmari, D. Mijin, R. Vukićević, B. Božić, N. Valentić, V. Vitnik, Ž. Vitnik, G. Ušćumlić (2012) Synthesis, structure and solvatochromic properties of some novel 5-arylazo-6-hydroxy-4-phenyl-3-cyano-2-pyridone dyes, Chem. Cent. J., 6, 71. https://doi.org/10.1186/1752-153X-6-71

[32] A.D. Mašulović, J.M. Lađarević, A.M. Ivanovska, S.Lj Stupar, M.M. Vukčević, M.M. Kostić, D.Ž. Mijin (2021) Structural insight into the fiber dyeing ability: Pyridinium arylazo pyridone dyes, Dyes Pigments, 195, 109741. https://doi.org/10.1016/j.dyepig.2021.109741

[33] B.Đ. Božić, A.S. Alimmari, D.Ž. Mijin, N.V. Valentić, G.S. Ušćumlić (2014) Synthesis, structure and solvatochromic properties of novel dyes derived from 4-(4-nitrophenyl)-3-cyano-2-pyridone, J. Mol. Liq., 196, 61–68. https://doi.org/10.1016/j.molliq.2014.03.026

[34] Q. Peng, M. Li, K. Gao, L. Cheng (1991) Hydrazone-azo tautomerism of pyridone azo dyes: Part II: Relationship between structure and pH values, Dyes Pigments,15(4), 263–274. https://doi.org/10.1016/0143-7208(91)80011-W

[35] J. Lađarević, B. Božić, L. Matović, B. Božić Nedeljković, D. Mijin (2019) Role of the bifurcated intramolecular hydrogen bond on the physicochemical profile of the novel azo pyridone dyes, Dyes Pigments, 162, 562–572, https://doi.org/10.1016/j.dyepig.2018.10.058

[36] M.J. Kamlet, J.M. Abboud, M.H. Abraham, R.W. Taft (1983) Linear Solvation Energy Relationships. 23. A Comprehensive Collection of the Solvatochromic Parameters, π*, α, and β, and Some Methods for Simplifying the Generalized Solvatochromic Equation, J. Org. Chem., 48(17), 2877–2887. https://doi.org/10.1021/jo00165a018.

[37] Y. Marcus (1993)The properties of organic liquids that are relevant to their use as solvating solvents, Chem. Soc. Rev.,22, 409–416. https://doi.org/10.1039/CS9932200409

[38] J. Catalán (2009) Toward a Generalized Treatment of the Solvent Effect Based on Four Empirical Scales: Dipolarity (SdP, a New Scale), Polarizability (SP), Acidity (SA), and Basicity (SB) of the Medium, J. Phys. Chem. B, 113(17), 5951–5960. https://doi.org/10.1021/jp8095727

[39] F.A.S. Chipem, A. Mishra, G. Krishnamoorthy (2012) The role of hydrogen bonding in excited state intramolecular charge transfer. Phys. Chem. Chem. Phys. 14, 8775–8790. https://doi.org/10.1039/C2CP23879A

[40] J. Lađarević, D. Mijin, L. Antonov (2020) Tautomerism in 8-(phenyldiazenyl)quinolin-5-ol: An attempt for pH activated rotary switch, Dyes Pigments, 182, 108628. https://doi.org/10.1016/j.dyepig.2020.108628

[41] P. Wang, Y. Song, Z. Tang, Z. Li, K.R. Ansari, M. Talha, A. Singh, Y. Lin (2024) Systematic Analysis of the Effect of Benzene on the Corrosion Inhibition Performance of Imidazoline Derivatives: Experimental and Theoretical Research,Langmuir, 40(51), 26903 – 26917. https://doi.org/10.1021/acs.langmuir.4c03256

IZVOD

TAUTOMERIJA I SOLVATOHROMIZAM 5-(SUPSTITUISANIH FENILAZO)-3-CIJANO-6-HIDROKSI-4-METIL-2-PIRIDONA

U okviru rada, sintetisano je deset molekula 5-(supstituisanih fenilazo)-3-cijano-6-hidroksi-4-metil-2-piridona, koji se međusobno razlikuju prema položaju i prirodi supstituenata na fenilnom prstenu. Sintetisane boje su detaljno okarakterisane tačkom topljenja i spektroskopskim tehnikama (FT-IR, NMR i UV-Vis). Budući da su elektronska gustina i hemijska struktura organskih molekula od ključne važnosti za njihovu primenu kao inhibitora korozije, ovaj rad se fokusira na određivanje specifičnog tautomernog oblika boja u čvrstom stanju i različitim rastvaračima. Apsorpcioni spektri su određeni u 21 rastvaraču različitih svojstava. Uticaj rastvarača na apsorpcione maksimume određen je LSER metodom (Kamlet-Taft i Catalan modeli). U oba slučaja dobijene su odlične linearne zavisnosti izračunatih talasnih brojeva od eksperimentalnih vrednosti. LSER analiza je pokazala da je solvatohromizam ovih boja prvenstveno određen nespecifičnim interakcijama između molekula boje i rastvarača. Na osnovu analize efekata supstituenata na raspored elektronske gustine ovih boja, boje sa metoksi-grupom u –orto i -para položajima fenilnog jezgra izdvojile su se kao potencijalni kandidati za inhibitore korozije.

Ključne reči*: piridonske azo boje, tautomerija, hidrazon, LSER*

Naučni rad
Rad primljen: 06.03.2025.
Rad korigovan: 28.05.2025.
Rad prihvaćen: 02.06.2025.

Jelena Lađarević	https://orcid.org/ 0000-0002-5554-7295
Bojan Božić	https://orcid.org/0000-0001-9910-2741
Dušan Mijin	https://orcid.org/0000-0001-5691-2971
Luka Matović	https://orcid.org/0000-0003-4945-7776
Nataša Valentić	https://orcid.org/0000-0002-5466-7738
Evica Ivanović	https://orcid.org/0000-0002-5055-4568
Nebojša Banjac	https://orcid.org/0000-0002-4359-6276

Farzet Bikić, Dejana Kasapović

Faculty of Engineering and Natural Sciences, University of Zenica, Zenica, Bosnia and Herzegovina

Scientificpaper
ISSN 0351-9465, E-ISSN 2466-2585
https://doi.org/10.62638/ZasMat1400

Zastita Materijala 67 (1)
133 - 138 (2026)

Investigation of pitting corrosion in austenitic stainless steels AISI304L and AISI317L: With particular emphasis on the role of molybdenum

ABSTRACT

Austenitic stainless steels are among the most widely used stainless steel grades, with the American Iron and Steel Institute (AISI) 300 series being particulary common.Beginning with the base alloy 304 (Fe-19Cr-10Ni), the incorporation of molybdenum enhances pitting corrosion resistance (2-3 wt.% in AISI 316 and 3-4 wt.% in AISI 317). To prevent sensitisation caused by chromium depletion during welding and other thermal processes, and the resulting risk of intergranular corrosion, low-carbon variants such as 304L, 316L, 317L (with carbon content ≤ 0.03 wt.%) are employed. Alternatively, stabilization can be achieved by alloying with titanium (AISI 321) or niobium and tantalum (AISI 347), which bind carbon at elevated temperatures. Chromium contributes to oxidation resistance, whilst nickel improves ductility and workability at ambient conditions. This paper investigates the pitting corrosion behaviour of low-carbon austenitic stainless steels, specifically AISI317Land AISI304L. The experimental results are presented through cyclic potentiodynamic polarization curves. Findings indicate that the severity of pitting corrosion decreases with reduced temperatures in a 1.5% NaCl solution and that the presence of molybdenum in AISI317L notably enhances corrosion resistance.

Keywords:*austenitic stainless steels, molybdenum, pitting corrosion, temperature, chemical composition, cyclic polarization curves*

1. INTRODUCTION

Austenitic stainless steels are among the most commonly applied stainless steeltypes. Within this category, the American Iron and Steel Institute (AISI) 300 series alloys are especially prevalent.The base alloy, AISI 304 (Fe-19Cr-10Ni), may be modified through the addition of molybdenum to improve pitting corrosion resistance. Typical molybdenum content ranges from 2 to 3 wt.% in AISI316, and from 3 to 4 wt.% in AISI 317. Sensitisation, which arises from chromium depletion during welding or heat treatment processes and can lead to intergranular corrosion, may be avoided by using low-carbon variants such as 304L, 316L, 317L, where the carbon content is limited to a maximum of 0.03 wt.%.Alternatively, stabilisation can be achieved by alloying with titanium (AISI 321) or with niobiumand tantalum (AISI 347), which facilitate the formation of stable carbides at elevated temperatures. In addition to corrosion restance, chromium also enhaces oxidation stability, while nickel improves ductility and workability at ambient temperatures[1]. Stainless steels are valued not only for their corrosion resistance, but also for their mechanical strength, aesthetic appeal, and structuralversatility [2].

Pitting corrosion of stainless steel is manifested by the rapid growth of current flow after achieving specific values of anode potential, known as the pitting potential, after pits formation [3]. It can be prevented if the anions present in solution hinder the adsorption of chlorides, or push them from the metal surface. The introduction of competing anions containing chlorides (i.e. chromate, nitrate, environmentally-friendly organic compounds etc.) in the solution moves the value of pitting potential in anodic area. The resistance to pitting corrosion can be enhanced by increasing the content of chromium, molybdenum, and nitrogen in the alloy composition. Among these elements, molybdenum is particularly effective and is commonly added to stainless steels for this purpose[4].

This study focuses on the pitting corrosion behaviour of low-carbonaustenitic stainless steels,

---

*Corresponding author: Farzet Bikić
E-mail: farzet.bikic@unze.ba

Paper received: 09. 03. 2025.
Paper accepted: 25. 05. 2025.

specifically AISI 304 L and AISI 317 L. The high corrosion resistance of stainless steel is attributed to the formation of a protective passive film on its surface. The properties of this film have been the subject of extensive investigation.Using direct imaging of native passive film on 304 stainless steels, Hamada demonstrated the enrichment of chromium in the film and the accumulation of nickel in the matrix side closest to the passive film/matrix interface [5].While this oxide layer is capable of rapid self-repair in clean acid environments, its protective capacity diminishes in the presence of aggressive ions, particularly chlorides, and under elevated temperatures [6].

2. EXPERIMENTAL PART

Low-carbon gradesof austenitic stainless steels, specifically AISI304L and AISI317L, were selected for pitting corrosion testing. For the sake of clarity and brevity, these materials will hereafter be referred to as304L and 317L, respectively. The nominal chemical compositions of both steels are given in Table 1.

Pitting corrosion testing of the selected austenitic stainless steels was performed at three temperatures: 20°C, 30°C, and 40°C, in a 1.5% NaCl solution. The experiments were conducted in a corrosion cell in accordancewith ASTM G5 standard, using a Princeton Applied Research potentiostat/galvanostat (model 263A-2) operated viaPowerCORR® software [7]. To evaluate the susceptibility to pitting corrosion, the electrochemical direct current (DC)cyclic polarization method wasemployed.

Table 1. Chemical composition of the tested austenitic stainless steels

Chemical element	Chemical composition, mas.%	
	AISI 304L	AISI 317L
C	≤ 0,03	≤ 0,03
Si	≤ 1,00	≤ 1,00
Mn	≤ 2,00	≤ 2,00
P_{max}	0,045	0,045
S	≤0,015	≤0,015
N	≤ 0,11	≤ 0,11
Cr	18 -20	17,5-19,5
Mo	-	3-4
Ni	10-12	13-16

This technique includes scanning the electrode potential in the anodic direction up to a predefined vertex potential, followed by a reverse scan once a critical current threshold has been reached. The potentialscan rate was maintained at 0.5 mVs^{-1}. Pitting corrosion in stainless steels is typically observed as a sudden increase in current upon reaching a specific anodic potential, known as the pitting potential (Epitt), as illustrated in Figure 1. This potential marks the onset of pit formation and corresponds to the point at which the current on the polarization curve beginsto rise.According to the present understanding of the pitting corrosion process the Epitt represents a critical threshold value, where metastable pits nuclei within the passive state of the stainless steel may be transformed into stable growingpits when the passive formation breaks down [8].

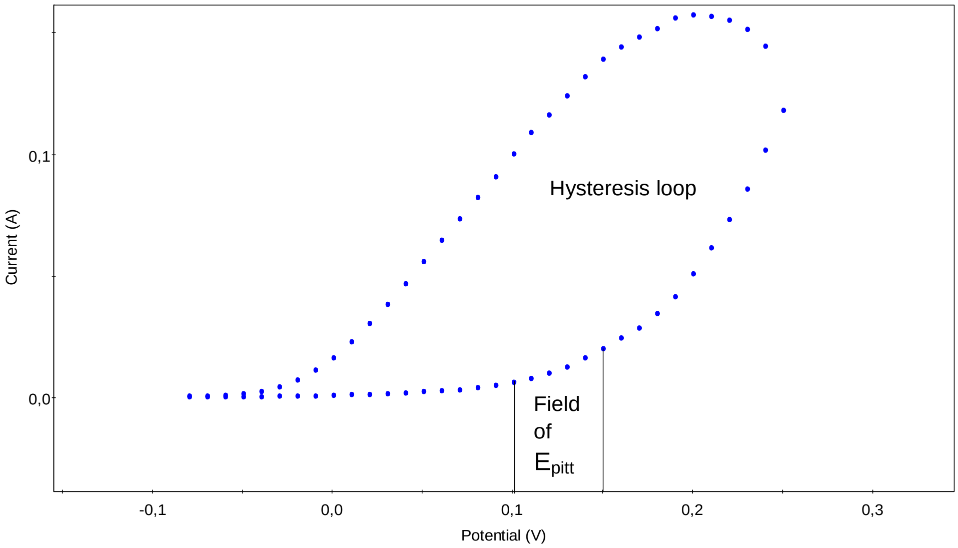

Figure 1. Cyclic polarization curve [3]

Negativepitting potential values indicate a greater susceptibility of stainless steels to pitting corrosion. The area enclosed by the hysteresis loopon a cyclic polarization curve serves as a qualitative measure of pitting corrosion severity (Figure 1). Alarger loop area generally corresponds to a higher intensity of pitting corrosion.

3. RESULTS AND DISCUSSION

The results of the pitting corrosion tests for the investigated stainless steels are given in Figures 2 to 6, and summarizedin Table 2. Figures 2 to 6 show cyclic polarization curves for 304L and 317L were obtained in the1.5% NaCl solution at three different temperatures (20 °C, 30 °C and 40 °C). Table 2 provides the corresponding pitting potential (Epitt) valuesin the specified solution and temperatures.Figures 2 and 3 specifically show the effect of temperature on the pitting corrosion behaviour of austenitic stainless steels 304L and 317L.

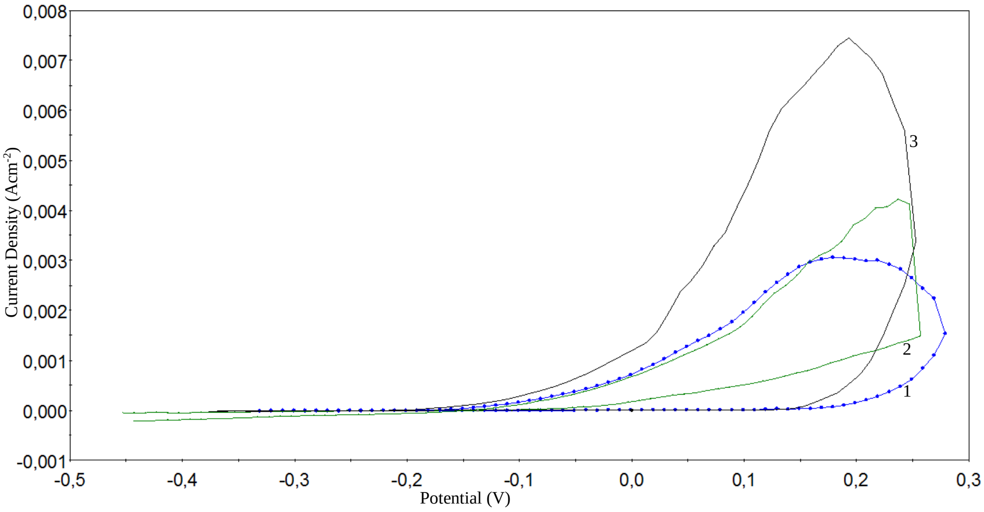

Figure 2. Cyclic polarization curves of type 304L stainless steel (1- 20 °C, 2 - 30 °C, 3 - 40 °C)

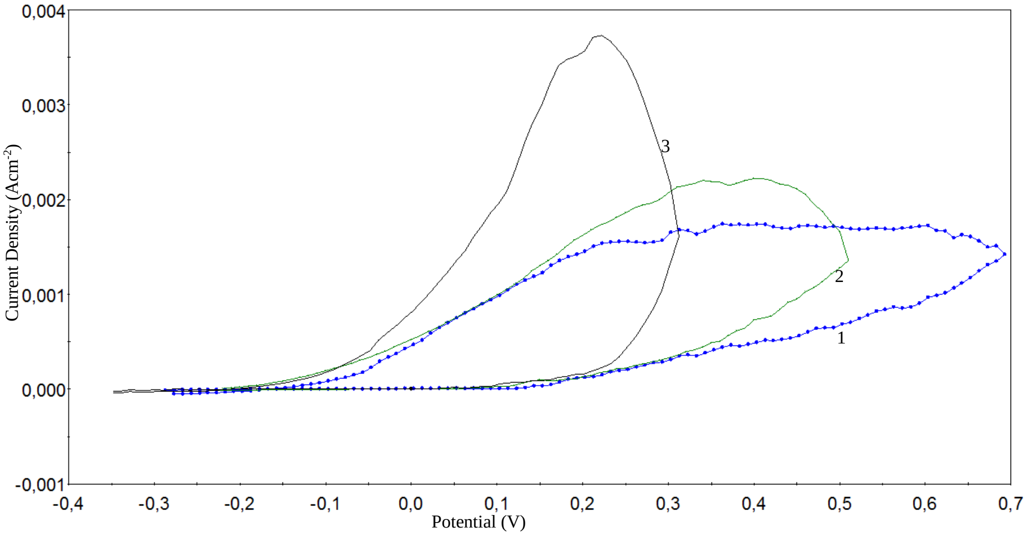

Figure 3. Cyclic polarization curves of type 317L stainless steel (1- 20 °C, 2 - 30 °C, 3 - 40 °C)

Temperature plays a significant role in the corrosionbehaviour of stainless steels. In general, a rise in temperature leads to a decrease in corrosion resistance [9]. Escrivàreported that passive films formed at elevated temperatures are likely to be more defective [10]. This was beneficial for the mitigation of aggressive ions inside the passive film and consequently could accelerate the dissolution process and the exchange kinetics between the electrode surface and the electrolyte [11].

The results shown in Figures 2 and 3 indicate that the severity of pitting corrosion in both tested austenitic stainless steels, 304L and 317L, increases with rising temperature in the 1.5% NaCl solution.

Figures 4, 5 and 6 illustrate the influence of chemical compositionon pitting corrosionbehaviour in 304L and 317L,withparticular emphasis on the role of molybdenum.

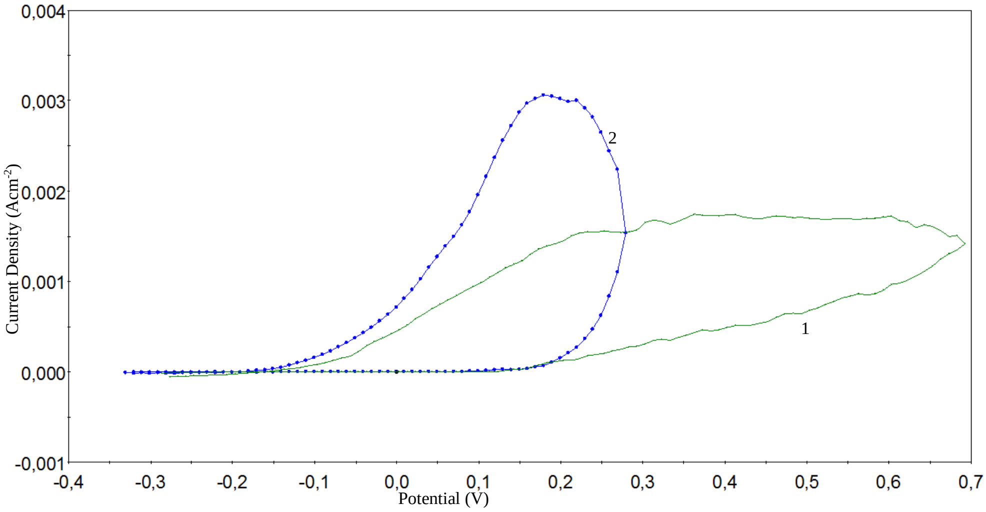

Figure 4. Cyclic polarization curves of stainless steels treated at 20 °C (1 - 317L, 2 - 304L)

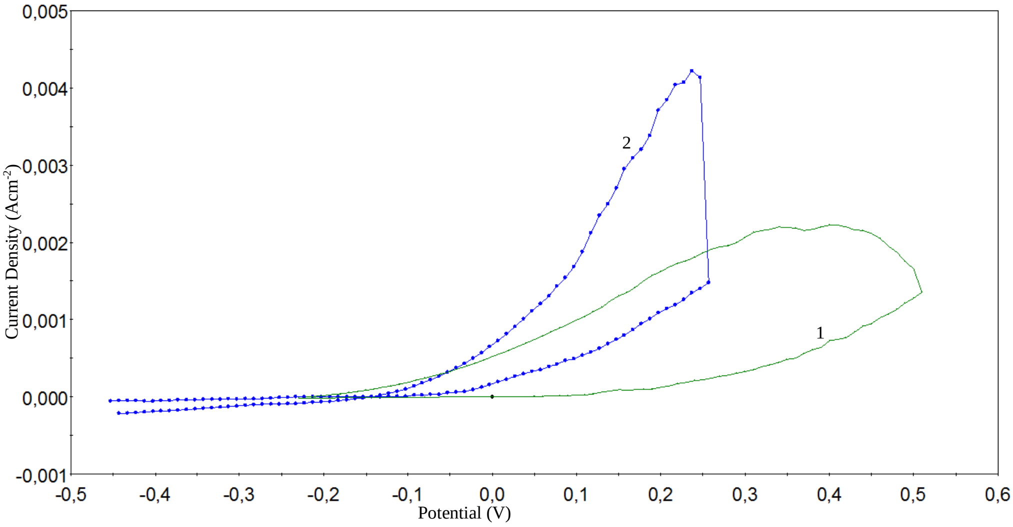

Figure 5. Cyclic polarization curves of stainless steels treated at 30 °C (1 - 317L, 2 - 304L)

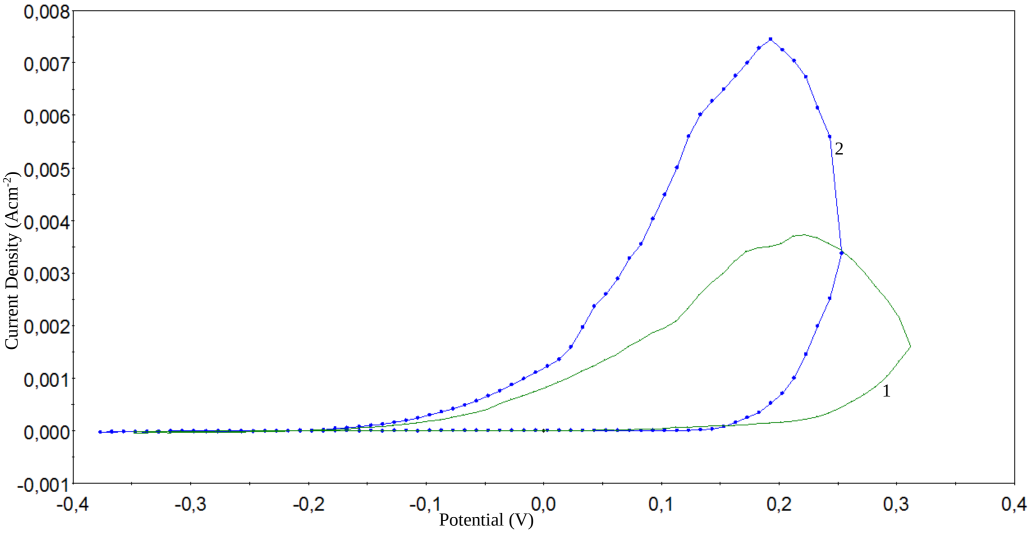

Figure 6. Cyclic polarization curves of stainless steels treated at 40 °C (1 - 317L, 2 - 304L)

Table 2. Pitting potential of tested stainless steels

t, °C	AISI	Pitting potential,± 10 mv
20	304L	199
	317L	233
30	304L	27
	317L	220
40 6	304L	163
	317L	212

A comparative analysis of the hysteresis loop areas (Figures 4, 5 and 6) and the measured pitting potentials(Table 2),reveals that all the tested samples of 317L exhibit lowerpitting corrosion activity than those of 304L.Samples of 317L austenitic stainless steel have a smaller hysteresis loop area (Figures 4, 5 and 6) and more positive pitting potential values (Table 2) compared to samples of 304L stainless steel. This difference in corrosion performance can be attributed to the presence of molybdenum in the chemical compositionof 317L, which is absent in 304 L. Given that the primary compositional distinction between these two steel grades lies in the molybdenum content, it reasonable to associate the enhanced corrosion resistance of 317L with alloying effect of molybdenum. In general, the addition of molybdenum to wrought austenitic stainless steels is known to improve their corrosion resistance [12].

4. CONCLUSIONS

Based on the conducted tests examining the influence of temperature and chemical composition, particularly molybdenum content, on the pitting corrosionbehaviour of austenitic stainless steels, the following conclusions can be drawn:

- An increase in the temperature of the 1.5% NaCl solution leads to a higher rate of pitting corrosion in both tested steel grades,304L and 317L
- 317Ldemonstrates superior resistance to pitting corrosion compared to 304L. This improved performance is attributed to the presenceof molybdenum in the 317 alloy, which is absent in the composition
- Overall, the results confirm that the addition of molybdenum enhances the pitting corrosion resistance of austenitic stainless steels.

5. REFERENCE

[1] F. King (2009) Corrosion Resistance of Austenitic and Duplex Stainless Steels in Environments Related to UK Geological Disposal, A Report to NDA RWM, QuintessaLimited, QRS-1384CR1,Version 1.2, UK.

[2] E. Kikuti, R. Conrrado, N. Bocchi, S.R. Biaggio Rocha, R.C. Filho (2004) Chemical and Electrochemical Coloration of Stainless Steel and Pitting Corrosion Resistance Studies, J. Braz. Chem. Soc., 15(4), 472-480.

[3] F.Bikić, D. Mujagić (2014) Investigation of possibility for reducing AISI 303 stainless steel pitting corrosion by microalloying with boron or zirconium, Bulletin of the Chemists and Technologists of Bosnia and Herzegovina, 42, 41 -46.

[4] ASM International (1992) Handbook Volume 13, Corrosion, ASM International Committee, USA.

[5] E. Hamada, K. Yamada, M. Nagoshi, N. Makiishi, K. Sato, T. Ishii, K. Fukuda, S. Ishikawa, T. Ujiro (2010) Direct imaging of native passive film on Stainless steel by aberration corrected STEM, Corros. Sci., 52, 3851– 3854.

[6] C. Q. Jessen (2011) Stainless Steel and Corrosion, Damstahl a/s, Denmark.

[7] ASTM G5 (1994) Standard Reference Test Method for Making Potentiostatic and Potenciodynamic Anodic Polarization Measurements.

[8] R.T. Loto(2013) Pitting corrosion evaluation of austenitic stainless steel type 304 in acid chloride media, J. Mater. Environ. Sci., 4 (4), 448-459.

[9] Z.Wang, Z. Feng, L. Zhang (2020) Effect of high temperature on the corrosion behavior and passive film composition of 316L stainless steel in high H_2S-containing environments, Corrosion Science, 174, 08844.

[10] C. Escrivà-Cerdán, E. Blasco-Tamarit, D.M. García-García, J. García-Antón, A. Guenbour (2012) Passivation behaviour of Alloy 31 (UNSN08031) in polluted phosphoric acid at different temperatures, Corros. Sci.,56 ,114–122.

[11] H.Iken, R. Basseguy, A. Guenbour, A.B. Bachir (2007) Classic and local analysis of corrosionbehaviour of graphite and stainless steels in polluted phosphoric acid, Electrochim.Acta, 52, 2580–2587.

[12] A. Szewczyk-Nykiel, (2015) The influence of molibdenum on corrosion resistance of sintered austenitic stainless steels, Tehnical Transactions Mechanics, 4-M (26), 131–142.

IZVOD

ISPITIVANJE PITTING KOROZIJE AUSTENITNIH NEHRĐAJUĆIH ČELIKA TIPOVA AISI304L I AISI317L: S POSEBNIM NAGLASKOM NA ULOGU MOLIBDENA

Austenitni nehrđajući čelici su među najčešće korišćenim vrstama nehrđajućeg čelika, a posebno je uobičajena serija 300 Američkog instituta za gvožđe i čelik (AISI). Počevši od osnovne legure 304 (Fe-19Cr-10Ni), ugradnja molibdena poboljšava otpornost na koroziju u obliku tačkaste korozije (2-3 tež.% kod AISI 316 i 3-4 tež.% kod AISI 317). Da bi se sprečila senzibilizacija izazvana smanjenjem hroma tokom zavarivanja i drugih termičkih procesa, i rezultirajući rizik od interkristalne korozije, koriste se varijante sa niskim sadržajem ugljenika kao što su 304L, 316L, 317L (sa sadržajem ugljenika ≤ 0,03 tež.%). Alternativno, stabilizacija se može postići legiranjem sa titanijumom (AISI 321) ili niobijumom i tantalom (AISI 347), koji vezuju ugljenik na povišenim temperaturama. Hrom doprinosi otpornosti na oksidaciju, dok nikl poboljšava duktilnost i obradivost u ambijentalnim uslovima. Ovaj rad istražuje ponašanje niskougljeničnih austenitnih nehrđajućih čelika, posebno AISI317L i AISI304L, usled tačkaste korozije. Eksperimentalni rezultati su predstavljeni kroz ciklične potenciodinamske polarizacione krive. Rezultati ukazuju na to da se intenzitet tačkaste korozije smanjuje sa smanjenjem temperature u 1,5% rastvoru NaCl i da prisustvo molibdena u AISI317L značajno poboljšava otpornost na koroziju.

Ključne reči: *Austenitni nehrđajući čelici, molibden, tačkasta korozija, temperatura, hemijski sastav, ciklične polarizacione krive*

Naučni rad
Rad primljen:09.03.2025.
Rad prihvaćen: 25.05.2025.

Farzet Bikić: https://orcid.org/0009-0002-9797-8883
Dejana Kasapović: https://orcid.org/0009-0003-2066-6053

Nnaemeka Uwaezuoke, Emmanuel Ojecho,*
Onyebuchi Ivan Nwanwe, Stanley Ibuchi Onwukwe

Department of Petroleum Engineering, Federal University of Technology, Owerri, Nigeria.

Scientific paper
ISSN 0351-9465, E-ISSN 2466-2585
https://doi.org/10.62638/ZasMat1280

Zastita Materijala 67 (1)
139 - 148 (2026)

Batch adsorption using *C. aurantiifolia* peel as bio-adsorbent for the treatment of heavy metals in produced water from petroleum production

ABSTRACT

Most produced water treatment techniques are ineffective in reducing impurities and concentration of metals. This causes difficulty in achieving disposal levels. The effectiveness of a biomaterial for produced water treatment for a Niger Delta oilfield is presented. The produced water sample was collected from a Niger Delta oilfield and preserved at ambient temperature of 28 °C, further characterized, and the result showed lead (0.0082 mg/l). nickel (0.0084 mg/l), cadmium (0.0051 mg/l), copper (0.94 mg/l), iron (0.26 mg/l), magnesium (0.068 mg/l), chromium (0.0071 mg/l), zinc (1.17 mg/l) and manganese (0.053 mg/l). Citrus aurantiifolia peel was used as an adsorbent and it was purchased from a local market in Eziobodo, Nigeria. After peeling, the bioadsorbent (lime peel) was prepared by thoroughly washing it with distilled water to get rid of any extraneous materials (such as dirt or impurities) stuck on its surface. The washed lime peel was then cut to pieces and sun-dried for at least 48 hours, after which it was also oven-dried after preheating to 55°C to prevent burning for 2-3 hours. The dried peels were then milled into finer particles, and packed in high-density polyethylene (HDPE, 0.77 mm thickness) bags. Experiments on batch adsorption were used to determine the effects of time of contact, dose of adsorbent, and speed of agitation. The samples were treated with the bioadsorbent on the magnetic stirrer in which various adsorption tests were carried out at different time intervals to obtain the optimum desired results for the removal of the metals. The Atomic Absorption Spectrophotometer technique was used in the study where the digested samples were analyzed for heavy metal content. Their concentrations were reduced after the treatments to Pb (0.0016 mg/l), Ni (0.0021 mg/l), Cd (0.00013 mg/l), Cu (0.019 mg/l), Fe (0.014 mg/l), Mg (0.0016 mg/l), Cr (0.0010 mg/l), Zn (0.21 mg/l), and Mn (0.0015 mg/l). The percentage of adsorption of Pb, Ni, Cd, Cu, Fe, Mg, Cr, Zn, and Mn were 80.49%, 75.00%, 97.45%, 97.98%, 94.62%, 97.65%, 85.92%, 82.05%, and 97.17%, respectively. The Citrus aurantiifolia peels exhibited potential as adsorbent for heavy metals treatment in produced water.

Keywords: *heavy metals, produced water, Citrus aurantiifolia peel, bio-adsorbent*

1. INTRODUCTION

Produced water comes from the reservoir rock [1], and often produced with hydrocarbons [2]. It could also be injected water containing production chemicals and formation water [3], and the contents determine the treatment and handling method [1]. Organic and inorganic substances such as dissolved gases, formation minerals, production chemicals, dispersed oil compounds, and solids (asphaltenes, waxes, formation solids, and corrosion products) can also be found [2].

Permission is often given due salinity, treating chemicals, heavy metals, and radionuclides [2]. It can cause erosion [5] and makes up approximately 80% of residuals and wastes obtained during gas production [6]. For its prevention, (i) use of technologies to control its production, (ii) recycle and reuse, and if neither of the two steps above is feasible, (iii) disposal of the produced water is considered [2] are considered.

The highest estimates include the USA (21,000,000,000 bbl/yr.), Oman (1,840,000,000 bbl/yr.), Australia (207,570,000 bbl/yr.), Iraq (105,853,190 bbl/yr.), and China (45,917,000 bbl/yr.) [4]. Various management options exist [7], but re-injection is common [8]. Its use include petroleum industry and beyond [9], and quality values are given (Table 1).

---

*Corresponding author: Nnaemeka Uwaezuoke
E-mail: nnaemeka.uwaezuoke@futo.edu.ng
Paper received: 28.03. 2025.
Paper accepted: 07. 05.2025.

Table 1. Common produced water quality values in comparison with some criteria 10].

Parameter	End-use criteria (ppm)			CBM water	Non-CBM (Conventional gas well) water
	Drinking	Irrigation	Livestock		
pH	6.5-8	-	6.5-8	7-8	6.5-8
TDS, mg/L	500	2,000	5,000	4,000-20,000*	20,000-100,000
Benzene, ppb	5	5	5	<100	1,000-4,000
SAR*	1.5-5	6	5-8	Highly varied	Highly varied
Na^+, mg/L	200	See SAR	2,000	500-2,000	6,000-35,000
Barium, mg/L	-	-	-	0.01-0.1	0.1-40
Cl^-, mg/L	250	-	1,500	1,000-2,000	13,000-65,000
HCO_3^-, mg/L	-	-	-	150-2,000	2,000-10,000

*Total Dissolved Solids (TDS) range estimated for the lower 50 percentile

**Sodium Absorption Ratio (SAR) – a function of a ratio of Na to Ca and Mg levels

The water quality standards are comparatively lower for conventional gas wells when compared to drinking, livestock and other produced water reuse methods [11]. The heavy metals occur naturally in the subsurface and can be divided into three groups, (i) toxic metals; Sn, Co, As, Cd, Ni, Cu, Zn, Pb, Cr, Hg, etc, (ii) precious metals; Au, Ag, Ru, Pt, Pd etc, and (iii) radionuclides; Ra, U, Th, Am, etc. [1]. They can have effects on the soil, plants, aquatic environment, and human health [12]. Table 2 shows common heavy metals with maximum contamination levels (MCL) in water and their harmful effects.

Table 2. Harmful effects of the heavy metals [13]

S/N.	Heavy Metal	Maximum Contamination Level (mg/L)	Harmful Effects
1	Cu	0.25	liver damage, convulsions, insomnia.
2	Zn	0.80	skin irritation, nausea, depression, anaemia, and neurological symptoms.
3	Ni	0.20	carcinogen, dermatitis, gastrointestinal disorder, lung and kidney damage.
4	Cr	0.05	carcinogen, nausea, diarrhea.
5	Cd	0.01	carcinogen, kidney dysfunction.
6	As	0.05	skin problems, visceral cancer.
7	Pb	0.006	central nervous system damage, cerebral disorders, kidney, liver, and reproductive system dysfunction.
8	Hg	0.00003	neurotoxin, kidney dysfunction, circulatory and neurological disorders.

Adsorption is generally used for the treatment process because adsorbents can easily be overloaded with organics [14]. Also, adsorption isotherms and models give an estimate of the amount of adsorbate or solutes that have been adsorbed after adsorption has taken place per unit weight at constant temperature. The common models are Langmuir and Freundlich isotherms. Others include Redlich and Peterson, Sips, Radke and Prausnitz, Toth, and Koble, and Corrigan [13] [15]. Adsorbents could be natural or synthetic. Natural adsorbents include clays, charcoal, ores, zeolites, and minerals. Synthetic adsorbents are commonly prepared from agricultural and industrial wastes, etc. Some commonly used agricultural wastes and industrial wastes for the removal of heavy metals are shown in Table 3 and Table 4, respectively.

Adsorbent selection factors include high adsorbent capacity, low cost, and its effectiveness for a wide range of pollutants. Four identified efficient mechanisms for the adsorption of impurities/pollutants include physisorption, chemisorption, ion exchange, and precipitation. Similarly, functional groups in organic compounds [16] on carbon surfaces, such as *Citrus aurantiifolia* peel. These heteroatoms are surface functional groups [17]. Hydrogen bonding also bond electrostatically to other compounds [18]. Solute are also soluble due to forces that are large enough [19]. The oxygen functional groups determine the surface properties of a bio-adsorbent, and therefore the quality of the adsorbent [20]. The carboxyl and hydroxyl groups are great contributors to heavy metals adsorption such as Ni, Pb, Hg, Cd, and Cr ions onto a variety of carbon adsorbents such as the *Citrus aurantiifolia* [21].

Table 3. Common agricultural wastes for heavy metal removal [13]

S/N.	Type of Wastewater	Type of Adsorbent	Adsorbent Dosage (g)	Metal Ion	Amount Adsorbed (mg/g)	Contact Time (min)	Temperature (^{o}C)
1.	hospital wastewater	cassava peels	10.0	Pb^{2+} Cu^{2+}	5.80 8.00	20-120	39.85
2.	aqueous solution	ash gourd peel powder	6.0	Cr^{6+}	18.70	40-60	28.0
3.	aqueous solution	barley straw	1.0	Cu^{2+}	4.64	120	25.0
4.	aqueous solution	cashew nut	3.0	Ni^{2+}	18.86	30	30.0
5.	electroplating wastewater	chemically modified orange peel	2.0	Cu^{2+}	289.0	180	30.0
6.	aqueous solution	modified lawn grass	0.5	Pb^{2+}	137.12	400	29.85
7.	aqueous solution	grapefruit peel	2.0	U^{6+}	140.79	60-80	24.85
8.	aqueous solution	peanut shell	1.0	Cr^{6+}	4.32	360	30.0
9.	aqueous solution	sugarcane & orange peel biochar	1.0	Pb^{2+}	86.96 and 27.86	30	25.0
10.	electroplating wastewater	mango peel	5.0 5.0 5.0	Ni^{2+} Cu^{2+} Zn^{2+}	39.75 46.09 28.21	120	25.0
11.	aqueous solution	wheat shell	10.0	Cu^{2+}	17.42	60	25.0
12.	aqueous solution	sulfonated biochar	2.0	Pb^{2+} Cd^{2+}	191.07 85.76	5	180.0

Table 4. Common industrial wastes for removing heavy metals [13]

S/N.	Type of Wastewater	Type of Adsorbent	Adsorbent Dosage (g)	Metal Ion	Amount Adsorbed (mg/g)	Contact Time (min.)	Temperature (^{o}C)	pH
1.	dye and heavy metal wastewater	fly ash	2.0	Cd^{2+} Cu^{2+} Ni^{2+}	6.36 12.78 1.66	60	25.0	4.8-5.3
2.	aqueous solution	coal fly ash	2.5	Cu^{2+} Ni^{2+}	158.0 99.0	120 60	20.0	8.0
3.	aqueous solution	fly ash geopolymer	2.0	Cu^{2+}	152.0	120	45.0	6.0
4.	aqueous solution	fly ash bottom ash	2.0	Cd^{2+}	142.9 23.3	240	25.0	5.0-6.0
5.	aqueous solution	red mud	1.0	Cu^{2+}	5.3	60	30.0	5.5
6.	aqueous solution	activated red mud	4.0	Zn^{2+}	14.9	480	25.0	6.0
7.	aqueous solution	red mud	1.0	Co^{2+}	18.0	15	30.0	5.0
8.	aqueous solution	activated red mud	4.0	Pb^{2+}	6.0	30	30.0	4.0
9.	aqueous solution	basic oxygen furnace slag	0.5	Cu^{2+}	245.2	60	20.0	3.5
10.	synthetic water	LD slag geopolymer raw LD slag	2.0	Ni^{2+}	84.8 14.3	1440	45	10.0 10.0

Previous studies have shown that activated carbon have adsorption capacity up to 77.68% with oxygen functional groups onto the adsorption sites [22]. An adsorbent's surface area depends on how it's structured. As adsorption occurs, the carbon will usually experience expansion as a result of immersion, known as adsorption-swelling or adsorption-extension [23]. Also, (i) solids that are finely divided and (ii) porous substances are known to be good adsorbents [24]. Some researchers also suggest that the distribution of functional groups on an adsorbent surface depends on its pore size due to the presence of heteroatoms (usually oxygen, nitrogen, and sulfur) [25].

Activated carbon when used as adsorbents is not cost effective. An inexpensive adsorbent foundational material is the citrus fruits peel. They are of commercial value, readily available, and have average absorption capacity of 96% [26] [27]. Furthermore, study shows that agricultural materials contain lignin, protein, and polysaccharides which are linked with some functional groups and function as adsorbents for metal ions [28], with citrus peel regarded as one of the most important low-cost adsorbents [29]. This is due to their strong potential in the adsorption process due to their pectin (galacturonic acid), high content of cellulose, hemicellulose, and lignin [28]. Citrus fruits include orange peel, lime peel, lemon peel, etc. of the same genus of plant family group with similar biological, physical, and chemical properties. Their adsorption is through biosorption. The Freundlich Isotherm forms the basis for adsorption onto heterogeneous binding sites; the metal ions [27]. Biosorption is affected by the nature of the derived product or biomass, how it is applied, concentration, and surface area. The age, nutrition, and growth of the biomass also influence biosorption due to extracellular product formation, and changes in cell size, etc. [30].

2. MATERIALS AND METHOD

2.1. Materials

These include produced water samples from a Niger Delta oilfield and *Citrus aurantiifolia* peel (local adsorbent material). *Citrus aurantiifolia* is characterized by plant type (fruits, trees, shrubs), plant family (Rutaceae), genus (citrus), water needs (average), soil type (loam), soil pH (acid, neutral), soil drainage (moist but well-drained), and tolerance (clay soil). It grows under various climate zones under full sun exposure.

2.2. Method

2.2.1.Collection of samples/materials

The sample was collected from a Niger Delta oilfield (Fig.1) and preserved at ambient temperature of 28 ^{o}C. However, from multiple research analyses and tests, produced water commonly contains heavy metals such as Cd, Pb, Cu, Fe, Mg, Cr, Zn, and Mn. The adsorption experimentation and process would test for those ions. *Citrus aurantiifolia* peel (Fig. 2) was used as an adsorbent and it was purchased from a local market in Eziobodo, Nigeria.

Figure 1. Raw-produced water samples from the Niger Delta

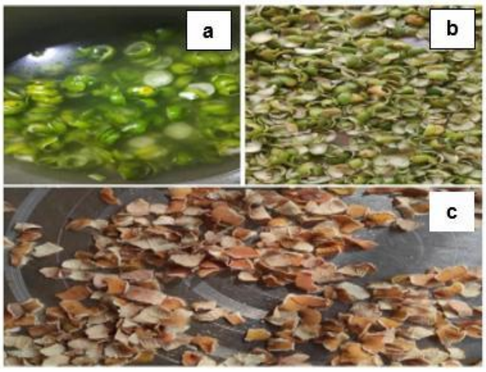

Figure 2. Raw Citrus aurantiifolia peel (local adsorbent material) (a) freshly peeled (b) initial drying stage (c) final drying stage

2.2.2. Atomic Absorption Spectrophotometer (AAS) technique and test procedure

The AAS technique was used in the study. The heavy metals were tested individually to first obtain the source absorbance value for each of the metals. These values were recorded and used as reference points through the adsorption experiment. The light absorbed by each metal, measured in nm, helps to determine the concentration amount of a metal in the solution. Three main parameters were considered for the AAS metal test procedure. Wavelength is the amount of light absorbed by a metal and the value of the wavelength is determined by the concentration amount of the metal in the solution. Slit allows for the entry of broad or narrow light wavelengths into the AAS monochromator and its width is expressed in mm. The detection limit is the highest/lowest signal or concentration of a metal that can be detected with the AAS method. For the experiment carried out it's also the sum of all the concentrations for each specific metal detected during the experimental procedure, from the highest to the lowest. Each metal was assigned different wavelength, slit & detection limit values according to when they get detected by the AAS due to the light absorbed by each respective metal for a given test.

The digested samples were analyzed for heavy metal content using Atomic Absorption Spectrophotometry (AAS) at a Research Laboratory in the Federal University of Technology, Owerri. The procedure involved aspirating the digested sample into an air-acetylene flame, where the solvent evaporated, and free metal atoms were vaporized in a process known as atomization. A hollow cathode lamp emitting light in the UV-visible spectrum was used to excite the metal atoms electronically. The absorbance of this light was then measured using a UV-visible dispersive spectrometer equipped with a photomultiplier detector. Each metal analysis was conducted in triplicate, and the instrument automatically provided the mean concentration values of the analyzed metals, including Lead, Nickel, Cadmium, Copper, Iron, Magnesium, Chromium, Zinc, and Manganese.

2.2.3 Preparation of Citrus aurantiifolia peel for experimental procedure

After peeling, the local adsorbent was prepared by thoroughly washing it with distilled water to get rid of any extraneous materials (such as dirt or impurities) stuck on its surface. The washed lime peel was then cut to pieces and sun-dried for at least 48 hours, after which it was also oven-dried after preheating to 55ºC to prevent burning for 2-3 hours. At that condition, the peels would have dried out and begin to curl or snap and don’t bend. This was done to reduce moisture content and adsorbed gases on the surface. The dried peels were then milled into finer particles (Fig. 3), and packed in high-density polyethylene (HDPE, 0.77 mm thickness) bags, and heat-sealed with a sealing machine to shield them from the external environment.

Figure 3. Finely grounded peel

2.2.3. Experiments performed with the adsorbent on the wastewater

Experiments on batch adsorption were used to determine the effects of these factors on the wastewater sample collected from the Niger Delta (Fig. 1).

i. Time of contact (mins.)

ii. Dose of adsorbent (g)

Iii. Speed of agitation (rpm)

1g of the *Citrus aurantiifolia* peel was added to a 50ml beaker with 30ml effluent-produced water with 7.1 as the initial pH. The beaker was kept on a magnetic stirrer at an ambient temperature of 30 ± 2°C. A speed of 150 rpm was maintained and agitated at a time interval of 5-60 mins for contact time effect. It was also aimed at determining the optimum time of the process of adsorption.

i. Effect of contact time

1g constant dose of the adsorbent (*Citrus aurantiifolia* peel) was stored in 18 polyethylene bottles which contain 30ml of the produced water. Agitation was achieved with a magnetic stirrer at 150 rpm and 5, 10, 15, 20, 25, 30, 40, 50, and 60-minute time intervals. The ambient temperature of 30 ± 2°C was recorded, and a pH of 7.1 was recorded. At the predetermined time intervals, the samples were collected from the stirrer and filtered. The filtrates were collected for further analysis.

ii. Effect of adsorbent dose

30ml of the effluents and 0.5, 1, 1.5, 2, 2.5, and 3g of the adsorbents were placed into 12 polyethylene bottles. They were agitated for 25 mins. and 30mins. optimum times for the bottle set that contains lime peels, respectively. It was performed at ambient temperature and a pH of 7.1. They were taken out of the stirrer and filtered. The filtrates were taken for further analysis. The percentage reductions in the pollution causative factors are calculated using Eq.1:

$$\% \text{ Reduction}=[(\text{initial conc.}-\text{final conc.})/ / (\text{initial conc.})] \times 100 \qquad (1)$$

iii. Effect of agitation speed

Adsorbent selection factors include high adsorbent capacity, low cost, and its effectiveness for a wide range of pollutants. Four identified efficient mechanisms for the adsorption of impurities/pollutants include physisorption, chemisorption, ion exchange, and precipitation. Similarly, functional groups in organic compounds [16] on carbon surfaces, such as *Citrus aurantiifolia* peel. These heteroatoms are surface functional groups [17]. Hydrogen bonding also bond electrostatically to other compounds [18]. Solute are also soluble due to forces that are large enough [19]. The oxygen functional groups determine the surface properties of a bio-adsorbent, and therefore the quality of the adsorbent [20]. The carboxyl and hydroxyl groups are great contributors to heavy metals adsorption such as Ni, Pb, Hg, Cd, and Cr ions onto a variety of carbon adsorbents such as the *Citrus aurantiifolia* [21].

Adsorbent doses in the range of 0.5-3g were used and agitation speeds of 50-150rpm were also conducted for their effects. Whattman No.1 filter paper (pore size: 11µm particle retention) was used, and studies were carried out on the filtrates. Also, *Design-Expert® software version 13* was engaged. This software when applied established the optimum values and their treatment efficiencies. Finally, these optimum values were then re-visited experimentally to confirm them, and the kinetic parameter was established at those optimum values of the process variables.

3. RESULTS AND DISCUSSION

The wastewater was initially characterized, and the result showed lead (0.0082 mg/l). nickel (0.0084 mg/l), cadmium (0.0051 mg/l), copper (0.94 mg/l), iron (0.26 mg/l), magnesium (0.068 mg/l), chromium (0.0071 mg/l), zinc (1.17 mg/l) and manganese (0.053 mg/l). The CCD for each factor is also shown (Table 5).

There were three main factors included for each metal. They include (i) sample runs, (ii) concentration, and (iii) absorbance values (Table 6). The percentage reductions and AAS sample results are shown in Table 7. These three factors apply to all the nine metals used in the experimental procedure. The sample is also referred to as batch number. This describes the number of batch experiments/adsorption tests carried out for a particular metal. From the test, there were a total of 20 batch experiments.

Table 5. Central Composite Design (CCD) for each factor

Factor	Name	Axial low	Low	Mean	High	Axial High
A	Mass Dosage	0.727	0.50	6.00	1.00	12.727
B	Contact Time	9.546	30.00	60.00	150.00	110.454
C	Agitation Speed	331.821	600.00	500.00	900.00	668.179

Nine metals were constantly tested for every batch. Different values of three parameters that influence the adsorption process were assigned to each batch. The parameters are (i) mass dosage, (ii) contact time, and (ii) agitation speed. For example, in batch 1 (or sample run 1), a mass dosage of 6g, contact time of 60 mins, and agitation speed of 500 rpm were used as a constant assigned parameter value for each metal tested in batch 1. The varying adsorption results were then recorded for each respective metal. The AAS sample results and the standard chart for the metals are presented in Table 7 and Fig. 4. The calibrations of the heavy metals are shown with R^2 of Pb (0.994), Ni (0.997), Cd (0.981), Cu (0.997), Fe (0.993), Mg (0.993), Cr (0.993), Zn (0.987) and Mn (0.996).

3.1. Batch analysis result

Table 6. Design of experiment for heavy metals removal (concentration)

Runs	Mass Dosage (g)	Contact Time (Mins)	Agitation Speed (RPM)	Concentration								
				Pb (mg/L)	Ni (mg/L)	Cd (mg/L)	Cu (mg/L)	Fe (mg/L)	Mg (mg/L)	Cr (mg/L)	Zn (mg/L)	Mn (mg/L)
1	6	60	500	0.0038	0.0032	0.00014	0.038	0.038	0.0055	0.0026	0.74	0.0072
2	2	30	400	0.0026	0.0040	0.00037	0.041	0.041	0.0032	0.0019	0.57	0.0071
3	6	60	500	0.0019	0.0038	0.00024	0.036	0.025	0.0016	0.0015	0.38	0.0020
4	6	60	500	0.0025	0.0057	0.00016	0.081	0.051	0.0047	0.0015	0.32	0.0081
5	10	90	400	0.0044	0.0061	0.00028	0.053	0.036	0.0028	0.0037	0.46	0.0063
6	6	60	500	0.0031	0.0039	0.00035	0.019	0.052	0.0041	0.0025	0.31	0.0087
7	6	9.54622	500	0.0025	0.0034	0.00026	0.037	0.017	0.0033	0.0010	0.63	0.0072
8	6	110.454	500	0.0040	0.0047	0.00031	0.042	0.028	0.0044	0.0041	0.69	0.0036
9	10	30	600	0.0048	0.0056	0.00032	0.037	0.046	0.0024	0.0016	0.27	0.0071
10	12.7272	60	500	0.0033	0.0064	0.00027	0.041	0.014	0.0034	0.0027	0.22	0.0058
11	8	60	500	0.0041	0.0031	0.00025	0.025	0.030	0.0048	0.0017	0.48	0.0089
12	6	60	331.821	0.0035	0.0042	0.00017	0.056	0.047	0.0043	0.0035	0.36	0.0020
13	2	90	600	0.0027	0.0037	0.00040	0.040	0.056	0.0028	0.0041	0.21	0.0051
14	2	30	600	0.0016	0.0050	0.00035	0.039	0.035	0.0041	0.0032	0.51	0.0021
15	10	30	400	0.0039	0.0045	0.00013	0.051	0.040	0.0039	0.0015	0.98	0.0015
16	6	60	668.179	0.0043	0.0040	0.00034	0.034	0.029	0.0035	0.0047	0.58	0.0063
17	4	60	500	0.0053	0.0039	0.00041	0.052	0.052	0.0018	0.0041	0.71	0.0037
18	10	90	600	0.0028	0.0021	0.00026	0.023	0.037	0.0022	0.0018	0.44	0.0043
19	2	90	400	0.0042	0.0032	0.00019	0.044	0.043	0.0023	0.0023	0.63	0.0074
20	0.727171	60	500	0.0034	0.0043	0.00024	0.047	0.031	0.0045	0.0040	0.62	0.0062

Table 7. Source data, concentration reduction and AAS sample results

Heavy metal		Pb	Ni	Cd	Cu	Fe	Mg	Cr	Zn	Mn
Source	Concentration [mg/L]	0.0082	0.0084	0.00510	0.940	0.260	0.0680	0.0071	1.17	0.0530
	Absorbance	0.5864	0.7263	0.5140	4.9526	9.5510	1.5848	0.5169	4.0782	0.9116
Concentration reduction [%]		80.49	75.00	97.45	97.98	94.62	97.65	85.92	82.05	97.17
AAS sample results										
Name		Pb	Ni	Cd	Cu	Fe	Cr	Zn	Mg	Mn
Wavelength, nm		283	341	228.9	324.8	248.3	357.9	213.9	285.2	279.5
Silt, nm		0.7	0.2	0.7	0.7	0.2	0.7	0.7	0.7	0.7
Detection limit, mg/l		0.08	0.1	0.01	0.005	0.05	0.04	0.005	0.005	0.03

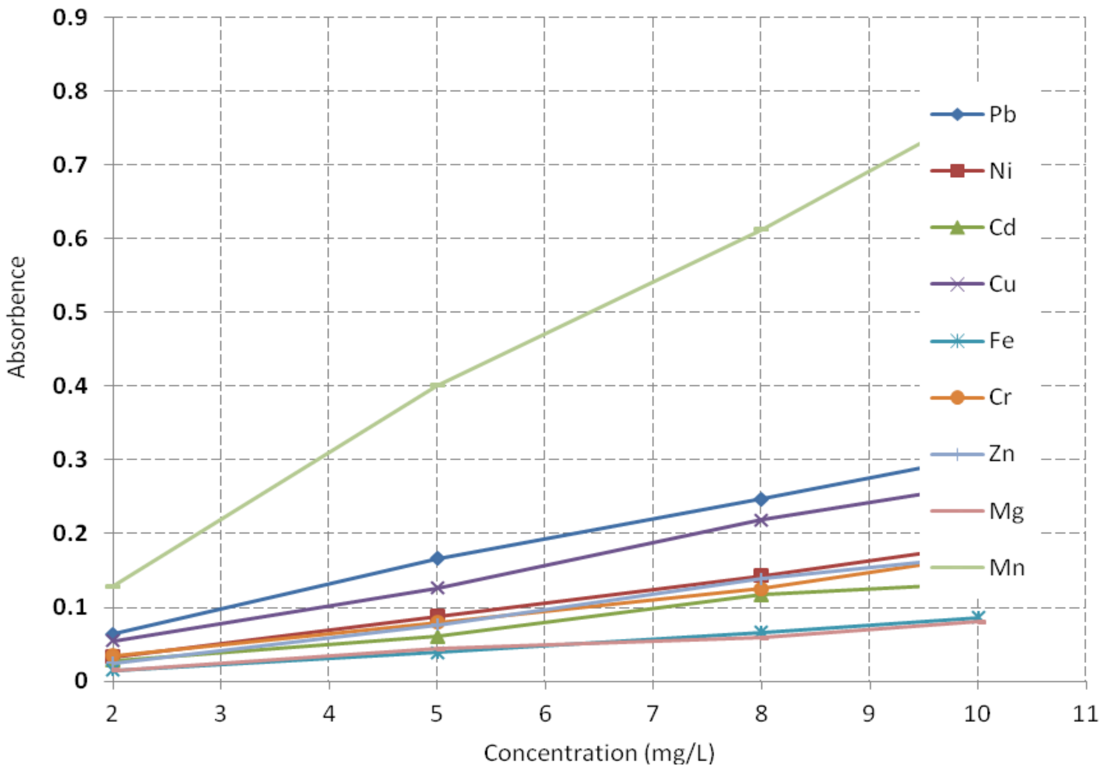

Figure 4. Standard chart for the heavy metals

Concentration is the second factor for each metal. This describes the concentration amount of the metal left after the adsorption of that batch has taken place. There's a sub-factor known as the "source". For the section on concentration factor, the source indicates the initial concentration of the metal before any batch adsorption was carried out. It's recorded for each metal and it's a constant value that's compared to every batch. The metal concentration amount left in the produced water after batch adsorption is completed is usually compared to the source concentration to deduce the percentage reduction of that metal for the respective batch. For example, the concentration of lead metal Pb in batch 1 (or sample run 1): was reduced from its source concentration, 0.0082 mg/L to 0.0038mg/L. In Batch 2, it was reduced from a source concentration of 0.0082mg/L to 0.0026mg/L, etc. After 20 runs or batch adsorption were conducted, Pb was best reduced to its lowest concentration of 0.0016 mg/L in batch 14 when compared to the other batches. That yielded a concentration reduction of 80.49% as shown in Table 7. Similar observations were made for the other heavy metals.

Similarly, absorbance values, measured in AU (absorbance unit), at every numbered row (batch number) were recorded. This describes the quantity of light absorbed by each metal when tested in the AAS after the adsorption process of that batch has taken place. The sub-factor known as "source" also applies to this. For the section on absorbance value, the source indicates the initial absorbance of the metal before any batch adsorption was carried out. It's recorded for each metal and it's a constant value that's compared to every batch. The closer the absorbance value is to 1.0 or greater than 1.0, it's an indication of the high concentration amount of that metal.

20 runs were performed on the wastewater to obtain optimum results. From the batch adsorption results obtained during the experiment, the concentration of heavy metals in the produced water was successfully reduced. Moreover, this reduction is affected by three main parameters. They include mass dosage (g), contact time (mins), and agitation speed (rpm). It is observed that each of these parameters has a different concentration reduction effect on each of the metals that were tested. On the 14th run, Pb had the lowest concentration value of 0.0016 mg/L at an agitation speed of 600 rpm using an adsorbent mass dosage of 2g for 30 minutes. The traces of Ni dropped to the lowest (0.0021) with an agitation speed of 600 rpm using a mass dosage of 10g for 90 minutes and this was achieved in the 18th run. The lowest concentration value of Cd was 0.00013 using 10g of mass dosage for 30 minutes with a 400 rpm on the 15th run. Cu was also reduced to a low value of 0.019 mg/L after agitating with a speed of 500 rpm for 60 minutes at an adsorbent dosage of 6g. The concentration of Fe decreased to 0.014mg/L with the highest dosage amount of 12.73g used in the 10th run at a speed of 500 rpm for 60 minutes. The 3rd run produced the lowest value 0.0016 mg/L of Mg with a mass dosage of 6g and, a contact time of 60 minutes at 500 rpm. The level of Cr dropped to its lowest (0.0010) during the 7th run with an agitation speed of 500 rpm and, an adsorbent mass dose of 6g for 60 minutes. Zn and Mn had a low of 0.21 and 0.0015 with agitation speeds of 600 and 400 rpm, and mass dosages of 2g and 10g for 90 and 30 mins on the 13th and 15th runs, respectively.

The lowest concentrations of heavy metals were achieved at varying agitation speeds, contact times, and adsorbent mass doses. It proved the advantage of the batch adsorption process for optimal results. From the experiment, the best value of the adsorption parameters obtained during the experiment for an effective reduction of each of the heavy metals using *Citrus aurantiifolia* peel as an adsorbent is given in Table 8.

Table 8. Adsorption parameters for an effective reduction of heavy metals

Name	Agitation speed, rpm	Mass dosage of adsorbent, g	Contact time, min.
Pb	600	2	30
Ni	600	10	90
Cd	400	10	30
Cu	500	6	60
Fe	500	12.73	60
Mg	500	6	60
Cr	500	6	60
Zn	600	2	90
Mn	400	10	30

With the specific parameters, the metal concentrations in the water sample with Pb, Ni, Cd, Cu, Fe, Mg, Cr, Zn, and Mn were decreased from 0.0082, 0.0084, 0.0051, 0.940, 0.260, 0.0680, 0.0071, 1.17 and 0.053 to 0.0016, 0.0021, 0.00013, 0.019, 0.014, 0.0016, 0.0010, 0.21 and 0.0015, respectively.

4. CONCLUSION

The procedures involve the use of standard solutions prepared at ambient temperature in the laboratory. The produced water samples had impurities and traces of heavy metals. All experiments were performed at ambient temperature, while the parameters considered during the tests were time, mass dosage of adsorbent, and agitation speed. The tests were carried out at a constant temperature, and reduction of the heavy metals' concentration at ambient temperature at varying time intervals, mass dosage, and agitation speed. The Atomic Absorption Spectrophotometer was used to detect the concentration of the metals treated with the local bio-adsorbent. Also, the research showed that the concentration of the heavy metals was in excess as compared to allowable values for re-use or discharge. After the produced water samples were treated with the local bio-adsorbent in the batch adsorption process, metal concentration was reduced to the desired values in the samples. The percentage of adsorption of Pb, Ni, Cd, Cu, Fe, Mg, Cr, Zn, and Mn were 80.49%, 75.00%, 97.45%, 97.98%, 94.62%, 97.65%, 85.92%, 82.05%, and 97.17%, respectively. Time was considered a major parameter since it was required for effective adsorption. It is concluded that the bio-nature of the adsorbents such as *Citrus aurantiifolia* and orange peels which are agricultural wastes, as observed by other researchers, have high amounts of cellulose, tannin, hemicelluloses, and lignin. Similarly, they have fibrous materials and functional groups which immensely contribute to adsorption from fresh water. The contents of these materials enable them to effectively bind metal ions. Hence, the adsorbent used has excellent binding abilities.

Conflict of interest

No known conflict of interest has been declared by the authors.

5. REFERENCES

[1] S.G. Udeagbara, S.O. Isehunwa, N.U. Okereke, I.U. Oguamah, A. Kerunwa, O. Nwanwe (2021) Treatment of produced water from Niger Delta oil fields using a sequential mixture of bio-adsorbents. *Cogent Engineering, 8(1),* 1 – 3, https://doi.org/10.1080/23311916.2021.1939927

[2] F. Ahmadun, P. Alireza, L.C. Abdullah, D.R.A. Biak, S.S. Madaeni, Z.Z. Abidin (2009) Review of technologies for oil and gas-produced water treatment. Journal of Hazardous Materials, 170(2–3), 530-551, https://doi.org/10.1016/j.jhazmat.2009.05.044

[3] J. Neff, K. Lee, E.M DeBlois (2011) Produced water: an overview of Composition, fates, and effects. Produced Water: *Environmental Risks and Advances in Mitigation Technologies*, 3-54, http://dx.doi.org/10.1007/978-1-4614-0046-2_1

[4] A.J. Abbas, H.A. Gzar, M.N. Rahi (2021) Oilfield-produced water characteristics and treatment technologies: a mini-review. IOP Conference Series: *Material Science* and *Engineering,* 3, https://doi.org/10.1088/1757-899X/1058/1/012063

[5] K. Guerra (2011) Oil and gas produced water management and beneficial use in the western United States, Issue *157 of Science and Technology Program Report*. Retrieved from, https://books.google.com.ng/books/about/Oil_and_Gas_Produced_Water_Management_an.html?id=MB84twAACAAJ&redir_esc=y

[6] [6] K. Azetsu-Scott, P. Yeats, G. Wohlgeschaffen, J. Dalziel, S. Niven, K. Lee (2006) Precipitation of heavy metals in produced water: influence on contaminant transport and toxicity. *Marine Environmental Research*, 63(2), 146-167, http://dx.doi.org/10.1016/j.marenvres.2006.08.001

[7] J.D. Arthur, ALL Consulting, LLC (2005) Technical Summary of Oil & Gas Produced Water Treatment Technologies.

[8] C.E. Clark, J.A. Veil (2009) Produced water volumes and management practices in the United States. *Argonne National Laboratory,* 15, https://doi.org/10.2172/1007397

[9] E. Allison, B. Mandler (2018) *Using produced water*: recycling oilfield water in the oil and gas industry and beyond. *Petroleum and the Environment*, *Part 5/24,* Retrieved from https://www.americangeosciences.org/geoscience-currents/using-produced-water

[10] T.D. Hayes, D. Arthur (2004) Overview of emerging produced water treatmenttechnologies. Health and Environmental Research Online (HERO) http://ipec.utulsa.edu/Conf2004/Papers/hayes_arthur.pdf

[11] H. Li (2013) *Produced water quality characterization and prediction for Wattenberg field* (Master's thesis, Colorado State University, Fort Collins, United States), http://hdl.handle.net/10217/79104

[12] J. Singh, A.S. Kalamdhad (2011) Effects of heavy metals on soil, plants, human health and aquatic life. *International Journal of Research in Chemistry and Environment (IJRCE), 1(2),* 15 – 21. Retrieved from. http://www.ijrce.org/index.php/ijrce/article/view/78

[13] A. Hussain, S. Madan, R. Madan (2021) Removal of heavy metals from wastewater by adsorption. *Heavy Metals - Their Environmental Impacts and Mitigation, IntechOpen,* http://dx.doi.org/10.5772/intechopen.95841

[14] E.I. Igunnu, G.Z. Chen (2014) Produced water treatment technologies. *International Journal of Low- Carbon Technologies,* 9(3), 157-177, https://doi.org/10.1093/ijlct/cts049

[15] R. Yousef, H. Qiblawey, M.H. El-Naas (2020) Adsorption as a process for produced water treatment: a review. *processes, 8(12),* 1657 https://doi.org/10.3390/pr8121657

[16] A.Y. El-Khateeb (2020) Practical approach for the identification of functional groups in organic compounds. *Progress in Chemical and Biochemical Research, 3(2), 147-168*, https://doi.org/10.33945/SAMI/PCBR.2020.2.9

[17] C. Higginbotham (2021) *Introductory Organic Chemistry.* Retrieved from, https://openoregon.pressbooks.pub/introductoryorganic/

[18] J.G. Smith (2007) Introduction to organic molecules and functional Groups, Chapter 11 Lesson 2. Retrieved from, https://www.youtube.com/watch?v=dkvGkSWDYvY

[19] B. Davarcioglu (2011) The general characteristic of weak intermolecular interactions in liquids and crystals. *International Journal of Modern Engineering Research (IJMER),1(2),* 443-454, http://www.ijmer.com/

[20] S. Dey, S.R. Basha, G.V. Babu, T. Nagendra (2021) Characteristic and biosorption capacities of orange peels biosorbents for removal of ammonia and nitrate from contaminated water, *Cleaner Materials, 1, 1000001,* https://doi.org/10.1016/j.clema.2021.100001

[21] Y. Xiadong, Y. Wan, Y. Zheng, F. He, Z. Yu, J. Huang, H. Wang, Y.S. Ok, Y. Jiang, B. Gao (2019) Surface functional groups of carbon-based adsorbents and their roles in the removal of heavy metals from aqueous solutions: A critical review. *Chemical Engineering* Journal, 366, 608-621, https://doi.org/10.1016/j.cej.2019.02.119

[22] X. Ruzhen, Y. Jin, Y. Chen, W. Jiang (2017) The importance of surface functional groups in the adsorption of copper onto walnut shell derived activated carbon. *Water Science & Technology,* 76(11), 3022-3034, http://dx.doi.org/10.2166/wst.2017.471

[23] E.A. Flood, F.M. Farhan (1963) Stresses and strains in adsorbent-adsorbate systems: V.

Thermodynamic Theory of Adsorption-Extension Phenomena, Canadian *Journal of Chemistry, 41(7)*, https://doi.org/10.1139/v63-245

[24] Byju's (2022) Factors affecting adsorption of gases on solids. Retrieved from, https://byjus.com/chemistry/factors-affecting-the-extent-of-adsorption/

[25] J. Barkauskas, D. Maryte (2004) An investigation of the functional groups on the surface of activated carbons. Journal of the Serbian Chemical Society, 69(5), 364, http://dx.doi.org/10.2298/JSC0405363B

[26] N. Mahato, P. Agarwal, D. Mohapatra, M. Sinha, A. Dhyani, B. Pathak, M.K. Tripathi, S. Angaiah (2021) Biotransformation of citrus waste-II: bio-sorbent materials for removal of dyes, heavy metals, and toxic chemicals from polluted water. *processes, 9(9),* 1544, https://doi.org/10.3390/pr9091544

[27] A. Kumar, A. Balouch, A.A. Pathan, A.M. Mahar Abdullar, M.S. Jagirani, F.A. Mustafai, M. Zubair, B. Laghari, P. Panah (2017) Remediation techniques applied for aqueous system contaminated by toxic Chromium and Nickel ion. *Geology, Ecology, and Landscapes,* 1(2),143-153, https://doi.org/10.1080/24749508.2017.1332860

[28] F. Gönen, D.S. Serin (2012) Adsorption study on orange peel: removal of Ni (II) ions from aqueous solution. *African Journal of Biotechnology 11(5),* 1250-1258, https://doi.org/10.5897/AJB11.1753

[29] K. Jusufi, B. Korça, A. Berisha, J. Halili, T. Selimi, M. Sadiku, N. Troni, F. Ferataj, J. Hasanaj, V. Mehmeti, A. Halili (2016) Potential application of orange peels as bio-sorbents in the removal of organic molecules from wastewater. RAD *Conference Proceedings,1, 176-178,* https://doi.org/10.21175/RadProc.2016.41

[30] G.M. Gadd (2008) Biosorption: a critical review of scientific rationale, environmental importance and significance for pollution treatment, *Journal of Chemical Technology* and *Biotechnology, 84(1),* 13-28, https://doi.org/10.1002/jctb.1999

IZVOD

ŠARŽNA ADSORPCIJA KORIŠĆENJEM KORE *C. AURANTIIFOLIA* KAO BIO-ADSORBENTA ZA TRETMAN TEŠKIH METALA U PROIZVEDENOJ VODI IZ PROIZVODNJE NAFTE

Većina tehnika tretmana proizvedene vode je neefikasna u smanjenju nečistoća i koncentracije metala. Ovo uzrokuje poteškoće u postizanju nivoa odlaganja. Prikazana je efikasnost biomaterijala za tretman proizvedene vode za naftno polje delte Nigera. Uzorak proizvedene vode je sakupljen sa naftnog polja Delta Nigera i čuvan na temperaturi okoline od 28^{o}C, dalje karakterisan, a rezultat je pokazao olovo (0,0082 mg/l). nikl (0,0084 mg/l), kadmijum (0,0051 mg/l), bakar (0,94 mg/l), gvožđe (0,26 mg/l), magnezijum (0,068 mg/l), hrom (0,0071 mg/l), cink (1,17 mg/l) i mangan (053 mg/l). Citrus aurantiifolia kora je korišćena kao adsorbent i kupljena je na lokalnom tržištu u Eziobodu, Nigerija. Nakon ljuštenja, bioadsorbent (limetova kora) je pripremljen temeljnim pranjem destilovanom vodom da bi se uklonili svi strani materijali (kao što su prljavština ili nečistoće) zaglavljeni na njegovoj površini. Oprana kora limete je zatim isečena na komade i sušena na suncu najmanje 48 sati, nakon čega je, takođe, sušena u rerni nakon zagrevanja na 55^{o}C da bi se sprečilo zagorevanje 2-3 sata. Osušene kore su zatim mlevene u sitnije čestice i pakovane u kese od polietilena visoke gustine (HDPE, debljine 0,77 mm). Eksperimenti sa šaržnom adsorpcijom su korišćeni da bi se odredili efekti vremena kontakta, doze adsorbenta i brzine mešanja. Uzorci su tretirani bioadsorbentom na magnetnoj mešalici u kojoj su vršeni različiti testovi adsorpcije u različitim vremenskim intervalima da bi se dobili optimalni željeni rezultati za uklanjanje metala. Tehnika atomskog apsorpcionog spektrofotometra je korišćena u studiji gde su digestirani uzorci analizirani na sadržaj teških metala. Njihove koncentracije su nakon tretmana smanjene na Pb (0,0016 mg/l), Ni (0,0021 mg/l), Cd (0,00013 mg/l), Cu (0,019 mg/l), Fe (0,014 mg/l), Mg (0,0016 mg/l), Cr (0,0010 mg/l) i Mn2 (0,0010 mg/l). (0,0015 mg/l). Procenat adsorpcije Pb, Ni, Cd, Cu, Fe, Mg, Cr, Zn i Mn bio je 80,49%, 75,00%, 97,45%, 97,98%, 94,62%, 97,65%, 85,92%, 82,05%, odnosno 97,17%. Citrus aurantiifolia kore su pokazale potencijal kao adsorbent za tretman teških metala u proizvedenoj vodi.

Ključne reči: *teški metali, proizvedena voda, kora Citrus aurantiifolia, bio-adsorbent*

Naučni rad
Rad primljen: 28.03.2025.
Rad prihvaćen: 07.05.2025.

ORCID: https://orcid.org/0000-0002-4729-4072

Azuka N. Amitaye[1,2]*, Elias E. Elemike*[2]*, Terngu T. Uzah*[2]*,**

[1]*Department of Chemistry, Nigeria Maritime University, Okerenkoko, P.M. B. 1005, Warri South-West, Nigeria,* [2]*Department of Chemistry, Federal University of Petroleum Resources, P.M.B 1221, Effurun, Nigeria*

Scientific paper
ISSN 0351-9465, E-ISSN 2466-2585
https://doi.org/10.62638/ZasMat1406

ZastitaMaterijala 67 (1)
149 - 158 (2026)

Valorization of african giant land snail shell waste (*Archachatinamarginata)* by extraction of chitosan from it

ABSTRACT

The African giant land snail (Archachatinamarginata) is one of the most commonmollusks in southern Nigeria. It has a shell that constitutes more than half of its body mass and it is usually discarded as waste.The goal of the present study is to valorize snail shell wastes by extracting chitosan, a versatile and top-demanding biopolymer from it. Chitosan was extracted by chemical methods and characterized by Fourier transformed infrared spectroscopy, and powdered X-ray diffraction. Quality parameters such as solubility, moisture content, ash value and degree of deacetylation were determined for snail shell-chitosan. The results show that snail shell chitosan is of comparable quality to commercially marketed shrimp chitosan. Snail shell chitosan has a DD value of 78.4 %, solubility of 95.35 %, moisture of 1.42 %, and ash value of 1.61 % which affirms snail shell-chitosan as a sustainable and suitable feedstock for commercial production of chitosan. The yield of chitosan based on snail shells was 14.83 % which is comparable to yield from crustacean shell wastes.

Keywords: *Archachatinamarginata, shell waste, chitosan, quality parameters, valorization*

1. INTRODUCTION

The increasing awareness of the nutritional benefits of snail meat has continued to drive its consumption by humans of all classes. Snail meat, popularly known as ‘Congo meat’ is a rich source of protein, calcium, iron, and other essential minerals. Snail meat is edible for persons of all ages and nationalities and there is no cultural and religious restriction on the use and consumption of snail meat and its parts.

Snail is a member of the phylum *Mollusca*, with its muscular and soft parts partly covered by a protective shell. The African giant land snail (*Archachatinamarginata*) is one of the most common*mollusks* in southern Nigeria. It has a shell that constitutes more than half of its body mass and it is usually discarded as waste. As snail meat consumption increases, the mass of snail shell wastes is expected to increase and may constitute a nuisance in the environment. This is because snail shell waste is highly underutilized and its biodegradability rate is very low.

However, snail shell wastes can be harnessed as feed-stock for the production of industrial-grade chemicals such as chitin, chitosan, oligochitosan and so on. Chitin and chitosan are essential biopolymers due to their bioactivity, biodegradability, non-toxicity, sorbent strength, and antimicrobial activities.

Although chitosan is not found free, it is derived from chitinous-based biomaterials such as exoskeletons of crustaceans, insects, *mollusks*, and cell walls of some fungi [1-3]. Commercial-grade chitosan is extracted from shrimp chitin [4] and used in many biomedical applications. Chitosan has been extracted from the shells of crabs, crayfish, squillas, turtles, and external parts of millipedes and mosquitoes but the shrimp chitosan is of superior grade [5].

The quality of chitin and chitosan is defined by parameters such as moisture content, viscosity, ash value, solubility, molecular weight, and degree of deacetylation (DD). These quality parameters vary for different chitinous-based sources. Each chitinous-based source yield chitin of different properties [2, 6]. The quality of chitin extracted from shrimp and crabs at different growth stages by the same method differs significantly [7]. Quality parameters also depend on the extraction methods and conditions adopted to derive chitin and chitosan from feedstocks [3, 8].

Chitin and chitosan have a similar structural framework as cellulose but with unique functional groups that make them distinct as shown in Figure 1. Chitosan is a derivative of chitin but chitin is not

---

*Corresponding author: Terngu T. Uzah
E-mail: uzah2t@gmail.com

Paper received: 21.03. 2025.
Paper corrected: 01.05. 2025.
Paper accepted: 10. 05.2025.

a derivative of cellulose. Also, chitin and chitosan are not obtained from cellulosic-based biomass.

Chitosan is a family of polymers with at least 51 % degree of deacetylation. It is a copolymer of N-acetyl-D-glucosamine linked to D-glucosamine units by β-1, 4 glycosidic bonds, as its monomeric units [2, 9]. The ratio of N-acetyl-D-glucosamine to D-glucosamine subunits of chitosan monomeric units is far less than unity hence; the D-glucosamine unit is the dominant structural component of chitosan.

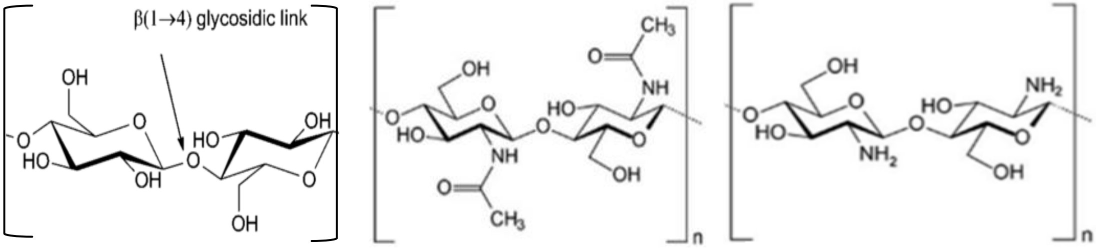

(a). Cellulose *(b). Chitin* *(c). Chitosan*

Figure 1. Chemical structure of cellulose [10], chitin (completely acetylated chitin) [11,12]; and chitosan (completely deacetylated chitosan) [13]

However, chitosan is more exploited for industrial applications compared to chitin due to its high pH sensitivity [14], biodegradability, physiological compatibility, biodigestibility, adsorption, and chelating capacity [5, 15]. Industries such as food, pharmaceutical, cosmetics and medicine are the main areas of applications of chitosan but the food and nutrition industry are the most important users of chitosan [15-17].

Chitosan is used in drug formulation as a carrier [18]; in wound dressing materials due to its adsorptive and antimicrobial properties [18-21]. It is also used in wastewater treatment due to its antimicrobial, adsorptive capacity, and eco-friendliness [22]. Chitosan's application in plastic production is due to its biodegradability [23]. It has been used as filler in paper production [3, 24,25]. This is why the global chitosan market has continued to grow in a positive trend. In 2019, the global transactions of chitosan were valued at USD 6.8 billion and the average return on investment in chitosan is expected to grow at a rate of 24.7 % annually by 2027 [18].

The isolation of chitosan from biomass comprises the removal of minerals (particularly, calcium carbonate), proteins and lipids, and acetyl groups [26]. However, the quality and properties of chitosan are affected by the extraction procedure, the nature of the chitinous feedstock, and the conditions under which chitin was extracted [27].

The extraction of chitosan of good quality from shrimp shell materials was executed using 3 % hydrochloric acid (as demineralized), 4 % sodium hydroxide (as deproteinized) and 50 % NaOH as deacetylating agent [28].

Therefore, the extraction of chitosan from African giant land snail shell waste is expected to valorize it as there are many existing and new potential markets for chitosan. Further still, valorization of snail shell waste will mitigate or eliminate potential negative environmental impact of shell wastes on the long run. Therefore, the present study is designed to extract chitosan from snail shell wastes and ascertain the potentiality for its exploitation as commercial feedstock for chitosan production.

2. MATERIALS AND METHODS

2.1. Materials

Snail shell from African giant land snail, *Archachatinamarginata*, represented in figure 2,is indigenous to West Africa [29]. The shells of about 2 years old snail were collected by the authors from Facha Integrated farms withinObiaruku in Delta State, Nigeria on the 12th April, 2022. The place is geographically situated between latitudes 5°2and 5°3 and longitude 5°4and 5°4.Chemical reagents were of analytical grade, used without further purification.

Figure 2. African giant land snail (Archachatinamarginata)

2.2. Methods

2.2.1. Preparation of snail shell powder from snail shell wastes

The snail shells were processed for chitosan extraction by approaches used by Oyekunle and co [30] and Thillai and co [1] with some modifications.

The snail shells were washed over running tap water to remove debris and then broken into smaller particles with a cleaned metallic hammer, to loosen tissue and organics. The tissue-free particles were further washed in hot tap water (90 ℃) and then rinsed with warm deionized water to remove any foreign matter before it was sun-dried for 14 days in a dust-free environment.

The sun-dried snail shells were further downsized in a mortar and then pulverized using an industrial-grade blender into fine particles as shown in Figure3. The residual fine particles were sieved using an industrial sieve to obtain fine particles of sizes below 600 microns. Finally, the shell powder was stored in cleaned air-tight containers at ambient temperature.

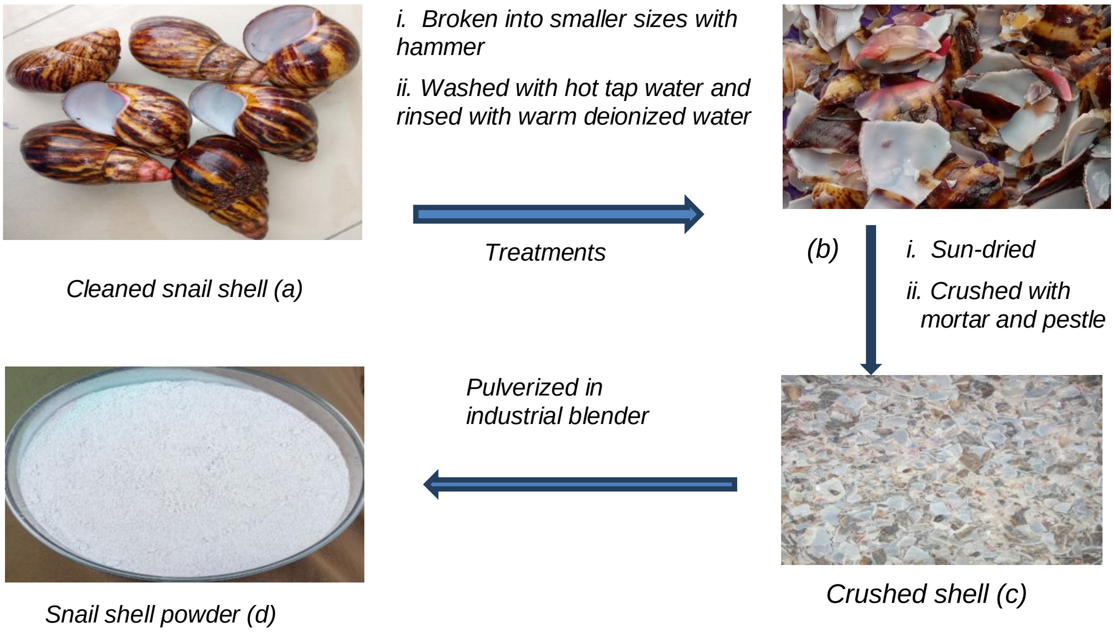

Figure 3. Fresh Snail shell powder from snail shell

2.2.2. Extraction of chitin from the snail shell powder

Chitin was extracted from the snail shell powder by consecutive acid and alkaline treatments of the shell powder under different experimental conditions of temperature, concentration, and retention time. The extraction entails demineralization and deproteinization using hydrochloric acid and sodium hydroxide as demineralizer and deproteinizer respectively. For optimal deproteinization efficiency, shell powder was demineralized first [31].

Demineralization of snail shell powder

The demineralization was performed according to the method used by Thillai and Co to demineralized shrimp shells [1] with slight modifications to suit the present biomass. About 18 g snail shell powder was demineralized in 420 mL of 7 % HCl, in the ratio of 3:70 g shell power to mL HCl solution. The shell powder was slowly added to 7 % (v/v) HCl solution in500 mL flask to avoid effervescence. Thereafter, the reaction flask was stir-heated at 150 rpm and 80 ℃ for 4hours over a magnetic stirrer, to remove carbonates and phosphates of calcium. The demineralized sample was filtered and washed repeatedly with deionized water to remove any trace of HCl and soluble impurities before it was oven-dried at 70 ℃ for 6 hours to achieve constant weight and then stored in an air-tight container.

Deproteinization of demineralized shell sample

The deproteinization was performed according to the procedure used by Thillai et al[1]with some modifications. The demineralized snail shell powder was deproteinized in 5 % (w/v) NaOH solution in the ratio of 3:70 g dried demineralized snail shell powder to mL NaOH solution (w/v) at 80 ℃ with constant stirring at 200 rpm for 3 hours. The resulting solid was filtered and the residue bathed in 5 % NaOH to obtain a clear solution, which marked the end of deproteinization. The deproteinized sample (residue) was washed to neutrality with hot deionized water (100-120℃). The pure deproteinized sample (chitin) was then oven-dried at 70 ℃ for 6 hours to achieve constant weight.

2.2.3. Extraction of chitosan from chitin by deacetylation

The snail shell chitin was deacetylated by heterogeneous alkaline hydrolysis at 120 ℃. The acetyl group was removed from the chitin based on the procedures used by Chang et al [32], Tsai et al [33], and Boukhlifi [34] with minor modifications. The chitin was deacetylated in 50 % (w/v) NaOH solution in the ratio of 1:20 g dried chitin to mL NaOH solution (w/v) at 120 ℃ with constant stirring at 250 rpm for 6 hours. The residual mixture was filtered and the residue (chitosan) was washed to neutrality with hot deionized water (100-120℃) and then dried in an oven at 120 ℃ for 3 hoursto constant weight. The dried chitosan obtained was quantified and recorded as a percent of the original weight of the snail shell sample [35] and then stored in airtight containers.

Table 1 shows the process parameters for the extraction of chitosan from snail shell waste.

Table 1. Chitosan extraction parameters

S/N	Parameter	Level
1	Weight of shell powder	18 g
2	Particle size	0.3-0.5 mm
3	Temperature	80 ℃
4	Concentration of demineralized	7 % HCl
5	Shell powder to acid ratio	3:70
6	Concentration of deproteinized	5 % NaOH
8	Concentration of deacetylating agent	50 % NaOH
9	Deacetylation temperature	120 ℃

2.3. Determination of percentage yield

The yield percent was obtained based on the original weight of snail shell powder used in the extraction process as expressed in the equation,Eq. 1

$$Yield\ (\%) = \left({W_y}/{W_{sp}} \right) \times\ 100 \qquad (1)$$

where W_y=Weight yield of chitosan (g) and W_{sp} = Weight of snail shell powder used

2.4. Characterization of snail shell chitosan

The formation and purity of the snail shell chitosan were confirmed by Fourier transformed-infrared (FT-IR) spectroscopy and powdered x-ray diffraction (pXRD). The model and operating condition of the FT-IR: Thermo Nicolet iS10 Smart ITR spectrophotometer (Thermo Fisher Scientific, USA), equipped with an OMNIC-Software, a DTGS detector, and a Ge-on-KBr beam splitter) in the wavelength range of 500 cm^{-1} and 4000 cm^{-1} and the solid-state using potassium bromide (KBr) pellets.

The powdered x-ray diffractometer (a Bruker D2PHASER diffractometer, Karlsruhe, Germany) furnished with a Ni 24 filtered Cu Kα-radiation (λ = 1.5406 Å), generated at voltage of 40 kV and intensity of 40 mA, and a diffracted beam monochromator. Each of the dried powdered samples was viewed in the diffraction angles (2θ) in the range of 5°–80° and a counting time of 5.0 s/angle step (that is step size of 0.05).

2.5. Determination of chitosan quality parameters

The quality of snail shell chitosan was ascertained by the following parameters: moisture content, solubility, ash value, and degree of deacetylation (DD).

2.5.1. Determination of moisture content

The moisture content was determined by gravimetric method according to the procedure used by Pereda and co-workers [36] and calculated by equation, Eq. 2. The process was repeated three times and the average moisture content was recorded.

$$Moisture\ content\ (\%) = \frac{W_1 - W_2}{W_1 - W_0} \times 100 \qquad (2)$$

Where = Weight of empty crucible (g); = Weight of fresh sample plus crucible (g); = Weight of dried sample plus crucible (g).

2.5.2. Ash value

The ash value was determined by dry ashing 1.0 g of sample in mufflefurnace according to the procedure used by Jiang [37] and Mohan and co-workers [38] with some modification. The sample was placed on a pre-weigh crucible and transferred into mufflefurnace that was pre-heated to 55. The sample was allowed to tar in the furnace for 6 hours and then allowed to cool to <200 °C in the furnace before it was transferred into a desiccator with a vented top to further cool to room temperature. The ash value was calculated by equation, Eq. 3. The process was repeated twice and the average value was recorded.

$$Ash\ value\ (\%) = \frac{W_{res}}{W_{sam}} \times 100 \qquad (3)$$

Where W_{res} = Weight of residue (ash) (g) and W_{sam} = Weight of sample (g)

2.5.3. Determination of solubility of chitosan

The solubility test was performed according to the procedure used by Adekanmi and co-workers [31] with minor modifications. A sample of 1.0 g was dissolved in 100 mL of 1 % (v/v) acetic acid solution. The resulting mixture was stirred at 400 rpm for 2 hours at ambient temperature and subsequently made to pass through a pre-weighed filter paper, dried to constant weight at 80 ℃ in an oven. At the end of filtration, the filter paper was re-dried to constant weight and re-weighed.

The solubility of chitosan was calculated by equation, Eq. 4.

$$Solubility = \frac{Amount\ of\ sample\ that\ dissolved\ into\ solution}{Original\ amount\ of\ sample} \times \quad (4)$$

2.5.4. Determination of the degree of deacetylation (DD)

The DD value of chitosan was determined by the elemental method. The CHN elemental analyzer was used to determine the carbon-nitrogen ratio of chitosan and the degree of acetylation (DA) and DD were calculated by the equations,Eq. 5 and 6 respectively.

$$DA = \left\{\frac{({}^{C}/_{N} - 5.14)}{1.72}\right\} \times 100 \qquad (5)$$

where ‘*C*’ and ‘*N*’ are the percent carbon and nitrogen content in the biopolymer respectively

$$DD\ (\%) = 100 - DA \qquad (6)$$

3. RESULTS AND DISCUSSION

The formation and purity of snail shell chitosan were confirmed by the appearance of characteristic absorption bands in its Fourier transformed-infrared spectrum shown in Figure 4.

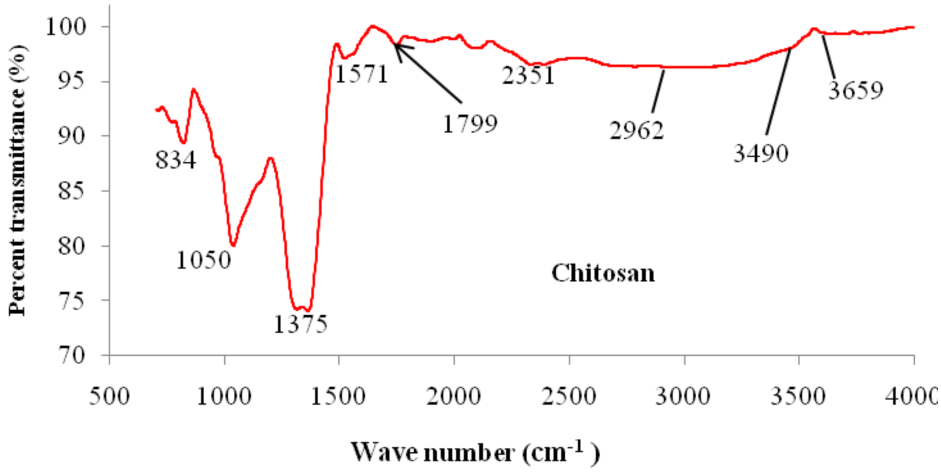

Figure 4. Fourier transformed-infrared spectrum of snail shell-chitosan

The broad peak at 3490 cm^{-1} corresponds to O-H stretching vibration [39, 40]. The peak around 2351 cm^{-1} is due to the absorption of atmospheric CO_2 by the chitosan [41].

Furthermore, the spectrum of snail shell-chitosan did not show a peak at 1500 cm^{-1} which is associated with amide band of protein [40]. This implies that snail-chitosan was sufficiently deproteinized and it is expected to manifest in the solubility of the biopolymer in acetic acid.

The intense peak at 1375 cm^{-1} indicates the CH_3 of the amide group [42]. Comparing the sharpness of this peak to that of the amino group at 1571 cm^{-1} indicates that snail shell-chitosan was insufficiently deacetylated as many molecules of acetyl-amide appeared to be in the sample. The polysaccharide component is represented by the band at 834 cm^{-1} [43].

Figure 5 is the powdered x-ray diffraction (XRD) pattern of snail shell chitosan. The formation of snail shell-chitosan was confirmed by the appearance of two characteristic peaks at $2θ$ = 18.19˚ and 29.50˚ which correspond to the (110) and (241) planes of orthorhombic crystalline structure based on JCPDS card no: 39-1894 and some literature [44-46].

The peak at $2θ = 34.22˚$ is indicative of mineral contamination [47]. The multiple peaks in the XRD spectrum of chitosan show that the snail shell-chitosan is polycrystalline. Therefore, the snail shell-chitosan is orthorhombic in structure and polycrystalline material in nature.

The properties of chitosan from snail shell wastes as displayed in Table 2 was compared to the quality indices of standard chitosan in Table 3 to establish quality of snail shell-chitosan.

Table 2. Snail shell-chitosan quality parameters

Parameters	Snail shell-chitosan
Moisture content (%)	1.42
Ash value (%)	1.61
Solubility (%)	85.2
DD (%)	67.44

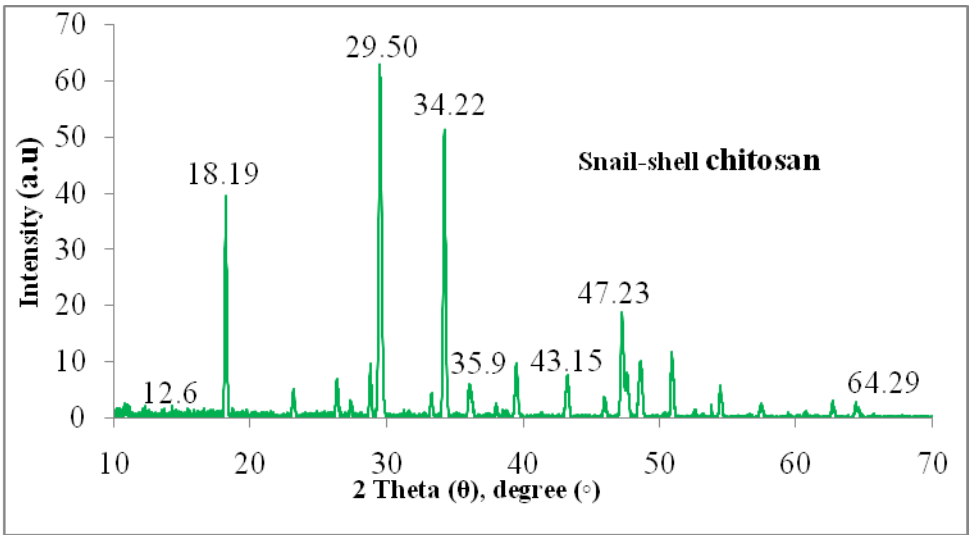

Figure 5. Powdered X-ray diffractogram of snail shell-chitosan

DDis the degree of deacetylation basedon the carbon-to-nitrogen ratio.

Table 3. Quality parameters of commercial/ standard chitosan

Parameters	Chitosan from crustacean (shrimp and crab) shell	Ref.
Moisture content (%)	<10	[48, 49]
Ash value (%)	< 1	[50, 51]
Solubility (%)	97.65	[5]
DD (%)	81.24	[5]
	80 (for high quality chitosan)	[2, 50]

3.1. Percent yields

Crustacean shells, especially shrimp and crab shells, contain 13-42 % of chitin and chitosan which is one of the reasons for their exploitation as main commercial sources of chitin and chitosan [52]. However, the extraction of the biopolymers from these feedstocks is strongly associated with the efficiencies of demineralization and deproteinization processes [4]. Most research groups had reported 15-25 % yield of chitosan from shrimp shell wastes [5, 53-54].

The chitosan yield of 2.67 g which corresponded to 14.83 % was obtained from snail shell waste. This yield percent is comparable to those of crustacean shell wastes as such snail shell is a potential feedstock for commercial production of chitosan.

3.2. Moisture content of snail shell chitosan

Chitosan is hygroscopic hence; it isstored in airtight container. Chitosan of good quality has low moisture content for prolonged self-stability and storage [55-56]. Chitosan of excessive moisture content deteriorates quickly in quality as high moisture encourages fungal growth [31]. This is why the moisture content of most commercial chitosan is less than 10 % [48].

The moisture content of chitosan derived from snail shells is 1.42 % which is far less than the 10 % benchmark [48, 49] but above the range of 1.00-1.30 % reported for most shrimp shell wastes [57-59]. The high moisture content of the snail shell chitosan may be due to high atmospheric moisture (high humidity) at the time of extraction. Moreover, 7.56 % and 7.62 % moisture levels have been reported for shrimp and crab shells respectively by Parthiban and co [5].

3.3. Ash value of snail shell-chitosan

Ash value is a quality parameter that measures the extent to which a chitinous feedstock has been demineralized. Ash in chitosan is an indication that mineral salts were incompletely removed by demineralization [60]. The significance of ash value of chitosan is the effect it has on other quality parameters such as molecular weight, solubility, and viscosity [5, 55, 57]. As such, the ash value of chitosan of high quality is less than 1 % [61].

However, the ash value of snail shell-chitosan was 1.61 %. The implication is that 7 % of the demineralizer was insufficient for the complete removal of mineral salts from the snail shell powder. Hence, increasing the concentration of demineralizer as well as the retention time for demineralization might enable adequate removal of mineral salts.

Nevertheless, a high concentration of demineralizer could cause depolymerization via glycosidic cleavage (via hydrolysis), which might reduce the polymer's molecular weight and chain length [5].

3.4. Solubility of snail shell-chitosan

Chitosan is insoluble in water. Chitosan becomes soluble when its amino groups are protonated at low pH conditions. The implication is that solubility is a function of the degree of deacetylation[47, 62]. Crystallinity, which is the order of arrangement of monomers in a polymer, is another factor that influences the solubility of chitosan [62].

Chitosan of high solubility, 97.65 % in 1 % acetic acid, is of excellent biological value [5]. However, solubility of the snail shell-chitosan in 1 % acetic acid is 85.2 %. Ahing and coworkers reported solubility of 99.0-99.7 % for shrimp shell chitosan in 1 % acetic acid solution [63]. The low solubility of snail shell chitosan relative to shrimp chitosan was due to its ash value as the FT-IR spectrum in Figure 4 had indicated no protein contamination because of the absence of absorption bands at 1500 cm^{-1} [30, 64]. Protein contamination and residual ash value are responsible for low solubility of chitosan [5,57]. Residual protein in chitosan results from incomplete deproteinization of its chitin, and it has tremendous effect on solubility.

3.5. Degree of deacetylation (DD)

The degree of deacetylation (DD) is the mole fraction of D-glucosamine in chitosan (N-acetyl-D-glucosamine and D-glucosamine) [65]. It is the mole fraction of deacetylated units of the chitosan chain [34, 66-68]. The DD is a functional parameter whose value affects other physico-chemo-biological properties of chitosan. Properties such as solubility, chemical reactivity, antimicrobial and antioxidant activities, biodegradability, chelation, and mucoadhesive capacities of chitosan are affected by DD value [69-71].

The DD value of the snail shell-chitosan sample was determined by elemental analysis. The percent carbon and nitrogen in chitosan were 38.76 % and 6.80 % respectively hence, the DD value of snail shell chitosan was 67.44 %.

4. CONCLUSION

Chitosan was extracted from the shell waste of *Archachatinamarginata* by demineralization, deproteinization, and deacetylation processes. The resultant chitosan was characterized by FT-IR and pXRD spectroscopy. Based on quality parameters, snail shell chitosan is of comparable quality to commercial/standard chitosan. Hence, snail shell waste is a potential feedstock for sustainable and commercial production of chitosan.

Acknowledgements

The authors are thankful to the Federal University of Petroleum Resources and management for providing laboratory equipment essential to carry out this research successfully. This work is supported by Tertiary Education Trust Fund (TETfund) Nigeria on grant number TETF/DASTD; UNIV/DELTA/TSAS/2020/VOL 1.

Conflict of Interest

The authors declare that there is no conflict of interest.

5. REFERENCES

[1] N. S.Thillai,N., Kalyanasundaram, S. Ravi (2017) *Extraction and characterization of chitin and chitosan from Achatinodes*,Nat. Prod. Chem. Res.,5, 281-284. http://dx.doi.org/10.4172/2329-6836.1000281

[2] J.Cheng, H.Zhu, J.Huang, J.Zhao, B.Yan, S.Ma, H. Zhang, D. Fan (2020) *The physicochemical properties of chitosan prepared by microwave heating*,FoodSci.Nutr., 8(4), 1987-1994. http://dx.doi.org/10.1002/fsn3.1486

[3] A.N.Amitaye, E.E.Elemike, H.B.Akpeji, E.Amitaye, I. Hossain, J. I. Mbonu, A. E. Aziza (2024) *Chitosan: A sustainable biobased material for diverse applications,*J. Environ. Chem. Eng., 12, 113208, http://dx.doi.org/10.1016/j.jece.2024.113208.

[4] B.T.Iber, D.Torsabo, C.E.Chik, F.Wahab, S. Abdullah, H.B.Hassan, N. Kasan (2022) *The impact of re-ordering the conventional chemical steps on the production and characterization of natural chitosan from biowaste of Black Tiger Shrimp, Penaeusmonodon,* J. Sea Res., 190, 102306, https://doi.org/10.1016/j.seares.2022.102306

[5] F.Parthiban, S.BalaSundari, A. Gopalakannan (2017) *Comparison of the Quality of Chitin and Chitosan from Shrimp, Crab and SquillaWaste,*Curr. World Environ., 12(3), 672-679. http://dx.doi.org/10.12944/CWE.12.3.18

[6] T.K.Varun, S.Senani, N.Jayapal, J.Chikkerur, S.Roy, V.B.Tekulapally, M.Gautam, N.Kumar (2017) *Extraction of chitosan and its oligomers from shrimp shell waste, their characterization and antimicrobial effect*,Vet. World, 10 *(2)*, 170-175. http://dx.doi.org/0.14202/vetworld.2017.170-175

[7] K. W.Omari, J. E.Besaw, F. M. Kerton (2012) *Hydrolysis of chitosan to yield levulinic acid and 5-hydroxymethylfurfural in water under microwave irradiation*,Green Chem., 14*(5)*, 1480–1487. https://doi.org/10.1039/C2GC35048C

[8] M.Yanat, K.Schroen (2021) *Preparationmethods and applications of chitosan nanoparticles; with an outlook toward reinforcement of biodegradable packaging,*React. Funct. Polym., 161, 104849-52. https://doi.org/10.1016/j.reactfunctpolym.2021.104849

[9] E. M.Costa, S.Silva, C.,Pina, F. K.Tavaria, M. M. Pintado (2012) *Evaluation and insights into chitosan antimicrobial activity against anaerobic oral pathogens*,Anaerobe, 18(3), 305-309. https://doi.org/10.1016/j.anaerobe.2012.04.009

[10] S.Eyley, W.Thielemans (2014) *Surface modification of cellulose nanocrystals*. Nanoscale*,* 6, 7764-7779, DOI:10.1039/c4nr01756k.

[11] W. M.Kedir, G. F.Abdi, M. M.Goro, L. D. Tolesa (2022) *Pharmaceutical and drug delivery applications of chitosan biopolymer and its modified nanocomposite: A review*,Heliyon*,* 8, 1-10, DOI:10.1016/j.heliyon.2022.e10196.

[12] I.Younes, M.Rinaudo (2015)*Chitin and chitosan preparation from marine sources, structure, properties and applications*,Mar. Drugs*,* 13(3), 1133-1174.https://doi.org/10.3390/md13031133

[13] J.Dutta, A Priyanka (2022)*Facile approach for the determination of the degree of deacetylation of chitosan using acid-base titration,*Heliyon*,* 8(7), e09924, DOI:10.1016/j.heliyon.2022.e09924.

[14] R. N.Wijesena, N.Tissera, Y. Y.Kannangara, Y.Lin, G. A.Amaratunga, K. M. De Silva (2015) *A method for top-down preparation of chitosan nanoparticles and nanofibers*,Carbohydr. Polym.*,* 117, 731–738. https://doi.org/10.1016/j.carbpol.2014.10.055

[15] E. A.Azmy, H. E.Hashem, E. A.Mohamed, N. A. Negm (2019) *Synthesis, characterization, swelling, and antimicrobial efficacies of chemically modified chitosan biopolymer*,J.Mol.Liq.*,* 284, 748-754: Doi: 10.1016/j.molliq.2019.04.054.

[16] T.J.Gutiérrez (2017) *Chitosan applications in textile and food industry* In S. Ahmed, S. Ikram, *Chitosan-derivatives, composites and applications,* New York: Scrivener Publishing LLC, Wiley, 2, 185–232. DOI:10.1002/9781119364894.ch8.

[17] T.Philibert, B. H.Lee,N. Fabien (2017)*Current status and new perspectives on chitin and chitosan as functional biopolymers*,Appl. Biochem. Biotechnol., 181, 1314–1337. DOI:10.1007/s12010-0162286-2.

[18] V.Kumar, N.Sharma, P.Janghu, R.Pasrija, M. Umesh, P.Chakraborty,S.Sarojini, J.Thomas (2023) *Synthesis and characterization of chitosan nanofibres for wound healing and drug delivery application*,J. Drug Deliv.Sci. Techn.*,*87, 104858. Doi:10.1016/j.jddst.2023.104858.

[19] G.Martua, M.Mihai, D.C.Vodnar (2019)*The use of chitosan, alginate, and pectin in the biomedical and food sector-biocompatibility, bioadhesiveness, and biodegradability*,Polym. (Basel)*,* 11(11), 1837. DOI:10.3390/polym11111837.PMID.

[20] H.Hamedi, S.Moradi, S.M.Hudson, A.E.Tonelli (2018) *Chitosan-based hydrogels and their applications for drug delivery in wound dressings: a review,*Carbohydr.Polym.*,* 199, 445–460, DOI:10.1016/j.carbpol.2018.06.114.

[21] G.Granata, S.Stracquadanio, M.Leonardi, E. Napoli, G.Malandrino,V. Cafiso, S. Stefani, C. Geraci (2021) *Oregano and thyme essential oils encapsulated in chitosan nanoparticles as effective antimicrobial agents against foodborne pathogens*, Mol.*,* 26(13), 40-55. DOI:10.3390/moleculess26134055

[22] F.Boukhlifi, A.Bencheikh, H. Ahlafi (2011) *Characterization and adsorption of chitin toward copper* Cu^{2+}*,*Phys. Chem. News*,* 58, 67-72. http://dx.doi.org/10.5772/intechopen.89708

[23] M. A.Elsawy, G. A.Saad, A. M. Sayed (2016) *Mechanical, thermal, and dielectric properties of poly(lactic acid)/chitosan nanocomposites,*Polym. Eng. Sci.*,* 56, 987–994. http://dx.doi.org/10.1002/pen.24328

[24] A. B.Pitaloka, A. H.Saputra, M. Nasikin (2013) *Water Hyacinth for Superabsorbent Polymer Material,*World Appl. Sci. J.*,*22(5), 747-754. http://dx.doi.org/10.5829/idosi.wasj.2013.22.05.262

[25] S.Habibie, M.Hamzah, M.Anggaravidya, E. Kalembang 92016)*The effect of chitosan on the physical and mechanical properties of paper*. J.Chem.Eng.Mater.Sci.*,* 7(1), 1-10. DOI: 10.5897/JCEMS2015.0235.

[26] M. H.Mohammed, P. A.Williams, O. Tverezovskaya (2013)*Extraction of chitin from prawn shells and conversion to low molecular mass chitosan*. Food Hydrocoll.*,* 31*(2)*, 166–171. http://dx.doi.org/10.1016/j.foodhyd.2012.10.021

[27] P. Ramasamy, N. Subhapradha, T. Thinesh, J. Selvin, K. M. Selvan, V. Shanmugam (2017) *Characterization of bioactive chitosan and sulfatedchitosanfromDoryteuthissinghalensis (Ortmann, 1891)*,Int.J.Biol.Macromol.*,* 99, 682-691. https://doi.org/10.1016/j.ijbiomac.2017.03.041

[28] N. V. Toan (2009)*Production of chitin and chitosan from partially autolyzed shrimp shell materials,*OpenBiomater.J.*,* 1, 21-24. http://dx.doi.org/10.2174/1876502500901010021

[29] F. A. Aluko, E. A. Adesina, A. M. Akanji, H. A. Awojobi, G. A. Adeleke, E. S. Apata (2017) *Assessment of phenotypic traits of Archachatinamarginatasututralis snails in the derived Savannah zone of Ogun State, Nigeria*, Ethiop.J. Environ. Stud. Mgt,10, 1350-1356. DOI: v10i10.11

[30] T. D.Oyekunle, A. J. Omoleye (2019) *New process for synthesizing chitosan from snail shells*,J. Phys.Conf.Ser.*,*1299, 1-6. http://dx.doi.org/10.1088/1742-6596/1299/1/012089

[31] A.A.Adekanmi, U.T.Adekanmi, A.S.Adekanmi, L.K.Ahmad, O.O.Emmanuel (2023) *Production and characterization of chitosan from chitin of snail shells by sequential modification process*. Afr.J. Biotechnol., 22(2), 39-53. https://doi.org/10.5897/AJB2020.17135

[32] J.S.Chang, K.L.Chang, M.L.Tsai (2007) *Liquid–crystalline behavior of chitosan in malic acid.*J. Appl. Polym. Sci.*,*105, 2670–2675. http://dx.doi.org/10.1002/app.26475

[33] M. L.Tsai, S. W.Bai, R. H. Chen (2008)*Cavitation effects versus stretch effects resulted in different size and polydispersity of ionotropic gelation chitosan–sodium tripolyphosphate nanoparticle*. Carbohydr. Polym.*,* 71, 448–457. https://doi.org/10.1016/j.carbpol.2007.06.015

[34] F. Boukhlifi (2020) *Quantitative Analysis by IR: Determination of Chitin/Chitosan DD,* In M. Khan, G. M. Nascimento,M. El-Azazy, *Modern spectroscopic techniques and applications*, London: Intechopen Limited, 107-131.

[35] K. O.Amoo, O. A.Olafadehan, T. O. Ajayi (2019) *Optimization studies of chitin and chitosan production from Penaeusnotialis shell waste,* Afr.J. Biotechnol.*,* 18(27), 670-688. DOI: 10.5897/AJB2019.16861

[36] M.Pereda, M. I.Aranguren, N. E.Marcovich (2009) *Water vapor absorption and permeability of films based on chitosan and sodium caseinate,*J. Appl. Polym. Sci.,11(6), 2777-2784. http://dx.doi.org/10.1002/app.29347

[37] T. D. Jiang (2001),*Chitosan,* Chemical Industry Press, Beijing, China.

[38] C. O. Mohan, S. Gunasekaran, C. N. Ravishankar (2019) *Chitosan-capped gold nanoparticles for indicating temperature abuse in frozen stored products*, Sci. food, 3(2), htpps://doi.org/10.1038/s41538-019-0034-z

[39] Y.Zhang, C.Xue, Y.Xue, R.Gao, X. Zhang (2005) *Determination of the degree of deacetylation of chitin and chitosan by X-ray powder diffraction*, Carbohydr.Res.,340, 1914-1917, DOI:10.1016/j.carres.2005.05.005.

[40] P.Zhu, Z.Gu, S.Hong, H. Lian (2017) *One-pot production of chitin with high purity from lobster shells using choline chloride–malonic acid deep eutectic solvent*,Carbohydr.Polym.,177, 217-223. https://doi.org/10.1016/j.carbpol.2017.09.001

[41] A.N. Amitaye, E.E. Elemike, T.T. Uzah (2024) *Multifarious Techniques for Resolving Chitosan's Degree of Deacetylation (DD)*,*Mater. Int.,*6(2), 1-24. DOI:10.33263/Materials62.01

[42] A.Pawlak, M. Mucha (2003)*Thermogravimetric and FTIR studies of chitosan blends*. *Thermochim. Acta.,*396(1–2), 153-166. https://doi.org/10.1016/S0040-6031(02)00523-3

[43] T. Nicolet (2001)*Introduction to Fourier Transform Infrared Spectrometry,* Thermo Nicolet Corporation, Madison, USA.

[44] A.Kocyigit, M.Yilmaz, S.Aydogan, U. S. Incekara (2020) *The performance of chitosan layer in Au/n-Si sandwich structures as a barrier modifier*. Polym.Test., 89, 106546, DOI:10.1016/j.polymertesting.2020.106546.

[45] M. Rajkumar, K. Kavitha, M. Prabhu, N. Meenakshisundaram, V. Rajendran (2013) *Nanohydroxyapatite–chitosan–gelatin polyelectrolyte complex with enhanced mechanicaland bioactivity.* Mater. Sci. Eng. C,33, 3237–3244. DOI:10.1016/j.msec.2013.04.005.

[46] K. R.Desnelli, F.Alfarado, A. Mara,M. Said (2023) *Methylene blue degradation using chitosan-*Fe_2O_3*,* Rev. Colomb. Quim.,52(2),36–42, DOI:10.15446/rev.colomb.quim.v52n2.109625.

[47] S.Kumari, S.H.Annamareddy, S.Abanti, P.K.Rath (2017) *Physicochemical properties and characterization of chitosan synthesized from fish scales, crab and shrimp shells,*Int.J.Biol. Macromol., 104, 1697-1705.doi/10.1016/j.ijbiomac.2017.04.119

[48] K. K. Sukumaran (1987) *Squilla (Mantis shrimp) fishery of Karnataka state*,Mar.Fish.Resour.Mgt.,18, 1-3.http://dx.doi.org/10.1016/0165-7836(93)90048-C

[49] M.Anand, R.Kalaivani, M.Maruthupandy, A.K. Kumaraguru, S. Suresh (2014) *Extraction and characterization of chitosan from marine crab and Squilla collected from the Gulf of Manner region, South India*. J. Chitin chitosan Sci., 2(4), 280-287. https://doi.org/10.1166/jcc.2014.1053

[50] H.K.No, S.P.Meyers (1989) *Crawfish Chitosan as a coagulant in recovery of organic compounds from seafood processing streams,* J. Agric. Food Chem., 37(3), 580-583. https://doi.org/10.1021/jf00087a002

[51] K. Ssekatawa, D. K. Byarugaba, E. M. Wampande, T. N. Moja, E. Nxumalo, M. Maaza, J. Sackey, F. Ejobi, J.B.Kirabira (2021) *Isolation and characterization of chitosan from Uganda edible mushrooms, Nile perch scales and banana weevils for biomedical applications*, Sci Rep., 11, 4116. https://doi.org/10.1038/s41598-021-81880-7.

[52] F.Croisier, C.Jerome (2013) *Chitosan-based biomaterials for tissue engineering*,Eur. Polym. J., 49(4), 780-792. https://doi.org/10.1016/j.eurpolymj.2012.12.009.

[53] W. William, N. Wid (2019)*Comparison of extraction sequence on yield and physicochemical characteristic of chitosan from shrimp shell waste*, J. Phys. Conf. Ser. 1358 (1) https://doi.org/10.1088/1742-6596/1358/1/012002.

[54] S. Pati, A. Chatterji, B. P. Dash, B. R. Nelson, T. Sarkar, S. Shahimi, H. A. Edinur, T. S. B. AbdManan, P. Jena, Y. K. Mohanta, D. Acharya (2020) *Structural characterization and antioxidant potential of chitosan by γ-irradiation from the carapace of horseshoe crab*. Polymers 12 (10), 1–14. https://doi.org/10.3390/ polym12102361.

[55] N.Subhapradha, P.Ramasamy, V.Shanmugam, P. Madeswaran, A.Srinivasan, A. Shanmugam (2013) *Physicochemical characterization of beta-chitosan from Sepioteuthislessonianagladius*, Food Chem., 141(2), 907-913. https://doi.org/10.1016/j.foodchem.2013.03.098

[56] F. C.K. Ocloo, E. T.Quayson, A.Adu-Gyamfi, E. A. Quarcoo, D.Asare, Y.Serfor-Armah, B. K. Woode (2011) *Physicochemical and functional characteristics of radiation-processed shrimp chitosan,* Radiat. Phys. Chem.,80(7), 837-841. DOI: 10.1016/j.radphyschem.2011.03.005.

[57] M. S.Hossain, A. Iqbal (2014) *Production and characterization of chitosan from shrimp waste*,J. Bangladesh Agric.Univ.,12(1), 153-160. http://dx.doi.org/10.3329/jbau.v12i1.21405

[58] V.Mohanasrinivasan, M.Mishra, J. S.Paliwal, S. K.Singh, E.Selvarajan, V.Suganthi,C. S. Devi (2014). *Studies on heavy metal removal efficiency and antibacterial activity of chitosan prepared from shrimp shell wastes*,Biotech.,4(2), 167-175. DOI: 10.1007/s13205-013-0140-6

[59] P. S.Saravana, T. C.Ho, S.J.Chae, Y.J.Cho, J.S.Park, H.J.Lee,B. S. Chun (2018)*Deep eutectic solvent-based extraction and fabrication of chitin films from crustacean*,Carbohydr.Polym. DOI: 10.1016/j.carbpol.2018.05.018.

[60] S. O. Fernandez-Kim (2004)*Physicochemical and functional properties of Crawfish chitosan as affected by different processing protocols,* Graduate faculty of Seoul National University, Seoul. https://repository.lsu.edu/gradschool_theses/1338?utm_source=repository.lsu.edu%2Fgradschool_theses%2F1338&utm_medium=PDF&utm_campaign=PDFCoverPages

[61] H. K.No, M. Y. Lee (1995)*Isolation of chitin from crab shell waste*. J. Korean Soc.FoodNutr., *24*(1), 105-113.https://doi.org/10.1021/jf00087a001

[62] L.Riu, M.Xie, B.Hu, L.Zhou, M.Saeeduddin, X. Zeng (2017) *Enhanced solubility and antioxidant activity of chlorogenic acid-chitosan conjugates due to the conjugation of chitosan with chlorogenic acid*, Carbohydr. Polym., 170, 206-216. https://doi.org/10.1016/j.carbpol.2017.04.076

[63] F. A. Ahing, N. Wid (2016) Extraction and characterization of chitosan from shrimp shell waste in Sabah,Trans. Sci. Technol.,3(1-2), 227-237. https://doi.org/10.4236/ojopm.2018.83003

[64] A.Wasko, P.Bulak, M. Polak-berecka, K.Nowak, C.Polakowski, A. Bieganowski (2016)*The first report of the physicochemical structure of chitin isolated from Hermetiaillucens*,Int. J. Biol. Macromol., 92, 316-320. https://doi.org/10.1016/j.ijbiomac.2016.07.038

[65] Y.Shigemasa, H.Matsuura, H.Sashiwa, H. Saimoto (1996)*Evaluation of different absorbance ratios from infrared spectroscopy for analyzing the degree of deacetylation in chitin*,Int. J. Biol. Macromol.,18, 237-242.https://doi.org/10.1016/0141-8130(95)01079-3

[66] M.Rinaudo, M.Milas, P. Ledung (1993) *Characterization of chitosan-Influence of ionic -strength and degree of acetylation on chain expansion*,Int.J. Biol.Macromol., 15(5), 281-285. https://doi.org/10.1016/0141-8130(93)90027-J

[67] W.Wei, S. Q.Bo, S. Q.Li, Q. Wen (1991) *Determination of the mark–Houwink equation for chitosans with different degrees of deacetylation*, Int.J. Biol.Macromol., 13(5), 281-285. https://doi.org/10.1016/0141-8130(91)90027-r

[68] A. N. Amitaye, E. E. Elemike, T. T. Uzah (2024) *Multifarious Techniques for Resolving Chitosan’s Degree of Deacetylation (DD)*, Mater. Int., 6 (2), 1-24. DOI: 10.33263/Materials62.016

[69] G.Lamarque, M.Cretenet, C.Viton, A.Domard (2005) *The new route of deacetylation of alpha and beta-chitins using freeze-pump-out-thaw-cycles*. Biomacromol., 6, 1380-1388. http://dx.doi.org/10.1021/bm049322b

[70] M. A.Matica, F. L. Bachmann, A.Tøndervik, H. Sletta, V. Ostafe (2019)*Chitosan as a Wound Dressing Starting Material: Antimicrobial Properties and Mode of Action,*Int.J.Mol.Sci.,20, 5889. DOI:10.3390/ijms20235889.

[71] J.Kumirska, M. X.Weinhold, J.Thoming, P. Stepnowski (2011) *Biomedical activity of chitin/ chitosan-based materials-Influence of physic-ochemical properties apart from molecular weight and degree of N-acetylation*,Polym., 3, 1875-1901. https://doi.org/10.3390/polym3041875

IZVOD

VALORIZACIJA OTPADA LJUŠTURE AFRIČKOG DŽINOVSKOG KOPNENOG PUŽA (*ARCHACHATINAMARGINATA*) EKSTRAKCIJOM HITOZANA IZ NJEGA

Afrički džinovski kopneni puž (Archachatinamarginata) jedan je od najčešćih mekušaca u južnoj Nigeriji. Ima ljušturu koja čini više od polovine njegove telesne mase i obično se odbacuje kao otpad. Cilj ove studije je valorizacija otpada ljušture puža ekstrakcijom hitozana, svestranog i veoma zahtevnog biopolimera iz njega. Hitozan je ekstrahovan hemijskim metodama i okarakterisan Furijeovom transformisanom infracrvenom spektroskopijom i difrakcijom X-zraka praha. Parametri kvaliteta kao što su rastvorljivost, sadržaj vlage, vrednost pepela i stepen deacetilacije određeni su za hitozan iz ljušture puža. Rezultati pokazuju da je hitozan iz ljušture puža uporedivog kvaliteta sa komercijalno prodajnim hitozanom iz škampa. Hitozan iz ljuštura puževa ima DD vrednost od 78,4%, rastvorljivost od 95,35%, vlagu od 1,42% i vrednost pepela od 1,61%, što potvrđuje da je hitozan iz ljuštura puževa održiva i pogodna sirovina za komercijalnu proizvodnju hitozana. Prinos hitozana na bazi ljuštura puževa bio je 14,83%, što je uporedivo sa prinosom iz otpada ljuštura rakova.

Ključne reči: *Archachatinamarginata, otpad ljuštura, hitozan, parametri kvaliteta, valorizacija*

Naučni rad
Rad primljen: 21.03.2025.
Rad korigovan: 01.05.2025.
Rad prihvaćen: 10.05.2025.

Azuka N. Amitaye:	0000-0002-4069-5359
Elias E. Elemike:	0000-0001-9253-5093
Terngu T. Uzah:	0000-0003-3556-2049

Ahlem Chahinez Kadri[1]*, M'hamed Ouadah*[1]**,*
Abderrahmane Younes[2]*, Sofiane Chabane*[3]

[1]*Ecole Nationale Supérieure des Technologies Avancées, Place des Martyrs, 16001 Algiers, Algeria,* [2]*Research Center in Industrial Technologies (CRTI), Cheraga, Algiers, Algeria,* [3]*CIMA+, Montreal, Quebec, Canada*

Scientific paper
ISSN 0351-9465, E-ISSN 2466-2585
https://doi.org/10.62638/ZasMat1418
Zastita Materijala 67 (1)
159 - 170 (2026)

Assessing the impact of AC, DC and hybrid AC/DC stray currents on cathodic protection efficiency

ABSTRACT

Ensuring the efficiency of cathodic protection (CP) is critical for maintaining the integrity of buried pipelines. Stray currents, particularly those originating from high-voltage power lines, can interfere with CP systems, leading to accelerated corrosion. This study investigates the effects of alternating current (AC), direct current (DC), and hybrid AC/DC stray currents on CP performance. Electrochemical measurements and finite element modeling (FEM) were employed to evaluate the impact of these currents on X70 steel pipelines. Results indicate that AC stray currents reduce CP effectiveness by shifting protection potentials to more electropositive values, increasing corrosion risk. DC stray currents affect CP voltage settings, while hybrid AC/DC interference exacerbates both effects. Findings provide insights into pipeline protection strategies, particularly in environments with mixed AC/DC stray currents.

Keywords: *AC stray current, DC stray current, hybrid AC/DC interference, corrosion, cathodic protection, finite element method (FEM)*

1. INTRODUCTION

Cathodic protection (CP) stands as one of the most commonly employed methods to safeguard pipelines against corrosion, either through impressed current anodes or by connecting them to sacrificial materials acting as anodes [1-5]. There are two primary types of CP systems(Fig.1): impressed current (ICCP) and sacrificial anode (SACP). In the ICCP system, an electrical current is supplied from an external source (rectifier), which is electrically connected between an anode and the pipeline cathode. Conversely, in the SACP system, the pipeline is electrically linked to the sacrificial anode.

Cathodic protection (CP) is widely used to mitigate pipeline corrosion, utilizing either impressed current cathodic protection (ICCP) or sacrificial anode cathodic protection (SACP) [1-5]. As shown in Figure 1, ICCP relies on an external power source to supply protective current, whereas SACP employs sacrificial materials that corrode in place of the pipeline.

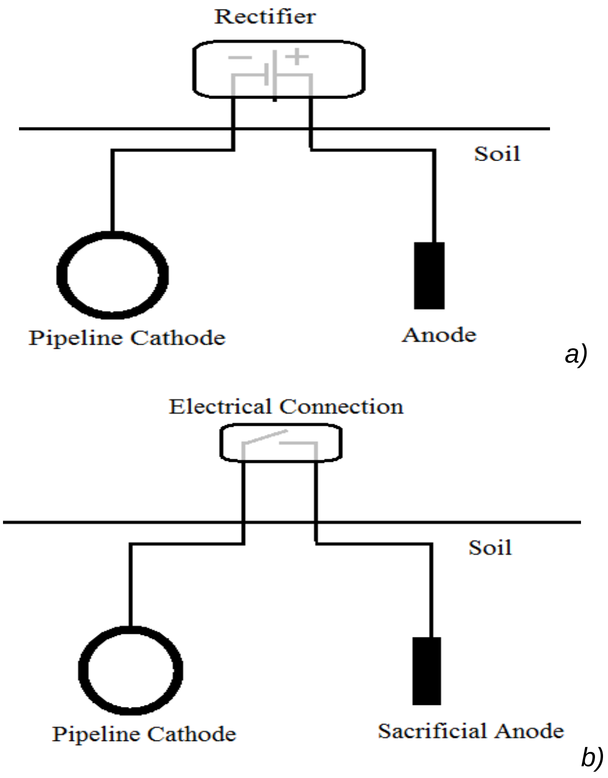

Figure 1. Cathodic protection system:
a) Impressed current cathodic protection,
b) Sacrificial anode cathodic protection

---

*Corresponding author: M'hamed Ouadah
E-mail: mhamed.ouadah@ensta.edu.dz

Paper received: 27.03. 2025.
Paper accepted: 28. 05.2025.

Stray currents can originate from either alternating current (AC) or direct current (DC), depending on their source [6,7]. For instance, AC stray currents may occur when alternating current flows through power line conductors, generating an electromagnetic field around these conductors. This field can couple with adjacent buried pipelines, inducing AC stray currents [8-15].

DC Stray currents can be categorized as either dynamic or static [16-17]. Dynamic stray currents are characterized by variations in amplitude and/or changes in the direction of current flow. These currents may originate from both manmade and natural sources. Manmade sources include DC welding equipment and DC electrical railway systems [18-23]. Telluric currents, on the other hand, are naturally occurring stray currents induced by disturbances in the Earth's magnetic field due to sunspot activity. In contrast, static stray currents maintain a constant amplitude and follow consistent geographical paths. Examples of static stray currents include high voltage direct current (HVDC) ground electrodes and cathodic protection systems.

Both AC and DC stray currents pose significant risks to buried steel pipelines, as they can cause corrosion and reduce the efficiency of cathodic protection [24-33]. In references [25] and [26], the impact of AC stray currents resulting from electromagnetic induction caused by high voltage power lines on cathodic protection performance (both sacrificial anode and impressed current cathodic protection) was investigated. The authors demonstrated that the protection potential becomes more electropositive with increasing AC stray current. This indicates that the likelihood of AC corrosion rises with higher induced AC stray currents, even when the pipeline is under cathodic protection. AC stray currents not only affect cathodic protection performance but also shift the applied cathodic protection potential on pipelines away from its intended design value.

This study presents a detailed assessment of the impact of AC, DC, and hybrid AC/DC stray currents on the cathodic protection (CP) performance of buried pipelines. By combining electrochemical measurements with finite element modeling (FEM), it quantifies how stray currents interfere with CP efficiency and contribute to corrosion acceleration in X70 steel pipelines. The findings offer valuable insights for enhancing pipeline protection strategies, particularly in areas influenced by high-voltage power lines.

To achieve this, a methodology was developed to evaluate the effects of stray currents on CP performance, utilizing electrochemical parameters obtained from experimental tests on X70 steel pipelines. These parameters serve as boundary conditions in a cathodic protection model, ensuring a more accurate representation of real-world conditions.

The results demonstrate that as AC stray current density increases, the CP potential shifts in a more electropositive direction, reducing its protective effectiveness and heightening corrosion risk, even under CP. Additionally, the presence of a nearby pipeline further disturbs the CP potential of the protected pipeline, increasing its vulnerability to corrosion. Notably, at the intersection of two pipelines, when subjected to AC stray currents of 100 and 200 A/m², the second pipeline experiences a negative current density, causing stray currents to exit the pipeline. This phenomenon leads to a partial cathodic protection effect on the first pipeline, mitigating its corrosion risk.

This study enhances the understanding of stray current interference in CP systems and provides a foundation for developing mitigation strategies to improve pipeline longevity and reliability.

2. METHODOLOGY

This study focuses on diagnosing the effects of AC, DC, and combined AC/DC stray currents on cathodic protection (CP) performance. Electrochemical tests were conducted to determine X70 steel's response to stray currents. The study considered three scenarios: (1) a pipeline under AC stray current interference, (2) the impact of an intersecting pipeline on CP performance, and (3) the combined influence of AC and DC stray currents. Experimental polarization curves and electrochemical impedance spectroscopy (EIS) data were integrated into a finite element model to simulate real-world CP conditions.

The experimental setup included a three-electrode system with a saturated calomel electrode (SCE) as a reference, a platinum counter electrode, and an X70 steel working electrode. Stray current densities of 0 A/m², 100 A/m², and 200 A/m² were applied, and their effects on CP potential, corrosion rate, and polarization behavior were analyzed.

This study focuses on diagnosing the effects of AC, DC, and combined AC/DC stray currents on cathodic protection (CP) performance. The methodology relies on electrochemical measurements to determine the electrochemical parameters of X70 steel pipelines.Stray current densities of 0 A/m², 100 A/m², and 200 A/m² were applied to the X70 steel using two electrodes connected to an AC stray current source as presented in Fig.2. This allowed for the extraction of polarization corrosion parameters (such as Tafel slopes, corrosion current densities, and corrosion potentials) under various AC stray current densities. These parameters serve as boundary conditions in a Finite Elements Method (FEM) cathodic protection model. To assess the effects of AC, DC, and combined AC/DC stray currents on CP performance, we examined two intersecting pipelines at a 90° angle. Pipeline n°1 is protected from corrosion by an impressed current cathodic protection system, while Pipeline n°2 intersects Pipeline n°1 without applied cathodic protection. Three Scenarios were developed:

Scenario 01: The first case involves only Pipeline n1 under the influence of AC stray current (Fig. 3).

Scenario 02:the pipeline n°1 without the influence of AC stray current intersecting Pipeline n2 (Fig. 4).

Scenario 03: Combines the effects of both scenarios (Figure 5).

The pipelines, measuring 40m in length, have an outside radius of 210 mm and a wall thickness of 10 mm.

Figure 2. Electrochemical test bench

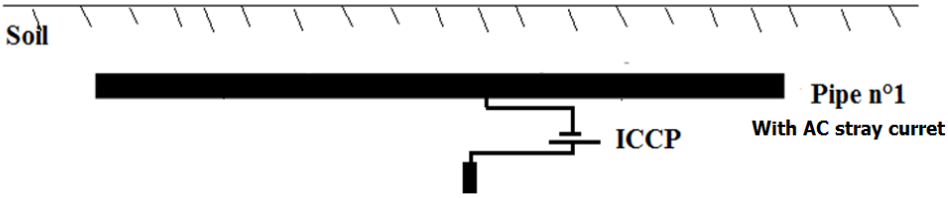

Figure 3. The Schematic representation of the system used to identify the impact of AC stray current on the cathodic protection performance

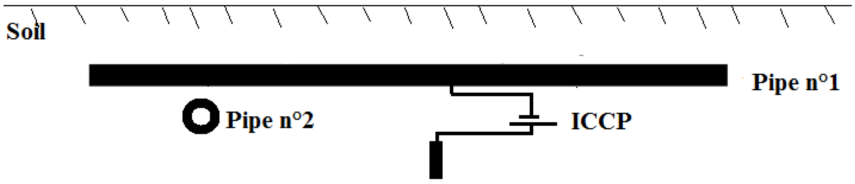

Figure 4.The Schematic representation of the system used to identify the impact of DC on the cathodic protection performance

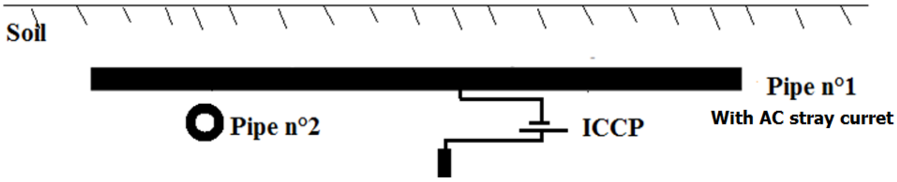

Figure 5. Schematic representation of the system employed to assess the influence of combined AC and DC stray currents on cathodic protection performance

2.1. Cathodic Protection Model

The fundamental components of the cathodic protection system include: the anode (Γ_1), the cathode (Γ_2), and the electrolyte (Ω). Designing the CP system necessitates solving Laplace's equation $\nabla^2 V = 0$ with appropriate boundary conditions to determine the potential and current density distribution within the solution domain. Figure 6 illustrates the various boundary conditions utilized based on the nature of the boundary.

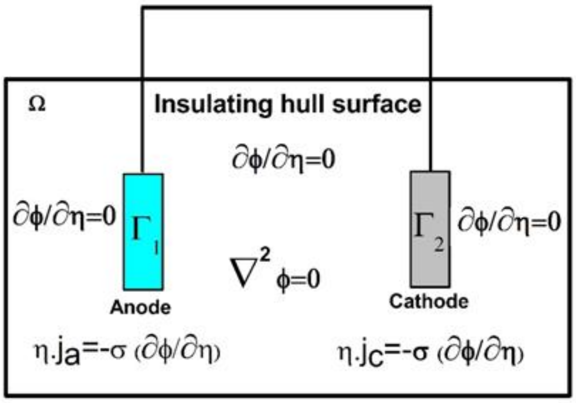

Figure 6. Principle of the cathodic protection system boundary conditions: $\Gamma 1$ is the anode, $\Gamma 2$ is the cathode and Ω is the electrolyte

For symmetry boundaries, the following boundary condition was applied:

$$\frac{\partial V}{\partial n} = n.\nabla V = 0 \qquad (1)$$

Where V represents the electrical potential and n denotes the normal to the boundary surface.

- Along the anode, the CP system imposes an output current regulated by a rectifier. The current flowing out of the anode surface is uniform. Therefore, the anode boundary condition can be expressed as follows:

$$I = I_{anode} = 0 \qquad (2)$$

- Along the pipeline surface, the utilized boundary condition is as follows:

$$n.J_c = -\sigma \frac{\partial V}{\partial n} = f_c(V) \qquad (3)$$

Where $f_c(V)$ represents the electrochemical relationship between the current densities (J_c) and the potentials *(V).* This relationship is depicted by nonlinear curves, referred to as polarization curves, obtained through electrochemical measurements.

2.1. Materials and experimental procedures

In this study, the X70 steel pipeline was utilized. The XRD pattern depicted in Figure 7 typically reveals peaks corresponding to the ferrite (α-Fe) phase, the primary constituent of X70 steel, with small amounts of pearlite potentially present depending on the composition and processing conditions.

The sharpness and intensity of the peaks provide insights into the material's crystallinity and residual stress levels, both critical for pipeline applications, where high crystallinity and minimized residual stress are essential to ensure mechanical reliability.

The microstructure of the X70 steel matrix, illustrated in Figure 8, predominantly features a ferritic-pearlitic structure, where ferrite imparts ductility, and pearlite enhances strength.

A refined grain structure is vital for optimizing the steel's strength and toughness, especially in demanding low-temperature conditions. Further more, reducing non-metallic inclusions through advanced steelmaking techniques is crucial to enhancing weldability and minimizing the likelihood of fractures, thereby ensuring superior performance and reliability in pipeline applications.

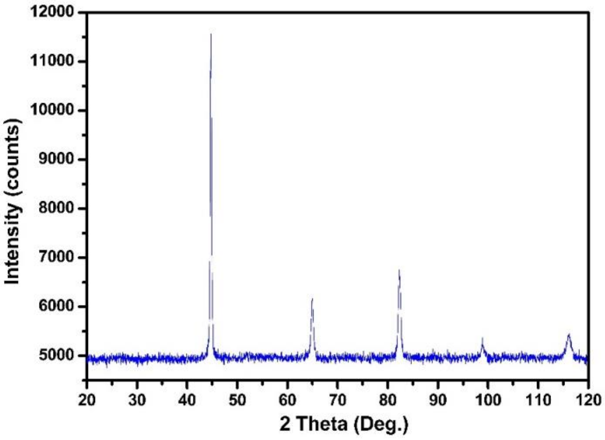

Figure 7. An X-ray diffraction (XRD) analysis of the X70 steel.

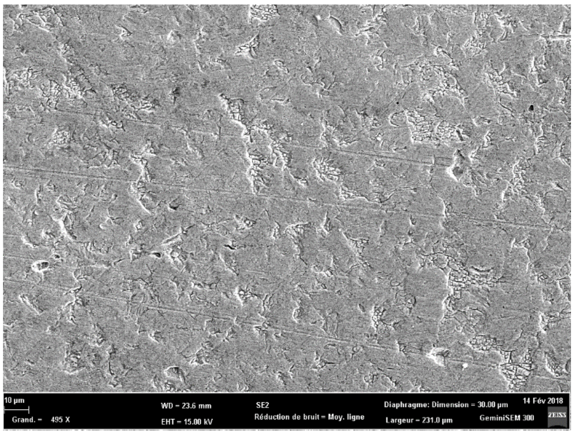

Figure 8. Microstructure of X70 pipeline steel

Electrochemical measurements were conducted using a Bio-Logic SP-150 electrochemical workstation controlled by a PC. A three-electrode system was employed: TheX70 steel specimen served as the working electrode (WE), a saturated calomel electrode (SCE) was utilized as the reference electrode (RE), and a platinum wire acted as the counter electrode (CE). The electrolyte utilized in this investigation was a simulated soil solution, consisting of MgSO4·7H_2O (0.131g), $CaCl_2 \cdot 2H_2O$ (0.18g), KCl (0.122g), and $NaCO_3$ (0.483g) [34].

Electrochemical Impedance Spectroscopy (EIS) is an effective technique for evaluating the corrosion resistance of X70 steel in simulated soil solution affected by AC interference. Figures 9-12 show the Nyquist plots and bode plots of X70 steel in simulated soil solutions at different AC densities. The electrochemical impedance spectroscopy data were fitted using the equivalent circuit shown in Fig. 12, where a constant phase element, C, represents a double-layer capacitor, R1 represents the solution resistance, and R2 denotes the double-layer resistance. The fitting results are listed in Table 1, indicating that as the AC current density increased, R2 decreased, suggesting a reduction in the corrosion resistance of X70 steel. This indicates that the corrosion rate increased with higher AC current density values. Also, it can be seen that the diameter of the capacitive loop gradually decreased with increasing AC current density, indicating that the AC corrosion rate increased with increasing AC current density.

Bode plot analysis shows that at low frequencies the impedance amplitude is lower, suggesting a more active corrosion process. Under the influence of AC interference, this amplitude generally decreases, indicating reduced corrosion resistance. Also, it can be seen from the phase angle that the decrease in phase angle in the low-frequency region suggests increased corrosion activity, as the system becomes more resistive and less capacitive.

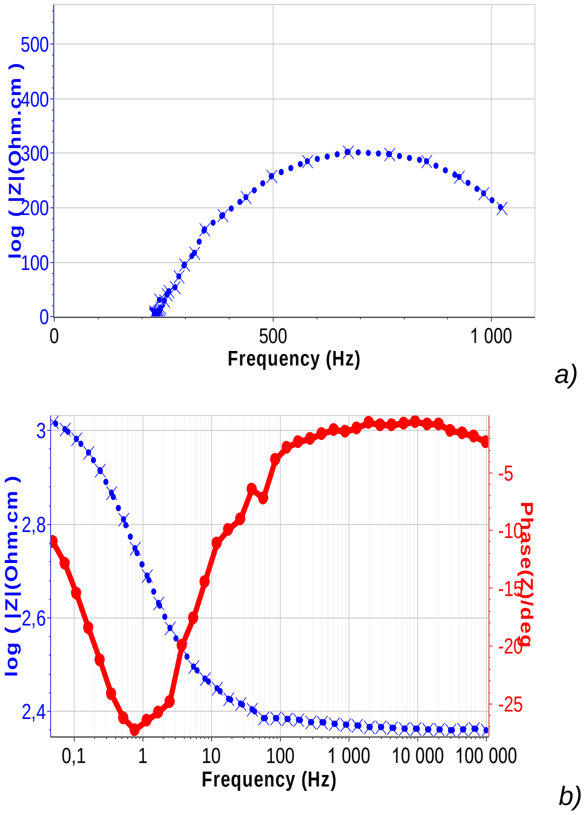

a)

b)

Figure 9. Nyquist plots (a) and Bode plots (b) of X70 steel in simulated soil solutions

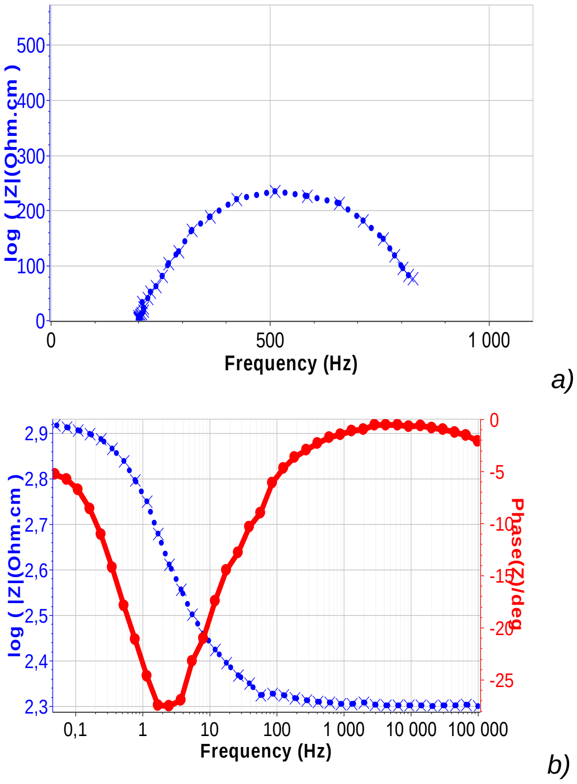

a)

b)

Figure 10. Nyquist plots (a) and Bode plots (b) of X70 steel in simulated soil solutions under a current density of 100 A/m²

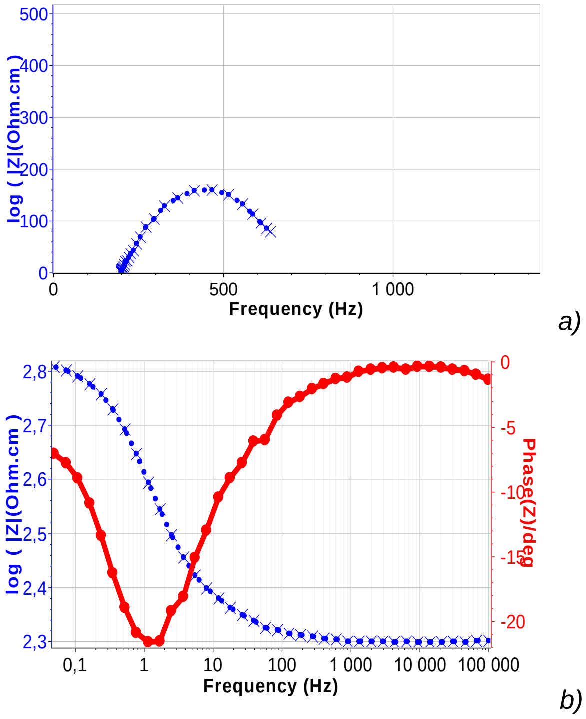

a)

b)

Figure 11. Nyquist plots (a) and Bode plots (b) of X70 steel in simulated soil solutions under a current density of 200 A/m²

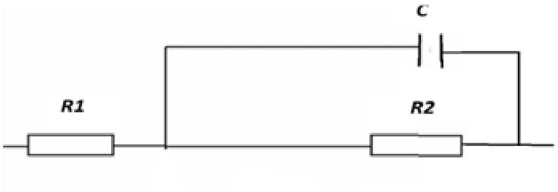

Figure 12. Equivalent circuit diagram

Table 1. Fitting results of EIS data of X70 steel in simulated soil solution under No AC current density, 100 A/m² and 200 A/m²

AC current density	R1(Ωcm)	C(F)	R2(Ωcm)
No AC current density	201,8	44,84e-9	1001,1
With 100 A/m²	201,3	63,07e-6	653,5
With 200 A/m²	199,7	67,48e-6	485,8

Figute 13 illustrates the polarization curve of X70 steel in the simulated soil solution under various AC stray current densities. The results derived from fitting the polarization curves shown in Figure 13 are summarized in Table 2, presenting the corrosion current density (Icorr), corrosion potential (Ecorr), and Tafel slopes (b_{anodic}, $b_{cathodic}$).

The polarization curves reveal a clear trend of increased corrosion activity with rising AC interference. As the AC stray current density increases from 0 to 200 A/m², the corrosion potential (Ecorr) shifts positively from -769.39 mV.SCE to -710.26 mV.SCE, indicating a higher electrochemical reactivity of the steel surface. Simultaneously, the corrosion current density (Icorr) rises significantly from 12.64 µA/cm² at 0 A/m² to 46.36 µA/cm² at 200 A/m², demonstrating that AC stray currents accelerate the corrosion process. The anodic Tafel slope (ba) increases slightly, while the cathodicTafel slope (bc) shows a sharp rise, suggesting that AC stray currents primarily influence the cathodic reaction, potentially altering oxygen reduction kinetics. These findings indicate that AC stray currents not only enhance the overall corrosion rate but also modify electrochemical behavior, with significant implications for cathodic protection strategies in AC-interfered environments.

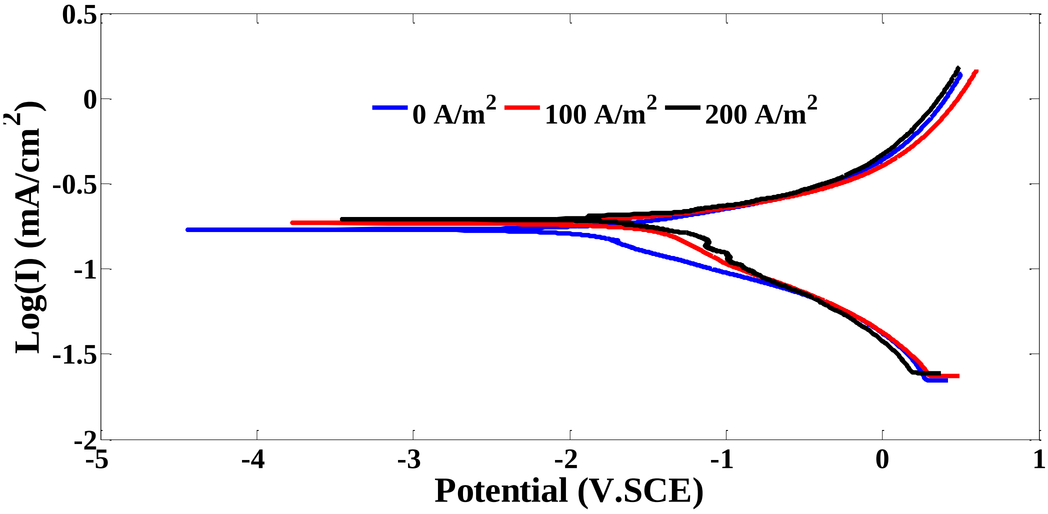

Figure 13. Polarization curves of X70 steel under various AC stray current densities

Table 2. Tafel slopes, corrosion current densities, and corrosion potentials obtained from polarization curves under various AC stray current densities

AC stray current density, (A/m²)	ba (mV)	bc (mV)	Icorr (µA/cm²)	Ecorr (mV.SCE)
0	173.1	247.1	12.64	-769.39
100	175.5	466.3	31.41	-731.39
200	204.0	671.6	46.36	-710.26

3. RESULTS AND DISCUSSION

3.1. Scenario 01:AC Stray Current Effects on CP Performance

To investigate the impact of AC stray current on cathodic protection performance, the scenario depicted in Fig. 3 was considered. The simulation model comprises the following elements: pipeline n°1 protected from corrosion by an impressed current cathodic protection system, with an anode output current of 4 A. Pipeline n°1 is subjected to AC stray current densities of 0 A/m2, 100 A/m², and 200 A/m².

For the 4 A output current, Figure 14 illustrates the distribution of CP potential along the pipeline under the influence of AC stray current densities of 0, 100, and 200 A/m². It is evident from this figure that, in the absence of stray current (0 A/m²), the CP potential ranges between -1.37 V and -0.81 V vs. SCE, with the surface area facing the anode exhibiting the lowest value of -1.37 V vs. SCE. According to references [35, 36], the recommended effective cathodic protection potential (E-protection) for buried steel pipelines is less than -0.780 V vs. SCE. Therefore, for an output current of 4 A, the pipeline is fully protected against corrosion.

Furthermore, it can be observed from this figure that induced AC stray current densities cause a deviation of the cathodic protection potential from its design value. The CP potential becomes more positive with increasing AC stray current densities. This indicates that the likelihood of corrosion increases with higher AC stray current densities, even when the pipeline is under cathodic protection.

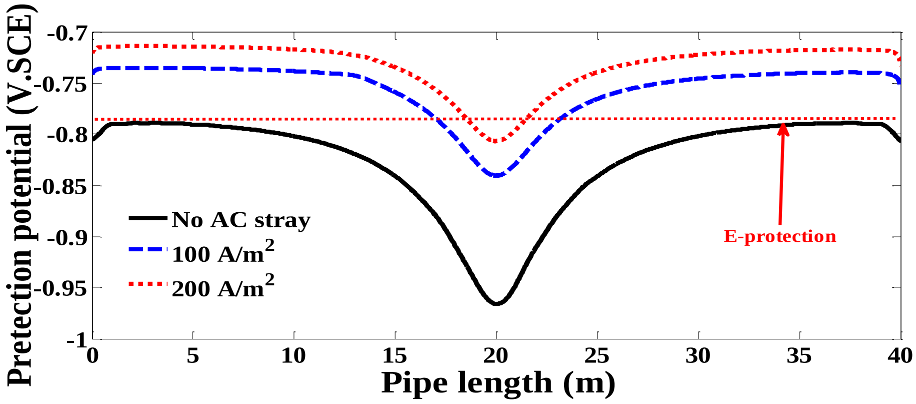

Figure 14. Effects of the AC stray current densities on the CP performance

3.2. Scenario 02:DC Stray Current Effects on CP Performance

Considering the scenario of two intersecting pipelines (Pipeline n°1 and Pipeline n°2) as illustrated in Fig.4, the simulation model comprises the following elements: Pipeline n°1 is protected from corrosion by an impressed current cathodic protection system, with an anode output current of 4 A. Pipeline n°2 intersects pipeline n°1 but does not have any applied cathodic protection.

Figure 15 illustrates the distribution of cathodic protection potential along pipeline n°1 concerning pipe length, both with and without the presence of pipelinen°2. In the absence of pipeline n°2, pipeline n°1 exhibits full protection against corrosion. However, the introduction of pipeline n°2 significantly alters the cathodic protection potential of pipeline n°1, particularly at the intersection point, where a noticeable increase in potential occurs. This shift indicates that the presence of pipeline n°2 disrupts the cathodic protection potential of pipeline n°1 from its intended design, consequently increasing the probability of corrosion despite being under cathodic protection.

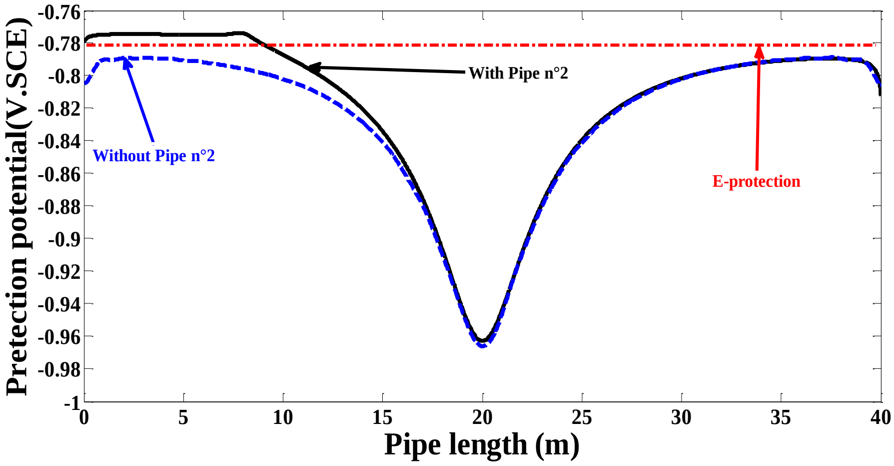

Figute 15. Cathodic protection potential distribution along pipelinen°1 as a function of pipe length with and without the presence of pipelinen°2

Figure 16 depicts the distribution of cathodic protection current density along the pipeline n°1 with respect to pipe length. Near the intersection, the protection current density diminishes, reaching nearly zero at the point of intersection between the two pipelines. Consequently, the effectiveness of pipeline cathodic protection is compromised around the intersection, resulting in inadequacy.

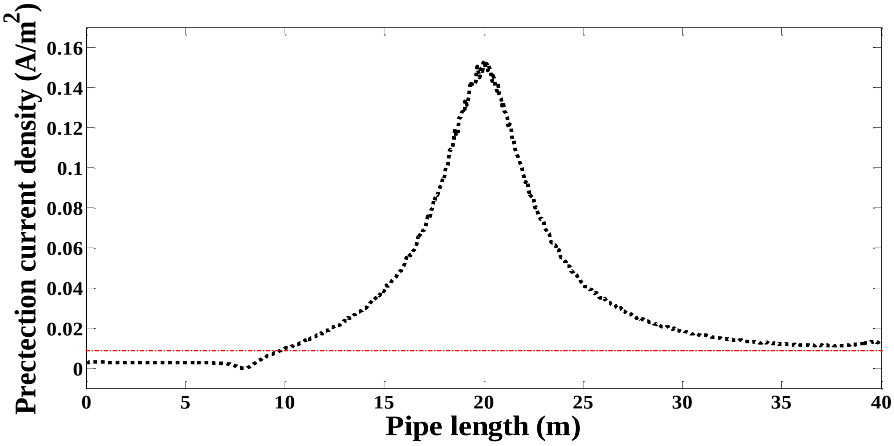

Figure 16. Cathodic protection current density distribution along pipelinen°1 as a function of pipe length

Figures 17 and 18 portray the potential and stray current density distributions along Pipeline n°2 concerning pipelinelengths, respectively. Notably, significant changes in potential distribution are observed at the intersection of the two pipelines, indicating the substantial impact of the intersection. Moreover, the stray current density is nearly negligible at the intersection point between the two pipelines.

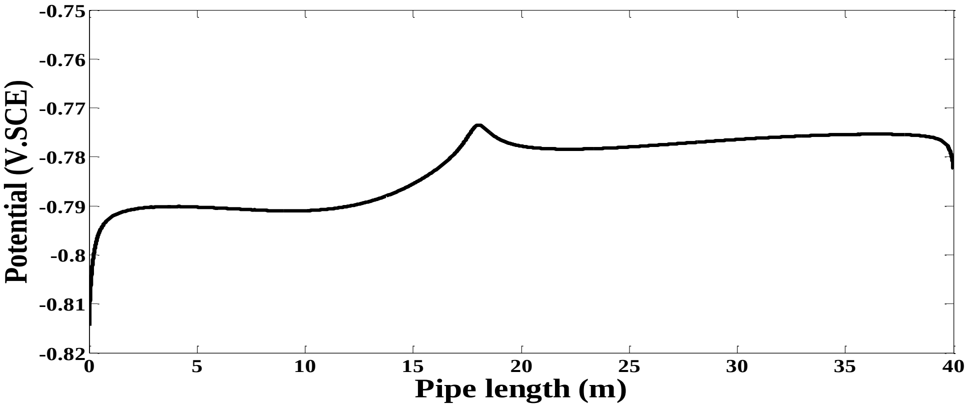

Figure 17. Potential distribution along pipelinen°2 as a function pipe length

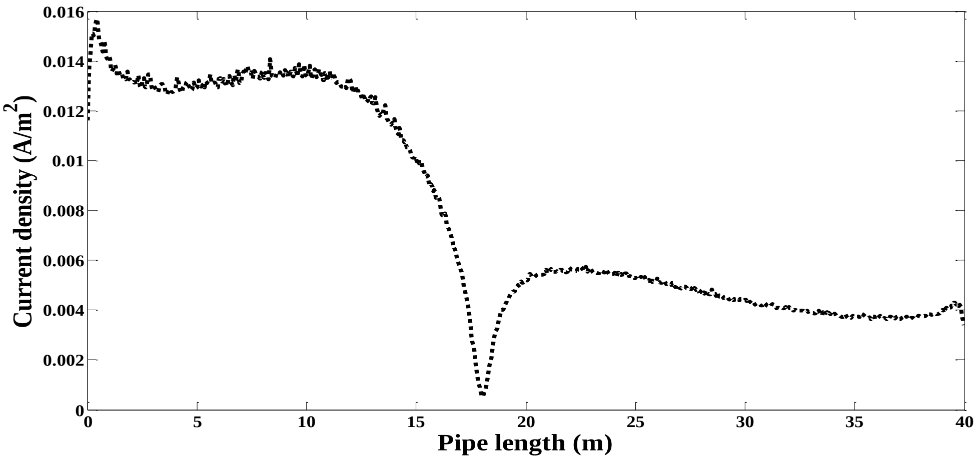

Figure 18. Stray current density distribution along pipelinen°2 as a function pipe length

3.3. Scenario 03: Hybrid AC/DC Stray Current Effects

In the preceding sections of this paper, we examined the impact of AC and DC stray currents on cathodic protection performance. Now, we delve into the effects of combined AC/DC stray currents on cathodic protection efficacy. We consider the scenario of two intersecting pipelines (pipeline n°1 and pipelinen°2), as illustrated in Fig. 5.

The simulation model comprises the following: Pipe n1 is shielded from corrosion by an impressed current cathodic protection system with an anode output current of 4 A. Pipelinen° 1is subjected to AC stray current densities of 0, 100 A/m^2, and 200 A/m2. Pipelinen°2 intersects pipelinen°1 but lacks cathodic protection.

Figures 19 and 20 depict the distributions of cathodic protection potential and current density along pipelinen°1 concerning pipe length under the influence of AC stray current densities of 0, 100, and 200 A/m^2, with the presence of pipelinen°2. The cathodic protection potential becomes more positive with increasing AC stray current. At the intersection of the two pipelines and for AC stray current densities of 100 and 200 A/m^2, we observe that as the AC stray current densities increase, the protection potential of pipelinen°1 becomes more negative, accompanied by an increase in protection current density. This indicates that pipelinen°1 receives some cathodic protection, mitigating corrosion.

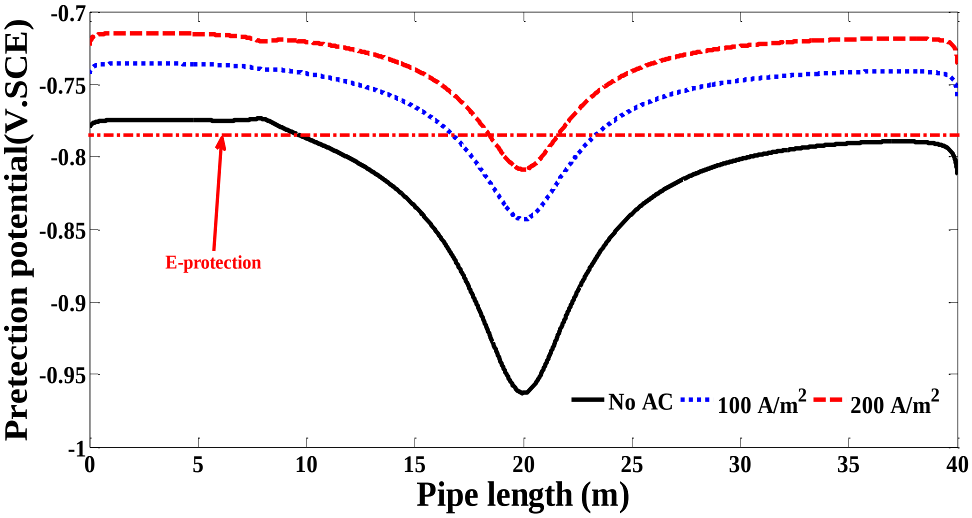

Figure 19. Distribution of cathodic protection potential along pipeline n°1 as a function of pipe length, considering the influence of AC stray current densities of 0, 100 A/m^2, and 200 A/m^2 in the presence of pipeline n°2

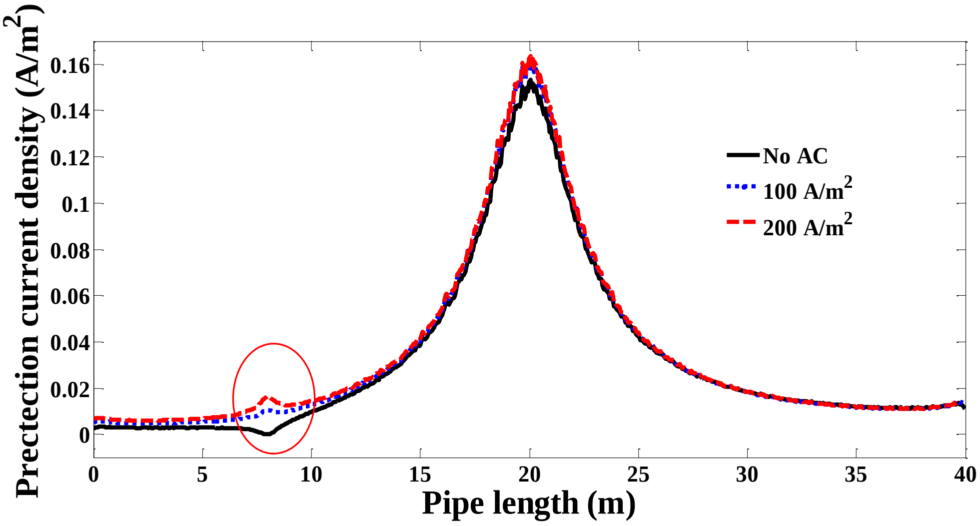

Figure 20. Distribution of cathodic protection current density along pipeline n°1 as a function of pipe length, considering the influence of AC stray current densities of 0, 100 A/m^2, and 200 A/m2 in the presence of pipeline n°2

Figures 21 and 22 illustrate the distributions of stray current density and potential along Pipe n°2 concerning pipe length for AC stray current densities of 0, 100, and 200 A/m^2, respectively. At the intersection of the two pipelines and for AC stray current densities of 100 and 200 A/m^2, the stray current density of pipelinen°2 is negative, signifying that the stray current flows out of pipelinen°2. Consequently, that section of the pipeline acts as an anode, with its potential higher than the corrosion potential of the X70steel , exacerbating corrosion on pipelinen°2.

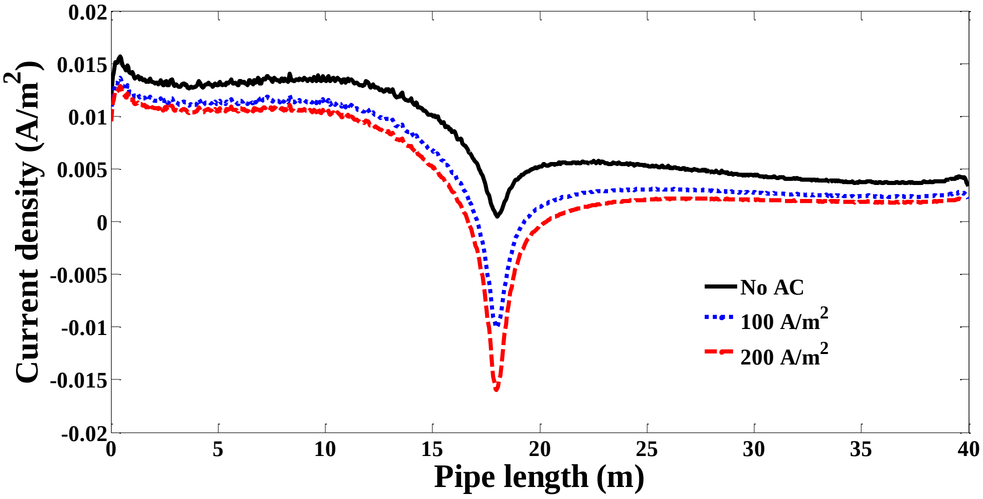

Figute 21. Stray current density distribution along pipelinen°2 as a function of pipe length for AC stray current densities of 0, 100 A/m^2 and 200 A/m^2

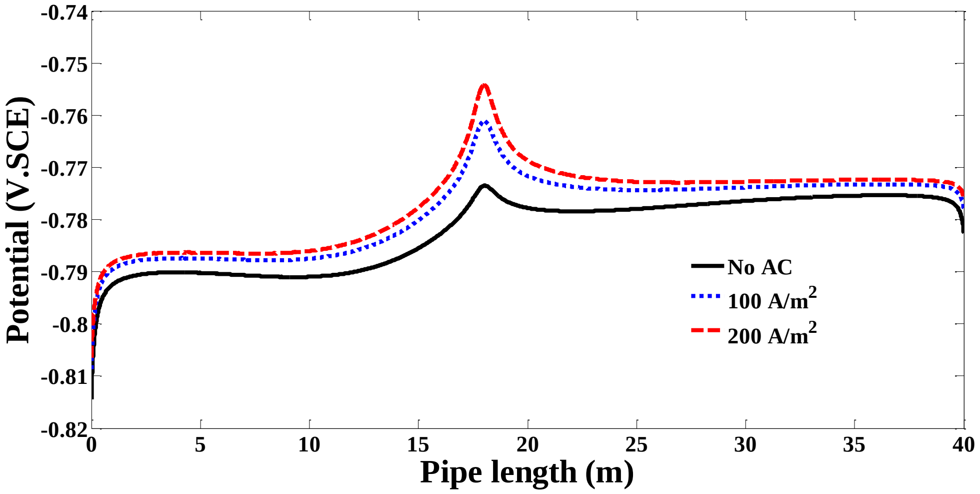

Figure 22. Potential distributions along pipelinen°2as a function of pipe length for of AC stray current densities of 0, 100 A/m^2 and 200 A/m^2

4. CONCLUSION

In this paper, we investigated the effects of AC, DC, and combined AC/DC stray currents on the cathodic protection (CP) performance of the X70 steel pipeline. Our findings reveal several important insights:

- The likelihood of corrosion increases with higher AC stray current densities, even when the pipeline is under cathodic protection.
- The presence of pipeline n°2 significantly impacts the cathodic protection potential of pipeline n° 1 at their intersection.
- Pipelinen°2's presence shifts the cathodic protection potential of pipeline n°1 away from its design values.
- The presence of pipeline n°2 increases the risk of corrosion for pipeline n°1, even with cathodic protection applied.
- At the intersection of the two pipelines and for AC stray current densities of 100 and 200 A/m^2, pipeline n°1's protection potential becomes more negative, and the protection current density increases.

- Sections of pipeline n°1 experiencing increased current density receive some level of cathodic protection, reducing corrosion.
- At the intersection of the two pipelines and for AC stray current densities of 100 and 200 A/m^2, pipeline n°2 exhibits negative current density, indicating stray current flow out of the pipeline.

5. REFERENCES

[1] D.Lauria,M.Pagano,C.Petrarca,C.Pisani (2015) A novel approach to design cathodic protection system for high-voltage transmission cables,IEEE Trans.Ind.Appl.,51(6),5415–5420. https://doi.org/10.1109/TIA.2015.2411735

[2] H.M.H.Farh, M.E.A.B.Seghier, T.Zayed (2023) A comprehensive review of corrosion protection and control techniques for metallic pipelines, Eng. Fail. Anal., 143, 106885. https://doi.org/10.1016/j.engfailanal.2022.106885

[3] D.Lauria,S.Minucci,F.Mottola,M.Pagano,C.Petrarca (2018) Active cathodic protection for HV power cables in undersea application,Electr. Power Syst.Res.,163,590–598. https://doi.org/10.1016/j.epsr.2017.11.016

[4] C.Christodoulou,G.Glass,J.Webb,S.Austin,C.Goodier (2010) Assessing the long term benefits of impressed current cathodic protection, Corros. Sci.,52(8),2671 2679. https://doi.org/10.1016/j.corsci.2010.04.018

[5] I.D. Kim, E. C. Nho (2005) Module-type switching rectifier for cathodic protection of underground and maritime metallic structures, IEEE Trans.Ind. Electron., 52(1),181–189. https://doi.org/10.1109/TIE.2004.841094

[6] X.H.Wang et al. (2013) Study on AC stray current corrosion law of buried steel pipelines, Appl. Mech.Mater.,263–266,448–451.

[7] D.Paul (2016) DC stray current in rail transit systems and cathodic protection [History],IEEEInd.Appl. Mag., 22(1),8 13. https://doi.org/10.1109/MIAS.2015.2481754.

[8] H.Zhang,G.Karady,J.Hunt (2011) Effect of various parameters on the inductive voltage and current on pipelines, IEEE PES General Meeting, 17. https://doi.org/10.1109/PES.2011.6038882.

[9] G.Lucca (2018) Different approaches in calculating AC inductive interference from power lines on pipelines,IET Sci. Meas.Technol.,12(6),802–806. https://doi.org/10.1049/iet-smt.2018.0086

[10] K.B. Adedeji (2016) Effect of HVTL phase transposition on pipelines induced voltage, IJEEI, 4(2), 93–101. https://doi.org/10.52549/ijeei.v4i2.209

[11] A.Popoli, A.Cristofolini, L.Sandrolini (2021) A numerical model for the calculation of electromagnetic interference from power lines on nonparallel underground pipelines, Math. Comput. Simul., 183,221–233. https://doi.org/10.1016/j.matcom.2020.02.015

[12] L.Qi,H. Yuan, Y.Wu, X.Cui (2013) Calculation of overvoltage on nearby underground metal pipeline due to lightning strike on UHV AC line tower, Electr. Power Syst.Res.,94,54–63. https://doi.org/10.1016/j.epsr.2012.06.011

[13] D.Micu, G.Christoforidis, L.Czumbil (2013) AC interference on pipelines due to double circuit power lines: A detailed study,Electr.Power Syst. Res., 103, 1–8. https://doi.org/10.1016/j.epsr.2013.04.008

[14] F.Dawalibi (1986) Electromagnetic fields generated by overhead and buried short conductors.Part 1 - Single conductor,IEEE Trans.Power Deliv., 1(4), 105–111. https://doi.org/10.1109/TPWRD.1986.4308036

[15] K.B.Adedeji et al. (2018) AC induced corrosion assessment of buried pipelines near HVTLs: A case study of South Africa, PIER B. https://doi.org/10.2528/PIERB18040503

[16] C.A.Charalambous, P.Aylott (2014) Dynamic stray current evaluations on cut-and-cover sections of DC metro systems,IEEE Trans. Veh. Technol., 63(8), 3530–3538. https://doi.org/10.1109/TVT.2014.2304522

[17] M.Ormellese, S.Beretta, F.Brugnetti, A.Brenna (2021) Effects of non-stationary stray current on carbon steel buried pipelines under cathodic protection, Constr.Build.Mater.,281,122645. https://doi.org/10.1016/j.conbuildmat.2021.122645

[18] G.Cui, Z.L.Li, C.Yang, M.Wang (2016) The influence of DC stray current on pipeline corrosion, Pet.Sci., 13, 135–145. https://doi.org/10.1007/s12182-015-0064-3

[19] A.Dolara, F.Foiadelli, S.Leva (2012) Stray current effects mitigation in subway tunnels,IEEE Trans. Power Deliv.,27(4),2304–2311.

[20] A.Ogunsola, L.Sandrolini, A.Mariscotti (2015) Evaluation of stray current from a DC-electrified railway with integrated electric–electromechanical modeling and traffic simulation,IEEE Trans.Ind.Appl.,51(6),5431–5441.

[21] J.V.Rodriguez, J.S.Feito (2013) Calculation of remote effects of stray currents on rail voltages in DC railway systems,IETElectr.Syst.Transp., 3(2),31–40.

[22] S.Aatif,H.Hu,F.Rafiq,Z.He(2021)Analysis of rail potential and stray current in MVDC railway electrification system,Railw.Eng.Sci.,29,394–407. https://doi.org/10.1007/s40534-021-00243-0

[23] S.Lin, Q.Zhou, X.Lin, M.Liu, A.Wang (2020) Infinitesimal method based calculation of metro stray current in multiple power supply sections,IEEE Access, 8, 96581–96591. https://doi.org/10.1109/ACCESS.2020.2994125

[24] A.Brenna,S.Beretta,F.Bolzoni,M.Pedeferri,M.Ormellese (2017) Effects of AC-interference on chloride-induced corrosion of reinforced concrete, Constr. Build. Mater.,137,76-84. https://doi.org/10.1016/j.conbuildmat.2017.01.087

[25] M.Ouadah,O.Touhami,R.Ibtiouen (2016) Diagnosis of the AC current densities effect on the cathodic

protection performance of steel X70 for a buried pipeline due to EMI caused by HVPTL, Prog. Electromagn. Res.M.,45,163–171.

[26] M.Ouadah, O.Touhami, R.Ibtiouen (2017) Method for diagnosis of the effect of AC on the X70 pipeline due to inductive coupling caused by HVPL, IETSci. Meas. Technol.,11(6),766–772. https://doi.org/10.1049/iet-smt.2016.0519

[27] D.Kuang, Y.F.Cheng (2017) Effects of AC interference on cathodic protection potential and its effectiveness for corrosion protection of pipelines, Corros.Eng.Sci.Technol.,52(1),22–28. https://doi.org/10.1080/1478422X.2016.1175773

[28] A.K.Thakur, A.K.Arya, P.Sharma (2020) The science of AC-induced corrosion: A review of pipeline corrosion due to HV AC lines, Corros. Rev., 38(6), 463–472. https://doi.org/10.1515/corrrev-2020-0044

[29] M.Ouadah, O.Touhami, R.Ibtiouen, A.Bouzida (2019) Diagnoses and mitigation of corrosion due to EMI between HVPTL and buried pipeline,IEEE CAGRE.https://doi.org/10.1109/CAGRE.2019.8713291

[30] C.Wen, J.Li, S.Wang, Y.Yang (2015) Experimental study on stray current corrosion of coated pipeline steel,J.Nat.Gas Sci.Eng.,27(3),1555–1561.

[31] S.A. Memon, P. Fromme (2014) Stray current corrosion and mitigation in DC transit systems,IEEE Electr.Mag.,2(3),22–31.

[32] M.Ouadah, O.Touhami, R.Ibtiouen, M. F. Belmnaouar, M.Zergoug (2017) Corrosive effects of electromagnetic induction caused by HVPL on buried pipelines,Int.J.Electr.Power Energy Syst., 91 (2), 34–41. DOI:10.1016/j.ijepes.2017.03.005

[33] M.Ouadah, O.Touhami, R.Ibtiouen (2016) Diagnosis of AC corrosion on buried pipeline due to HV power line,J.Electr.Eng.,16(2),76–83.

[34] R.N.Parkins, W.K.Blanchard, B.S.Delanty (1994) Transgranular SCC of high-pressure pipelines in near-neutral pH,Corrosion,50(5),394–408.

[35] H.H.Uhlig, R.W.Revie (1985) Corrosion and corrosion control,John Wiley,New York.

[36] D.M.Kaufman (2003) Applying educational theory in practice,BMJ,326(7382),213–216. https://doi.org/10.1136/bmj.326.7382.213

IZVOD

PROCENA UTICAJA AC, DC I HIBRIDNIH AC/DC LUTAJUĆIH STRUJA NA EFIKASNOST KATODNE ZAŠTITE

Obezbeđivanje efikasnosti katodne zaštite (KZ) je ključno za održavanje integriteta zakopanih cevovoda. Lutajuće struje, posebno one koje potiču iz visokonaponskih dalekovoda, mogu ometati KP sisteme, što dovodi do ubrzane korozije. Ova studija istražuje efekte naizmenične struje (AC), jednosmerne struje (DC) i hibridnih AC/DC lutajućih struja na performanse KZ. Elektrohemijska merenja i modeliranje konačnih elemenata (FEM) korišćeni su za procenu uticaja ovih struja na čelične cevovode X70. Rezultati pokazuju da AC lutajuće struje smanjuju efikasnost KZ pomeranjem potencijala zaštite na elektropozitivnije vrednosti, povećavajući rizik od korozije. DC lutajuće struje utiču na podešavanja napona KZ, dok hibridna AC/DC interferencija pogoršava oba efekta. Rezultati pružaju uvid u strategije zaštite cevovoda, posebno u okruženjima sa mešovitim AC/DC lutajućim strujama.

Ključne reči: *AC lutajuća struja, DC lutajuća struja, hibridna AC/DC interferencija, korozija, katodna zaštita, metoda konačnih elemenata (FEM)*

Naučni rad
Rad primljen: 27.03.2025.
Rad prihvaćen: 28. 05.2025.

Ahlem Chahinez Kadri: https://orcid.org/0009-0004-3703-923X
M’hamed Ouadah: https://orcid.org/0000-0003-3444-0787
Abderrahmane Younes: https://orcid.org/0000-0003-2446-1568
Sofiane Chabane: https://orcid.org/0000-0003-3720-1239

Abdelmadjid Atassi[1],Mounir Djellab[1,2],Hamza Bentrah[1,2],*
Abdelouahad Chala[1],Mohamed Cherif Ben Ameur[3],
Slimane Kherief[1],Ridha Azzouz[1,4],Amir Eddine Kabouia[1],
Bouzid Bouamra[1]

[1]Laboratory of Physics of Thin Films and Applications, University of Biskra, B.P. 145, Biskra, R.P. 07000 Algeria, [2]Laboratoire de Génie des procédés chimiques et de l'environnement, University of Biskra, B.P. 145, Biskra, R.P. 07000 Algeria, [3]Politecnico di Milano, Department of Chemistry, Materials and Chemical Engineering "Giulio Natta", Via Mancinelli, 7, 20131 Milano MI, Italy, [4]Centre de recherche scientifique et technique des régions arides de Biskra, University of Biskra, B.P. 145, Biskra, R.P. 07000 Algeria.

Scientific paper
ISSN 0351-9465, E-ISSN 2466-2585
https://doi.org/10.62638/ZasMat1393

Zastita Materijala 67 (1)
171 - 180 (2026)

Corrosion inhibitionefficiency of the Myrrh Gum on API 5CTP110 tubing in hydrochloric acid

ABSTRACT

The corrosion inhibition properties of Myrrh Gum (MG) on API 5CTP110 tubing in a 0.5 M HCl solution were investigated using electrochemical techniques, including electrochemical impedance spectroscopy and potentiodynamic polarization. The study demonstrated that MG exhibits exceptional inhibitory performance, achieving an efficiency of 92% at an optimal concentration of 3 g/L. The analysis revealed that the adsorption of MG molecules onto the steel surface follows the Langmuir isotherm model, indicating a process dominated by physical adsorption. Additionally, MG acts as a mixed-type inhibitor, effectively mitigating both anodic and cathodic reactions. These findings highlight the potential of Myrrh Gum as a cost-effective and environmentally friendly corrosion inhibitor for industrial applications, particularly in acidic environments. The use of MG aligns with sustainable practices, providing a viable alternative to traditional synthetic inhibitors and contributing to the development of green corrosion prevention strategies.

***Keywords**: Eco-friendly corrosion inhibitor, API 5CTP110 tubing, Myrrh Gum,Hydrochloric acid, EIS*

1. INTRODUCTION

Carbon steels play a pivotal role in the petroleum industry, serving as the primary material for constructing vital oil and gas pipelines that facilitate exploration, extraction, and transportation processes within petroleum fields[1, 2]. Despite their widespread use driven by economic factors, carbon steel pipelines may encounter corrosion resistance challenges compared to alternative steel types [3]. While carbon steel is cost-effective and boasts properties essential for industrial applications, its susceptibility to corrosion in acidic environments is notable [4].This vulnerability becomes particularly significant during industrial procedures such as acid descaling, oil well acidification, and acid pickling, which often involve handling mineral acids in elevated concentrations [5], leading to substantial damage to the carbon steel infrastructure.

Acidizing in petroleum oil wells is a critical technique for enhancing oil production, involving the injection of high-temperature acidic solutions into the wellbore to create channels in rock formations, allowing for improved oil and gas flow. This process also serves to dissolve debris within ageing wells, restoring and maximizing productivity. Various acids, including hydrofluoric acid (HF), acetic acid (CH_3COOH), chloroacetic acid ($ClCH_3COOH$), formic acid (HCOOH), and sulfamic acid (H_2NSO_3H), are utilized in acidizing treatments, with hydrochloric acid (HCl) being the most commonly employed acid, typically ranging from 5% to 28% concentration by weight. The acidizing method exposes the carbon steel pipelines of oil wells to a highly aggressive and corrosive environment [6].

Corrosion control in oil wells typically relies on four main methods: employing corrosion-resistant materials, implementing cathodic protection, applying coatings, and utilizing corrosion inhibitors. Among these approaches, corrosion inhibitors are particularly favoured for their practicality, cost-effectiveness, and efficiency in safeguarding oil wells against corrosion [7].

Inhibitors are added to the acid solution during the acidizing process to reduce the aggressive attack of the acid on oil wells. The effective acidizing inhibitors that are usually found in commercial formulations [1] are acetylenic alcohols [8], alkenylphenones [9], aromatic aldehydes [10],

---

*Corresponding author: Prabin Kumar Mahato
Email: pkmahatoru@gmail.com

Paper received: 30.03.2025.
Paper accepted: 25.04.2025.

nitrogen-containing heterocyclics [11], and condensation products of carbonyls and amines [12]. Although effective at elevated concentrations, these inhibitors pose toxicity risks and are not environmentally friendly[13]. Consequently, the utilization of inorganic inhibitors is discouraged due to their detrimental impacts on human health and the environment [14]. In the 21st Century, the exploration of "green" or environmentally friendly corrosion inhibitors has become a focal point, aiming to deploy cost-effective molecules with minimal or zero environmental footprint. As of now, numerous alternative eco-friendly organic and inorganic inhibitors have been identified and explored [15, 16].

In the present study, the researchers aimed to investigate Myrrh Gum extract (MG) [17] as an eco-friendly corrosion inhibitor [18] which possesses several advantages such as low cost [19], environmental safety, and high inhibition efficiency [17].

2. EXPERIMENTAL

2.1. Material

The API 5CTP110 tubing served as the study's working electrode. Every sample intended for use in electrochemical tests was divided into squares of 3 x 3 x 1 cm. The supplier guaranteed the chemical composition of the steel under study, which included the following: C 0.24, Mn 1.37, Si 0.2, P 0.011, S 0.027, Cr 0.11, Ni 0.08, Mo 0.03, Al 0.01, Cu 0.1 and the remaining Fe. Every working electrode in contact with the electrolyte had a surface area of 2.85 cm^2. Before every examination, the surface was ready by a wet polishing process using silicon carbide abrasive sheets (grades 320 up to 800), followed by a distilled water rinse, and lastly with acetone degreasing.

2.2. Medium

Hydrochloric acid of analytical reagent grade 37% and distilled water were utilized to make the electrolyte solutions (0.5 mol/L).

2.3. Inhibitor

Myrrh Gum is a solid substance extracted from a small tree in the Commiphora genus. It is commonly used to produce perfumes, incense, and medicinal products due to its content of volatile oils, alcohol-soluble resins, and water-soluble gums. The primary natural components of Myrrh Gum are L-arabinose, 4-methyl D-glucuronic acid, and D-galactose acid, in a ratio of 1:3:4[20].Glucuronic acid, which is one of its key constituents, contains a carboxyl group (-COOH)[21, 22]attached to the first carbon (C1) in its structure, a defining characteristic of uronic acids.The molecular structure of glucuronic acid is presented in Fig.1 [23].

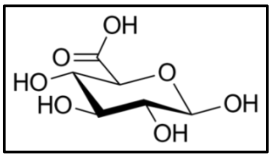

Figure 1. Molecular structure of Glucuronicaci

2.4. Electrochemical Techniques

Potentiodynamic polarization (PDP) and electrochemical impedance spectroscopy (EIS) were used to investigate the inhibitory impact of Myrrh for API 5CTP110 tubing in 0.5 mol/L M hydrochloric acid at 20°C. The Para Cell Electrochemical Cell Kit was used for all testing. It was made to accommodate a working, reference (Ag/AgCl), and counter (graphite) electrode. The working electrode and the graphite counter electrode were positioned in opposition to one another. The Gamry Instruments Potentiostat/ Galvanostat/ZRA (Reference 3000) was linked to the electrochemical cell. The Gamry system incorporated specific software components, namely the GamryEchem Analyst software for data processing and the Gamry Instruments Framework for hardware control. All electrochemical assessments of the API 5CTP110 tubing were conducted in a 0.5 mol/L hydrochloric acid medium, both in the absence (blank) and presence of the inhibitor (Myrrh Gum), following a 30 minutes immersion at 20°C. Tafel curves were generated by automatically varying the working electrode potential within the range of –0.25 to +0.25 V versus the open-circuit potential (OCP) at a scan rate of 0.5 mV/s. The anodic (*ba*) and cathodic (*bc*) Tafel slopes were extrapolated to determine the corrosion current (*Icorr*). The inhibition efficiency (η_{pol}) was computed using (Eq. 1)

$$\eta_{Pol}\% = \frac{Icorr - Icorr(inh)}{Icorr} \times 100 \qquad (1)$$

Where *Icorr(inh)*and *Icorr* denote the corrosion current values in the presence and absence of the inhibitor, respectively. Electrochemical impedance spectroscopy (EIS) experiments were executed under potentiostatic conditions spanning a frequency spectrum from 20 kHz to 50 mHz, with a 10mV peak-to-peak amplitude. The inhibition efficiency (η_{EIS}) was determined by contrasting the charge transfer resistance values in the presence (*Rt*) and absence ($\acute{R}t$) of Myrrh Gum, according to the following formula (Eq.2):

$$\eta_{EIS}\% = \frac{Rt - \acute{R}t}{Rt} \times 100 \qquad (2)$$

Surface Study by Scanning Electron Microscopy (SEM-EDX)

The surfaces of API 5CTP110 tubing specimens subjected to analysis included exposure to 0.5 mol/L hydrochloric acid both in the absence and presence of Myrrh Gum at 20°C. Utilizing the TESCANVEGA3 scanning electron microscope, we obtained images through scanning electron microscopy (SEM) and conducted energy-dispersive X-ray spectroscopic analysis (EDX).

3. RESULTS AND DISCUSSION

3.1. FT-IR spectroscopic analysis of MG

From Fig.2, a broad peak recorded at 3358cm^{-1} presented the stretching vibration of O–H (hydroxyl group). An absorption band around 2926 cm^{-1} was attributed to asymmetric and symmetric stretching vibrations of −CH2– groups (-CH group). In addition, the peak absorption recorded at 2103 cm^{-1} indicated the existence of stretching of carboxylic groups[24]. The peaks at 1732 cm^{-1} and 1633 cm^{-1} characterizes the C=O group and the C=C group respectively (which confirmed the presence of both ester and carboxyl groups). The peak located at 1424 cm^{-1} is attributed to −COO– symmetric stretching. The peak at 1370 cm^{-1} signifies the -CN group. Two peaks appeared 1235 cm^{-1} and 1017 cm^{-1} that are attributed to the vibration of the -CO group.

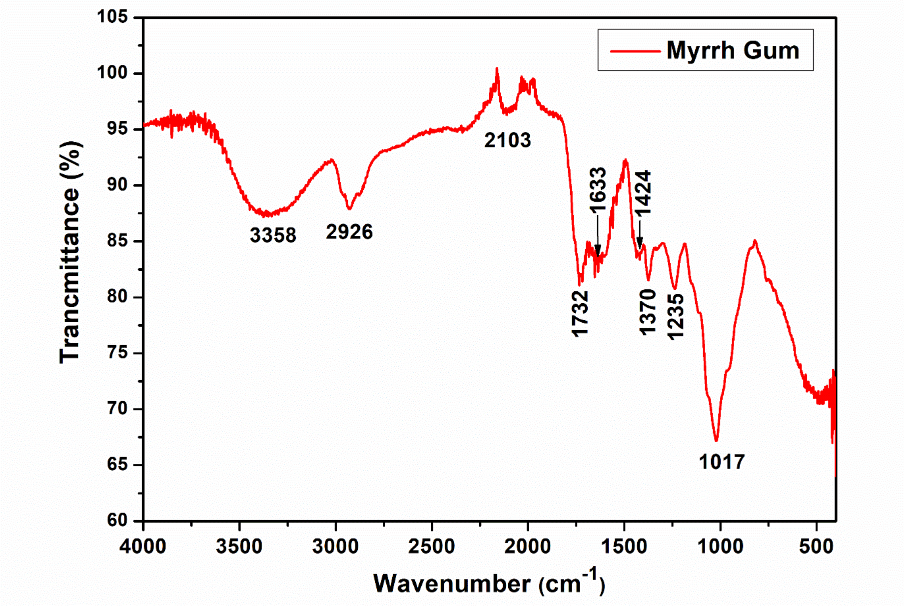

Figure 2. FTIR spectra of the Myrrh Gum (MG)

3.2. Inhibition effect of Myrrh Gum (MG)

Impedance measurements

Impedance tests were conducted to understand the properties and dynamics of the electrochemical reactions at the interface between API 5CTP110 tubing and HCl, both with and without MG. Fig.3 shows the Nyquist, Bode modulus, and Bode phase diagrams from the EIS data gathered during the corrosion of API 5CTP110 tubing in a 0.5 M HCl solution, considering both scenarios where MG is absent and present in varying concentrations.

The Nyquist plot (Fig.3.a) reveals depressed semicircles in both scenarios, with and without MG, indicating that the corrosion reactions are dominated by charge transfer processes[25, 26]. Regardless of the presence of MG, all Nyquist plots maintain a similar configuration featuring a single capacitive loop, pointing to the geometric blocking effect as MG's mode of inhibition[27]. An increase in the diameter of the Nyquist plots with rising MG concentrations shows MG's effectiveness in reducing the corrosion of API 5CTP110 tubing. However, careful estimation of the Rt (charge transfer resistance) is necessary as the centers of these depressed semicircles are positioned below Zi = 0. The consistent shape of the Nyquist plots, whether MG is present or not, indicates that the inhibitor does not alter the dissolution mechanism of the steel but significantly affects the electrical properties of the double layer. Using the Impedance Model Editor from GamryEchem Analyst, an attempt was made to fit these results with an equivalent circuit model (Fig.4). The circuit consists of the solution resistance *Rs*, the constant phase element that represents the double-layer capacitance (CPE), and the charge transfer resistance *Rt*. The corresponding EIS data derived from this equivalent circuit model are displayed in Table1. Also, Fig.4 presents both the simulated and experimentally derived impedance curve for API 5CTP110 tubing immersed in 0.5 M hydrochloric acid solution with 3.00 g/L of MG.

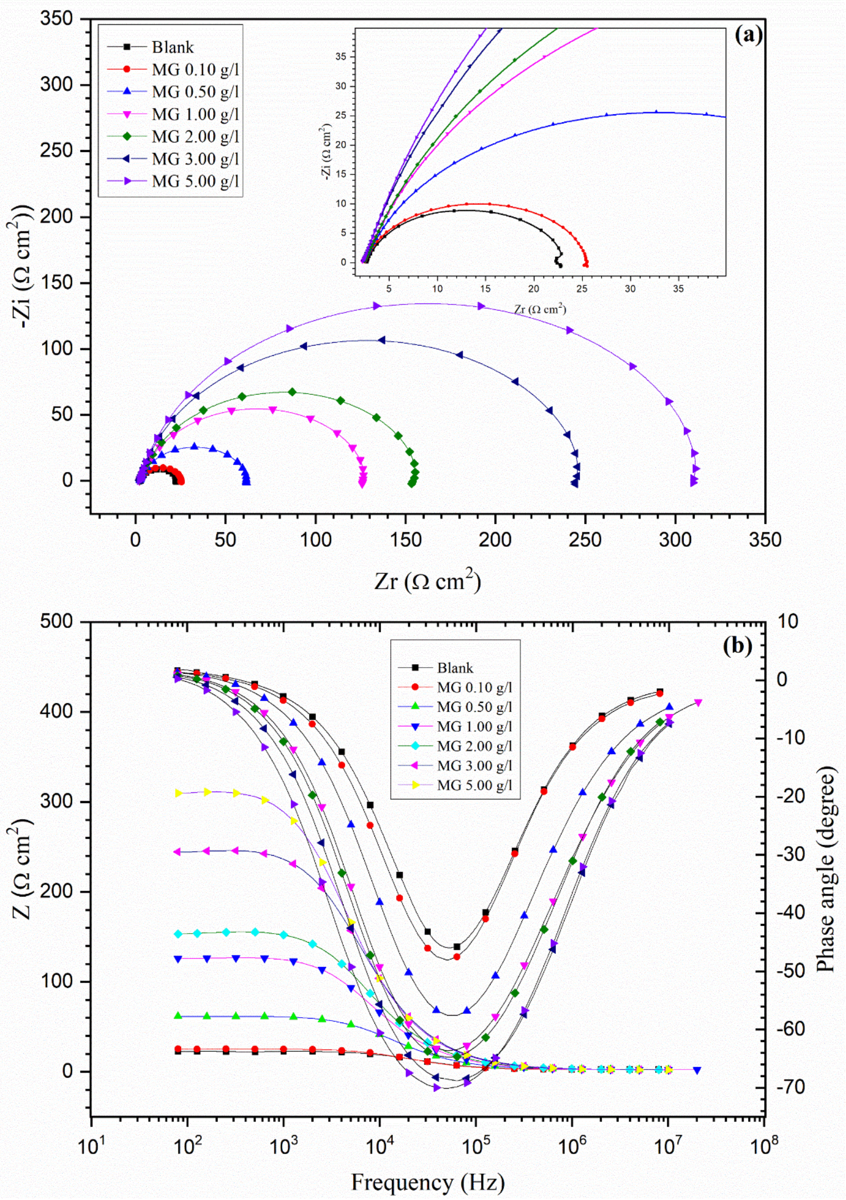

Figure 3. EIS plots for API 5CTP110 tubing in 0.5 M HCl medium without and with different concentrations of MG at 20°C, (a) Nyquist, (b) Bode modulus and Bode phase angle representations

Table1.EIS parameters for API 5CTP110 tubing in 0.5 M HCl without and with different concentrations of MG at 20°C

System/concentration	Rs, (Ω cm^2)	Y_0, (μΩ S^n cm^{-2})	n	Rt, (Ω cm^2)	Cdl, (μF cm^{-2})	η_{EIS}%
Blank	*2.7*	*686*	0.9*0*	*020.25*	423	-
0.10 g/L	*2.5*	*752*	0.88	*023.15*	421	*12*
0.50 g/L	*2.4*	*454*	0.8*7*	*060.54*	265	*66*
1.00 g/L	*2.2*	*342*	0.8*6*	*128.8*	204	*84*
2.00 g/L	*2.4*	*292*	0.8*7*	*157.5*	170	*87*
3.00 g/L	*2.2*	*214*	0.90	*250.1*	154	*92*
5.00 g/L	*2.2*	*225*	0.87	*317.8*	152	*93*

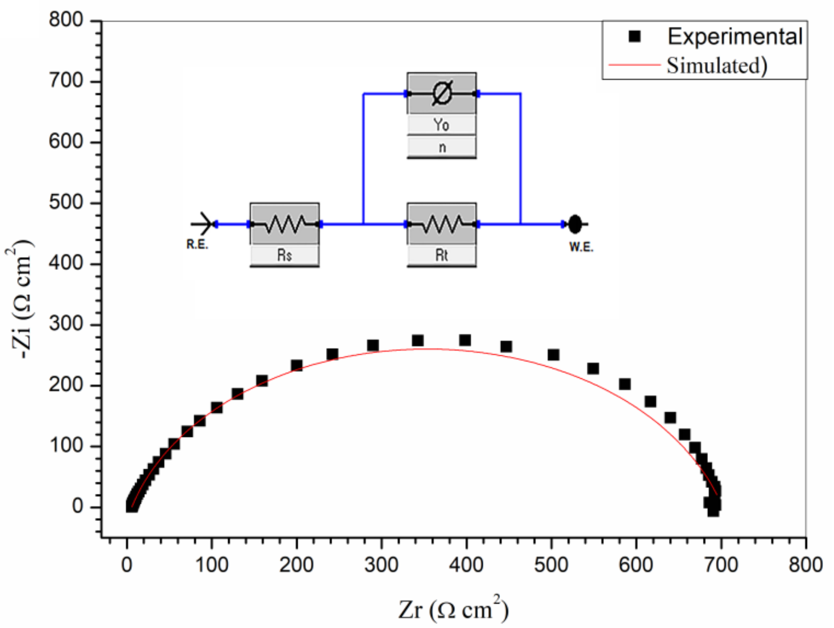

Figure 4.Nyquist plot of simulated data and experimental data, together with the equivalent circuit used to fit the impedance data, recorded for API 5CTP110 tubing in 0.5 M HCl containing 3 g/L MG

As the concentration of MG increased, there was a notable rise in the charge transfer resistance (*Rt*) of API 5CTP110 tubing. Specifically, the *Rt* value increased from 20.25Ωcm2 without MG to 250.1 Ω cm2 at a MG concentration of 3.00 g/L. It is important to note that at this concentration of 3.00 g/L, the Rt value reached a plateau and showed little further change. At a MG concentration of 3.00 g/L, the η_{EIS} exceeded 92%, demonstrating MG's efficacy as a corrosion inhibitor for API 5CTP110 tubing in an HCl solution. For more accurate fitting results, constant phase elements (CPE) were utilized in place of capacitors. The impedance of the CPE depends on the frequency, but its phase angle remains constant across frequencies (Eq.3)[28].

$$Z_{CPE} = Y_0^{-1}\left(j\omega\right)^{-n} \tag{3}$$

Here, Z_{CPE} denotes the impedance of a CPE, Y_0 is a scale factor indicative of the combined characteristics of the surface and electroactive species, independent of frequency, *j* represents the imaginary unit, *ω* is the angular frequency, and *ω* equals *2πf*, where *f* is the frequency. The parameter *n* represents a phase shift and relates to the slope of the log |*Z*| versus log *f* curve, typically ranging from 0.5 to 1. Eq.4 was used to compute the double layer capacitance C_{dl}[29].

$$C_{dl} = Y_0\left(2\pi f_{max}\right)^{n-1} \tag{4}$$

In this equation, f_{max} is the frequency at which the imaginary component of the impedance is at its maximum. Conversely, an increase in inhibition effectiveness is associated with a reduction in the metal's capacitance, as evidenced by the marked decrease in C_{dl} values from 423 μFcm^{-2} in the solution without MG to 152 μFcm^{-2} in the solution containing the highest MG concentration (3.00 g/L) at a temperature of 20°C.

3.3. Potentiodynamic polarization measurements

Fig.5 depicts the outcomes of potentiodynamic polarization tests conducted at 20°C on the surface of API 5CTP110 tubing in 0.5MHCl solutions, both with and without various concentrations of MG. The summarized results in Table2 include parameters such as corrosion current density, corrosion potential, anodic Tafel slope, and cathodicTafel slope, with the inhibition efficiency of MG calculated using Eq.1.Analysis of Fig.5 reveals a decrease in both cathodic and anodic current densities with increasing concentrations of MG, while the corrosion potential (*Ecorr*) remains unchanged, suggesting that MG acts as a mixed inhibitor[30].Further analysis of Fig.5 shows that the cathodic branches in both inhibited and uninhibited solutions of API 5CTP110 tubing display parallel Tafel lines, indicating that the corrosion reaction mechanism remains consistent and is governed by charge transfer processes, including hydrogen evolution and reduction of H$^+$ ions. However, the data in Table2 also shows a significant reduction in *Icorr* values as MG concentration increases, attributing to decreased hydrogen evolution and steel dissolution in the cathodic and anodic reactions, respectively, due to the inhibitor[31]. The effectiveness of an inhibitor in reducing corrosion can be influenced by two mechanisms: reducing the available reaction surface through geometric blocking and altering the activation energy of redox reactions. It is difficult to ascertain which mechanism predominates. If the geometric blocking effect is more significant, there would be no notable change in *Ecorr* after adding the inhibitor. The lack of substantial variation in *Ecorr* supports the dominance of the geometric blocking effect over activation energy changes[32].As the concentration of MG increases, the efficacy of the inhibitor peaks at 91% at 3.00 g/L, as shown in Table2, demonstrating a strong correlation between the data from EIS and potentiodynamic polarization tests.

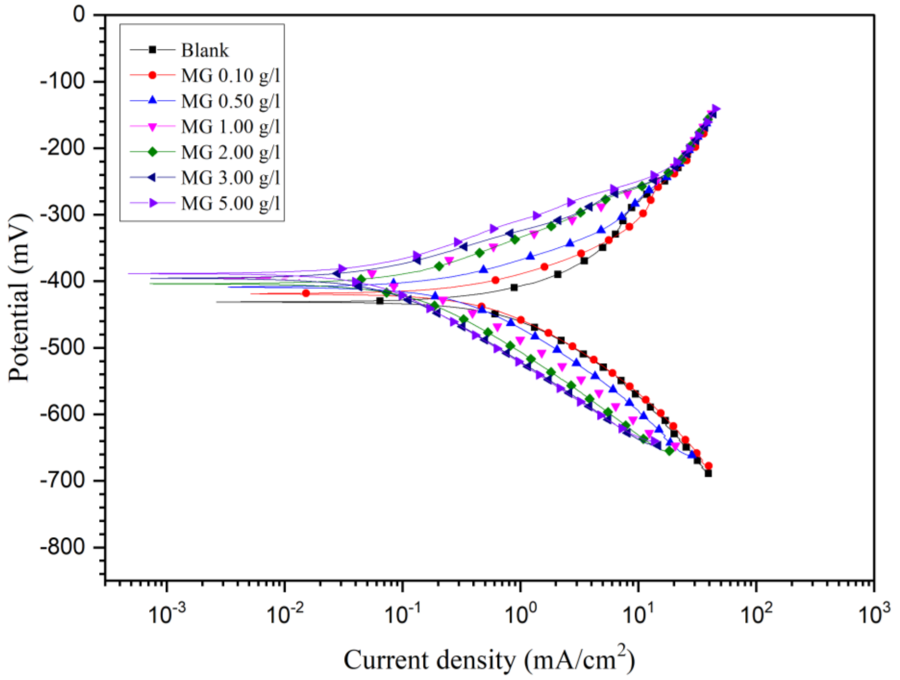

Figure 5.Potentiodynamic polarization curves for API 5CTP110 tubing in 0.5 M HCl without and with different concentrations of MG at 20°C

Table 2.Potentiodynamic polarization parameters for API 5CTP110 tubing in 0.5 M HCl without and with different concentrations of MG at 20°C

System/Concentration	Ecorr, (mV)	Icorr, (µA)	- *bc*, (mV dec^{-1})	Ba,(mV dec^{-1})	η_{pol}, %
Blank	*-426*	*948*	14*2*	*101*	-
0.10 g/L	*-419*	*844*	14*1*	*99*	*11*
0.50 g/L	-4*07*	*367*	*127*	*75*	*61*
1.00 g/L	*-390*	190	129	70	*80*
2.00 g/L	-400	144	124	75	84
3.00 g/L	-396	87	116	64	91
5.00 g/L	-389	71	116	68	92

3.4. Adsorption isotherm and standard free energy of adsorption

The present study assessed various adsorption isotherms and identified the Langmuir adsorption isotherm as the most appropriate model to describe the adsorption behaviour of the investigated inhibitor, as depicted in Fig.6. This isotherm establishes a relationship between the surface coverage ($\theta = \eta_{EIS}\%/100$) and the inhibitor concentration (*C*) in the electrolyte[33].

$$\frac{C}{\theta} = \frac{1}{K_{ads}} + C \qquad (5)$$

The adsorption process is characterized by the adsorption constant K_{ads}, which can be derived from the linear plots of C/θ against C, yielding slopes close to unity. Additionally, the standard free energy of adsorption ΔG°_{ads} is calculated using K_{ads} through Eq.6 [33, 34].

$$\Delta G^{\circ}_{ads} = -RT\ \ ln(1\times10^{6} K_{ads}) \qquad (6)$$

where 1 x 10^6 represents the concentration of water molecules in mg/L, *R* is the universal gas constant, and *T* is the absolute temperature. The values of $\Delta G_{ads}$and *Kads* are presented in Table3. The value of *Kads* serves as an indicator of the strength of the adsorption forces between the inhibitor molecules and the metal surface[28].

Table 3. Langmuir adsorption isotherm parameters for API 5CTP110 tubing in 0.5 M HCl solution containing MG at 20°C

Isotherm mode	Linear correlation coefficient	Slope	*Kads* (L/g)	ΔG°_{ads} (kJmol^{-1})
Langmuir	0.99673	0.98592	2.7993	-19.67

In general, if the ΔG°_{ads} value is up to -20 kJ/mol, it indicates physical adsorption between charged molecules and a charged metal due to electrostatic interaction. On the other hand, if the ΔG°_{ads} value is below -40 kJ/mol, it shows chemisorption, which involves charge sharing or transfers from the inhibitor to the metal surface to form a coordinate bond[35].In this investigation, the value of ΔG°_{ads} is 9.99 kJ/mol demonstrating that the adsorption of MG on API 5CTP110 tubing surface includes physical adsorption. This conclusion is supported by similar findings from the study of Ebenso et all.[36].

3.5. Surface analysis by SEM-EDX

Fig.6 presents microscope images and corresponding chemical analysis for the polished metal surfaces, both with and without the inhibitor (MG), to demonstrate the effectiveness of MG as confirmed by EIS and polarization curve methods. When the pipeline steel was immersed in 0.5 M HCl, a corrosion product formed on its surface, as shown in Fig.6.a, due to the ongoing corrosion process. In contrast, the microscopy image of the specimen treated with the inhibitor (Fig.7.b) shows no visible corrosion product.

To identify the surface components of API 5CTP110 tubing after 72 hours of exposure to 0.5 M HCl, Energy Dispersive X-ray Spectroscopy (EDX) analysis was performed (Table4). In the absence of the inhibitor, the EDX spectra revealed prominent peaks for oxygen and chloride elements. However, for the API 5CTP110tubing exposed to 0.5 M HCl containing 3 g/L of MG, the spectra indicated a reduction in the oxygen and chloride ratios, likely due to the adsorption of MG on the tubing surface.

Table 4.Content of elements obtained from EDX spectra for API 5CTP110 tubing

Element	Weight %	
	Steel + 0.5 M HCl	Steel + 0.5 M HCl + 3 g/L GM
Iron	77.17	90.78
Oxygen	16.14	6.41
Chlorine	6.69	2.81

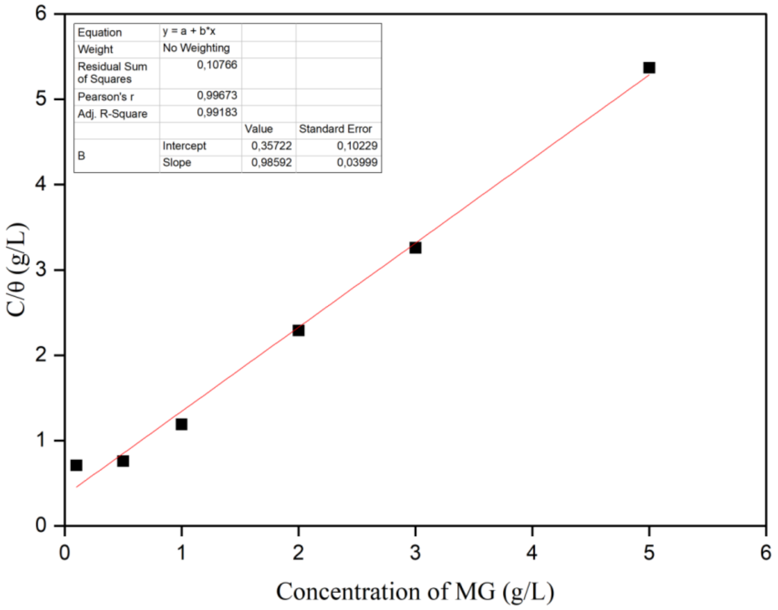

Figure 6.Langmuir isotherm adsorption mode of MG on the API 5CTP110 tubing in 0.5 M HCl at 20°C (from EIS measurements).

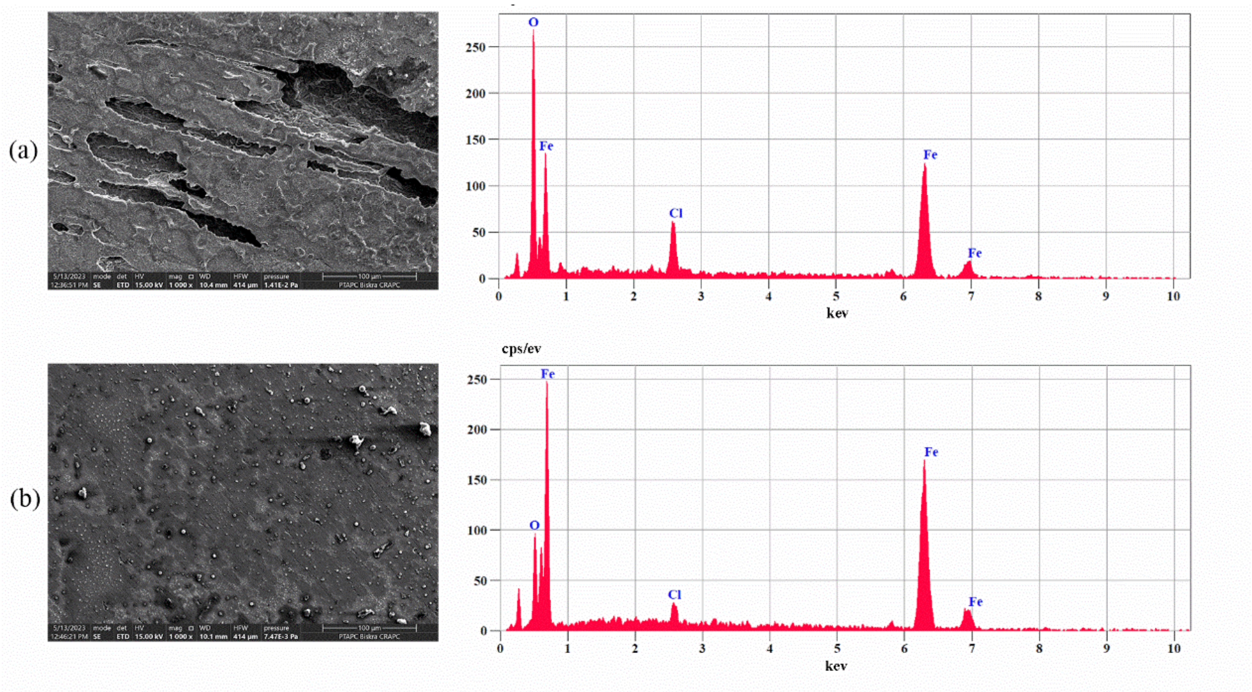

Figure 7.SEM images of API 5CTP110 tubing in 0.5 M HCl at 20°C before and after 72 h immersion: (a) in 0.5 M HCl without and (b) in 0.5 M HCl with 2 g/L MG

3.6. Mechanism of Corrosion Inhibition

Dominant component of MG is polysaccharides with a carboxyl functional group (glucuronic acid)[20]. The free energy of adsorption of MG is –19.67 kJ mol/L, which indicates that the adsorption mechanism of the MG on API 5CTP110 steel surface is a physical absorption. Glucuronic acid molecules can be adsorbed on the steel surface via electrostatic interaction between the protonated glucuronic acid molecules and the charged metal surface. The API 5CTP110 steel surface has a positive charge in the hydrochloric acid[37], so due to the electrostatic repulsion, the protonated glucuronic acid molecules cannot get close to the steel surface. Since the anions of Cl^- could be specifically adsorbed on the API 5CTP110 steel surface, the latter becomes negatively charged and therefore increases the tendency of adsorption of the protonated glucuronic acid chains on API 5CTP110 steel surface by electrostatic interaction (physisorption).

4. CONCLUSIONS

This study on the corrosion inhibition properties of Myrrh Gum (MG) for API 5CTP110 tubing in hydrochloric acid (*H*Cl) solution yielded the following key findings:

MG is an effective inhibitor for API 5CTP110 tubing in 0.5 M HCl, with inhibition efficiency increasing with concentration and reaching a maximum of 92% at 3 g/L.

The adsorption behaviour of MG on the tubing surface aligns with the Langmuir adsorption isotherm.

The calculated ΔG°_{ads} value confirms that the adsorption of MG on the steel surface occurs predominantly through physical adsorption mechanisms.

Potentiostatic polarization data indicate that MG functions as a mixed-type inhibitor, affecting both anodic and cathodic reactions.

Electrochemical impedance spectroscopy (EIS) and polarization studies suggest that the inhibition mechanism of MG primarily involves a geometric blocking effect, reducing the active surface area exposed to the corrosive medium.

5. REFERENCES

[1] K. Haruna, I. Obot, N. Ankah, A. Sorour, T. Saleh (2018) Gelatin: A green corrosion inhibitor for carbon steel in oil well acidizing environment, J. Mol. Liq., 264, 515-525. DOI: 10.1016/j.molliq.2018.05.058.

[2] W. Zhang, H.-J. Li, M. Wang, L.-J. Wang, F. Shang, Y.-C. Wu (2018) Halogen-substituted acridines as highly effective corrosion inhibitors for mild steel in acid medium, J. Phys. Chem. C, 122, 25349-25364. DOI: 10.1021/acs.jpcc.8b07015.

[3] A.H. Alamri (2020) Localized corrosion and mitigation approach of steel materials used in oil and gas pipelines – An overview, Eng. Fail. Anal., 116, 104735.

DOI: https://doi.org/10.1016/j.engfailanal.2020.104735.

[4] M.A.M. El-Haddad, A. Bahgat Radwan, M.H. Sliem, W.M.I. Hassan, A.M. Abdullah (2019) Highly efficient eco-friendly corrosion inhibitor for mild steel in 5 M HCl at elevated temperatures: experimental & molecular dynamics study, Sci. Rep., 9, 3695. DOI: 10.1038/s41598-019-40149-w.

[5] M. Goyal, S. Kumar, I. Bahadur, C. Verma, E.E. Ebenso (2018) Organic corrosion inhibitors for industrial cleaning of ferrous and non-ferrous metals in acidic solutions: A review, J. Mol. Liq., 256, 565-573. DOI: https://doi.org/10.1016/j.molliq.2018.02.045.

[6] A. Singh M.A. Quraishi (2015) Acidizing corrosion inhibitors: a review, J. Mater. Environ. Sci, 6, 224-235.

[7] D. Dwivedi, K. Lepková, T. Becker (2017) Carbon steel corrosion: a review of key surface properties and characterization methods, RSC Adv., 7, 4580-4610. DOI: https://doi.org/10.1039/C6RA25094G

[8] A. Frignani, C. Monticelli, F. Zucchi, G. Trabanelli (2014) Acetylenic alcohols as inhibitors of iron acid corrosion. Improvement of the inhibition efficiency of a class of substances based on their action mechanism, Int. J. Corros. Scale Inhib, 3, 105. DOI: 10.17675/2305-6894-2014-3-2-105-119.

[9] M. Salman, K. Ansari, V. Srivastava, D.S. Chauhan, J. Haque, M. Quraishi (2021) Chromeno naphthyridines based heterocyclic compounds as novel acidizing corrosion inhibitors: Experimental, surface and computational study, J. Mol. Liq., 322, 114825. DOI: https://doi.org/10.1016/j.molliq.2020.114825.

[10] M. Galai, M.E. Touhami, M. Oubaaqa, K. Dahmani, M. Ouakki, M. Khattabi, Z. Benzekri, R. lachhab, S. Kaya, N. Bulut, S. Briche, S. Boukhris (2023) Electrochemical, Characterization, and Quantum Chemical Studies of Two Newly Synthesized Aromatic Aldehydes-Based Xanthene Diones as Corrosion Inhibitors for Mild Steel in 1 M Hydrochloric Acid, J. Bio- Tribo-Corros., 9, 63. DOI: 10.1007/s40735-023-00778-1.

[11] J. Wang, L. An, J. Wang, J. Gu, J. Sun, X. Wang (2023) Frontiers and advances in N-heterocycle compounds as corrosion inhibitors in acid medium: Recent advances, Adv. Colloid Interface Sci., 103031. DOI: https://doi.org/10.1016/j.cis.2023.103031.

[12] M. Yadav, S. Kumar, P. Yadav (2013) Corrosion Inhibition of Tubing Steel during Acidization of Oil and Gas Wells, J. Pet. Eng., 2013. DOI: 10.1155/2013/354630.

[13] D. Singh A. Dey (1993) Synergistic effects of inorganic and organic cations on inhibitive performance of propargyl alcohol on steel dissolution in boiling hydrochloric acid solution, Corrosion, 49, 594-600. DOI: https://doi.org/10.5006/1.3316090.

[14] F.G. Liu, M. Du, J. Zhang, M. Qiu (2009) Electrochemical behavior of Q235 steel in saltwater saturated with carbon dioxide based on new imidazoline derivative inhibitor, Corros. Sci., 51, 102-109. doi: https://doi.org/10.1016/j.corsci.2008.09.036.

[15] X. Li, S. Deng, H. Fu, G. Mu (2010) Synergistic inhibition effect of rare earth cerium(IV) ion and sodium oleate on the corrosion of cold rolled steel in phosphoric acid solution, Corros. Sci., 52, 1167-1178. DOI: https://doi.org/10.1016/j.corsci.2009.12.017.

[16] X. Li, S. Deng, H. Fu, G. Mu (2009) Synergistic inhibition effect of rare earth cerium(IV) ion and 3,4-dihydroxybenzaldehye on the corrosion of cold rolled steel in H2SO4 solution, Corros. Sci., 51, 2639-2651. DOI: https://doi.org/10.1016/j.corsci.2009.06.047.

[17] S.Y. Al-Nami A.E.-A.S. Fouda (2020) Corrosion Inhibition Effect and Adsorption Activities of methanolic myrrh extract for Cu in 2 M HNO3, Int. J. Electrochem. Sci., 15, 1187-1205. doi: https://doi.org/10.20964/2020.02.23.

[18] B. Tan, B. Xiang, S. Zhang, Y. Qiang, L. Xu, S. Chen, J. He (2021) Papaya leaves extract as a novel eco-friendly corrosion inhibitor for Cu in H2SO4 medium, J. Colloid Interface Sci., 582, 918-931. doi: https://doi.org/10.1016/j.jcis.2020.08.093.

[19] N. Hossain, M. Asaduzzaman Chowdhury, M. Kchaou (2021) An overview of green corrosion inhibitors for sustainable and environment friendly industrial development, J. Adhes. Sci. Technol., 35, 673-690. DOI: 10.1080/01694243.2020.1816793.

[20] M. Rinaudo (2014) Biomateriales basados en un polisacárido natural: el alginato, TIP Revista Especializada en Ciencias Químico-Biológicas, 17, 92-96.

[21] H. Hu, J. Li, W. Jiang, Y. Jiang, Y. Wan, Y. Wang, F. Xin, W. Zhang (2024) Strategies for the biological synthesis of D-glucuronic acid and its derivatives, World J. Microbiol. Biotechnol., 40, 94. DOI: 10.1007/s11274-024-03900-8.

[22] A. Wadouachi J. Kovensky (2011) Synthesis of Glycosides of Glucuronic, Galacturonic and Mannuronic Acids: An Overview, Molecules, 16, 3933-3968. doi: 10.3390/molecules16053933.

[23] A. Richel, F. Nicks, P. Laurent, B. Wathelet, J.-P. Wathelet, M. Paquot (2012) Efficient microwave-promoted synthesis of glucuronic and galacturonic acid derivatives using sulfuric acid impregnated on silica, Green Chemistry Letters and Reviews, 5, 179-186. doi: 10.1080/17518253.2011.607852.

[24] C.-S. Wu (2009) Renewable resource-based composites of recycled natural fibers and maleated polylactide bioplastic: Characterization and biodegradability, Polym. Degrad. Stab., 94, 1076-1084. https://doi.org/10.1016/j.polymdegradstab.2009.04.002.

[25] A. Singh, K.R. Ansari, D.S. Chauhan, M.A. Quraishi, H. Lgaz, I.-M. Chung (2020) Comprehensive investigation of steel corrosion inhibition at macro/micro level by ecofriendly green corrosion inhibitor in 15% HCl medium, J. Colloid Interface Sci., 560, 225-236.

doi: https://doi.org/10.1016/j.jcis.2019.10.040.

[26] M. Djellab, H. Bentrah, A. Chala, H. Taoui, S. Kherief, B. Bouamra (2020) Synergistic effect of iodide ions and bark resin of Schinus molle for the corrosion inhibition of API5L X70 pipeline steel in H2SO4, Mater. Corros., 71, 1276-1288. DOI: https://doi.org/10.1002/maco.202011533.

[27] D. Wang, Y. Li, B. Chen, L. Zhang (2020) Novel surfactants as green corrosion inhibitors for mild steel in 15% HCl: Experimental and theoretical studies, Chem. Eng. J., 402, 126219. doi: https://doi.org/10.1016/j.cej.2020.126219.

[28] S.A. Umoren (2016) Polypropylene glycol: A novel corrosion inhibitor for ×60 pipeline steel in 15% HCl solution, J. Mol. Liq., 219, 946-958. DOI: https://doi.org/10.1016/j.molliq.2016.03.077.

[29] M. Djellab, H. Bentrah, A. Chala, H. Taoui (2019) Synergistic effect of halide ions and gum arabic for the corrosion inhibition of API5L X70 pipeline steel in H2SO4, Mater. Corros., 70, 149-160. doi: https://doi.org/10.1002/maco.201810203.

[30] R. Solmaz, G. Kardaş, M. Çulha, B. Yazıcı, M. Erbil (2008) Investigation of adsorption and inhibitive effect of 2-mercaptothiazoline on corrosion of mild steel in hydrochloric acid media, Electrochim. Acta, 53, 5941-5952. doi: https://doi.org/10.1016/j.electacta.2008.03.055.

[31] I.B. Obot, A. Meroufel, I.B. Onyeachu, A. Alenazi, A.A. Sorour (2019) Corrosion inhibitors for acid cleaning of desalination heat exchangers: Progress, challenges and future perspectives, J. Mol. Liq., 296, 111760. doi: https://doi.org/10.1016/j.molliq.2019.111760.

[32] H. Taoui, H. Bentrah, A. Chala, M. Djellab (2019) Bark resin of Schinus molle as an eco-friendly inhibitor for API 5L X70 pipeline steel in HCl medium, Mater. Corros., 70, 511-520. doi: https://doi.org/10.1002/maco.201810477.

[33] O. Sotelo-Mazon, S. Valdez, J. Porcayo-Calderon, M. Casales-Diaz, J. Henao, G. Salinas-Solano, J.L. Valenzuela-Lagarda, L. Martinez-Gomez (2019) Corrosion protection of 1018 carbon steel using an avocado oil-based inhibitor, Green Chemistry Letters and Reviews, 12, 255-270. DOI: 10.1080/17518253.2019.1629698.

[34] M.M. Solomon, S.A. Umoren, A.U. Israel, I.G. Etim (2016) Synergistic inhibition of aluminium corrosion in H2SO4 solution by polypropylene glycol in the presence of iodide ions, Pigment Resin Technol., 45, 280-293. doi: 10.1108/PRT-01-2015-0010.

[35] H. Bentrah, Y. Rahali, A. Chala (2014) Gum Arabic as an eco-friendly inhibitor for API 5L X42 pipeline steel in HCl medium, Corros. Sci., 82, 426-431. DOI: https://doi.org/10.1016/j.corsci.2013.12.018.

[36] E. Ebenso, N. Eddy, A. Odiongenyi (2009) Corrosion Inhibition and Adsorption Properties of Methocarbamol on Mild Steel in Acidic Medium, Port. Electrochim. Acta, 27, 13-22. DOI: 10.4152/pea.200901013.

[37] S. Kherief, M. Djellab, H. Bentrah, A. Chala, B. Bouamra, H. Taoui (2023) Corrosion Inhibition Efficiency of Ghars Date Extract on API 5L X70 Pipeline Steel in Hydrochloric Acid, Protection of Metals and Physical Chemistry of Surfaces, 59, 1306-1314. doi: 10.1134/S2070205123701162.

IZVOD

EFIKASNOST INHIBITORA KOROZIJE GUME MIRTE NA CEVIMA API 5CTP110 U HLOROVODONIČNOJ KISELINI

Ispitivana su svojstva inhibicije korozije gume mirte (MG) na cevima API 5CTP110 u rastvoru HCl od 0,5 M. Studija je pokazala da MG pokazuje izuzetne inhibitorne performanse, postižući efikasnost od 92% pri optimalnoj koncentraciji od 3 g/L. Analiza je otkrila da adsorpcija molekula MG na površinu čelika prati model Langmirove izoterme, što ukazuje na proces kojim dominira fizička adsorpcija. Pored toga, MG deluje kao inhibitor mešovitog tipa, efikasno ublažavajući i anodne i katodne reakcije. Ovi nalazi ističu potencijal gume mirte kao isplativog i ekološki prihvatljivog inhibitora korozije za industrijske primene, posebno u kiselim sredinama. Upotreba MG je u skladu sa održivim praksama, pružajući održivu alternativu tradicionalnim sintetičkim inhibitorima i doprinoseći razvoju zelenih strategija za sprečavanje korozije.

Ključne reči: *Ekološki inhibitor korozije, API 5CTP110 cevi, guma mirte, hlorovodonična kiselina, EIS*

Naučni rad
Radprimljen: 30.03.2025.
Rad prihvacen: 25.04.2025.

Valentina Loganina[1]*, Vadim Pylaev*[1]*, Roman Fediuk*[2,3]***,
Bassam A. Tayeh[4]*,Sergey Klyuev*[5,6]*,Alexander Klyuev*[5]*,
Svetlana Shambina*[6]*, German Fediuk*[2]

[1]*Penza State University of Architecture and Construction, Penza, Russia,*[2]*Far Eastern Federal University, Vladivostok, Russia,*[3]*Branch of the Federal State Budgetary Institution "CNIIP of the Ministry of Construction of Russia" Far Eastern Scientific Research, Design and Technological Institute for Construction, Vladivostok, Russia,* [4]*Civil Engineering Departmet, Faculty of Engineering, Islamic University of Gaza, P.O. 108, Gaza Strip, Palestine,* [5]*Belgorod State Technological University n.a. V.G. Shukhov, Belgorod, Russia,* [6]*RUDN University, Moscow, Russia*

Scientific paper
ISSN 0351-9465, E-ISSN 2466-2585
https://doi.org/10.62638/ZasMat1429

Zastita Materijala 67 (1)
181 - 190 (2026)

Lime compositions with polysaccharides for building walls restoration ad protection

ABSTRACT

Preserving historical heritage is a significant priority in contemporary urban planning. However, enhancing the durability of lime coatings used in the restoration of cultural heritage sites remains a challenge. This study aims to identify a method for improving the crack resistance of lime-based coatings using polysaccharide additives. The study examines water-soluble modified polysaccharides AtrenCemHV and AtrenCem LV. The maximum adsorption values of these additives on lime were determined, with AtrenCemHV at 1.83 g/g and AtrenCem LV at 1.66 g/g. Findings indicate that the adsorption of polysaccharides onto the surface of $Ca(OH)_2$ *lime particles leads to the formation of a composite structure containing inter- and intercrystalline organic molecules, which enhances the crack resistance of the coatings. The research also provides insights into the carbonization process of lime coatings containing polysaccharide additives, revealing that these additives increase the thickness of the carbonized layer. Lime compositions with polysaccharides demonstrate greater cohesive strength due to a high calcite content. Additionally, the formation of a composite structure with organic molecules contributes to a reduction in the elastic modulus and hardness of the coatings. Lime coatings with the AtrenCem LV additive endured 35 cycles of freezing and thawing. Thus, the new findings on lime compositions with polysaccharide additives are crucial for restoring building walls.*

Keywords: *lime; polysaccharides; monomolecular adsorption; carbonization; crack resistance; coatings*

1. INTRODUCTION AND RESEARCH AIM

The challenge of preserving historical heritage is a central concern in today's urban planning [1]. Natural stone and exterior finishes of building facades deteriorate due to physical weathering and harsh environmental conditions [2]. Restoration and rehabilitation efforts rely on specialized materials that not only restore the visual appeal of structures but also ensure their usability[3,4]. Lime-based compositions are frequently used in the restoration of historical buildings. Among the most widely used commercial lime paints for such restorations are “Holvi,” “Kalcemur,” “Silacra-lime,” “Antik 1,” and “Antik 2,” among others [5,6]. Some of these paints maintain traditional compositions, which help protect old surfaces and make them ideal for heritage restoration, while others are enhanced with cellulose fibers to improve coverage and ease of use while retaining technical and protective qualities.

Lime compounds are known to harden slowly, complicating the finishing process [7,8]. To speed up hardening and boost the strength of lime composites, various additives are incorporated into their formulation, such as sodium aluminate, sodium fluoride, potassium carbonate, calcium chloride, amorphous aluminum oxide, lithium carbonate, calcium formate, and finely dispersed amorphous silica[9,10].

Improving the resilience of mineral binder composites has increasingly focused on the use of colloidal silicon dioxide dispersions to address technological challenges [11,12]. Silicon oxide nanoparticles, reacting with Ca(OH)2 over time to form calcium silicate hydrate, play a significant role

---

*Corresponding author: Roman Fediuk
E-mail: roman44@yandex.ru

Paper received: 24.04. 2025.
Paper corrected: 31.05.2025.
Paper accepted: 04. 06.2025

in reducing pore sizes (by up to 30%) as they fill the pores with sol particles and reaction products[13,14].

The use of a modified silica sol, known as “Hardness-C,” has been proposed for the formulation of dry construction mixtures [15,16]. To further accelerate the hardening of lime, adding natural zeolites to the mixture is also suggested [17,18].

Research by [19,20]shows that incorporating zeolite-containing rock particles into cement systems can result in the formation of insoluble compounds between fluorine and calcium ions, which fill the pores in the cement-zeolite paste. This reduces fluoride ion concentration, thickens the diffusion layer, lowers hydration temperature by reducing the cement content when a filler is added, enhances cement paste strength, and results in the release of free lime[21,22].

Considering the limited availability and varying properties of natural zeolites, synthetic zeolites are a promising alternative for use in mineral binder compositions [23,24,25,26].Research by [27,28]suggests that synthesized calcium silicate hydrates can enhance the durability of lime coatings. A dry lime composition has been developed for wall finishing and restoration, containing a calcium silicate hydrate filler. This allows for the creation of mortar mixtures with water retention rates of 98-99%, a drying time of 15-20 minutes to reach degree "5," and a working time of 1-1.5 hours. These coatings have a vapor permeability coefficient of 0.05 mg/m·h·Pa, adhesive strength of 0.6-0.9 MPa, and compressive strength of 3-4 MPa. For restoring historical masonry, studies by [29,30]recommend lime-metakaolin mixtures. These mortars have been used in Genoa's white plasters, and it was found that increasing the metakaolin-to-lime ratio raises the amount of chemically bound water, reduces pore size (to 0.1 μm), and enhances compressive strength up to 9 MPa. [30]also proposed using lime compositions with organic components (such as polysaccharides, proteins, and fatty acids) in restoration projects. [31]found that adding animal glue can double the mechanical strength of the mortar, extend the carbonization front, and reduce porosity and pore size. Historically, plant extracts, glutinous rice, fruit juices, oils, and animal fats were added to slaked lime in various regions to improve the properties of lime mortars and plasters[32,33]. For instance, Vitruvius's "De Architectura" recommends adding oil (Oleo subacta) to lime for waterproofing. In the Americas, ancient Mayan masons also used plant extracts, as supported by ethnohistorical, archaeological, and analytical evidence.

In this context, evaluating the applicability of the theory of monomolecular adsorption is crucial. This theory posits that adsorption occurs at specific active centers on the adsorbent surface, where each center interacts with only one adsorbate molecule, forming a single molecular layer[34,35]. The process is balanced by dynamic equilibrium between adsorption and desorption. Despite significant research on improving the durability of lime composites, many aspects, especially those related to restoring cultural heritage sites, remain unresolved. A promising approach for developing lime compositions involves a biomimetic method that creates a lime composite with meso-nanostructural properties similar to calcite biominerals, thereby greatly enhancing the long-term performance of the restoration material.

This article aims to develop lime compositions enhanced with polysaccharide additives for building wall restoration. To achieve this, the study focuses on analyzing the structure formation process of lime compositions with polysaccharides, examining the surface activity of polysaccharides in water solutions, and applying the theory of monomolecular adsorption to understand the adsorption behavior of polysaccharide additives on lime.

2. MATERIALS AND METHODS

This study utilized slaked lime with a true density of 2230 kg/m³, a bulk density of 280 kg/m³, and an activity level of 83%. The organic additives used were water-soluble modified polysaccharides AtrenCemHV and AtrenCem LV, both based on cellulose ether (hydroxyethylcellulose) produced through the reaction of alkali cellulose with ethylene oxide. These additives differ primarily in their molecular weight, with AtrenCemHV having a higher molecular weight. According to standard guidelines, the additives were used in proportions ranging from 0.2% to 1.0% of the binder's weight. During the production of the lime composition, the water-to-lime (W/L) ratio was maintained at 1.0 for all formulations to avoid excessive liquidity. The AtrenCemHV and AtrenCem LV additives were introduced into the mixture during the addition of mixing water.

The true and bulk densities of the slaked lime were measured by weighing a specified volume in both compacted and loose states. The lime's activity was assessed according to the Russian standard GOST 22688-2018. For this, a 1 g lime sample was placed in a 250 ml conical flask, and 150 ml of distilled water was added along with three to five glass beads. The flask was covered with a watch glass and heated to the boiling point for 7 minutes. After cooling to 20-30°C, the flask's walls and the watch glass were rinsed with boiled distilled water, and a few drops of a 1% phenolphthalein alcohol solution were added. The solution was then titrated with a 1 N hydrochloric acid solution while stirring continuously until complete discoloration occurred. The active calcium and magnesium oxides (A, %) in the hydrated lime were calculated using the formula:

$$A = \frac{VT_{CaO}}{W(100 - W)} 100\%$$

where:

W: moisture content of hydrated lime

V: volume of 1 N hydrochloric acid solution used for titration, in ml

T_{CaO}: titer of 1 N hydrochloric acid solution, expressed in grams of CaO

The moisture content of the hydrated lime was determined by placing a 10 g lime sample in a pre-dried weighing bottle, which was then dried in an oven at 105°C to 110°C until a constant mass was reached. The moisture content (W, %) was calculated using the formula:

$$W = \frac{m - m_1}{m} \cdot 100\%$$

where:

m: initial mass of the lime sample, in grams

m_1: mass of the lime sample after drying, in grams

The structure of the hardened lime composite was analyzed using a D8Advans powder diffractometer (Germany), utilizing CuKα radiation with sample rotation. The measurements were conducted for lime composite powder in continuous mode (1 degree per minute) and step-by-step mode (0.02° step size, 10 seconds exposure) across a 2Θ angle range of 5°–100°. X-ray diffraction-based quantitative phase analysis methods leverage the fact that each substance generates a unique set of interference lines. While the ratio of line intensities for each phase remains constant, individual line intensities are proportional to phase content and are influenced by the sample's absorption coefficient.

A TESCAN Vega 3 scanning electron microscope (SEM) was used to examine pre-polished samples(50×25×8 mm). The adsorption behavior of AtrenCemHV and AtrenCem LV additives on lime was studied during the structure formation process of the lime composite. The adsorption was quantified by observing changes in the surface tension (σσσ) of the polysaccharide solution due to a reduction in adsorbent concentration upon adding lime. The stalagmometric (drop counting) method was used for surface tension measurements. To determine the amount of adsorption, lime was mixed into the additive solution, stirred, and allowed to settle until adsorption equilibrium was reached. Adsorption measurements were taken at intervals of 15 minutes and 48 hours after mixing. Data processing followed the equation:

$$\mathrm{a} = \frac{\mathrm{a}_\infty b C_p}{1 + b C_p}$$

where:

a: adsorption value, kg/m²

a_∞: maximum adsorption at complete mineral surface coverage, kg/m² or g/g

b: constant representing the adsorption capacity of additives, 1/%

C_p: equilibrium concentration in the solution, %

Graphical methods were used to determine the maximum adsorption (a_∞) and the constant *b* according to the Langmuir equation, with plots of $\frac{C_p}{a} - C_p$ coordinates.

The elastic modulus of the lime coatings was evaluated using tensile testing, while Vickers hardness was assessed by pressing a tetrahedral diamond pyramid into a 4×4×16 cm sample, with a 136° angle between opposing faces (Figure 1). The surface area of the indentation was calculated using the diagonal (*d*) measured under a microscope.

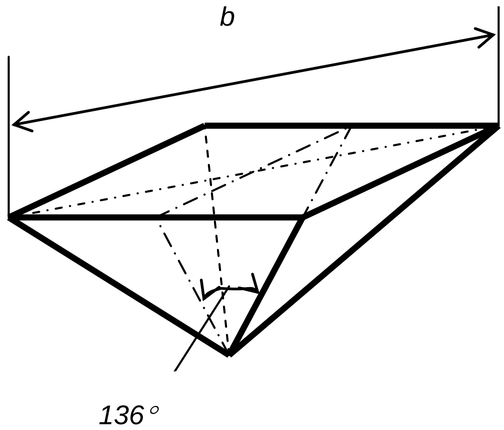

Figure 1. Tetrahedral diamond pyramid for hardness determination by the Vickers method

$$HV = \frac{2P \cdot \sin\frac{\alpha}{2}}{d^2}$$

where:

P: load on the indenter, N

α: angle between opposite faces of the Vickers indenter

d: diagonal of the indentation, mm

The tensile (cohesive) strength of the samples was measured using an IR 5057-50 tensile testing machine (Russia) according to the Russian standard GOST 18299-72*. Tests were conducted at 20°C and 60% relative humidity. The samples (10×10×50 mm) were clamped in the machine, with force applied evenly along their axis. A deformation rate of 0.06 m/hr was used, and only samples that fractured within the designated working section were considered. The tensile strength (R_{cog}), in Pa, was calculated using:

$$\boldsymbol{R_{cog}} = \frac{\boldsymbol{F_{Pi}}}{\boldsymbol{S_{Oi}}}$$

where:

F_{Pi}: tensile load at rupture, N

S_{Oi}: initial cross-sectional area, m²

The elastic modulus (*E*) was derived from the stress-strain curve as the slope of the tangent to the initial linear section:

$$\boldsymbol{E} = \frac{\boldsymbol{R'_{cogi}}}{\boldsymbol{\varepsilon'_i}} \cdot 100$$

where:

R'_{cogi}: tensile strength at the point where the tangent detaches from the curve, Pa

ϵ'_i: relative elongation at this point, m/m

Cohesive strength was calculated based on the axial tensile strength using samples with a cross-sectional area of 10×10×50 mm:

$$R = \frac{P}{F}$$

where:

P: failure force, N

F: initial cross-sectional area, m²

Crack formation in polymer coatings was assessed using the correlation between crack length, the Vickers indentation size, and fracture toughness. The critical stress intensity factor (K_{1c}) was calculated as follows:

$$K_{1c} = 0{,}028HVa^{0{,}5}(E/HV)^{0{,}5}(C/a)^{-1{,}5}$$

where:

HV: Vickers hardness

*C:*half-length of radial cracks

a*:* half-length of the indentation diagonal

Frost resistance, a key durability measure for lime coatings in various climates, was also tested. For each analysis, six samples were prepared.

3. RESULTS AND DISCUSSION

The cohesive strength of the newly developed lime coatings was measured, and the results are presented in Table 1.

Table 1. Cohesive strength (tensile strength) of the lime samples

Composition	Cohesive Strength (MPa)	Standard Deviation (%)
Curing Age: 28 days		
Control (lime + water)	0.22	<1
AtrenCem LV (0.5% by weight of lime)	0.23	<1
AtrenCemHV (0.5% by weight of lime)	0.24	<1
AtrenCem LV (1% by weight of lime)	0.24	<1
AtrenCemHV (1% by weight of lime)	0.25	<1
Curing Age: 3 months		
Control (lime + water)	0.26	<1
AtrenCem LV (0.5% by weight of lime)	0.38	<1
AtrenCemHV (0.5% by weight of lime)	0.40	<1
AtrenCem LV (1% by weight of lime)	0.47	<1
AtrenCemHV (1% by weight of lime)	0.51	<1

These results indicate that the addition of Atren Cem LV and Atren Cem HV improves the tensile strength of lime-based coatings, likely due to structural changes in the lime matrix. The incorporation of these additives promotes the formation of inter- and intercrystalline organic macromolecules, enhancing the durability of the coatings. This structural improvement was confirmed through analysis using SEM images(Fig. 2).

The microstructural analysis revealed low-contrast, nanoscale areas within the calcite crystals, corresponding to the amorphous organic phase (Fig. 2b). The integration of polysaccharides into the calcite matrix was further confirmed through adsorption studies, which measured changes in the surface tension of the mortar with varying concentrations of AtrenCem LV.

As shown in Figure 3, increasing the concentration of AtrenCem LV reduces the surface tension of the solution until it stabilizes at around 1% concentration, achieving a surface tension of $56.62 \cdot 10^{-3}$ J/m². This stabilization indicates the saturation of adsorption sites. Similar behavior was observed for AtrenCemHV, which stabilized at $54.5 \cdot 10^{-3}$ J/m².

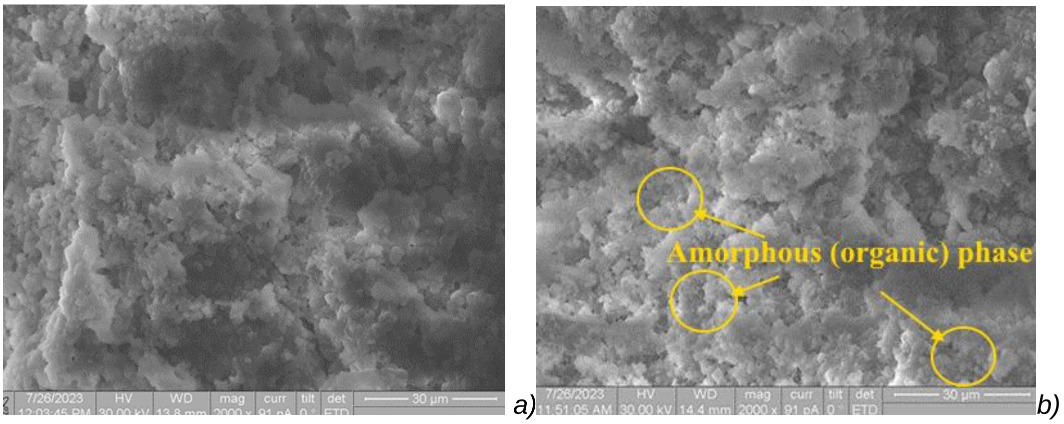

a) b)

Figure 2.Structure of Lime Hardened Paste:(a)Control composition (lime + water); (b)Composition with AtrenCemHV (0.5%)

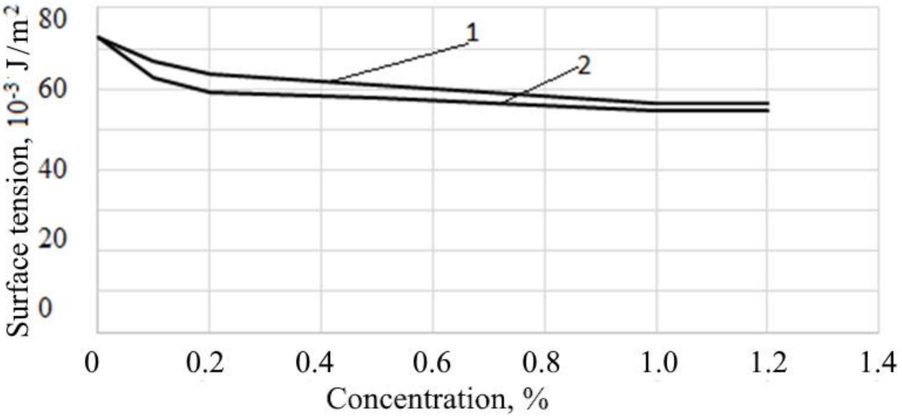

Figure 3.Change in Surface Tension of Polysaccharide Solution AtrenCem LV (1) AtrenCemHV (2)

Adsorption measurements demonstrated that the amount of AtrenCem LV adsorbed on lime after 15 minutes and 48 hours was similar, at approximately 0.909 g/g for a 1% solution. In comparison, AtrenCemHV showed a higher adsorption capacity of 1.1 g/g. The maximum adsorption values were determined to be 1.83 g/g for AtrenCemHV and 1.66 g/g for AtrenCem LV, as shown in Figure 4.

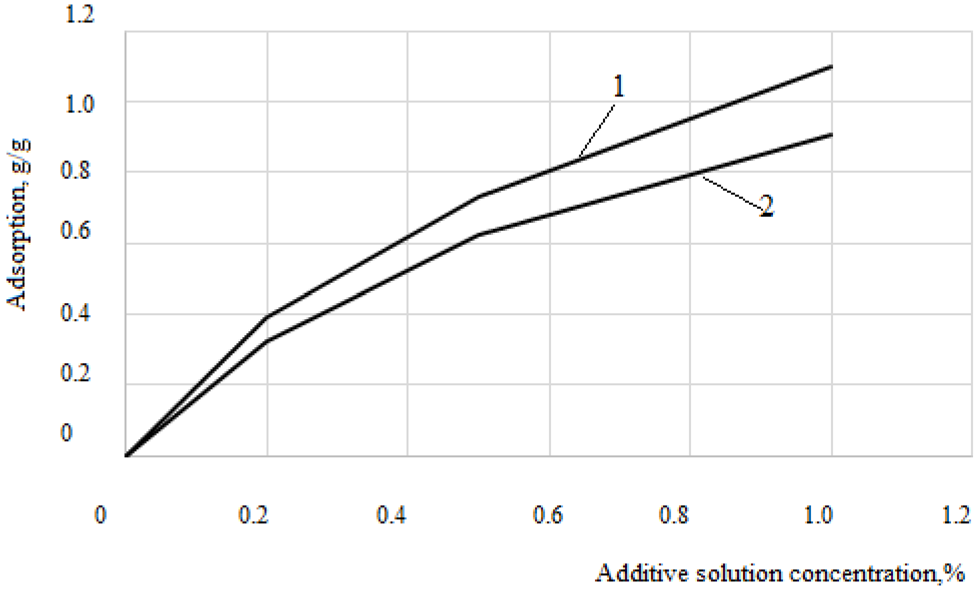

Figure 4.Adsorption of Polysaccharides on Lime Depending on Concentration (AtrenCemHV (1), AtrenCem LV (2))

These results suggest that the theory of monomolecular adsorption can be applied to describe the adsorption of Atren Cem LV and Atren Cem HV on lime surfaces.

The adsorption isotherm (Fig. 5) plotted in coordinates $\frac{1}{a_{\infty}b}.C$ confirmed this relationship, allowing the calculation of the adsorption equilibrium constant b. For Atren Cem LV, b was calculated as $1.18\,{}^{1}/_{\%}$ and for Atren Cem HV, $1.30\ {}^{1}/_{\%}$.

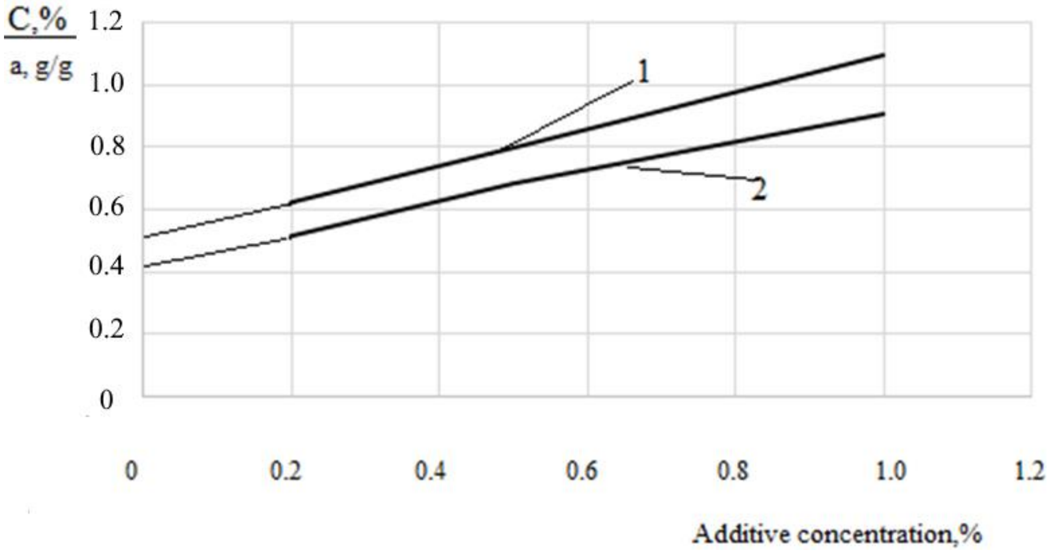

Figure 5. Adsorption Isotherm of Additives in Coordinates $1/a = f(C)$: AtrenCem LV (1); AtrenCemHV (2)

The study further showed that the presence of polysaccharides in the lime composite aids in the carbonization process, leading to a thicker carbonized layer. Figure 6 illustrates this carbonization, which starts from the surface and gradually progresses inward. Samples with AtrenCem LV showed better carbonization, indicated by the lighter coloration and a higher carbonized thickness at 21% humidity.

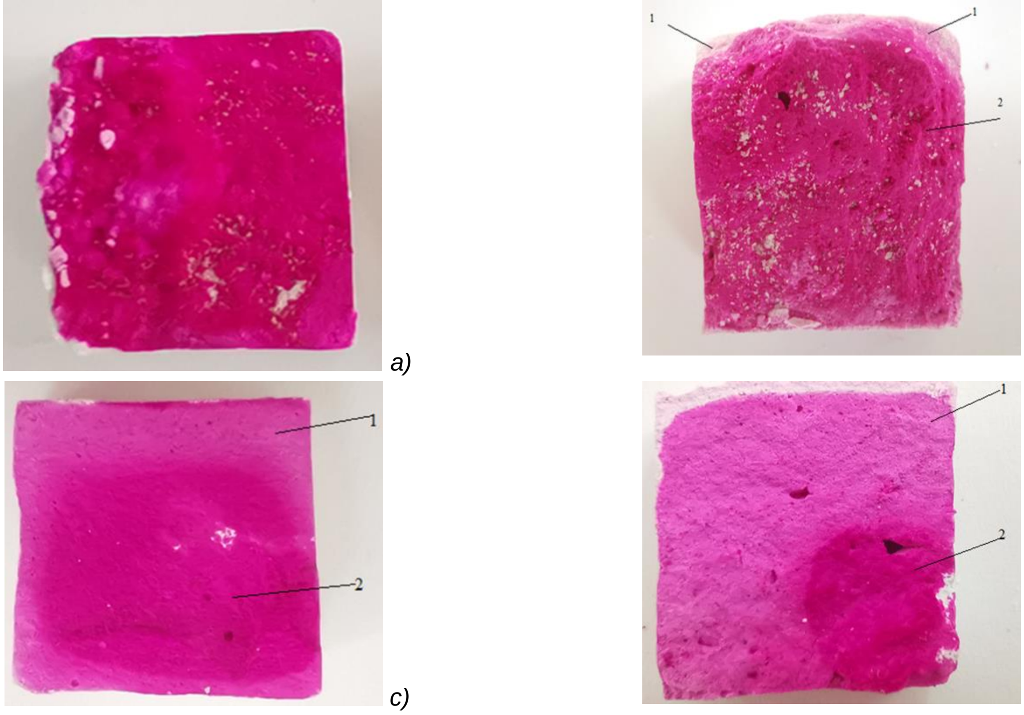

a) *b)* *c)* *d)*

Figure 6.Carbonized Layer Changes in Lime Samples at 4 (a, b) and 10 (c, d) Days: (a, c) Control composition; (b, d) Composition with 1 wt. % AtrenCemLV;1 - the carbonated part is indicated in light color; 2 - the low-carbonated part is indicated in dark color

X-ray diffraction analysis confirmed the increased calcite content in modified samples, with 92.02% calcite in control samples and 96.21% in those with 1% AtrenCemHV (Fig. 7). This increase in calcite content suggests enhanced durability of the modified coatings.

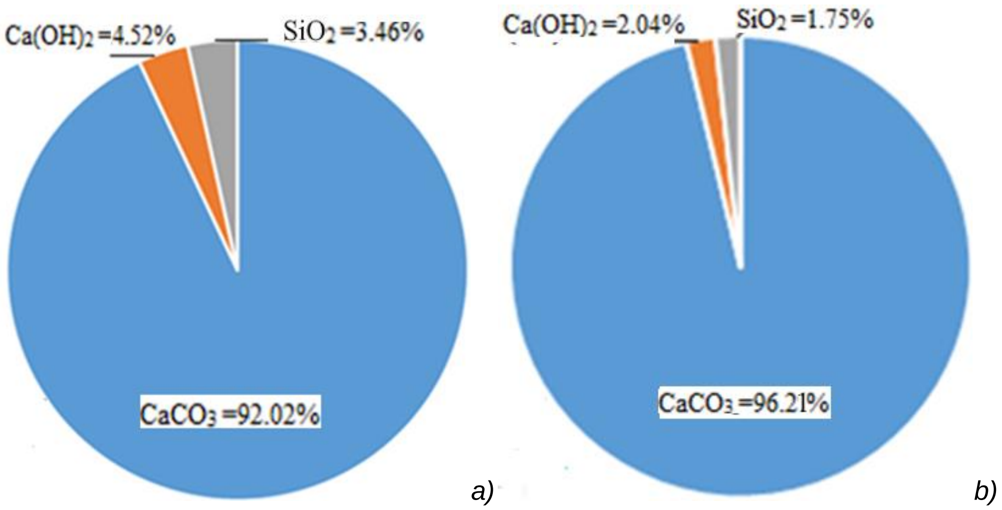

Figure 7.Mineral Content: (a) Control sample (lime) (b) Lime + 1 wt. % AtrenCemHV

The inclusion of organic molecules improves the deformation properties of the coatings. This is evident from the reduced elastic modulus of 0.925 MPa in samples with 1% AtrenCem LV, compared to 0.987 MPa in control samples (Fig. 8).

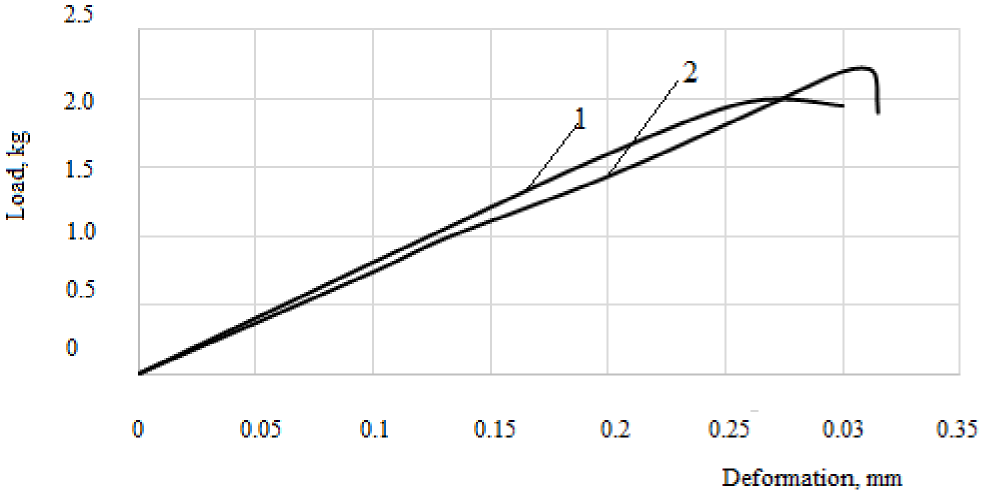

Figure 8.Tensile Deformations of Lime Coatings: (a) Control sample (lime) (b) Lime + 1 wt. % AtrenCemHV

Vickers hardness tests showed a reduction in hardness from 1.890 kgf/mm² in the control composition to 1.448 kgf/mm² with AtrenCem LV, leading to improved crack resistance. These modified lime coatings endured 35 freeze-thaw cycles without notable changes in their appearance.

In terms of resistance to freeze-thaw cycles, Table 2 provides the stress intensity factor (K_1C) and microhardness values after 25 cycles.

Measuring the hardness of coatings using the Vickers method showed that the Vickers hardness of coatings based on the control composition (without polysaccharide additives) is HV = 1.890kgf/mm^2, and that of coatings based on the composition with the addition of AtrenCem LV is 1.448 kgf/mm^2. This ensures higher crack resistance of coatings during operation. Lime coatings containing the AtrenCem LV additive in the formulation withstood 35 cycles of alternating freezing and thawing without significant changes in the quality of appearance.

When assessing the hardness of the coatings and the stress intensity factor after 25 freeze-thaw cycles, it was found that cracks appeared in the control lime coating already at a load of 2 kgf (Table 2).

Table 2. Stress Intensity Factor $K_{1C}$and Microhardness After 25 Freeze-Thaw Cycles

Load, kgf	Stress intensity factorK1C, MPa·m		Average diagonal length of imprint, mm		Average crack length, mm	
	Control sample without additives	Sample with additive Atrencem LV	Control sample without additives	Sample with additive Atrencem LV	Control sample without additives	Sample with additive Atrencem LV
0.5	0.00226	0.0020	0.7	0.8	0	0
1.0	0.002678	0.0027	1.0	0.9	0	0
1.5	0.00299	0.00303	1.2	1.1	0	0
2.0	0.010*	0.00321	1.5	1.3	0.7	0
2.5	-	0.00346	-	1.4	-	0
3.0	-	0.0266*	-	1.5	-	0.4

*Critical value of stress intensity factor K_{1c}.

In coatings with Atren Cem LV, cracks appeared only at a load of 3 kgf, while control samples cracked at 2 kgf. The critical stress intensity factor (K_{1C}) for control samples was 0.010 MPa·m^{½}, compared to 0.0266 MPa·m^{½} for samples with Atren Cem LV, demonstrating significantly improved crack resistance with the additive.

4. CONCLUSIONS

The development of lime compositions with polysaccharide additives for restoring building walls has led to the following key conclusions:

Structural Formation: The inclusion of polysaccharide additives Atren Cem HV and Atren Cem LV in lime composites facilitates the formation of a structure containing inter- and intercrystalline organic molecules. This is due to the adsorption of these additives on the lime surface, which enhances the elastic modulus and hardness of the lime coatings.

Surface Activity: The study confirmed the surface activity of Atren Cem LV and Atren Cem HV polysaccharides in aqueous solutions.

Adsorption Theory Application: It was demonstrated that the theory of monomolecular adsorption is applicable for describing the adsorption behavior of Atren Cem LV and Atren Cem HV on lime. The specific adsorption parameters for these polysaccharide additives were identified.

Acknowledgments

This work was conducted as part of the flagship university development program at Belgorod State Technological University named after V.G. Shukhov, utilizing the facilities of the High Technology Center at BSTU named after V.G. Shukhov.

5. REFERENCES

[1] C.L.S. Blavier, H.E. Huerto-Cardenas, N. Aste, C. Del Pero, F. Leonforte, S. Della Torre(2023) Adaptive measures for preserving heritage buildings in the face of climate change: A review, Build. Environ. 245,110832. https://doi.org/10.1016/j.buildenv.2023.110832.

[2] S. Bianchi, C. Andriotis, T. Klein, M. Overend(2024) Multi-criteria design methods in façade engineering: State-of-the-art and future trends, Build. Environ. 250,111184. https://doi.org/10.1016/j.buildenv.2024.111184.

[3] S.Pescari, L.Budău, C.–B.Vîlceanu(2023) Rehabilitation and restauration of the main façade of historical masonry building –Romanian National Opera Timisoara, Case Stud. Constr. Mater. 18, e01838. https://doi.org/10.1016/j.cscm.2023.e01838.

[4] A.M.Petrov, R.M.Magomedov, S.V. Savina (2023) Ecological Safety of Construction in the Concept of Sustainable Development, Construction Materials and Products. 6 (1), P. 5 – 17. https://doi.org/10.58224/2618-7183-2023-6-1-5-17.

[5] Z. Valančius, R. Vaickelionienė, G. Vaickelionis, P. Makčinskas (2022) Use of an industrial by-product phosphogypsum in the production of white textured paints, J. Clean. Prod. 380, 134888. https://doi.org/10.1016/j.jclepro.2022.134888.

[6] M.Kharun, S.Klyuev, D.Koroteev, P.C. Chiadighikaobi, R.Fediuk, A.Olisov, N.Vatin, N. Alfimova(2020)Heat treatment of basalt fiber reinforced expanded clay concrete with increased strength for cast-in-situ construction, Fibers. https://doi.org/10.3390/fib8110067.

[7] H.R. de C. Veloso Moura, L.G.Pedroti, M.M. Salgado Lopes, J.M. Franco de Carvalho, J.C. Lopes Ribeiro, J.C.Bernardes Dias(2023) Influence of biocide and dispersant additives on the performance and durability of building paints produced with granite waste, Constr. Build. Mater. 409, 134112. https://doi.org/10.1016/j.conbuildmat.2023.134112.

[8] A.V.Klyuev, N.F.Kashapov, S.V.Klyuev, S.V. Zolotareva, N.A. Shchekina, E.S.Shorstova, R.V. Lesovik(2023) Experimental studies of the processes of structure formation ofcomposite mixtures with technogenic mechanoactivated silica component, Construction Materials and Products. 6, 5–18. https://doi.org/10.58224/2618-7183-2023-6-2-5-18.

[9] M.M.S. Lopes, L.G. Pedroti, A.F. de Oliveira, J.C.L. Ribeiro, J.M. Franco de Carvalho, A. Fiorini de Carvalho, F. de P. Cardoso, G.H. Nalon, G.E.S. de Lima(2021) Optimization of performance of

sustainable paints using granite waste through the variation of particle size and pH, J. Clean. Prod. 326, 129418. https://doi.org/10.1016/j.jclepro.2021.129418.

[10] R.S.Fediuk, Y.G. Yevdokimova, A.K.Smoliakov, N.Y.Stoyushko, V.S. Lesovik(2017) Use of geonics scientific positions for designing of building composites for protective (fortification) structures. IOP Conference Series: Materials Science and Engineering. 221(1), 012011. https://doi.org/10.1088/1757-899X/221/1/012011

[11] F. Han, Z. Zhang(2022) Micromechanical properties of 4-year-old composite binder pastes with different mineral admixtures using nanoindentation technique, J. Build. Eng. 61, 105264. https://doi.org/10.1016/j.jobe.2022.105264.

[12] R.S. Fediuk, V.S. Lesovik, A.P. Svintsov, N.A. Gladkova, R.A. Timokhin, et al. (2018) Self-compacting concrete using pretreatmented rice husk ash. Magazine of Civil Engineering. 79(3), pp. 66-76.https://doi.org/10.18720/MCE.79.7

[13] D. Koňáková, V. Pommer, K. Šádková, M. Záleská, M. Böhm, M. Keppert, E. Vejmelková(2024) Heat-resistant composites based on ternary binders with a low cement content: Characterization and performance, Dev. Built Environ. 18, 100400. https://doi.org/10.1016/j.dibe.2024.100400.

[14] S. Klyuev, R. Fediuk, M. Ageeva, E. Fomina, A. Klyuev, E. Shorstova, S. Zolotareva, N. Shchekina, A. Shapovalova, L. Sabitov(2022)Phase formation of mortar using technogenic fibrous materials, Case Stud. Constr. Mater. 16, e01099. https://doi.org/10.1016/j.cscm.2022.e01099.

[15] M.Z.Y. Ting, W. Li, Y. Yi(2023) Two-phase changes in workability of sand-bentonite mixture triggered by seawater and binder during seepage cut-off wall construction in marine environment, Constr. Build. Mater. 401, 132900. https://doi.org/10.1016/j.conbuildmat.2023.132900.

[16] R.Fediuk, R. Timokhin, A. Mochalov, K. Otsokov, I. Lashina (2019) Performance properties of high-density impermeable cementitious paste, Journal of Materials in Civil Engineering. 31(4), 04019013. https://doi.org/10.1061/(ASCE)MT.1943-5533.0002633

[17] J. Krejsová, D. Koňáková, V. Pommer, L. Poláková, R. Černý, J. Maděra, E. Vejmelková(2024) Valorization of waste wood fly ash in environmentally friendly lime-based plasters with enhanced strengths for renovation purposes, J. Build. Eng. 87, 109056. https://doi.org/10.1016/j.jobe.2024.109056.

[18] T.E.S. de Lima, A.R.G. de Azevedo, M.T. Marvila, V.S. Candido, R. Fediuk, S.N. Monteiro (2022) Potential of Using Amazon Natural Fibers to Reinforce Cementitious Composites: A Review Polymers, 14 (3), 647. https://doi.org/10.3390/polym14030647

[19] S. Afzal Basha, A. Vinod Kumar, S. Akhil Tej, C.G. Mohan Babu(2023) Evaluation of zeolite as supplementary cementing material, Mater. Today Proc. https://doi.org/10.1016/j.matpr.2023.02.318.

[20] R.Fediuk, A.Yushin(2016) Composite binders for concrete with reduced permeability, IOP Conf. Ser. Mater. Sci. Eng. https://doi.org/10.1088/1757-899X/116/1/012021.

[21] W.R. Wise, S.J. Davis, W.E. Hendriksen, D.J.A. von Behr, S. Prabakar, Y. Zhang(2023)Zeolites as sustainable alternatives to traditional tanning chemistries, Green Chem. 25,4260–4270. https://doi.org/10.1039/D3GC00381G.

[22] R.S. Fediuk, V.S. Lesovik, A. V. Mochalov, K.A. Otsokov, I. V. Lashina, R.A. Timokhin(2018) Composite binders for concrete of protective structures, Mag. Civ. Eng.. https://doi.org/10.18720/MCE.82.19.

[23] E. Koohsaryan, M. Anbia, M. Maghsoodlu(2020) Application of zeolites as non-phosphate detergent builders: A review, J. Environ. Chem. Eng. 8, 104287. https://doi.org/10.1016/j.jece.2020.104287.

[24] J. Hou, J. Yuan, J. Xu, Y. Fu, C. Meng(2013) Template-free synthesis and characterization of K-phillipsite for use in potassium extraction from seawater, Particuology. 11, 786–788. https://doi.org/10.1016/j.partic.2013.02.003.

[25] H. Luan, Q. Wu, J. Wu, X. Meng, F.-S. Xiao(2024) Templates for the synthesis of zeolites, Chinese J. Struct. Chem. 43, 100252. https://doi.org/10.1016/j.cjsc.2024.100252.

[26] V.I. Loganina, M.V. Frolov, Y.P. Skachkov(2016) Lime composition for the walls of buildings made of aerated concrete, in: Proc. Int. Symp. Mech. Eng. Mater. Sci., Atlantis Press, Paris, France. https://doi.org/10.2991/ismems-16.2016.29.

[27] V. Loganina, I.Pyshkina(2015) Calcareous finishing compounds using fillers on the basis of synthesized hydrosilicates, Bull. South Ural State Univ. Ser. Construction Eng. Archit. 15, 36–39. https://doi.org/10.14529/build150406.

[28] R.S. Fediuk, V.S. Lesovik, Y.L. Liseitsev, R.A. Timokhin, A. V. Bituyev, M.Y. Zaiakhanov, A.V. Mochalov (2019) Composite binders for concretes with improved shock resistance, Mag. Civ. Eng. https://doi.org/10.18720/MCE.85.3.

[29] A. Bakolas, R. Bertoncello, G. Biscontin, A. Glisenti, A. Moropoulou, E. Tondello, E. Zendri(1995) Chemico-Physical Interactions Among the Constituents of Historical Walls in Venice, MRS Proc. 352, 771. https://doi.org/10.1557/PROC-352-771.

[30] A.Bakolas, E.Aggelakopoulou, A. Anagnostopoulou, S.Moropoulou(2006) Evaluation of pozzolanic activity and physico-mechanical characteristics in metakaolin–lime pastes, J. Therm. Anal. Calorim. 84, 157–163.

[31] C.Genestar, C.Pons(2003) Ancient covering plaster mortars from several convents and Islamic and Gothic palaces in Palma de Mallorca (Spain). Analytical characterisation, J. Cult. Herit. 4, 291–298. https://doi.org/10.1016/j.culher.2003.02.001.

[32] E.R.Littmann(1960) Ancient Mesoamerican Mortars, Plasters, and Stuccos: The Use of Bark Extracts in Lime Plasters, Am. Antiq. 25, 593–597. https://doi.org/10.2307/276642.

[33] D.Magaloni, R.Pancella, Y.Fruh, J.CaÑetas, V. CastaÑo(1995) Studies on The Mayan Mortars Technique, MRS Proc. 352, 483. https://doi.org/10.1557/PROC-352-483.

[34] A.S.Balykov, T.A.Nizina, D.B.Chugunov, N.S. Davydova, V.M. Kyashkin (2025) Photocatalysts based on Zn-Ti layered double hydroxide and its calcination products for selfcleaning concretes: Structure formation and photocatalytic activity. Construction Materials andProducts.8 (1), 2. https://doi.org/10.58224/2618-7183-2025-8-1-2

[35] G.V. Nesvetaev, Yu.I. Koryanova, T.A. Khezhev (2025) Heat dissipation of cement and design the composition of concrete for massive structures. Construction Materials and Products. 8 (1), 3. https://doi.org/10.58224/2618-7183-2025-8-1-3

IZVOD

KOMPOZICIJE KREČA SA POLISAHARIDIMA ZA RESTAURACIJU I ZAŠTITU ZIDOVA ZGRADA

Očuvanje istorijskog nasleđa je značajan prioritet u savremenom urbanističkom planiranju. Međutim, poboljšanje trajnosti krečnih premaza koji se koriste u restauraciji lokaliteta kulturne baštine ostaje izazov. Cilj ove studije je da se identifikuje metod za poboljšanje otpornosti na pucanje premaza na bazi kreča korišćenjem polisaharidnih aditiva. Studija ispituje modifikovane polisaharide rastvorljive u vodi AtrenCemHV i AtrenCem LV. Određene su maksimalne vrednosti adsorpcije ovih aditiva na kreču, sa AtrenCemHV na 1,83 g/g i AtrenCem LV na 1,66 g/g. Rezultati ukazuju da adsorpcija polisaharida na površinu čestica kreča Ca(OH)2 dovodi do formiranja kompozitne strukture koja sadrži inter- i interkristalne organske molekule, što poboljšava otpornost premaza na pucanje. Istraživanje takođe pruža uvid u proces karbonizacije krečnih premaza koji sadrže polisaharidne aditive, otkrivajući da ovi aditivi povećavaju debljinu karbonizovanog sloja. Krečne kompozicije sa polisaharidima pokazuju veću kohezionu čvrstoću zbog visokog sadržaja kalcita. Pored toga, formiranje kompozitne strukture sa organskim molekulima doprinosi smanjenju modula elastičnosti i tvrdoće premaza. Krečni premazi sa aditivom AtrenCem LV izdržali su 35 ciklusa smrzavanja i odmrzavanja. Stoga su nova saznanja o sastavima kreča sa aditivima polisaharida ključna za restauraciju zidova zgrada.

Ključne reči: *kreč, polisaharidi; monomolekularna adsorpcija, karbonizacija; otpornost na pucanje, premazi*

Naučni rad
Radprimljen: 24.04.2025.
Rad korigovan: 31.05.2025.
Rad prihvaćen: 04.06.2025.

Valentina Loganina	https://orcid.org/0000-0001-7532-0074
VadimPylaev	https://orcid.org/0009-0005-7761-5606
Roman Fediuk	https://orcid.org/0000-0002-2279-1240
Bassam A. Tayeh	https://orcid.org/0000-0002-2941-3402
Sergey Klyuev	https://orcid.org/0000-0002-1995-6139
Alexander Klyuev	https://orcid.org/0009-0007-0262-5425
Svetlana Shambina	https://orcid.org/0000-0002-9923-176X
German Fediuk	https://orcid.org/0009-0005-4670-0461

---

*Vladimir D. Jović**

University of Belgrade - Institute for Multidisciplinary Research, National Institute of the Republic of Serbia, Belgrade, Serbia

Scientific paper
ISSN 0351-9465, E-ISSN 2466-2585
https://doi.org/10.62638/ZasMat1671

Zastita Materijala 67 (1)
191 – 198 (2026)

Adsorption of iodide anions onto Ag(111)

ABSTRACT

In this work, adsorption process of iodide anions onto Ag(111) wasinvestigated using cyclic voltammetry (CV), Electrochemical Impedance Spectroscopy (EIS) and differential capacitance (C_{diff} vs. ω) measurements. Fitting of experimental results was performed by using commercial program for fitting defined by Gamry Instruments Inc. in EIS 300 software, as well as by equation for C_{diff} vs. ω dependence defined in previous investigations for anion adsorption, containing Constant Phase Element – corresponding to the double layer capacitance (CPE_{dl}) connected in parallel with adsorption capacitance (C_{ad}) and adsorption resistance (R_{ad}). Although the C_{diff} vs. ωdependences were obtained from the EIS measurements, significant difference in parameters for anion adsorption obtained by both procedures indicated that the analysis of C_{diff} vs. ω dependence is more reliable.

***Keywords**:Ag(111), iodideadsorption, adsorption mechanism, EIS, C_{diff} vs. ω dependence.*

1. INTRODUCTION

Iodide anions adsorption/desorption processes on silver single crystal surfaces have been investigated by C_{diff} vs. E, CV and surface analytical techniques [1-8].CVs were characterized by the presence of a broad peak at more negative potentials and a sharp peak at less negative potentials, with a broad peakcorresponding to the formation of randomly distributed ad-layer at potentials negative of –0.8 V vs. Ag/AgCl and its transformation into a $(\sqrt{3}x\sqrt{3})R30^{o}$ ordered structure between –0.8 and –0.4 V vs. Ag/AgCl and a sharp peak detected at potentials slightly positive of –0.4 V vs. Ag/AgCl corresponding to compression of $(\sqrt{3}x\sqrt{3})R30^{o}$structure into (8 x 8) iodide structure[1,2].

*In situ*STM and *ex situ* LEED studies of Yamada etal.[3] confirmed continuous compression of the iodide ad-lattice from square$(\sqrt{3}x\sqrt{3})R\text{-}30^{o}$, via $(\sqrt{3}qR\beta^{o}x\sqrt{3}R–30^{o})$ ($q \approx 1$, $0 \leq \beta \leq 30$), to $(\sqrt{3}$ x $\sqrt{3})R30$atpotentials between -1.2 V and -0.8 V. Atpotentials more positive than sharp peak $(\sqrt{3}$ x $\sqrt{3})R(30^{o}+\alpha^{o})$ has been detected [3].

Although the structure of the adsorbed iodide ad-layers has been extensively studied, practically no attempt was made to analyze the mechanism of iodide adsorption and define the equivalent circuit for such process. In previous works [9-12] chloride and bromide anions adsorption onto Ag single crystals, as well as hydroxide anions adsorption onto Cu single crystals has been analyzed by predicting equivalent circuit for anion adsorption. Equivalent circuit was composed of C_{dl} connected in parallel with C_{ad} and R_{ct}[9,10], as well as of CPE_{dl} connected in parallel with C_{ad} and R_{ad} [11,12]. It has been shown that such equivalent circuits could be used for fitting experimental results by the analysis of C_{diff} vs. ω dependences.

1.1. Differential capacitance for different cases of anion adsorption

C_{diff} vs. Edependences were introduced in electrochemistry with the beginning of double layer structure investigations as a suitable technique for determining the double layer capacitance (C_{dl}) on both, liquid (mercury) and solid metal electrodes [13,14]. This technique was very convenient for determining the potential of zero charge, E_{pzc} on solid electrodes as a minimum on C_{diff} vs. E curves [13-15]. Since the minimum existed only in the presence of a diffuse part of the double layer [16,17], these experiments were performed in dilute

---

*Corresponding author:Vladimir D. Jović

E-mail:vladajovic@imsi.bg.ac.rs

Paper received: 01. 12. 2025.

Paper accepted: 25. 12. 2025.

solutions of the concentrations lower than 10^{-2} M, usually of the order of 10^{-3} M [18,19]. In all these experiments ohmic resistance had to be compensated in order to obtain the real value of C_{dl}. In such a case the value of C_{diff} was equal to the value of C_{dl} and was independent of frequency. Accordingly measurement at one frequency was sufficient to determine the value of the double layer capacitance.

With introduction of single crystal surfaces, this technique in combination with CV, has frequently been used for determining E_{pzc} as well as adsorption behavior of different anions. Typical frequencies for these measurements varied between 10 Hz and 20 Hz [19], while the sweep rate used was usually 5 - 10 mV s^{-1}. For interpretation of the obtained results concerning adsorption of anions it was assumed that the “specific adsorption” of anions does not involve the charge transfer between the electrode surface and adsorbed anions.

About 25 years ago the equivalent circuit composed of C_{dl} connected in parallel with the charge transfer resistance (R_{ct}) and C_{ad} was used for the first time for the analysis of adsorption of fluoride, sulfate, acetate and chloride anions onto silver single crystals[9,10]. The same equivalent circuit, with adsorption resistance (R_{ad}) instead of R_{ct} has later been used for the analysis of OH^- species adsorption onto Cu(111) from fluoride or sulfate containing solutions of different pH [20].

Z. Kerner et al. [21] demonstrated that the frequency dependence of capacitance on solid electrodes was due to the atomic scale inhomogeneities rather than due to the geometry aspect of roughness. They criticized old physical theories used for explaining capacitance dispersion as a function of surface roughness [22,23] and pointed out physico-chemical approach of T. Pajkossy [24,25], claiming that the origin of the capacitance dispersion can be allocated in the double layer and that it can be attributed to the presence of atomic scale inhomogeneities – “disorder” of the electrode surface, together with the presence of some kinetic process, most probably with the “specific adsorption” of anions [21].

Introduction of *in situ* techniques (STM and surface X-ray scattering) in the investigation of the structure of adsorbed anions onto single crystal faces provided significant contribution to the understanding of the process of anion adsorption [26-30], showing that in the case of chloride and bromide anions adsorption onto Au single crystals incommensurate, hexagonal-close-packed monolayers, compressing uniformly with increasing potential were formed [29-31]. The ad-atom spacing of these compressed structures was found to approach van der Waals diameter, indicating at least partial discharge of anions [29-31]. *In situ* X-ray absorption fine structure (XAFS) studies of bromide adsorption onto Ag(111) revealed the formation of AgBr(111) monolayer with the Br-Ag bond distance of 2.72±0.05 Å, indicating complete charge transfer between bromide anions and Ag(111) surface [32].

In this paper the dependence of C_{diff} vs. ω for different cases of simple and complex anion adsorption processes for ideal, homogeneous and “real surfaces” (introducing *CPE* instead of C_{dl} [33-35]) have been analyzed. Two cases were considered: 1) double layer capacitance represented by a parallel plate condenser (assuming ideal, homogeneous surface) and 2) double layer capacitance represented by a *CPE* (assuming nonhomogeneous charge distribution at the surface).

1.2. Ideal, homogeneous surface

Equivalent circuit for ideal double layer behavior of the electrode impedance is presented by ohmic resistance $R_\Omega$and double layer capacitance C_{dl} connected in series. Differential capacitance is by definition imaginary component of electrode admittance over frequency and for such equivalent circuit is given by the equation:

$$C_{diff} = \frac{Y''}{\omega} = \frac{C_{dl}}{1+\omega^2 C_{dl}^2 R_\Omega^2} \tag{1}$$

In most cases $1 >> \omega^2 C_{dl}^2 R_\Omega^2$ and accordingly $C_{diff} \approx C_{dl}$. On the other hand in dilute solutions with high value of R_Ω the value of C_{diff} could be influenced by the R_Ω, as shown in equation (1). Hence, imaginary component of electrode admittance should be corrected for $R_\Omega$in order to obtain the real value of C_{dl}. This could be done either by compensating R_Ω during differential capacitance measurements (using IR compensation technique on the potentiostat), or by subtracting it from the real component of electrode impedance, $Z'_{corr} = Z' - R_\Omega$ and calculating Y''_{corr} by following equation (R_Ω - determined from the high frequency intercept of impedance diagrams, or by some other technique):

$$Y'' = \frac{Z''}{(Z'_{corr})^2 + (Z'')^2} \tag{2}$$

Hence, by using Y''_{corr} for determining C_{diff} ($Y''_{corr}/\omega = C_{diff}$) it is possible to obtain the real value of differential capacitance.

In the presence of specific adsorptionre presented by the R_{ad} and C_{ad} connected in series, C_{diff}(corrected for R_{Ω}) should depend on frequency [9-12]. The simplest case of specific adsorptionat "real electrode surface" is usually represented by the equivalent circuit shown in Figure 1, where the R_{ad} and C_{ad} connected in series are placed in parallel with the CPE_{dl}(representing double layer capacitance of "real electrode surface".

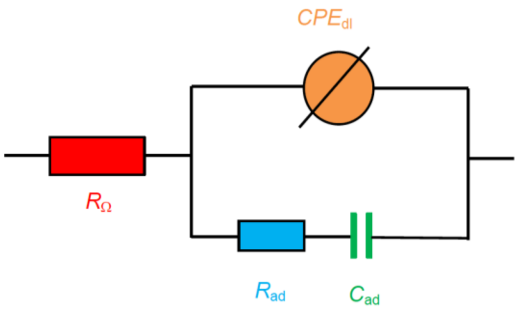

Figure 1. Equivalent circuit for anion adsorption

1.3. Real surface

Taking into account that even single crystal faces contain significant number of monoatomic terraces and cannot be considered as ideal (homogeneous) surface, introduction of *CPE* defined as $CPE = Z_{dl}(j\omega)^{-\alpha}$ [33-35] is mandatory.

For the case of simple anion adsorption, presented by the equivalent circuit shown in Figure 1, differential capacitance as a function of frequency (using the definition given in equation (2)) is defined by the following equation:

$$C_{diff} = C_{dl}\omega^{\alpha-1}\sin\left(\frac{\alpha\pi}{2}\right) + \frac{C_{ad}}{1+\omega^2 C_{ad}{}^2 R_{ad}{}^2} \qquad (3)$$

Hence, by plotting C_{diff} vs. ω dependences obtained for constant potential from EIS measurements it is possible to fit these dependences by the equation (3) and obtain the values of C_{dl}, α, R_{ad} and C_{ad}.

It is also possible to obtain these parameters by fitting EIS measurements with the commercial software, either by using Bode diagrams, or Z' vs. ω and $-Z''$ vs. ω dependences.

2. EXPERIMENTAL

All experiments were carried out in a two–compartment electrochemical cell at 25 ±1 °C. The single crystal electrode (Monocrystals Company, d = 0.9 cm) was sealed in epoxy resin in such a way that only the (111)disc surface was exposed to the solution. The surface area of the electrode exposed to the electrolyte was 0.636 cm^2. The counter electrode (CE) was a Pt sheet and was placed parallel to the working electrode. The reference electrode (RE) was a saturated silver chloride electrode (Ag/AgCl).The RE was placed in a separate compartment and connected to the working compartment by means of a Luggin capillary. Solution of 0.1 M NaI was made from supra pure (99.999% – Aldrich) chemicals and extra pure UV water (Smart2PureUV, TKA).

The single crystals were prepared by a mechanical polishing procedure followed by chemical polishing in the solution containing NaCN and H_2O_2 as explained in previous paper [36]. Before each experiment, the electrolyte was purged with high purity nitrogen (99.999%) for 45 min., while a nitrogen atmosphere was maintained over the solution during the experiment to prevent contamination with oxygen.

All experiments were performed using potentiostat Reference 600(PHE 200 and EIS 300 software -Gamry Instruments Inc.). EIS measurements were performed at constant potentials, in the frequencies range from 5000 Hz to 10 Hz, with the RMS amplitude of 10 mV and 10 points per decade.

3. RESULTS AND DISCUSSION

3.1. Iodide adsorption/desorption in 0.1 M NaI

CVs recorded at the sweep rates of 100 mV s^{-1}and 50 mV s^{-1}in 0.1 M NaIare presented in Figure 2. The process of iodide adsorption/desorption is characterized by one pear of broad peaks, composed of several small, sharp peaks in the negative potential region (from ~ –0.8 to ~ –1.2 V) [37] and one pear of sharp peaks at less negative potentials (around –0.36 V). The sudden increase of cathodic current density corresponding to the hydrogen evolution wasrecorded immediately after the cathodic limit on the presented CVs.

Byintegrating the total surface under the cathodic and anodic parts of the CVs shown in Figure2 corresponding chargeswere obtained,with the maximum anodic charge (Q_a) of ~ 90 μC cm^{-2} and the maximum cathodic charge(Q_c) of ~ 97 μC cm^{-2}. Taking into account that the theoretical charge (assuming complete charge transfer) for the (√3 x √3)R30°iodide ad-layeramounts to 74 μCcm^{-2}, it appeared that this ad-layer is formed under the broad peak [1-8,37].

3.2. The use of commercial program for fitting the EIS results

In order to obtain data for the mechanism of iodide anions adsorption EIS measurements were performed at constant potentials in the range of potentials presented in Figure 2.

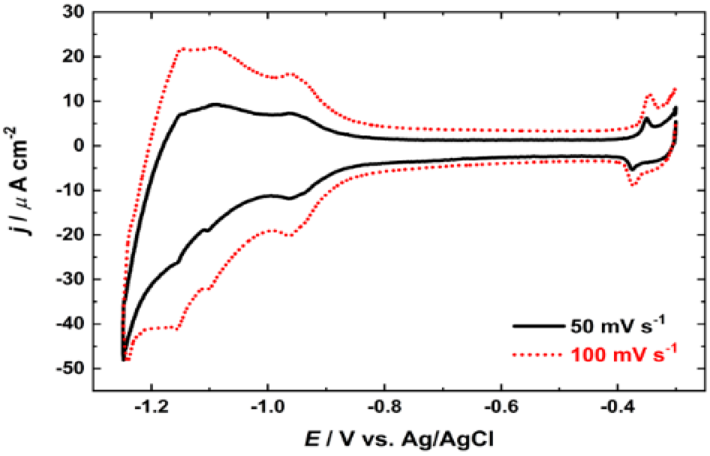

Figure 2. CVs recorded at 100 mV s^{-1} and 50 mV s^{-1} for the process of adsorption/desorption of iodide anions onto Ag(111) in 0.1 M NaI

Since there are three different regions, measurements in the region of broad peak (between -0.9 V and -1.2 V) were taken at 50 mV difference, in the double layer region (between -0.8 V and -0.4 V) at 100 mV difference, while in the region of sharp peak (between -0.4 V and -0.32 V) at 20 mV difference. Since Z' vs. ω and $-Z''$ vs. ω dependences were necessary for calculating C_{diff} (equation (2)) these dependences were plotted and fitted. Typical examples of Z' vs. ω and $-Z''$ vs. ω dependences fitted with the commercial program, recorded in the region of broad (E = -1.0 V) and the region of the flat portion of the CV (just before a sharp peak, E= -0.4 V), are presented in Figure 3. Fitting lines are seen not to deviate from experimental points, indicating precise fitting procedure.

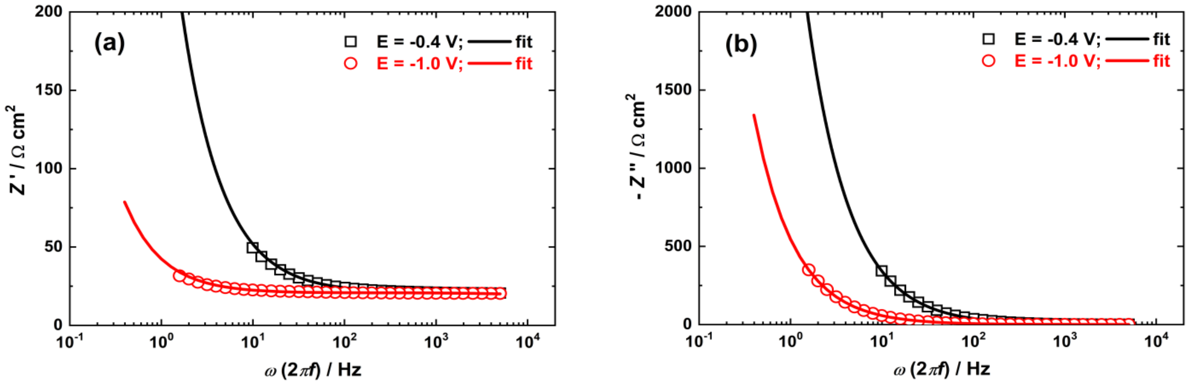

Figure 3. Z' vs. ω (a) and -Z'' vs. ω (b) dependences fitted with the commercial program, recorded in the different potential regions of the CV

Unfortunately, one result could not be fitted (EIS at E = -1.2 V) with the commercial program, actually some of the parameter values for C_{dl}, α, C_{ad} and R_{ad} were unrealistic. The results for C_{dl} vs. E, C_{ad} vs. E and R_{ad}vs. Eobtained by fitting procedure are presented in Figure 4(a,b,c) respectively. It is obvious that, although fitting procedure gave high precision (in all cases so called “goodness of fit” was lower than 1 x 10^{-4} corresponding to the deviation lower than 1 %), obtained results seem to be unrealistic.Generally, extremely high values for C_{ad} and R_{ad} at potentials more negative than -0.8 V are unexpected. Concerning R_{ad} it should be stated that this resistance represents a sum of two resistances: R_{ad}^{mt} – corresponding to the adsorption of anions at the edge of monoatomic terraces and defects on the surface and R_{ad}^{os} - corresponding to the adsorption of anions at the flat part of monoatomic terraces, representing adsorption resistance for the formation of ordered structures. Unfortunately, these two resistances cannot be separated and determined independently, at least not by using equivalent circuit shown in Figure 1. With the use of different equivalent circuit, as shown in Ref. [38], it is possible to separate and determine these two resistances, but the problem arises in the physical meaning of such equivalent circuit.

The value of α was found to vary between 0.8 and 0.9.

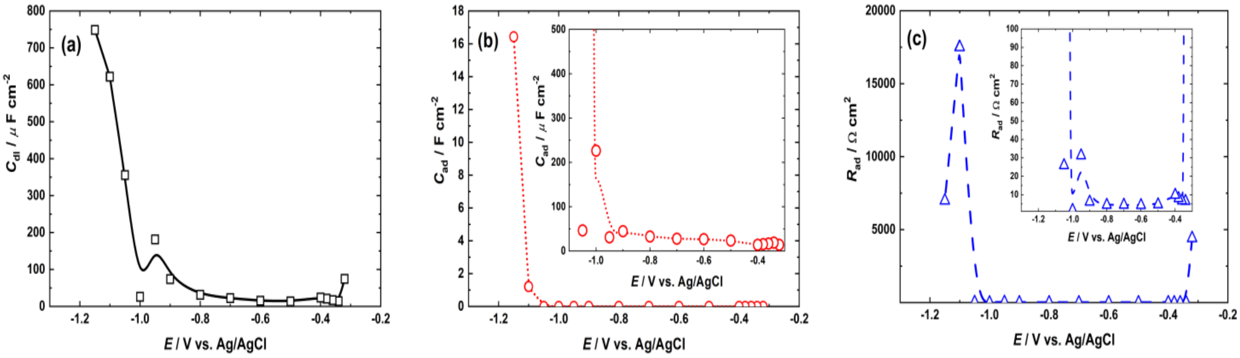

Figure 4. (a) C_{dl} vs. E, (b) C_{ad} vs. E and (c) R_{ad} vs. E dependences obtained by using commercial program for fitting experimental results. In the inset of (b) and (c) are presented C_{ad} vs. E and R_{ad} vs. E dependences at higher sensitivities of C_{ad} and R_{ad}

3.3. The use of equation (3) for fitting C_{diff} vs. ω dependences

As already stated Z' vs. ω and $-Z''$ vs. ω dependences for each applied potential were used to calculate C_{diff} vs. ω dependences. Obtained C_{diff} vs. ω dependences were plotted and fitted by equation (3) using non-linear curve fitting in Origin program. Experimental points and fitted curves for each applied potential are presented in Figure 5. As can be seen all fits are excellent. The values of parameters C_{dl}, C_{ad} and R_{ad} obtained by fitting procedure are presented in Figure 6(a,b).

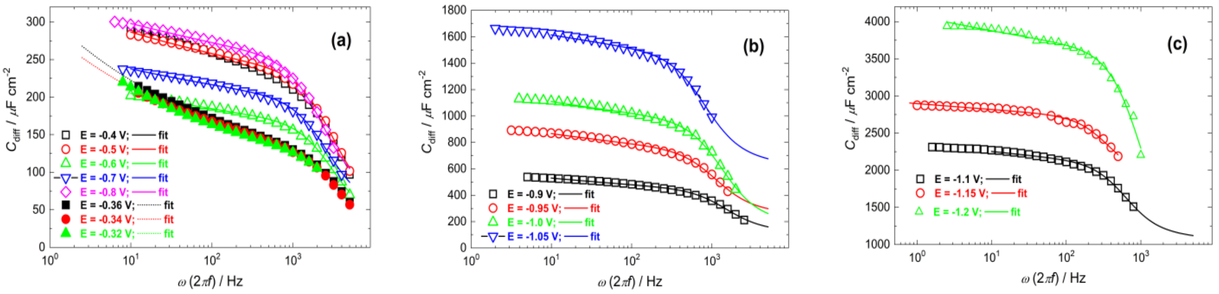

Figure 5. C_{diff} vs. ω dependences recorded for each applied potential (designated in the figure) are presented with points, while fitting results are presented with lines.

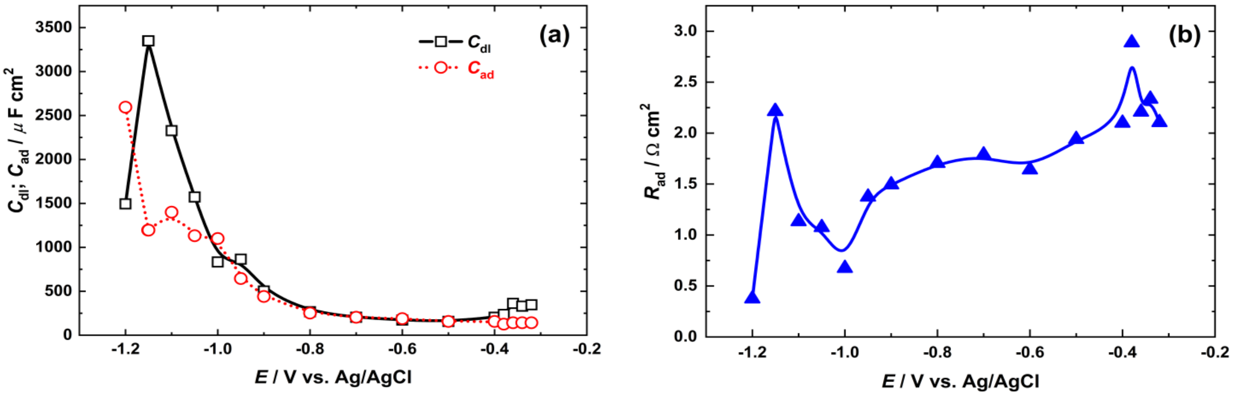

Figure 6. (a) C_{dl} vs. E, C_{ad} vs. E and (b) R_{ad} vs. E dependences obtained by fitting C_{diff} vs. ω dependences

Presented results seem more realistic, being in accordance with the CVs. The values of $C_{dl}$and C_{ad} are quite high in the region of iodide adsorption, while in the region of final phase transformation [37] (between -0.4 V and -0.32 V) C_{ad} is practically constant indicating that there is no additional adsorption of iodide anions during the final phase transformation (compression of (√3 x √3)R30 structure into (8 x 8) iodide structure[1,2]).

It should be stated that although commercial fits are precise, the values of $R_{ad}$and C_{ad} are practically quite insensitive to a fitting procedure. This software is giving fitted results and possible error in their determination. One, actually the worse example, of the table with fitting results is presented in Table 1. Goodness of fit of 16.08e^{-6} is quite satisfactory, but the errors for $R_{ad}$and C_{ad} are unacceptable.

Table 1. Probably the worse example for presented results in commercial fitting program

Parameter	Value	± Error	Dimensions
R_s	31.00	1.186	ohm
Y_{dl}	34.06e^{-6}	12.79e^{-6}	*S*s^α*
α_{dl}	939.8e^{-3}	36.47e^{-3}	
C_{ad}	20.77e^{-6}	13.78e^{-6}	*F*
R_{ad}	6.965	5.404	ohm
Goodness of Fit	16.08e^{-6}		
-0.8V.DTA			

Another factor that could influence the precision of fitting with the commercial program might be the number of points, actually the range of frequencies used for the EIS measurements. Frequencies from 5000 Hz to 10 Hz are satisfactory for C_{diff} vs. ω dependences, but it seems that for fitting with the commercial program it is necessary to extend the frequency range from 100 kHz to 0.01 Hz and probably extend the number of points per decade to 20?

With a present knowledge of fitting procedure in the commercial EIS 300 software it is not possible to make any reasonable explanation for the difference in the fitting results, but it could be stated that the use of equation (3) for fitting C_{diff} vs. ω dependences is much more realistic.

4. CONCLUSIONS

The CVs of the process of iodide anions adsorption onto Ag(111) are characterized by three potential regions: from -1.2 V to -0.8 V (broad peaks) adsorption/desorption of randomly distributed iodide anions with a formation of ordered structure (√3 x √3)R30° at about -0.8 V; double layer region from -0.8 V to -0.4 V (flat CVs); further compression of (√3 x √3)R30° into (8 x 8) ad-layer of iodide expressed by the sharp peaks between -0.4 V and -0.32 V.

Extremely high values ofC_{dl} and C_{ad} in the region of adsorption/desorption peaks, their constant values in the double layer region and constant value of C_{ad} in the region of phase transformation (compression into (8 x 8) iodide ad-layer) are in accordance with the CVs.

Finally, it was shown that fitting of C_{diff} vs. ω dependences using equation (3) produces more realistic results for C_{dl} vs. *E,* C_{ad} vs. *E* and R_{ad} vs. *E*dependences than the use of commercial fitting procedure.

5. REFERENCES

[1] M.L.Foresti, G. Aloisi, M. Innocenti, H. Kobayashi, R. Guidelli (1995) Crystal face effects on adsorption of ionic and non-ionic species on Ag electrodes: an electrochemical and STM study, Surf. Sci. 335-241. https://doi.org/10.1016/0039-6028(95)00423-8

[2] K.J. Stevenson, X.Gao, D.W. Hatchett, H.S. White (1998)Voltammetric measurement of anion adsorption on Ag(111), J. Electroanal. Chem. 447, 43-51. https://doi.org/10.1016/S0022-0728(98)00021-7

[3] T. Yamada, K. Ogaki, S. Okubo, K. Itaya(1996) Continuous variation of iodine adlattices on Ag(111) electrodes: in situ STM and ex situ LEED studies, Surf. Sci. 369, 321-335. https://doi.org/10.1016/S0039-6028(96)00880-1

[4] G.N. Salaita, F. Lu, L. Laguren-Davison, A.T. Hubbard (1987) Structure and composition of the Ag (111) surface as a function of electrode potential in aqueous halide solutions, J. Electroanal. Chem. 229, 1-17. https://doi.org/10.1016/0022-0728(87)85127-6

[5] J.H. Schott, H.S. White, (1994) Halogen adlayers on silver (111), J. Phys. Chem. 98, 291-297. https://doi.org/10.1021/j100052a049

[6] J.H. Schott, H.S. White (1994) Tunneling spectroscopy of halogen adlayers on silver (111) surfaces,J. Phys. Chem. 98 297-302. https://doi.org/10.1021/j100052a050

[7] J.H. Schott, H.S. White (1994) Halogen chemisorption on silver(111). Scanning tunneling microscopy of coadsorbed halogen atoms, Langmuir 10, 486-491. https://doi.org/10.1021/la00014a024

[8] M. Kawasaki, H. Ishii (1995) Preparation and Surface Characterization of Ag(111) Film Covered with Halide Monolayer,Langmuir 11, 832-841. https://doi.org/10.1021/la00003a026

[9] V.D. Jović, B.M. Jović, R. Parsons(1990) Acetate adsorption on the (111) oriented silver single crystal surface,J. Electroanal. Chem. 290, 251-262. https://doi.org/10.1016/0022-0728(92)80461-C

[10] V.D. Jović, R. Parsons, B.M. Jović (1992) Anion absorption on the (111) face of silver, J. Electroanal. Chem. 339, 327-337. https://doi.org/10.1016/0022-0728(92)80461-C

[11] V.D. Jović, B.M. Jović (2003) EIS and differential capacitance measurements onto single crystal faces in different solutions. Part I - Ag(111) in 0.01MNaCl, J. Electroanal. Chem. 541, 1-11. https://doi.org/10.1016/S0022-0728(02)01309-8

[12] V.D. Jović, B.M. Jović (2003) EIS and differential capacitance measurements onto single crystal faces in different solutions. Part II - Cu(111) and Cu(100) in 0.1MNaOH, J. Electroanal. Chem. 541, 13-21.https://doi.org/10.1016/S0022-0728(02)01310-4

[13] D.C. Grahame (1954) Differential Capacity of Mercury in Aqueous Sodium Fluoride Solutions. I. Effect of Concentration at 25°, J. Am. Chem. Soc. 76, 4819-4823.https://doi.org/10.1021/ja01648a014

[14] R. Reeves, The Double Layer in the Absence of Specific Adsorption,in: J. O'M. Bockris,B.E. Conway, E. Yeager(Eds.), Comprehensive Treatise of Electrochemistry, vol. 1, Plenum, New York and London, 1980, Chapter 3, pp. 83.134.

[15] G. Vallete (1989) Double layer on silver single crystal electrodes in contact with electrolytes having anions which are slightly specifically adsorbed: Part III. The (111) face, J. Electroanal. Chem. 269, 191-203. https://doi.org/10.1016/0022-0728(89)80112-3

[16] G. Valette, A. Hamelin (1973) Structure et propriétés de la couche double électrochimique à l'interphase argent/solutions aqueuses de fluorure de sodium, J. Electroanal. Chem. 45, 301-319. https://doi.org/10.1016/S0022-0728(73)80166-4

[17] G.H. Bolt (1955) Analysis of the validity of the Gouy-Chapman theory of the electric double layer, J. Coll. Sci. 10, 206-218. https://doi.org/10.1016/0095-8522(55)90027-1

[18] G. Valette (1982) Double layer on silver single crystal electrodes in contact with electrolytes having anions which are slightly specifically adsorbed: Part II. The (100) face,J. Electroanal. Chem. 138, 37-54. https://doi.org/10.1016/0022-0728(82)87126-X`

[19] A. Hamelin, Double-layer properties at *sp*and *sd*metal single-crystal electrodes, in: B. E. Conway, J. O'M. Bockris, R. White (Eds.), Modern Aspects of Electrochemistry, vol. 16, Plenum, New York, 1985, Chapter 1.

[20] S.Härtinger, K.Doblhofer(1995) The electrochemical interface between copper(111) and aqueous electrolytes,J. Electroanal. Chem. 380, 185-191. https://doi.org/10.1016/0022-0728(94)03650-R

[21] Z. Kerner,T.Pajkossy (2000) On the origin of capacitance dispersion of rough electrodes, Electrochim. Acta 46, 207-211. https://doi.org/10.1016/S0013-4686(00)00574-0

[22] R. de Levi, Electrochemical response of porous and rough electrodes, in: P. Delaney, Ch. W. Tobias (Eds.), Advances in Electrochemical Engineering, vol. 6, Wiley, New York, 1967.

[23] M. Sluyters-Rehbach, J. Sluyters, in A. Bard (ed.), Electroanalytical Chemistry, vol. 4, Marcel Dekker, New York, 1970, pp. 75-80.

[24] T. Pajkossy, T. Wandlowski, D.M. Kolb (1996) Impedance aspects of anion adsorption on gold single crystal electrodes,J. Electroanal. Chem. 414, 209-220. https://doi.org/10.1016/0022-0728(96)04700-6

[25] T. Pajkossy (1994) Impedance of rough capacitive electrodes, J. Electroanal. Chem. 364, 111-125. https://doi.org/10.1016/0022-0728(93)02949-I

[26] G.Aloisi, A.M.Funtikov, T.Will (1994) Chloride adsorption on Ag(111) studied by in-situ scanning tunnelling microscopy, J. Electroanal. Chem. 370, 297-300.https://doi.org/10.1016/0022-0728(93)03140-K

[27] O. Magnussen, B.M. Ocko, R.R. Adžić, J.X. Wang (1995) X-ray diffraction studies of ordered chloride and bromide monolayers at the Au(111)-solution interface, Phys. Rev. B 51, 5510-5518. https://doi.org/10.1103/PhysRevB.51.5510

[28] O. Magnussen, B.M. Ocko, J.X. Wang, R.R. Adžić (1996) In-Situ X-ray Diffraction and STM Studies of Bromide Adsorption on Au(111) Electrodes, J. Phys. Chem. B 100, 5500-5508. https://doi.org/10.1021/jp953281j

[29] J.X. Wang, R.R. Adžić, B.M. Ocko, In Situ X-ray Scattering Studies of Electrosorption, in: A. Wieckowski (Ed.), Interfacial Electrochemistry: Accomplishments and Challenges, Marcel Dekker Inc., New York, 1999, pp. 175-185.

[30] Th. Wandlowski, J.X. Wang, B.M. Ocko (2001) Adsorption of bromide at the Ag(100) electrode surface, J. Electroanal. Chem. 500, 418–434. https://doi.org/10.1016/S0022-0728(00)00380-6

[31] Z. Shi, J. Lipkowski (1996) Chloride adsorption at the Au(111) electrode surface, J. Electroanal. Chem. 403, 225-239. https://doi.org/10.1016/0022-0728(95)04313-6

[32] O. Endo, D. Matsumura, K. Kohdate, M. Kiguchi, T. Yokoyama, T. Ohta (2000) In-situ XAFS studies of Br adsorption on the silver(111) electrode, J. Electroanal. Chem. 494, 121-126. https://doi.org/10.1016/S0022-0728(00)00338-7

[33] J.R. Macdonald, Impedance Spectroscopy Emphasizing Solid Materials and Systems, Wiley, New York, Chichester, Brisbane, Toronto, Singapore, 1987.

[34] G.J.Brug, A.L.G.Van Den Eedem, M.Sluyters-Rechbach, J.H.Sluyters (1984) The analysis of electrode impedances complicated by the presence of a constant phase element, J. Electroanal. Chem. 176, 275-295. https://doi.org/10.1016/S0022-0728(84)80324-1

[35] C.H.Hsu, F.Mansfeld (2001) Technical Note: Concerning the Conversion of the Constant Phase Element Parameter Y0 into a Capacitance, Corr. 57, 747-748. doi:10.5006/1.3280607

[36] J.N. Jovićević, V.D. Jović, A.R. Despić (1984) The influence of adsorbing substances on thelead upd onto (111) oriented silver single crystal surface-I,Electrochim. Acta 29, 1625-1638. https://doi.org/10.1016/0013-4686(84)89002-7

[37] V.D. Jović, B.M. Jović(2011) Processes of adsorption/desorption of iodides and cadmium cations onto/from Ag(111), J. Serb. Chem. Soc. 76, 283–303. doi:10.2298/JSC100701026J

[38] V.D. Jović (2009) Differential Capacity of Bromide Anions Adsorption onto Ag(100) in the Absence, and onto Ag(poly) in the Presence of $NaClO_4$, Chem. Biochem. Eng. Q.23, 1–12. https://doi.org/10.15255/CABEQ.2014.319

IZVOD

ADSORPCIJA ANJONA JODIDA NA Ag(111)

U ovom radu, proces adsorpcije jodidnih anjona na Ag(111) je ispitan korišćenjem ciklične voltametrije (CV), elektrohemijske impedansne spektroskopije (EIS) i merenja diferencijalnog kapaciteta (Cdiff vs. ω). Fitovanje eksperimentalnih rezultata je izvršeno korišćenjem komercijalnog programa za fitovanje definisanog od strane Gamry Instruments Inc. u EIS 300 softveru, kao i jednačinom za zavisnost Cdiff vs. ω definisanu u prethodnim istraživanjima za adsorpciju anjona, koja sadrži element konstantne faze – koji odgovara dvoslojnom kapacitetu (CPEdl) povezanom paralelno sa adsorpcionim kapacitetom (Cad) i adsorpcionim otporom (Rad). Iako su zavisnosti Cdiff vs. ω dobijene iz EIS merenja, značajna razlika u parametrima za adsorpciju anjona dobijenim oba postupka ukazala je da je analiza zavisnosti Cdiff vs. ω pouzdanija.
Ključne reči: *Ag(111), adsorpcija jodida, mehanizam adsorpcije, EIS, zavisnost Cdiff vs. ω.*

Naučni rad
Rad primljen: 01.12.2025.
Rad prihvaćen: 15.12.2025.

UPUTSTVO ZA PRIPREMU RADA

Radi ujednačavanja izgleda radova, koji se objavljuju u časopisu ***Zaštita materijala*****,** autori se moraju pridržavati uputstva za pripremu radova. Rukopisi u kojima ova uputstva nisu poštovana biće odbijeni bez recenzije. Urednik zadržava pravo da formatiranje rada uskladi sa standardima časopisa. Tekst rukopisa treba da bude u jednoj koloni, a formatiranje teksta što jednostavnije, zato što će se veći deo formatiranja prilikom obrade rukopisa ukloniti i zameniti. Treba, međutim, koristiti podebljana slova (*bold*), kurziv (*italic*), superskripte, subskripte itd. Za obradu teksta treba koristiti program MS Word, format .doc, font Arial sa proredom 1,5. Na stranicama formata A4 margine treba da budu: gornja i donja 3 cm, leva i desna 2,2 cm. Treba numerisati sve redove i sve strane rukopisa.

Kompletan rukopis treba da sadrži: naslov, izvod (apstrakt, na srpskom i engleskom jeziku), ključne reči (na srpskom i engleskom jeziku), uvod, eksperimentalni deo, rezultate, diskusiju, zaključak, reference, tabele i slike. Pozicije slika i tabela treba obeležiti u tekstu (slike i tabele ne treba inkorporirati u datoteku koja sadrži rukopis; oni se dostavljau kao posebne datoteke u odgovarajućim formatima). Nazivi slika ispisuju se ispod slika, a nazivi tabela iznad tabela. Na kraju rukopisa iza slika i tabela, na posebnoj strani treba dati spisak naziva slika i tabela po redu navođena u manuskriptu. **Nazivi slika i tabela daju se na srpskom i engleskom jeziku.**

Kako bi se izbegle nepotrebne gramatičke i pravopisne greške, autorima radova napisanih na engleskom jeziku savetujemo da prilikom pisanja koriste funkcije "spell-check" i "grammar-check".

Naslov treba da bude jasan sam po sebi i ne preterano dugačak (ne više od 15 reči, Arial *bold*, velika slova veličine 14). Puno ime autora (ime i prezime – Arial *bold-italic*, veličina slova 12) navodi se ispod naslova. Afilijacija i kompletna poštanska adresa autora navode se odmah ispod punog imena autora (Arial, *italic*, veličina slova 11). Kada rad ima više od jednog autora, svako ime treba obeležiti arapskom cifrom u superskriptu, a autora za korespondenciju treba obeležiti zvezdicom (*) iznad imena. Takođe, puno ime i e-mail adresu autora za korespodenciju treba napisati u fusnoti na prvoj stranici rukopisa.

Izvod, ne bi trebalo da bude duži od 250 reči (10–15 redova; Arial, *italic*, veličina slova 11) i trebalo bi da sadrži kratak pregled metoda i najvažnije rezultate rada, tako da se može koristiti prilikom indeksiranja u referentnim periodičnim publikacijama i bazama podataka. U izvodu ne treba navoditi reference.

Ključne reči (pojmovi, geografske lokacije, rezultati; Arial, *italic*, veličina slova 11) se navode u posebnom redu na kraju izvoda. Ključne reči moraju biti relevantne za temu i sadržaj rada. Dobar izbor ključnih reči preduslov je za ispravno indeksiranje rada u referentnim periodičnim publikacijama i bazama podataka.

NAPOMENA: Ukoliko je rad napisan na srpskom jeziku onda naslov rada, izvod i ključne reči trebalo bi prevesti na engleski jezik i dodati tekstu iza spiska referenci.

Uvod (Arial, veličina slova 12) treba da sadrži ciljeve rada i kratak pregled relevantnih prethodnih istraživanja, izbegavajući pri tom detaljan pregled literature i rezultata.

Eksperimentalni deo (Arial, veličina slova 12) trebalo bi da sadrži dovoljno detalja da bi se obezbedila reproducibilnost eksperimenata. Metode koje su opisane u već objavljenim publikacijama ne treba opisivati u radu, već samo treba navesti relevantne reference i opisati one elemente koji se razlikuje u odnosu na objavljene metode i postupke.

Rezultati i diskusija (Arial, veličina slova 12) ne bi trebalo da sadrže ono što se već nalazi u tabelama i na slikama. Rezultati bi trebalo da budu jasni i koncizni. Diskusija treba da objasni značaj rezultata istraživanja, a ne da ih ponavlja ili opisuje. Treba izbegavati detaljno navođenje objavljene literature i raspravu o istoj.

Zaključak (Arial, veličina slova 12) treba da sadrži samo pregled osnovnih naučnih doprinosa rada. Treba predstaviti samo glavne zaključke do kojih se došlo na osnovu rezultata. U zaključku ne treba navoditi reference.

Formule, simboli i skraćenice. Formule bi trebalo kucati kurzivom (preporučujemo Equation Editor of Microsoft Office 2003) i trebalo bi da budu navedene i obeležene u samom rukopisu, osim ako ne zahtevaju neko posebno formatiranje. Formule treba numerisati sa desne strane, između zagrada:

$$a^3 = 3M / 4N \qquad (1)$$

Pozivanje na jednačinu/jednačine u tekstu: (jed. 1) ili jednačine (1-4) itd.

Složenije hemijske formule trebalo bi prikazati kao slike.

Skraćenice treba definisati prilikom prvog pominjanja u izvodu i u glavnom delu teksta; treba ih navoditi dosledno, uvek na isti način, od početka do kraja teksta.

Tabele i ilustracije treba suštinski da doprinesu boljem razumevanju i tumačenju rezultata rada. Slike, crteži i druge ilustracije treba da budu jasni i dobrog kvaliteta.

Ilustracije moraju biti u jednom od sledećih formata:

•TIFF (ili JPEG): u boji ili sivim tonovima (polutonovima), od minimum 300 dpi.

•TIFF (ili JPEG): crno-beli linearni crteži, od minimum 1000 dpi.

•TIFF (ili JPEG): kombinacije linearnih crteža i površina u boji, odnosno sivim tonovima (polutonovima), od minimum 500 dpi.

Molimo vas ne činite:

• uz rukopis dostavljati ilustracije optimizovane za korišćenje na ekranu (npr, GIF, BMP, Pict, WPG); one obično imaju nisku rezoluciju i mali raspon boja;

• dostavljati ilustracije koje imaju rezolucije manje od gore navedenih;

• dostavljati ilustracije nesrazmerno velikih dimenzija u odnosu na format rukopisa.

Legende za tabele i slike treba dostaviti uz rukopis, ali ih ne treba inkorporirati u tekst. Slike treba označiti kao "Sl." (Sl. 1) i numerisati arapskim brojevima prema redosledu kojim su navedene u tekstu. Mesta za tabele i slike treba jasno naznačiti u rukopisu. Nazivi slika ispisuju se ispod slika, a tabela iznad tabela. Na kraju rukopisa iza slika i tabela, na posebnoj strani treba dati spisak naziva slika i tabela po redu navođena u manuskriptu, na oba jezika - srpskom i engleskom.

Zahvalnica/Acknowledgements treba da se nalazi u posebnom odeljku na kraju članka, a ispred spiska referenci.

Reference. Spisak referenci, navedenih na jeziku na kom su objavljene, treba da sadrži **samo** radove koji su citirani u tekstu. Citirani radovi navode se u listi referenci po redosledu citiranja u tekstu. U tekstu se broj reference navodi u uglastim zagradama, [ ]. Kod radova koji su prihvaćeni za objavljivanje ali još uvek nisu dobili paginaciju treba staviti napomenu „u štampi“ ili „in press“.

Primeri navođenja referenci su dati u nastavku:

Navođenje radova: [1] I.Ilić, M.Sokić, N.Vučković, V.Matković (2005) Electrochemical process of obtaining glucose**,** Tehnika, 56(3), 9-14.

Ostali časopisi i novine: [1] S. Petrović, Washington Post, 4 Okt. 2005, p. 6

Navođenje knjige: [1] M.Jaić, R.Živanović-Trbojević (2000) Wood finishing, Technical Press, Belgrade.

Citiranje knjiga na CD-ROM i DVD: [1] M.Petrović (2002) Opšta hemija [CD-ROM]; Nolit, Beograd.

[2] G.Jakšić (2002) Analitička hemija [DVD]; Nolit, Beograd.

Čapter u knjizi: [1] M. Stojanovic, Č.Lačnjevac, Z.Lopičić (2012) Corrosion and Corrosion Behavior of depleted uranium, knjiga Corrosion and Protection of Materials, Izdavač ITNMS, Belgrade, pp 223-281.

Navođenje simpozijuma/skupa: [1] M.Petrović, M.Stojanović, M.Mihajlović (2013) 16. YUCORR, Tara, Serbia, proceedings, p.235-242.

[2] M.Pavić, K.Stojanović, M.Mihić (2013) 16. CORR, Beograd, Serbija [CD-ROM];

Doktorske teze: [1] S. Petrović, Modelovanje transporta zagađujućih materija u aluvijalnim sedimentima reke Dunav, doktorska teza, Univerzitet u Novom Sadu, jun 2011.

Patenti: [1] **P.**Wait (1989), Device for Elementary Analyses. USA Patent, No. *123456*.

Tekst sa Web site: [1] M.Arslanagić, S.Kandic - Maglajlić (2011) Manual for the source of scientific papers (http://www.efsa.unsa.ba/ef/docs/handbooks/ manual_economic_web.pdf, 01.12.2013.)

[2] Međunarodna unija za čistu i primenjenu hemiju*, http://www.iupac.org/dhtml_home.html (24 April 2005).*

Proverite da li su sve reference navedene u tekstu navedene i u spisku referenci (i obrnuto).

NAPOMENA:

- **Recenzija i objavljivanje radova su besplatni.**
- **Autorima će PDF datoteka koja sadrži njihov prihvaćeni rad biti poslata besplatno, elektronskom poštom. Štampana verzija sveske u kojoj se nalazi prihvaćeni rad besplatno će biti dostavljena autoru za korespondenciju.**
- **Elektronska verzija rada biće dostupna na internet stranici časopisa, www.idk.org.rs/casopis, i može se koristiti u skladu sa uslovima licence Creative Commons Attribution 4.0 International license (https://creativecommons.org/licenses/by/4.0/)**

UREĐIVAČKI ODBOR
Časopis ZAŠTITA MATERIJALA

MANUSCRIPT PREPARATION

Authors must follow the instructions for authors strictly, failing which the manuscripts would be rejected without review. Editor reserves the right to adjust the formatting style to conform to the standards of the journal. The text layout should be in single-column format. Keep the layout of the text as simple as possible. Most formatting codes will be removed and replaced on processing the manuscript. However, do use bold face, italics, subscripts, superscripts etc. The manuscript should be written in Microsoft Word format.doc, font Arial with 1.5 spacing. On the pages of the manuscript size A4 margins should be: top and bottom 3 cm, left and right 2.2 cm. Add the line numbering and page numbers.

The complete manuscript should contain the title, abstract, keywords, introduction, experimental part, results, discussion, conclusion, references, drawings, tables and pictures. Mark the position of figures and tables in the text. Each figure must have a title below the figure and each table must have a title above the table. Figure and table captions should be listed at the end of the manuscript.

To avoid unnecessary errors, it is strongly advised to use the "spell-check" and "grammar-check" functions of your word processor.

Title should be clear, not too long but explanatory (no more than 15 words; Arial bold, all caps, 14 points). The full name(s) of the author(s) (first name, then last name, in Arial bold 12 points) should be written below the title. The affiliation(s) and complete postal address(es) of the author(s) should be provided immediately after the full name of the authors and written with Arial 11 points. When the paper has more than one author, their names should be followed by a mark (Arabic numeral) as superscript; for the corresponding author, an asterisk symbol should be added using *Word_Insert_Reference_Footnote_Symbol* sequence. Also, the full and e-mail addresses of the corresponding author should be provided in the footer of the first page.

Abstract, not exceeding 250 words (10-15 lines), written in Arial, 11 points, italic, should contain a short review of the method and the most important results of work, so that its original text can be used in referential periodicals and databases. Do not include citations in the Abstract.

Keywords (concepts, locations, results) written with Arial 11 points, italic, are listed in a separate line at the end of the abstract. Keywords should be relevant to the topic and content of the paper. An accurate list of keywords will ensure correct indexing of the paper in referential periodicals and databases.

Introduction, written in Arial, 12 points, should include the objectives of the work and provide an adequate background, avoiding a detailed literature survey or a summary of the results.

Experimental, written in Arial, 12 points – provide sufficient detail to allow the work to be reproduced. Methods already published should be indicated by a reference: only relevant modifications should be described.

Results and Discussion written in Arial, 12 points, should not contain what has been already explained by tables and figures. Results should be clear and concise. Discussion should explore the significance of the results of the work, not repeat them. Avoid extensive citations and discussion of published literature.

Conclusion written in Arial 12 points should contain only essential contributions made to science. The main conclusions drawn from results should be presented. Do not include citations in this section.

Formulae, symbols and abbreviations. Formulae will be typeset in Italics (preferably with the Equation Editor of Microsoft Office 2003) and should be written or marked as such in the manuscript, unless they require a different styling. The formulae should be numbered on the right side, between brackets:

$$a^3 = 3M / 4N \qquad (1)$$

Always refer in the text to the Equations as (Eq. 1), Eqs. (1-4) etc. Complex Chemical Formulae should be presented as Figures.

Abbreviations should be defined when first mentioned in the abstract and in the main body of the text and ensure consistency of abbreviations throughout the article.

Tables and figures should essentially contribute to better understanding and interpretation of the results. Photos, drawings and other illustrations should be clear and of good quality. The acceptable image formats include:

- TIFF (or JPEG): Color or grayscale photographs (halftones), keep to a minimum of 300 dpi.

- TIFF (or JPEG): Bitmapped (pure black & white pixels) line drawings, keep to a minimum of 1000 dpi.TIFF (or JPEG): Combinations bitmapped line/half-tone (color or grayscale), keep to a minimum of 500 dpi.

Please do not:

• Supply files that are optimized for screen use (e.g., GIF, BMP, PICT, WPG); these typically have a low number of pixels and limited set of colors;

• Supply files that are too low in resolution;

• Submit graphics that are disproportionately large for the content.

Table and Figure titles, should accompany the manuscript and **should not be inserted** in the text. **Illustrations** should be labeled "**Fig.**", **(Fig.1),** and numbered consecutively in Arabic numerals in the order in which they are referred to in the text.

Places for tables and figures should be clearly indicated in the manuscript.

Each figure must have a title below the figure and each table must have a title above the table. Figure and table captions should be listed at the end of the manuscript.

Acknowledgements. Include acknowledgements in a separate section at the end of the article before the references.

References. The list of References should only include works that are cited in the text. References are listed in the order in which they appear in the text. Citation in the text is done by specifying the number of references in square brackets, in the original language. Papers which have been accepted for publication should be included in the list of references with the name of the journal and the specification "in press".

Examples of citations are given below:

Journal papers: [1] I.Ilić, M.Sokić, N.Vučković, V.Matković (2005) Electrochemical process of obtaining glucose**,** Tehnika, 56(3), 9-14.

Nonscientific Journals and Newspapers: [1] S. Petrović, The Washington Post,Oct 4, 2005, p. 6

Books: [1] M.Jaić, R.Živanović-Trbojević (2000) Wood finishing, Technical Press, Belgrade.

Chapter in the Books: [1] M.Stojanovic, C.Lacnjevac, Z.Lopičic (2012) Corrosion and Corrosion Behavior of depleted uranium, book Corrosion and Protection of Materials, ITNMS, Belgrade, pp 223-281.

Recommended formats for CD-ROM and DVD books:

[1] M.Petrović (2002) General Chemistry [CD-ROM]; Nolit, Belgrade.

[2] G.Jakšić (2002) Analitical Chemistry [DVD]; Nolit, Belgrade.

Symposium/Congress: [1] M.Petrović, M.Stojanović, M.Mihajlović (2013) 16. YUCORR, Tara, Serbia, proceedings, p.235-242.

[2] M.Pavić, K.Stojanović, M.Mihić (2013) 16. CORR, Belgrade, Serbia [CD-ROM];

Patents: [1] **P.**Wait (1989), Device for Elementary Analyses. USA Patent, No. *123456*.

Text from the Web site: [1] M.Arslanagić, S.Kandic - Maglajlić (2011) Manual for the source of scientific papers (http://www.efsa.unsa.ba/ef/docs/handbooks /manual_economic_web.pdf, 01.12.2013.)

[2] International Union of Pure and Applied Chemistry, *http://www.iupac.org/dhtml_home.html* (April 24, 2005).

Please ensure that every reference cited in the text is also present in the reference list (and vice versa).

NOTE:

- **Review and publications are free of charge.**
- **The authors will be provided with a .pdf file containing the paper, via e-mail, free of charge. A hard copy of the journal issue is sent to the corresponding author for free.**
- Copies of papers available on the website of the journal can be used in accordance with the **Creative Commons Attribution 4.0 Internationa license (https://creativecommons.org/licenses/by/4.0/)**

EDITORIAL BOARD
MATERIAL PROTECTION

EcoMet Reciklaža DOO
Loznica

JOVANA CVIJIĆA 11
https://ecomet.rs